XXIX INTERNATIONAL SYMPOSIUM ON

MODERN TECHNOLOGIES, EDUCATION AND PROFESSIONAL PRACTICE

IN GEODESY AND RELATED FIELDS

CONFERENCE PROCEEDINGS BOOK

05 – 06 NOVEMBER 2019

ISTANBUL - TURKEY

© Copyright 2019, The Organizing Committee of the the XXIX International Symposium on
“Modern Technologies, Education and Professional Practice in Geodesy and Related Fields”

XXIX INTERNATIONAL SYMPOSIUM ON MODERN TECHNOLOGIES, EDUCATION AND PROFESSIONAL PRACTICE IN GEODESY AND RELATED FIELDS

CONFERENCE PROCEEDINGS BOOK

05 – 06 NOVEMBER 2019
ISTANBUL -TURKEY

The electronic version of this booklet can be found at
http://www.gravity.itu.edu.tr/symp2019/

Organizers

ITU Geomatics Engineering Department (ITU - GE)

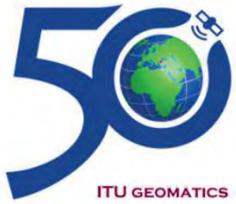

https://www.geomatik.itu.edu.tr/

Union of Surveyors and Land Managers in Bulgaria (USLMB)

http://www.geodesy-union.org/

ITU Gravity Research Group (ITU - GRG)

http://www.gravity.itu.edu.tr/

Istanbul Technical University (ITU)

http://www.itu.edu.tr/

Editorial

Dear Colleagues,

XXIX International Symposium on “Modern Technologies, Education and Professional Practice in Geodesy and Related Fields” has been successfully organized as ITU-USLMB joint symposium in İstanbul, Turkey and held by Istanbul Technical University (ITU), Geomatics Engineering Department on November 5-6, 2019. In this year’s meeting, we had 107 participants with 67 oral and poster presentations with contribution of the authors from eleven different countries including Bulgaria, Russia, Iran, China, United States, Poland, Italy, Syria, Maldives, Brunei and Turkey. The presentations and discussions in the ten oral sessions constituted a scientific and multidisciplinary platform for the participating colleagues for exchanging knowledge and experiences on the relevant fields of Geodesy. In the sessions, while the visionary content of the keynote speeches described the modern face of the geodesy, the presentations on the case studies showed us how the Geodesy meets the evolving and changing needs of the today’s society. As a tradition of USLMB symposia, this year’s meeting scheduled two young researchers’ session as well in order to enable the active participation of the young colleagues. The 31 of the presented studies are included as full texts in this proceedings book and provided for further reading of interested colleagues.

We are proud to hold the XXIX International Symposium on “Modern Technologies, Education and Professional Practice in Geodesy and Related Fields” in 2019 at Istanbul Technical University that we are also celebrating the 70th year of the Geodetic Education in Turkey, and the 50th year of that at Istanbul Technical University.

As symposium organizing committee, we appreciate the valuable contributions of the participants, and acknowledge Istanbul Technical University at first and all the sponsor companies for their support in organization.

Yours Sincerely,

Istanbul
December 2019

Assoc. Prof. Dr. Bihter EROL
Symposium Organizing
Committee Chair

Foreword

Dear Participants,

The 29th International Symposium - "MODERN TECHNOLOGIES, EDUCATION AND PROFESSIONAL PRACTICE IN GEODESY AND RELATED FIELDS" was held in Istanbul on 05-06 November 2019 in Turkey.

The symposium is being implemented in accordance with the recommendations of the International Symposium "Modern technologies, education and professional practice in geodesy and related fields", held in Sofia on 08-09 November 2018.

Modern methods and technologies, education and professional practice are inextricably linked and are a prerequisite for the development of modern society. In many areas they are developing at an extremely rapid rate. In this regard, a good example is geodesy and related fields, such as photogrammetry, cartography, satellite systems - methods and technologies, spatial planning, cadastre, geodynamics, geographic information systems, engineering and natural sciences, and many others. Modern methods and geospatial technologies offer rich possibilities for acquisition, storing, processing and efficient use of various and especially spatial information - geospatial information. It finds multilateral applications in various fields of science and practice and offers exceptional, potential opportunities for new ones. This, together with social development, necessitates the need to keep professionals constantly informed about the current state of these problems and their development trends, as well as their diverse, in many ways, interdisciplinary application.

The papers that have been submitted and received are relatively large in number, totaling 67 and covering virtually all of the main issues raised by the symposium.

The program is in line with the stated main problems raised for the symposium.

The present symposium continues the established tradition of the Union of Surveyors and Land Managers in Bulgaria to organize an International Symposium every year on particularly topical issues, approved by a corresponding resolution of the previous symposium. This is a 29th symposium successfully organized by Turkish colleagues, with assistance from Bulgaria.

Thanking the organizers and co-organizers sponsors and participants, we wish this successful event to become a tradition.

Yours Sincerely,

Prof. Dr. Eng. Georgi Milev
Honorary President of USLMB

Dr. Ivan Kaltchev
President of USLMB

Committees

COMMITTEE OF USLMB SYMPOSIA

Prof. Dr. Georgi Milev, BAS, USLMB
Assoc. Prof. Dr. Asparuch Kamburov, USLMB
Dr. Ivan Kaltchev, USLMB
Ivanka Koleva, USLMB

ORGANIZING COMMITTEE

Assoc. Prof. Dr. Bihter Erol (Chair)
Assist. Prof. Dr. Serdar Bilgi (Co-Chair)
Prof. Dr. Dursun Zafer Şeker
Prof. Dr. Mustafa Yanalak
Prof. Dr. Reha Metin Alkan
Prof. Dr. Şinasi Kaya
Assoc. Prof. Dr. Serdar Erol
Lec. Dr. Ufuk Özerman

LOCAL SECRETARIES

Res. Assist. M. Serkan Işık
Res. Assist. Alper Kuçak
Res. Assist. Volkan Özbey
Res. Assist. M. Raşit Çevikalp

SCIENTIFIC AND ADVISORY COMMITTEE

Prof.Dr. Bülent Bayram, Turkey
Prof.Dr. Cengizhan İpbüker, Turkey
Prof.Dr. Elif Sertel, Turkey
Prof.Dr. Georgi Milev, Bulgaria
Prof.Dr. Georgi Valev, Bulgaria
Prof.Dr. H. Hakan Denli, Turkey
Prof.Dr. Haluk Özener, Turkey
Prof.Dr. Hande Demirel, Turkey
Prof.Dr. Ilias Tziavos, Greece
Prof.Dr. Jadu Dash, UK
Prof.Dr. Jon Mills, UK
Prof.Dr. Keranka Vassileva, Bulgaria
Prof.Dr. Michael G. Sideris, Canada
Prof.Dr. Murat Yakar, Turkey
Prof.Dr. Nebiye Musaoğlu, Turkey
Prof.Dr. Rahmi Nurhan Çelik, Turkey
Prof.Dr. Şenol Hakan Kutoğlu, Turkey
Prof.Dr. Uğur Doğan, Turkey
Prof.Dr. Uğur Şanlı, Turkey
Assoc.Prof.Dr. Arzu Erener, Turkey
Assoc.Prof.Dr. Aslı Garagon Doğru, Turkey
Assoc.Prof.Dr. Bahattin Erdogan, Turkey
Assoc.Prof.Dr. Claudia Tocho, Argentina
Assoc.Prof.Dr. Emine Tanır, Turkey
Assoc.Prof.Dr. Füsun Balık Şanlı, Turkey
Assoc.Prof.Dr. George Vergos, Greece
Assoc.Prof.Dr. Hakan Yavaşoğlu, Turkey
Assoc.Prof.Dr. Himmet Karaman, Turkey
Assoc.Prof.Dr. İbrahim Tiryakioğlu, Turkey
Assoc.Prof.Dr. M. Tevfik Özlüdemir, Turkey
Assoc.Prof.Dr. Mohammad A. Sharifi, Iran
Assoc.Prof.Dr. Mohamed Elhabiby, Egypt
Assoc.Prof.Dr. Özgün Akçay, Turkey
Assoc.Prof.Dr. R. Cüneyt Erenoğlu, Turkey
Assoc.Prof.Dr. Ramazan Alpay Abbak, Turkey
Assoc.Prof.Dr. Todor Kostadinov, Bulgaria
Assoc.Prof.Dr. Vassilis Gikas, Greece
Assoc.Prof.Dr. Wouter van der Wal, Netherlands
Assoc.Prof.Dr. Zaide Duran, Turkey
Assist.Prof.Dr. Balaji Devaraju, India
Assist.Prof.Dr. Uğur Algancı, Turkey
Dr. Ivan Kaltchev, Bulgaria
Dr. Jean-Yves Pirlot, Belgium
Dr. Matthias Weigelt, Germany
Dr. Rossen S. Grebenitcharsky, Saudi Arabia

Content

Content

PROCEEDINGS

Archaeoseismology of the North Black Sea - Bulgaria-Russia expeditions

Boyko Ranguelov[1*]Orlin Dimitrov[2], Andrey Korzhenkov[3], Evgeny Rogozhin[3]
Alexandr Ovsyuchenko[3]

[1] Mining and Geology University, Geophysics Department 1700 Sofia, Bulgaria
Phone: +359 2 8060 436, E-mail: branguelov@gmail.com

[2] Institute of Oceanology "Fr.Nansen" Bulgarian Academy of Sciences, Varna, Bulgaria
Phone: +359 2 8060 436, E-mail: ovdimitrov@gmail.com

[3] Schmidt's Institute of the Physics of the Earth – RAS, Moscow, Russia
Phone: +7 (916) 226-90-92, E-mail: korzhenkov@ifz.ru

ABSTRACT

Significant number of expeditions to the Bulgarian and Russian costal areas has been performed during the last years in the frame of the bilateral scientific cooperation (common projects, unified methodologies, integrated complex geological and geophysical investigations, etc.). The main aim of these expeditions was to reveal the relationships between the seismic effects on the archaeological objects, (discovered and excavated) and the influence of the strong earthquakes occurred in ancient and historical times in depth, when they exist or not and to present the areas where such dependencies are adequate. Such approach is newly performed and is targeted to the increased completeness to the earthquakes catalogues, data about secondary effects (such like tsunamis, landslides, turbidities, etc.). The only source of similar information up to now was the written documents by different chroniclers. The massive measurements in situ, visual documentation, comparative studies, timing and destructions, damages or other effects to the ancient structures can help drastically to fulfill the missing data into the earthquakes catalogue time series. The combination between archeological findings and artifacts, surface and deeper active faults, geophysical characteristics of the local and regional seismic sources are these fundamentals which help the discovery and deeper archaeoseismology investigations and understanding. The results obtained are targeted to the new seismic zoning procedures, which do not consider up to now this significant source of information – the archaeoseismology.

KEYWORDS: Archaeoseismology, new data; complex investigations

1. INTRODUCTION

There are a lot of studies related to the northern Bulgarian Black Sea coast earthquakes. [1], [2] Ranguelov, Gospodinov, 1994; Ranguelov, 1996; Ranguelov, 2011; Ranguelov, 2013, etc.] The seismogenic area Shabla-Kaliakra is the main source of the strongest earthquakes occurred during the historical times. Several events with the magnitude 7 and above occurred in this area creating a lot of destructions, victims and many secondary effects accompanying such high energy seismic events – Table 1.

Table 1. Earthquakes in Shabla-Kaliakra seismic zone with M>5 since ancient times to the present days (according to the Balkan Catalogue, 1972 with some new data and modifications)

Year	Month/Day	Time	Lat(E)	Long(N)	Depth	M
46-45 c. BC			(43,5?)	(28,3?)	20(?)	7.6 (?)
3rd c.BC			43,4	28,4	20	7,0
543			43,5	28,3	20	7,6
1444	XI		43,2	28,1	20	7,5
1832			43,4	28,7	14	6,5
1858	I / 8	01:15	43,4	28,7	20	5,2
1869	I / 10		43,6	28,7		6,5
1901	III /31	7:10:24	43,4	28,6	14	7,2
1901	III /31	11:30	43,6	28,8	25	5,0
2009	VIII/5	7:49:27	43,38	28,77	8	5,0

Despite the relatively well documented catalogue data about the local seismicity, a lot of unknown and not proved facts exist, especially related to the ancient seismic events. This area is famous with the development of multihazard natural disasters such like earthquakes, landslides, tsunamis, floods, storm surges etc., frequently generating each other and thus creating so called domino effects [3], [4]. Because of its location on the Black Sea shore the area was inhabited since very ancient times. Due to this a lot of historical descriptions exist about different hazardous events observed since a long time ago. Such situation combined with the earthquake source located in the aquatory of the sea creates still a lot of interest especially among the specialists in seismology, geodynamics, geomorphology, seismostratigraphy and archaeology. Same situation was expressed for the Russian part of the Black Sea - Kerch and especially Taman peninsula.

2. MATERIAL AND METHOD

To combine the seismological investigations with the archaeology, the previously developed methodology was used [5, 6]

The methodology in this study was limited due to the specifics of:

- Earthquake source location in the sea

- The multihazards chains of disastrous events (earthquakes, landslides, water level changes, tsunamis, surge storms, etc.) frequently affected the ancient inhabited areas [7], [8].

- Archaeological excavations and disclosures of the preserved sediments, destructions and disturbances limited in space and time, and frequently a lack of finances for extended arhaeoseismology research when necessary.

- Removal of the deposits during the excavations, which almost always eliminated all signs of disaster affection to the historical and archaeological sites.

According to the developed archaeoseismological studies before, the following methodology was applied in depths to support both studies – in Russia and in Bulgaria:

- Data collection by filed observations, measurements, documentation, interpretation and seismic intensity assessment

- Seismic sources formalization, based on known past earthquakes and seismic zoning.

- New interpretation of the seismic source formalization.

- Use of the referent seismic event (M7.2 31st March, 1901) relatively well documented with an extended macroseismic map – fig 4, good description of the effects of this strong event (secondary effects generated by it – subsidence, rockfalls, landslides, tsunami, etc.- and their influence to the environment) to create the calibration curve – intensity vs. distance [4].

- Creation of the calibration curve itself, considering the sea location of the epicenter, the azimuth distribution of the intensities, intensity attenuation, destructions and disturbances, etc.

- Selection of the most affected part of the coastal area with the investigated objects.

3. RESULTS AND DISCUSSION

The following archaeological sites have been visited, observations made and interpretations done according to the described methodology:

3.1. Russia

Several national and international expeditions in the frame of Russia-Bulgaria bilateral project cooperation focused on:

Gorgippia – ancient city (Greek colony) located in the centre of Anapa city. Many seismic effects have been observed.

Raevskoe – ancient fort, mostly under the recent sediments.

Utrish – natural reserve area with a lot of expressions of the paleosesimogenic dislocations, landslides and silt volcanoes.

Fanagoria – huge ancient city located to the bay of Taman peninsula. Many archaeological layers are discovered which preserve a lot of seismic deformations.

The study of ancient objects has revealed a number of seismically induces deformations and destructions: systematic tilts and shifts of upper parts of the walls, as well as their arch-like warping in plan; shear ruptures; rotations of different components of walls and other building elements around vertical axis; squashing of water wells' mouths and stems. Some of mentioned deformations can be formed during strong historical earthquakes in 3rd and 1st centuries BC, as well as in 1st and 3rd century AD. There seismic events were accompanied by local destructions and fires. Summarizing the data on historical earthquakes of the Taman's Peninsula it can be concluded that regional seismic potential is determined by a possibility of $M \geq 7.0$ crust earthquake occurrence with average recurrence interval – one seismic event if few hundred years. Seismic oscillations in the source zone from such natural events are about Io=IX or even more [9].

3.2. Bulgaria

Several national and international expeditions in the frame of Bulgaria-Russia bilateral project cooperation to the sites:

Durankulak - very ancient site developed in long time interval from Neolithic structures to the medieval buildings with observed seismic effects.

Balchik – famous with its Cybela temple destroyed by a complex disaster (earthquake, tsunami, landslide)

Kavarna – ancient Greek colony Bisone, flooded by tsunami generated by huge landslide, generated by an earthquake.

Kaliakra – ancient city, castle and fort, source of many paleoseismodislocations.

Varna – old city Odessos, with observed seismic affects on its preserved ancient structures

Pobiti kamani. – natural reserve preserved a long lasted geological history of seismic effects in situ to the stones

Almost all seismic effects to the investigated archaeological sites, structures (excavated or surface), or rocks are expressed as fallen stones or bricks or cracks to the direction of the possible epicenter. The calibration curve derived from the macroseismic map of the M7.2 seismic event of 31st March, 1901 is essential for the investigated objects, observed seismic effects and assessed intensities. The variations in distances (respective intensities) cover the observed effects and give the possibility of eventual reconstruction of the acting forces, their directions and correct interpretation of the observations. There are a lot of effects observed on the archeological sites, paleoseismological and recently active faults and their activated segments, which could be considered as sources of the seismic effects to the investigated sites and objects. The most difficult to asses parameter is the time of the seismic event, affected the respective site and structures. Sometimes integrated effects of several seismic effects are impossible to separate.

4. CONCLUSION

The reach material was collected during the expeditions on the Bulgarian and Russian Black Sea coastal areas. Many objects have been discovered, documented and investigated and new data collected.

As the huge information is available the detailed interpretation will follow by the Russian and Bulgarian specialists.

The promising results are expected due to the systematic deformations to all archaeological objects located in the areas of high seismicity. But due to the huge volume of information this will be product of the future work of the teams – both consisted from Russian and Bulgarian specialists.

ACKNOWLEDGEMENT

Several projects supported these studies:

"Research of the Consequences of Strong Earthquakes in the Coastal Areas of Bulgaria and the Taman Peninsula. Program for bilateral cooperation between Bulgaria and Russia. Funded by the Research Fund (Contract No: DNTS / Russia 02/20 of 25.06.2018.)

RFFI grants - №№ 19-55-53017 ГФЕН_а; 18-55-18014 Болг_а; 18-05-01004 А

The National Science Program "Environmental Protection and Reduction of Risks of Adverse Events and Natural Disasters", supported by the Ministry of Education and Science (MES) of Bulgaria (Agreement No : D01-230/06.12.2018).

REFERENCES

1. Bonchev, E.K.; Bune V.I.; Christoskov L.V.; Karagjuleva J.B.; Kostadinov V.B.; Reisner G.I.; Rizikova S.V.; Shebalin N.V.; Sholpo V.I.; Sokerova D.C. A method for compilation of seismic zoning prognostic maps for the territory of Bulgaria; Geol. Balc., 1982 12, 2, p.3-48

2. Ranguelov B.K.; Seismicity and Tsunamis in the Black Sea., Proc. Seismology in Europe. XXV Gen. Ass. ESC, 9-14 Sept. Reykjavik, Island, 1996, p. 667-673.

3. Ranguelov B.K.; Dimitrova S.D.. The secondary effects of earthquakes. Vulnerability, objects at risk and risk reduction., Proc. Intl. Conf. VSU'2004., Sofia, Bulgaria, 2004, pp.V-6 – V-11.

4. Ranguelov, B.; Natural Hazards and nonlinearities. BAS, Sofia, Bulgaria 2011; pp. 1–232.

5. Ranguelov B., Historical macroseismic observations - a tool for the quake parameters determination., Book of papers, XXVI Gen. Ass. ESC, Tel Aviv, Israel, 1998; p.306-310

6. Ranguelov B., The archeoseismology in Bulgaria – Present and Expectations., Proc. 31st Gen.Ass. ESC., Hersonissos, Greece, 2008, pp. 372-378 (on CD).

7. Ranguelov B. Bojkova A. Archaeoseismology in Bulgaria, Proc. Conf. Geoarchaeology and Archaelomineralogy., Sofia, Bulgaria, 2008; pp.341-346

8. Ranguelov B., E.Mircheva, I.Lazarenko., R. Encheva., 2008. The archaeological site – possible evidence about multihazard ancient events, Proc. Conf. Geoarchaeology and Archaelomineralogy., Sofia, Bulgaria 2008; 347-352 pp.

9. Molev E.A., Korzhenkov A.M., Ovsyuchenko A.N., Larkov A.S. Potential traces of earthquakes in the ancient city of Kytaia, Kerch Peninsula, Crimea. // Geodesy and Geodynamics. 2019. No. 10. pp. 321-330.

10. Korzhenkov A.M., Mazor E. Structural reconstruction of seismic events: Ruins of ancient buildings as fossil seismographs; Sci. and New Technol. 1999. N 1. pp. 62–74.

11. Paneva Zl., B.Ranguelov., 2011. Archaeoseismology and reconstruction of the ancient environment in Bulgaria., Proc. 3rd EMUNI student research multi-conference. 2011. p. 82-89.

Ocean tide loading displacements observed by very long baseline interferometry during IVS-CONT14 campaign

Kamil Teke

[1]Hacettepe University, Department of Geomatics Engineering 06800 Ankara, Turkey
Phone: +90 312 297 6990, E-mail: kteke@hacettepe.edu.tr

ABSTRACT

Ocean tide loading (OTL) displacements can be predicted by convolution software, e.g. SPOTL [1], which convolves the elastic load Green's function over the gridded values of global ocean tide models such as FES2014 [2] for the whole oceans. Besides, ocean tide loading (OTL) displacements can be observed with space geodetic techniques. In this study, the amplitudes and Greenwich phase lags for each coordinate component, i.e., radial, west, and south of the principal semi-diurnal (M_2, S_2, N_2, K_2) and -diurnal tides (K_1, O_1, P_1, Q_1) of OTL displacements were estimated at the very long baseline interferometry (VLBI) sites of the 15 days long continuous VLBI campaign, CONT14, carried out by the International VLBI Service for Geodesy and Astrometry (IVS). In the estimation of the amplitudes and Greenwich phase lags of the tidal constituents, hourly VLBI station coordinate time series were used as observations derived through analyzing 1 hour VLBI sessions of the CONT14 campaign. The estimated amplitudes and Greenwich phase lags of the principal constituents of OTL displacements were compared with the predictions of the state-of-the-art ocean tide models, among others, FES2012 [3,4], FES2014 [2] and TPXO8 [5,6]. Both the amplitudes and the phases between CONT14 estimates and ocean tide models agree to some extent for the M_2, S_2, N_2, K_1, and O_1 tides at most of the sites and coordinate components. However, for K_2, P_1, and Q_1 tides CONT14 estimates do not converge to those of the model amplitudes and/or phases. Because such a small duration of 15 days long hourly station coordinate time series does not satisfy the minimum period of Rayleigh criterion [7] to distinguish between neighboring frequencies.

KEYWORDS: VLBI; CONT14 hourly sessions; ocean tide loading displacements

1. INTRODUCTION

Tidal variations of the pressure exerted by the ocean mass to the seafloor, cause harmonic displacements on the crust so-called ocean tide loading (OTL) displacements. Tidal harmonic constituents of the OTL displacements are predicted through convolving several ocean tide models as well as these tides would be resolved from the observations of space geodetic techniques using the so called static and kinematic methods. In the static approach, real (in-phase) and imaginary (out-of-phase) parts of OTL displacement constituents are estimated along with the daily station coordinates as part of daily solutions. Then, the daily estimates of tidal constituents and their covariance information are stacked in a combined solution e.g. using a Kalman Filter e.g., [8-18]. In kinematic approach, station coordinate time series and their formal errors are estimated at sub-daily intervals without reducing the OTL displacements from the observations a priori to the parameter estimation, then the amplitudes and phases of OTL displacement tidal constituents are decorrelated using harmonic analysis e.g., [19-26].

In literature, several OTL displacement estimation studies based on analyzing the observations of VLBI and/or GNSS techniques can be cited. For example, [8] first demonstrated that applying ocean tide model loading corrections to the a priori coordinates of the VLBI stations located near ocean coasts and on islands reduce the post-fit residuals of the VLBI delays (observations) as well as change VLBI station coordinates up to a few centimeters, suggesting the ocean tide loading can be monitored using VLBI. [9] estimated the vertical components of the OTL displacement semidiurnal (M_2, S_2, K_2, N_2) and diurnal tidal constituents (K_1, P_1, O_1, Q_1) at six VLBI sites from the analysis of daily VLBI sessions carried out every 5th and 7th day of the week since 1984 till late 1992 with linear least-squares when horizontal amplitudes and phases were fixed to those of ocean tide model from [27]. They compared the estimated vertical amplitudes at the corresponding sites to those of the [27] and [28] models. The accuracy of the VLBI observations at that time was not high enough to determine the vertical amplitudes better than 1 mm at diurnal and semidiurnal frequencies as concluded by [9]. [13] estimated vertical tidal displacements using 3 years of observations derived at 353 globally distributed Global Positioning System (GPS) stations and found a good agreement of GPS observed OTL displacement vertical amplitude and

phase parameters of M_2, N_2, S_2, and O_1 constituents with those of model predictions except for K_1 and K_2 due to multipath effects, solar radiation as well as their high correlation with GPS constellation repeat period and orbital period [16,29,30]. [15] estimated OTL displacement tidal constituents of M_2, S_2, N_2, O_1, and Q_1 through performing a Kalman filter estimation using 90 days of GPS observations.

In this study, the troposphere delays estimated from 24 hour sessions (external delays) were reduced from the observations a priori to the analysis of 1 hour VLBI sessions of CONT14 campaign. Besides, in the analysis of 1 hour VLBI sessions, the CONT14 specific terrestrial reference frame (TRF) and Earth orientation parameters (EOP) series were used which had been estimated from a global solution through stacking the normal equations of daily sessions of CONT14. By means of handling the estimated hourly station positions as observations along with their formal errors, OTL displacement constituents of principal semi-diurnal and diurnal tides are intended to be resolved.

2. IVS CONT14 CAMPAIGN AND ANALYSIS OF HOURLY SESSIONS

International VLBI Service for Geodesy and Astrometry (IVS, [31-33]) carries out 15 days continuous VLBI sessions every three years in order to demonstrate the state-of-art capabilities of the current VLBI technology. Among others, the observations of CONT14 campaign were analyzed for this study, carried out from 6 (0 UT) to 20 (24 UT) May 2014. 17 VLBI stations located at 16 sites were contributed to CONT14 (see Figure 1).

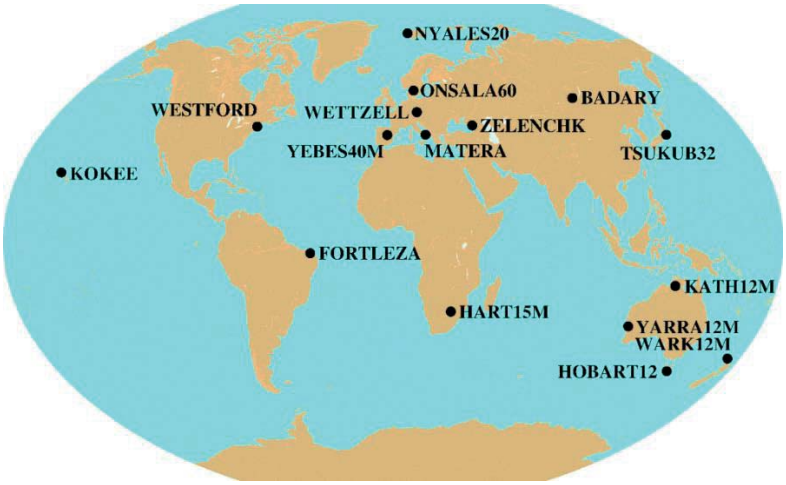

Figure 1. VLBI stations participating to CONT14 campaign [34]

The geodetic VLBI stations contributed to CONT14 campaign are listed in Table 1. For further information on CONT14 campaign readers are referred to [34].

Table 1: Geodetic VLBI stations participated to CONT14.

Observatory name	Country	VLBI Acronym
Ny-Ålesund	Norway	NYALES20
Onsala	Sweden	ONSALA60
Badary	Russia	BADARY
Wettzell	Germany	WETTZELL
Zelenchukskaya	Russia	ZELENCHK
Westford	USA	WESTFORD
Matera	Italy	MATERA
Yebes	Spain	YEBES40M
Tsukuba	Japan	TSUKUB32
Kokee Park	USA	KOKEE
Fortleza	Brazil	FORTLEZA
Katherine	Australia	KATH12M
Hartebeesthoek	South Africa	HART15M
Yarragadee	Australia	YARRA12M
Warkworth	New Zealand	WARK12M
Hobart	Tasmania	HOBART26
Hobart	Tasmania	HOBART12

The high correlation between the parameters in hourly sessions results in troposphere delays and antenna coordinates propagate into each other and unreliable estimates (e.g. [35,36]). To overcome this restriction, external troposphere slant delays ΔL estimated from 24 hour sessions were reduced from the observations of hourly sessions a priori to the adjustment and residual troposphere delays were not estimated. The CONT14 VLBI observations were analyzed using Vienna VLBI and Satellite Software (VieVS, [37]). The parameters were estimated using classical Gauss Markov least-squares adjustment method. The observations were not removed below a certain elevation angle and not down-weighted. Source coordinates were fixed to ICRF2 (International Celestial Reference Frame, [38]). The high-frequency variations of Earth rotation parameters were modeled as recommended by the IERS Conventions 2010 [39]. Troposphere zenith hydrostatic delays (ZHD) were computed from local surface pressure measurements at the sites using [40-42] and mapped to the observation directions with the VMF1. Tidal and nontidal atmospheric loading [43], as well as tidal ocean loading based on the ocean model FES2014 [2], were introduced to each observation a priori to the adjustment. Finally, the OTL displacements were assumed to be unveiled by the estimated hourly station positions.

3. ESTIMATING THE PRINCIPAL SEMI-DIURNAL AND DIURNAL TIDES FROM THE HOURLY OTL DISPLACEMENTS OBSERVED BY VLBI

The tidal harmonic displacements on the Earth crust, caused by the seafloor pressure variations due to the ocean tide loading (OTL), $\Delta_{n,k}$ for the k'th coordinate component (i.e. radial, west, or south) at a site, n and at a particular time t can be formulated with the harmonic function

$$\Delta_{n,k} = \sum_j A_{n,j,k} \cos(\chi_j(t) - \varphi_{n,j,k}) \qquad (1)$$

where χ_j denotes the astronomical phase of the j'th tidal constituent which is computed from fundamental astronomical arguments [39]. In Eq. 1, A_{nj} and φ_{nj} are the amplitude and the phase lag with respect to the j'th tidal potential at Greenwich meridian, respectively.

Principal lunar semidiurnal tide, M_2 is the strongest tidal constituent that has a frequency of 2 cycles per lunar day (period: 12.42 hour). Other principal tides mostly considered are namely; principal solar semidiurnal S_2 that has a period of 12 hour, principal lunar elliptic semidiurnal N_2 (12.66 hour), lunisolar semidiurnal K_2 (11.97 hour that is one-half a sidereal day), lunar diurnal K_1 (23.93 hour, one sidereal day), principal solar declination P_1 (24.07 hour), principal lunar diurnal O_1 (period: 25.82 hour), lunar elliptic diurnal Q_1 (26.87 hour), lunisolar fortnightly M_f (13.66 day), lunar monthly evectional constituent M_m (27.55 day), and solar semiannual S_{sa} (182,62 day) [44].

For the calculations of OTL displacements from models according to Eq. 1, the amplitudes and phase lags of principal tides were derived from "Ocean Tide Loading Provider", a web-based facility provided by M.S. Bos and H.-G. Scherneck [45] that uses OLFG/OLMPP algorithm [27] and the Green's functions using Gutenberg-Bullen standard Earth model to determine the deformation due to point loads [46]. Tidal coefficients were selected as not to correct for geocenter motion due to ocean tides. In first place, as a simulation study, hourly OTL displacements were calculated from Eq. 1 using the real and imaginary parts of 342 tidal constituents that were derived from a spline interpolation of 11 principal tidal constituents as recommended by the IERS2010 conventions [39]. Then, assuming these calculated OTL displacements as observations the amplitudes and phase lags of 8 principal semi-diurnal and diurnal constituents were estimated using the linear form of Eq. 1. Before the estimation, fortnightly, monthly, and semi-annual tidal terms provided from FES2014 were reduced from the hourly positions of the stations. The estimated amplitudes and phase lags of all the 8 semidiurnal and diurnal tides were found as exactly identical to those of the FES2014 model. This one to one agreement suggests that the amplitudes and phases of several semi-diurnal and diurnal principal tidal constituents can be resolved from the 15 days of hourly but errorless OTL displacements even such a short time span of data is highly vulnerable to observational errors. Then, the real hourly series of station positions and their formal errors were used as observations. The results are presented in the following chapter.

4. RESULTS AND DISCUSSION

Clear signals of OTL displacements were derived from the hourly station position estimates e.g. the radial component of the geodetic colocation site Kokee is shown in Figure 2. The estimated amplitudes and phases as well as their formal errors of all principal semi-diurnal and diurnal tides at the coastal CONT14 VLBI sites (located in 150 km distance from the coast) are presented in Table 2. Depending on the number and quality of the observations per station, the formal errors of the estimated amplitudes were found similar for most of the tidal constituents, ranging from 0.1 to 0.3 mm in the radial and 0.1 to 0.2 mm in the horizontal components except for the VLBI stations at Hartebeesthoek and Fortaleza of which formal errors of the amplitudes are large about 0.5 mm in radial and 0.3-0.4 mm in horizontal components. The formal errors of the phase angles are found mostly on the order of 5-10 degrees despite for K_2, P_1 and Q_1 tides at the VLBI stations; Hartebeesthoek (HART15M), Fortaleza, Warkworth and Hobart (HOBART12 and HOBART26) they reach up to a few tens of degrees and generally seen in the tangential components. These large formal errors seen on the phases should be resulted from the small amplitudes of these tides.

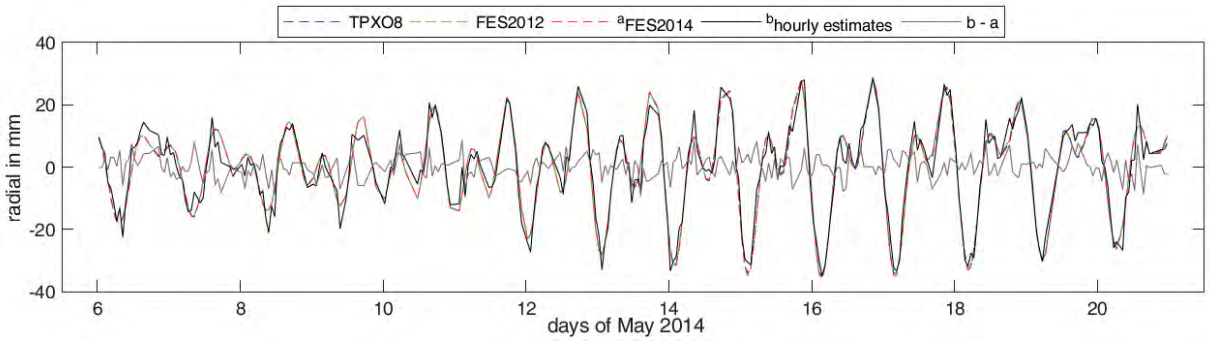

Figure 2. *Radial components of the hourly coordinate estimates of KOKEE (Kauai island, Hawaii, USA) station when the ocean tide model corrections were not introduced to the coordinates a priori to the adjustment.*

The best agreement of the estimated radial amplitudes of M_2 tide with respect to those of ocean tide models was found at the sites Onsala, Badary, Wettzell, Zelenchukskaya, Matera, Tsukuba, Kokee and Yarragade varying in 0.01-0.40 mm whereas the worst agreement is seen at Fortaleza and Ny-Ålesund and Yebes sites with the radial amplitude differences extend to about 1.5 mm. There are also large discrepancies of M_2 tide radial amplitudes between the

CONT14 estimates and model values at Hobart and Yebes VLBI sites with the values of about 0.9 mm. At most of the stations, the tangential amplitudes of M_2 vary from 0.03 mm (at Matera) to 0.4 mm (at Katherine). It is worth to note that there is a large M_2 tide radial amplitude difference of about 0.7 mm between TPXO8 model and both FES2014 and FES2012 models at Ny-Ålesund. When M_2 tide Greenwich phase lags are considered, the agreement between estimates and the models do agree within 1 to 5 degrees for most of the stations in all coordinate components. However, the estimated west phases of M_2 tide at Badary differ from the models at about 10 degrees as well as at Hartebeesthoek (HART15M) the difference with the model values are on the order of about 13 degrees.

The worst agreement of the estimated radial amplitudes of S2 tide to the model values are seen at the sites Yebes, Hartebeesthoek (HART15M), Fortaleza, and Warkworth ranging in 0.7-2 mm. The agreement of S_2 tide at the remaining sites does not exceed 0.4 mm in all components. At all of the sites, the estimated phases of S_2 tide are varying in about 5 degrees with respect to those of TPXO8 and FES2014 models whereas at the Ny-Ålesund, Onsala and Wettzell sites the differences in south phases and at Yarragade the difference in radial phase with respect to FES2012 model are larger with the values of 11.0, 9.2, 10.9, and 7.7 degrees, respectively.

Comparing the level of agreement of the estimated radial amplitudes of N_2 tide with respect to the those of ocean tide models 0.2 to 0.3 mm differences are found at most of the sites. Large radial amplitude differences of N_2 tide between the estimates and model values at the sites Westford, Fortaleza, and Warkworth are seen as 0.4 mm, 0.5 mm, and 0.8 mm, respectively. Most of the west and south amplitude estimates of N_2 tide do not differ from the model predictions more than 0.2 mm. The agreement of estimated N_2 phases to those of TPXO8 and FES2014 vary in 5 degrees for all sites, tides and coordinate components while the south components of Westford and Wettzell, and radial component of Badary compared to those of FES2012 are larger about 8, 11 and 10 degrees, respectively.

From the phasor vector plots (see e.g. Figure 3) it can be seen that the agreement of the amplitudes and phases between CONT14 estimates and ocean tide models do agree well for the M_2 tide at most of the sites and coordinate components. However, for K_2, P_1, and Q_1 tides at most of the sites and coordinate components CONT14 estimates do not converge to those

of the model amplitudes and/or phases. The large formal errors of the estimated amplitudes and phases of K_2, P_1, and Q_1 tidal constituents seen at most the sites also indicate that these tides cannot be well resolved from CONT14 hourly coordinate time series (see also Table 2).

Table 2: The amplitudes and phase lags of OTL displacement semi-diurnal and diurnal constituents with their formal errors estimated from CONT14 hourly sessions at coastal stations (located in 150 km distance from the coast) in millimeter and arc degrees, respectively. The stations are sorted from north to south.

Stations		A_{M_2}	φ_{M_2}	A_{S_2}	φ_{S_2}	A_{N_2}	φ_{N_2}	A_{K_2}	φ_{K_2}	A_{K_1}	φ_{K_1}	A_{O_1}	φ_{O_1}	A_{P_1}	φ_{P_1}	A_{Q_1}	φ_{Q_1}
	R	9.27±0.11	177.3±0.6	2.50±0.09	-141.3±2.1	2.05±0.11	156.3±2.0	0.18±0.09	-132.9±28.7	1.14±0.09	-46.2±4.6	1.40±0.09	-122.0±3.2	0.19±0.11	116.6±21.6	0.11±0.11	-161.2±27.7
NYALES20	W	2.83±0.06	-18.2±1.1	0.81±0.05	34.6±3.8	0.60±0.05	-38.9±4.3	0.06±0.05	40.9±52.6	0.24±0.05	103.6±5.6	0.47±0.04	55.5±5.0	0.11±0.06	96.3±4.5	0.00±0.05	163.6±>100
	S	1.51±0.05	-23.8±1.9	0.58±0.05	23.7±4.9	0.36±0.05	-30.9±6.3	0.27±0.06	25.9±8.1	0.83±0.05	136.7±3.4	0.35±0.05	66.3±5.5	0.12±0.05	127.6±22.1	0.06±0.06	0.6±9.2
	R	3.25±0.05	-64.4±0.8	0.87±0.05	-37.8±3.2	0.59±0.06	-88.0±0.3	0.16±0.05	-39.1±17.2	2.11±0.05	-55.2±1.3	1.14±0.06	-105.5±1.3	0.79±0.05	-56.8±3.1	0.09±0.06	-162.2±18.6
ONSALA60	W	1.42±0.05	85.1±0.5	0.35±0.04	118.2±5.7	0.19±0.04	57.8±9.7	0.05±0.04	120.7±38.8	0.32±0.05	96.5±1.9	0.43±0.04	36.6±5.3	0.16±0.05	92.0±0.9	0.05±0.05	-0.4±10.9
	S	0.68±0.05	112.7±3.0	0.14±0.04	142.5±16.5	0.18±0.05	91.4±0.6	0.01±0.04	141.8±>100	0.26±0.04	45.9±9.9	0.11±0.05	-43.7±24.0	0.22±0.05	37.4±11.6	0.06±0.06	-157.5±31.2
	R	7.58±0.13	-168.6±1.0	1.51±0.14	-164.8±4.0	1.45±0.16	175.4±1.6	0.05±0.15	-165.1±75.0	3.43±0.14	-6.6±2.0	2.18±0.14	0.8±2.0	1.47±0.19	-4.6±1.7	0.34±0.15	-0.8±2.7
WESTFORD	W	3.58±0.08	-129.7±1.3	0.31±0.08	-132.2±13.6	0.87±0.08	-154.2±3.8	0.03±0.07	-139.2±>100	0.34±0.09	-8.1±16.7	0.21±0.07	24.3±16.9	0.05±0.14	-2.0±33.8	0.16±0.06	43.0±22.7
	S	1.84±0.10	-18.0±2.8	0.52±0.10	18.1±8.1	0.50±0.09	-31.4±8.1	0.12±0.10	-158.3±28.3	0.25±0.10	176.5±18.8	0.16±0.08	-48.2±24.0	0.18±0.14	-176.6±9.3	0.03±0.10	10.6±60.9
	R	7.79±0.10	50.3±0.7	3.84±0.10	70.3±0.8	1.13±0.10	64.1±3.4	0.74±0.10	66.7±4.5	9.65±0.09	-137.2±0.6	7.34±0.09	-154.0±0.6	4.39±0.10	-139.9±1.3	0.72±0.11	-166.0±3.2
TSUKUB32	W	2.59±0.08	-10.7±1.8	1.24±0.08	30.1±3.5	0.43±0.08	-22.8±6.9	0.41±0.09	25.9±8.1	2.02±0.09	-169.4±2.4	1.51±0.08	172.8±2.0	1.08±0.12	-172.0±2.0	0.13±0.08	160.4±17.1
	S	1.92±0.05	-76.7±0.8	0.58±0.05	-63.9±3.7	0.46±0.06	-84.6±1.0	0.09±0.05	-66.1±20.4	1.43±0.06	90.7±0.1	1.20±0.05	70.4±1.4	1.01±0.06	87.9±0.2	0.08±0.04	52.6±30.5
	R	12.19±0.23	-121.2±1.0	4.42±0.25	-118.9±2.4	2.10±0.21	-127.6±5.4	0.98±0.22	-128.3±12.4	10.60±0.24	60.9±1.1	6.04±0.20	54.9±1.8	4.91±0.23	59.6±2.1	0.72±0.20	50.2±15.5
KOKEE	W	2.92±0.19	153.8±3.6	0.81±0.20	-172.3±10.7	0.52±0.18	156.0±13.5	0.01±0.24	-171.7±>100	2.05±0.17	38.7±4.7	1.30±0.18	12.7±5.4	0.93±0.18	36.4±10.6	0.08±0.20	0.3±19.6
	S	4.41±0.14	97.3±0.5	1.55±0.12	126.4±4.1	0.71±0.15	93.0±0.9	0.30±0.13	119.0±18.8	1.68±0.13	111.9±2.7	1.23±0.14	93.5±0.6	0.75±0.14	108.1±5.1	0.10±0.15	82.5±16.2
	R	36.85±0.41	33.5±0.6	9.48±0.39	55.4±2.1	8.14±0.46	20.9±1.8	2.22±0.37	52.2±9.0	1.88±0.50	96.9±2.7	2.46±0.39	32.3±7.8	1.86±0.47	90.4±0.1	0.36±0.51	174.9±11.4
FORTLEZA	W	5.14±0.34	22.3±3.1	1.52±0.28	43.9±10.7	0.49±0.40	8.0±11.0	0.83±0.29	39.7±19.0	0.14±0.32	155.2±>100	0.34±0.35	-14.4±28.7	0.44±0.28	139.1±36.4	0.02±0.28	138.8±>100
	S	5.80±0.30	51.4±2.8	1.67±0.36	83.6±2.1	1.24±0.31	27.7±10.4	0.65±0.34	82.4±5.7	0.75±0.29	123.6±19.8	0.94±0.34	95.4±2.9	0.29±0.28	119.2±43.2	0.33±0.32	73.2±24.0
	R	3.56±0.16	146.7±2.3	0.42±0.15	-110.6±11.4	0.81±0.17	104.4±4.5	0.29±0.15	-115.5±19.3	7.61±0.18	11.7±0.9	6.06±0.16	8.9±0.8	3.57±0.19	10.3±1.0	0.83±0.17	-0.3±1.1
YARRA12M	W	2.27±0.12	-128.5±2.8	0.75±0.12	-72.4±4.5	0.58±0.12	-152.9±8.6	0.20±0.13	-72.8±16.2	1.53±0.12	148.4±4.2	0.56±0.10	144.3 ±10.0	0.82±0.12	145.9±7.4	0.05±0.10	136.6±>100
	S	2.52±0.14	-158.7±3.2	0.84±0.15	-99.4±2.6	0.49±0.17	-179.5±4.4	0.10±0.15	-104.5±33.2	0.64±0.13	-66.3±7.8	0.45±0.14	-103.5±6.6	0.17±0.16	-73.8±22.4	0.06±0.12	-118.3±88.8
	R	26.15±0.19	56.7±0.4	4.42±0.19	121.2±2.1	3.71±0.19	30.0±2.3	0.64±0.19	116.1±11.4	3.72±0.22	-174.0±1.9	0.56±0.21	118.6±16.1	2.10±0.27	-179.0±1.1	0.08±0.19	47.9±>100
WARK12M	W	8.58±0.15	-21.5±0.9	0.94±0.19	8.1±7.5	1.89±0.12	-40.9±3.6	0.31±0.20	-12.6±13.4	0.60±0.14	-23.6±12.9	0.76±0.12	-62.5±7.2	0.27±0.16	-28.1±25.5	0.17±0.15	-86.2±5.0
	S	5.73±0.19	18.5±1.7	1.02±0.17	31.3±8.7	1.38±0.23	-0.9±1.6	0.09±0.20	-155.5±85.6	0.90±0.17	-148.2±9.5	0.56±0.20	-174.2±8.9	0.66±0.20	-153.6±12.0	0.10±0.20	172.7±22.5
	R	10.34±0.16	151.7±0.8	0.97±0.16	-114.2±5.9	2.62±0.14	130.3±2.9	0.03±0.15	56.4±>100	6.54±0.17	86.5±0.1	5.64±0.13	56.5±1.2	2.99±0.16	79.6±0.8	1.02±0.12	44.7±6.9
HOBART26	W	4.26±0.12	103.5±0.7	1.86±0.10	135.0±3.2	0.61±0.12	105.8±4.6	0.65±0.10	129.7±8.7	0.94±0.13	-161.1±5.7	0.37±0.12	-161.4±11.7	0.62±0.14	-162.9±6.3	0.11 ±0.13	-175.3±10.1
	S	1.11±0.15	103.6±3.3	0.40±0.15	98.2±4.7	0.07±0.16	92.6±8.7	0.12±0.18	-84.2±12.2	1.12±0.13	-142.6±6.4	1.15±0.15	-162.8±4.4	0.71±0.14	-145.4±10.1	0.30±0.17	-174.0±5.3
	R	10.14±0.16	152.0±0.8	1.05±0.15	-114.1±5.3	2.50±0.13	130.4±3.0	0.04±0.15	-123.0±>100	6.33±0.17	86.5±0.1	5.83±0.13	56.4±1.1	2.85±0.17	79.5±0.9	1.08±0.12	44.6±6.5
HOBART12	W	4.35±0.14	103.2±0.8	1.64±0.12	134.9±4.1	0.64±0.13	105.8±4.9	0.39±0.11	129.8±16.1	0.99±0.15	-160.2±6.3	0.18±0.13	-161.7±27.2	0.37±0.16	-163.0±11.7	0.03±0.15	8.1±58.3
	S	1.05±0.16	103.7±3.7	0.38±0.16	98.2±5.4	0.08±0.17	92.6±8.1	0.33±0.18	-84.2±4.5	1.18±0.14	-142.7±6.5	1.31±0.16	-164.6±4.0	1.13±0.14	-145.4±6.5	0.41±0.17	-174.2±4.0

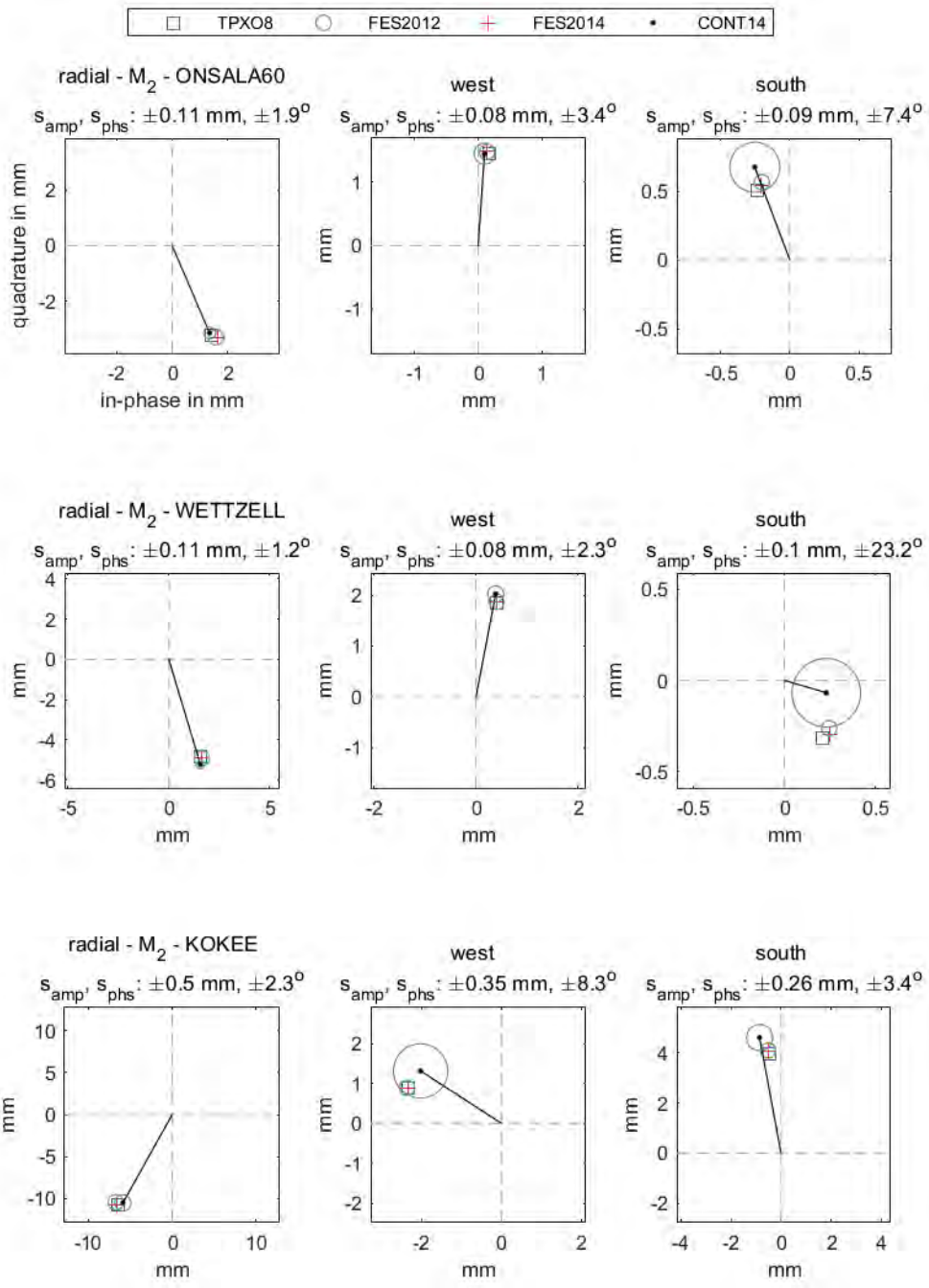

Figure 3. *Phasor vectors of OTL displacement M_2 constituent with one sigma error ellipses at ONSALA60 (Sweden), WETTZELL (Germany) and KOKEE (Hawaii, USA) stations. The horizontal axis represents the in-phase component, and the vertical axis the out-of-phase component relative to the tidal potential at Greenwich. The Greenwich phase lag is zero along the positive direction in the horizontal axis and the phase angle increases counterclockwise.*

5. CONCLUSION

The amplitudes of phasor vector differences between CONT14 estimates and those of ocean tide models are below 0.4 mm at the inland sites: Badary, Wettzell, Matera and Zelencuhkskaya as well as at the coastal site Onsala for all principal semi-diurnal and diurnal tides. The worst agreement between CONT14 estimates and ocean tide models in terms of phasor vector differences are seen at the sites Warkworth and Fortaleza where the differences in radial components for both semi-diurnal and diurnal tides vary in 0.8 to 2.0 mm. The latter is due to the high humidity during the CONT14 period that results in the errors of troposphere delays to propagate to the estimated OTL displacements. While the large median formal errors of the hourly coordinate estimates at station Warkworth as 8.1 mm, 4.8 mm, and 7.5 mm in radial, south, and west directions might results in the radial amplitudes of the phasor vector differences to vary in 0.5-1.5 mm at all tides.

As an overall assessment, the RMS of the radial amplitudes of phasor vector differences (radial RMS misfits) between the CONT14 estimates and those of ocean tide models i.e. FES2014, FES2012 and TPXO8 is found about two times larger than those of tangential components. Likewise, the RMS misfits over coastal stations are about two times larger than those of inland stations for all tides. The best agreement between CONT14 and considered ocean tide models in radial component is seen for N_2 tide with the RMS misfits of about 0.2 mm across inland sites and 0.4 mm across the coastal sites. The amplitudes and phases between CONT14 and ocean tide models do partly agree for S_2, N_2, K_1, and O_1 tides at most of the sites and coordinate components. However, for K_2, P_1, and Q_1 tides CONT14 estimates mostly do not converge to those of the model amplitudes and/or phases.

Unmodeled portions of troposphere delays comprise the largest part of the total errors in the observations of space geodetic techniques and significantly propagate to the station coordinates when station coordinates are estimated at sub-diurnal intervals. To improve the accuracies of semi-diurnal and diurnal tidal constituents, estimated from a short time span of sub-daily station coordinates, further developments on the troposphere delay model is necessary.

ACKNOWLEDGEMENT

This work is supported by The Scientific and Technological Research Council of Turkey (TÜBİTAK), project number: 115Y244. The author acknowledges the International VLBI Service for Geodesy and Astrometry for providing the observations of CONT14 campaign.

REFERENCES

1. Agnew, D.C. SPOTL: Some Programs for Ocean-Tide Loading, SIO Technical Report 2012, Scripps Inst of Oceanogr., University of California.

2. Carrère, L.; Lyard, F.; Cancet, M.; Guillot, A.; Picot, N. Finite Element Solution FES2014, a new tidal model - Validation results and perspectives for improvements, presentation to ESA Living Planet Conference, 2016, Prague.

3. Lyard, F.; Lefevre, F.; Letellier, T.; Francis, O. Modelling the global ocean tides: Modern insights from FES2004. Ocean Dyn 2006, 56(5-6), 394-415.

4 Carrère, L.; Lyard, F.; Cancet, M.; Guillot, A.; Roblou, L. A new global tidal model taking advantage of nearly 20 years of altimetry. In: Proceedings of Meeting "20 Years of Altimetry", 2012, Venice.

5. Egbert, G.D.; Erofeeva, S.Y. Efficient inverse modeling of barotropic ocean tides. Journal of Atmospheric and Oceanic Technology 2002, 183-204.

6. Egbert, G.D.; Erofeeva, S.Y.; Ray, R.D. Assimilation of altimetry data for nonlinear shallow-water tides: Quarter-diurnal tides of the Northwest European Shelf. Cont Shelf Res 2010, 30(6), 668-679.

7. Foreman, M. Manual for tidal heights analysis and prediction. Pac Mar Sci Rep 1977, 77–10, 1–58.

8. Schuh, H.; Möhlmann, L. Ocean loading station displacements observed by VLBI. Geophys Res Lett 1989, 16:1105-1108.

9. Sovers, O.J. Vertical ocean loading amplitudes from VLBI measurements. Geophys Res Lett 1994, 21, 357-360.

10. Haas, R.; Schuh, H. Ocean loading observed by geodetic VLBI. In Proceedings of the 13th International Symposium on Earth Tides 1998, edited by B. Ducarme and P. Paquet, pp 111-120.

11. Scherneck, H.G.; Haas, R.; Laudati, A. Ocean loading for, in and from VLBI. In IVS 2000 General Meeting Proceedings 2000, Greenbelt, edited by N. Vandenberg and K. Baver, 257-262.

12. Dach, R.; Dietrich, R. The Ocean Loading Effect in the GPS Analysis: A Case Study in the Antarctic Peninsula Region. Marine Geodesy 2001, 24:1, 13-25.

13 Schenewerk, M.S.; Marshall, J.; Dillinger, W. Vertical ocean-loading deformations derived from a global GPS network. J Geod Soc Jpn 2001, 47(1), 237–242.

14. Petrov, L.; Ma, C.P. Study of harmonic site position variations determined by very long baseline interferometry. J Geophys Res 2003, 108(B4):2190.

15. Allinson, C.R.; Clarke, P.J.; Edwards, S.J.; King, M.A.; Baker, T.F.; Cruddace, P.R. Stability of direct GPS estimates of ocean tide loading. Geophys Res Lett 2004, 31, L15603.

16. King, M.A.; Penna, N.T.; Clarke, P.J.; King, E.C. Validation of ocean tide models around Antarctica using onshore GPS and gravity data. J Geophys Res 2005, 110, B08401.

17. Thomas, I.D.; King, M.A.; Clarke, P.J. A comparison of GPS, VLBI and model estimates of ocean tide loading displacements. J Geod 2007, 81(5), 359-368.

18. Yuan, L.; Chao, B.F.; Ding, X.; Zhong, P. The tidal displacement field at Earth's surface determined using global GPS observations. J Geophys Res Solid Earth 2013, 118, 2618-2632.

19. Vey, S.; Calais, E.; Llubes, M.; Florsch, N.; Woppelmann, G.; Hinderer, J.; Amalvict, M.; Lalancette, M.F.; Simon, B.; Duquenne, F.; Haase, J.S. GPS measurements of ocean loading and its impact on zenith tropospheric delay estimates: a case study in Brittany, France. J Geod 2002, 76, 419-427.

20. Khan, S.A.; Scherneck, H.G. The M2 ocean tide loading wave in Alaska: Vertical and horizontal displacements, modelled and observed. J Geod 2003, 77(3– 4), 117–127.

21. King, M.A. Kinematic and static GPS techniques for estimating tidal displacements with application to Antarctica. J Geodyn 2006, 41(1-3), 77-86.

22. Yun, H.S.; Lee, D.H.; Song, D.S. Determination of vertical displacements over the coastal area of Korea due to the ocean tide loading using GPS observations. J Geodyn 2007, 43(3-5), 528-541.

23. Melachroinos, S.A.; Biancale, R.; Llubes, M.; Perosanz, F.; Lyard, F.; Vergnolle, M.; Bouin, M.N.; Masson, F.; Nicolas, J.; Morel, L.; Durand, S. Ocean tide loading (OTL) displacements from global and local grids: comparisons to GPS estimates over the shelf Brittany, France. J Geod 2008, 82(6), 357-371.

24. Vergnolle, M.; Bouin, M.N.; Morel, L.; Masson, F.; Durand, S.; Nicolas, J.; Melachroinos, S.A. GPS estimates of ocean tide loading in NW-France: Determination of ocean tide loading constituents and comparison with a recent ocean tide model. Geophys J Int 2008, 173(2), 444-458.

25. Penna, N.T.; Clarke, P.J.; Bos, M.S.; Baker, T.F. Ocean tide loading displacements in western Europe: 1. Validation of Kinematic GPS estimates. J Geophys Res Solid Earth 2015, 120, 6523-6539.

26. Martens, H.R.; Simons, M.; Owen, S.; Rivera, L. Observations of ocean tidal response in South America from subdaily GPS positions. Geophys J Int 2016, 205, 1637-1664.

27. Scherneck, H.G. A parameterized solid earth tide model and ocean tide loading effects for global geodetic baseline measurements. Geophys J Int 1991, 106(3):677-694.

28. Pagiatakis, S.D. The response of a realistic earth to ocean tide loading. Geophys J Int 1990, 103, 541-320.

29. Urschl, C.; Dach, R.; Hugentobler, U.; Schaer, S.; Beutler, G. Validating ocean tide loading models using GPS. J Geod 2005, 78(10):616-625.

30. Zhong, P.; Ding, X.L.; Yuan, L.G.; Xu, Y.L.; Kwok, K.; Chen, Y.Q. Sidereal filtering based on single differences for mitigating GPS multipath effects on short baselines. J Geod 2010, 84: 145-158.

31. Nothnagel, A.; Artz, T.; Behrend, D.; Malkin Z. International VLBI Service for Geodesy and Astrometry - Delivering high-quality products and embarking on observations of the next generation. J Geod 2019, 91(7), 711–721.

32. Behrend, D. Data Handling within the International VLBI Service. Data Science Journal 2013, Vol. 12, pp. WDS81–WDS84.

33. Schuh, H.; Behrend, D. VLBI: A fascinating technique for geodesy and astrometry. J Geodyn 2012, 61, 68–80.

34. International VLBI Service for Geodesy and Astrometry. Available online: https://ivscc.gsfc.nasa.gov/index.html (accessed on 4 August 2019).

35. Rothacher, M.; Beutler, G. The Role of GPS in the study of Global Change. Physics and Chemistry of the Earth 1998, 23(9/10):1029-1040.

36. Teke, K.; Böhm, J.; Nilsson, T.; Krasna, H. Sub-daily antenna position estimates from the CONT11 campaign. Proceedings of the 21st Meeting of the European VLBI Group for Geodesy and Astrometry (EVGA), Reports of the Finnish Geodetic Institute 2013, edited by N. Zubko and M. Poutanen, Helsinki, Finland, 131-134.

37. Böhm, J.; Böhm, S.; Boisits, J.; Girdiuk, A.; Gruber, J.; Hellerschmied, A.; Krasna, H.; Landskron, D.; Madzak, M.; Mayer, D.; McCallum, J.; McCallum, L.; Schartner, M.; Teke, K. Vienna VLBI and Satellite Software (VieVS) for Geodesy and Astrometry. Publications of the Astronomical Society of the Pacific 2018, 130(986), 044503; 1 – 6.

38. Fey, A.; Gordon, D.; Jacobs, C.S. The second realization of the International Celestial Reference Frame by Very Long Baseline Interferometry. IERS Technical Note 2009, vol. 35.

Verlag des BundesamtsfürKartographie und Geodasie, Frankfurt am Main, ISBN 3-89888-918-6.

39. Petit, G.; Luzum, B. IERS Conventions 2010, IERS Technical Note 2010; 36. Verlag des Bundesamts für Kartographie und Geodasie, Frankfurt am Main.

40. Saastamoinen, J. Atmospheric correction for the troposphere and stratosphere in radio ranging of satellites. In the use of artificial satellites for geodesy, Geophys Monogr Ser 1972, 15, Amer. Geophys. Union, 274–251.

41. Saastamoinen, J. Contribution to the theory of atmospheric refraction (in three parts). Bull Geod 1973, 105–107, 279–298.

42. Davis, J.L.; Herring, T.A.; Shapiro, I.I.; Rogers, A.E.E.; Elgered, G. Geodesy by radio interferometry: effects of atmospheric modeling errors on estimates of baseline length. Radio Sci 1985, 20 (6), 1593–1607.

43. Petrov, L.; Boy, J.P. Study of the atmospheric pressure loading signal in Very Long Baseline Interferometry observations. J Geophys Res 2004, 109 (B3), B03405.

44. Doodson, A.T. The Harmonic Development of the Tide-Generating Potential. Proceedings of the Royal Society A: Mathematical, Physical and Engineering Sciences 1921, 100 (704): 305-329.

45. Ocean tide loading provider – Chalmers. Available online: http://holt.oso.chalmers.se/loading (accessed on 4 August 2019).

46. Farrell, W.E. Deformation of the Earth by surface loads. Rev Geophys Space Phys 1972, 10(3):761-797.

The state of the art about drought monitoring in Turkey observed by the new satellite-based techniques

Gonca Okay Ahi [1]

[1]Hacettepe University, Geomatics Engineering Department 06800 Ankara, Turkey
Phone: +90 312 297 69 90, E-mail: goncaokayahi@hacettepe.edu.tr

ABSTRACT

Drought is a long-lasting shortage in water supply in the atmosphere, surface and groundwater expressing itself with (i) less than average precipitation (meteorological drought), (ii) followed by a damage in crop production or in the ecology, if below-average precipitation period is extended (agricultural drought) and also with (iii) significant fall of water reserves such as in aquifers, lakes (hydrological drought). Thus, drought monitoring is crucial for the economy and water resources management for a country, however, it cannot be achieved properly in national scale with the traditional observation methods. Satellite-based techniques for drought monitoring are very promising for this purpose. In this study, by using Center for Space Research (CSR)'s Level 3, Release 5 (RL05) data observed by Gravity Recovery and Climate Experiment (GRACE) satellite, German Research Center (GFZ)'s Level 3, Release 6 (RL06) data observed by GRACE/GRACE-FO (GRACE-Follow-On) satellite, Tropical Rainfall Measuring Mission (TRMM) precipitation data, Global Land Data Assimilation System (GLDAS) data and finally drought indices (El Niño–Southern Oscillation: ENSO, North Atlantic Oscillation: NOA, Self-calibrating Palmer Drought Severity index: SCPDSI), a state of the art about drought monitoring in Turkey, is presented. The results propose to find answers about how to reveal the dominant drought periods, get notable information about the spatial distribution, observe spatial and temporal change rate and understand several prominent reasons of the drought events observed in Turkey. Moreover, the results of the statistical approach used for the prediction of GRACE/GRACE-FO derived Total Water Storage (TWS) time series is discussed. According to our results, the spatial distribution of the drought is primarily affected by the precipitation history but also by uncontrolled human usage of water resources, especially in Central Anatolia according to GRACE and GRACE-FO results. The contrast leading to a spatial change from Eastern part to Western part, with a rate of 1 cm/yr, is less obvious according to GRACE-FO derived amplitude of TWS section. Recent, GRACE-FO amplitude sections of TWS shows in the general sense, the increasing impact of drought observed in Turkey.

KEYWORDS: Total Water Storage (TWS); GRACE; GRACE-FO, GLDAS, TRMM, drought; Turkey

1. INTRODUCTION

Turkey, situated between 36-42° N, 26-45° E coordinates, is surrounded by Black sea (Northern part), Aegean Sea (Western part) and Mediterranean Sea (Southern part). The country has ~83 million populations and one of the main economy of the country is based on the agriculture. According to National Aeronautics and Space Administration (NASA) study the recent drought that began in 1998 in the Eastern Mediterranean Levant region, which comprises also Turkey, is likely the worst drought of the past 900 years [1]. [2] states that Turkey needs to make plans for its drinking water requirements, meet its demand for hydroelectric energy from sustainable alternatives, and implement agricultural irrigation methods that can withstand droughts. In this context, drought monitoring has a special importance for national resources management. However, traditional techniques are not sufficient for an understanding in national scale neither make possible a monitoring. With the development of satellite technology, new missions are incorporated making possible to remotely sense the interested region. For example, Gravity Recovery and Climate Experiment (GRACE), with a mission lifetime (2002-2017), and the following mission namely GRACE-Follow-on (GRACE-FO), launched in 2018 and still operating can be cited as the new gravimetric satellite technologies. Besides, gravimetric missions, for drought monitoring hydrological models, a terrestrial modeling system incorporating satellite and ground-based observations (e.g. Global Land Data Assimilation System: GLDAS [3] with NOAH [4] , MOS [5], VIC [6], CLM [7] models), satellite-based precipitation data (e.g. Tropical Rainfall Measuring Mission: TRMM [8]) and in-situ data can be used to make better interpretations and to validate the results. In Turkey, using GRACE data, some important studies have been performed covering a time period till max. 2014 [9–11]. More recent study integrating the GRACE, GLDAS, TRMM data and drought indices is also performed [12] whose results supports this study aiming to give a general guideline about drought monitoring with the available methods, to discuss about the personal ongoing researches on this domain and the latest results obtained with the GRACE-FO data in 2019 pointing out, in the general sense, a continuous drought in Turkey.

2. DROUGHT MONITORING

The interested parameter when interpreting drought, is a functional of the gravity field called as Total Water Storage (TWS) which is an integrated parameter of the available surface water, ice and/or snow layer, biosphere, soil moisture and groundwater as shown in Figure 1A. The TWS can be expressed in Eq.1.:

$$\Delta\eta_{land}(\theta,\phi,t) = \frac{a\rho_{ave}}{3\rho_w}\sum_{l=0}^{\infty}\sum_{m=0}^{l}\tilde{P}_{lm}(\cos\theta)\frac{2l+1}{1+k_l}\left(\Delta C_{lm}\cos(m\phi)+\Delta S_{lm}\sin(m\phi)\right) \quad (1)$$

where ρ_{ave} is the average density of the Earth, ρ_w is the density of fresh water, a is the equatorial radius of the Earth, $\tilde{P}_{lm}$ is the fully-normalized Legendre associated function of degree l and order m, k_l is the Love number of degree l, θ is the spherical co-latitude (polar distance), and ϕ is the longitude.

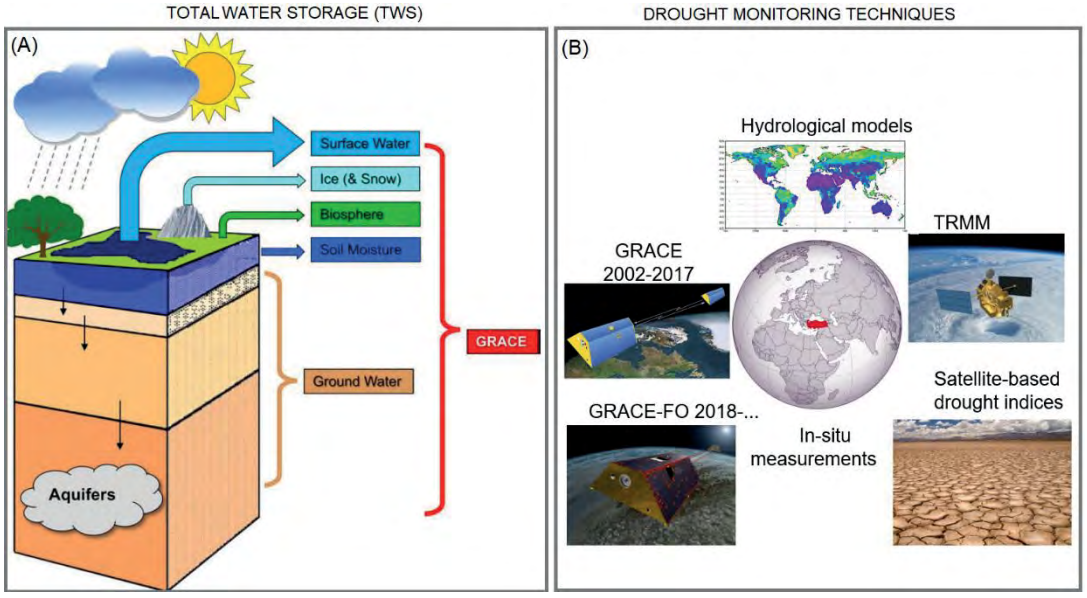

Figure 1. *(A) Schematic diagram of TWS measured by GRACE* [13], *(B) Commonly used techniques for drought monitoring: GRACE satellite data, Hydrological models, precipitation data (e.g. TRMM), drought indices, In-situ measurements, GRACE-FO data.*

When using different data sets (Figure 1B), sometimes, TWS parameter is directly accessed (e.g. GRACE) or it is derived as for the case of hydrological models expressed in Eq.2.:

$$TWS_{GLDAS} = \Delta SM + \Delta SWE + \Delta CWS \quad (2)$$

where, TWS_{GLDAS} is the change in terrestrial water storage from GLDAS, ΔSM is the change in soil moisture (kg/m^2), ΔSWE is the change in the snow moisture equivalent (kg/m^2), and ΔCWS is the change in canopy water storage (kg/m^2). Soil moisture values are averaged before integrating them into the TWS calculation, according to the three-layer model for VIC and MOS, and the four-layer model for NOAH [12]. Moreover, another way to interpret the results is to jointly compare the corresponding two parameters such as TWS and precipitation or TWS and soil moisture derived from hydrological models etc. In this context, hydrological models offer an important numbers of auxiliary parameters to study the relation with the TWS such as soil moisture, snow water equivalent and canopy water storage, rainfall, snowmelt, evapotranspiration. Another way of studying the drought event is the study of the groundwater reserve and its change in basin scale. There exist many researches incorporating GRACE data to estimate groundwater and its variability [14–18]. Turkey's Euphrates Tigris basin, the biggest basin of the country with 180 000 km^2, is also being investigating in the scope of drought monitoring studies [19–22]. The Eq.3 expresses the groundwater component of total water storage after [20]:

$$G' = S' - SWE' - SW' - SM' \quad (3)$$

where *G* is groundwater storage, *S* is total water storage, *SWE* is snow water equivalent, *SW* is surface water storage, *SM* is soil moisture, and the primes indicate anomalies with respect to the mean of the particular component during the study period. Besides, for a proper natural resources management, statistical prediction with the time series analysis methods can also be studied in order to have an idea about the future of the total water storage. As an example of one of this kind studies [23] can be cited which also deserve a scientific focus because gravimetric missions might be interrupted due to some instrumental problems leading to missing data and also the lifetime of the mission might expire. For whole studies in this context, the Table 1. give a short summary about the links of the possible data which might be useful for the drought monitoring studies.

Table 1. Web addresses of the useful data for the drought monitoring studies.

GRACE (CSR)	https://podaac.jpl.nasa.gov/dataset/GRACE_GSM_L2_GRAV_CSR_RL06. https://podaac.jpl.nasa.gov/dataset/TELLUS_GRAC_L3_CSR_RL06_LND
GRACE (GFZ)	https://podaac.jpl.nasa.gov/dataset/GRACE_GSM_L2_GRAV_GFZ_RL06 https://podaac.jpl.nasa.gov/dataset/TELLUS_GRAC_L3_GFZ_RL06_LND
GRACE (JPL)	https://podaac.jpl.nasa.gov/dataset/GRACE_GSM_L2_GRAV_JPL_RL06. https://podaac.jpl.nasa.gov/dataset/TELLUS_GRAC_L3_JPL_RL06_LND
GRACE-FO (CSR)	https://podaac.jpl.nasa.gov/dataset/GRACEFO_L2_CSR_MONTHLY_0060 https://podaac.jpl.nasa.gov/dataset/TELLUS_GRFO_L3_CSR_RL06_LND
GRACE-FO (GFZ)	ftp://isdcftp.gfz-potsdam.de/grace-fo/Level-2/ (Release 6) ftp://isdcftp.gfz-potsdam.de/grace/GravIS/GFZ/Level-3/TWS
GRACE-FO (JPL)	https://podaac.jpl.nasa.gov/dataset/GRACEFO_L2_JPL_MONTHLY_0060 https://podaac.jpl.nasa.gov/dataset/TELLUS_GRFO_L3_JPL_RL06_LND
TRMM In-situ	http://mirador.gsfc.nasa.gov/# https://mgm.gov.tr/eng/forecast-cities.aspx
GLDAS	https://disc.sci.gsfc.nasa.gov/services/grads-gds/gldas
Drought indices	
SCPDSI	https://crudata.uea.ac.uk/cru/data/drought/
ENSO	http://www.cpc.ncep.noaa.gov/data/indices/
NAO	https://www.cpc.ncep.noaa.gov/products/precip/CWlink/pna/nao.shtml.

3. RESULTS AND DISCUSSION

After giving a general review about drought monitoring and studying the available literature for Turkey in this scope, it is possible to state how the drought periods, spatial distributions and its change, the possible reasons of drought can be studied. The Figure 2. present a general view about the actual state in Turkey derived from GRACE, GRACE-FO, GLDAS (e.g. MOS), TRMM, in-situ measurements, drought indices, statistical prediction and propose a methodological example.

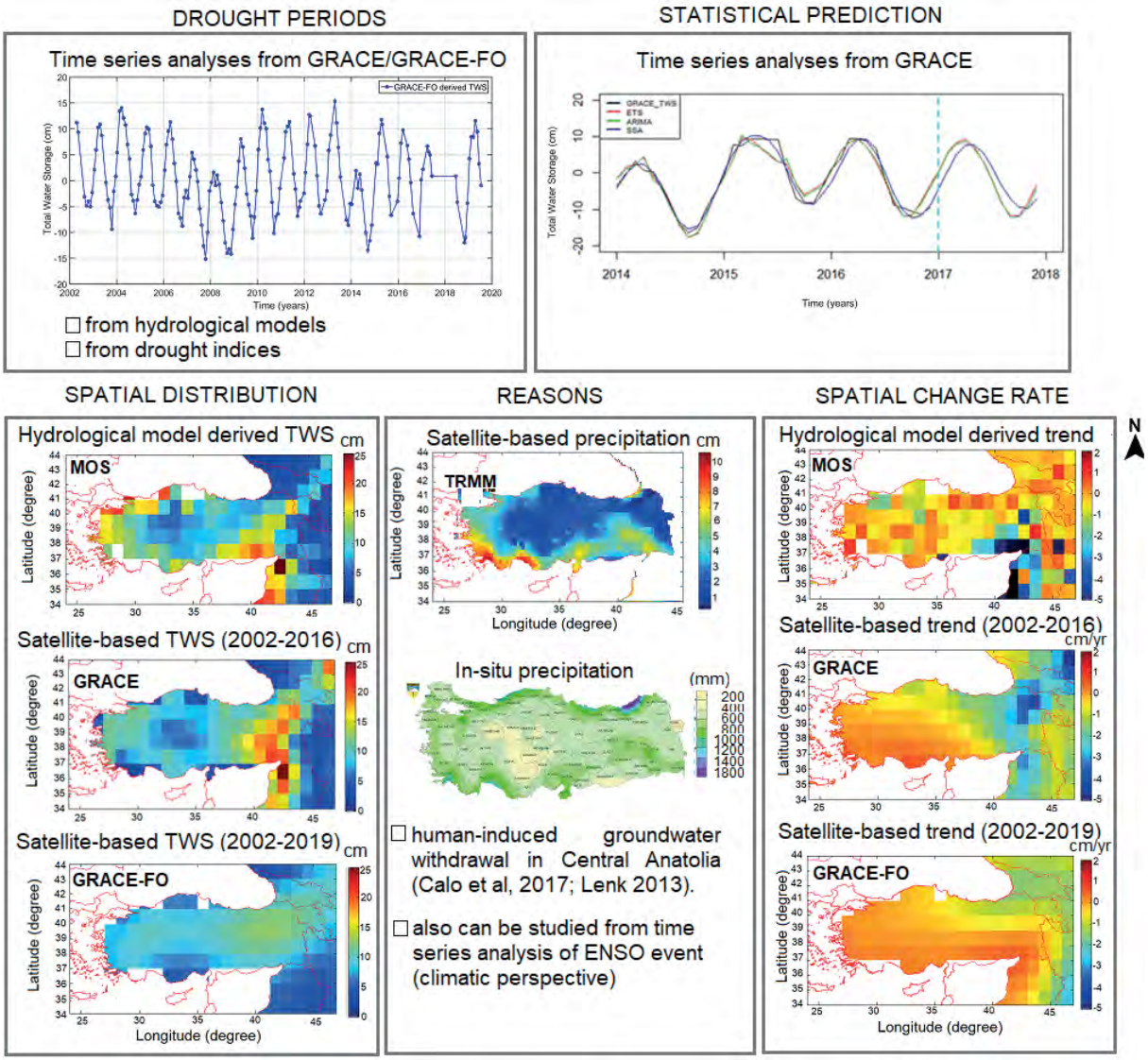

Figure 2. *State of the art and the interpretation strategies about drought monitoring in Turkey.*

The analysis of TWS time series derived from GRACE/GRACE-FO data may reveal, with a decreasing signal, important drought periods in Turkey. However, the gravimetry derived TWS signal is suggested to be validated by hydrological models or by drought indices. At this stage, drought indices, according to the sensibility of the indicator (e.g. to hydrological drought) may give a priori idea about the reason of the decrease. After performing a least-square adjustment to the data with an appropriate mathematical model (e.g. [24]) and obtaining the amplitude, phase (not shown here) and trend components, 2D sections of the interested parameter can be plotted to interpret spatially either the spatial distribution (amplitude) or spatial change (trend) of the drought. The same processing steps might be applied to hydrological model derived TWS data, to get the same plot and to validate the results. However, this give just a general overview about the distribution and do not contribute to our understanding about the possible causes. To comment, satellite based and in-situ precipitation plots should be associated and a joint interpretation is needed. If a forecasting is needed, then time series analysis methods can be used for this purpose with a proper test-train set choice having an impact on the forecasting results.

4. CONCLUSION

According to our finding, Turkey observe important drought periods in 09/2004, 09/2008 and 10/2014 and 11/2018. In the Eastern part and in coastlines, relatively more important anomalies are observed (20 cm) compared to the Central Anatolia having lower values (2 cm) according to GRACE and GRACE-FO amplitude sections. However, after processing more recent GRACE/GRACE-FO data, the range of the TWS data is observed to be smaller with a variation between 2-12 cm. This outlines a general decrease about the TWS in Turkey. The spatial distribution of the drought is primary controlled by the precipitation and by uncontrolled groundwater withdrawal from the Central Anatolia. However, the contrast between Eastern and Central part observed from GRACE-FO is less important compared to the ones observed from the former GRACE sections. There still exists a spatial change with a rate at about 1 cm/yr from Eastern part to Western part. Concerning, statistical prediction study, the preliminary results showed the adapted time series analysis method (Singular Spectrum Analysis: SSA) for forecasting over Turkey TWS time series. As perspective, drought monitoring with GRACE-FO and with up-to-date auxiliary data should continue. Besides, basin scales studies should also

have focused. In term of statistical predictions, with the new GRACE/GRACE-FO time series, this time by incorporating other data (e.g. precipitation) and other strategies for test-train data sets selection, a multivariate statistical prediction is envisaged.

REFERENCES

1. Drought in eastern Mediterranean worst of past 900 years. Available online: https://climate.nasa.gov/news/2408/drought-in-eastern-mediterranean-worst-of-past-900-years/ (accessed on 01.11.2019)

2. Kurnaz, L. Drought in Turkey, Istanbul Policy center, Sabancı University, 1–4, 2014.

3. Rodell, M.; Houser, P.R.; Jambor, U.; Gottschalck, J.; Mitchell, K.; Meng, C.J; Arsenault, K.; Cosgrove, B.; Radakovich, J.; Bosilovich, M.; Entin, J.K.; Walker, J.P.; Lohmann, D.; Toll, D. The Global Land Data Assimilation System. Bull. Am. Meteorol. Soc.2004, 85(3), 381-394.

4. Koren, V.; Schaake, J.; Mitchell, K.; Duan, Q.Y.; Chen, F.; Baker, J.M. A parameterization of snowpack and frozen ground intended for NCEP weather and climate models. J. Geophys. Res. Atmos.1999, 104(D16), 19569-19585.

5. Koster, R.D; Suarez, M.J. Energy and Water Balance Calculations in the Mosaic LSM United States: Greenbelt, Maryland : National Aeronautics and Space Administration, Goddard Space Flight Center, Laboratory for Atmospheres, Data Assimilation Office : Laboratory for Hydrospheric Processes, 1996.

6. Liang, X.; Lettenmaier, D.P.; Wood, E.F. One-dimensional statistical dynamic representation of subgrid spatial variability of precipitation in the two-layer variable infiltration capacity model. J. Geophys. Res. Atmos.1996, 101(D16), 21403-21422.

7. Dai, Y.; Zeng, X.; Dickinson, R.E.; Baker, I.; Bonan, G.B.; Bosilovich, M.G.; Denning, A.S.; Dirmeyer, P.A.; Houser, P.R.; Niu, G.; Oleson, K.W.; Schlosser, C.A.; Yang, Z.L. The common land model. Bull. Am. Meteorol. Soc.2003, 84(8), 1013-1024.

8. Huffman, G.J.; Bolvin, D.T.; Braithwaite, D.; Hsu, K.; Joyce, R.; Kidd, C.; Nelkin, E.J.; Sorooshian, S.; Tan, T.; Xie, P. Algorithm Theoretical Basis Document (ATBD) Version 5.2 NASA - NASA Global Precipitation Measurement (GPM) Integrated Multi-satellitE Retrievals for GPM (IMERG) - Algorithm Theoretical Basis Document (ATBD) Version 5.2 IMERG Algorithm Theor. Basis Doc.2018

9. Atayer, E.S. Yeryuvarı Gravite alanının aylık GRACE çözümleri ile izlenmesi ve duyarlılığı üzerine bir inceleme. MSc, Yıldız Teknik University, Istanbul, 2012.

10. Lenk, O. Satellite based estimates of terrestrial water storage variations in Turkey. J.

Geodyn. 2013, 67**,** 106–110.

11. Yıldırım, Y.Ö. GRACE uydu verileri ile Türkiye'nin uzun dönemli su kütle değişiminin incelenmesi. MSc, Gebze Technical University, Kocaeli, 2015

12. Ahi, G.O.; Jin, S. Hydrologic mass changes and their implications in Mediterranean-climate Turkey from GRACE measurements. Remote Sens., 2019, 11(2), 120.

13. Cazenave, A.; Chen, J. Time-variable gravity from space and present-day mass redistribution in the Earth system. Earth Planet. Sci. Lett., 2010, 298, 263–274.

14. Liesch, T; Ohmer, M. Comparison of GRACE data and groundwater levels for the assessment of groundwater depletion in Jordan. Hydrogeol. J., 2016, 24(6), 1547-1563.

15. Feng, W.; Shum, C.K; Zhong, M.; Pan, Y. Groundwater storage changes in China from satellite gravity: An overview. Remote Sens., 2018, 10(5), 674.

16. Henry, C.M.; Allen, D.M.; Huang, J. Groundwater storage variability and annual recharge using well-hydrograph and GRACE satellite data. Hydrogeol. J., 2011, 19(4), 741-755.

17. Huang, J.; Halpenny, J.; Van Der Wal, W.; Klatt, C.; James, T.S.; Rivera, A. Detectability of groundwater storage change within the Great Lakes Water Basin using GRACE. J. Geophys. Res. Solid Earth, 2012, 117(B8).

18. Huang, J.; Pavlic, G.; Rivera, A.; Palombi, D.; Smerdon, B. Mapping groundwater storage variations with GRACE: a case study in Alberta, Canada. Hydrogeol. J., 2016, 24(7), 1663-1680.

19. Chao, N.; Luo, Z.; Wang, Z.; Jin, T. Retrieving Groundwater Depletion and Drought in the Tigris-Euphrates Basin Between 2003 and 2015. Groundwater, 2018, 56(5), 770-782

20. Voss, K.A.; Famiglietti, J.S.; Lo, M.; De Linage, C.; Rodell, M.; Swenson, S.C. Groundwater depletion in the Middle East from GRACE with implications for transboundary water management in the Tigris-Euphrates-Western Iran region. Water Resour. Res., 2013, 49, 904–914.

21. Yilmaz, M.T.; Karasu, I.G.; Yilmaz, K.K.; Tufekci-Avsar, N.; Selek, B.; Aras, M.; Ozaltin, A.M.; Duygu, M.B.; Kirmencioglu, B. Analysis Of Terrestrial Water Storage Change Using Grace-Based Observations Over Euphrates-Tigris Basin. Türkiye Ulusal Jeodezi ve Jeofizik Birliği Bilimsel Kongresi, 30 Mayıs – 2 Haziran 2018, İzmir.

22. Joodaki, G.; Wahr, J.; Swenson, S.; Estimating the human contribution to groundwater depletion in the Middle East, from GRACE data, land surface models, and well observations. Water Resour. Res., 2014, 50(3), 2679-2692.

23. Ahi, G.O.; Çekim, H.Ö. GRACE Uydusu Zaman Serisinin İstatiksel Yaklaşımlarla Kestirimi. Harit. Derg., 2019, 162, 25–35.

24. Jin, S.; Park, J.U.; Cho, J.H.; Park, P.H. Seasonal variability of GPS-derived zenith tropospheric delay (1994-2006) and climate implications. J. Geophys. Res. Atmos., 2007, 112 D09110.

Multi-GNSS Contribution to Single-Frequency Precise Point Positioning

Berkay Bahadur[1], Metin Nohutcu[1]

[1] Hacettepe University, Department of Geomatics Engineering, 06800 Ankara, Turkey,
Phone: +90 312 297 6990, E-mail: berkaybahadur@hacettepe.edu.tr,
mnohutcu@hacettepe.edu.tr

ABSTRACT

Over the past decade, Precise Point Positioning (PPP) has been a highly popular topic within the Global Navigation Satellite System (GNSS) community because of its unprecedented benefits such as operational simplicity, cost-effectiveness, elimination of base station requirements, etc. The traditional PPP approach employs the dual-frequency ionosphere-free combination of code and phase measurements. However, the number of dual-frequency GNSS receivers which are mostly used in geodetic applications requiring high positioning accuracy is quite limited. On the other hand, single-frequency GNSS receivers still dominate the GNSS market due to their considerably low costs. Therefore, single-frequency PPP (SF-PPP) has been increasingly taking attention in GNSS-related researches. Nevertheless, the positioning accuracy obtained from SF-PPP is mainly dependent on the number of available satellites. In recent years, the emergence of new navigation systems, e.g. Galileo and BeiDou, together with the completion of the GLONASS constellation provides important opportunities to enhance the positioning performance of SF-PPP. In this context, the main objective of this study is to evaluate the contribution of multi-GNSS integration that includes GPS, GLONASS, Galileo and BeiDou satellites to the SF-PPP performance. For this purpose, the SF-PPP model used in the study, which is based on the single-frequency ionosphere-free combination of code and phase measurements (GRAPHIC) is presented firstly. The related model also comprises the approach utilized to combine multi-constellation data. The study also includes an experimental test in which daily observation datasets collected at five IGS stations during the 1-week period of August 25–31, 2019 were processed under two different modes; GPS-only and multi-GNSS SF-PPP. Then, the solutions of two PPP modes were statistically analyzed in terms of positioning accuracy and convergence time. The results indicate that the integration of four constellations improves the positioning performance of SF-PPP considerably in comparison with the GPS-only mode.

KEYWORDS: Multi-GNSS; PPP; Single-frequency, GRAPHIC

1. INTRODUCTION

Precise Point Positioning (PPP) is a positioning technique that enables centimeter- or millimeter-level positioning accuracy on a global scale using a single receiver only [1,2]. The main strength of PPP lies behind the employment of precise orbit and clock products obtained from a global network, e.g. International GNSS Service (IGS). Typically, PPP employs the ionosphere-free combination of dual-frequency code and phase observations to mitigate ionospheric delay on GNSS signals. Currently, PPP is a powerful tool for a lot of geoscience applications, such as atmospheric sensing, geohazard monitoring, structural health monitoring, aerial triangulation, etc. [3–7]. In recent years, implementation of the PPP method with single-frequency receivers, which are still dominant in the GNSS market, has been attracting considerable interest due to their low costs.

For single-frequency GNSS users, mitigation of ionospheric delays is one of the critical issues since it is not possible to use dual-frequency ionosphere-free combinations. There are several approaches to mitigate ionospheric delays in SF-PPP. The first approach is to employ the ionosphere models, such as the Klobuchar model [8] and its refined versions [9–11], NeQuick model [12], NTCM model [13], etc., however, their accuracies are not decent enough to reach relatively high-accurate positioning solution. On the other hand, Global Ionosphere Maps (GIMs), which are provided by different analysis centers of IGS, is another option to eliminate ionospheric delay for single-frequency users. However, final GIMs, which typically have an accuracy of 2–8 TECU (Total Electron Content Unit) can be acquired only with a latency 1-14 days and they cannot be employed in real-time positioning solutions [14]. Finally, single-frequency ionosphere-free observable, i.e. Group and Phase Ionospheric Correction (GRAPHIC) combination, is able to eliminate the ionospheric delays without any external data or correction [15,16]. Since GRAPHIC combination, which is formed by combining code and phase observations, contains the non-integer phase ambiguity parameter, it requires a relatively long initial time to converge a sufficient accuracy. Still, the GRAPHIC combination can provide higher positioning accuracy in comparison with the other ionospheric mitigation approaches [17,18], so it is utilized to eliminate the ionospheric delays in this study.

In recent years, the GNSS community has been facing significant changes with the advent of new navigation systems, such as Galileo and BeiDou, in addition to the completion of GLONASS constellation. The integration of multi-constellation has offered considerable

opportunities to improve positioning performance as it provides additional satellite and signal sources for positioning, navigation and timing applications. Recent studies have concluded that the combinations of multi-GNSS improve the positioning performance of PPP significantly in terms of positioning accuracy and convergence time [19¬21]. At the same time, the positioning performance of SF-PPP can be enhanced with the integration of multi-constellation because the limited number of visible satellites is one of the factors restricting the positioning performance of SF-PPP in most cases.

Consequently, the main objective of this study is to assess the contribution of multi-GNSS integration, which includes GPS, GLONASS, Galileo and BeiDou satellites, to the SF-PPP performance. In this study, we mainly focus on how the increasing number of satellites influences the positioning performance of SF-PPP in both static and kinematic processing modes. In this context, this study constitutes an introduction of the multi-GNSS SF-PPP model that is based on the GRAPHIC combination as well as the presentation of the results obtained from an experimental test to evaluate the SF-PPP performance under GPS-only and multi-GNSS scenarios.

2. MULTI-GNSS SINGLE-FREQUENCY PPP MODEL

Code pseudorange (P) and carrier phase (L) observation equations can be written as follows:

$$P_{i,r}^{s,j} = \rho_r^{s,j} + cdt_r^s - cdT^{s,j} + T_r^{s,j} + I_i^{s,j} + b_{i,r}^s - b_i^{s,j} + \varepsilon(P_{i,r}^{s,j}), \quad (1)$$

$$L_{i,r}^{s,j} = \rho_r^{s,j} + cdt_r^s - cdT^{s,j} + T_r^{s,j} - I_i^{s,j} + \lambda_i^s N_i^{s,j} + B_{i,r}^s - B_i^{s,j} + \varepsilon(L_{i,r}^{s,j}), \quad (2)$$

where subscripts r and i indicate the receiver and the frequency index of navigation signal, respectively; superscripts s and j indicate the GNSS index (G: GPS, R: GLONASS, E: Galileo and C: BeiDou) and the satellite number, respectively. Moreover, $\rho_r^{s,j}$ is the geometric range, c is the speed of light; cdt_r^s and $cdT^{s,j}$ are the receiver and satellite clock offsets, respectively; $T_r^{s,j}$ is the tropospheric delay; $I_i^{s,j}$ is the first-order ionospheric delay on frequency i; $b_{i,r}^s$ and $b_i^{s,j}$ are the receiver and satellite code hardware biases on frequency i; $B_{i,r}^s$ and $B_i^{s,j}$ are the receiver and satellite phase hardware biases on frequency i, respectively; $N_i^{s,j}$ is the integer ambiguity parameter; λ_i^s is the wavelength of the corresponding frequency; and ε is the observation noise.

GRAPHIC combination can be formed by

$$\Phi_{i,r}^{s,j} = \frac{P_{i,r}^{s,j} + L_{i,r}^{s,j}}{2} \tag{3}$$

$$\Phi_{i,r}^{s,j} = \rho_r^{s,j} + cdt_r^s - cdT^{s,j} + T_r^{s,j} + \frac{\lambda_i^s N_i^{s,j}}{2} + \frac{\left(b_{i,r}^s - b_i^{s,j}\right)}{2} + \frac{\left(B_{i,r}^s - B_i^{s,j}\right)}{2} + \varepsilon\left(\Phi_{i,r}^{s,j}\right) \tag{4}$$

In general, precise products generated by IGS are used to eliminate the satellite orbit and clock errors in the SF-PPP model. In recent years, IGS has started to produce precise orbit and clock products for newly emerging satellite systems as a part of the Multi-GNSS Experiment Project (MGEX) [22]. Thanks to MGEX's precise products generated in the same reference system and timescale, integration of multi-constellation has been possible. Similar to the standard IGS products, MGEX products are also generated depending on dual-frequency ionosphere-free combinations of code and phase observations [23]. Therefore, the satellite clock corrections provided by IGS include the code hardware biases of the ionosphere-free combination ($b_{IF}^{s,j}$). On the other hand, the receiver hardware biases are traditionally assimilated into the receiver clock errors because of their high-correlation. Consequently, after applying precise orbit and clock corrections, we can reorganize Equation 4 as follows:

$$\Phi_{i,r}^{s,j} = \rho_r^{s,j} + \widetilde{cdt_r^s} + T_r^{s,j} + \widetilde{N_i^{s,j}} + \varepsilon\left(\Phi_{i,r}^{s,j}\right) \tag{5}$$

$$\widetilde{cdt_r^s} = cdt_r^s + \frac{\left(b_{i,r}^s + B_{i,r}^s\right)}{2} \tag{6}$$

$$\widetilde{N_i^{s,j}} = \frac{\lambda_i^s N_i^{s,j}}{2} - \frac{\left(b_i^{s,j} + B_i^{s,j}\right)}{2} + b_{IF}^{s,j} \tag{7}$$

where $\widetilde{cdt_r^s}$ is the reorganized clock offset term and $\widetilde{N_i^{s,j}}$ is the float ambiguity parameter. As it can be seen in Equation 7, the float ambiguity parameter additionally contains the satellite code and phase hardware biases. Herein, the Differential Code Bias (DCB) products can be employed to correct the code hardware biases.

Equation 5 includes different receiver clock offset parameters for each navigation system. Instead of estimating different receiver clock offsets, a more convenient way is to introduce the system time difference parameters for GLONASS, Galileo and BeiDou with respect to GPS clock offset. The reason lies behind is that most of the GNSS receivers currently use the GPS system time as a reference timescale and the satellite clock corrections produced by IGS are referred to the GPS time [24–26]. If the system time-difference parameters

($cdt_{sys}^{R}, cdt_{sys}^{E}, cdt_{sys}^{C}$) are introduced, the multi-GNSS SF-PPP model can be obtained as follows:

$$\Phi_{i,r}^{G,j} = \rho_r^{s,j} + \widetilde{cdt_r^G} + T_r^{s,j} + \widetilde{N_i^{s,j}} + \varepsilon\left(\Phi_{i,r}^{s,j}\right) \quad (8)$$

$$\Phi_{i,r}^{R,j} = \rho_r^{s,j} + \widetilde{cdt_r^G} + cdt_{sys}^{R} + T_r^{s,j} + \widetilde{N_i^{s,j}} + \varepsilon\left(\Phi_{i,r}^{s,j}\right) \quad (9)$$

$$\Phi_{i,r}^{E,j} = \rho_r^{s,j} + \widetilde{cdt_r^G} + cdt_{sys}^{E} + T_r^{s,j} + \widetilde{N_i^{s,j}} + \varepsilon\left(\Phi_{i,r}^{s,j}\right) \quad (10)$$

$$\Phi_{i,r}^{C,j} = \rho_r^{s,j} + \widetilde{cdt_r^G} + cdt_{sys}^{C} + T_r^{s,j} + \widetilde{N_i^{s,j}} + \varepsilon\left(\Phi_{i,r}^{s,j}\right) \quad (11)$$

In the model, the estimated parameters constitute the three-position components, one receiver clock bias, three system time-difference parameters, one tropospheric delay and one real-valued ambiguity parameter for each of the observed satellites.

3. TEST AND RESULTS

3.1 Data Description

In this study, 24-h observation dataset collected at five IGS MGEX stations during the 1-week period of August 25–31, 2019 were acquired from IGS servers. The related observation files contain both GPS, GLONASS, Galileo and BeiDou satellites. Figure 1 depicts the geographical locations of stations used in this study. Also, the observation sampling interval is 30-sec for each observation file. Furthermore, precise products generated by GFZ (GeoForschungsZentrum Potsdam), which is one of the MGEX analysis centers, were utilized in this study to eliminate the satellite orbit and clock products for multi-constellation. The sampling interval of satellite orbit and clock products are 300 and 30 seconds, respectively.

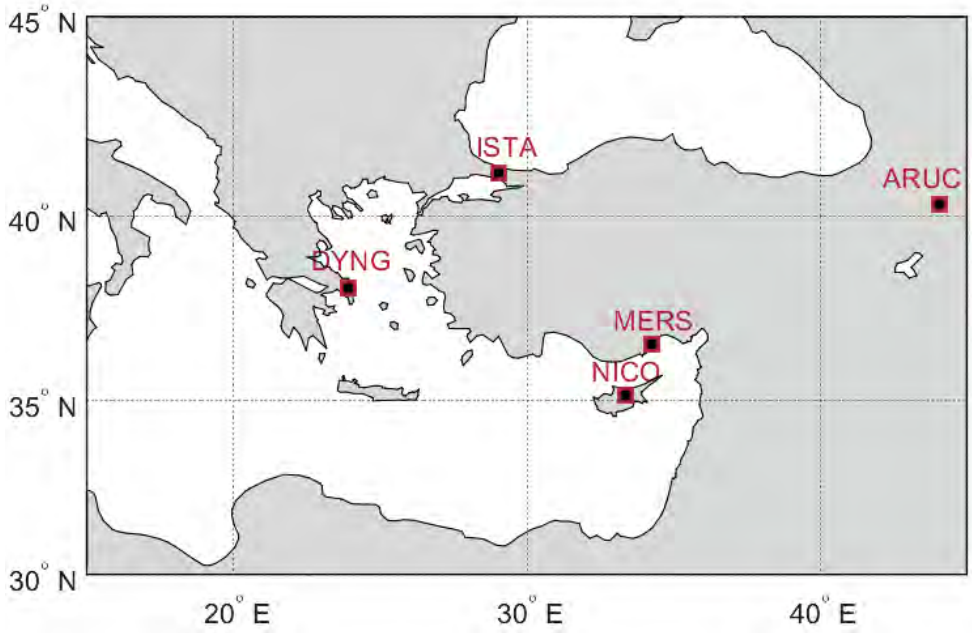

Figure 1. *Geographical locations of IGS stations used in this study.*

3.2 Processing Strategy

In this study, an extended version of PPPH [22], which is an open-source GNSS analysis software to integrate multi-constellation, was used to perform SF-PPP processes in static and kinematic modes. The processing strategies employed in the software are summarized in Table 1.

The position components are assumed to be constant in static mode, while spectral density values for position components are set as $10^2\ m^2/s$ for kinematic processes. The receiver clock and time-difference parameters are estimated as random walk (RW) process with a spectral density value of $10^5\ m^2/s$. The ambiguity parameters are estimated as floating numbers and they are assumed to be constant for each continuous arc. Furthermore, the tropospheric delay is typically separated into a dry (hydrostatic) and a wet (non-hydrostatic) part. The dry component of the tropospheric delay can be easily modeled at zenith direction and projected to the satellite elevation angle using a mapping function [27]. Therefore, only the wet component of the tropospheric delay is to be estimated as a RW process with a spectral density value of $10^{-9}\ m^2/$.

Table 1: PPP processing strategies applied in the study.

Constellation and related signals	GPS (G1), GLONASS (R1), Galileo (E1), and BeiDou (B1)
Processing mode	Static and kinematic
Satellite orbit and clock	Final GFZ products
Satellite antenna phase center offsets (PCOs) and its variations (PCVs)	IGS absolute antenna model (Antex)
Receiver antenna PCOs and PCVs	IGS absolute antenna model (Antex)
Troposphere	
Dry component	Modeled by Saastamoinen [27] with Global Pressure and Temperature 2 model [30]
Wet component	Estimated
Mapping function	Vienna Mapping Function [31]
Gradients	Not applied or estimated
Relativistic effects	Corrected [32]
Phase wind-up	Corrected [33]
Site displacements effects	Solid Earth tides and ocean loading are corrected [34]
Adjustment method	Extended Kalman filter
Elevation mask	8^{o}
Weighting method for observation	Elevation dependent (sin(el)), correlations ignored

Choosing appropriate stochastic characteristics for code and phase observations is an important point for SF-PPP. The GRAPHIC observation is a combination of original code and phase observations, which are assumed to be uncorrelated. Considering normal error propagation, the initial variances of GRAPHIC combination can be acquired from the original variances of code (σ_P^2) and phase (σ_L^2) observations and it is equal to $0.25\sigma_P^2 + 0.25\sigma_L^2 \cong 0.25\sigma_P^2$. The initial code variance for GPS satellites is set to 0.3 m. Since GLONASS code observations have a higher code noise level because of its lower code chipping rate [28] and satellite inter-frequency biases caused by the FDMA (Frequency Multiple Division Access) signal structure [29], the initial variances of GLONASS code observations are down-weighted and selected as 0.6 m. Also, initial variances of Galileo and BeiDou code observations are set to 0.6 m since their satellite orbit and clock products are assumed to be relatively lower than GPS satellites [22].

3.2 Experimental Test

This section presents the results of the experimental test that have been conducted to investigate the contribution of multi-GNSS to SF-PPP performance. Firstly, the observation dataset has been evaluated in terms of visible satellite numbers for GPS, GLONASS, Galileo, and BeiDou. Figure 2 indicates the average number of available satellites per epoch for quad-constellation as well as their minimum and maximum satellite numbers considering the whole epochs over the one week. The figure shows that GPS has the highest number of visible satellites in each station, and it still dominant constellation for GNSS applications. At the same time, it can be seen from the figure that the other systems provide considerable satellite resources, and it is clear that there is substantial potential to improve SF-PPP performance.

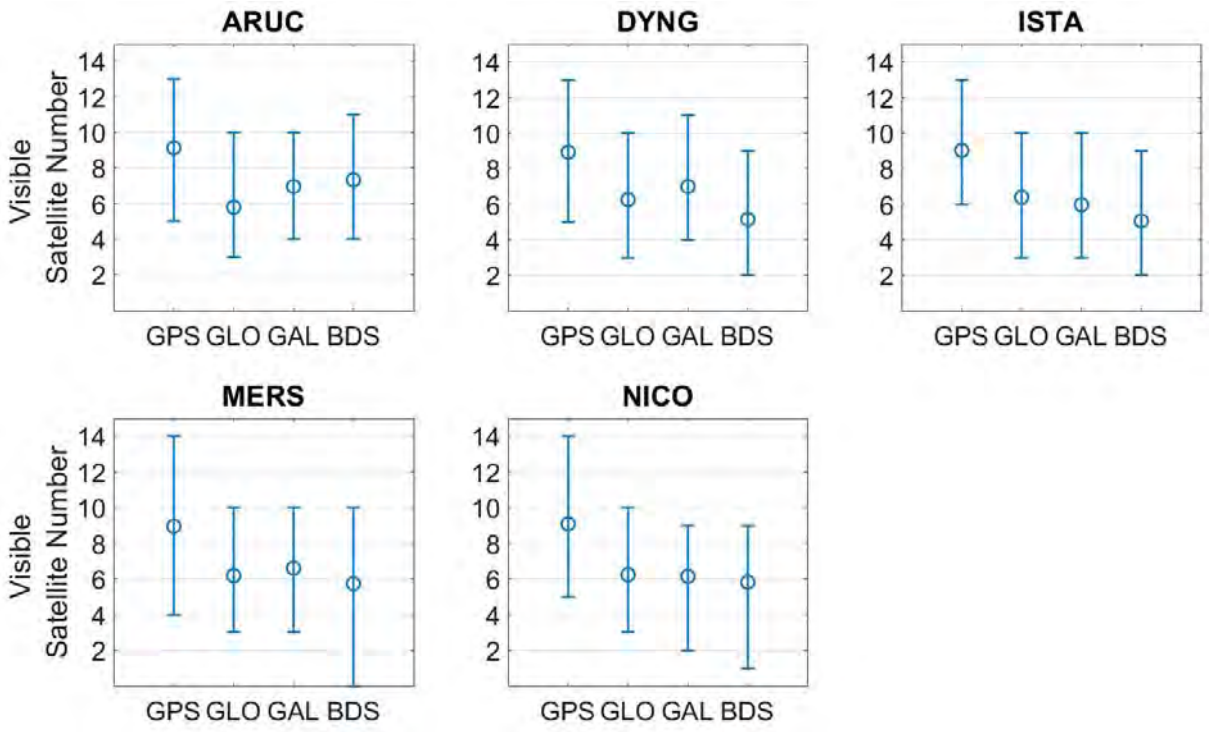

Figure 2. *Epoch-wise minimum, maximum and average numbers of visible satellites for GPS, GLONASS, Galileo and BeiDou in five IGS stations.*

The positioning solution obtained from SF-PPP processes in static mode under two different scenarios, GPS-only and multi-GNSS, are evaluated in terms of positioning accuracy. In this

study, the coordinate difference between the position obtained from the corresponding PPP solution and ground truth is referred to as the positioning error, where precise station coordinates from IGS weekly solutions were assumed as the ground truth. Note that the positioning errors were calculated in the local coordinate system (north, east and up directions).

Figure 3 depicts the positioning errors in the north, east and up directions for GPS-only and multi-GNSS solutions in static mode at ARUC station on August 25, 2019. From the figure, it can be seen that positioning errors decrease with the integration of multi-constellation. The multi-GNSS has significantly improved the SF-PPP performance of GPS-only processing mode in the short observation periods, especially in two hours. This figure summarizes the impact of multi-GNSS on the SF-PPP performance basically.

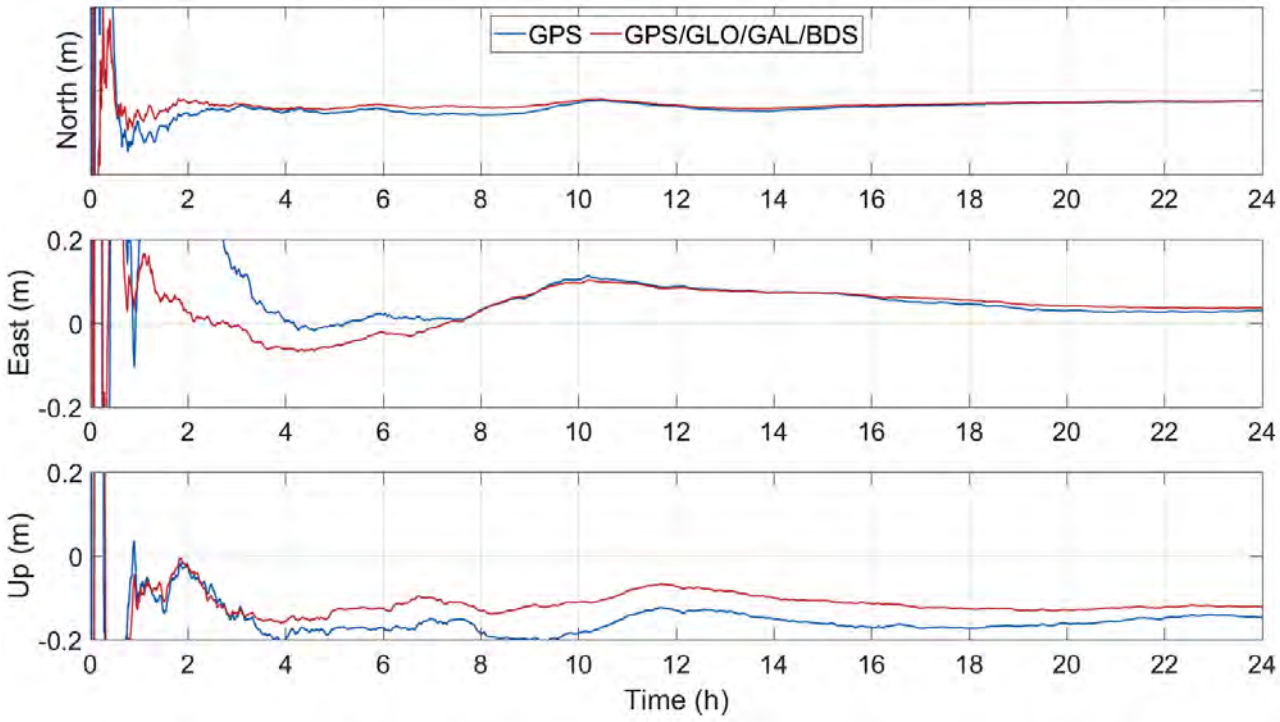

Figure 3. *Static SF-PPP positioning errors for GPS-only and multi-GNSS processing modes at ARUC station on August 25, 2019.*

Table 2 provides the root mean square (RMS) values for positioning errors in the north, east and up directions as well as the 3D positioning errors with different observation lengths of 15 min, 30 min, 1 hour, 2 hours, 4 hours, 8 hours, 12 hours and 24 hours. RMS values are computed considering the whole SF-PPP solutions for all the stations during the one week. Besides, the

table presents the improvement percentages in the 3D positioning errors for the multi-GNSS SF-PPP solutions in comparison with that of GPS-only solutions. The results show that the increase in observation lengths enhances SF-PPP performance in all components. Also, the use of additional satellites, multi-GNSS, substantially improves the positioning accuracy for all observation lengths. Multi-GNSS SF-PPP improves the 3D positioning accuracy of GPS-only solution by a rate of 40% at the end of the first hour, whereas the rate decreases to 5.3% after a four-hour observation length. From the table, it is concluded that the improvement percentage is higher in the short observation lengths, especially within the two hours.

Table 2: RMS values of positioning errors obtained from static SF-PPP solutions under GPS-only and multi-GNSS modes with different observation lengths and their improvements compared with GPS-only SF-PPP solutions.

GPS-Only	**15 min**	**30 min**	**1 h**	**2 h**	**4 h**	**8 h**	**12 h**	**24 h**
North (m)	0.5298	0.2434	0.0939	0.0412	0.0228	0.0232	0.0187	0.0138
East (m)	1.9666	0.8548	0.3535	0.3040	0.0494	0.0276	0.0587	0.0370
Up (m)	1.3668	0.5543	0.2187	0.2051	0.1055	0.0917	0.0653	0.0548
3D (m)	2.4528	1.0475	0.4261	0.3691	0.1187	0.0985	0.0898	0.0675
Multi-GNSS	**15 min**	**30 min**	**1 h**	**2 h**	**4 h**	**8 h**	**12 h**	**24 h**
North (m)	0.3654	0.1547	0.0639	0.0244	0.0206	0.0188	0.0174	0.0163
East (m)	0.8151	0.2835	0.1239	0.0965	0.0476	0.0264	0.0553	0.0365
Up (m)	1.1682	0.4762	0.1491	0.1294	0.0997	0.0869	0.0583	0.0537
3D (m)	1.4706	0.5754	0.2041	0.1633	0.1124	0.0928	0.0818	0.0629
3D Positioning Improvement (%)	40.0	45.1	52.1	55.8	5.3	5.9	8.9	6.9

Figure 4 shows the distribution of positioning errors in the north, east and up directions for GPS-only and multi-GNSS solutions taking the whole epochs into account. In other words, the figure indicates the distribution of positioning errors obtained from total 100800 epochs. Instead of frequencies, the figure depicts the probability percentages computed from the ratio of frequencies to the total number of epochs. For the GPS-only SF-PPP solutions, the absolute means of positioning errors are 3.48, 10.15 and 10.22 cm in the north, east and up directions, whereas corresponding values for the multi-GNSS SF-PPP solutions are 2.86, 7.07 and 8.58

cm, respectively. Also, the RMS values for GPS-only solutions are computed as 22.98, 43.72 and 40.74 cm, while the RMS values for multi-GNSS solutions are 14.73, 19.37 and 28.17 cm. From these results, it can be concluded that the integration of multi-constellation enhances the SF-PPP performance considerably in static solutions.

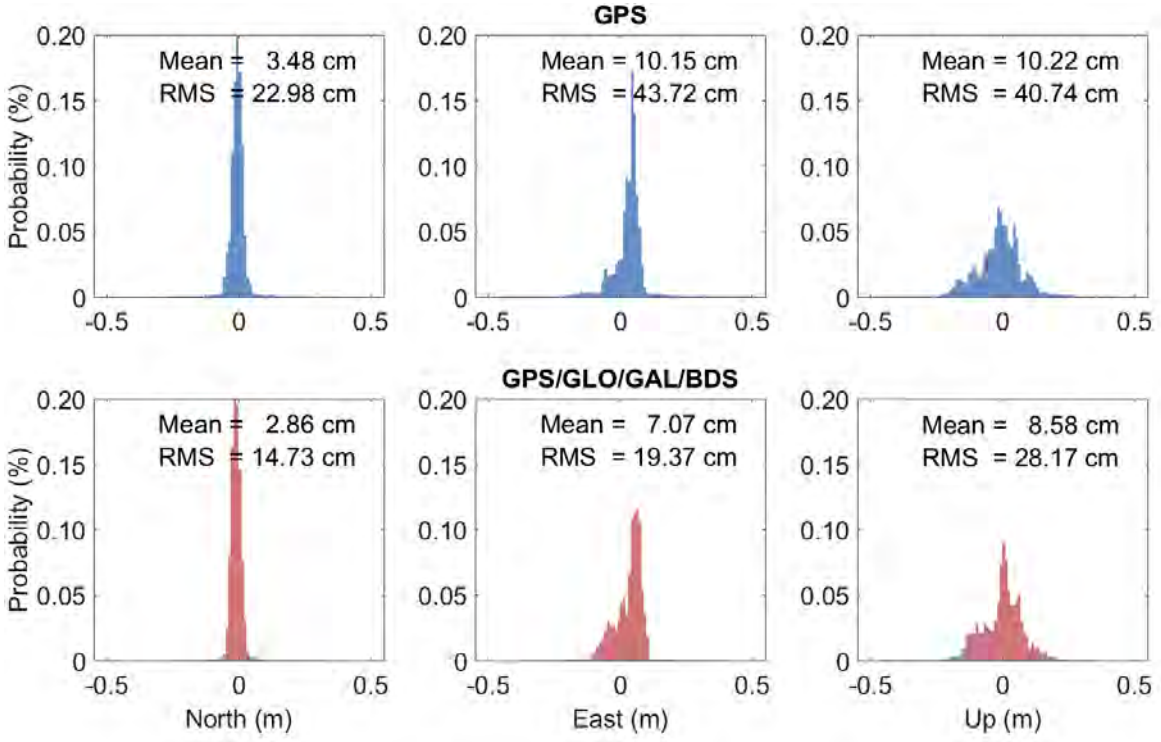

Figure 4. *Distribution of epoch-wise positioning errors in the north, east and up directions for static GPS-only and Multi-GNSS SF-PPP solutions.*

Also, the same dataset used in static processes were processed also in the kinematic mode under GPS-only and multi-GNSS SF-PPP scenarios. Similarly, Figure 5 shows the positioning errors in the north, east and up directions for GPS-only and multi-GNSS solutions in kinematic mode at ARUC station on August 25, 2019. From the figure, it can be seen that the positioning errors of the multi-GNSS solution are lower than those of GPS-only solutions. In order to evaluate the contribution of multi-constellation in more detail, the distribution of positioning errors for the whole epochs is depicted in Figure 6. In a similar way, the probability percentages acquired from the proportion of frequencies to the total number of epochs. The absolute mean positioning errors of GPS-only kinematic solutions are 18.49, 23.79 and 32.43 cm in the north, east and up directions. These errors are computed as 9.5, 11.22 and 19.56 cm for multi-GNSS kinematic

solutions. While the RMS values of GPS-only kinematic solutions are equal to 47.96, 63.63 and 78.89 cm in the north, east and up directions, they are 19.70, 24.23 and 36,69 for the multi-GNSS kinematic solutions. Consequently, it can be said that the combination of multi-constellation contributes to the SF-PPP performance in both static and kinematic modes significantly.

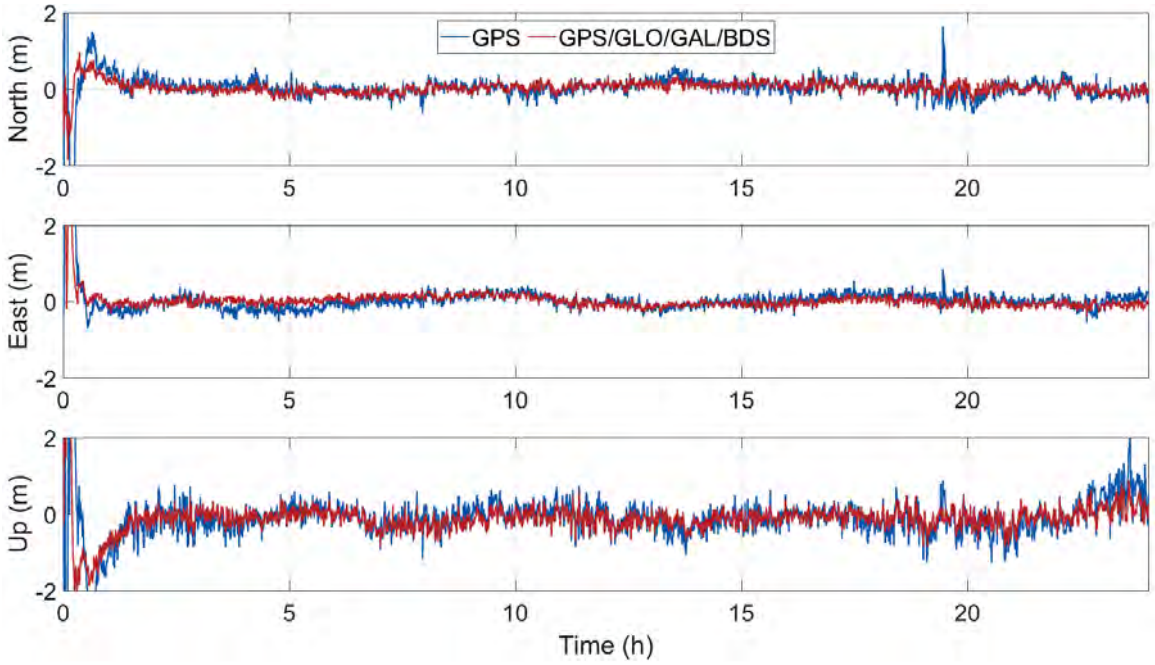

Figure 5. *Kinematic SF-PPP positioning errors for GPS-only and multi-GNSS processing modes at ARUC station on August 25, 2019.*

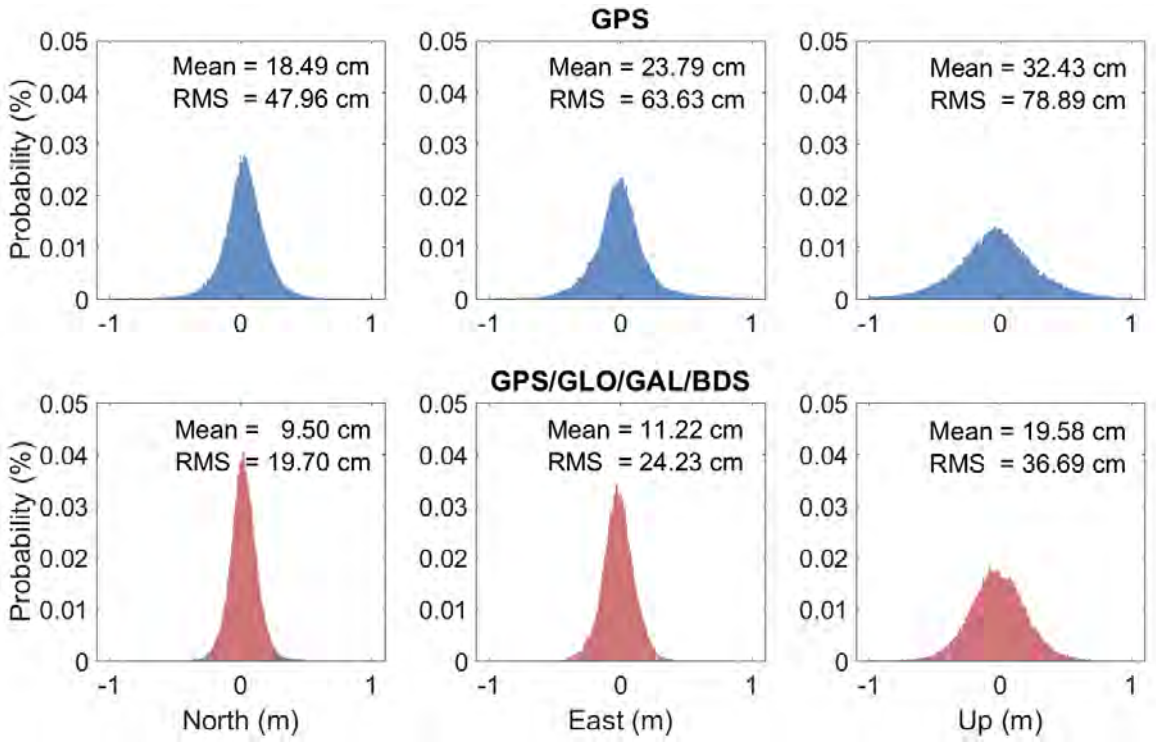

Figure 6. *Distribution of epoch-wise positioning errors in the north, east and up directions for kinematic GPS-only and Multi-GNSS SF-PPP solutions.*

4. CONCLUSIONS

Single-frequency PPP has been attracting a lot of attention within the GNSS community because it can provide relatively high positioning accuracy with low-cost receivers. Still, SF-PPP requires an initial time to achieve sufficient positioning accuracy due to the convergence of the non-integer ambiguity parameter. In recent years, the emergence of new satellite systems and completion of the GLONASS constellation offer considerable opportunities to enhance the SF-PPP performance because of providing additional satellites and signals. The main objective of this study is to assess the contribution of multi-GNSS to SF-PPP performance.

In this study, an experimental test containing 24-hour observation datasets collected at five IGS stations over 7 consecutive days between 25-31 August 2019 was conducted. Firstly, the dataset was analyzed in terms of the number of visible satellites for GPS, GLONASS, Galileo, and BeiDou. The evaluation showed that GPS is still the dominant constellation but the other system can provide additional satellites substantially. The results also indicate that the combination of

multi-GNSS increases the positioning accuracy of GPS-only SF-PPP solutions. In static processing, the mean absolute errors of GPS-only solutions were reduced from 3.48, 10.15 and 10.22 cm to 2.86, 7.07 and 8.58 cm in the north, east and up directions with the integration of multi-constellation. For kinematic processing, the improvements were from 18.49, 23.79 and 32.43 cm to 9.5, 11.22 and 19.56 cm in the north, east and up directions, respectively. On the other hand, the RMS values of positioning errors were improved by integrating multi-constellation, especially in the short observation lengths. Improvement percentages of multi-GNSS were between 40 and 52% within the first two hours, while the improvement percentage decreased under 10% at the end of the day. Consequently, this study concludes that the integration of multi-GNSS has contributed to SF-PPP positioning performance significantly.

ACKNOWLEDGEMENT

This study was supported by TUBITAK CAYDAG under Project No. 118Y410.

REFERENCES

1. Zumberge, J.F., Heflin, M.B., Jefferson, D.C., Watkins, M.M., Webb, F.H. Precise point positioning for the efficient and robust analysis of GPS data from large networks. J. Geophys. Res.-Solid Earth. 1997, 102 (B3), 5005-5017.

2. Kouba, J., Héroux, P. Precise Point Positioning Using IGS Orbit and Clock Products. GPS Solut. 2001, 5 (2), 12-28.

3. Hernández-Pajares, M., Roma-Dollase, D., Garcia-Fernàndez, M. et al. Precise ionospheric electron content monitoring from single-frequency GPS receivers. GPS Solut. 2018, 22:102.

4. Krietemeyer, A., Ten Veldhuis, M-C., Van der Marel, H., Realini, E., van de Giesen, N. Potential of Cost-Efficient Single Frequency GNSS Receivers for Water Vapor Monitoring. Remote Sens. 2018, 10 (9), 1493.

5. Paziewski, J., Sieradzki, R., Baryla, R. Multi-GNSS high-rate RTK, PPP and novel direct phase observation processing method: application to precise dynamic displacement detection. Meas Sci Technol. 2018, 29 035002.

6. Yigit, C.O., Gurlek, E. Experimental testing of high-rate GNSS precise point positioning (PPP) method for detecting dynamic vertical displacement response of engineering structures. Geomat Nat Hazards Risk. 2017, 8 (2), 893–904.

7. Shi, J., Yuan, X., Cai, Y., Wang, G. GPS real-time precise point positioning for aerial triangulation. GPS Solut. 2017, 21 (2), 405-414.

8. Klobuchar, J. A. Ionospheric time-delay algorithm for single-frequency GPS users. IEEE Trans Aerosp Electron Syst. 1987, 23(3), 325–332.

9. Yuan, Y., Huo, X., Ou, J., Zhang, K., Chai, Y., Wen, D., Grenfell, R. Refining the Klobuchar ionospheric coefficients based on GPS observations. IEEE Trans Aerosp Electron Syst. 2008, 44(4), 1498–1510.

10. Bi, T., An, J., Yang, J., Liu, S. A modified Klobuchar model for single-frequency GNSS users over the polar region. Adv Space Res. 2017, 59(3), 833–842.

11. Chen, J., Huang, L., Liu, L., Wu, P., Qin, X. Applicability analysis of VTEC derived from the sophisticated Klobuchar model in China. ISPRS Int J Geo-Inf. 2017, 6(3), 75.

12. Nava, B., Coïsson, P., Radicella, S.M. A new version of the NeQuick ionosphere electron density model. J Atmos Terr Phys. 2008, 70(15), 1856–1862.

13. Hoque, M.M., Jakowski, N. An alternative ionospheric correction model for global navigation satellite systems. J Geod. 2015, 89(4), 391–406.

14. Roma-Dollase, D., Hernández-Pajares, M., Krankowski, A., Kotulak, K., Ghoddousi-Fard, R. et al. Consistency of seven different GNSS global ionospheric mapping techniques during one solar cycle. J Geod. 2018, 92(6), 691–706.

15. Yunck, T.P. Coping with the atmosphere and ionosphere in precise satellite and ground positioning, Washington DC. Am Geophys Union Geophys Monogr Ser. 1993, 73, 1–16.

16. Choy, S.L. An investigation into the accuracy of single frequency precise point positioning. Ph.D. thesis. RMIT University, Australia.

17. Cai, C., Liu, Z., Luo, X. Single-frequency ionosphere-free precise point positioning using combined GPS and GLONASS observations. J. Navig. 2013, 66, 417–434.

18. Montenbruck, O. Kinematic GPS positioning of LEO satellites using ionosphere-free single frequency measurements. Aerosp. Sci. Technol. 2003, 7, 396–405.

19. Cai, C., Gao, Y., Pan, L., Zhu, J. Precise point positioning with quadconstellations: GPS, BeiDou, GLONASS, and Galileo. Adv. Space Res. 2015, 56 (1), 133–143.

20. Tegedor, J., Øvstedal, O., Vigen, E. Precise orbit determination and point positioning using GPS, GLONASS, Galileo and BeiDou. J. Geod. Sci., 2014, 4 (1), 65–73.

21. Bahadur, B., Nohutcu, M. PPPH: a MATLAB-based software for multi-GNSS precise point positioning analysis. GPS Solut., 2018, 22:113.

22. Montenbruck, O., Steigenberger, P., Prange, L., Deng, Z., Zhao, Q., Perosanz, F., Romero, I., Noll, C., Stürze, A., Weber, G., Schmid, R., MacLeod, K., Schaer, S. The Multi-GNSS Experiment (MGEX) of the International GNSS Service (IGS) – Achievements, prospects and challenges. Adv. Space Res. 2017, 59 (7), 1671-1697.

23. Steigenberger, P., Hugentobler, U., Loyer, S., Perosanz, F., Prange, L., Dach, R., Uhlemann, M., Gendt, G., Montenbruck, O. Galileo orbit and clock quality of the IGS Multi-GNSS Experiment. Adv. Space Res. 2015, 55 (1), 269-281.

24. Cai, C., Gao, Y. Modeling and assessment of combined GPS/GLONASS precise point positioning. GPS Solut. 2013, 17 (2), 223-236.

25. Li, X., Ge, M., Dai, X., Ren, X., Fritsche, M., Wickert, J., Schuh, H. Accuracy and reliability of multi-GNSS real-time precise positioning: GPS, GLONASS, BeiDou, and Galileo. J. Geodesy. 2015, 89 (6), 607-635.

26. Abd Rabbou, M., El-Shazly, A., Ahmed, K. Comparative analysis of multi-constellation GNSS single-frequency precise point positioning. Surv. Rev. 2018, 50 (361), 373-382.

27. Saastamoinen, J. Contributions to the theory of atmospheric refraction. Bull. Geod. 1972, 105 (1), 279–298.

28. Hauschild, A., Montenbruck, O., Sleewaegen, J.M., Huisman, L. and Teunissen, P.J.G. Characterization of Compass M-1 signals. GPS Solut. 2012, 16(1), 117–126.

29. Wanninger, L. Carrier-phase inter-frequency biases of GLONASS receivers, J. Geodesy. 2012, 86 (2) 139-148.

30. Lagler, K., Schindelegger, M., Böhm, J., Krásná, H., Nilsson, T. GPT2: Empirical slant delay model for radio space geodetic techniques. Geophys. Res. Lett. 2013, 40 (6),1069-1073.

31. Böhm, J., Werl, B., Schuh, H. Troposphere mapping functions for GPS and Very Long Baseline Interferometry from European Centre for Medium-Range Weather Forecasts operational analysis data, J. Geophys. Res. 2006, 111, B02406.

32. Kouba, J., Héroux, P. Precise Point Positioning Using IGS Orbit and Clock Products. GPS Solut. 2001, 5 (2), 12-28.

33. Xu, P., Shi, C., Fang, R., Liu, J., Niu, X., Zhang, Q., Yanagidani, T. High-rate Precise Point Positioning (PPP) to measure seismic wave motions: an experimental comparison of GPS PPP with inertial measurement units. J. Geodesy. 2013, 87 (4), 361-372.

34. Petit, G., Luzum, B. IERS Conventions 2010, IERS Technical Note 36, Frankfurt am Main: Verlag des Bundesamts für Kartographie und Geodäsie, 2010, 179 pp., ISBN 3-89888-989-6.

Methodology Assessment on Orbit Determination of LEO Satellites in Purpose of Global Geopotential Model Validation

Rewa Alkahal[1], Bihter Erol[2]

[1]Istanbul Technical University, Geomatics Engineering Department 34469 Istanbul, Turkey
E-mail: alkahal15@itu.edu.tr

[2]Istanbul Technical University, Geomatics Engineering Department 34469 Istanbul, Turkey
Phone: +90 212 285 3414, E-mail: bihter@itu.edu.tr

ABSTRACT

The determination of Earth's gravity field, vertical datum and height unification, geophysical and geodynamical phenomena have become reliant on the Global Geopotential Models. These models are generally derived by satellite-only, terrestrial, or combined data. An assessment of these global geopotential models is essential to determine their accuracy to be used in various applications. Therefore, models derived specific parameters may be assessed by the comparison with other conventionally derived parameters. However, precise orbit determination for the validation of global geopotential models has been approved in theory. The accuracy of Earth's gravity field depends potentially on the orbit of the satellite's mission. Conversely, the determination of satellites orbits is affected by the accuracy of the gravitational forces, and merely on the gravity field models that represent the effect of Earth's gravity. Particularly, the harmonic expansion of the models is employed in measuring gravitational perturbations in the dynamic orbits determination procedure. In this study, the validation of Earth's gravity field models by precise orbit determination is discussed. Additionally, the effects of perturbation potential on the orbital elements are analyzed by modeling the orbital motion of Gravity Field and Steady-State Ocean Circulation Explorer (GOCE) satellite mission by the short arc approach. Which is, in this case, half of one revolution of the satellite – 45 minutes. Applying numerical integration methods, a single-step Runge Kutta method, and a multistep Adams and Bashforth method to estimate the orbit. The Precise Science Orbit of GOCE is taken as a reference orbit solution to compare the results. The RMS-fit value between the two orbital models is used as an assessment tool between global geopotential models employed separately in deriving the predicted orbit.

KEYWORDS: *Global Geopotential Models; Earth's Gravity Field; Orbit determination; Low Earth Orbit satellites ; GOCE mission*

1. INTRODUCTION

The gravity field of the Earth is defined as a vector force field that is merely composed of the gravitational attraction and the centrifugal forces of the Earth. It changes physically with respect to time and position. The gravitational force is conservative; hence, it is expressed as the gravitational potential by means of three-dimensional scalar quantities. The gravitational potentials can be derived by using many techniques and methods such as the gravimetric measurements to measure the gravity gradients, astronomic leveling to derive the deflection of vertical, and satellite altimetry to cover the surface heights [22]. Global Gravity Models, or in other words, Global Geopotential Models are mathematical models that represent the gravity field of the Earth. Although the mentioned techniques are very efficient in obtaining accurate Earth's gravity models, it is inconvenient to attain the same accuracy for Global Gravity Models because of the requirements of the very high effort in terms of time, cost, and human contribution. The Global Gravity Models are improved with the rise of Earth's constellation satellites. The recent development of the gravimetric satellite missions is, in turn, able to replace the conventional techniques to accomplish the gravimetric measurements by the help of the gradiometers and accelerometers mounted on the satellites. Besides the gravimetric measurements, an orbital determination is equivalently important in terms of deriving the Global Gravity Models. The force of gravity affects the fine ellipsoidal shape of the Keplerian orbits, which interferes in the calculation of the real orbits by the name of orbital perturbations. Therefore, the orbit perturbation effect is used for the determination of the flattening of the Earth, followed by other harmonic expansions of the gravity field **[2].** The derivation of spherical harmonic expansions by means of Keplerian elements was introduced in the theory of satellite geodesy [18]. Thereafter, a Precise Orbit Determination is crucial in order to obtain highly accurate Global Gravity field Models, and this fact is reversible, to determine a precise orbit, there is a need for an accurate Global Gravity Model [16]. In order to evaluate the reliability of the accuracy of the derived models, a continuous evaluation is preferred to be done prior to each usage [34]. The evaluation methods are varied between relative, i.e., the comparison of differences between the coefficients derived from the models, and external evaluations which are done using data obtained from other sources such as, GPS/leveling, gravity anomalies, and orbit parameters [34]. Each assessment technique shows its advantages and disadvantages in terms of the models employed, and the spectral and spatial resolution of

the models. The terrestrial evaluations of the models have been done by different scientists all around the globe [1]. [23], [14], [17]. Nevertheless, it is more reliant on the spatial resolution of the models and less on the spectral resolution. In turn, in order to assess the models solely on their spectral resolution, orbit parameters methods give reliable interpretations [16]. In this study, the Global Gravity Models are validated in terms of their spectral resolution using the orbit determination methodology. Similar studies can be found in the literature, studies done by [3], [16], [24], [26], [27].

In the light of the mentioned studies, the current methodology follows the short-arc orbit determination of the Gravity field and steady-state Ocean Circulation Explorer (GOCE) satellite mission that was launched by the European Space Agency in 17th of March 2009. The final orbit product was compared to the Precise Science Orbit that was published in the documentation of the satellite mission of GOCE. The orbital computation technique is based on the numerical integration of the equation of motion of the satellite. There are two employed techniques, the first one is a single-step numerical integration method specified to solve second order differential equations, followed by a multi-step method to solve for the same purpose in a compact manner. The single-step method is chosen to be the 7th order Runge – Kutta – Nyström introduced by [10]. On the other hand, the 4th order Adams and Bashforth multi-step method are referred to [15].

The Global Gravity Models that were used for the validation were individually used as a background force model in the orbital determination procedure. The models were chosen to be satellite-only derived models, specifically GOCE-only models, and one combined model. Respectively ordered as; (ITG-GRACE2010s), (TIM-R1), (TIM-R5), (SPW-R1), (SPW-R5), (DIR-R1), (DIR-R5), and the newly GOCE derived models; (TIM-R6), (DIR-R6) models, and the combined model; (EGM2008). The assessment of the chosen GGMs is made corresponding to the RMS of fit of the product orbit to the reference orbit. The resulted RMS values were compared for each model, and the models' behaviors were evaluated concerning degree and order between 100 and 200. The results showed the advanced enhancement of GOCE-derived models than the other models, specifically the new models (TIM-R6) & (DIR-R6). This, indeed, leads to the conclusion that the enhancement of GOCE models is worthy to be taken into

considerations for further studies on GOCE-derived data, and for better Precise Orbit Determination results.

2. MATERIAL AND METHOD

The methodology is based upon the theory of the determination of satellites orbit using dynamic forces as background models by studying the equation of motion of the satellite. The employed dynamic force models were only the gravitational forces, basically, the gravity field forces that affect the satellite's motion by perturbations. There exist other gravitational forces affecting on the satellites, however, since the aim of the study is to assess the Global Gravity Models, it is much measurable to employ the gravity field models as the only forces contributing to the orbital motion [3].

The process of the assessment is structured by, firstly computing the Gravity Gradients from the GGMs, substituting them in the equation of motion, numerically integrating the equation of motions, and finally computing the RMS of fit for each model referred to PSO from GOCE. The following diagram describes the assessment procedure briefly;

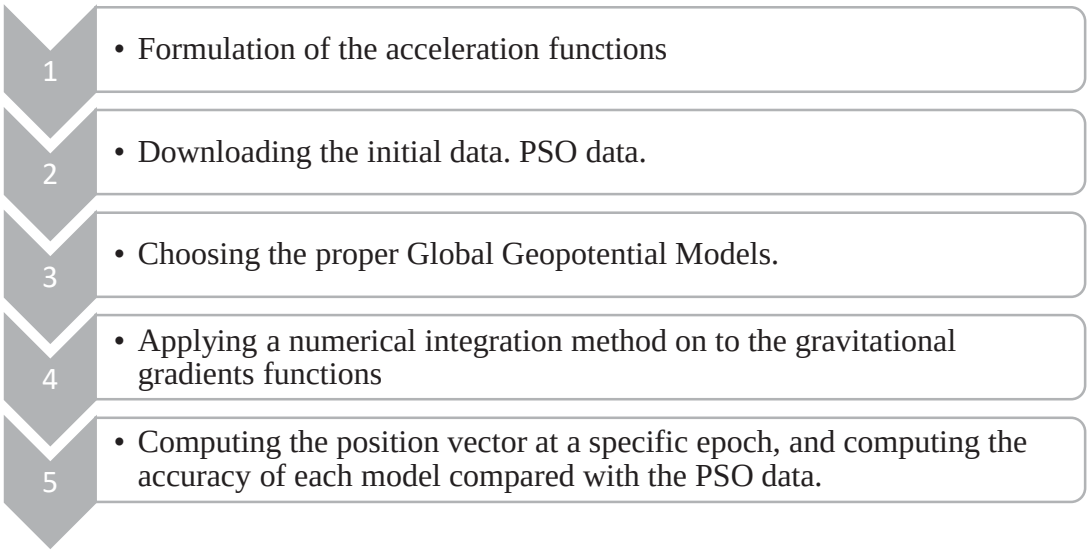

Figure 1. Summary of the integration and evaluation procedure.

2.1. Satellite orbit determination by the short-arc method

The short-arc method for orbit determination has been introduced by [28], [30], [31], with efficient numerical algorithms that facilitate orbit estimation aims. The method provides an advantageous solution for computing a partial arc from the whole satellite orbit in order to avoid the high computation costs, i.e., hardware and time processing. Authors as in [27] followed the proposed procedure for validation purposes. Other authors implemented it as an approach for gravity field recovery from the satellite motion [8]. This study is aimed to compute the satellite orbits of GOCE mission which has an approximate altitude of 254 km [19].

The initial value problem is introduced in order to assess the computations. The initial values are obtained from the Precise Science Orbit data (PSO) of GOCE satellite mission. The Precise Orbit Data, (PSO) had been processed by the Astronomical Institute in the University of Bern (AIUB) directly after the mission launch within the High-level Processing Facility for the final use in the second level (Level-2). The GPS solution of the orbit had been processed using undifferentiated solutions based on the Precise Point Positioning method providing accuracy with 2 cm. The PSO data had been solved for the reduced – dynamics orbits, and the kinematic orbits, the mean 3D RMS of fit between the two models had been obtained as 1.82 cm, and claimed to be consistent with the accuracy of the orbital determination [4]. The data sampling of the Reduced-Dynamic orbits is 10s, whereas it had been computed every 1 second for the kinematic orbital solution. The background force models that had been used in the processing of the reduced-dynamic orbits are the gravitational forces (EIGEN-5S & EIGEN-5C), Solid Earth and Ocean Tides Models (IERS 3004, FES2004), and the Luni-Solar-Planetary gravity (DE4055). Moreover, the data product had been given in the Earth-Centered Earth Fixed reference frame (ECEF), together with the transformation quaternions to the Inertial Earth Centered reference frame (ECI) [12]. Further information about the level-2 GOCE data product can be found in the GOCE level-2 Product Data Handbook [11].

Following, the acceleration functions are formulated by the equation of motion added to its disturbing potentials (1) where the gravity gradients are taking place in the disturbing part of the equation with their harmonic expansion (2).

$$\ddot{r} = -\frac{GM}{r^3}\boldsymbol{r} + ks \tag{1}$$

$$\frac{\partial V}{\partial r} = -\frac{GM}{r^2}\left\{1 - \sum_{n=2}^{\infty}\sum_{m=0}^{n}\left(\frac{R}{r}\right)^n [C_{nm}\cos m\lambda + S_{nm}\sin m\lambda]P_{nm}(\sin\varphi)\right\}$$

$$\frac{\partial V}{\partial \varphi} = \frac{GM}{r}\left\{\sum_{n=0}^{\infty}\sum_{m=0}^{n}\left(\frac{R}{r}\right)^n [C_{nm}\cos m\lambda + S_{nm}\sin m\lambda]P'_{nm}(\sin\varphi)\right\} \tag{2}$$

$$\frac{\partial V}{\partial \lambda} = \frac{GM}{r}\left\{\sum_{n=0}^{\infty}\sum_{m=0}^{n}(n+1)\left(\frac{R}{r}\right)^n [C_{nm}\cos m\lambda + S_{nm}\sin m\lambda]mP_{nm}(\sin\varphi)\right\}$$

Where the $\ddot{r}$ is the positional acceleration, GM is the gravitational constant, **r** is the positional vector of the satellite, R is the equatorial radius of the Earth. n & m are the degree and order of the spherical harmonic expansion of the Earth's gravity field. Pnm and P'nm are the normalized Lagrange Polynomials, and their first order derivatives respectively, C & S are the spherical harmonic coefficients derived to the degree and order, in this scenario, from the Global Geopotential Models. Finally, r, λ, φ are the geocentric spherical coordinates in the Earth Centered Earth Fixed Reference Frame. Since the initial position is taken from the PSO data, firstly, the coordinates are transformed from the Cartesian to the spherical coordinates following equations (3). Then, the Gravity Gradients are derived with respect to the spherical coordinates followed by the transformation to the Cartesian system (4) in order to integrate the acceleration vectors in the Cartesian coordinate system.

$$\begin{aligned} x &= r\cos\varphi\ \cos\lambda \\ y &= r\cos\varphi\ \sin\lambda \\ z &= r\sin\varphi \end{aligned} \tag{3}$$

$$\frac{\partial V}{\partial x} = \frac{\partial V}{\partial r}\frac{x}{r} - \frac{\partial V}{\partial \varphi \cos\varphi}\frac{z\,x}{r^3} - \frac{\partial V}{\partial \lambda}\frac{y}{r^2\cos\varphi^2}$$
$$\frac{\partial V}{\partial y} = \frac{\partial V}{\partial r}\frac{y}{r} - \frac{\partial V}{\partial \varphi \cos\varphi}\frac{z\,y}{r^3} + \frac{\partial V}{\partial \lambda}\frac{x}{r^2\cos\varphi^2} \quad (4)$$
$$\frac{\partial V}{\partial z} = \frac{\partial V}{\partial r}\frac{z}{r} + \frac{\partial V}{\partial \varphi\, r}\sqrt{1-\frac{z^2}{r^2}}$$

The acceleration functions are then computed by the formula (5);

$$\ddot{x} = \frac{\partial V}{\partial x} + 2\,\omega\,\dot{y} + \omega^2 x$$
$$\ddot{y} = \frac{\partial V}{\partial y} - 2\,\omega\,\dot{x} + \omega^2 y \quad (5)$$
$$\ddot{z} = \frac{\partial V}{\partial z}$$

Since the reference orbit is in the ECEF reference frame, there is no need to transform to the inertial reference frame [32]. Accordingly, the effect of the rotation around the Earth's rotation axis should be eliminated from the calculations; hence, the Earth's rotation angle ω is multiplied by the velocity of the Satellite and subtracted/added to the acceleration of the Satellite.

2.2. Computational procedure

The followed algorithm is developed by the author in the MatLab language, *the computational algorithm of the gravity gradients was taken from the open source GRACETOOLS provided by [9]*.

The numerical integration procedure is divided into two steps. Firstly, the 7th order Runge-Kutta-Nystrom single-step numerical integration method is implemented, after that, the 4th order Adams-Bashforth & Moulton method is used to complete the entire orbit in a much time effective algorithm. Generally, the single-step methods are formulated from independent steps, they are directly dependent on the initial value assigned (6).

$$y(t_i) = y(t_0) + f\big(t, y(t)\big) * h + \frac{f'\big(t, y(t)\big)}{2!} * h^2 \tag{6}$$

On the other hand, the multi-step methods efficiently make use of the last computed value from the previous step, yet, the multi-step methods require a previous implementation of single-step methods to define more than one initial value [21]. According to previous studies [20], [25], the use of the high order single-step methods alone provides high accuracy, however, it requires a long time to process. Hence, the mentioned studies proposed to divide the orbit determination process into two steps employing both methodologies. These facts justify the reason of using the two methods in the computation. Furthermore, according to [33], the predictor-corrector method, i.e., the Adams-Bashforth-Moulton method was proved to be an adequate technique used if a precise orbit determination is required. The predictor-corrector method is composed by two main steps, the predicting step, which computes the approximate values from the initial state values, then, a correcting step is added to ensures the correctness of the value by inserting the predicted value into the function (7).

$$\begin{aligned} y^p(t_{i+1}) &= y(t_i) + f(t, y(t_i)) * h \\ f^p{}_{i+1} &= f(t_{i+1}, y^p(t_{i+1})) \\ y(t_{i+1}) &= y(t_i) + f^p{}_{i+1} * h \\ f_{i+1} &= f(t_{i+1}, y(t_{i+1})) \end{aligned} \tag{7}$$

Further details about the parameters and coefficients of both methods can be found in [21].

3. RESULTS AND DISCUSSION

3.1. Numerical Results

The implementation of the numerical integration methods requires initial values in order to start in the computation, these values are taken from the reference orbit, which is the reduced dynamic orbit solution from PSO data. The orbit started by 16th of January, 2013 at 12.00 AM and computed until after 45 minutes, that is, approximately half of one revolution of the satellite. The step size of both numerical methods was fixed as 1 second in order to obtain higher accuracy. The used models were expanded to the degree/order between 100 and 200, up to the

last available value by the model. When the model has a lower degree/order than 200, it was truncated up to its maximum value. EGM2008, has a very long wavelength which its higher resolution doesn't contribute to the precision of orbit determination [29]. The reason of choosing this range, i.e., between 100 and 200, is that the productivity of the GOCE-derived models commons in this range, besides the fact that this range of degree and order has a refinement on the precision of the Low Earth Orbiters [19]. The models were chosen as the satellite-only models, specifically, the newly derived GOCE-only models were compared with the oldest version of GOCE-only models, together with one GRACE-only derived model and a combined model (Table 1).

Table 1. List of the employed models.

Global Geopotential Models	Maximum degree/order	Year	Data
ITG-GRACE2010S	180	2010	S(GRACE)
EGM2008	2190	2008	A, G, S(GRACE)
GO_CONS_DIR_R6	300	2019	S(GOCE)
GO_CONS_DIR_R5	300	2014	S(GOCE), S(GRACE), S(LAGEOS)
GO_CONS_DIR_R1	240	2010	S(GOCE)
GO_CONS_TIM_R6	300	2019	S(GOCE)
GO_CONS_TIM_R5	280	2014	S(GOCE)
GO_CONS_TIM_R1	224	2010	S(GOCE)
GO_CONS_SPW_R5	330	2017	S(GOCE)
GO_CONS_SPW_R1	210	2010	S(GOCE)

As it was mentioned, the results were obtained in the Cartesian coordinate system referred to ECEF reference frame; hence, the comparison with the positions of the PSO data can be directly

made. Following, the results obtained along X, Y, and Z axes (Table 2), (Table3), (Figure 2), (Figure 3), (Figure 4);

Table 2. Orbit differences (m) between the PSO data and the computed orbits along 45 minutes for every GGM truncated to the d/o between 100&200 and the corresponding full expansion.

d/o		DIR_R6	DIR_R5	DIR_R1	TIM_R6	TIM_R5	TIM_R1	SPW_R5	SPW_R1	EGM2008	ITGGRACE2010S
100	X	1.2250	1.2214	5.1463	-0.0853	0.7075	4.5173	-0.0834	-0.1016	-0.1465	-0.0387
	Y	1.4495	1.4284	-7.7675	-1.1583	0.5179	-2.411	-1.2702	-1.2046	-1.1834	-1.2790
	Z	6.4901	6.458	-14.6334	-0.9400	2.2879	-5.4225	-1.0097	-0.9670	-0.9378	-1.0781
120	X	3.5377	3.5335	-0.1313	0.1428	3.4832	0.7178	0.1171	0.1113	0.0942	0.1816
	Y	1.9739	1.9544	4.6382	-1.0631	3.7842	4.9434	-1.1509	-1.0952	-1.0904	-1.1901
	Z	1.9270	1.8969	5.6818	-0.9714	6.175	5.5474	-1.0107	-0.9785	-0.9620	-1.1196
150	X	0.8733	0.8669	-0.9977	0.1038	-1.4362	-0.2989	0.0786	0.0835	0.0656	0.1439
	Y	1.7955	1.7824	0.5548	-1.0757	1.8474	-0.3228	-1.1698	-1.1302	-1.1093	-1.2049
	Z	1.8510	1.8282	1.9495	-0.9469	1.807	1.1959	-0.9936	-0.9852	-0.9460	-1.1037
180	X	-0.5356	-0.5465	-0.0349	0.0955	0.1141	0.011	0.0724	0.0739	0.0582	0.1317
	Y	-0.5734	-0.5947	-0.8558	-1.0409	-0.2618	-0.9373	-1.1412	-1.0961	-1.0761	-1.1666
	Z	0.7138	0.6819	-0.5031	-0.8869	0.0789	-0.5972	-0.9423	-0.9266	-0.8865	-1.022
200	X	0.0331	0.0237	0.1144	0.0877	-0.0799	-0.0053	0.0646	0.0678	0.051	-
	Y	-0.6307	-0.6539	-1.1092	-1.0277	-0.8241	-0.8491	-1.1275	-1.0896	-1.0613	-
	Z	-0.5985	-0.6318	-0.9034	-0.8558	-0.5465	-0.5907	-0.9110	-0.9124	-0.8542	-
MAX	X	0.0479	0.0384	0.0667	0.084	0.0304	-0.0137	0.0617	-	0.0474	-
	Y	-1.0396	-1.0594	-1.0601	-1.0259	-1.0146	-0.8500	-1.1258	-	-1.0602	-
	Z	-0.8008	-0.8295	-0.8715	-0.8496	-0.7674	-0.5646	-0.9056	-	-0.8492	-

Table 3. 3D (m) RMS of fit between the PSO data and the computed orbits along 45 minutes for every GGM truncated to the d/o between 100&200 and the corresponding full expansion.

d/o	DIR_R6	DIR_R5	DIR_R1	TIM_R6	TIM_R5	TIM_R1	SPW_R5	SPW_R1	EGM2008	ITGGRACE2010S
100	3.9040	3.8832	10.0159	**0.8627**	1.4146	4.3059	0.9381	0.8938	0.8759	0.966
120	2.5901	2.5757	4.2353	**0.8355**	4.6398	4.3099	0.8869	0.8504	0.8413	0.9492
150	1.5719	1.5568	1.3043	0.8296	1.7069	**0.7357**	0.8873	0.8670	0.8426	0.9470
180	0.6124	0.6103	0.5735	0.7914	**0.1711**	0.6417	0.8554	0.8298	0.8057	0.8986
200	**0.5061**	0.5251	0.8286	0.7738	0.5728	0.5972	0.8378	0.8215	0.7871	-
MAX	0.7582	0.7772	0.7933	0.7706	0.7347	**0.5892**	0.8350	0.8215	0.7847	0.8986

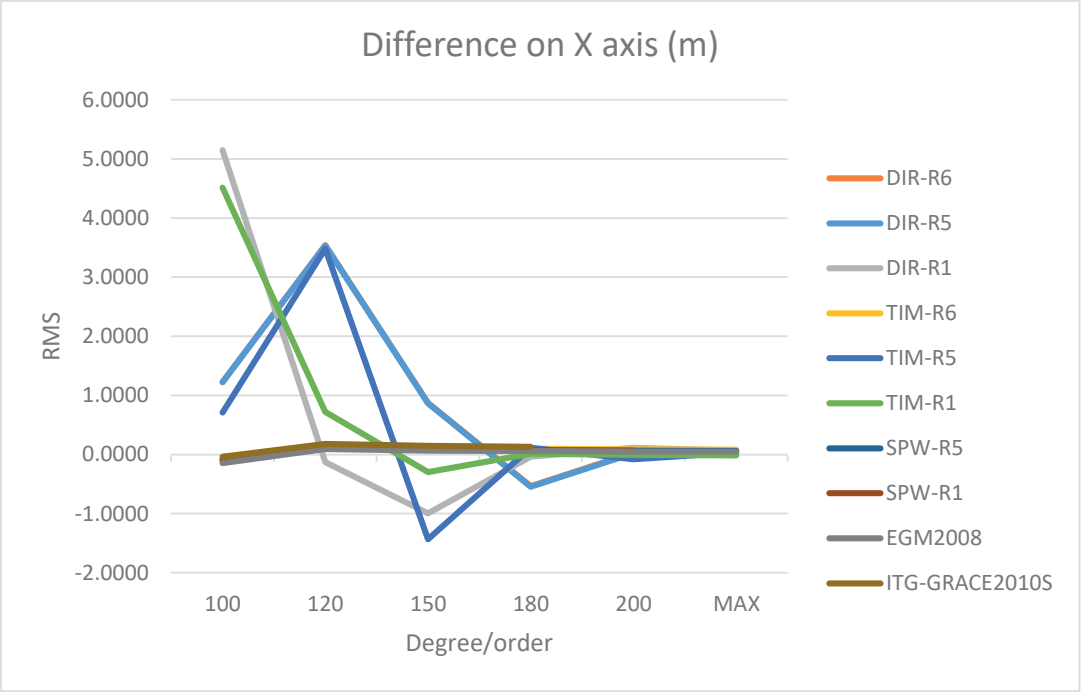

Figure 2. Orbit differences on X-axis in meters.

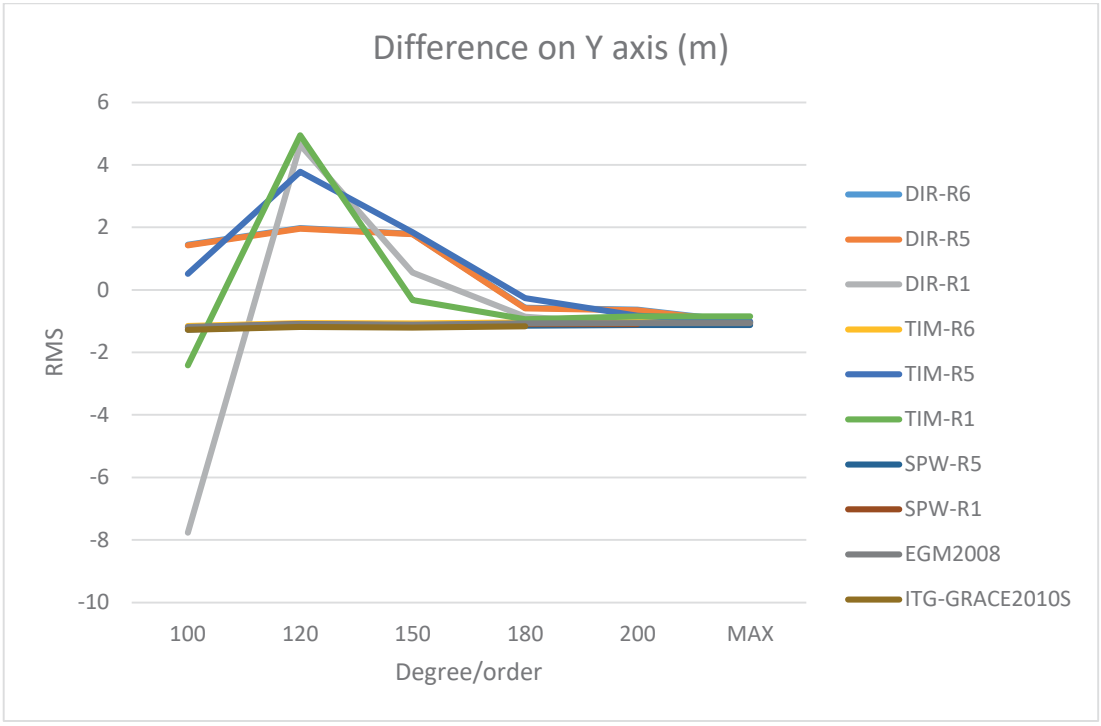

Figure 3. Orbit differences on Y-axis in meters.

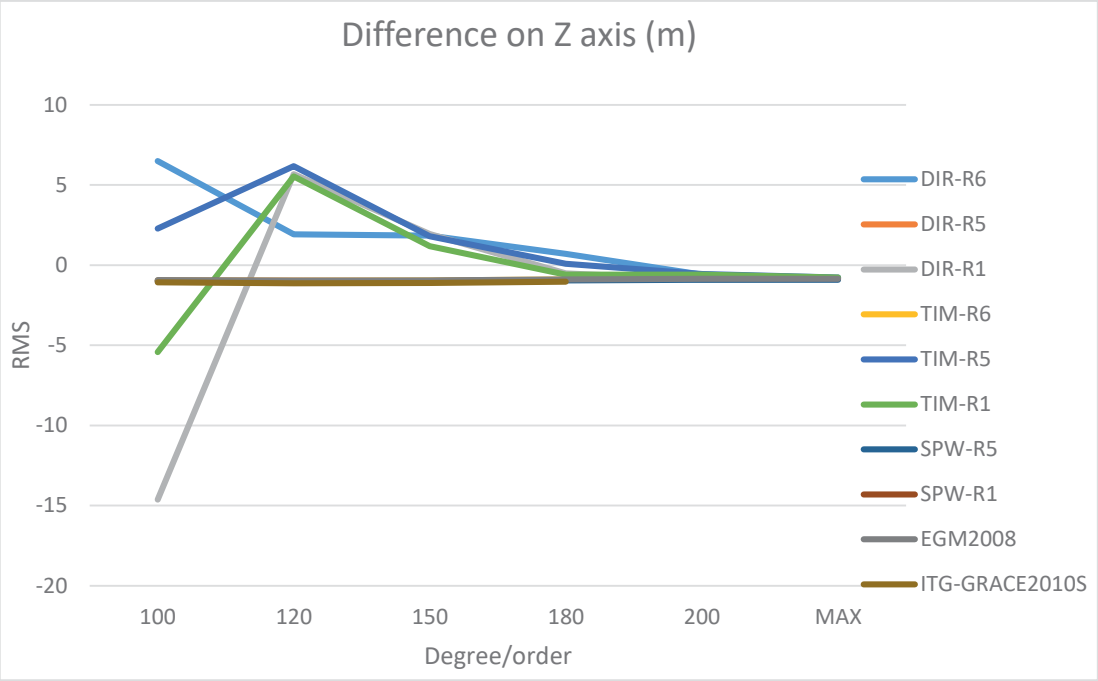

Figure 4. Orbit differences on Z-axis in meters.

3.2. Results Evaluation

A spectral evaluation of the chosen GGMs (DIR-R6, DIR-R5, DIR-R1, TIM-R6, TIM-R5, TIM-R1, SPW-R5, SPW-R1, ITG-GRACE2010s, and EGM2009) can now be done externally using the satellite orbit determination method. The orbit determination strategy used in this study is based on numerical integration algorithms which showed an acceptable performance in terms of time and hardware requirements when it comes to the short-arc approach, used here as 45 minutes arc. The results shown in (Table 2) and (Figures 2, 3, 4), reflect radical changes in the orbits' accuracy on each axis when the wavelength ranges of the models were employed between 100 and 180. These changes occurred basically on the GOCE-derived models, specifically, the TIM and DIR models. Whereas the SPW models, the EGM2009 and ITG-GRACE2010S models showed much stabilized results all over the studied wavelength ranges (approximately 80 cm). This fact points out the importance of choosing the proper expansion of the degree and order of the model to be used for certain applications. The results tend to smooth above the range of 180 and show the highest accuracy in the centimetric levels. Meaning that the models produce the best performance between the 180-200 degree and order. The

accuracy is reduced for longer wavelengths; yet, the models that showed stability all over the wavelength provided their best results on their maximum truncation (between 200, 300 and 330). Moreover, these models gave the least accuracy among other models. Table 4 shows each model's best 3D RMS values on a specific degree/order. The best result is given by **TIM-R5** model, which is a solely GOCE-derived model [5], followed by DIR models having (DIR-R6) with 2 cm ahead. The TIM-R6 model showed similar behavior as other models, such as SPW models, the model has been published in 2019 [6], it is claimed that the same data input was used, except for the data period since a specific technique was applied to overcome the polar gaps in the data [6].

Additionally, the DIR-R6 model is a GOCE-derived combined model with GRACE, LAGEOS, and LARES data was used in the computation of the gravity model. In comparison with its previous version(s), DIR-R6 was the first model that includes data from LARES and used the reduced-dynamic technique for orbit estimation from GOCE Satellite to Satellite Tracking data (SST_PRD_2) whereas, the DIR-R5 used kinematic data (SST_KIN_2) [13], [7].

Table 4. The best 3D RMS values produced by each model on different degree and order.

	DIR_R6 (200)	DIR_R5 (200)	DIR_R1 (180)	TIM_R6 (300)	TIM_R5 (180)	TIM_R1 (224)	SPW_R5 (330)	SPW_R1 (200)	EGM2008 (330)	ITGGRACE2010S (180)
3D RMS	0.5061	0.5251	0.5735	0.7706	**0.1711**	0.5892	0.8350	0.8215	0.7847	0.8986

The differences between all the models is concentrated between the centimetric level, which is a considerable quantity when it is used for the precise orbit determination, and generally in applications that require high level of accuracy. It is also important to note that the best obtained accuracy by the TIM-R5 model is ahead of the accuracy of other models by decimetric levels. Hence, it is essential to notice the TIM series models effectiveness and contributions to the precise orbit determination of the Low Earth Orbiters, which in turn, provides the necessity to focus on the TIM series in further studies.

4. CONCLUSION

The study of Gravity Field of the Earth has an important influence on the dynamic motion and the mass density structure of the Earth. Observation of gravity by satellite gravimetry missions had been a great improvement in the resolution of gravity signals. Consequently, Global Geopotential/Gravity Models have become essential to offer static or temporal gravity models measured by satellite only or combined data products. When it comes to the global evaluation of GGM signals, the prediction of satellites position in orbits is claimed to be an advantageous method since it provides an unbiased assessment to a specific area, i.e., a specific spatial resolution. In this method, the spectral behavior can be fairly assessed for shorter wavelengths, indeed, it doesn't require longer wavelengths to be considered. The methodology follows the computation of satellites' positions by benefitting from numerical integration methods, in essence, integrating the equation of motion that is derived by means of gravity gradients represented in terms of an initial position of the satellite which is taken from the reference orbital model (the reduced-dynamic PSO data). Since the reduced-dynamic solutions of GOCE PSO data are in the ECEF reference frame, the process excludes any transformation to ECI reference frame and all the computations were in the same reference frame as the reference orbital data. The applied numerical methods were chosen according to their efficiency in integrating a short-arc orbit, i.e., 45 minutes of arc. The forces affecting the orbital motion are beyond the gravity field effects; there are other gravitational and non-gravitational forces that if considered in the determination process provide higher accuracy [3]. However, these forces were neglected in order to be able to assess Global Gravity Models purely. The employed GGMs were chosen as mostly satellite-only derived models. The behavior of the models was seen to be stable all over the considered wavelength range for some models (TIM-R6, SPW-R5, SPW-R1, EGM2008, & ITG-GRACE2010S). The smooth behavior of the models decreased the chance for the models to produce better accuracy. However, other models (TIM-R5, TIM-R1, DIR-R6, DIR-R5, & DIR-R1) had a fluctuated behavior over different wavelengths. These models were able to provide the best RMS of fit in the 3-dimensions of the orbit comparing with the reference orbit. The best accuracy was obtained from the TIM-R5 model having a 3D RMS of 17 cm with a degree and order of 180, while it produced 4.64 meters RMS value when the degree/order was set to 120.

The mentioned fact remarks on the importance of the choice of the degree and order expansion of each model. For further studies, the reliability of employing the TIM and DIR models in GOCE orbital determination should be assessed since they proved to have the most accurate results compared to other models. Furthermore, to test the efficacy of these models in precise orbit determination, it is important to employ them in the computation of longer orbital arcs, and their behavior can be evaluated accordingly. Other methodologies for the orbit determination can be done, as it is already employed in the literature, by using different estimation techniques together with numerical integration methods. These techniques give the opportunity to produce independent satellite orbit models without considering a priori model in the computation, but only for accuracy testing reasons.

ACKNOWLEDGEMENT

Special acknowledgement to the providers of the open-source GRACETOOLS software (Darbeheshti, 2018), which was very beneficial in computing the gravity gradients with its speed and highly efficient results. Other acknowledgements go to the High Level Processing Facility that provides the solutions of GOCE satellite without any compensation. Lastly, to the ICGEM that collects, archives and delivers the Global Gravity Models as an open source website.

REFERENCES

1. Avsar, N. B.; Erol, B.; Kutoglu, S. H. Evaluation of GOCE-Based Global Geopotential Models Versus EGM2008 and GPS/Levelling Data in Northwest of Turkey. In: Jin S., Barzaghi R. (eds) IGFS 2014. International Association of Geodesy Symposia, Volume 144. Springer, Cham. 2015.
2. Barthelmes, F. Global Models, in Grafarend, E. (Ed.) Encyclopedia of Geodesy, Springer International Publishing, 2014.
3. Bobojć, A. Assessment of chosen GRACE-related gravity models based on the GOCE satellite precise science orbit, Acta Geophys. 2019, Volume 67, Issue 4, pp. 1265-1275 doi: https://doi.org/10.1007/s11600-019-00317-y
4. Bock, H.; Jäggi A.; Meyer, U.; Visser, P.; van den IJssel, J.; van Helleputte, T.; … Hugentobler, U.. GPS-derived orbits for the GOCE satellite. Journal of Geodesy 2011, Volume 85, Issue 11, pp. 807–818. doi:10.1007/s00190-011-0484-9
5. Brockmann, J. M. On High Performance Computing in Geodesy -- Applications in Global Gravity Field Determination; Phd thesis, Institute of Geodesy and

Geoinformation, University of Bonn. No. 22, 2014. doi: http://nbn-resolving.de/urn:nbn:de:hbz:5n-38608

6. Brockmann, J. M; Schubert, T.; Mayer-Gürr, T.; Schuh, W. D. The Earth's gravity field as seen by the GOCE satellite an improved sixth release derived with the time-wise approach. GFZ Data Services. 2019. Doi: http://doi.org/10.5880/ICGEM.2019.003
7. Bruinsma, S. L., Forste, C., Abrikosov, O., Marty, J. C., Rio, M. H., Mulet, S., Bonvalot, S.; The new ESA satellite-only gravity field model via the direct approach; Geophysical Research Letters, Volume 40, No. 14, pp. 3607-3612, 2013, doi: 10.1002/grl.50716
8. Chen, Q.; Shen, Y.; Zhang, X.; Hsu, H.; and Chen, W., Global Earth's gravity field solution with GRACE orbit and range measurements using modified short arc approach. Acta Geod Geophys 2015, Volume 50, Issue 2, pp. 173-185
9. Darbeheshti, Neda; Wöske, Florian; Weigelt, Matthias; Mccullough, Christopher; Wu, Hu. GRACETOOLS—GRACE Gravity Field Recovery Tools. Geosciences 2018, Volume 8, no. 9: 350.
10. Dormand J. R.; Prince P. J. New Runge–Kutta algorithms for numerical simulation in dynamical astronomy**;** Cel. Mech 1978. Volume 18**,** pp. 223–232**.**
11. ESA (2010a). GOCE Level 2 Product Data Handbook. Available online: https://earth.esa.int/documents/10174/1650485/GOCE_Product_Data_Handbook_Level-2 (accessed on 24 November 2019)
12. ESA (2010b). GOCE Standards. Available online: https://earth.esa.int/c/document_library/get_file?folderId=14168&name=DLFE-572.pdf (accessed on 24 November 2019)
13. Förste, Ch.; Abrykosov, O.; Bruinsma, S.; Dahle, Ch.; König, R.; Lemoine, J. M. ESA's Release 6 GOCE gravity field model by means of the direct approach based on improved filtering of the reprocessed gradients of the entire mission. GFZ Data Services. 2019, doi: http://doi.org/10.5880/ICGEM.2019.004
14. Goyal, R.; Dikshit, O.; Balasubramania, N, Evaluation of global geopotential models: a case study for India. Survey Review 2019, Volume 51, pp. 402-412.
15. Grigorieff R. D.; Numerik gewöhnlicher Differentialgleichungen 2; Teubner Verlag, Stuttgart, 1977.
16. Gruber, Th.; Visser, P. N. A. M; Ackermann, Ch.;Hosse M. Validation of GOCE gravity field models by means of orbit residuals and geoid comparisons. Journal of Geodesy 2011, Volume 85, Issue 11, pp. 845–860.
17. Ibrahim Yahaya, S.; El Brirchi, E. H.; El Azzab, D., Assessment of Global Geopotential Models for GNSS Levelling in Niger, In 3ème Edition du Colloque International des utilisateurs du SIG-The 3rd International conference of GIS Users, 2016.
18. Kaula, William M. The Theory of Satellite Geodesy: Application of Satellites to Geodesy, Blaisdell Publ. Comp., London, 1966.
19. Meijde, M.; Pail, R.; Bingham, R.; Floberghagen, R. GOCE data, models, and applications: a review. International Journal of Applied Earth Observation and Geoinformation (JAG) 2013, Volume 35 (Part A), pp. 4-15. doi: https://doi.org/10.1016/j.jag.2013.10.001
20. Montenbruck O. Numerical integration methods for orbital motion. Celest Mech Dyn Astron 1992, Voume 53, pp: 59-69.

21. Montenbruck O., and Gill E. Satellite orbits – models, methods and applications. Springer, Berlin. 2000.
22. Novak, P. Direct modeling of the gravitational field using harmonic series, Acta Geodyn. Geomater 2010. Volume 7, No. (1-157), pp: 35–47.
23. Odera, P.A.; Fukuda, Y**.** Evaluation of GOCE-based global gravity field models over Japan after the full mission using free-air gravity anomalies and geoid undulations. Earth Planets Space 2017, Volume 69**,** doi:10.1186/s40623-017-0716-1
24. Papanikolaou, T.D.; Tsoulis, D. Assessment of Earth Gravity Field Models in the Medium to High Frequency Spectrum Based on GRACE and GOCE Dynamic Orbit Analysis. Geosciences 2018, Volume 9, Issue 12, No. 441.
25. Papanikolaou, T.D.; Tsoulis, D. Assessment of numerical integration methods in the context of low Earth orbits and inter-satellite observation analysis, Acta Geod Geophys 2016, Volume 51, Issue 4. pp: 619–641. Doi: 10.1007/s40328-016-0159-3
26. Papanikolaou, T.D.; Tsoulis, D. Dynamic orbit parameterization and assessment in the frame of current GOCE gravity models, Physics of the Earth and Planetary Interiors 2014,Volume 236, pp. 1-9. doi: 10.1016/j.pepi.2014.08.003
27. Papanikolaou, T.D.; Tsoulis, D. Degree-wise validation of satellite-only and combined Earth gravity models in the frame of an orbit propagation scheme applied to a short GOCE arc, Acta Geod Geophys 2013, Volume 48, Issue 13, pp: 305-316. doi: https://doi.org/10.1007/s40328-013-0020-x
28. Rooba, J. An efficient short-ARC orbit computation, Journal of Geodesy 1983 Volume 57, (1-4), pp: 138-145. doi: 10.1007/BF02520920.
29. Sansò F.; Sideris M.G. Geoid determination: Theory and methods. Lecture Notes in Earth System Sciences, Volume 110. Springer-Verlag, Berlin, Heidelberg, 2013.
30. Schrama, E. Orbit integration based upon interpolated gravitational gradients. Master's Thesis, Delft University of Technology, Delft 1984. doi: 10.13140/RG.2.1.2367.2160
31. Seeber, G. Satellite Geodesy (2nd ed.), De Gruyter, 2003.
32. Shou, H. N. Orbit Propagation and Determination of Low Earth Orbit Satellites. International Journal of Antennas and Propagation 2014. Volume 2014. Doi: http://dx.doi.org/10.1155/2014/903026
33. Somodi, B., & Földváry, L. Application of numerical integration techniques for orbit determination of state-of-the-art LEO satellites. Periodica Polytechnica Civil Engineering, 2011, Volume 55, Issue 2, pp. 99-106. Doi: https://doi.org/10.3311/pp.ci.2011-2.02
34. Ustun, A.; Abbak, R. A. On global and regional spectral evaluation of global geopotential models, Journal of Geophysics and Engineering 2010, Volume 7, Issue 4, pp.369–379, doi: https://doi.org/10.1088/1742-2132/7/4/003

GEODETIC MONITORING OF DISPLACEMENTS AND DEFORMATIONS FOR ASSESTMENT OF EFFECT FROM SUSPEND OF EXPLOITATION OF PERNIK MINES

Ivan Kaltchev[1], Maria Kaltcheva[2]

[1]GEO PLUS LTD., 215 Tzar Boris III blvd, 1618 Sofia, Bulgaria,
Phone: +359885956312, E-mail: ikaltchev@geoplus-bg.com
[2]GEO PLUS LTD., 215 Tzar Boris III blvd, 1618 Sofia, Bulgaria,
Phone: +359888145895, E-mail: mkaltcheva@geoplus-bg.com

ABSTRACT

The Pernik Coal Basin is the oldest in Bulgaria - its operation starts on 17.08.1891. Depth of bedding of coal beds is small (10-130m). In the last years, after the mining operations were stopped on 2000, emergency situations occurred on the territory of the town of Pernik, which are directly related to the mining activity carried out in the Pernik basin. Risky and emergency situations potentially affect all types of engineering facilities on the terrain of the city of Pernik (buildings, streets, roads, railways, bridges, stadiums, other facilities) as well as elements of the underground engineering infrastructure (water mains, sewerage, cable routes, etc.). The main goal of the project is to carry out studies and analyses and to propose design solutions for the development of the geodetic network for surveying of the movements and deformations of the land surface and the mining mass with objects in order to organize specialized monitoring as a preventive measure for the purpose of conservation of objects and facilities from the harmful influence of the mining works and the consequences of stopping their operation in region of Pernik Mining. Different methods and instruments were applied for performing of precise geodetic measurements for deformation monitoring for last 9 years. Some results and conclusions are presented in the report based on collected 4D data base.

KEYWORDS: Deformations and movements monitoring; Precise geodetic measurements - methods and instruments

1. INTRODUCTION

1.1. The object of interest

The Pernik Coal Basin is the oldest in Bulgaria - its operation starts on 17.08.1891.

Figure 1. *Underground galleries of Mini Pernik at the past and now*

Depth of bedding of coal beds is small (10-130m). Seized underground spaces and burrows extend over a large part of the residential quarters and built engineering infrastructure of the town of Pernik.

In the last years, after the mining operations were stopped on 2000, emergency situations occurred on the territory of the town of Pernik, which are directly related to the mining activity carried out in the Pernik basin.

Independent of the type of used abutment, the present conditions of the underground mining galleries can be described as one of the following variants:

a) The abutments are not fully degraded yet, but in each next moments can change to Variant
b) The gallery is repaired with complete disassembly of the fastening and breaking at the end of their existence. It is the better variant;
c) The abutment is already degraded on 90% and the top is ruined with a large cavity - a high vault above the top.

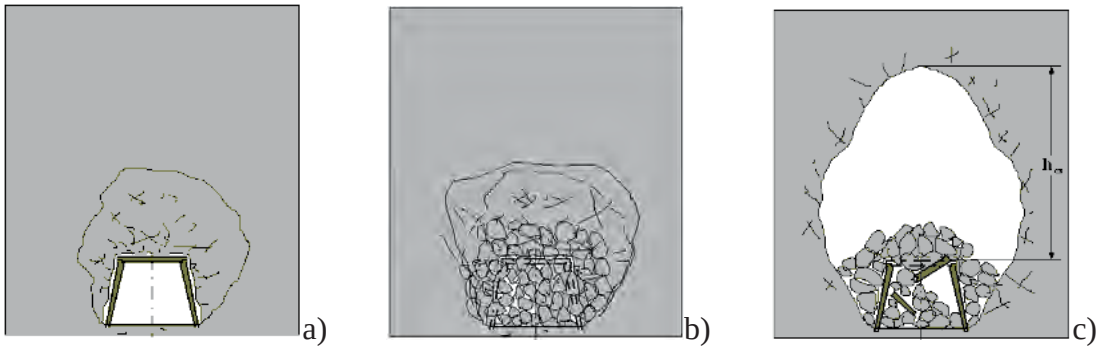

Figure 2. *Variants of the conditions of the underground galleries*

Risky and emergency situations potentially affect all types of engineering facilities on the terrain of the city of Pernik (buildings, streets, roads, railways, bridges, stadiums, other facilities) as well as elements of the underground engineering infrastructure (water mains, sewerage, cable routes, etc.).

1.2. The project for geodetic monitoring for displacements and deformations

The scope of the project is to design and develop a spatial network for geodetic monitoring of the ground surface, the rock massive and objects of engineering infrastructure on the ground and performing precis geodetic measurements for monitoring of displacements and deformations of the most threatened objects by interrupted underground mining activities of the Pernik Minings in the City of Pernik with a goal to control and prevent the structures from the harmful influence of the performed mining activities and aftereffect of stopping of their exploitation.

The design defined objects, which are subject to protection from harmful influence of the underground mining works. All objects, for which are received official complaints by citizens, ware included; the objects with social importance; buildings and constructions, which are

above of "crosses" of mining galleries as potentially most dangerous places for occurrence of deformation processes; profile lines on the streets as infrastructural objects; buildings situated on or near to borders of seized spaces on the coal layers and near to profile lines on the streets. The configurations of the buildings, the number of floors, the occupied area, the construction, foundation and condition are taken into account during selection of the buildings and were included only the buildings with massive structure.

Figure 3. *Objects, which are subject to protection from harmful influence of the underground mining works*

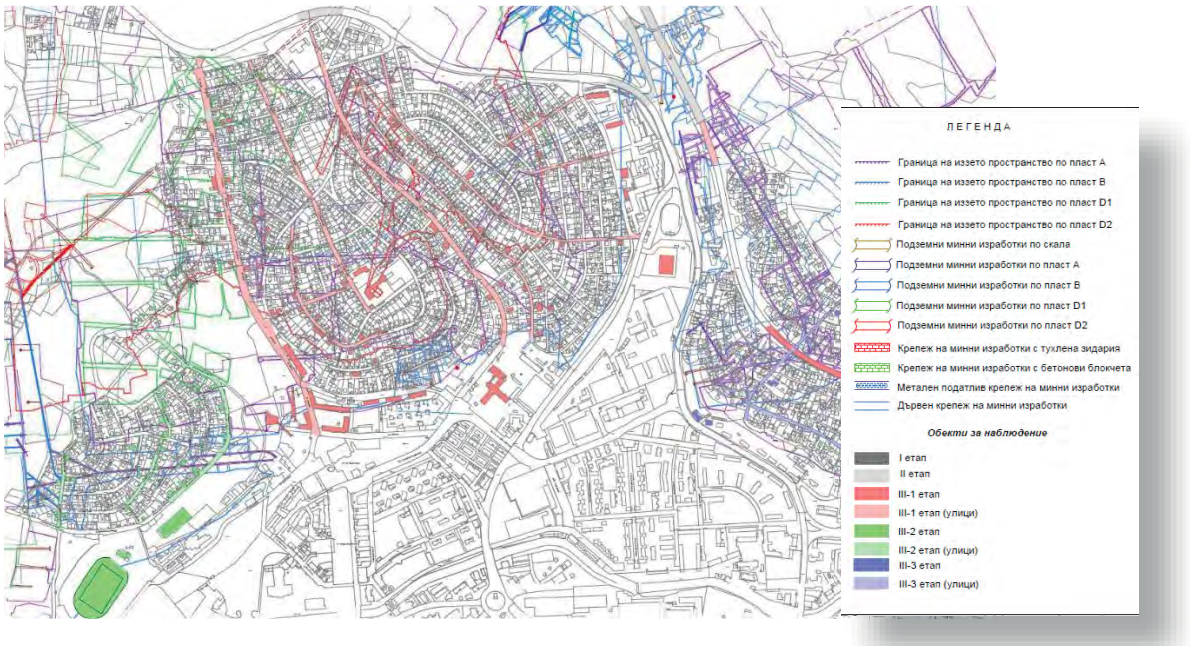

Figure 4. *Defining and classification of the objects, which are subject to protection from harmful influence of the underground mining works – stages and underground objects*

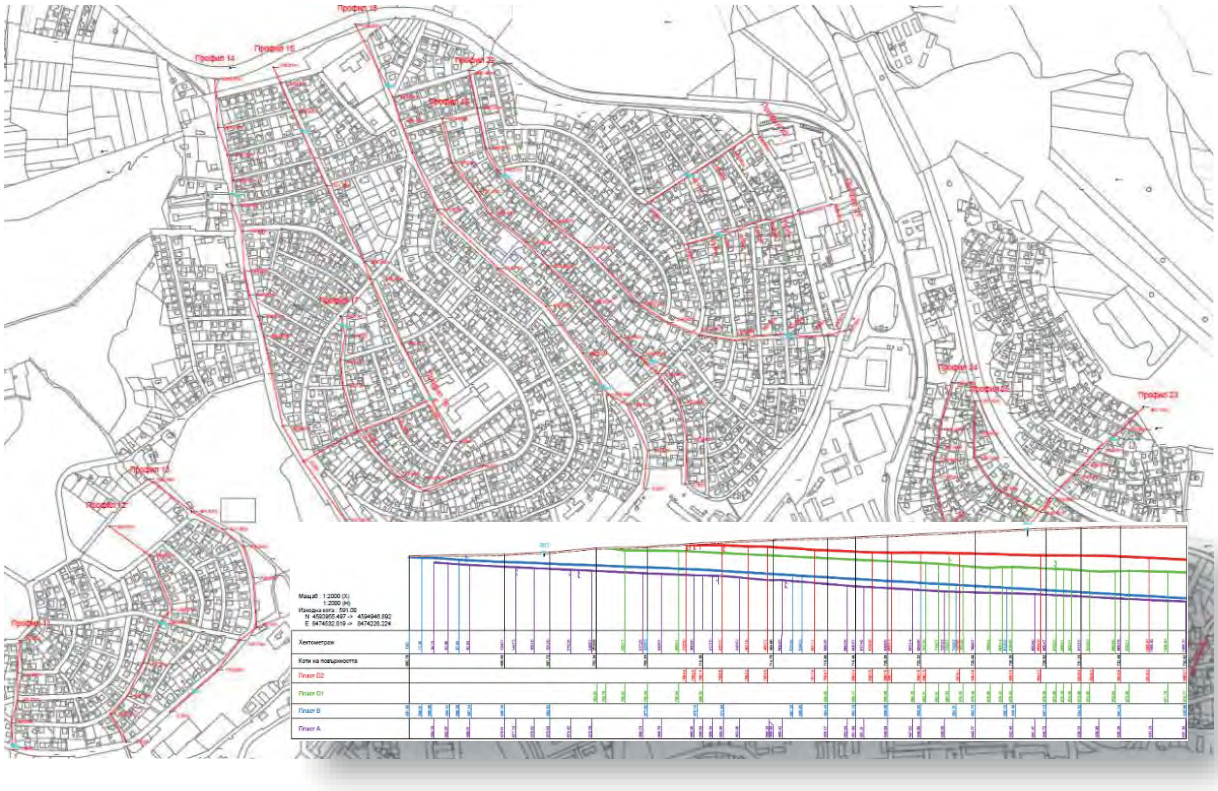

Figure 5. *Defining and classification of the objects, which are subject to protection from harmful influence of the underground mining works – profiles*

The defined groups of objects ware categorized in respect of „Instruction for protection of the objects and structures from harmful influence of the underground mining activities in coal basins" from 1983.

Table 1: Categorization of the objects and structures for monitoring of deformations with limits of values of maximum parameters of deformations

№	Category	General description of protected objects and structures	Limits (maximum) for deformations			
			Slope *i*, mm/m	Curvature *K*, mm/m2	Radius of curvature *R*, m	Horizontal deformation *ε*, mm/m
1	I	Residential and public buildings highest than 5 floors	**4**	**0.2**	**5000**	**2**
2	II	Nurseries and kindergartens, regardless of the number of floors with a length of 50 m; Railway bridges up to 20 m long; 3, 4 floors public and residential buildings over 40m in length.	**8**	**0.4**	**2500**	**3**
3	III	One-floor buildings over 20 m in length; Two-floors residential and public buildings up to 40 m in length; Single floor warehouses over 40 m in length; Railroad.	**12**	**0.6**	**1700**	**6**
4	IV	One-floor buildings up to 20 m in length; All roads within the scope of the project.	**20**	**0.8**	**-**	**10**

On the base of preliminary investigations were defined the boundaries and the coverage of the territory under the project - about 213ha, including 7 residential areas in the centre of City of Pernik:

Figure 6. *The boundaries and coverage of the territory under of the project*

The basic principal for the choice of the type of monitored movements and deformations for different type of objects are adopted the following:

- For all buildings, bridges and other structures the vertical displacements and deformations of their bases and foundations are measuring;
- For all streets, roads and railways the vertical and horizontal displacements and deformations are measuring.

2. GEODETIC MONITORING FOR DISPLACEMENTS AND DEFORMATIONS

The following tree types of geodetic marks for stabilization of the points, included in spatial geodetic network, are used – deep levelling benchmarks, wall benchmarks, combined land marks for horizontal and vertical measurements:

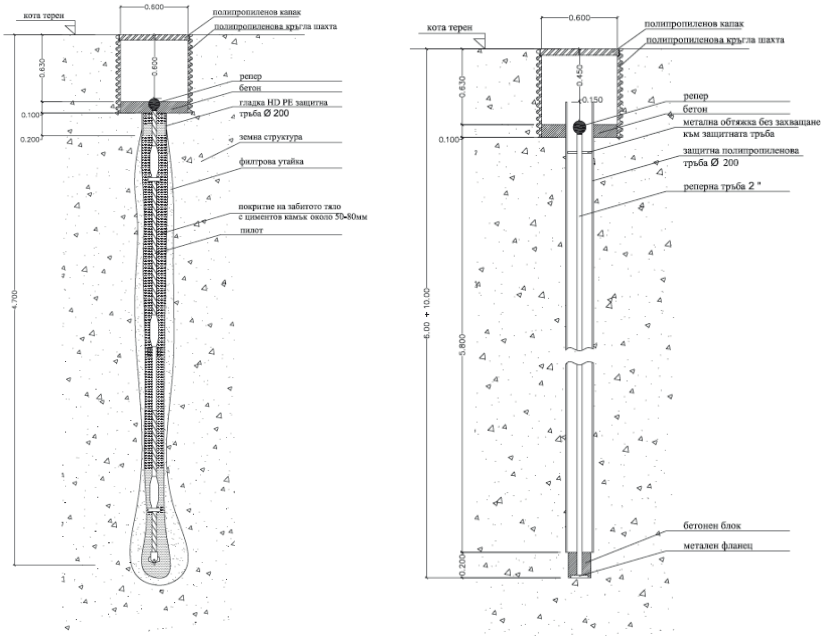

Figure 7. *Constructions for built deep levelling benchmarks*

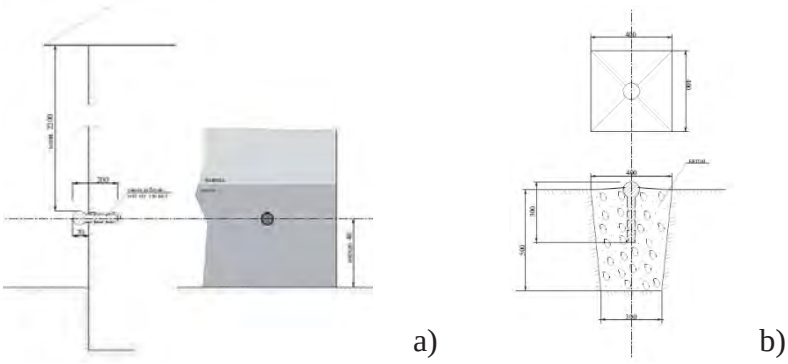

a) b)

Figure 8. *Types of built geodetic marks – a) wall benchmarks; b) combined landmarks for horizontal and vertical measurements*

The positions of the geodetic marks are determined on the base of the existing information from the planes of underground galleries and cadastral map of the city. The geodetic network included about 362 combined landmarks, 708 controlled wall benchmarks and 27 deep levelling benchmarks now.

On the results of analysis of existing geodetic base in the area of interest the reference points were selected – 6 existing ground benchmarks and 2 existing points from State Geodetic Network with known coordinates.

The methodology and technology for performing of precise geodetic measurements ware well-founded. To ensure the necessary accuracy of the observed vertical displacements and deformations, the absolute heights above sea level of the controlled benchmarks are determined by precise geometric levelling II^{-nd} class with standard deviation of ≤ 0.70 mm on 1km double run distance. The levelling is performed by set of high-precise digital levels and invar levelling staffs.

The horizontal displacements and deformations of the objects above underground mining galleries in this project are determined from measured coordinates by using combination of GNSS and trigonometrical methods. The accuracy of determined bases between points by each two GNSS receivers is in the limits of m_S=2.5-5mm. The angular and distance measurements are performed by tri stative method with electronical total station with standard deviation of measured angle $m_\beta \leq \pm 2$" and for measured distance $m_S \leq \pm$(2-3mm+2ppm):

Figure 9. *Examples of used precise geodetic instruments*

The period between of the measurement campaigns was accepted by 6 months and additional measurements in cases of force major events such earthquakes, water floods and appearing of visible disruptions of the constructions. For the period of past 9 years of organized observations such kind of exceptional measurements were not performed nevertheless that on 2012 was a huge earthquake in Pernik region.

2.1 Geodetic measurements

The last 15 campaign of geodetic measurements for monitoring of displacements and deformations were performed April - May 2019.

2.1.1. Precise geometric levelling

The precise geometric levelling was realized by high-precise digital levels LEICA NA3003 and LEICA DNA03 with set of twins of invar barcode levelling staffs. The method BFFB (Back-Fore-Fore-Back) was used for measuring of the height differences between stations of the instruments. Double-run measurements (in one and opposite directions) were performed for whole levelled lines.

The total length of double run levelled lines in the network is 54 253 m. The number of double run levelled height differences is 1115 (2230 measured differences in total) and the total number of included benchmarks (fixed and controlled) is 938:

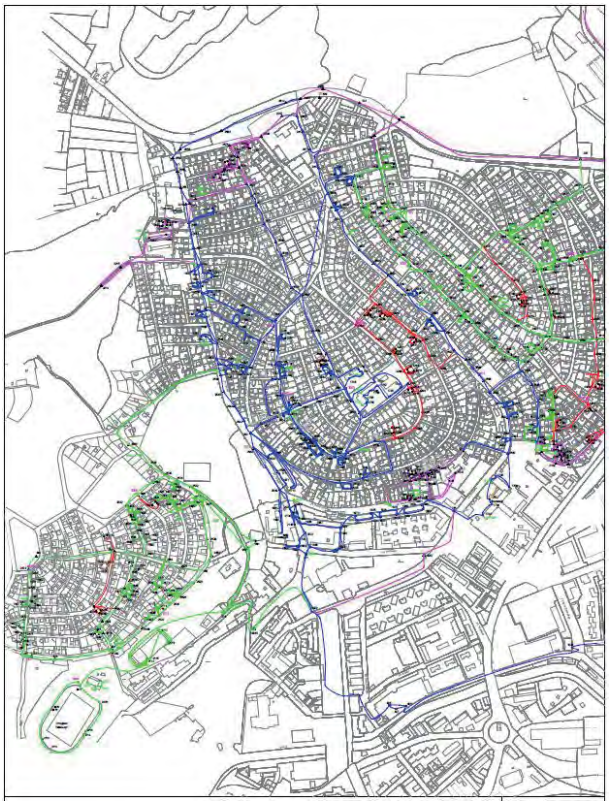

Figure 10. *A part of the schema of the precise levelling geodetic network*

2.1.2. GNSS observations

To connect the network of controlled points for geodetic measurements of horizontal displacements and deformations with reference points from the State Geodetic Network the precise GNSS observations were performed.

The observations were realized by professional geodetic GNSS receivers LEICA GPS SYSTEM 530 (5 items), SOKKIA RADIAN-IS (4 items) и CHC HUACE X91/X900 (3 items) in set with standard accessories for mount the antennas on wooden tripods and centric with optical plummets.

The total number of the points, which coordinates were determined by GNSS observations, is 145. The total number of the determined spatial vectors in the network is 436 (1308

coordinate differences). Because of the large number of simultaneously used GNSS receivers not only vectors between reference base stations and new points were determined, but a large number of vectors between rovers new points also were determined.

2.2.3. Precise polygonometry (angle – distance) measurements

Due to the fact, that a big part of the controlled points for monitoring of horizontal displacements and deformations are situated in the city canyon of Pernik, where conditions for GNSS observations are not good, in these regions of the plane network were performed additional geodetic measurements by conventional technology. This decision is based on the main goal to receive reliable end results for coordinates of the controlled points, which were situated on specific places according existing underground galleries. The places of controlled points were fixed by the needs of the monitored objects and cannot move them because of limits of used technologies for measurements.

The measurements were performed by two precise total stations LEICA TC1610 (angular accuracy of 5^{cc} and distance accuracy of 3mm+2ppm) with standard set of accessories for mount the instruments and reflectors on wooden tripods and centric by optical plummet.

The total number of points, which coordinates were determined by polygonometry, is 300. For the calculations were used as reference 85 points, determined by GNSS observations. The total number of angle-distance measurements, used in calculations of the network, is 917 per each.

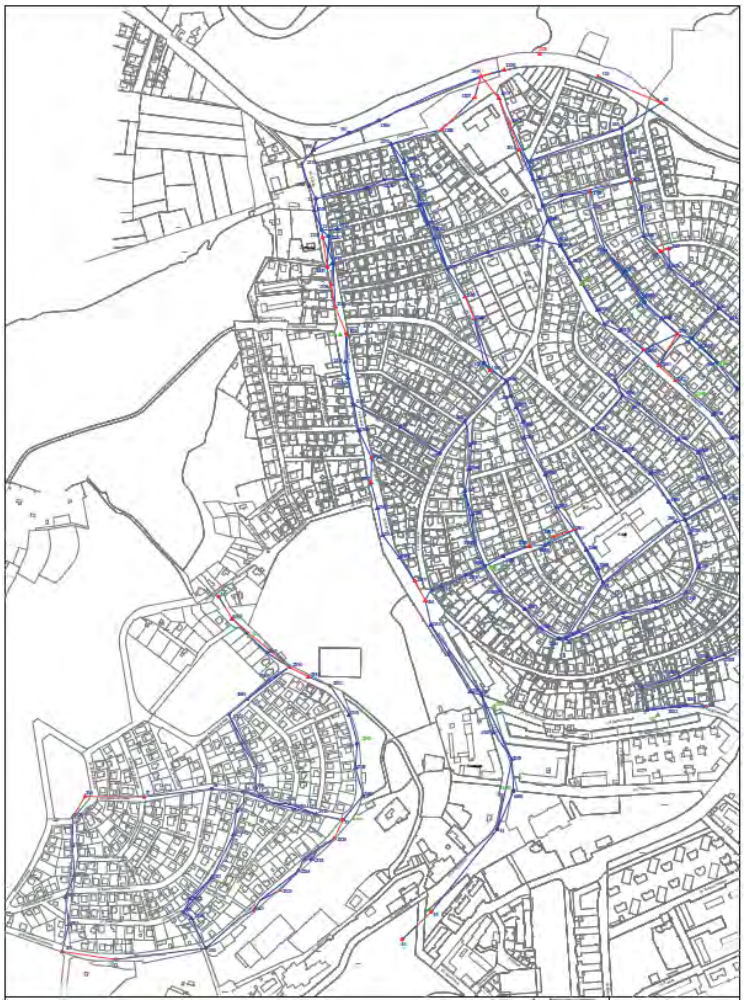

Figure 11. *A part of the schema of the precise polygonometry and GNSS geodetic network*

2.2. Processing the geodetic measurements

2.2.1. Processing the precise geometric levelling measurements

The processing of collected data from performed levelling measurements is realized by specialized software DigitalLeveling - our own application, developed especially for big geodetic networks as in case of Pernik Minings. A preliminary asset of the measured height differences and distances in the levelling network was performed by closed loops. The determined values of the measured height differences were adjusted by strict parametrical adjustment by Least Square Method (LSM). The results from this adjustment shows that, the highest value of standard deviation of adjusted elevation is 0.99mm. The standard deviation

for measurement with weight equal one for whole network is Me=0.3mm, which correspond with a priory value of the standard deviation of the used instruments (0.4mm).

2.2.2. Processing the GNSS observations

The processing of GNSS observations was realized in the environment of specialized software Leica Geo Office. All spatial vectors between occupied points were calculated by the GNSS measurements. During these calculations were determined the errors (standard deviations) of the coordinate differences dX, dY, dZ, formed each vector, on the base of multiply measurements. The maximum value of the standard deviation of the adjusted coordinates is 3.5mm.

2.2.3. Processing of the linear-angular measurements

The processing of performed angle-distance measurements was realized in the environment of specialized software WIN TPLAN. A preliminary asset of the measured angles and distances in the polygonometry network by closed loops. The received values of measured angles and distances in the network were adjusted by strict parametrical adjustment by LSM. The results from this adjustment processing shows that the maximum value of the standard deviation of adjusted coordinates is m_s=7.98mm. The standard deviation for measurement with weight equal one for whole network is Me=5.7^{CC}, which is corresponding with the accuracy of the used total station.

3. RESULTS AND DISCUSSION

All results from performed campaigns of geodetic measurements are collected in specialized data base, created for the project in the GIS environment and analyzed by GIS functionality and office software.

3.1. Analysis of the vertical displacement data

In order to perform comparative analysis of the data, collected by campaigns of measurements, the vertical displacements were calculated from determined elevations of controlled benchmarks in different campaigns. The absolute displacements were calculated for the period from the date of first to date of last campaigns and relative displacements were calculated for the period from date of the previous to date of the last campaigns. Annual displacements and velocities of the movements were calculated also. Results from these calculations were presented in tables as following:

Table 2: Results of comparative analysis of vertical displacements

Репери по обекти в участък			Абсолютни вертикални премествания , mm										
№ на репер	Тип обект	Местонахождение	11-0 29.03.2017г	Средна скорост mm/месец	12-0 29.09.2017г	Средна скорост mm/месец	13-0 30.03.2018г	Средна скорост mm/месец	14-0 30.09.2018г	Средна скорост mm/месец	№ на репер
1354	Сграда	Сграда на Пътя за Дивотино			-2.5		0.7	0.0	0.5	0.0	1354
2216	Път	Път за Дивотино	7.8	0.1	4.4	0.1	8.2	0.1	5.5	0.1	2216
2217	Път	Път за Дивотино	10.4	0.1	9.2	0.1	12.5	0.2	10.9	0.1	2217
2218	Път	Път за Дивотино	11.3	0.2	10.9	0.1	13.5	0.2	11.7	0.1	2218
131	Път	Път за Дивотино									131
132	Път	Път за Дивотино	-0.1	0.0	-2.0	0.0	7.3	0.1	6.7	0.1	132
141	Път	Път за Дивотино									141
142	Път	Път за Дивотино	-14.5	-0.2	-61.7	-0.8	5.3	0.1	-14.0	-0.2	142
151	Път	Път за Дивотино	-0.6	0.0	-3.6	0.0	5.6	0.0	2.8	0.0	151
152	Път	Път за Дивотино	20.3	0.3							152
153	Път	Път за Дивотино	25.7	0.4	20.2	0.3	27.1	0.3	26.9	0.3	153
154	Път	Път за Дивотино	15.0	0.2	3.1	0.0	16.1	0.2	2.4	0.0	154
1019	Път	Път за Дивотино	-5.6	-0.1	-9.1	-0.1	0.6	0.0	1.7	0.0	1019
1020	Път	Път за Дивотино	-17.6	-0.3	-37.2	-0.4	-13.4	-0.2	-14.2	-0.2	1020
2401	Път	Път за Дивотино	5.9	0.1	-14.7	-0.2	8.4	0.1	2.7	0.0	2401
2402	Път	Път за Дивотино	-8.7	-0.1	-27.1	-0.3	-9.5	-0.1	-17.1	-0.2	2402
2501	Път	Път за Дивотино	14.6	0.2	13.4	0.2	20.1	0.2	21.8	0.2	2501
2502	Път	Път за Дивотино	25.5	0.4	24.1	0.3	28.9	0.4	30.1	0.3	2502
2503	Път	Път за Дивотино	18.5	0.3	18.7	0.2	21.6	0.3	23.1	0.3	2503
2504	Път	Път за Дивотино									2504
2505	Път	Път за Дивотино									2505
2506	Път	Път за Дивотино	24.9	0.4	-1.4	0.0	26.9	0.3	10.2	0.1	2506
2507	Път	Път за Дивотино	14.1	0.2	-4.4	0.1	16.8	0.2	15.1	0.2	2507
2625	ЖП линия	ЖП линия Перник-Волуяк	-30.5	-0.7	-46.2	-0.9	-45.0	-0.8	-47.0	-0.7	2625
2624	ЖП линия	ЖП линия Перник-Волуяк	-54.2	-1.2	-66.8	-1.3	-69.4	-1.2	-79.6	-1.2	2624
2574	ЖП линия	ЖП линия Перник-Волуяк	-5.8	-0.1	-9.5	-0.2	-1.7	0.0	-4.7	-0.1	2574
1361	ЖП линия	ЖП линия Перник-Волуяк	-5.4	-0.1	-13.7	-0.3	-4.8	-0.1	-10.9	-0.1	1361
1362	ЖП линия	ЖП линия Перник-Волуяк	-10.8	-0.2	-42.5	-0.6	-13.1	-0.2	-19.9	-0.2	1362
1363	ЖП линия	ЖП линия Перник-Волуяк	-11.4	-0.2	-49.4	-0.7	-10.2	-0.1	-23.5	-0.3	1363
1364	ЖП линия	ЖП линия Перник-Волуяк	-3.3	0.0	-8.2	-0.1	-0.5	0.0			1364
1365	ЖП линия	ЖП линия Перник-Волуяк									1365
1366	ЖП линия	ЖП линия Перник-Волуяк	0.5	0.0	-0.7	0.0					1366
1367	ЖП линия	ЖП линия Перник-Волуяк	-5.9	-0.1	-5.4	-0.1	-2.9	0.0	-9.3	-0.1	1367
2313	ЖП линия	ЖП линия Перник-Волуяк	-44.7	-0.6	-63.5	-0.8	-40.5	-0.6	-56.1	-0.6	2313
2314	ЖП линия	ЖП линия Перник-Волуяк	-27.9	-0.4	-53.6	-0.7	-30.0	-0.4	-35.6	-0.4	2314
2315	ЖП линия	ЖП линия Перник-Волуяк	-26.2	-0.4	-45.8	-0.6	-25.3	-0.3	-32.6	-0.4	2315
2316	ЖП линия	ЖП линия Перник-Волуяк	-1.7	0.0	-33.6	-0.4	1.7	0.0	-20.8	-0.2	2316
2317	ЖП линия	ЖП линия Перник-Волуяк	-10.6	-0.2	-31.8	-0.1	-9.0	-0.1	-11.1	-0.1	2317
2318	ЖП линия	ЖП линия Перник-Волуяк	-49.0	-0.7	-91.2	-1.2	-52.1	-0.6	-70.6	-0.8	2318

The vertical displacements were showed graphically by linear changes of elevations of controlled benchmarks on profiles and objects in time and regression analysis for forecasting of the movements:

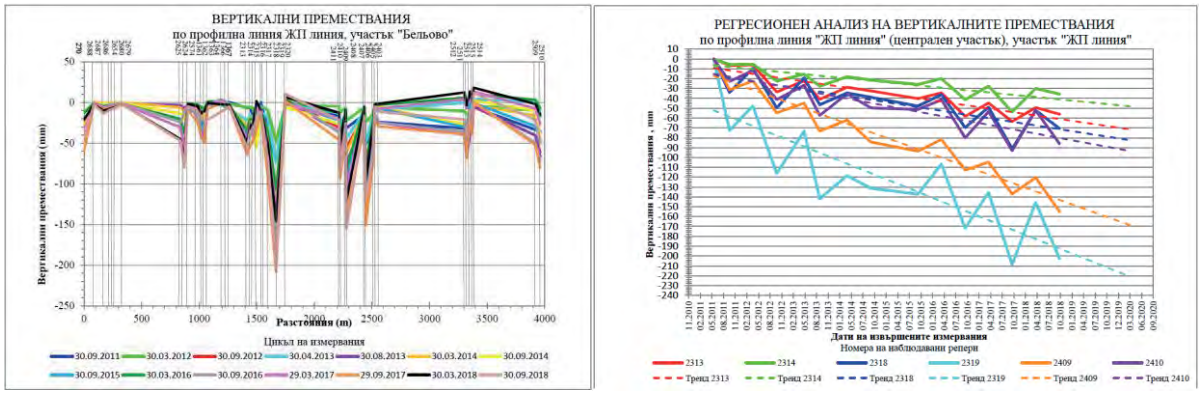

Figure 12. *Graph of linear changes of vertical displacements by profiles in time, by benchmarks in time and regression analysis*

It has been found that for most of the controlled benchmarks, the values of the observed vertical displacements are significantly greater than the accuracy of the method used to determine the elevations. This gives a high degree of credibility to claim that there have actually been vertical displacements in the controlled benchmarks and objects.

The vertical deformations were calculated on the base of the vertical displacements. The results were shown in tables with calculated values of the main deformation parameters according Instruction for the protection of the facilities and structure from the harmful influence of the underground mining works in the coal basins, issued by Ministry of Energy, Sofia 1983 – the inclination i (mm/m), curvature (mm/m²) and radius of the curvature R (m) for applied cases of objects (on buildings and linear objects – roads and railways).

3.2. Analysis of the data for horizontal displacements

The values of calculated coordinate differences dX, dY for the periods between dates of first and next campaigns of measurements and between consecutive campaigns were presented in table forms. By these coordinate differences were calculated the values of properties of the vectors of horizontal displacements – the length dS and bearing anlge α, as the velocity of the

the rate of horizontal displacements. The values of horizontal deformations ε (mm/m), calculated according Instruction, were presented in tables also.

To illustrate the comparative analysis of the results of the geodetic measurements, the combined schemes were presented, which containing:

- Positions of the elements of engineering infrastructure on the ground surface situated on the cadastral map of the City of Pernik;
- Positions of underground mines and fields;
- Positions of benchmarks and geodetic points;
- The calculated horizontal and vertical displacements on controlled points.

The horizontal displacements were presented graphically by trajectories of movements, by applying colour according to the period of their occurrence between the campaigns performed.

The colorized of vertical displacements are also used, depending on their size. An example of such a combined scheme is given in the following figure:

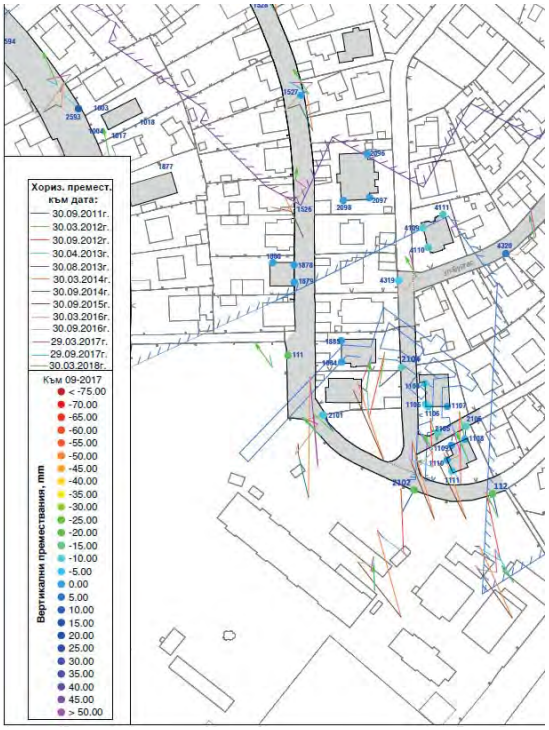

Figure 13. *A part of combined schema for graphical representation of changes of vertical and horizontal displacements*

For each measurement campaign, a detailed analysis of the observed displacements, deformations and rate of change is made, taking into account the location of the controlled points, the initial moment the observations, the type of the observed object, etc.

4. CONCLUSION

As a result, the correlation between the magnitude of vertical and horizontal displacements was found, i.e. in areas with more significant absolute shrinkage, higher values of horizontal displacements are also found.

There is a clear trend towards the horizontal displacement vector directions, which generally follow the direction of the terrain slope and the underground layers - an expected result that confirms the correctness of the observed data for horizontal movements. Particularly clear is the trend of horizontal displacements for the points on the railway line - the vectors have directions perpendicular to the axis of the line, depending on the position of the points in relation to the axis in opposite directions to the fall of the line embankment. It is noteworthy the cyclical nature of a diametrical change of direction of the horizontal displacement vectors with more significant values, the trajectory showing seasonal variations of the controlled points around the initial position, which coincide with the oscillations of the vertical displacements.

In result of provided data from geodetic monitoring for deformation processes occurring in sections of the railway structure, the responsible authority made decision to design and execute reinforcement activities to protect and prevent construction of this important object.

The developed GIS data base with collected actual geodetic data for the progress of deformation processes will be useful tool for the further design of strengthening measures for the prevention of the residential areas of the town of Pernik.

Executing the largest design for geodetic monitoring of displacements and deformations in Bulgaria for last 9 years our team acquired and further developed its professional qualifications and expand the practical and theoretical experience in this very specialized field of the geodetic science and practice.

Natural Hazards, Geophysical Characteristics and Some Ecology Problems on the Bulgarian Black Sea Coast

Boyko Ranguelov [1] , Orlin Dimitrov [2]

[1] Mining and Geology University, Geophysics Department 1700 Sofia, Bulgaria
Phone: +359 2 8060 436, E-mail: branguelov@gmail.com

[2] Institute of Oceanology "Fr.Nansen" Bulgarian Academy of Sciences Varna, Bulgaria
Phone: +359 2 8060 436, E-mail: ovdimitrov@gmail.com

ABSTRACT

An integrated approach to the new and interpreted geophysical data, natural hazards expressions and local natural resources is applied to reveal the relationships, dependencies and possible interactions between the potential geophysical fields, DEM and bathymetry, natural hazards developed in the regional geophysical context and the natural recourses explored and exploited since historical times up to the present days. The main aim of this study is to reveal relationships in depth, when they exist or not and to present the areas where such dependences are not adequate. Such approach is newly performed and is targeted to the scientists, decision makers, and local and regional authorities, to inform them about possible sustainable deployment of the natural resources and their effective exploitation in case if a strong multihazrds natural phenomena affect the study area and the possible effect to the environment. The side effect of this research is the deeper view to the possibilities of the recent geophysics to help the extended knowledge and mitigation measures in case if the strong disaster occurred and environmental pollution observed. The results of the study show sometime deeper relationships, and also frequently the lack of such intersection between the investigated parameters.

KEYWORDS: natural hazards, geophysical characteristics, Black Sea coast

1. INTRODUCTION

To study the influence of the natural hazards [1] and their effects on the development of the coastal society is an important task investigated from different point of view especially to the sustainability and human safety and infrastructural security. On the other hand the natural resources define the societal progress and provide high standard of life. The coastal societies usually develop tourism and entertainment as priority all over the world. The Bulgarian Black Sea coastal area is not an exception. But in parallel a lot of other social activities help the progress and sustainability. For example the gas and oil production, the development of port facilities, the extensive fishery and seafood production as well as other heavy industry activities such as energy sector development ore and mineral exploration and exploitation, etc. are of vital importance for the balanced and effective social life. The Bulgarian Black Sea coastal area both – on land and in the sea is threatened by different natural hazards which can destroy the sustainability for curtain interval of time. The ability to recover is an important task of the administration and local people. The natural resources and reserves are the basement of the fast recovery and progress. Using the knowledge about all known data and information as well as some new technology solutions we try to estimate all possible natural hazards and their destructive potential to the coastal society and on the other hand try to find all useful and potential resources which could be exploited in case of occurrence of hazardous events and their prevention and the possibility of sustainable development of the coastal society of Bulgaria.

2. MATERIAL AND METHOD

Full information about all known natural hazards and natural resources are summarized and studied in details [2], [3]. The methodology applied is the comparative analysis of the reflections of the known phenomena to the geophysical fields and their imminent characteristics. The results obtained are presented to a comparative table for easier understanding and common use.

2.1 Natural hazards in the Black Sea area and surroundings

- Collapsibility of loess. The hazard spreads to the north part of the Black sea coast. It is mixed with some karsts activities. The negative influence could be expected to the buildings constructions, underground mining and collapse of the agricultural land. The level of the destructive potential is low, because simple geology and geophysical prospecting can define clearly the areas of potential threat.

- Rock falls and cracked deposits. The hazard is located to the rocks near to the sea and can be localized easy. Low destructive potential.

- Active faults and mud flows. These are surface geodynamic factors with low destructive potential.

- Active faults and earthquakes. The typical representative seismic source is so called Shabla-Kaliakra source. According to the maps of the seismic hazard this is one of the most dangerous seismic active sources. Typical example is the earthquake from 1901 – magnitude 7.1, I max (intensity) X EMS. The location of the epicenter is in the sea about 10-15 km from the coast. The earthquake triggered big block subsidence (about 3 km2), large rock falls and landslides and even clear tsunami effects (about 3 meters local sea inundation in Balchik). The source has no clear origin. Some theories suspect the activation of the faults cross-section, another the fault's knot, but the observations did not confirm any of it. The source is characterized by very strong seismic events which occur irregularly, but there are a lot of historical descriptions about ancient strong earthquakes with very high magnitudes, strong destructive effects and triggering other destructive hazards like landslides, stone falls, tsunamis, etc. The destructive potential is very high and preventive, protective and safety measures are essential. The seismic source is one of the most active and hazardous all over the Black Sea coast

- Induced Seismicity – some data about man-made earthquakes with magnitude up to 4.5 are observed due to the exploitation of the huge salt body near Devnia. The method of solution extraction is supposed to be a trigger of stress redistribution and small earthquakes generation. The subsidence is also observed.

- Tsunamis. As it was mentioned some local earthquakes can trigger tsunami. The far field tsunamis of seismic origin have been also observed – sources from Crimea, North

Anatolian fault, Vrancea, etc. There are data about tsunamis generated by other phenomena – like underwater slides (turbidities), atmospheric disturbances as well as of not known origin. A typical representative event is this one from 7 May, 2007. It created local disturbances of the sea level with amplitude of about three meters. The models calculated on the basis of underwater landslide (because the seismic activity was not detected) as well as of atmospheric origin, does not confirm certainly the source of this tsunami generation mechanism. There are some hypotheses that large gas emissions and mud volcanoes can also trigger tsunamis. The model calculations for some typical cases show that the tsunami height can not go over 3 meters [4]. But other calculations show very specific effect of some local peculiarities of the bottom and coastal geometry, which can focus the tsunami energy to some local places. This could be very dangerous and needs special investigations and modeling. For now the destructive potential is assessed as middle.

- Landslides. Almost the whole area of the Bulgarian northern Black Sea coast consists of large active landslides which are active due to the rainfalls, underground waters' levels changes, triggered by earthquakes, etc. The destructive potential is very high and many roads, buildings and other facilities have been destructed during the historical times (Kavarna case - III c. BC) as well as recent constructions. To the south the Sarmatian lime stones (the main geological reason of the landslide process) are rarer and around Cape Emine the spreading of the active landslides is decreasing. The south part of the sea coast only rare cases can be observed [3].

- Erosion on land and on the costal rocks (abrasion) – widely spread all over the coast. Very clear expressed and could be avoided. Low destructive potential.

- Salt waters intrusion and silanization – widely spread and some salty lands are out of exploitation. Low destructive potential

- Floods. Flash floods are frequent event usually related to storms. The can affect the low lands and river estuaries and deltas. High destructive potential.

- Storms. The whole black Sea coast is vulnerable to storms. Surge storms and high sea water levels are frequently observed. Sometimes the sea level increased up to several meters. Wind storms are also frequent. High destructive potential due to the needs to close ports during

the wind storms. Hail and snow storms are usual during the winter time. In general - high destructive potential.

- Icing. The northern part of the coast is frequently affected by icing during the winter times. Sometimes even the sea is freezing.

- Natural and artificial (due to the flotation ore processes) radioactivity. Observed on some beaches (for example "Vromos") and waste deposits (for example near Rosen cooper mine)

2.2 Natural resources in the Bulgarian Black Sea area and coastal zone

The natural resources (mineral deposit, oil and gas, coal mining, etc.) are extracted from the general map of Bulgaria and show relative high concentration of different deposits in the coastal area [5].

- The Shabla (Kamen briag-Tulenovo) oil deposit. Small block structured deposit which produces still very small quantities of heavy oil.
- Dobrudja cool basin. Deep (~3500 m.) anthracite deposit with significant quantities, but due to the deep location and underground waters wait for innovative approach of exploitation.
- Manganese deposit. Huge deposit near Obrochishte. Mine exploitation. Potential for local people employment.
- Salt deposit near Devnya – base for chemical industry and potential of human employment.
- Gas seeps in the sea, related to the shallow depositions of methane. Predominantly located in the sea and near to the north coast. No industrial quantities are expected.
- The gas deposit Galata. Still produces gas. Some difficulties for the exploitation due to the high content of the abrasive material in the gas substrate.
- Healthy mud. High medically elective mud deposits near Balchik (Tuzlata) and Pomorie. High potential for health tourism.
- Hot mineral waters – wide spread to the north. Due to the Valangine water aquifer of lime stones. High potential for health tourism.
- Sapropel deposits due to the sea plants deposition. Considered as a resource with multiple application to the agriculture, pharmaceutics, etc.

- Sea salt production – open exploitation and production near Bourgas and Pomorie.
- Black Sea cool basin north of Bourgas. Mining activity and exploitation.
- Cooper and multi metal ore deposits south of Bourgas (mines Rossen, Varli briag and Gramatikovo deposits). Ore exploitation since ancient times up to the present days.
- H2S – the sea water contains solution of H2S especially for the depths deeper then 150-200 meters. There are expectations about industrial processing of this resource.
- Gas hydrates. Huge deposits in the sea around the cost. Considered as a huge source of energy. Expectations about industrial exploitation. Needs innovative approach
- The main and very large income factor is considered the tourism with all facilities and services. This is a very vulnerable sector of the natural hazards and strongly depends on the natural resources.

3. RESULTS AND DISCUSSION

The results are summarized in a comparative Table 1. presenting the locations, level of danger which the object can be for the people or infrastructure the natural resources (deposits) and the geophysical characteristics of any of the objects, as well as the indicators, which could be useful for the comparative analysis.

Table 1: Comparative table of the natural hazards, natural resources and their relationships with the geophysical characteristics.

Object	Location (source)	Level of danger	Geophysical characteristics	Indicators (geology & geophysics)
Natural hazard a) Earthquakes	Shabla-Kaliakra seismic source (SS) (location in the sea)	Very high	Generator of irregular strong earthquakes (up to M8), long lasted aftershocks	Historical and recent seismic catalogues and descriptions
b) Earthquakes	Sparse distribution in the sea north and east of Bourgas city	Middle	Magnitude up to 5.5 (Richter scale)	Recent active faults
c) Earthquakes	On land around Devnya town	Middle	Magnitude up to 5.0 (Richter)	Tectonic and anthropogenic origin
Tsunamis	Threaten the whole coastal areas by local or far field tsunamis	Middle	Conservative models calculated up to 3 meters height and hundreds of meters inundation. Local anomalies due to the costal geometry.	Local SS (Shabla-Kaliakra) Regional SS (Crimea, Caucasus and Turkish coasts) Sometimes atmospheric or turbidities origin
Landslides	North coast (largely distributed) and south coast (much rare)	High	Huge volumes, deep sliding - geological origin and gravitational processes	Frequent activated areas up to several hundred square acres. Triggered by earthquakes and rain
Rock falls	Cliffs areas all over the coast	Low	Single huge rocks and/or avalanche type of gravitational process	Triggered by erosion, abrasion and possibly earthquakes
Turbidities	Underwater avalanche type deposition flows on the continental slope	Low	Mudflows sometimes with huge dimensions developed on the sea shelf	Mainly triggered by earthquakes or other destabilization processes
Salt waters intrusion and silanization	Lowlands on the costal areas, river beds	Low	Changed electrical conductivity	Stalinization of surface layers (sometimes on the land)
Floods	On land (low lands and river beds are more vulnerable)	Very high	Water masses intruded to the land and flash floods in lowlands and river beds	Generated by sea storms (sea waters intrusion) or rain and/or snow melting
Storms.	The whole costal line	High	High wind speeds, sea waters level increase, huge rain and snow	Wind sea storms, storm surges, rain and snow storms on the land and sea.
Icing.	Winter hazard mainly to the north coastal area	Middle	Low temperatures, wind and snow	Freezing areas, disconnection of electricity, sometimes even the sea is freezing
Radioactivity	Areas around the cooper mining waste deposits	Low	Radioactivity over the natural background	Higher radioactivity over ancient mines and recent waste deposits.

Table 1: *Cont.*

Mineral recourses (deposits)	**Location (source)**	**Level of danger**	**Geophysical characteristics**	**Indicators (geology & geophysics)**
The Shabla oil deposit	Kamen briag-Tulenovo	Very low	Relatively low reflection to the gravity and magnetic fields	Low reflections to the seismic exploration data
Dobrudja cool basin.	Central Dobrudja	No	Low reflection to the gravity and magnetic fields	Low reflections to the seismic exploration data
Manganese deposit	Near Obrochishte village	Low	Low reflection to the gravity and magnetic fields	Geology evidences about deposits
Salt deposit	Near Devnya town	High due to the induced seismicity	Very high reflection to the gravity field. Low reflection to the magnetic field.	High reflection to the seismic exploration data
Gas seeps	Near and/or deeper to the sea costal area	Middle due to the possibility of inflaming	Bubbles and visible emissions	High relationships with the bottom underwater active faults
The gas deposit "Galata".	In the sea near to the Galata cape	Low	Low refection to the gravity and magnetic fields	High reflection to the seismic exploration
Healthy mud	Tuzlata (near Balchik) and Pomorie	No	No refection to the gravity and magnetic fields	No refection to the seismic exploration data. Visible deposits.
Hot mineral waters	Developed mainly to the north coast (so called Valangian layer)	No	No refection to the gravity and magnetic fields. The Valangian layer is detected by seismic exploration and electro conductivity (VES) methods.	Higher temperature. High electro conductivity and reflectivity to the seismic exploration of the Valangian.
Sapropel deposits	In the sea	No	No refection to the gravity and magnetic fields	Underwater exploration
Sea salt production	Near Pomorie and Bourgas	No	No refection to the gravity and magnetic fields	Visible deposits during the exploitation
Black Sea cool basin	North of Bourgas	Middle	Normal magnetic and gravity fields	Mining activity
Cooper and multi metal ore deposits	Around Bourgas	Middle	Intensive mosaic magnetic field. Positive gravity anomaly. Radioactivity.	Mining activity, waste deposits, ore exploitation high magnetic susceptibility
H2S	Everywhere in the sea water	High possible environ_ment pollution	Solution in the water, high chemical reduction potential	No life, conservation of objects due to the low O2 content

Gas hydrates	Depositions to the deeper parts of the sea	Low	Anomalous low temperatures and higher pressure	Frozen methane, easy vaporizing to the surface

4. CONCLUSION

natural hazards it is rather clear that a lot of disasters threaten the coastal area. Different in their physical properties and power, they are real danger for the population and infrastructure.

There is high probability of multihazards triggered by each other. For example, the earthquakes can trigger tsunamis and on land and the bottom sea landslides (also rock falls and/or mudslides) and then landslides can trigger again tsunamis. The high winds water level changes can trigger floods, water salt intrusion and salinization,

There are observations about radioactive pollution due to the natural and anthropogenic factors. The gas and oil exploitation can triggered sea waters and coastal lands pollution.

Regarding the natural resources and reserves is clear that there is a large potential together with the tourism about industrial development (natural resources, port facilities, suitable places for communication and energy links, etc.)

Energy potential seems to be future development sector due to the wind energy, oil and gas interconnectors, expected deposits, H2S and gas hydrates exploitation, etc.

Industrial potential and trading industry are also with possibilities to increase and together with tourism can bring large benefits.

Both – natural hazards and natural resources are interconnected and prevention and safety measures are essential to preserve the human lives, industrial infrastructure and tourism. This approach can satisfy the requirements of sustainability and future development of the region..

ACKNOWLEDGEMENT

This publication is supported by the Nat. Science Program "Environmental Protection and Reduction of Risks of Adverse Events and Natural Disasters" (Resolution Council of Ministries and Ministry of Education and Science) – Agreement No D01-230/06.12.2018 with BAS.

REFERENCES

1. Muco, B. A. Geohazards assessment and mapping of some Balkan Countries., Nat Hazards 2012 Volume 64,(2), p. 943–981,

2. Ranguelov B. Risk profiles and hazards for the Black Sea area. In Social and Economic Impact and Policies; Margottini C, Canuti P, Sassa K., Eds.; Springer-Verlag, Berlin, Heidelberg, Germany, 2013; Volume 7, pp. 3–9.

3. Brouchev I. Geological Hazards Map of Bulgaria. "Acad. M. Drinov" Publ. House, BAS, Sofia, Bulgaria, 1994; pp. 215.

4. Ranguelov B. Natural Hazards – Nonlinearities and Assessment. "Acad. M. Drinov" Publ. House, BAS, Sofia, Bulgaria, 2011; pp. 245.

5. Natural Resources map of Bulgaria. Available online: http//mining-enc.com/userfiles/images/bolgarija4.jpg (accessed on 07 07 2019)Author 1, A.B. (University, City, State, Country); Author 2, C. (Institute, City State, Country). Personal communication, 2012.

Usability of the New GNSS-based Positioning Technologies

Veli Ilci[1]

[1]Hitit University, Vocational School of Technical Sciences 19169 Corum, Turkey
Phone: +90 364 219 0800, E-mail: veliilci@hitit.edu.tr

ABSTRACT

This study aims to determine the positioning accuracy and the usability of the two of the state-of-the-art positioning technologies; Trimble CenterPoint RTX and CSRS-PPP. For this aim, we conducted GNSS observations at the seven different test points with 20 km intervals that were located from the Corum province to the Kirikkale province. The observation data were collected using a Trimble R10 dual-frequency GNSS receiver. The coordinates of the test points were obtained from CenterPoint RTX in real-time and CSRSS-PPP services 20 days after the observation time. These coordinates are compared with the reference coordinates obtained from differential solution using GrafNET post-processing software. The maximum errors in latitude, longitude, and position components are cm-level, while the maximum errors in height components are 2-dm level for both of the technologies. The average results show that both of the services provide cm-level accuracy for all of the components. The results also show that the obtained accuracies will meet the current requirements of the many positioning applications, and therefore the usage of these new technologies will increase in the near future due to the advantage of them comparing to the classical positioning techniques. The main limitation of the CenterPoint RTX service is the initialization time to obtain these levels of accuracies. The main limitation of the CSRS-PPP service is not to provide a real-time solution.

KEYWORDS: Precise Point Positioning; CSRS-PPP; CenterPoint RTX

1. INTRODUCTION

Nowadays, classical Global Positioning Satellite System (GNSS) techniques called real-time kinematic (RTK) and network-RTK are used in many surveying applications because they provide a three-dimensional, and real-time solution in cm-level accuracy. The classical RTK technique requires at least two GNSS receivers, named reference, and rover [1]. Furthermore, the range between these two receivers is limited to approximately 20 km due to satellite orbit, and atmospheric errors [2]. Also, it requires radio connection or internet access in data transmission. The Network-RTK technique offers a solution with a single GNSS receiver; thus, it provides a more economical solution compared to the conventional RTK technique. Network-RTK technique calculates the atmospheric and orbital errors for the entire network, and the correction data is transmitted to the network users via the GSM connection. However, the disadvantage of this technique is that the infrastructure cost of the existing system is very high [3]. Also, in some Network-RTK systems, the users have to pay a certain fee to get service. Another disadvantageous of this technique that the usage of the service is limited to the network [4].

The existing solutions have not been able to meet all the needs of the users. Therefore, developing satellite-based positioning technologies, techniques, and algorithms aim to come through the disadvantageous of the existing positioning techniques and also meet the needs and expectations of the positioning community.

In the last decade, state-of-the-art positioning technologies focused on providing a cm-level accurate solution with a single GNSS receiver without any connection or limitation. Precise Point Positioning (PPP) is one of the emerging technology that aims to meet the needs of the users since 1990s [5]. One other technology has developed to overcome the limitation of the traditional techniques is Real-Time eXtended (RTX) technology [6], [7]. In this study, we examine the usability of these two technologies in terms of accuracy, and initialization time at the surveying applications.

2. MATERIAL AND METHOD

2.1 CSRS-PPP

The Canadian Spatial Reference System (CSRS) Precise Point Positioning (PPP) is an online GNSS processing service that was developed by the Canadian Geodetic Survey of Natural Resources Canada [8]. CSRS-PPP service allows the users to upload their raw static or kinematic GNSS observation data collected by a single or dual frequency receiver to the web interface of the service. In a few minutes, the solution files were sent by the service via e-mail. GNSS users, anywhere in the world, can obtain accurate positioning solution using only one GNSS receiver. This service does not necessitate reference station installation and proximity to reference stations. Also, this service provides a solution in NAD83 and ITRF reference frames.

2.2 Trimble CenterPoint RTX

Trimble CenterPoint Real-Time eXtended (RTX) technology aims to provide high-accuracy position information to its users. This technology uses globally distributed monitoring station networks' data to eliminate GNSS error sources on a global scale using highly accurate models and algorithms [9]. The correction data are produced in the operation center and transmitted in CMRx message format to six geostationary Sky Terra satellites to transmit the L-band signal to the user receiver [10]. This correction data is also transmitted to the user directly via Internet delivery. In both ways, the user can determine its position in real-time. The receiver position is calculated in ITRF2014 datum, current epoch, and transformed to ITRFyy datum and 2005.0 epoch dependent on the receiver and field software. The general process of CenterPoint RTX technology is summarized in Figure 1.

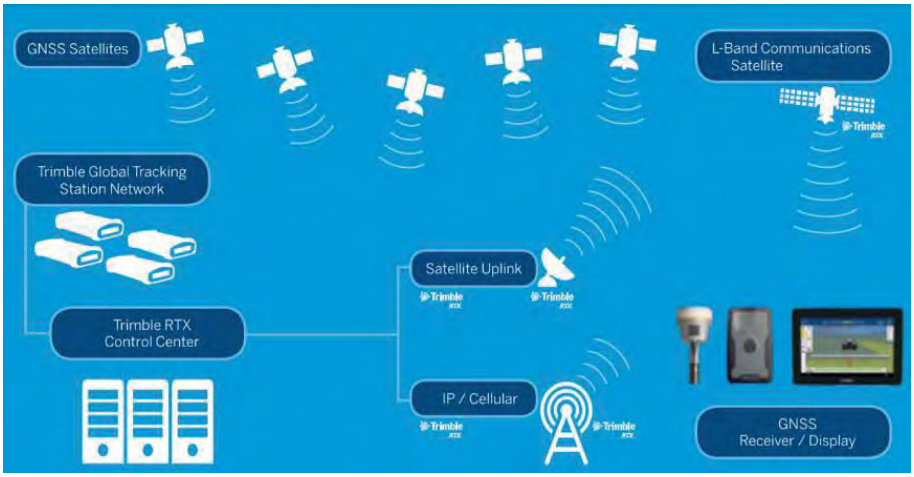

Figure 1. Process of CenterPoint RTX Technology [11]

CenterPoint RTX technology requires initialization time to solve uncertainties. This initialization time and the positioning accuracy may vary depending on some conditions such as the capacity of GNSS receiver and antenna, environmental characteristics, atmospheric conditions, the visible number and the distribution of the satellites, and multipath level [11]. The use of GPS, GLONASS, Galileo, Beidou, and QZSS satellite systems and the developed ionosphere correction models make a significant contribution to the solution and initialization time.

2.1 Study Area

This study was carried out along a 120 km long route covering Çorum and Kırıkkale provinces, see Figure 2. The test points are shown in red circles, and the TUSAGA-Active reference stations used in the solution are shown in black circles. The test points were selected in the direction from Çorum to Kırıkkale provinces with 20 km intervals and numbered from 1 to 7.

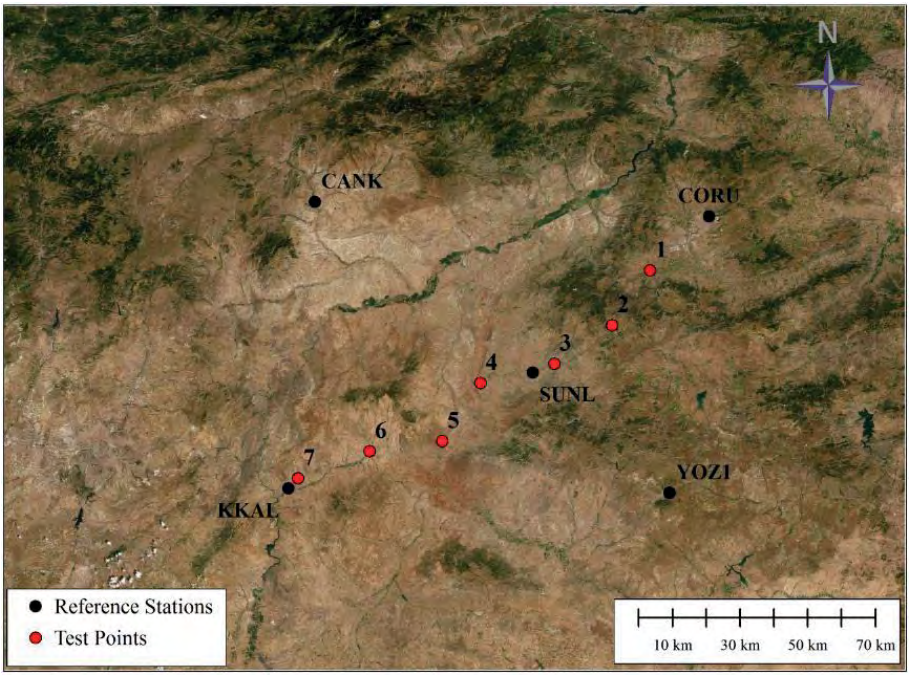

Figure 2. Study Area

2.2 Data Collection and Processing

GNSS observations at all of the test points were performed using a dual-frequency Trimble R10 receivers on June 2, 2018, see Figure 3. After the receiver had settled on a test point, the RTX data collection started as quickly as possible with the receivers' first data collection epoch to precisely determine the initialization time of the services. RTX correction data received via satellite connection through L-band for 75 minutes with a 1-second interval. At the same time, static GNSS data were collected for a minimum of 100 minutes for a 1-second interval. The GPS, GLONASS, GALILEO and BEIDOU satellite systems' data were collected at all of the test points. The satellite elevation angle was selected as 10 degrees. After the GNSS observation completed at a test point, the receiver was completely turned off, and the GNSS observation was started with cold-start at the one other test point.

Figure 3. Test measurements

1-second interval GNSS observations of CORU, SUNL, YOZ1, CANK, and KKAL reference stations for the related measurement day were obtained using the relevant web interface of TUSAGA-Aktif [12]. The satellite final ephemeris data for the measurement day was obtained from the relevant web-interface of the IGS service [13]. The 3D reference coordinates of the test points were determined by using GrafNet static network processing software developed by NovAtel.

The observation data of the test points uploaded to the CSRS-PPP services' web interface 20 days after the observation time to obtain the accurate coordinate values using final ephemerides data. For this process, we choose the kinematic solution and ITRF reference datum for the results. The related solution from CSRS-PPP received via e-mail in a few minutes, in ITRF2014 datum, current epoch. We calculate the reference coordinates of the test points at the same datum, and epoch to determine the accuracy of the CSRS-PPP solution.

RTX-PPP service offers a real-time solution in the ITRF2008 reference frame, 2005.0 epoch. To determine the accuracy of this technology, we calculate the test points' coordinates in this datum and epoch. We compare the results obtained from the CSRS-PPP service and CenterPoint RTX technology with that of reference coordinates epoch-by-epoch.

3. RESULTS

The differences between the reference coordinates of the test points and the obtained results from the two services are given in Figure 4 for latitude and longitude components, and in Figure 5 for 2D position and height components. When taking into consideration these figures, CSRS-PPP provides cm level accuracy for latitude, longitude, position, and height components from the first epoch of the observation. On the other hand, RTX provides cm-level accuracy after the 900-3000 epochs for latitude, longitude, position, and height components. As a result of this, Table 1 and Table 2 prepared for the differences data after 3000 epochs of the start of the observations.

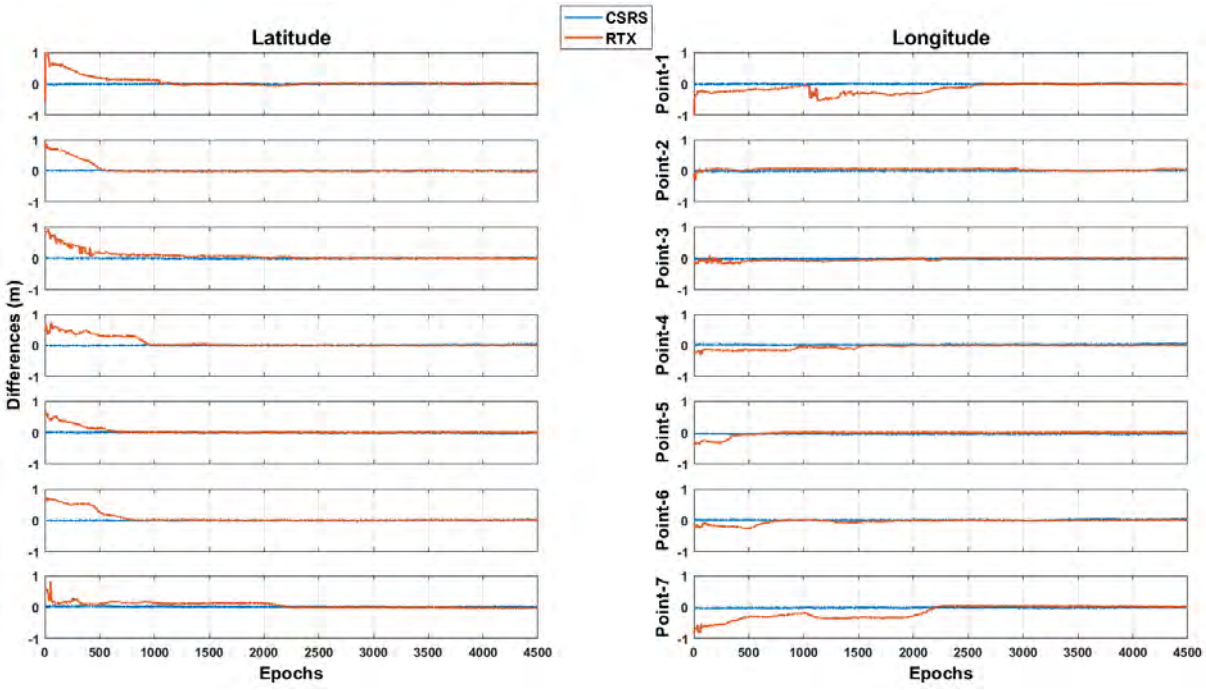

Figure 4. Differences in Latitude and Longitude Components

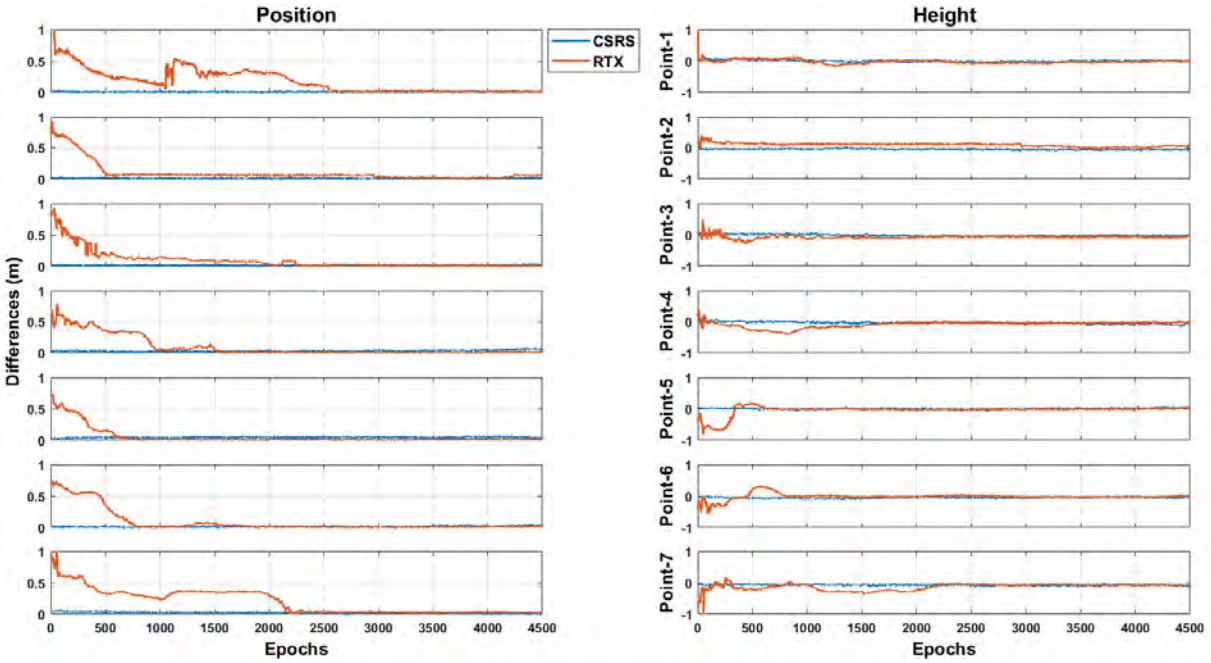

Figure 5. Differences in Position and Height Components

Table 1 gives some statistical data on the differences in latitude and longitude components. The latitude differences of CSRS-PPP and RTX are between -4 and 5 cm. The longitude differences of CSRS-PPP are between -6 and 6 cm, while RTX differences are between -3 and 7 cm.

Table 1: Statistics of Latitude and Longitude Components

	Latitude (m)						Longitude (m)					
	CSRS-PPP			RTX			CSRS-PPP			RTX		
PN	min.	max.	ave.	min.	max.	ave.	min.	max.	ave.	min.	max.	ave.
1	-0.03	0.03	0.00	-0.01	0.05	0.02	-0.04	0.02	0.00	-0.03	0.02	0.00
2	-0.02	0.04	0.01	-0.03	0.03	0.01	-0.01	0.03	0.01	-0.01	0.07	0.02
3	-0.01	0.04	0.01	-0.02	0.03	0.00	-0.03	0.01	-0.01	-0.01	0.02	0.01
4	-0.01	0.05	0.02	-0.02	0.03	0.00	0.01	0.06	0.04	-0.02	0.03	0.01
5	-0.04	0.01	-0.02	-0.01	0.04	0.01	-0.06	-0.02	-0.04	-0.01	0.03	0.01
6	-0.02	0.04	0.01	-0.01	0.02	0.01	-0.02	0.04	0.02	-0.02	0.03	0.00
7	-0.02	0.02	0.00	-0.04	0.00	-0.02	-0.04	0.01	-0.02	0.00	0.04	0.02

Table 2 gives some statistical data on the differences in position and height components. The position differences of CSRS-PPP are up to 8 cm, while differences of RTX are up to 7 cm. The average position differences are up to 5 and 3 cm in CSRS-PPP and RTX, respectively. The height differences are up to 13 cm in CSRS-PPP, and 12 cm in RTX. The average differences in height components are up to 7 cm in CSRS-PPP and RTX.

Table 2: Statistics of Position and Height Components

	Position (m)						Height (m)					
	CSRS-PPP			RTX			CSRS-PPP			RTX		
PN	min.	max.	ave.	min.	max.	ave.	min.	max.	ave.	min.	max.	ave.
1	0.00	0.04	0.01	0.00	0.05	0.02	0.00	0.05	0.01	0.00	0.10	0.03
2	0.00	0.04	0.02	0.00	0.07	0.03	0.02	0.10	0.06	0.00	0.10	0.04
3	0.00	0.04	0.02	0.00	0.03	0.01	0.00	0.06	0.02	0.00	0.12	0.06
4	0.02	0.08	0.04	0.00	0.04	0.01	0.00	0.13	0.06	0.00	0.09	0.03
5	0.02	0.07	0.05	0.00	0.04	0.02	0.00	0.06	0.02	0.00	0.06	0.01
6	0.00	0.05	0.02	0.00	0.03	0.01	0.01	0.08	0.04	0.00	0.06	0.03
7	0.00	0.04	0.02	0.01	0.04	0.03	0.01	0.13	0.07	0.02	0.11	0.07

4. CONCLUSION

CSRS-PPP and CenterPoint RTX are promising services that provide position information to GNSS users only using a single GNSS receiver. This study is conducted to reveal and compare the accuracy and usability of these services in GNSS applications. CSRS-PPP service provides a cm-level 2D position information (up to 8 cm) and 2-dm level height information (up to 13 cm) from the first measurement epoch. However, real-time position information can not be provided by the CSRS-PPP service. Because this service use ultra-rapid (available every 90 minutes, accuracy is +/- 15 cm), rapid (available the next day, accuracy +/- 5 cm), or final (available 13-15 days after the end of the week, accuracy +/- 2 cm) ephemerides data of the satellites that necessitate a latency time after the GNSS observations completed. In this study, we used the CSRS-PPP solutions that were processed using final ephemerides to obtain the best solutions of the seven test points. On the other hand, CenterPoint RTX technology can provide real-time position information. However, it necessitates the initialization time between 900-3000 epochs after the first measurement epoch. After the initialization time, RTX offers cm-level position (up to 7 cm), and 2-dm level (up to 12 cm) height accuracies. When taking into account the average values of both services, it can be concluded that cm-level position and height accuracies can be obtained using both services. Nevertheless, the main drawback of the RTX service is initialization time, while the main drawback of the CSRS-PPP service is not to provide real-time solutions.

REFERENCES

1. Alkan, R. M. Cm-level high accurate point positioning with satellite-based GNSS correction service in dynamic applications, J. Spat. Sci., 2019, pp. 1–9.

2. El-Mowafy, A. Analysis of Web-Based GNSS Post-Processing Services for Static and Kinematic Positioning Using Short Data Spans, Surv. Rev., 2011, 43(323), pp. 535–549.

3. Eissfeller, B. Real Time Kinematic and Precise Point Positioning: Status and Trends, Ger. J., 2012, vol. GPS 87, pp. 131–148.

4. Hutton, J. J.; Gopaul, N.; Zhang, X.; Wang, J.; Menon, V.; Rieck, D.J. J.; Kipka, A; Pastor, F. Centimeter-Level, Robust GNSS-Aided Inertial Post-Processing for Mobile Mapping Without Local Reference Stations, Int. Arch. Photogramm. Remote Sens. Spat. Inf. Sci. - ISPRS Arch., 2016, 41(July), pp. 819–826.

5. Zumberge, J. F.; Heflin, M. B.; Jefferson, D. C.; Watkins, M. M.; Webb, F. H. Precise point positioning for the efficient and robust analysis of GPS data from large networks, J. Geophys. Res., 1997, 102(B3), pp. 5005–5017.

6. Leandro, R.; Landau, H.; Nitschke, M.; Glocker, M.; Seeger, S.; Chen, X.; Deking, A.; BenTahar, M.; Zhang, F.; Ferguson, K.; Stolz, R.; Talbot, N.; Lu, G.; Allison, T.; Brandl, M.; Gomez, V.; Cao, W.; Kipka, A. RTX Positioning: The Next Generation of cm-accurate Real-Time GNSS Positioning, in Proceedings of the 24th International Technical Meeting of the Satellite Division of the Institute of Navigation (ION GNSS 2011), 2011, pp. 1460–1475.

7. Chen, X.; Allison, T.; Cao, W.; Ferguson, K.; Grünig, S.; Gomez, V.; Kipka, A.; Köhler, J.; Landau, H.; Leandro, R.; Lu, G.; Stolz, R.; Talbot, N. Trimble RTX, an Innovative New Approach for Network RTK, in 24th International Technical Meeting of the Satellite Division of the Institute of Navigation 2011, ION GNSS 2011, 2011, vol. 3, pp. 2214–2219.

8. Canadian Spatial Reference System-Precise Point Positioning (CSRS-PPP) Available Online: https://webapp.geod.nrcan.gc.ca/geod/tools-outils/ppp.php. (accessed on 01-Sep-2019).

9. Doucet, K.; Herwig, M.; Kipka, A.; Kreikenbohm, P.; Landau, H.; Leandro, R.; Moessmer, M.; Pagels, C. Introducing ambiguity resolution in web-hosted global multi-GNSS precise positioning with trimble RTX-PP, 25th Int. Tech. Meet. Satell. Div. Inst. Navig. 2012, ION GNSS 2012, vol. 2, pp. 1115–1125, 2012.

10. Leandro, R.; Landau, H.; Nitschke, M.; Glocker, M.; Seeger, S.; Chen, X.; Deking, A.; BenTahar, M.; Zhang, F.; Ferguson, K.; Stolz, R.; Talbot, N.; Lu, G.; Allison, T.; Brandl, M.; Gomez, V.; Cao, W.; Kipka, A. "Real-Time Extended GNSS Positioning: A New Generation of Centimeter-Accurate Networks," GPS World, 2012, vol. July, pp. 36–42.

11. Trimble CenterPoint RTX. Available online: https://www.trimble.com/Positioning-Services/CenterPoint-RTX. (accessed on 01-Sep-2019).

12. TUSAGA-Aktif. Available online: https://www.tusaga-aktif.gov.tr/Sayfalar/SistemeGiris.aspx. (accessed on 01-Sep-2019).

13. International GNSS Service (IGS). Available online: http://www.igs.org/. (accessed on 01-Sep-2019).

Accuracy Assessment of Satellite Positioning Techniques on Unmanned Aerial Vehicle (UAV) Photogrammetry

Ersin Turan[1], Bihter Erol[1], Ramazan Alper Kuçak[1], Serdar Erol[1]
[1]Istanbul Technical University, Geomatics Engineering Department, 34469 Istanbul, Turkey,
(turaners, bihter, kucak15, erol, @itu.edu.tr)

ABSTRACT

By the end of the 20th century, Unmanned Aerial Vehicles (UAV) were started to widely used on daily life in consequence of decreased production cost and increased options. UAV essentially is remotely controlled or autonomous aircraft that performs particular tasks and can carry payload without pilot on-board. Capability of carrying camera on-board enables to make use of it in photogrammetric technique. Main problem of photogrammetry is defining unknown parameters of collinearity equations (interior and exterior orientation parameters), these effectuate mathematical model. Photogrammetric cameras interior parameters are generally known. Yet, in classical airborne photogrammetry, exterior orientation parameters are computed by Ground Control Points (GCP), which are signaled and measured on the ground, via air triangulation. By the development of sensor systems, integration of Global Navigation Satellite System (GNSS) and Inertial Measurement Unit (IMU) with UAV brings up new approaches in photogrammetry. Obtaining instantaneous coordinates and rotation parameters can be utilized for orientation of images. Depending on GNSS measurement technique, accuracy of system can be increased with less ground points. Although classical absolute GNSS measurement has low accuracy, Real Time Kinematic (RTK) relative approach enhances point accuracy up to cm through GNSS methods. Within this scope; it is intended to analyze point accuracy and assess dependability of survey for geodetic applications by using RTK, and GCP outputs. By performing different approaches, it is aimed to eliminate dependency of GCP's on the photogrammetric mapping. With this object in mind, 17 ground points were set in ITU-Ayazağa Campus as GCP and test points and positioned by static GNSS measurement. Images which taken by DJI Phantom 4 RTK, are evaluated to produce orthophoto map. Outputs of each technique are compared between each other.

KEYWORDS: Accuracy; RTK; GCP; GNSS; Photogrammetry; UAV

1. INTRODUCTION

UAVs (Unmanned Aerial Vehicle) are widely used by various fields such as urban modeling, architecture, and geomatics applications. Owing to low cost and carrying payload like laser scanner and photogrammetric camera, UAVs are recently preferred in geodetic applications.

In conventional photogrammetry, image coordinates are global coordinates are connected with GCPs [1]. However, integration of GNSS and IMU systems on UAV photogrammetry enables to obtain exterior parameters; global coordinates of camera sensor center and rotation of axis (x, y, z and ω, φ, κ) directly. By means of advance satellite techniques like relative point positioning, point accuracy can be increased to cm level. RTK relative method is widely performed to get precise point coordinates through GNSS techniques.

In that article, it is intended to compare the point accuracies measured from orthomosaic by RTK, and GCP data; and also, estimate the dependability of techniques for geodetic and photogrammetric applications. Within this scope, it is desired to remove the dependence of GCPs by different approaches. While evaluation, SFM approach, which based on point detection and matching in images with or without coordinates, was applied.

2. MATERIAL AND METHOD

In order to compare different satellite positioning techniques, 3 orthophotos have been evaluated. UAV flight was performed over the ITU-Ayazağa Campus. During the flight, GNSS receiver on the UAV has observed satellites. Thanks to RTK, and Static GNSS methods, images are evaluated by aerial triangulation and direct geo-referencing.

Nowadays, by development of advance GNSS techniques it can be detect more accurate point positions. Point coordinate accuracy is affected by measurement time, satellite geometry, receiver and atmospheric conditions [2]. There are two different GNSS approaches; absolute and relative point positioning. Although, absolute positioning has high accuracy by means of corrections, relative approach provides more accurate results. In RTK method, errors common to base and rover are eliminated by taking corrections in real time [2]. RTK method is shown Figure 2.1.

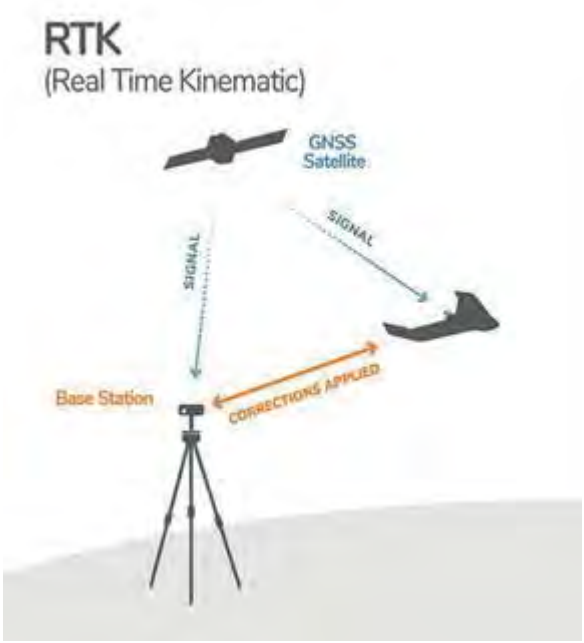

Figure 2.1: *Real Time Kinematic*

Integration on GNSS and IMU on flying vehicles enables implies to get directly exterior parameters that called direct geo-referencing [3]. In order to get precise orientation and point position, it enables to provide quantitative data acquisition with the GNSS-IMU sensors [4]. It allowed obtaining point position without GCPs and air triangulation via either a stereo pair of photographs, or a single photo and Digital Elevation Model (DEM). It is assumed that camera interior parameters are known precisely or well calibrated; also, Figure 2.2 shows direct geo referencing approach. Equation between global coordinates and local frame is

$$X_A = X_L - (Z - Z_L) * \frac{[(x-x_0)*m_{11}+(Y_A-Y_L)*m_{21}-(Z_A-Z_L)*m_{31}]}{[(x-x_0)*m_{13}+(Y_A-Y_L)*m_{23}-(Z_A-Z_L)*m_{33}]} \quad (2.1)$$

$$Y_A = Y_L - (Z - Z_L) * \frac{[(x-x_0)*m_{12}+(Y_A-Y_L)*m_{22}-(Z_A-Z_L)*m_{32}]}{[(x-x_0)*m_{13}+(Y_A-Y_L)*m_{23}-(Z_A-Z_L)*m_{33}]} \quad (2.2)$$

where, X_A, Y_A are object points, X_L, Y_L are camera coordiantes, x and y are image coordinates, x_0 and y_0 are image focal center offset and *m* is Rotation matrix elements.

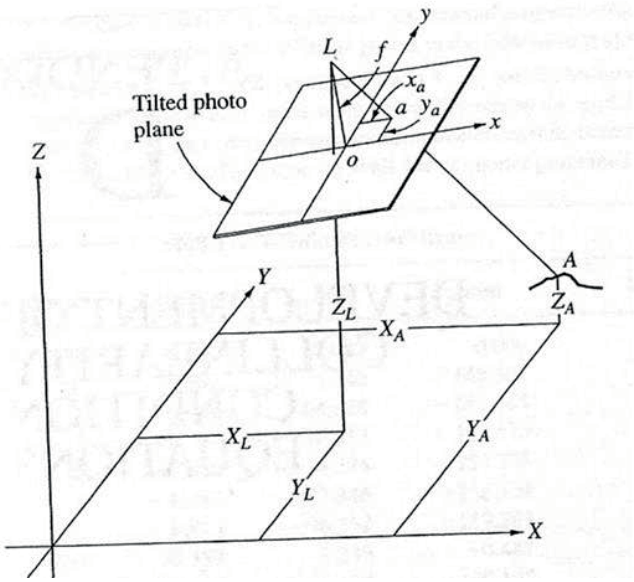

Figure 2.2: *Image referencing [5]*

2.1 Survey Area and UAV Photogrammetry

In this case study, around 950 photographs were obtained on ITU-Ayazaga Campus. 17 GCPs were measured by relative static GNSS method in study area (Figure 2.4a). All GCPs are painted with black and white colors. Every points positions are evaluated in office by using reference IGS ISTA reference stations. RMS values of GCPs are shown in Figure 2.3 DJI Phantom 4 RTK is chosen for flight to take images (Figure 2.4b). Obtained images were processed in automatic evaluation software, Agisoft Metashape Professional.

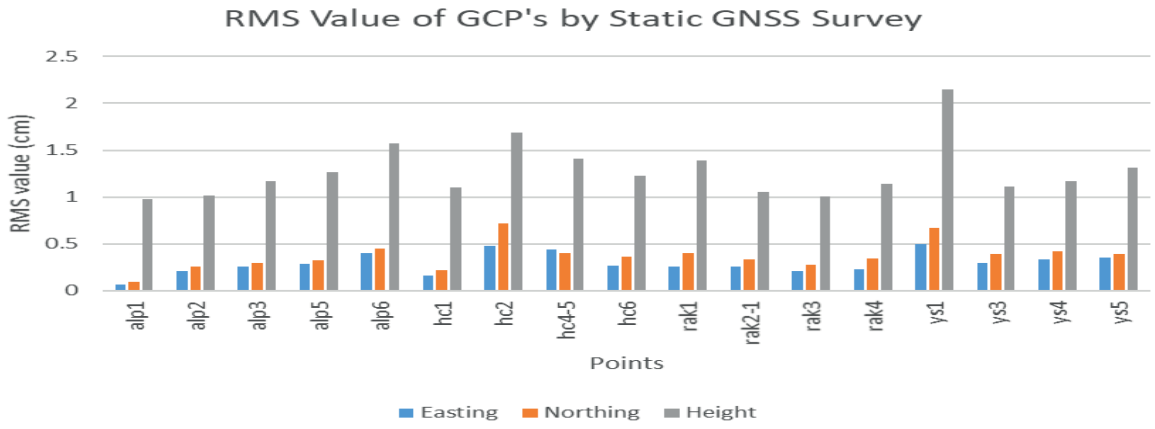

Figure 2.3: *RMS Values of GCPs*

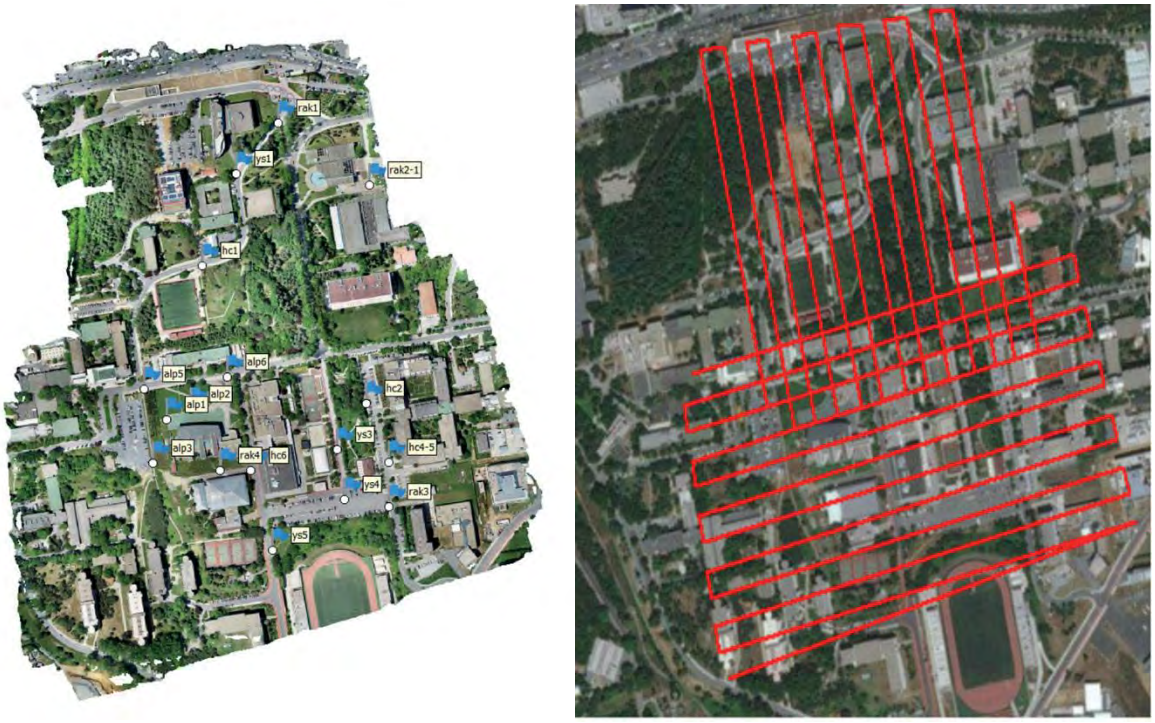

(a) **(b)**

Figure 2.4: *GCPs Locations and Flight Tracks*

RTK and GCP outputs were performed to evaluate three different orthomosaics. Two of them are produced individually by different models; yet, 10 GCPs and RTK values are merged and the new orthomosaic have been produced to figure out effects of GCPs on the RTK models in terms of accuracy.

3. RESULTS AND DISCUSSION

Each GCP positions are measured from different orthomosaics which modelled from RTK, GCP and RTK + GCP data. During comparison, relative static GNSS outputs were chosen as a reference coordinates, and each measurement extracted from reference coordinates. Differences between reference coordinates and coordinates extracted from models are shown in Figure 3.1, Figure 3.2 and Figure 3.3.

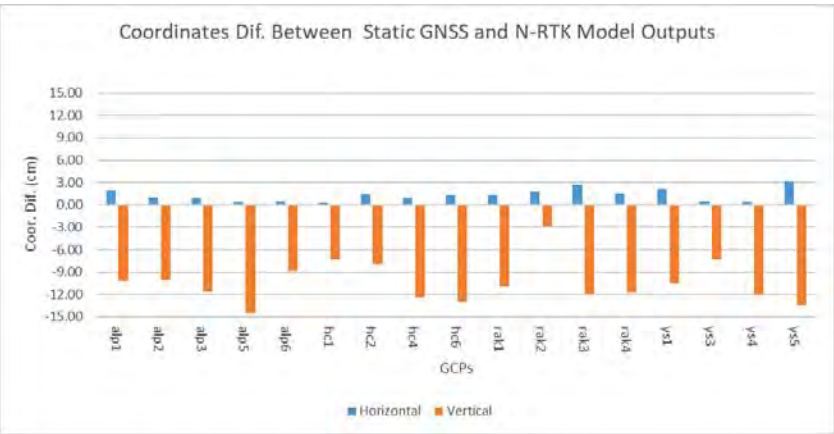

Figure 3.1: *Coordinate Differences between Reference and RTK model Outputs*

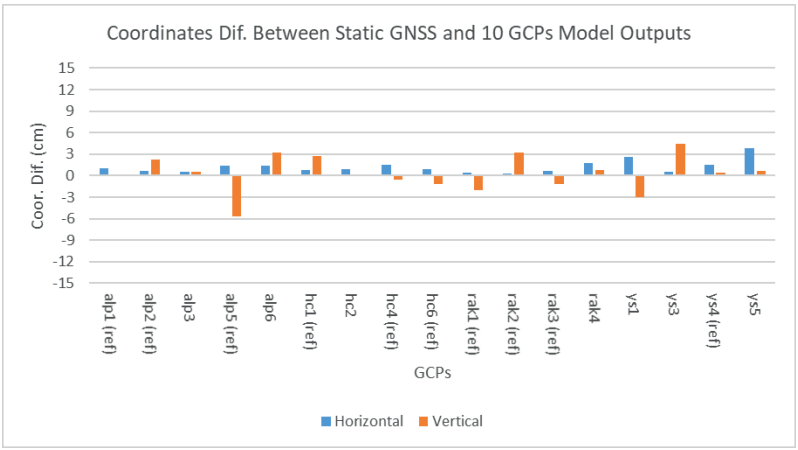

Figure 3.2: *Coordinate Differences between Reference and GCP model Outputs*

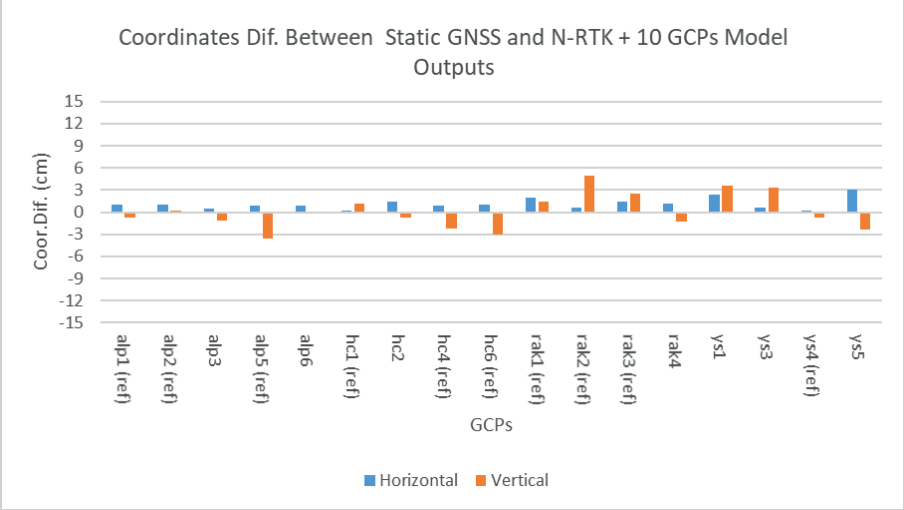

Figure 3.3: *Coordinate Differences between Reference and GCP+RTK model Outputs*

It is clearly seen, owing to RTK measurement were used in air-triangulation as initial values RTK+GCP model results are more reliable than others. RTK results figured out that method reliability can depend on RTK network accuracy, and also there is a bias in vertical component of RTK solution. On the other hand, Using GCP points while evaluating images with RTK measurements, vertical results are improved in models. RMS value of all differences are shown in Figure 3.4 (RMS values are estimated from test points differences.).

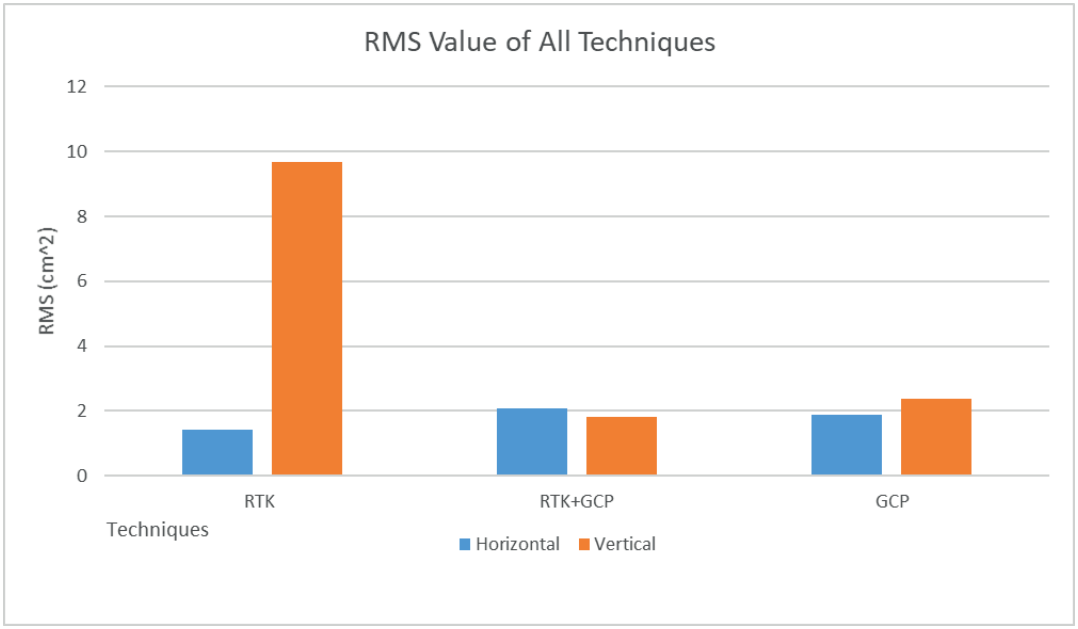

Figure 3.4: *RMS values of all coordinate differences*

4. CONCLUSION

In conclusion, it is desired to assess point accuracy of satellite positioning techniques on UAV photogrammetry. Hence RTK methods are performed on study area. As it is expected, best results are taken from orthomosaic modelled from RTK+ GCPs measurements. Even though providing best model, setting up and measurements of GCPs are costly and time consuming. The necessity of setting up GCPs can be eliminated by using RTK method to the desired position accuracy.

REFERENCES

1. Fazeli, H., Samadzadegan, F., & Dadrasjavan, F. (2016). Evaluating the potential of RTK-UAV for automatic point cloud generation in 3D rapid mapping. The International Archives of Photogrammetry, Remote Sensing and Spatial Information Sciences, 41, 221.

2. El-Rabbany, A. (2002). Introduction to GPS: the global positioning system: Artech house.

3. Remondino, F., Barazzetti, L., Nex, F., Scaioni, M., & Sarazzi, D. (2012). Uav Photogrammetry for Mapping and 3d Modeling – Current Status and Future Perspectives. ISPRS - International Archives of the Photogrammetry, Remote Sensing and Spatial Information Sciences, XXXVIII-1/C22, 25-31. doi:10.5194/isprsarchives-XXXVIII-1-C22-25-2011

4. Manual of Photogrammetry Fifth Edition, (2004), American Society for Photogrammetry and Remote Sensing.

5. Kraus, K. (2011). Photogrammetry: geometry from images and laser scans. Walter de Gruyter.

Refinement and Construction of Louisiana Local Gravity Grid for Precise Geoid Determination

Ahmed Abdalla[1], Clifford Mugnier[1], Bihter Erol[2], J. Anthony Cavell[1]

[1]Center for GeoInformatics, Louisiana State University, Baton Rouge, LA 70808, USA
E-mail: aabdalla1@lsu.edu

[2]Istanbul Technical University, Geomatics Engineering Department 34469 Istanbul, Turkey
Phone: +90 212 888 8888, E-mail: bihter@itu.edu.tr

ABSTRACT

In this study, the terrestrial and marine gravity data sets undergo refinement and validation for the sake the of precise geoid determination in Louisiana. The erroneous gravity data represent the main source of errors that can easily propagate into the geoid if not refined and eliminated. The purpose of this study is to ensure the integrity of the reliability of these data sets and merge them safely in the final gravity grid. This will highly reduce gross-error propagation into the geoid due to the inconsistency in the multipurpose collection of the gravity data. The NGS (National Geodetic Survey) goal aims for a 1 cm geoid across the states based on the GRAV-D project for airborne gravity measurements. For refinement of the terrestrial and marine gravity data we first cross-validate each dataset individually to assess their quality. We use bilinear interpolation method to predict the gravity values during the cross validation based on leave-one-out procedure within the specified search radius around the test point. The standard deviation is used as cut-off for outlier detection, it is set at ±10 mGal for the terrestrial gravity and ±5 mGal for the marine data after elimination of the crossovers. After that, we carry out another comparison to validate two combined global geopotential models (EGM2008 and XGM2016) to use the best-fit one in filling the gaps due to lack of gravity measurements. EGM2008 has a slight best-fit agreement compared to GM2016, therefore, it will be used in to restore and construct the gravity data. The construction of the gravity grid is carried out by means of remove-restore procedure using EGM2008 and terrain correction. A grid of a 1x1 arc-min resolution is constructed based on the spatial distribution of the sparse gravity data over Louisiana using search radius technique to count the number of points within the search radius. Different radius values are investigated in order to find the optimal choice of the sparse data to appropriately determine the interpolation and filling areas in the final grid. Numerical comparisons and analysis of the newly constructed grid of Louisiana are addressed and illustrated.

KEYWORDS: gravity data; geoid; gross-error; NGS; EGM2008; remove-restore; terrain correction; outliers.

1. INTRODUCTION

The characteristics of the local gravity field over specific regions are defined by the anomalous gravity field based on important gravimetric quantities such as the geoid heights, the gravity anomalies and the components of the deflection of vertical [1]. The geoid is defined as the surface that consists of points that have equal potentials, this surface closely coincides with mean sea level and extends below the continental areas [2]. The gravity anomaly is the difference between the real gravity measured on the earth by means of the acceleration of the free-fall and the corresponding gravity calculated on reference ellipsoid. The deflection of vertical is a small angle that is formed between the gravity vector (in the direction of the plumb line) and the gravity vector normal to the ellipsoid. The components of the deflection of the vertical are the components of the small angle of the deflection of the vertical into North-South and East-West for each component [1, 3, 4].

In physical geodesy, the gravity data are very important because they are used in the determination of the regional gravimetric geoid models. However, the lack and quality of the gravity measurements are the primary effectual factors in the accuracy of the geoid. The regional gravity field is compiled from the local gravity measurements such as terrestrial, airborne, and marine over the specified region. However, geoid heights derived by Stokes's formula are influenced by errors due to the lack of the gravity information in the remote zone areas. Hence, the global geopotential models (GGM) can be used as complementary for the local gravity field to reduce the far zone effect and improve the geoid quality [5].

Furthermore, an additional factor which can also have an influence on the geoid accuracy is the optimization of the computational parameters. The computational parameters include but are not limited to the agreement of GGMs with the ground truth data such as the gravity and GPS-levelling data, Least-squares (LS) modification parameters, and least-squares collocation (LSC) covariance fitting parameters [6-11]. Most of the available gravity data were collected discretely over decades for different purposes which makes the data consistency, and unification, and accuracy doubtful [12]. Therefore, it is most likely to acquire an erroneous geoid solution due to the unreliable data quality [13]. Gravity gridding and refinement techniques such as interpolation methods and gross-error detection were presented in previous studies, for more information we refer the readers to [14-18].

This paper consists of five sections, the organization of these sections is as follows: Following to this introductory section is the second section which briefly describes the study area and data sets (gravity data, GGMs, and DTM) utilized in this study. The third section describes the procedure and methodology, for instance, the leave-one-out cross-validation (LOOCV) technique, smoothing using GGM and terrain correction (remove-restore scheme), and bilinear interpolation [19-20]. Numerical investigations, results, and analyses are presented in the fourth section. The summary of this study and concluding remarks are drawn in the last section.

2. STUDY AREA AND LOUISIANA DATA SETS

2.1 Study area

The study area of the State of Louisiana is located in the southeastern part of the United States on the coast of the Gulf of Mexico to the south. It is bordered by 3 states, namely, Texas to the west, Arkansas to the north and Mississippi to the east (see Figure 1). The eastern boundary between Louisiana and Mississippi States is demarcated by the Mississippi River. Louisiana has one of the largest coastal wetlands in the United States of which the coastal zone extends from the western border of Texas to Mississippi in the Eastern border. Various processes such as mining activities, over-exploitation of groundwater and structural loading are claimed to have effectively contributed to land subsidence in Louisiana during the past 60 years [21]. It was noticed that Louisiana's large wetland areas created from the sediments deposited by the Mississippi River being lost because the land surface was rapidly sinking [22].

2.2 Data sets

2.2.1 Gravity data sets

Variation of rock densities causes changes in the gravity field of the Earth; these changes can be detected by the gravimeters. These advances in gravity data acquisition are supported by massive improvements in data processing and software programs. The accuracy of any work related to the gravity method is based on the reliability of the field measurements including planning, data acquisition, and processing. The values of the theoretical gravity field have slight

variation due to the fact that the spherical surface does have the same average radius and total mass with slight increase towards poles as seen in Figure 1.

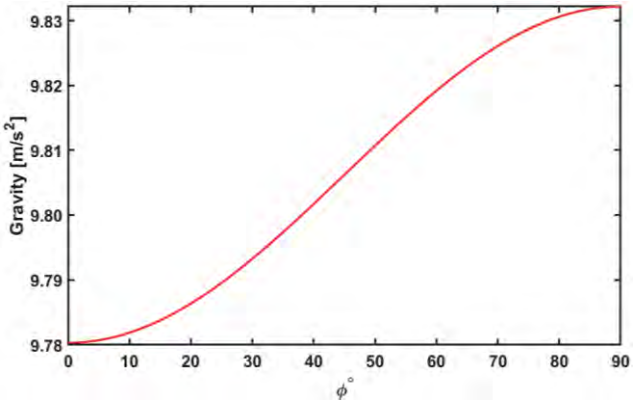

Figure 1. *Theoretical gravity field along in north-south latitudes using the international gravity formula 1967*

Two gravity data sets are used in this study were obtained from the international gravimetric bureau (BGI) in France [23]. A few sparse terrestrial gravity data (green dots in Figure 2) were collected in Louisiana in the period 1950-1982 by various institutions, organizations, and oil companies [24]. The current terrestrial gravity data are quite few and do not represent the total number of the collected data. The marine data over the Gulf of Mexico (Blue tracks) were similarly collected and belong to various owners. These gravity data sets will be gridded after the refinement and filter in order to be valid for the geoid determination.

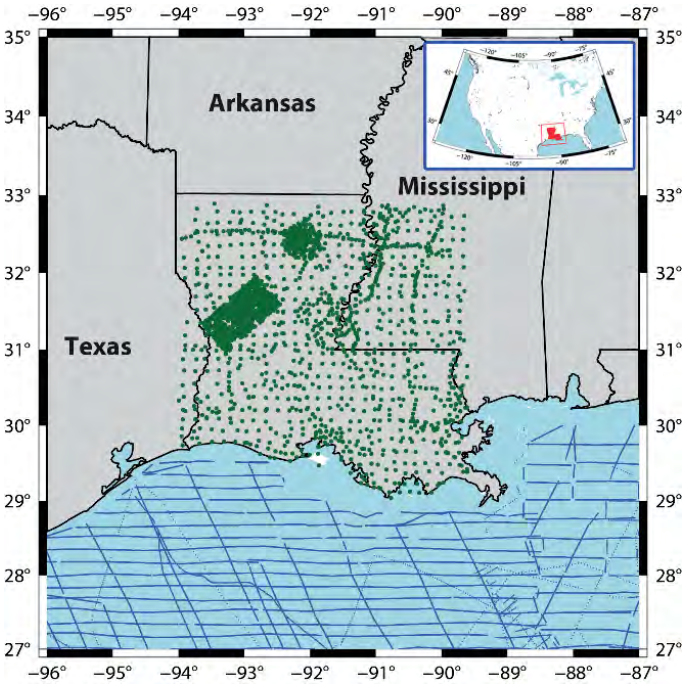

Figure 2. *Location of Louisiana and surrounding borders (States and Gulf of Mexico). The inset shows the location of Louisiana in the U.S map.*

2.2.2 Global Geopotential Models (GGMs)

The GGMs are used in this study to restore the missing areas in the final gridding. The combined GGMs are EGM2008 and XGM2016 [25, 26]. They will be validated by the local data sets at degree and order (d/o) 719. The EGM2008 was the first model developed to higher harmonic degree 20159 combined with ITG_GRACE03S model and its covariance matrix and terrestrial, airborne and altimetry data. On the other hand, XGM2016 was first released up to d/o 719, recently it is published as XGM2019e in 3 versions truncated to d/o 2160, 5540, and 760 [27]

2.2.3 Digital Elevation Model (DEM)

A digital elevation model SRTM-3S from the Shuttle Radar Topography Mission is used in this study. The DEM is a digital representation of the Earth's heights and usually used define the terrain characteristics such as the aspect, slope, watershed, and drainage networks. The topography features of Louisiana are depicted in Figure 3. The DEM is very important in the

geoid determination because it is employed in resolving the impact of the topographic masses above the geoid. The well-known remove-compute-restore procedure utilizes the DEM for obtaining short-wavelength frequencies by means of terrain corrections [6, 28]. The impact of the topography on the gravity anomaly will be calculated using the DEM, the terrain correction is used to smooth the terrestrial gravity data.

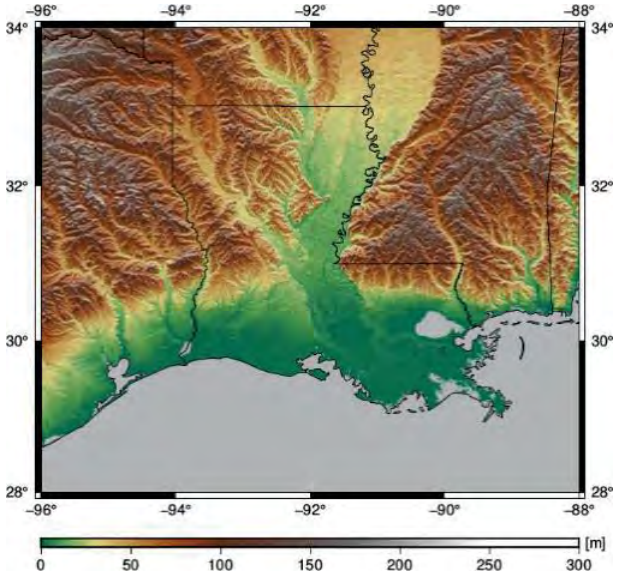

Figure 3. *The digital elevation model over Louisiana and the surrounding states (cw: Texas, Arkansas and Mississippi)*

3. METHODOLOGY

The free-air gravity anomalies are sensitive to the latitudinal changes on the reference ellipsoid according to the Geodetic Reference System 1980 (GRS80) as described in [30]. The free-air anomaly Δg_{FA} is the difference between the surface gravity on the Earth g_P and the normal gravity γ_Q calculated on the normal ellipsoid as follows:

$$\Delta g_{FA} = g_P - \gamma_Q \tag{1}$$

The normal gravity is given by means of the vertical gradient

$$\gamma_Q = \gamma_0 - \frac{\partial h}{\partial g} H \tag{2}$$

The Bouguer anomalies can be calculated by means of the free-air anomalies and the height *H* as follows:

$$\Delta g_B = \Delta g_{FA} - 0.011187H \tag{3}$$

The low-frequency contribution of the GGMs on the gravity can be obtained using their spherical harmonic coefficients to compute free-air anomalies Δg^{GGM} as follows:

$$\Delta g^{GGM} = \frac{GM}{a^2} \sum_{n=2}^{N_{max}} (n-1) \left(\frac{a}{r}\right)^{n+2} \sum_{m=-n}^{n} C_{nm} Y_{nm} \tag{4}$$

where GM is the geocentric gravitational constant, a is the GGM equatorial radius, r is the geocentric radius, N_{max} is the maximum degree of the GGM, n and m are the degree and order of the spherical harmonic coefficients, C_{nm} are the fully normalized spherical harmonic coefficients of the disturbing potential, and Y_{nm} are the fully normalized surface spherical harmonics.

The terrain correction is given by

$$T_c = \frac{G\rho R^2}{2} \iint_{\sigma} \frac{\left(H_p - H_Q\right)^2}{l^{-3}} d\sigma \tag{5}$$

where G stands for the Newtonian gravitational constant, ρ is the topographic mass-density density, R is the mean Earth radius, H_p is the height of the computation point, H_Q is the height of the running points, l is the planar distance between H_p and H_Q, and $d\sigma$ is the surface area element. The smoothed gravity data δg_c is given by subtracting the terrestrial/marine free-air anomalies Δg_{FA} from the GGM-based anomalies Δg^{GGM} and topography-effect anomalies T_c as follows

$$\delta g_c = \Delta g_{FA} - \Delta g^{GGM} - T_c \tag{6}$$

The prediction of the smoothed anomalies is obtained using the bilinear interpolation [31] based on LOOCV procedure [32]. The error δ_g between the predicted and smoothed data is obtained by the following comparison:

$$\delta_g = \delta g_c - \overline{\delta g_c} \tag{7}$$

3.1 Data smoothing

A preliminary refinement can be done by smoothing the gravity data using the GGM and TC using Eq. (6). The smoothed value δg_c is checked to find the potential cut-off value according to the differences between the real value and the corresponding GGM-based value. The Bouguer anomalies were compared with the normal gravity in Sudan for the computation of the gravimetric geoid (2008) in Sudan as explained in [19]. In this study, two GGMs (EGM2008 and XGM2016) are used to smooth the gravity data sets together with the terrain correction as mentioned in Equation 6.

3.2 LOOCV

Another refinement can be done by the cross-validation technique, which is followed to detect gross errors by comparing the smoothed anomalies and their predicted values. The idea behind LOOCV is to omit the observation from the data set and predict its value from the remaining (running) data, the difference between the value of the omitted observation and its predicted value is the prediction error as shown in Eq. (7). We have optimized this method to increase its speed using the truncation window, see [34, 35]. The truncation window is a small area that truncated around the computation point to reduce the search area instead of searching within the entire data. This reduces the search time and provides reliable values with respect to the spatial distribution of the data. The prediction error shows the quality of the predicted value, meaning that the smaller prediction error between the real and interpolated point, the better quality of the point selected for the prediction test [14]. Values with large prediction errors are considered as outliers and must be eliminated from data to prevent their use in the final interpolation to avoid propagating error into the final grid. The prediction of the values is obtained using the bilinear interpolation.

4. PRELIMINARY RESULTS AND ANALYSIS

The short and long wave-length components of the gravity field based on the GGM and DTM are computed, see Figure 4. The GGM-based free-air anomalies are computed to d/o 719 using XGM2016 model as seen in Figure 4a. XGM2016 slightly shows better agreement to the terrestrial gravity than EGM2013, we used standard deviation (SD) to differentiate between the models. A model with minimum SD should be used in smoothing and gridding. At this stage, XGM2016 (SD=3.17 mGal) was selected instead of the EGM2008 (SD=3.27 mGal) for building the gravity grid of Louisiana. The same degree and order (d/o) for XGM2016 will also be used to fill in the onshore gaps. The topography effect on the gravity field of Louisiana is also calculated from the DTM using terrain correction. It will be used in smoothing the terrestrial gravity data together with the GGM in order to carry out the interpolation. So for smoothing, the removal of the reference field and terrain effect are applied over inland areas, while only removal of reference field is applied over seaward areas.

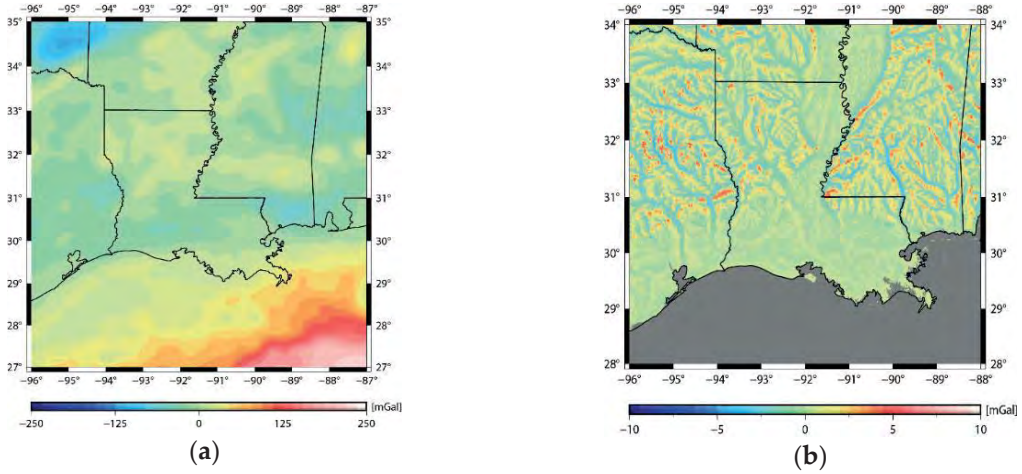

(**a**) (**b**)

Figure 4. a) *Free-air anomalies from XGM2019 (d/o=719), and b) topographic effect*

4.1 Smoothing and outlier detection

Figure 5 shows the impact of GGM and T_c on the refinement of the terrestrial data. Despite the slight improvement on the smoothing of the terrestrial gravity data the terrain correction is still important to be applied due to high sensitivity of free-air anomalies towards the topography. When removing the reference field (GGM-based anomalies) from the terrestrial gravity data, a small number of points (9 points) are detected as outliers. The differences of the eliminated

outliers reach 30 mGal in EGM2008 and 34 mGal in XGM2016, the current differences of the data vary between 10 and − 10 mGal. The impact of removing the EGM2008 reference field and topography effect showed more smoothing in the data, it reduced SD of the data differences from ±2.84 mGal to ±2.56 mGal. On the other hand, the removal of the combination of XGM2016 and topography effects have improved SD from ±2.73 mGal to ±2.47 mGal.

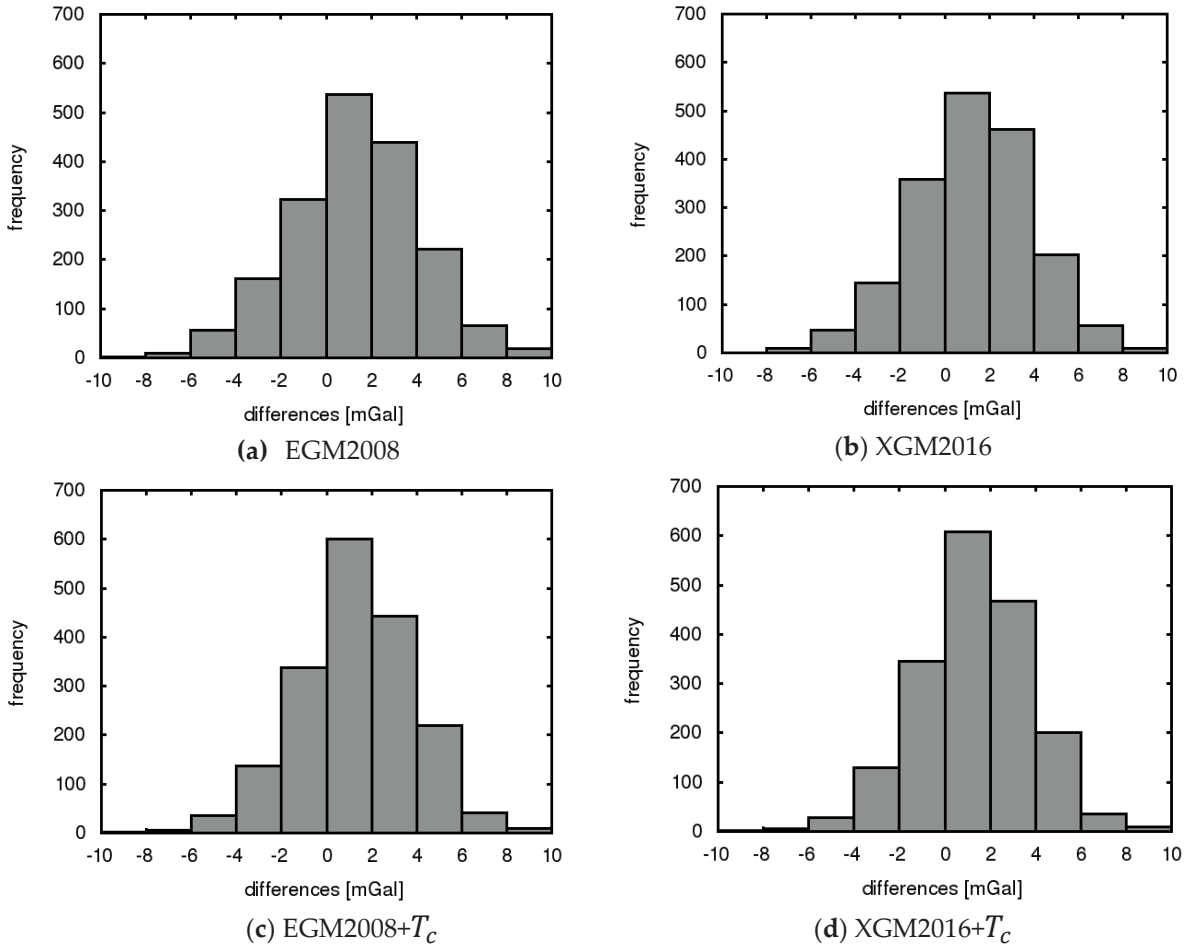

Figure 5. *Gravity smoothing by a) EGM2008, b) XGM2016, c) EGM2008 and T_c and d) XGM2016 and T_c*

The density of the differences after smoothing increased within ±4 mGal as shown in Figures 5.c and 5.d which confirms the visibility of the smoothing process, this represents about 85% of the entire data. The density distribution for the rest of the data is 13% for ±6 mGal, 3% for ±8 mGal and 1% for ±10 mGal. Here we consider removing the effect of topography due to the basic assumption which presumes that all Earth's masses above the geoid are harmonious. However, in fact the Earth's density varies, therefore, the topography must be removed before

starting the calculation of the geoid while the impact of the topography has to be recovered later after the computation of the geoid.

We further perform a refinement for the previously smoothed data (EGM2008 and XGM2016) using LOOCV (see Sect 2.2). In this refinement, the EGM2008 and XGM2016 combinations were cross-validated by LOOCV, where only two points were detected as outliers with prediction error $(\sim 11\ mGal)$. The remainders were confined together within a reasonable range of error of $(\pm 4\ mGal)$. Therefore, we can see that after two refinement procedures the total number of eliminated points as outliers is 11 points and the density of smoothed data $(\pm 3\ mGal)$ is about 94% of the entire data. Relatively few number of points (6%) were found to have prediction errors of $(\pm 5$ and $\pm\ 6\ mGal)$

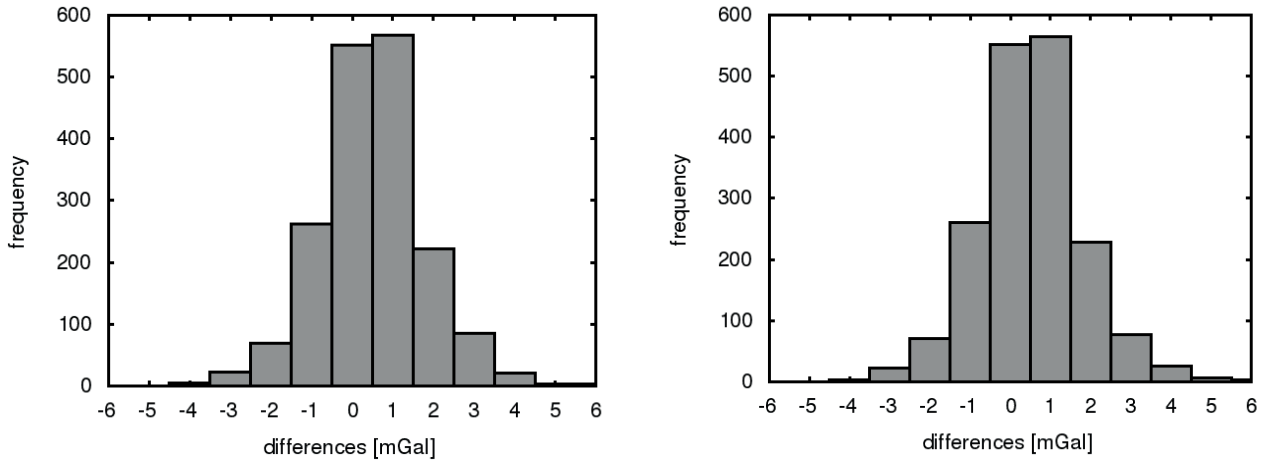

(a) EGM2008 (**b**) XGM2016

Figure 6. *LOOCV of smoothed data a) EGM2008 and T_c and b) XGM2016 and T_c*

The second refinement procedure assures that the current terrestrial gravity data are valid to be used in the final grid with low expectations of gross-errors after applying the two-step refinement procedure.

For the marine data, when removing the reference field by the geopotential models EGM2008 and XGM2016 at d/o 719, we found high consistency between the marine and GGMs anomalies of about 98% of existing data within $\pm 5\ uGal$ as seen in Figure 7. This high agreement makes it safe to utilize the GGM for the recovery of the outliers and the un-surveyed areas.

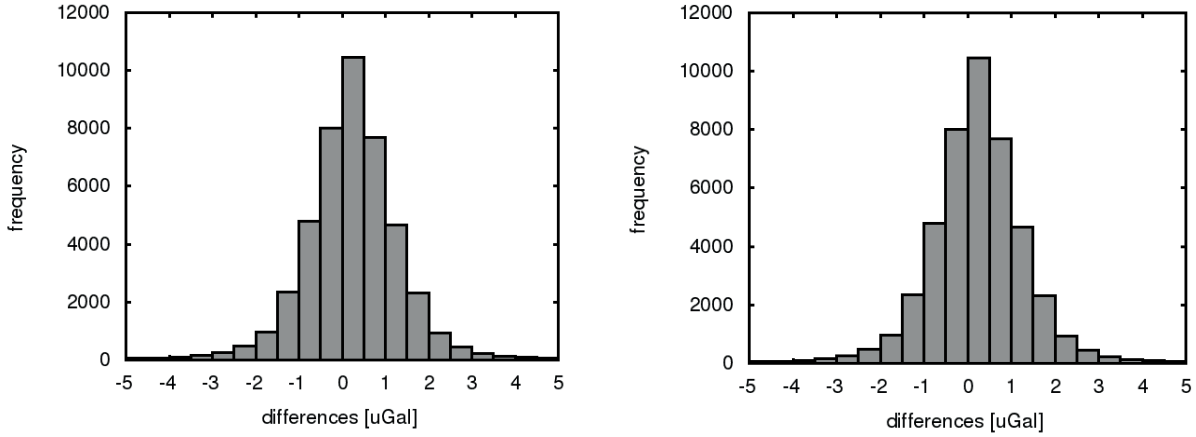

(a) EGM2008 (**b**) XGM2016

Figure 7. *The consistency between marine and global anomalies based using a) EGM2008 and b) XGM2016*

On the other hand, the rest of the marine data (~1.5%) still have a good consistency with up to ($\pm 3\ mGal$) , the rest of the data (~0.5%) are shown to vary between (± 3.5 to $\pm\ 10 mGal$) as seen in Figure 8. The outliers in the marine are selected for values beyond ($\pm 10\ mGal$) and only 10 points are suspect as outliers and eliminated from the data sets.

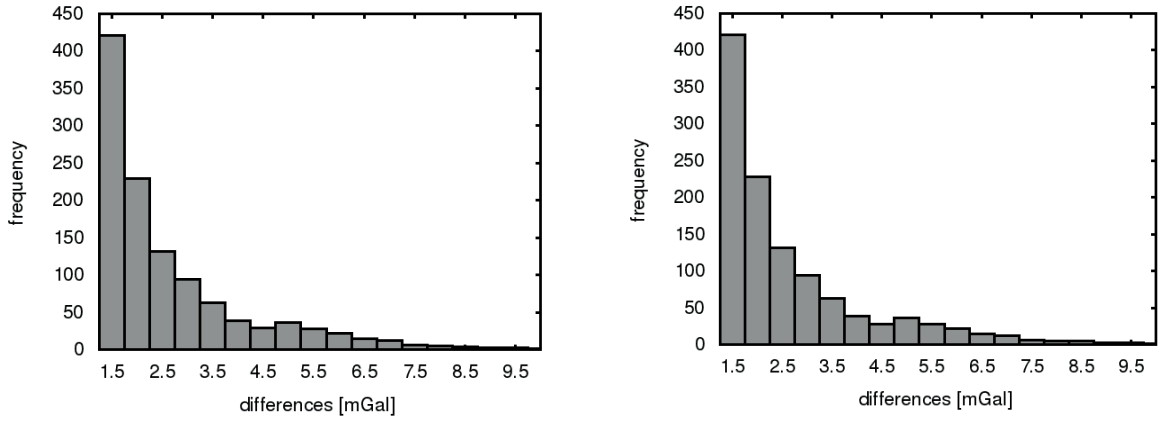

(a) EGM2008 (**b**) XGM2016

Figure 8. *Absolute differences between marine and global free-air anomalies from a) EGM2008 and b) XGM2016 models*

4.2 Interpolation points

A regular grid of 1×1 $arc - min$ is set for the interpolated values. The criterion of testing the valid interpolation points is based on the number of the scattered points around the location of the interpolated point. We set a moving search radius over each point in the regular grid, then we searched the scattered points in the vicinity within the limit of the search radius. The preliminary search radius $\sigma = 6$ arc-min shows a total number of points (7198 points) that can be kept on hold for the interpolation and the rest should be recovered by the GGM. When increasing the length to $\sigma = 7$ arc-min, the number of the interpolated points becomes 12841 points, 20296 points for $\sigma = 8$ arc-min and 29096 points for $\sigma = 8$ arc-min.

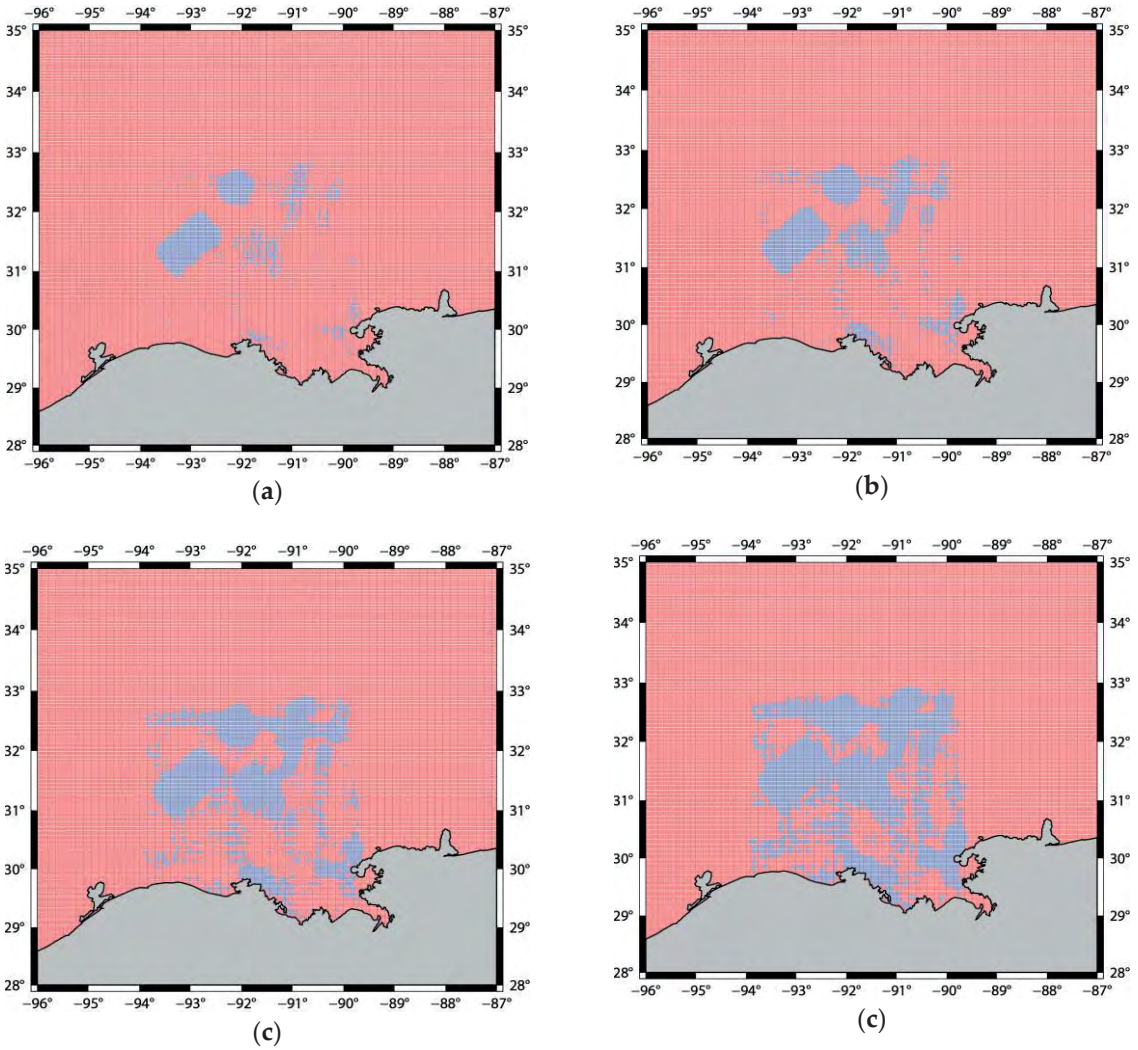

Figure 9. *Selection for inland interpolation points using search radius $\sigma = 6, 7, 8$ and 9 arc-min a, b, c and d, respectively.*

On the other hand, we similarly performed the search radius on the marine area to check the possibility of holding points over the Gulf of Mexico for the interpolation. The ship tracks were treated in the same way as the terrestrial data sets. However, in this case the length of the search radius was set to $\sigma = 4, 5, 6, 7$ arc-min. It is noticed that the interpolation points over the marine are denser due to the large number of the ship-track points and the limited area compared to the sparse and few terrestrial data over large area. Furthermore, the distribution of the marine tracks is mostly passing over the marine area of the Gulf of Mexico except narrow coastal strip as seen in Figure 10.

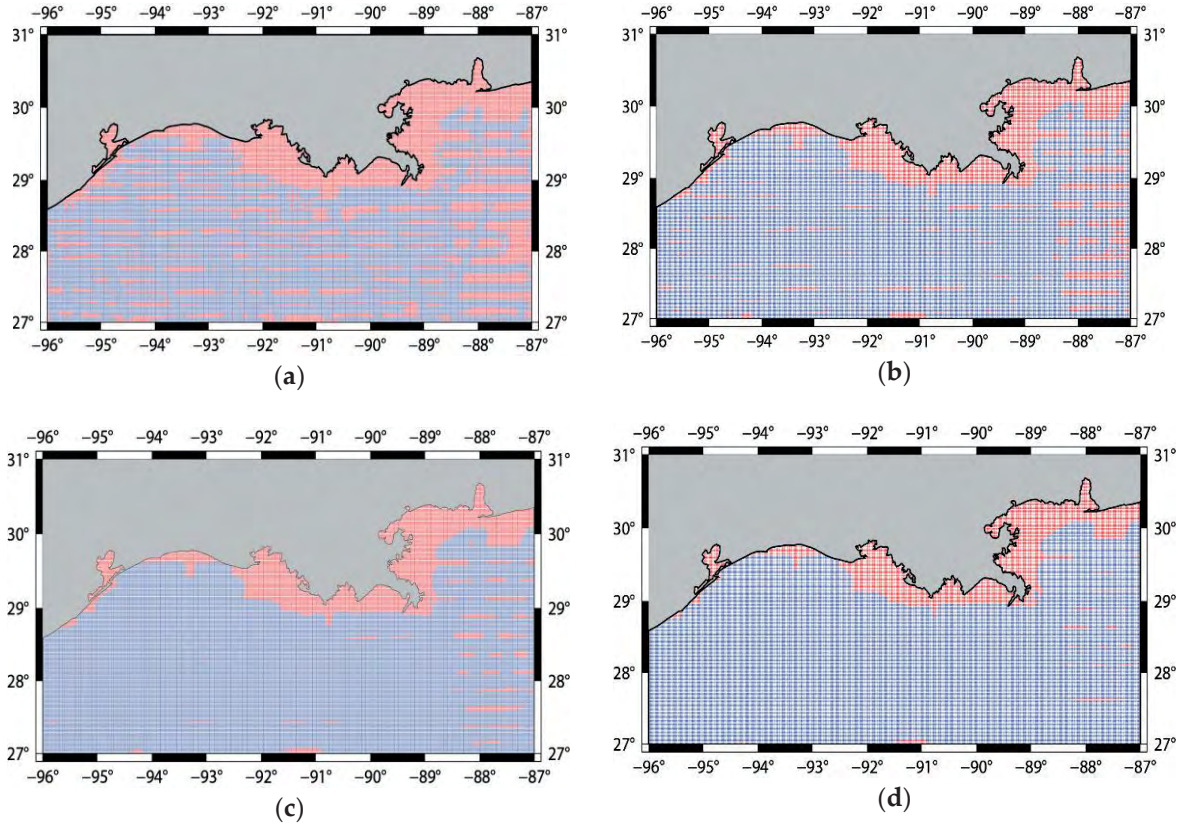

Figure 10. *Selection for marine interpolation points using search radius $\sigma = 4, 5, 6$ and 7 arc-min a, b, c and d, respectively.*

In this study, the search radius set to find the terrestrial/marine gravity data sets around the interpolation point is the maximum spherical distance between the interpolation point and the farthest located point on the circumference of the spherical cap. The criterion followed in the setting of the search radius is limited; it works over all points under the same conditions. Unfortunately, this makes the less and none-surrounding points not well treated because these

cases must have more specified options to include more surrounding points when the preliminary setting of the search radius is not fulfilled. Further improvements for the presented criterion can be achieved to provide alternative solutions for interpolation points with less or none-point vicinities.

4.3 Final grid

Due to the lack of the terrestrial gravity data over Louisiana State, most of the inland data are recovered by the GGM. In addition to the number of the gravity data over Louisiana, the gravity data over the surrounding States such as Texas, Oklahoma and Mississippi are not yet available to the authors to be included in this study. Similarly, GGM is also used to recover the points without interpolation for the marine area and the coastal strip.

The construction of the final gravity grid is based on the search radius which was described previously. The search radius is tested gradually with a step of 0.1 arc-min to detect more points within the search radius, after that the interpolation can be implemented. The implementation of the interpolation depends on the spatial distribution of the surrounding points detected within the search radius. This means that it is possible to detect a large number of points (≥ 5) within the search radius, but due to the bad distribution of these points around the interpolation point the interpolation can fail. We currently resolve this problem by using the GGM, but we intend to test using the mean value in further investigations. The GGM was also used to recover the interpolation points which have small number of points (< 5) within their principal search radius.

Finally, the terrestrial and marine gravity data sets are combined together to construct the gravity grid of Louisiana. The inland interpolated points are only 11% of the total inland points including parts of Texas, Oklahoma and Mississippi in addition to the area of the Louisiana State. The marine interpolated points represent 66% of the total marine points over the study part of the Gulf of Mexico. The coastal strip from Texas to Florida contains a number of points that are not interpolated according to the search radius criterion. Big coastal parts of Louisiana and Mississippi contain large numbers of these points, while a few points are shown in the coastal parts of Mexico and Florida over the study area. Figure 11 shows the final gravity grid is compiled over the study area. The southern part of Louisiana includes a few of the

interpolated points while the northern part includes more points compared to the southern part, we also noticed that the eastern part of the marine area is filled with the GGM.

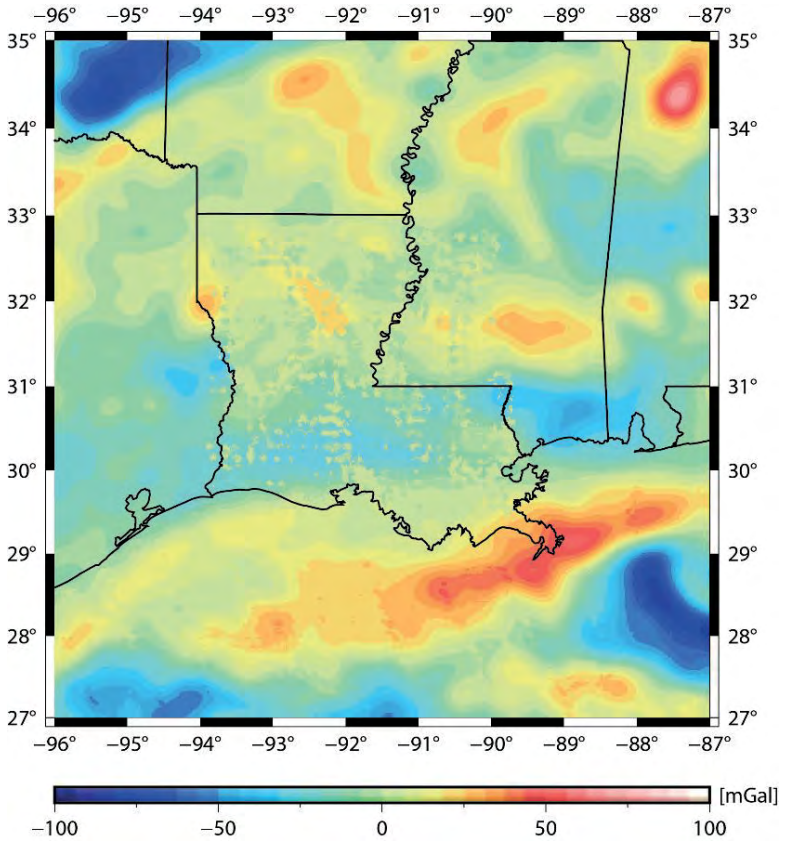

Figure 11. *Final gravity grid*

5. SUMMARY AND CONCLUSIONS

We refined the terrestrial and marine gravity in Louisiana and its gulf area for the purpose of construction of the local free-air gravity grid. For the construction of the gravity grid, the gravity grid is treated in a two-step procedure. Step1 is based on smoothing the free-air gravity anomalies by removing the reference field using the GGM and also by removing the topography effect on the gravity fields using terrain correction. We utilized the minimization of the standard deviation (SD) as the key parameter for determining the outliers, where SD beyond ± 10 mGal are considered to be outliers for the terrestrial data. On the other hand, the smoothing of the marine data, the smoothed marine gravity data are more consistent than the smoothed terrestrial data. We found that 98% of the smoothed data have differences within ± 5 uGal, the outliers are set for the differences with SD larger than ± 10 mGal. Step 2 is applying leave-one-out-

cross-validation (LOOCV) over the smoothed gravity data. We compared the differences between the smoothed value and its prediction value by means of LOOCV, the predicted values are obtained by the bilinear interpolation.

Furthermore, we tested the fully gridded points to check the possibility to get the tested point interpolated by applying the search radius over the test point to find possible terrestrial/marine data within the search radius. The terrestrial data were detected at a radius $\sigma = 8$ arc-min, while for marine data the search radius was selected at $\sigma = 6$ arc-min. The maximum number of points detected within the terrestrial data is 98 points while 112 points were detected in the marine gravity data. The minimum number of the data that were considered for performing the interpolation is 5 points per the search radius. For the interpolation points that have less than 5 gravity points are considered empty, in this case, the GGM will be used to calculate the gravity value over this point. Sometimes the interpolation can be conducted over the grid points due to the poor spatial distribution of the gravity data around the interpolation points. In this study, we also consider the GGM to recover the value of this point and similarly for points with less or non-point (empty).

Finally, the interpolated terrestrial and marine gravity data are combined together with the GGM-based inland and marine points to create the final gravity grid. Further improvements for the grid such as the utilization of the GGM full d/o, interpolation, search radius optimization and filtering are to be considered in the future work. Furthermore, the GRAV-D airborne gravity data and Altimetry data will be combined to the existing data to ensure high quality and precision for the final gravity grid.

REFERENCES

1. Heiskanen, W. A.; Moritz, H., Physical geodesy. W. H. Freeman, 1967

2. Kiamehr. R. Precise Gravimetric Geoid Model for Iran Based on GRACE and SRTM Data and the Least-Squares Modification of Stokes' Formula: with Some Geodynamic Interpretations, 2006, PhD Thesis.

3. Dragomir, V.; Ghitau, D.; Mihailescu, M.; Rotaru, M. Theory of the Earth's Shape, 1st ed., ser. Developments in Solid Earth Geophysics. Elsevier, 1982.

4. Fan, H. Theoretical Geodesy. 2006, Royal Institute of Technology.

5. Pail, R., N.; Kühtreiber, B.; Wiesenhofer, B.; Hofmann-Wellenhof, C.; Ullrich, N.; Höggerl, D.; Ruess, Imrek, E. The official Austrian geoid solution 2008: Data, Method and Results, vol. 11, Apr. 2009, p. 2974.

6. Moritz, H. Advanced Physical Geodesy. Wichmann, 1980

7. Ellmann, A. "Computation of three stochastic modifications of Stokes's formula for regional geoid determination," Computers & Geosciences, 2005, vol. 31, no. 6, pp. 742–755.

8. Ågren, J.; Sjöberg L. E.; and Kiamehr, R. The new gravimetric quasigeoid model KTH08 over Sweden," Journal of Applied Geodesy, vol. 3, no. 3, pp. 143-153, 2009.

9. Kiamehr, R.; Sjöberg, L. E. "An optimum way to determine a precise gravimetric geoid model based on the least-squares modificati on of Stokes' formula - A case study of Sweden," Acta Geodaetica et Geophysica Hungarica, 2010, vol. 45(2), pp. 148–164.

10. Abdalla, A. "Towards a precise gravimetric geoid model in the Saudi Arabia (SAGEO13)," 2013, Report.

11. Abdalla, A.; and Mogren, S. "Implementation of a rigorous least-squares modification of Stokes formula to compute a gravimetric geoid model over Saudi Arabia (SAGEO13)," Canadian Journal of Earth Sciences, 2015, vol 52 (10): pp. 823-832.

12. Ågren, J.; Sjöberg, L. E. Investigation of Gravity Data Requirements for a 5 mm-Quasigeoid Model over Sweden. In Gravity, Geoid and Height Systems, ser. International Association of Geodesy Symposia, U. Marti, Ed. Springer International Publishing, 2014, pp. 143–150.

13. Featherstone, W. E. Absolute and relative testing of gravimetric geoid models using Global Positioning System and orthometric height data," Computers & Geosciences, 2001, vol. 27 (7), pp. 807-814

14. Kiamehr, R. Qualification and refinement of the gravity database based on cross-validation approach: A case study of Iran," Acta Geodaetica et Geophysica Hungarica, 2007, vol. 42, no. 3, pp. 285–295.

15. Ellmann, A. An improved gravity anomaly grid and a geoid model for Estonia. Proc. Estonian Acad. Sci. Geol., 2002, vol.51(4), pp.199–214.

16. Ellmann, A.; All, T. L. E.; Oja, T. Towards unification of terrestrial gravity data sets in Estonia, Estonian Journal of Earth Sciences, 2009, vol 58(4), 229–245.

17. Märdla, S.; Ellmann, A.; Oja, T.; Jürgenson, H. Improving and Validating Gravity Data Over Ice-Covered Marine Areas. In IAG 150 Years, ser. International Association of Geodesy Symposia, C. Rizos and P. Willis, Eds. Springer International Publishing, 2016, pp. 263–270.

18. McCubbine, J. C.; Stagpoole, V.; Tontini, F. C.; Amos, M.; Smith, E.; Winefield, R. Gravity anomaly grids for the New Zealand region. New Zealand Journal of Geology and Geophysics, 2017, vol. 60(4), pp. 381–391.

19. Abdalla, A.; Fairhead, D. A new gravimetric geoid model for Sudan using the KTH method, Journal of African Earth Sciences, 2011, vol. 60(4), pp. 213–221.

20. Zalizniak, V. Interpolation and Approximation" in Essentials of Scientific Computing, V. Zalizniak, Ed. Woodhead Publishing, 2008, pp. 144–168.

21. Abdalla, A.; Fadil, A.; Fernandes, R.; Bos, M.; Mugnier, C.; Cavell J. A. Preliminary Results of Land Subsidence Monitoring in Louisiana from GNSS Observations. International Union of Geodesy and Geophysics (IUGG), 2019, Montreal, Canada.

22. Abdalla, A. Analysis of Geodetic Measurements for Land Subsidence research in Louisiana state," Center for GeoInformatics 2019 Outreach, Louisiana State University, Baton Rouge, USA, 2019.

23. International Gravimetric Bureau (BGI), http://bgi.obs-mip.fr (accessed on 19/10/2019)

24. BGI Data, "Louisiana Data Info: Terrestrial Gravity data," 2018.

25. Pavlis, N.; Holmes, S.; Kenyon, S. C., Factor, J. K. The development and evaluation of the Earth Gravitational Model 2008 (EGM2008). Journal of Geophysical Research: Solid Earth, 2012, vol. 117(B4), pp. 1-38.

26. Pail, R.; Fecher, T.; Barnes, D.; Factor, J. F.; Holmes, S. A.; Gruber,T.; Zingerle, P. Short note: the experimental geopotential model. Journal of Geodesy, 2018, Vol. 92(4), pp. 443–451

27. Zingerle, P.; Pail, R.; Gruber, T.; Xanthi, O. The experimental gravity field model XGM2019e. GFZ Data, 2019

28. Moritz, H. On the Use of the terrain correction in solving Molodensky's problem. Defense Technical Information Center, 1968

29. Forsberg, R. A Study of Terrain Reductions, Density Anomalies and Geophysical Inversion Methods in Gravity Field Modelling, Ohio State University, Columbus Dept of Godetic Science and Surveying, Technical Report, 1984, OSU/DGSS-355.

30. Moritz, H. Geodetic Reference System 1980," Journal of Geodesy, 2000, vol. 74(1), pp. 128–133.

31. Curry, W. Interpolation with prediction-error filters and training data, PhD Thesis, 2008, Stanford University.

32. Geisser, S. Predictive Inference. 1993, New York, NY: Chapman and Hall.

33. Molinaro, A. M.; Simon, R.; Pfeiffer, R. M., Prediction error estimation: a comparison of resampling methods. Bioinformatics, 2005, 21 (15): 3301–3307.

34. Abdalla, A. Green, C. GEOWARE: An optimized MATLAB software for determination of high-frequency geoid model using relational operators, 2018 International Conference on Computer, Control, Electrical, and Electronics Engineering (ICCCEEE), 2018, pp. 1–6.

35. Abdalla, A.; Ferreira, V.; Mugnier, C.; Elzein, A. On the optimization of spherical convolution integral: Efficiency analysis. International Conference on Computer, Control, Electrical, and Electronics Engineering 2019 (ICCCEEE19), 2019, Khartoum, Sudan

Estimation of sea level trend in the Black Sea from satellite and in-situ data

Nevin Betül Avşar[1,*], Şenol Hakan Kutoğlu[2], Shuanggen Jin[3]

[1]Zonguldak Bülent Ecevit University, Geomatics Engineering Department 67100 Zonguldak, Turkey
Phone: +90 372 291 2578, E-mail: nb_avsar@beun.edu.tr

[2]Zonguldak Bülent Ecevit University, Geomatics Engineering Department 67100 Zonguldak, Turkey
Phone: +90 212 285 3826, E-mail: kutogluh@hotmail.com

[3]Shanghai Astronomical Observatory, Chinese Academy of Sciences 200030 Shanghai, China
Phone: +86 21 34775292, E-mail: sgjin@shao.ac.cn

ABSTRACT

Sea level is a dynamical parameter related to climate change. Recently global sea level rise is accelerating in response to ocean thermal expansion and glaciers/ice sheet melting, and sea level change has a strong regional pattern. In this study, a comprehensive analysis of sea level change in the Black Sea is performed using satellite and in-situ data. Sea level observations from satellite altimetry and tide-gauge stations were used to estimate the trend of the Black Sea level and its periodicity. The present-day sea level changes in the Black Sea were investigated using multi-mission gridded satellite altimetry data covering nearly 24.5 years from January 1993 to May 2017. The mean rate of sea level rise has been detected as 2.5 ± 0.5 mm/year over the entire Black Sea. If considering the dominant cycles, until December 2014, the Black Sea level has risen at a rate of about 3.2 ± 0.6 mm/year. The maximum rate (~ 5 mm/year) was observed in the part which is between of 38°–40° northern latitudes and 41°–42° eastern longitudes of the Black Sea. Besides, coastal sea level changes were analyzed from 13 tide-gauge stations along the Black Sea coast. Accordingly, the relative sea level change were assessed using the available tide-gauge data, and generally seen a rise (except for the Bourgas station). The results also showed that there were significant vertical ground movements at some tide-gauge locations. For the nearly co-located Global Positioning System (GPS) and tide-gauge stations (at Trabzon, Sinop and Sile locations), after determining vertical motion from the GPS measurements, correlation coefficient between the trends obtained from altimetry and tide-gauges were greatly improved from 0.37 to 0.99. Furthermore, over the period of 2002–2017, the rate of seawater mass change in the Black Sea from the Gravity Recovery and Climate Experiment (GRACE) mascon solutions was 2.3 ± 1.0 mm/year. The sum of mass-induced and steric-induced (temperature + salinity) changes showed similar fluctuations with the total sea level changes obtained from altimetry.

KEYWORDS: Black Sea; sea level change; satellite altimetry; tide-gauge; GRACE

1. INTRODUCTION

High global surface temperatures lead to thermal expansion of oceans and rapid melting of glaciers/ice sheets resulting in sea level rise. In this context, sea level rise is an important parameter for monitoring the progression of climate change. Furthermore, sea level rise can affect human activities in coastal areas and alter ecosystems [1]. Potential sea level rise poses a significant threat to areas with low topography. Flooding, inundation, storm, erosion, habitat loss, ecosystem damage, contamination of underground water are mostly damaging/catastrophic impacts of sea level rise on coastal zones [2-5]. Therefore, a comprehensive assessment of present-day sea level change and its driving factors is important for adaption to its impacts, and associated socio-economic issues. Accurate estimation of future sea level changes, predetermination of regions which may be affected by sea level rise and taking precautions against possible impacts require monitoring of sea level change and its components.

Sea level changes are not geographically uniform. Satellite altimetry observations, which are available since 1993, show that there is a strong regional variability in sea level rates [6]. Regional sea level changes can deviate substantially from those of the global mean, and even in some regions can reveal a condition opposite to global trend [7]. In this sense, this study is focused on sea level changes in the Black Sea. It is aimed to make a reliable estimation of sea level rise by using data of tide-gauge stations along the Black Sea coast and satellite altimetry. Sea level observations from both the techniques are used to infer information on trend of the Black Sea level and its periodicity. Moreover, mechanisms driving sea level change in the Black Sea are investigated. The dynamic factors (mass variations, tectonic movements, etc.) which affect the sea level changes are analyzed to model the sea level changes correctly depending on time and location.

From past to present, numerous studies have been carried out to determine seasonal and interannual variability of the Black Sea level using tide-gauge and satellite altimetry data. A comprehensive analysis of these studies can be found in [8]. For example, according to [9], the Black Sea level increased by 20 cm in the last 100 years [10]. In [11] an average rate of sea level was determined as 27.3 ± 2.5 mm/year for a period of 6 years (1993–1998), by attributing it to the steric effect (mostly due to warming of surface waters). [10] also detected from along-track altimetry data that the Black Sea level rose at a rate of 13.4 ± 0.11 mm/year

over 1993–2008; in the western and eastern regions this rate become as 14.2 ± 0.16 and 12.8 ± 0.12 mm/year, respectively. They pointed out that the sea level changes in this period were closely related to annual fresh water flux (especially Danube River runoff). In addition, [12] also pointed out that due to the cyclonic Rim Current intensification the Black Sea level rises in the coastal areas that exceeded in the offshore by 1.5–2 times.

2. DATA AND METHOD

2.1 Data

In this study, satellite and in-situ data were used to investigate sea level change throughout the Black Sea.

Satellite altimetry provides accurate measurements of Sea Surface Height with near-global coverage. Accordingly, the altimetry dataset preferred in this study is Daily Sea Surface Heights (SSH)s from 1993-01-01 to 2017-05-15 for the Black Sea, provided from the Copernicus Marine Environment Monitoring Service. These multi-mission data in delayed-time are gridded (1/8° by 1/8°) Sea Level Anomalies (SLA)s computed with respect to a twenty-year 2012 mean. Necessary geophysical (solid earth, ocean and pole tides, ocean tide loading effect, sea state bias, and inverse barometer response of the ocean) and atmospheric (ionosphere, and dry/wet troposphere effects) corrections have been applied to the data set by the data center [13].

On the other hand, the existence of long-term data in many tide-gauge stations is one of the most important reasons for using these stations in sea level measurements. However, along the Black Sea coast most tide-gauge data are not up to date and tide-gauges' spatial distribution is poor. In this study, data of 13 tide-gauge stations on the Black Sea coast (including 1 station in the Bosporus) were used, which have different data periods. 7 tide-gauge stations (Poti, Batumi, Sevastopol, Tuapse, Varna, Bourgas, and Constantza) located at along the Black Sea coast have been chosen from the Permanent Service for Mean Sea Level (PSMSL) and other 6 tide-gauge (Amasra, Igneada, Istanbul, Trabzon, Sinop, and Sile) are from the Turkish Sea Level Monitoring System (TUDES). Figure 1 shows the locations of the tide-gauge stations in this study, and their data periods are given in Table 1. The Revised Local Reference (RLR) data from the PSMSL are the monthly averaged time series, spanning

from 65 to 140 years in the period of 1874–2013. As for the TUDES data, the data have been provided at 15-minute intervals in the Turkish National Vertical Control Network-1999 (TUDKA-99) datum. In the study, the monthly averaged time series of the TUDES data have been derived at each station. The record with the longest time period among these stations extends to mid-2001 at Amasra.

Moreover, this study focuses on coastal sea level changes along the Black Sea. For this purpose, the linear trends of sea level time series at the 8 tide-gauge stations used in this study (except for Istanbul, Sevastopol, Varna, Bourgas, and Constantza) were estimated from both tide-gauge and satellite altimetry data. The consistency of the results derived from both the observations were investigated and interpreted. Because of some problems in the tide-gauges, such as less data and short overlapping period, we concentrated on the analysis of coastal sea level change at only 8 tide-gauge locations along the eastern and southern coasts of the Black Sea.

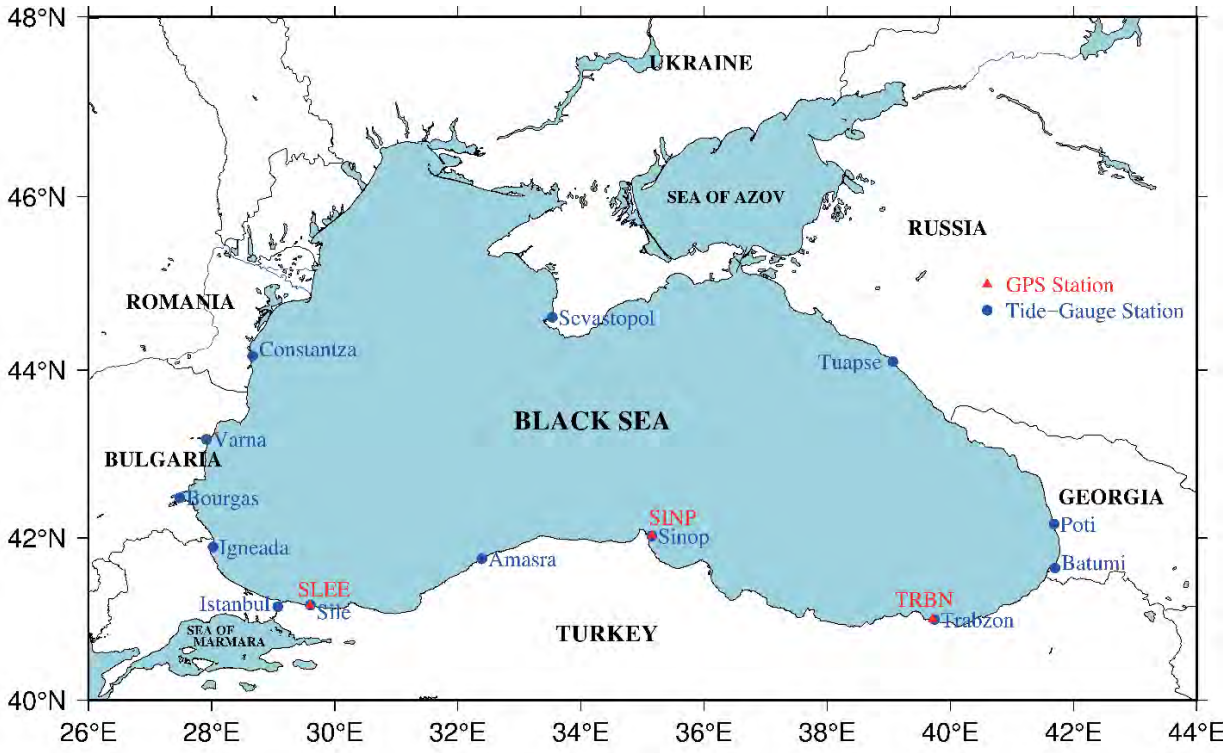

Figure 1. *Tide-gauge and GPS stations used in the study*

Since tide-gauge measurements reflect relative sea level change; if there is a vertical land motion at that tide-gauge location, the tide-gauge record is a combination of local sea level

change and vertical land motion at the location. Therefore, in order to obtain absolute coastal sea level change, the vertical land motion should be added from Global Navigation Satellite System (GNSS) observations. In this study, to estimate absolute sea level changes from the tide-gauges, 3 GPS stations (TRBN, SINP, and SLEE), which are nearly co-located tide-gauge stations (Figure 1), from the Turkish National Permanent Real Time Kinematic Network (TUSAGA-Active) were used. The GPS data were spanning from 1 January 2010 to 31 December 2014.

Table 1: Time-span on all the tide-gauge stations in this study.

Tide-gauge station (Country)	Data period
Poti (Georgia)	1874–2013
Batumi (Georgia)	1882–2013
Sevastopol (Ukraine)	1910–1994
Tuapse (Russia)	1917–2011
Varna (Bulgaria)	1929–1996
Bourgas (Bulgaria)	1929–1996
Constantza (Romania)	1933–1997
Amasra (Turkey)	2001–2014
Igneada (Turkey)	2002–2014
Trabzon (Turkey)	2002–2014
Sinop (Turkey)	2005–2014
Sile (Turkey)	2008–2014
Istanbul (Turkey)	2011–2014

Total change in sea level at seasonal and longer time scales is the sum of steric and mass (non-steric) induced changes. It is possible to estimate mass changes using satellite gravity data, and steric changes through in-situ and/or satellite measurements. Steric sea level changes

reflect volumetric expansion of the seawater due to density changes at shallow and deep. In the study, as steric data, global steric sea level (thermosteric, halosteric, and total) anomaly fields were used from the National Oceanic and Atmospheric Administration (NOAA)'s National Centers for Environmental Information (NCEI). These data are 3-month sea level anomalies [14]. They provide steric (thermosteric and halosteric) components of sea level change of the 0–700 m layer. Their time periods are 2005–present for total steric and halosteric sea levels, 1955–present for thermosteric sea level. On the other hand, water mass-induced sea level changes can be estimated from its time-variable gravity signals. In the study, to estimate water mass variations in the Black Sea, GRACE RL05 Mascon solutions from the University of Texas Center for Space Research (CSR) were preferred [15]. These GRACE products from April 2002 to June 2017 are monthly mass grids corresponding changes in equivalent water thickness relative to a time-mean baseline. Mass Concentration blocks (mascons) are essentially another form of gravity field basis functions (including spherical harmonics) to which GRACE's inter-satellite ranging observations are fit. Each mascon has a specific known geophysical location. These data are represented on a 0.5° lon-lat grid, but they represent the equal-area geodesic grid of size 1°x1° at the equator. Mascon solutions typically do not need to be destriped or smoothed unlike spherical harmonic coefficients. Moreover, they allow a better separation of land and ocean areas. Nevertheless, here, in order to minimize leakage along the coastline, an ocean mask were applied. The data also have a Glacial Isostatic Adjustment (GIA) correction.

2.2 Method

In this study, monthly averaged time series of all the sea level observations have been obtained to provide concurrent analysis. Sea level changes have a periodic character. In this sense, sea level time series exhibit a strong seasonality as well as a linear trend as mentioned in [16]. For sea level time series analysis, harmonic analysis method has been preferred in this study. So, a model including seasonal components (annual and semi-annual harmonics) and linear trend has been used [17]:

$$M(t) = M(t_0) + v(t - t_0) + \sum_{k=1}^{2} A_k \cos(\omega_k (t - t_0) + \varphi_k) + \varepsilon(t) \qquad (1)$$

where $M(t)$: sea level time series, t: time, t_0: beginning time (for example for altimetry: 1 January 1993), $M(t_0)$: mean sea level at t_0, v: the rate of sea level change (linear trend), k = 1 annual signal, k = 2 semi-annual signal, A: amplitude, ω: angular frequency, φ: phase, $\varepsilon(t)$: unmodelled residual term. Here, in order to estimate trend, phase and amplitude, the least squares method has been employed [18].

3. ANALYSIS AND RESULTS

3.1 Analysis of Long-Term Trend from Satellite Altimetry Data

In order to examine the inter-annual variability of the sea level time series, the seasonal components have removed from the monthly values (Figure 2a). The results show that the Black Sea level has risen at a rate of about 2.5 ± 0.5 mm/year between January 1993 and May 2017. On the other hand, the latest period for the available tide-gauge data in the Black Sea for this study is until to December 2014. Besides, the other dominant periodic behaviours (after removing seasonal cycles) in the altimetry time series have been determined using the Cycles Analysis & Timeseries Software (CATS) - v1.0 [19]. Figure 2b demonstrates the dominant cycles over the Black Sea level time series from January 1993 to May 2017. As seen in the figure, the period of January 1993 – December 2014 indicates a more apparent trend for this sea level time series. An average trend of 3.2 ± 0.6 mm/year over the Black Sea has been also determined for the period 1993–2014. The satellite altimetry observations from 1993 to 2014 yield the standard deviation of 7.5 cm for sea level anomalies in the Black Sea. In 2010 mean sea level anomaly was about 20 cm above the 1993 average. And this was the highest annual average in the satellite record from 1993 to present, and the record high sea level anomalies occurred in March 2010, January 2011 and April 2013. Figure 3 shows the spatial distribution of the Black Sea level trends over 1993–2014. As seen from the figure; the trend values were positive in whole basin, however they were not spatially uneven. Accordingly, over all the Black Sea basin, the rates of sea level change for the period 1993–2014 varied from 0.2 to 5.0 mm/year. The rate of sea level rise in coastal and shelf areas was greater than in the centre of the basin. Especially the southeastern region showed a larger rate of rise than the other parts in the Black Sea. According to [20], the observed spatial differences in the sea level rise were related to the basin dynamics, which redistributed water mass within the basin. Indeed, cyclonic Rim Current generally causes a higher sea level rise at

the coastal parts of the Black Sea. In particular, an extension of the Batumi anticyclone resulted in an excess sea level rise in the southeastern part of the basin over 1993–2014.

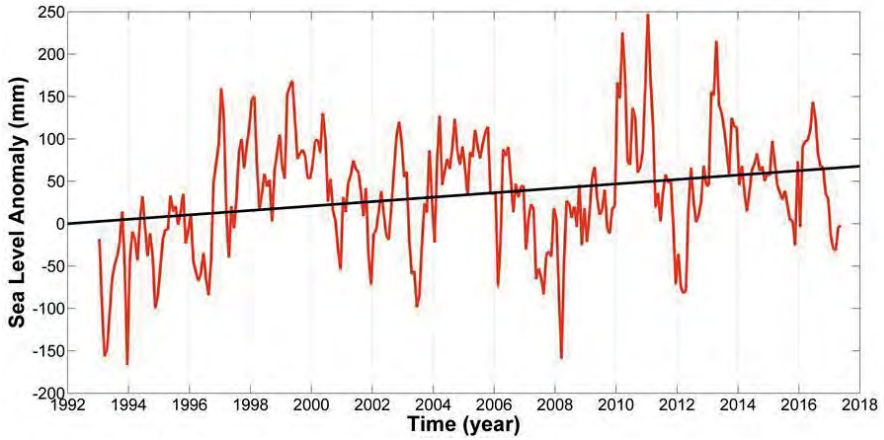

(a) *Non-seasonal sea level time series with its linear fitting*

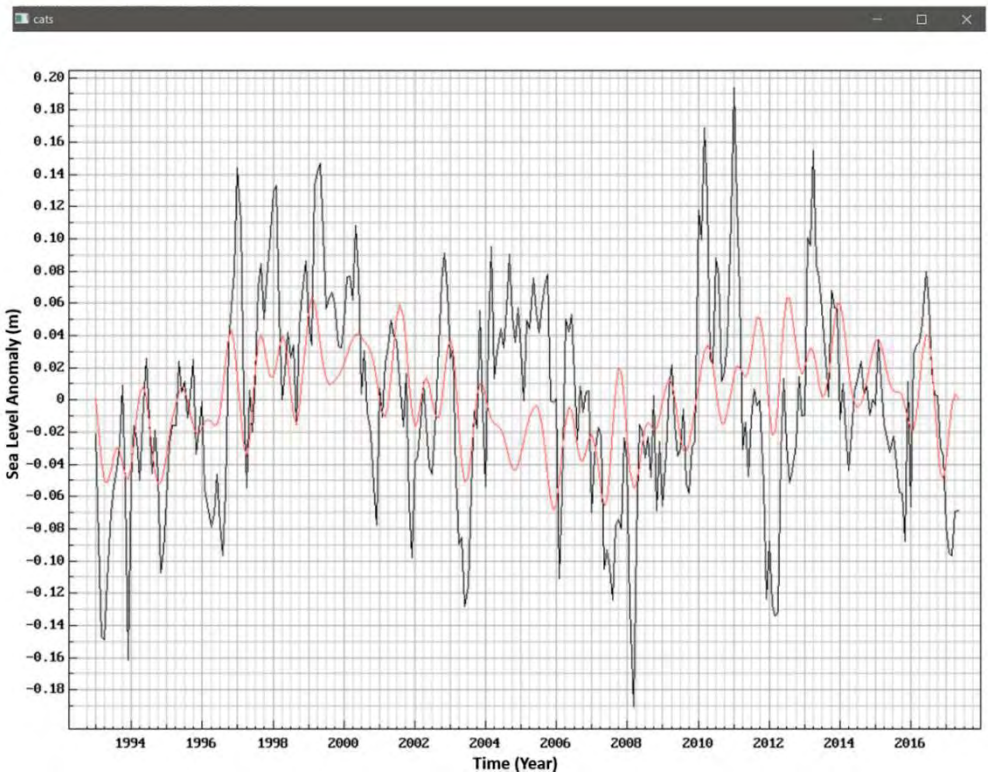

(b) *Dominant cycles (red) over the detrended and non-seasonal sea level time series (black)*

Figure 2. *Monthly non-seasonal sea level time series in the Black Sea over 1993–2017 from the satellite altimetry data*

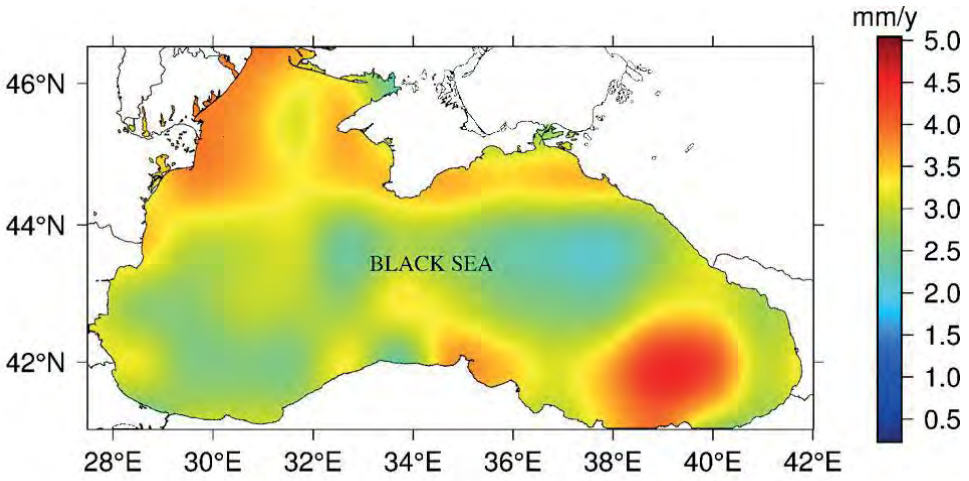

Figure 3. *Spatial distribution of sea level trend over the Black Sea from the multi-mission satellite altimetry data between January 1993 and December 2014 (Unit:mm/year)* [8]

3.2 Analysis of Long-Term Trend from Tide-Gauge Data

The least 50-year of data is needed for long-term sea level change studies [2]. However, sea level measurements from the TUDES network along the Black Sea coast are not long-term (< 20 years) while the tide-gauge time series provided from the PSMSL have an enough period for long-term trend estimation. Moreover, some tide-gauge time series (such as Bourgas, Batumi and Amasra) contain many missing observations. Eq.1 was used in the analysis of the relative sea level time series from the tide-gauge stations along the Black Sea coast. The data with less than 4 consecutive missing months were used through linearly interpolating, whereas the others were excluded from this analysis. Table 2 shows the linear variation with time of the observed sea level in the tide-gauge stations along the Black Sea. As an example, the trend and harmonic model of the Amasra tide-gauge data are represented in Figure 4. Consequently, nearly all the tide-gauge stations (except for Bourgas) indicated the rising sea levels. In addition, the Sinop station showed no significant sea level change.

Table 2: Trends of relative sea level changes in the Black Sea (The available longest data periods of the tide-gauges were used for the analysis).

Tide-gauge	Data period	Trend (mm/year)
Poti	August 1922 – December 2002	7.01 ± 0.12
Batumi	January 1925 – December 1996	3.52 ± 0.15
Sevastopol	September 1944 – December 1994	1.56 ± 0.22
Tuapse	January 1943 – December 2011	2.92 ± 0.14
Varna	January 1926 – November 1961	1.53 ± 0.48
Bourgas	February 1981 – January 1996	-7.52 ± 1.33
Constantza	January 1945 – December 1979	3.02 ± 0.46
Amasra	June 2001 – February 2011	3.43 ± 1.42
Igneada	June 2002 – December 2014	6.94 ± 2.18
Trabzon	July 2002 – December 2014	2.33 ± 1.75
Sinop	June 2005 – December 2014	0.43 ± 2.88
Sile	July 2008 – December 2014	5.03 ± 4.84
Istanbul	June 2011 – December 2014	36.77 ± 9.07

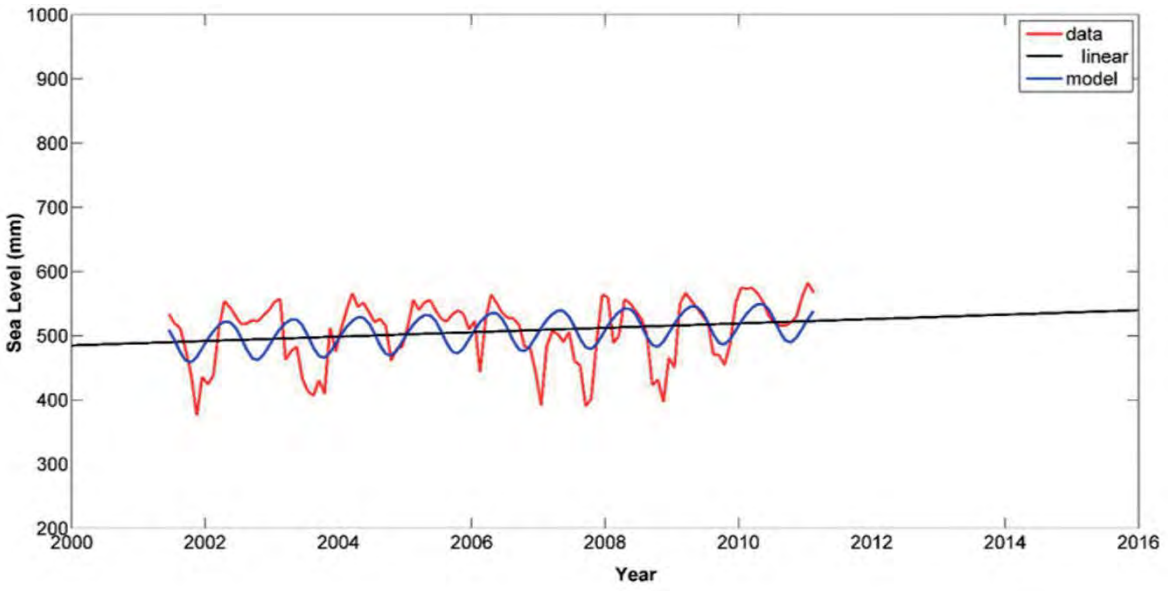

Figure 4. *Trend and harmonic model of ~ 10-year sea level time series at Amasra tide-gauge station* [8]

3.3 Analysis of Coastal Sea Level Change

According to the gridded satellite altimetry data used in the study, there are 3249 altimetric grid points in the Black Sea. In order to compare with tide-gauge results, the altimetry measurements at the closest points to the tide-gauge sites were selected; considering grid interval the altimetric points were chosen with less than 10 km to the tide-gauges (Table 3). For the comparison, the data after 1993 of the long-term tide-gauge records have been preferred in this study (Table 3). As stated before, the short overlapping periods of tide-gauges and altimetry enabled to analysis of sea level change at only 8 tide-gauges (Poti, Tuapse, Batumi, Amasra, Igneada, Trabzon, Sinop, Sile). Some tide-gauge time series included missing observations; therefore, the data gaps in these time series were eliminated. For example, at the Batumi station only 10-year record was useful for present study. As an example, the sea level time series at the Trabzon tide-gauge location are depicted in Figure 5. As seen in the figure, the time series from altimetry and tide-gauge measurements show almost similar behaviour in the sea level change.

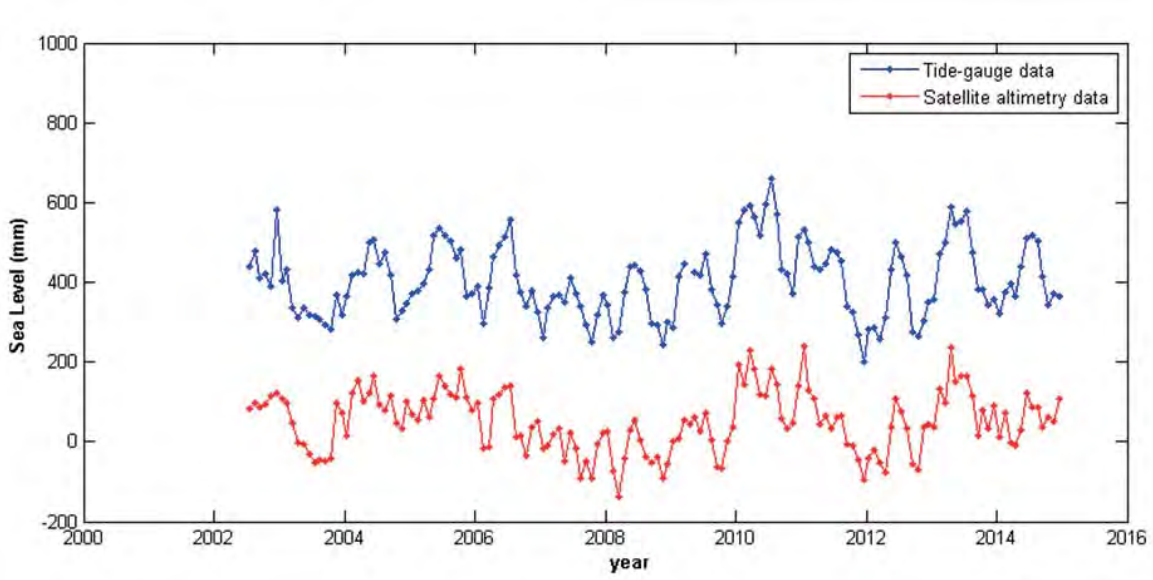

Figure 5. *Sea level time series at Trabzon tide-gauge location from satellite altimetry (red line) and tide-gauge (blue line)*

For the monthly time series of both the sea level measurements at 8 tide-gauge locations, the trends were estimated by calculating Eq.1 with the least squares method. The linear trends are shown in Table 3 and Figure 6 for each tide-gauge station. The results for the stations with long-term records such as Poti and Tuapse have a good agreement. At Amasra, the linear rates

of both observation data are not statistically significant. It may result from the short time-span or the data gaps.

Table 3: Trends of coastal sea level in the Black Sea, calculated from satellite altimetry and tide-gauge data at same time-span.

Tide-Gauge station	Distance (km)	Time-span	Trend (mm/year)	
			Satellite Altimetry	Tide-Gauge
Poti	2.4	Jan. 1993 – Dec. 2013	3.45 ± 0.78	4.13 ± 0.78
Tuapse	4.2	Jan. 1993 – Dec. 2011	3.42 ± 0.86	4.30 ± 0.88
Batumi	6.2	Sep. 2003 – Dec. 2013	1.38 ± 2.29	3.47 ± 2.56
Amasra	7.9	June 2001 – Dec. 2012	0.95 ± 1.72	0.07 ± 1.45
Igneada	7.9	July 2002 – Dec. 2014	2.19 ± 1.66	6.74 ± 2.08
Trabzon	8.6	July 2002 – Dec. 2014	-0.38 ± 1.65	2.33 ± 1.76
Sinop	6.0	June 2005 – Dec. 2014	7.05 ± 2.48	0.43 ± 2.88
Sile	5.5	July 2008 – Dec. 2014	3.61 ± 4.57	5.03 ± 4.84

As mentioned before, in this study, the vertical land motions at 3 tide-gauge sites along the southern Black Sea coast were estimated from nearby GPS stations (using Eq.1) (the distances between tide-gauge and GPS stations can be seen in Table 4), and added to the results obtained from the tide-gauge data. For this, the data belong to these continuous GPS stations (TRBN, SINP and SLEE) from the TUSAGA-Active have been processed using the GAMIT/GLOBK software [8]. Consequently, for Trabzon, Sinop and Sile tide-gauge locations, the trends obtained from tide-gauge + GPS are presented in Table 4 along with those computed from satellite altimetry. The results derived from satellite altimetry, tide-gauge, and tide-gauge + GPS are also shown in Figure 6. It is clearly seen that the trends obtained from satellite altimetry and tide-gauge + GPS have a better agreement. Especially for Sinop station, the difference between satellite altimetry and tide-gauge + GPS is much smaller than the difference between satellite altimetry and tide-gauge. When their relationships were further analyzed, it were seen that the correlation between satellite altimetry and tide-gauge + GPS were significantly improved (from 0.37 to 0.99). These results reveal that the vertical land motion varying at tide-gauge stations should be taken into account to get the absolute sea level change when using tide-gauges data.

Table 4: Trends obtained from satellite altimetry, and tide-gauge + GPS time series at 3 tide-gauge locations along the Black Sea coast.

Tide-Gauge station	GPS station	Distance (km)	Trend (mm/year)	
			Satellite Altimetry	Tide-Gauge + GPS
Trabzon	TRBN	2.8	-0.38 ± 1.65	1.21 ± 1.78
Sinop	SINP	0.8	7.05 ± 2.48	6.63 ± 3.81
Sile	SLEE	1.2	3.61 ± 4.57	4.44 ± 4.85

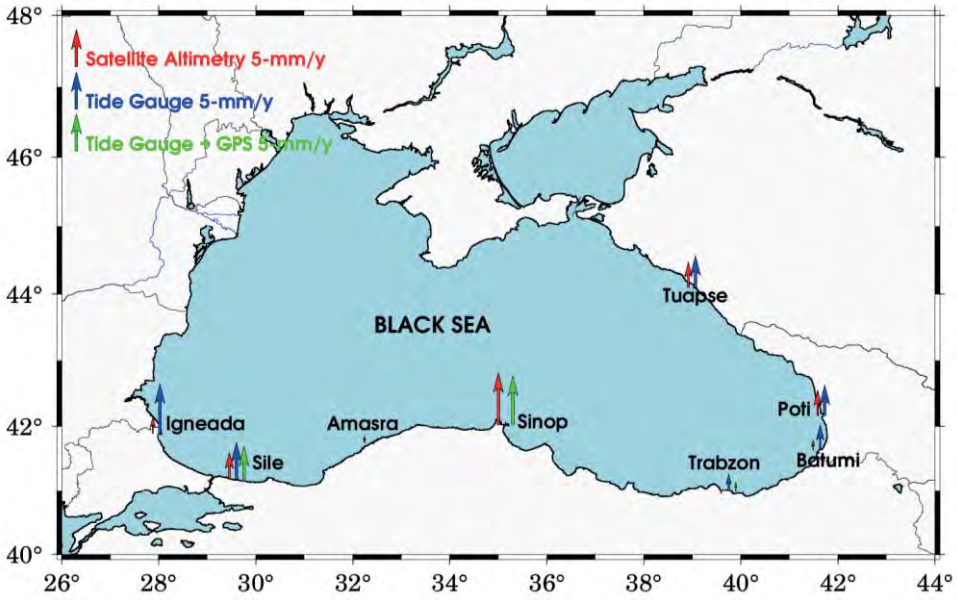

Figure 6. *Trends along the Black Sea coast from satellite altimetry (red arrows), tide-gauge (blue arrows), and tide-gauge + GPS (green arrows) (Unit: mm/year)*

3.4 Analysis of Steric and Mass-Induced Sea Level Changes

For this study, the Black Sea data were cut out from all the ocean steric data. Figure 7 demonstrates total steric sea level variations as well as individual contributions of thermal and haline expansion. In addition, Figure 7 includes 3-month altimetry-derived sea level changes from January 1993 to December 2014. Here, in order to remove datum differences between the related sea levels, transformations were performed via the calculated translation parameters.

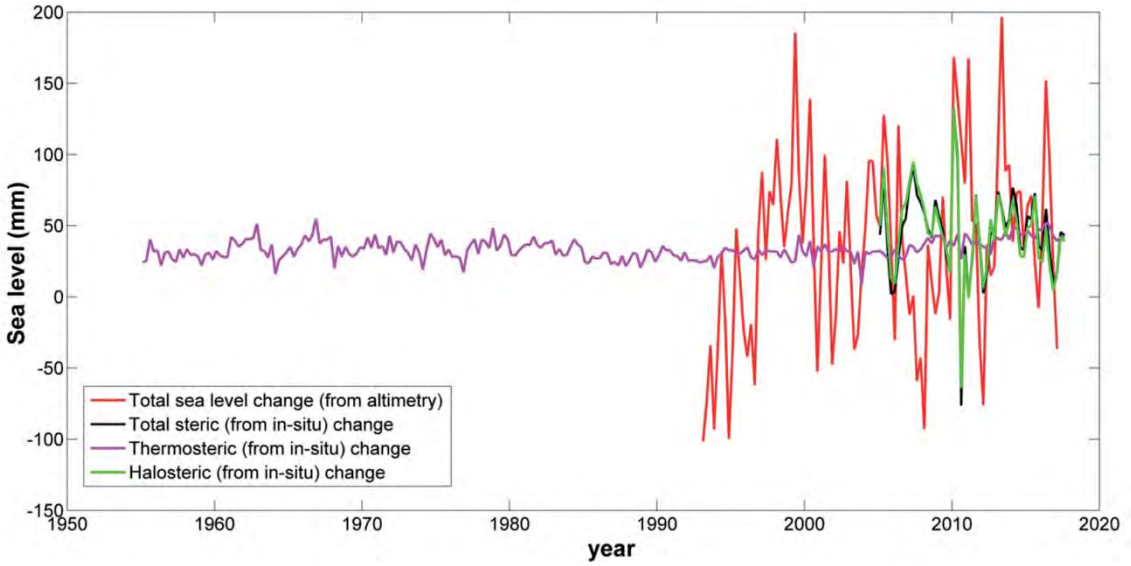

Figure 7. *Total and steric sea level changes in the Black Sea for 3-month time evolutions*

On the other hand, the basin-averaged time series of equivalent water thickness were obtained from 133 grid points covering the Black Sea. For the analysis, the 20 missing solutions (months) in the GRACE data between April 2002 and June 2017 have been interpolated linearly. Then, the mass-induced contribution to sea level change in the Black Sea was analysed using Eq.1. Accordingly, the result shows a rate of the non-seasonal seawater mass change of about 2.3 ± 1.0 mm/year over the last 15 years. Figure 8 depicts the monthly time series of the Black Sea level from April 2002 to May 2017 from satellite altimetry (in terms of sea level anomaly) and satellite gravity (in terms of equivalent water thickness). In figure, blue curve shows GRACE-derived equivalent water thickness, whereas green curve has been achieved by translating the equivalent water thickness with respect to the altimetry-derived sea level. Here, the altimetry-derived sea level has been interpolated at all the grid points of 0.5° associated with the mascon grid interval.

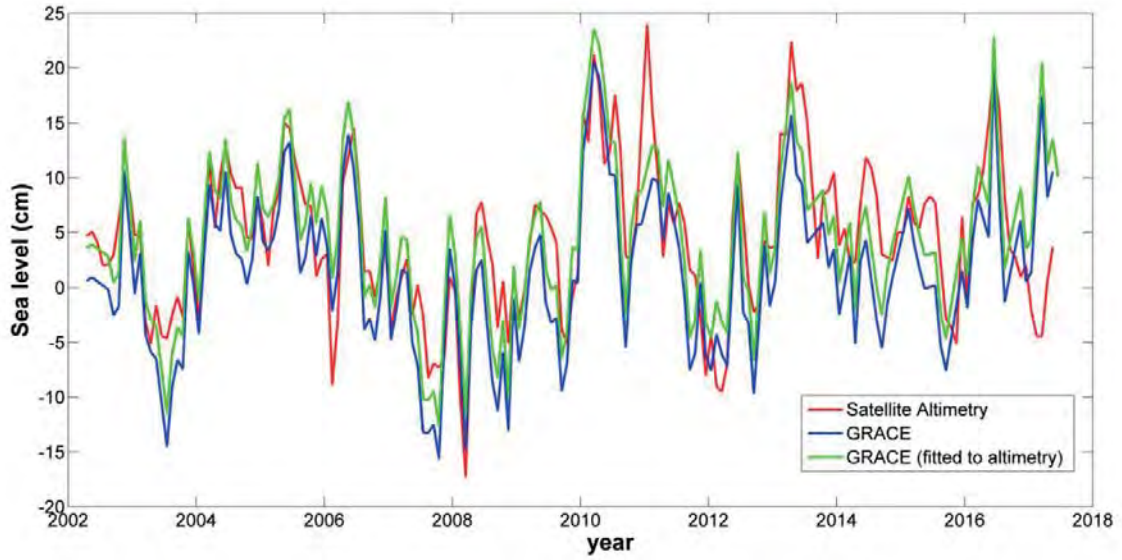

Figure 8. *Monthly sea level time series of the Black Sea from satellite altimetry and satellite gravity over 2002–2017 (Seasonal signals retained).*

Eventually, 3-month time evolution of sea level in the Black Sea are also charted in Figure 9. In spite of different uncertainties and systematic errors from altimetry, gravimetry and in-situ measurements; the 3-month time evolution of sea level shows that the observed sea level change and total of observed contributions almost exhibit similar fluctuations.

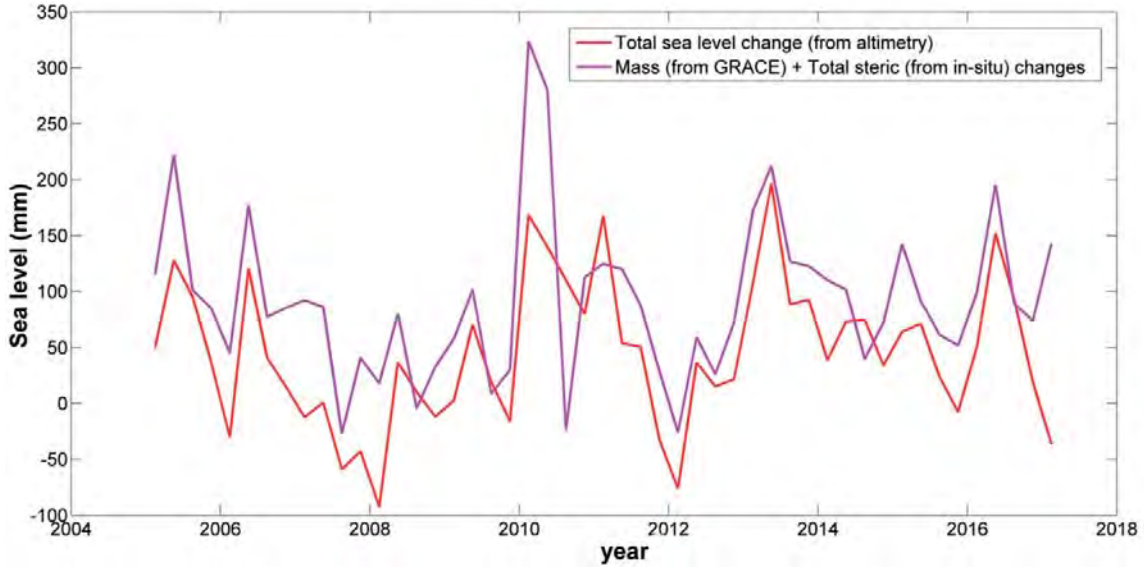

Figure 9. *Black Sea level changes from satellite altimetry data, and mass plus steric data for 2005–2017.*

4. CONCLUSION

In the Black Sea, which has a limited interaction with the Atlantic Ocean, sea level change is closely related to its hydrological balance. Recent studies based on altimetry and tide-gauge data have revealed the Black Sea level has risen. In this context, accurately determining the sea level change in the Black Sea and understanding the main driving forces of observed change are critical for determining its long-term variability and prevent its negative impacts. The results of this study show that accurately modelling of sea level changes depending on time and location in the Black Sea is crucial for risk assessments related to sea level rise, analysis of coastal change and planning of coastal area use.

In this study, the present-day sea level changes in the Black Sea were investigated using multi-mission gridded satellite altimetry data covering ~ 24.5 years from January 1993 to May 2017. When considering the dominant cycles, it detected the Black Sea level has risen at a rate of about 3.2 ± 0.6 mm/year. When the geographical distribution of sea level trends was investigated, the maximum rate (~ 5 mm/year) was observed in the southeastern part of the sea; this case should be considered. Using the available 13 tide-gauge data, relative sea level changes along the Black Sea were assessed, and generally seen a rise in the sea level. The results showed that at some tide-gauge locations, there were significant vertical movements. In order to detect the impact of vertical land motion on the coastal sea level change, the vertical movements at 3 Global Positioning System (GPS) stations (SINP, SLEE and TRBN), which were almost collocated with the Sinop, Sile and Trabzon tide-gauge stations, were analysed using GAMIT/GLOBK software. Consequently, at these 3 stations, the trends of absolute coastal sea level had a better agreement between satellite altimetry and tide-gauge + GPS.

On the other hand, mass contribution to the sea level change for the period 2002–2017 were detected as 2.3 ± 1.0 mm/year from the GRACE mascon solutions. 3-month total steric data as well as halosteric and thermosteric data of the water column in the Black Sea were also considered in this study. Along with mass-induced contributions, thermal and haline contributions exhibited a good agreement total sea level changes from satellite altimetry for the Black Sea.

ACKNOWLEDGEMENT

The authors are grateful to the organizations that provided the data, including Copernicus Marine Environment Monitoring Service (CMEMS), General Directorate of Mapping (Turkey) – GDM, Permanent Service for Mean Sea Level – PSMSL, National Oceanic and Atmospheric Administration (NOAA), and University of Texas Center for Space Research (UT-CSR).

REFERENCES

1. Field, C.B.; Barros, V.R; Dokken, D.J.; Mach, K.J.; Mastrandrea, M.D.; Bilir, T.E.; Chatterjee, M.; Ebi, K.L.; Estrada, Y.O.; Genova, R.C.; Girma, B.; Kissel, E.S.; Levy, A.N.; MacCracken, S.; Mastrandrea, P.R; White, L.L., Eds.; Climate Change 2014. Impacts, Adaptation, and Vulnerability. Part A: Global and Sectoral Aspects. Contribution of Working Group II to the Fifth Assessment Report of the Intergovernmental Panel on Climate Change; Cambridge University Press, Cambridge, United Kingdom and New York, NY, USA, 2014; 1132 pp.

2. Douglas, B.C. Sea level change in the era of the recording tide-gauge. In Sea Level Rise, History and Consequences, 1st ed.; Douglas, B.C., Kearney, M.S.; Leatherman, S.P., Eds.; Academic Press, USA, 2001; Volume 75, pp. 37–64.

3. Karaca, M.; Nicholls, R.J. Potential implications of accelerated sea-level rise for Turkey. J. Coast. Res. 2008, 24, 288–298.

4. Nicholls, R.J. Impacts of and responses to sea level rise. In Understanding Sea-Level Rise and Variability, Church, J.A.; Woodworth, P.; Aarup, T.; Wilson, W.S., Eds.; Wiley-Blackwell Publishing, London, UK, 2010; pp. 17–51.

5. Nicholls, R.J.; Cazenave, A. Sea-level rise and its impact on coastal zones. Science 2010, 328, 1517–1520.

6. Cazenave, A.; Palanisamy, H.; Ablain, M. Contemporary sea level changes from satellite altimetry: What have we learned? What are the new challenges?. Adv. Space Res. 2018, 62, 1639–1653.

7. Stammer, D.; Cazenave, A.; Ponte, R.M.; Tamisiea, M.E. Causes for contemporary regional sea level changes. Annu. Rev. Mar. Sci. 2013, 5, 21–46.

8. Avşar, N.B. Sea Level Changes In The Black Sea And Its Impacts On The Coastal Areas. PhD Thesis, Zonguldak Bülent Ecevit University, Graduate School of Natural and Applied Sciences, Department of Geomatics, Zonguldak, 2019.

9. Terziev, F.S., Ed.; Hydrometeorology and Hydrochemistry of the USSR Seas. Project: Seas of the USSR, Volume IV: The Black Sea, Issue 1: Hydrometeorological conditions, Gidrometeoizdat; St. Petersburg (in Russian), 1991.

10. Ginzburg, A.I.; Kostianoy, A.G.; Sheremet, N.A.; Lebedev, S.A. Satellite Altimetry Applications in the Black Sea. In Coastal Altimetry; Vignudelli, S.; Kostianoy, A. G.; Cipollini, P.; Benveniste, J., Eds.; Springer, Berlin, Heidelberg, 2011; pp. 367–387.

11. Cazenave, A.; Bonnefond, P.; Mercier, F.; Dominh, K.; Toumazou, V. Sea level variations in the Mediterranean Sea and Black Sea from satellite altimetry and tide-gauges, Global Planet Change 2002, 34, 59–86.

12. Kubryakov, A.A.; Stanichnyi, S.V. The Black Sea level trends from tide-gauges and satellite altimetry. Russ. Meteorol. Hydro+ 2013, 38, 329–333.

13. Product User Manual For Sea Level SLA Products, Copernicus Marine Environment Monitoring Service, REF: CMEMS-SL-PUM-008-032-062, 21.01.2019, Issue: 1.0, 40 pp.

14. Levitus, S.; Antonov, J.I.; Boyer, T.P.; Baranova, O.K.; Garcia, H.E.; Locarnini, R.A.; Mishonov, A.V.; Reagan, J.R.; Seidov, D.; Yarosh, E.S.; Zweng, M.M. World ocean heat content and thermosteric sea level change (0–2000 m), 1955–2010. Geophys. Res. Lett. 2012, 39, L10603.

15. Save, H.; Bettadpur, S.; Tapley, B.D. High-resolution CSR GRACE RL05 mascons. J. Geophys. Res.-Sol. Ea. 2016, 121, 7547–7569.

16. Cazenave, A.; Cabanes, C.; Dominh, K.; Mangiarotti, S. Recent sea level changes in the Mediterranean Sea revealed by TOPEX/POSEIDON satellite altimetry. Geophys. Res. Lett. 2001, 28, 1607e10.

17. Feng, G.; Jin, S.; Zhang, T. Coastal sea level changes in Europe from GPS, tide-gauge, satellite altimetry and GRACE, 1993–2011. Adv. Space Res. 2013, 51, 1019–1028.

18. Pugh, D.T. Tides, Surges and Mean Sea-Level. Reprinted with corrections; John Wiley & Sons Ltd., Chichester, UK, 1996; 486 pp.

19. CATS Cycles Analysis and Timeseries Software, Version 1.0, Ray Tomes and Radiance Trust, 2010; 30 pp.

20. Kubryakov, A.A.; Stanichny, S.V.; Volkov, D.L. Quantifying the impact of basin dynamics on the regional sea level rise in the Black Sea. Ocean Sci. 2017, 13, 443–452.

Physical Height Changes Estimated by GRACE Data: A Case Study Over Greenland

Emel Zeray Öztürk[1], Ramazan Alpay Abbak[2]

[1]Konya Technical University, Geomatics Engineering Department 42250 Konya, Turkey
Phone: +90 332 223 1930, E-mail: ezozturk@ktun.edu.tr

[2]Konya Technical University, Geomatics Engineering Department 42250 Konya, Turkey
Phone: +90 332 223 1898, E-mail: raabbak@ktun.edu.tr

ABSTRACT

Studies in recent years show that there are large mass variations in the Polar Regions of the Earth. Mass variations especially caused by global climate change necessitate modeling the redistribution of mass, investigation of its effect to the physical surface (e.g. vertical and horizontal displacements) of the Earth and evaluations of the future variations. The Gravity Recovery and Climate Experiment (GRACE) satellite mission, launched in 2002, contributed to the knowledge of temporal variations of geoid/quasigeoid heights induced by mass loading. With the implementation of the GRACE-Follow On (GRACE-FO) project, which is the continuation of the GRACE twin satellites that completed their mission in 2017, an important step was taken for the continuity of tracking Earth's mass movement across the planet. The main aim of this study is to estimate the physical height changes over Greenland where mass variations are intense. The effect of the mass redistribution to the physical height changes was investigated by means of the monthly release 6 GRACE based Global Geopotential Models (GGMs) developed by the CSR (Center of Space Research, the University of Texas at Austin) centre as well as Preliminary Reference Earth Model (PREM). The evaluated physical height changes were analysed using two different methods: the seasonal decomposition method and the Principal Component Analysis/Empirical Orthogonal Function (PCA/EOF) method. The main findings demonstrate that mass redistribution on a large scale over Greenland affects the physical height changes significantly. Vertical displacements vary from region to region but they increase more in particular in South Greenland, during the years 2004-2010 considerably.

KEYWORDS: geoid/quasigeoid heights; GRACE; Greenland; physical height changes; vertical displacements

1. INTRODUCTION

A precise national vertical reference system is essentially needed for each country. In order to realize this system with high accuracy, physical heights (i.e. the differences between ellipsoidal heights and geoid/quasigeoid heights) must be determined as precise as possible. The state of the art of geodetic science indicated that local/regional geoid/quasigeoid models can be developed with an accuracy of centimeter or sub-centimeter level [1]. It also should be mentioned that the deformation of the Earth's surface in the up component, e.g. ellipsoidal height changes, can be determined with the accuracy of a couple of millimeters [2,3].

In the past two decades, several studies emphasized the usefulness of geodetic satellite missions for the determination of temporal variations of geoid heights and Earth surface displacements induced from mass loading, and thereby the physical height (e.g. the orthometric/normal height) changes [4–9]. Among those missions, the Gravity Recovery and Climate Experiment [10] mission operated for the period between 2002 and 2017. The GRACE mission that has completed its activity, brought very useful information related to the elastic ground loading deformation in response to the Earth's mass variations [11,12]. The GRACE Follow-On (GRACE-FO) the continuation of the GRACE satellite mission was launched in May 2018 [13]. With the implementation of the GRACE-FO, the durableness of the monitoring Earth's mass variations is provided.

Greenland was selected as the research area. It is a region that mass variations are quite intense. Over the last two decades, a large number of scientific studies have been carried out on the geologic, geodetic and geophysical structure of the region due to the glacial melting. For example, Velicognia and Wahr [14] were estimated the acceleration of Greenland ice mass loss for the period from 2002 to 2006. They indicated that due to the accelerated rates of ice loss in southern Greenland, the rate of ice loss increased by 250 percent during the research period. In another study, Groh et al. [15] have been evaluated GRACE mass change time series for the Greenland ice sheet. They indicated that for the period from 2003-02 to 2013-12, estimated linear trends in ice mass vary between –252 Gt/yr and –274 Gt/yr.

The objective of this contribution is to investigate physical height changes over Greenland using the time series of GRACE mission data as well as to analyse and model the estimated physical height changes.

2. DATA AND METHOD

2.1 Research Area and Data Used

Greenland, the largest island of the world covers an area of around 2,166,086 km^2. Considering the spatial resolution of the GRACE (3º×3º on the equator) satellite mission data, Greenland was divided into 25 subareas consistent with the release 6 (RL06M v01) mass concentration (mascon) solutions provided by the Jet Propulsion Laboratory (JPL). The study area is illustrated in Figure 1. The application points (G1, G2,… G25) are the center points of those subareas.

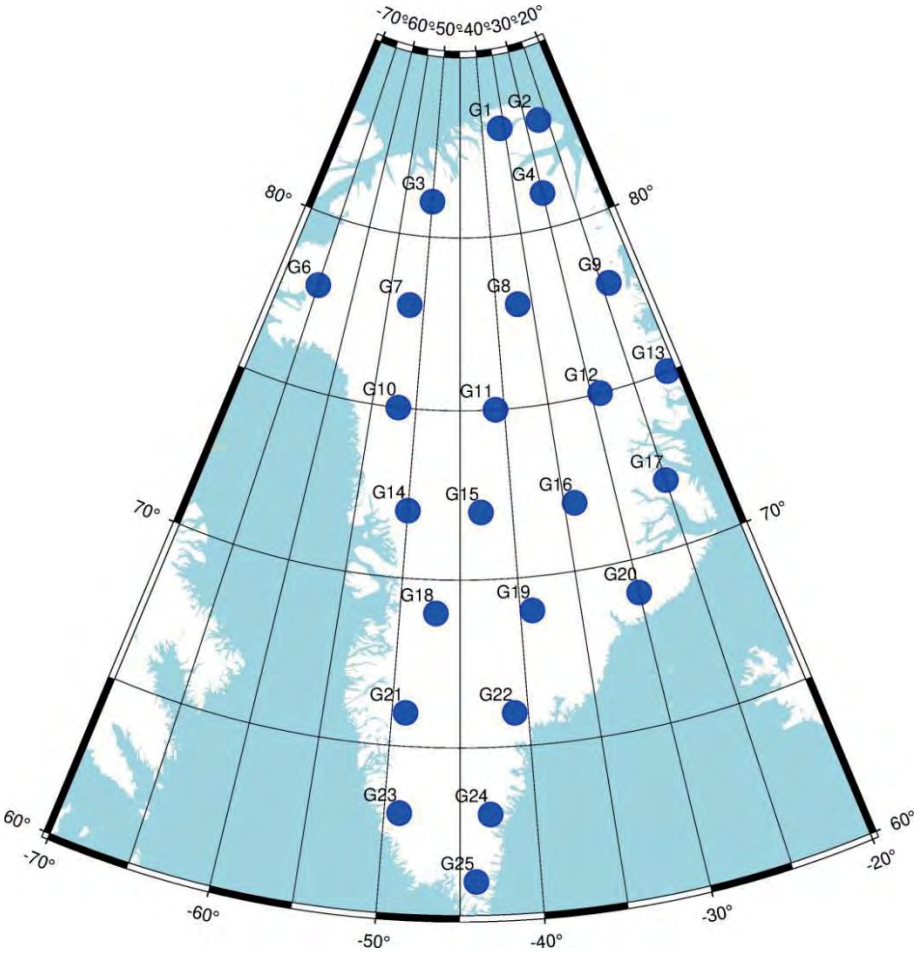

Figure 1. The study area Greenland, including 25 application points

The monthly release 6 (RL06) GRACE-based Global Geopotential Models (GGMs) with the decorrelation filter 3 (DDK3) developed by the Center of Space Research (CSR, Texas) were

used for the estimation of physical height changes. The CSR RL06 GRACE-based GGMs are convenient and without gaps for the period from January 2004 to December 2010. Therefore, the evaluation period is determined between 2004 and 2010 in the study. The GGMs were evaluated up to d/o 60 which corresponds to the spatial resolution of GRACE data. Load Love numbers [16] and the Preliminary Reference Earth Model (PREM) [17] were used to estimate Greenland's vertical displacements induced from surface mass loads.

2.2 Methodology

2.2.1 Computation of Physical Height Changes

The physical height changes ΔH obtained from temporal variations of geoid heights ΔN and surface displacements Δh were determined with the use of Eq. 1, Eq. 2 and Eq. 3 as follows [18]:

$$\Delta H = \Delta h - \Delta N \tag{1}$$

$$\Delta N_{(r,\varphi,\lambda)} = \frac{GM}{r\gamma}\sum_{l=2}^{l_{max}}\left(\frac{a}{r}\right)^{l}\sum_{m=0}^{l}P_{lm}(\sin\varphi)(\Delta C_{lm}^{T}\cos m\lambda + \Delta S_{lm}^{T}\sin m\lambda) \tag{2}$$

$$\Delta h = \frac{3a\rho_{\omega}}{\rho_{ave}}\sum_{l=0}^{l_{max}}\sum_{m=0}^{l}P_{lm}(\sin\varphi)\frac{h_l}{2l+1}(\Delta C_{lm}^{\sigma}\cos m\lambda + \Delta S_{lm}^{\sigma}\sin m\lambda) \tag{3}$$

where r, φ, and λ are geocentric radius, latitude, and longitude of the computation point, respectively, a is the semi-major axis of reference ellipsoid, GM is the product of the Newtonian gravitational constant G and the Earth's mass M, presents the normal gravity at the computation point, ΔC_{lm}^{T} and ΔS_{lm}^{T} are differences between the Stokes' coefficients of monthly GRACE-based GGMs and spherical harmonic coefficients of a selected reference GGM, P_{lm} are normalized Legendre functions of degree l and order m, and l_{max} is the applied maximum degree, h and k are the load Love numbers of degree l, ρ_{ave} is the Earth's average density and ρ_w is the water density. For the computation of ΔN and Δh values, IGiK–TVGMF (Instytut Geodezji i Kartografii-Temporal Variations of Gravity/Mass Functionals) software developed by Godah [19] was used.

2.2.2 Analysis and Modelling of Physical Height Changes

In the study, physical height changes were analysed and modeled using two different methods: the seasonal decomposition (SD) method, and the Principal Component Analysis/Empirical Orthogonal Function (PCA/EOF) method. Physical height changes are decomposed in the time domain by the SD method, on the other side physical height changes are analysed in spatio-temporal domain by the PCA/EOF method. The examined methods are expressed in short as follows:

In the seasonal decomposition method, physical height changes are separated into

$$\Delta H_i = T_i + S_i + E_i \tag{4}$$

where S is a seasonal component, T is a trend component and E is an unmodelled component. The sum of the seasonal and trend components gives the SD model of physical height changes ΔH^{SD}:

$$\Delta H^{\mathrm{SD}} = T + S \tag{5}$$

In the PCA/EOF method, the ΔH_i time series obtained over the study area (see Figure 1) are inserted to the matrix $\mathbf{\Delta H}$:

$$\mathbf{\Delta H} = \mathbf{T}\mathbf{P}^{\mathbf{T}} + \varepsilon \tag{6}$$

where $\mathbf{T}$ compose of PCA modes, $\mathbf{P}$ is the matrix of loading that describes the EOF loading patterns and indicates contributions of original variables to PCA modes. Lastly, ε is the unmodelled parts of ΔH time series. This method is based on finding $\mathbf{P}$ and $\mathbf{T}$ matrices. In this research, P and T were estimated using the Singular Value Decomposition (SVD) algorithm applied in the MATLAB software. The model of physical height changes $\Delta H^{\mathrm{PCA/EOF}}$ was obtained with the use of PCA/EOF method:

$$\Delta H^{\mathrm{PCA/EOF}} = \sum_{s=1}^{k} \mathrm{PCA}_s \cdot \mathrm{EOF}_s \tag{7}$$

where k presents the number of PCA modes and EOF loading patterns essential for the reflection of the significant signal of ΔH.

3. RESULTS AND DISCUSSION

3.1 Temporal Variations of Physical Height Changes

Physical height changes estimated with the use of Eq. 1, Eq. 2 and Eq. 3 are demonstrated in Figure 2. The figure indicates that minimum values are observed in February–April and maximum values are observed in August–October. It also shows that the separation between values at different epoch (e.g. March 2004 and September 2010) reach up to 60 mm in the subarea 22. It should be mentioned that the temporal variations of physical height changes increase towards South Greenland.

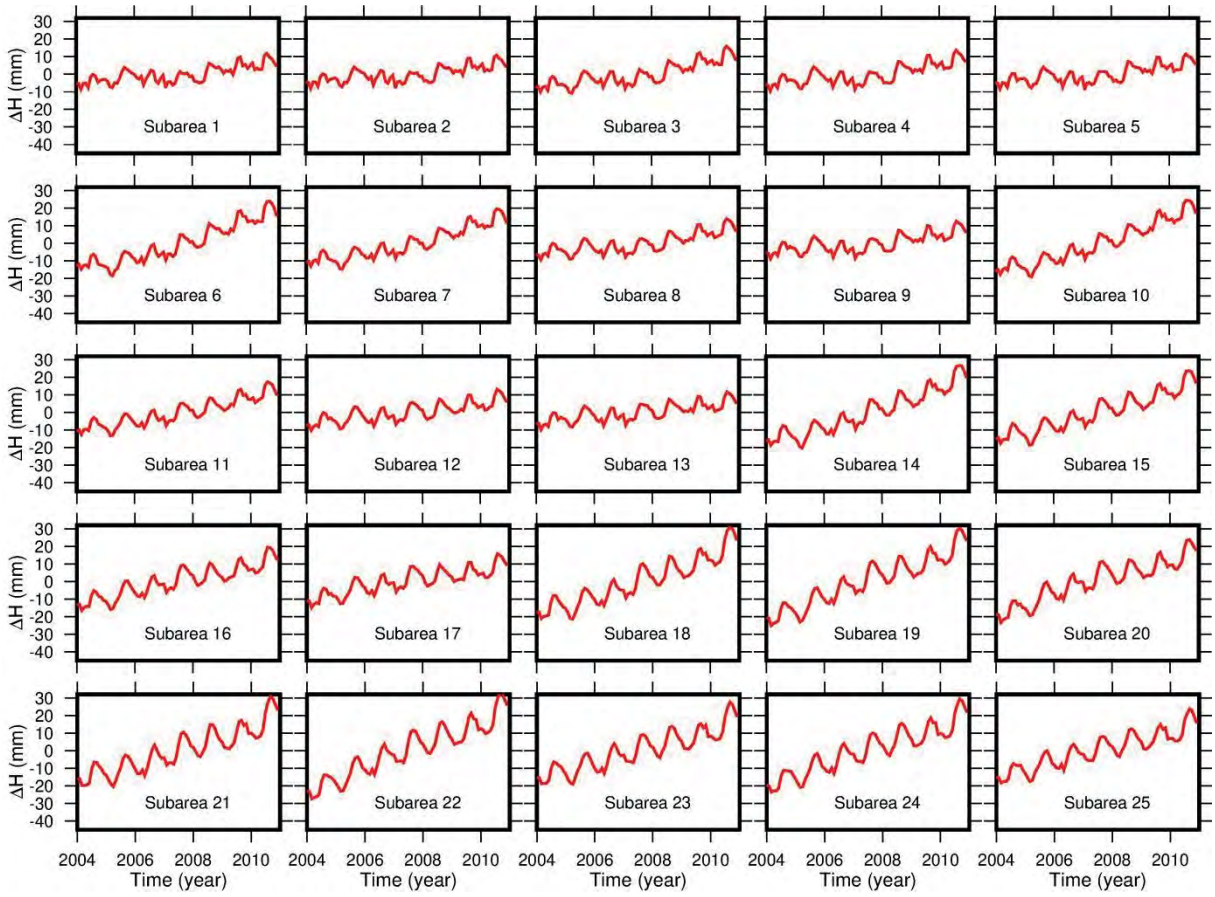

Figure 2. Time series of physical height changes ΔH over Greenland

3.2 Analysis and Modelling of Physical Height Changes

Physical height changes have been modelled and decomposed into the trend and seasonal components using the seasonal decomposition method. These components are shown in Figure 3. According to the figure, the trend components are quite effective especially in the subareas 6,10 and 14–25. Due to the mass variations, trend components show an increase of ~ 5.3 mm per year, totally 37 mm between 2004 and 2010.

The differences $\delta\Delta H^{SD}$ between the modelled ΔH^{SD} via the SD method and their corresponding ΔH data are demonstrated in Figure 4. According to the figure, the ΔH^{SD} models are compatible with their ΔH data. The differences $\delta\Delta H^{SD}$ are ranging from -4.7 mm to 6.7 mm.

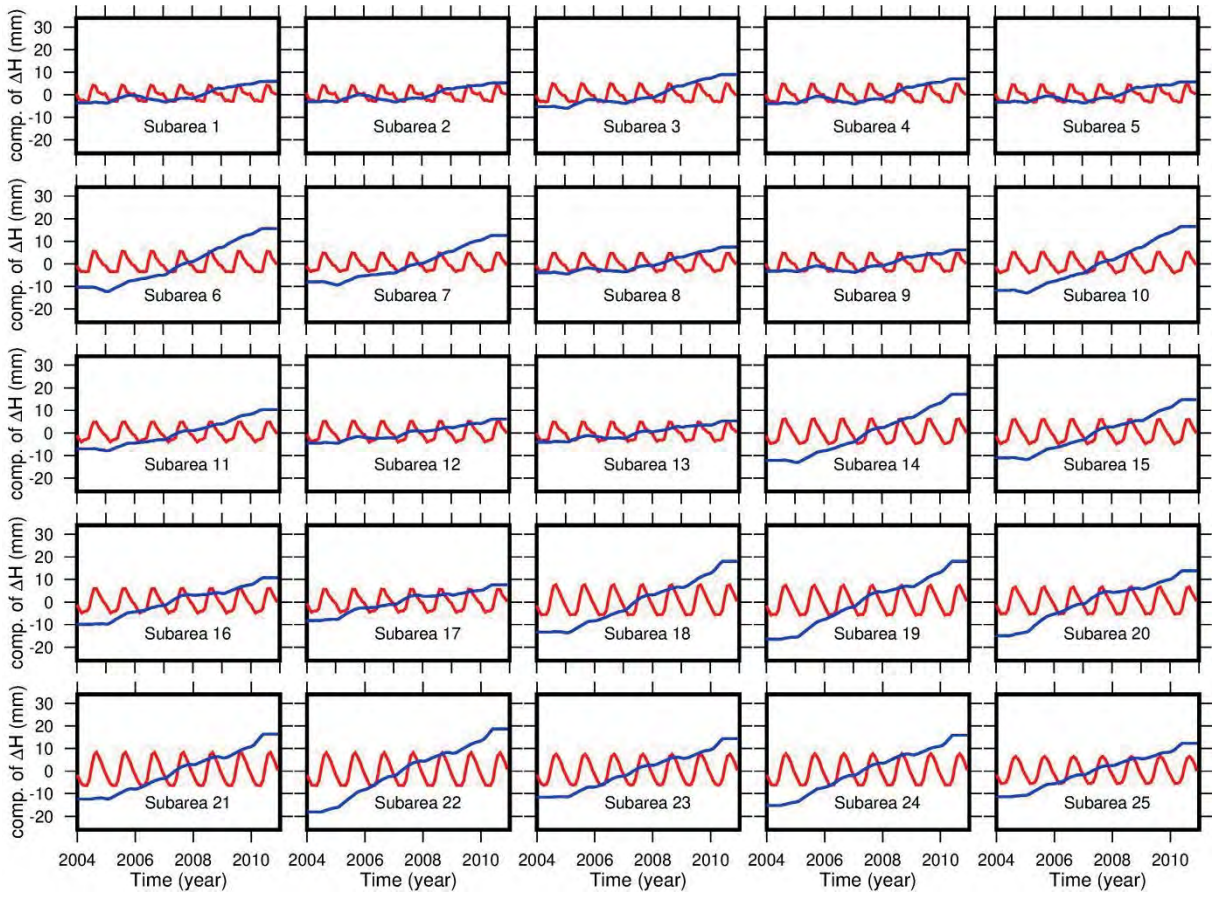

Figure 3. Time series of physical height changes and their seasonal *S* and trend *T* components [*S* (red line), *T* (blue line)]

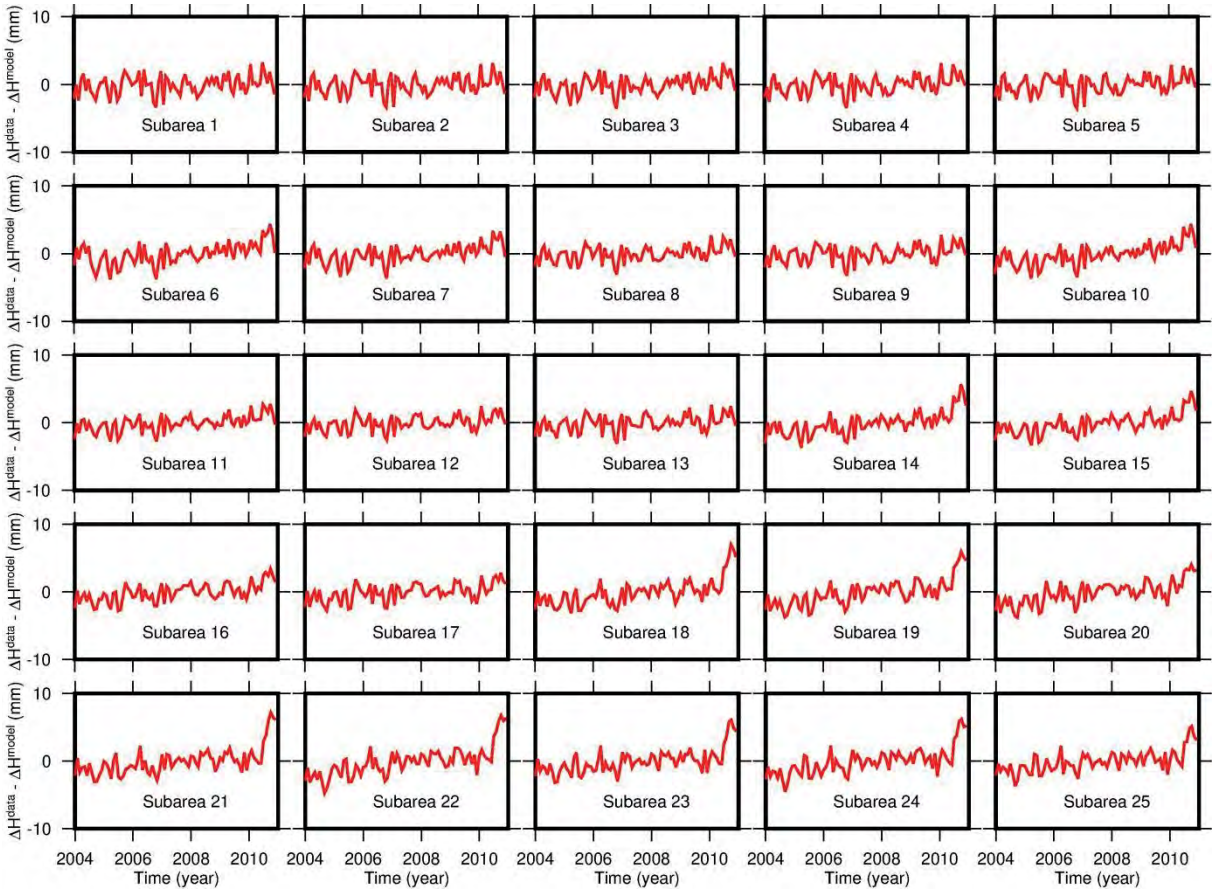

Figure 4. Differences $\delta\Delta H^{SD}$ between ΔH data and their corresponding ΔH^{SD} models

Physical height changes have been modelled and analysed using the PCA/EOF method as well. The percentages of the total variance of ΔH reflected by PCAs/EOFs are illustrated in Figure 5. It can be seen that the sum of the first two variances is 98.3% which means they reflect almost all ΔH signal. The time series of all four principal components are depicted in Figure 6. This figure indicates that a remarkable part of the ΔH signals can be estimated from the first PCA which shows a similar seasonal pattern to physical height changes. The second PCA was also utilized for the modeling of physical height changes. It shows a distinct horizontal character and it doesn't reflect the trend as much as the first PCA. The differences $\delta\Delta H^{PCA/EOF}$ between the modelled $\Delta H^{PCA/EOF}$ via the PCA/EOF method and their corresponding ΔH data are demonstrated in Figure 7. The inspection of this figure exhibits that the modelled $\Delta H^{PCA/EOF}$ and their corresponding data don't coincide with each other, especially towards the south subareas. The differences between minimum and maximum values can reach up to 67 mm in the subarea 22.

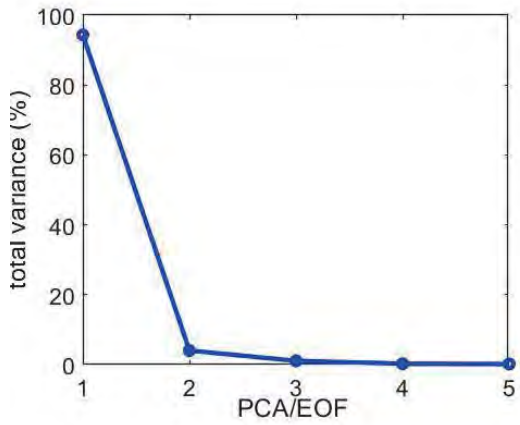

Figure 5. The percentages of the total variance of ΔH reflected by PCAs/EOFs

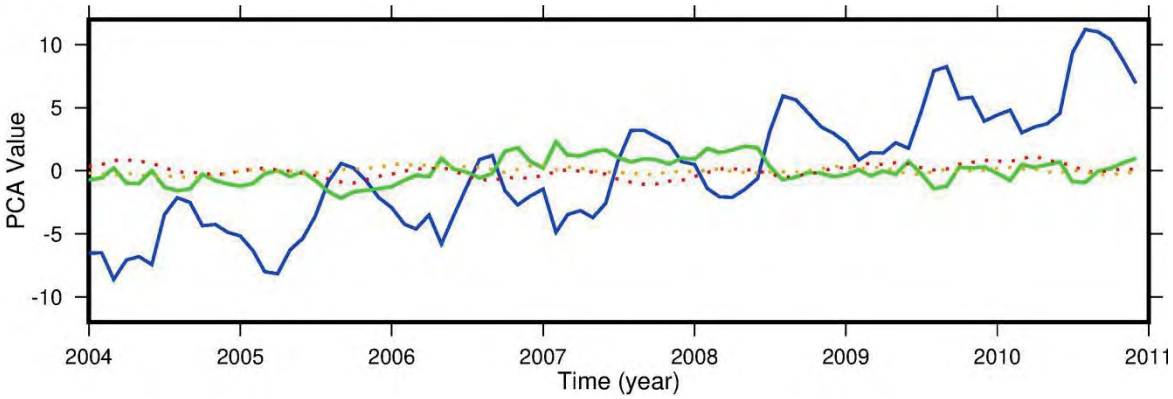

Figure 6. Time series of principal components [PCA1 (blue line), PCA2 (green line), PCA3 (red line), PCA4 (orange line)]

The statistical results of the $\delta\Delta H^{SD}$ and $\delta\Delta H^{PCA/EOF}$ are given in Table 1. It has been observed that $\delta\Delta H^{PCA/EOF}$ gives higher standard deviations than $\delta\Delta H^{SD}$ in all subareas. It may be concluded that the SD is a more suitable analysis method for the study area.

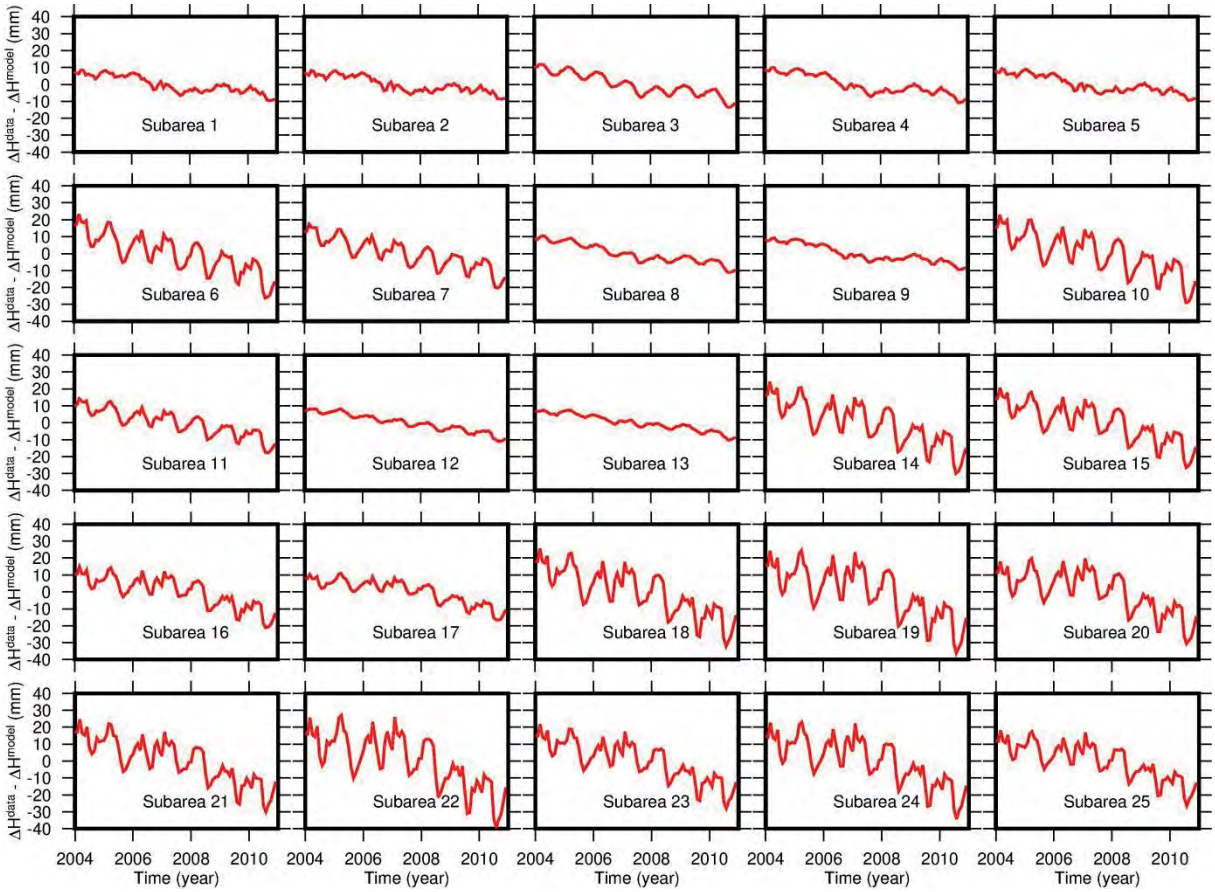

Figure 7. Differences $\delta\Delta H^{\mathrm{PCA/EOF}}$ between ΔH data and their corresponding $\Delta H^{\mathrm{PCA/EOF}}$ models

Table 1: Statistics of the differences [unit: mm] between (1) ΔH and ΔH^{SD} and (2) ΔH and $\Delta H^{PCA/EOF}$

	ΔH - ΔH^{SD}				ΔH - $\Delta H^{PCA/EOF}$			
Subareas	**min**	**max**	**mean**	**std.**	**min**	**max**	**mean**	**std.**
Subarea1	-3.3	3.2	0	1.4	-9.6	8.5	0	5.0
Subarea2	-3.3	3.1	0	1.4	-8.7	8.2	0	4.7
Subarea3	-3.6	3.1	0	1.3	-13.6	11.8	0	6.5
Subarea4	-3.5	3.1	0	1.3	-10.7	10	0	5.7
Subarea5	-3.5	2.9	0	1.3	-9.5	9.2	0	5.1
Subarea6	-3.8	4.3	0	1.6	-26.3	23.3	0	11.2
Subarea7	-3.7	3.3	0	1.3	-20.3	17.3	0	8.8
Subarea8	-3.1	2.7	0	1.1	-11.0	10.5	0	5.6
Subarea9	-3.3	2.7	0	1.2	-9.5	9.2	0	5.2
Subarea10	-3.7	4.3	0	1.5	-28.9	22.7	0	11.9
Subarea11	-2.7	2.8	0	1.2	-17.8	14.2	0	7.6
Subarea12	-2.5	2.4	0	1.1	-11.0	8.2	0	5.2
Subarea13	-3.1	2.6	0	1.2	-10.3	7.4	0	4.8
Subarea14	-3.7	5.6	0	1.7	-29.9	24.0	0	12.5
Subarea15	-3.3	4.6	0	1.5	-26.4	20.6	0	11.1
Subarea16	-2.8	3.4	0	1.3	-21.2	14.9	0	9.0
Subarea17	-2.8	2.8	0	1.3	-16.7	10.9	0	7.1
Subarea18	-3.1	7.0	0	1.9	-32.1	25.6	0	13.5
Subarea19	-3.7	5.9	0	1.9	-36.1	24.5	0	14.7
Subarea20	-3.8	4.0	0	1.7	-30.6	19.7	0	12.3
Subarea21	-3.1	7.1	0	2.0	-30.0	24.5	0	12.7
Subarea22	-4.7	6.7	0	2.2	-39.6	27.0	0	15.7
Subarea23	-3.2	6.1	0	1.8	-28.0	21.6	0	11.6
Subarea24	-4.5	6.2	0	1.9	-34.3	22.9	0	13.5
Subarea25	-3.7	5.1	0	1.6	-26.4	18.0	0	10.5

4. CONCLUSION

In this contribution, for the estimation, modeling, and analysis of the physical height changes, the study area Greenland has been divided into 25 subareas considering the JPL mascons. The DDK3 filtered CSR GGMs were used and truncated at d/o 60. Temporal variations of physical height changes were researched for the period between January 2004 and December 2010. In this period, the amplitude of the physical height changes can reach up to 60 mm and the values increases towards southern Greenland due to the increasing mass variations. The seasonal patterns are seen in the time series and the minimum values observed in spring and maximum values in autumn. The ΔH^{SD} models are consistent with corresponding ΔH data. Generally, trend components show an increase of 37 mm during the period. The differences $\delta\Delta H^{SD}$ can reach up to 12 mm over the region. The $\delta\Delta H^{SD}$ has fewer standard deviations than $\delta\Delta H^{PCA/EOF}$. Hence, the SD has been proposed as a more convenient method for modelling and analysis of the physical height changes in areas where mass variations are intense as in this study.

All in all, GRACE provides essential data for estimating temporal variations of physical height changes. In the future, the GRACE-FO mission which is the continuation of the GRACE project can play a crucial role for the next new generation dynamic leveling networks [20].

ACKNOWLEDGEMENT

The authors are thankful to the International Centre for Global Earth Models (ICGEM; http://icgem.gfz-potsdam.de/home) for providing the GFZ release 6 GRACE-based GGMs.

REFERENCES

1. Foroughi I., Vaníček P., Kingdon R.W., Goli M., Sheng M., Afrsteh Y., Novák P., Santos M. C., Sub-centimetre geoid. Journal of Geodesy, 2019, 92. 0949-7714.

2. Elaksher A., Kamtchang F., Wegmann C., Guerrero A., Assessing the quality of GEOID12B model through field surveys. Journal of Applied Geodesy,2018, 12(1), pp. 1-13.

3. Pa'suya M.F., Din A.H.M., Amin Z.M., Rusli N., Othman A.H., Accuracy Assessment of TanDEM-X DEM and Global Geopotential Models for Geoid Modeling in the Southern Region of Peninsular Malaysia. In: Saian R., Abbas M. (eds) Proceedings of the Second International Conference on the Future of ASEAN (ICoFA) 2017 – Volume 2. Springer, Singapore.

4. Godah W., Szelachowska M., Krynski J., Application of the PCA/EOF method for the analysis and modelling of temporal variations of geoid heights over Poland. Acta Geodaetica et Geophysica, 2018, 53 (1), 93–105.

5. Godah W., Szelachowska M., Zeray Öztürk E., and Krynski J., On the contribution of physical height changes estimated with the use of GRACE satellite mission data to the modernization of a national vertical system. In 2018 AGU Fall Meeting Abstracts.

6. Zeray Öztürk E., Godah W., Abbak R.A., Estimation of Physical Height Changes from GRACE Satellite Mission Data over Turkey. Acta Geodaetica and Geophysica (under review).

7. Sarmiento, C. J. S., Rizos, C., Roberts, C., Time-variable satellite gravity models application for the development of an archipelagic geoid-based height system. In Signal Processing & Its Applications (CSPA), 2018 IEEE 14th International Colloquium on (pp. 203-208).

8. Rangelova E., A dynamic geoid model for Canada, Ph.D Thesis, University of Calgary, Department of Geomatics Engineering, Report No. 20261., 2007.

9. Rangelova E., Sideris M.G., Contributions of terrestrial and GRACE data to the study of the secular geoid changes in North America. Journal of Geodynamics, 2008, 46(3):131–143.

10. Tapley B.D., Bettadpur S., Watkins M., Reigber C., The gravity recovery and climate experiment: mission overview and early results. Geophysical Research Letters, 2004, 31:L09607.

11. van Dam, T., Wahr J., Lavallée D., A comparison of annual vertical crustal displacements from GPS and Gravity Recovery and Climate Experiment (GRACE) over Europe. Journal of Geophysical Research: Solid Earth, 2007,112: B03404.

12. Tan W., Dongb D., Chena J., Wua B., Analysis of systematic differences from GPS measured and GRACE-modeled deformation in Central Valley, California. Advances in Space Research, 2016, 57(1): 19–29.

13. Koch A., Sanjuan J., Gohlke M., Mahrdt C., Brause N., Braxmaier C., Heinzel G., Line of sight calibration for the laser ranging interferometer on-board the GRACE Follow-On mission: on-ground experimental validation. Optics express, 2018, 26(20), 25892-25908.

14. Velicogna I., Wahr J., Acceleration of Greenland ice mass loss in spring 2004. Nature, 2006, 443(7109), 329.

15. Groh A., Horwath M., Horvath A., Meister R., Sørensen L. S., Barletta V. R., ..., Klees R., Evaluating GRACE Mass Change Time Series for the Antarctic and Greenland Ice Sheet—Methods and Results. Geosciences, 2019, 9(10), 415.

16. Wang H., Xiang L., Jia L., Jiang L., Wang Z., Hu B., Gao P., Load Love numbers and Green's functions for elastic Earth models PREM, iasp91, ak135, and modified models with refined crustal structure from Crust 2.0. Computers& Geosciences, 2012, 49:190–199.

17. Dziewonski A.M., Anderson D.L., Preliminary reference Earth model. Physics of the Earth and Planetary Interiors, 1981, 25:297–356.

18. Torge W., Müller J., Geodesy. Walter de Gruyter, 2012.

19. Godah W., IGiK–TVGMF: A MATLAB package for computing and analysing temporal variations of gravity/mass functionals from GRACE satellite based global geopotential models. Computers & Geosciences, 2019, 123:47–58.

20. Godah W., Szelachowska M., and Krynski J. The need for replacing static orthometric/normal heights with dynamic orthometric/normal heights. Journal of Geodesy (under review).

Analyzing the Interpolation Techniques by Computing the Height Transformation Surfaces Using GPS/Leveling Data

Onur Karaca[1], Bihter Erol[2]

[1] Istanbul Technical University, Geomatics Engineering Department, 34469 Ayazaga, Istanbul / Turkey, (onurkaraca_1903@hotmail.com)

[2] Istanbul Technical University, Geomatics Engineering Department, 34469 Ayazaga, Istanbul / Turkey, (bihter@itu.edu.tr)

ABSTRACT

The orthometric heights, which also play important role in many fields such as engineering surveying, flood management, coastal research, navigation, management of water sources, and risk analysis for earthquakes, etc., can be obtained by using the connection between geoid undulation and ellipsoidal height.

Within the scope of this study, local geoid models are determined by using different interpolation techniques in order to obtain geoid height information with high accuracy that directly affects the precision of transformed orthometric height through GNSS. Although there is no regional geoid model within 2-3 cm accuracy in Turkey yet, local GPS/Leveling surfaces (also called as "local geoid models") are computed in limited areas using sufficiently dense GPS/Leveling benchmarks.

In the content of research, the cross validation results belonging to the 12 interpolation techniques are investigated in order to test the consistence of computed grid values within themselves. In the light of obtained results, it can be stated that linear interpolation results for all of the gridding methods except minimum curvature, polynomial regression (simple planar surface, bilinear saddle) and moving average reveal the best performance with a standard deviation of 5.5 cm and 6.0 cm. The performances of the determined grids are examined at the reference benchmarks and test benchmarks, respectively by employing linear, nearest neighbor, cubic and spline interpolation methods. As a linear interpolation result of these testing processes of grids, biharmonic spline interpolation method draws the attention as the most accurate method, whose standard deviation is 1.2 cm at the reference benchmarks and 3.2 cm at test benchmarks. This results show that generated geoid model data can be used in all kind of engineering projects that require height information within cm accuracy.

In the evaluation of nearest neighbor interpolation at test points, the grid data that is obtained through natural neighbor method gives the most accurate result while moving average method gives the worst result. When considering cubic interpolation results, this can be said that triangulation with linear interpolation gives the best result; on the contrary, moving average gives the worst result. In the evaluation of spline interpolation results at test points, point Kriging gives the best results. On the other hand, moving average has the worst standard deviation value. This results show that generated geoid model data can be used in all kind of engineering projects that require height information within cm accuracy.

Keywords: *Local geoid modeling*; *height transformation*; *surface interpolation*; *GPS/Leveling*; *orthometric heights; geoid undulations*

1. INTRODUCTION

Within the scope of this study, local geoid models for Istanbul are employed via different interpolation algorithms and compared with each other since applied interpolation method is important in addition to surface type, sample size and design, data quality and density when performing a model (Li and Heap, 2008).

When realizing the study; 1204 Istanbul GPS Leveling Network 2005 (IGNA 2005) benchmark data, which is established to realize the height systems as geodetic infrastructure of Istanbul, and orthometric heights in regional vertical datum are operated for numerical evaluations.

In the study, firstly, blunders are detected visually and statistically and omitted from the data set. Then, data is gridded by using 7 interpolation methods which are stated below:

- Inverse Distance Weighting (IDW)
- Nearest Neighbor
- Triangulation with Linear Interpolation
- Local Polynomial
  - First Order Polynomial
  - Second Order Polynomial
  - Third Order Polynomial
- Radial Basis Function
  - Inverse Multiquadratic
  - Multilog
  - Multiquadratic
  - Natural Cubic Spline
  - Thin Plate Spline
- Biharmonic Spline Interpolation
- Kriging
  - Point Kriging
  - Block Kriging

The observed geoid undulations ($N = h - H$) depending on the GPS ellipsoidal heights (h) and the orthometric heights (H) of the benchmarks are modeled as independent variable. The rest

of the benchmarks are employed in order to test the calculated models hence obtaining more objective and realistic measures on the performances of the calculated surface models.

In order to evaluate the accuracies of geoid models objectively, gridded data with 1151 points are interpolated with linear, nearest, cubic and spline interpolation methods by using 50 test points.

The result of the study reveals that local GPS/leveling geoids can be the sensible solution for short-term applications that need high accuracy (< 5 cm). Besides, accuracies of the surface interpolation methods are compared with each other according to strength and weakness of their mathematical backgrounds.

2. SURFACE INTERPOLATION METHODS

Due to limitations of money, time, geological conditions etc., this is hard to obtain spatial continuous data at every point in working area. Therefore, spatial interpolation techniques, which can be described as an assumption of obtaining approximate values at unsampled locations for any geographic point by using known sample data, are required and performed (Robeson, 1997).

Spatial interpolation has wide range application area such as climate change investigation, crustal deformation monitoring, mine exploration, classification of soil properties, population density modelling, digital terrain modal (DTM) generation and use, chemical concentration modelling, soil Ph or moisture estimation and so on (Li and Heap, 2008).

Spatial interpolation methods are grouped into various classes in literature that are "point – areal", "Point Wise – Global Wise - Piece Wise", "Non Geostatistical – Geostatistical – Combined" , "Local Neighborhood – Geostatistical – Variational Approaches". In this study, interpolation methods are described as Deterministic and Geostatistical methods.

Due to the fact that most of the methods have same results for dense data, the choice of the method becomes vital for data with low density. This has to be said that interpolation methods give better results when the data get dense. Discontinuous surfaces, use of various data types in the sample application and high data noise cause poor results in interpolation. The sampling in

working area, which can be regular, random, stratified random, cluster, transect and contour type, also affect the performance of the interpolation (Li and Heap, 2008).

2.1. Inverse Distance Weighting (IDW) Method

In this one of the simplest and practical methods, the value at an unsampled point is evaluated via weighted average of sampled point within a certain cut-off distance. The Figure and equation of IDW are given below:

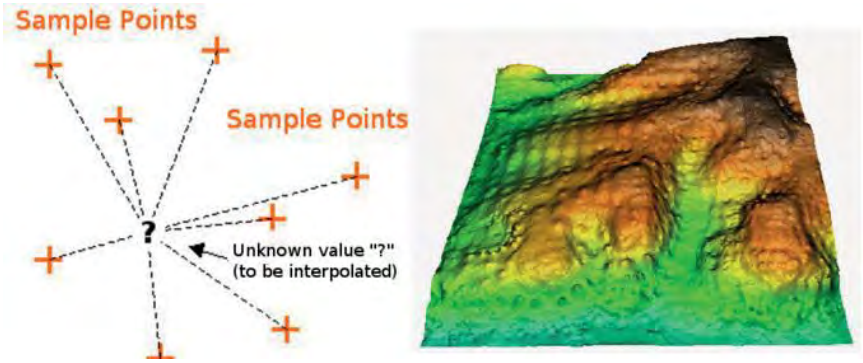

Figure 1: *Inverse distance weighting interpolation* (Sutton et al., 2009)

The equation of IDW is: (Li and Heap, 2008):

$$N_0 = \frac{\sum_{i=1}^{m} N_i P_i}{\sum_{i=1}^{m} P_i}, \qquad P_i = \frac{1}{{d_i}^k}, \qquad d_i = \sqrt{(x_i - x_0)^2 + (y_i - y_0)^2} \qquad (1)$$

where N_0 is the geoid height at the new point to be estimated, N_i is the geoid height at the new point, k is the power parameter, m is the number of sampled points used, d_i is the distance between the reference and interpolation point (x_0, x_i).

This exact interpolation method effective with dense data but does not allow extrapolation. Moreover, it tends to generate bull's eye patterns. Although interpolated values between data points lie within the range of the data point values, IDW method may not approximate valleys and peaks well (de Smith et al., 2015).

The main factor that affects the accuracy of this method is identified as power parameter "k" and there is inverse proportion with power parameter and weight for distance data. Likewise, the distance between the reference point and interpolation point, which will be predicted, decreases if weight increases. The relevant figure (see Figure 2) that illustrates the relationship between distance and relative weight is given below.

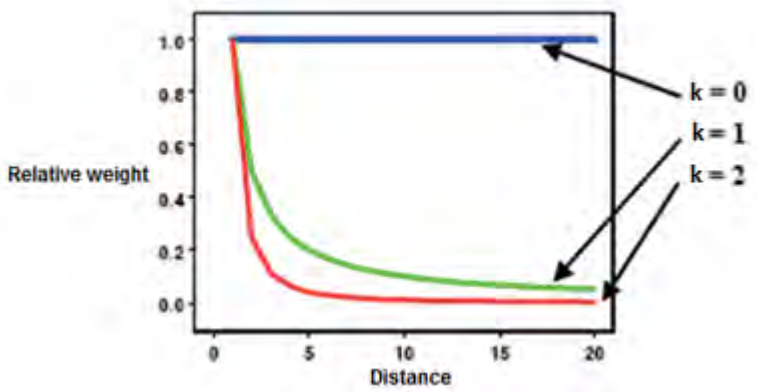

Figure 2: *The graphics on the effect of distance on relative weight (URL-2)*

2.2. Nearest Neighborhood (NN) Method

In Nearest neighbor method, geoid heights belong to unsampled points are acquired from nearest sampled points by using bisector between sampled points (n) like Voronoi (Thiessen) polygons (V_i, i=1,2,3,n) that are established by lining between neighbor points. Each sample has one polygon and samples are located in the center of these polygons (see Figure 3).

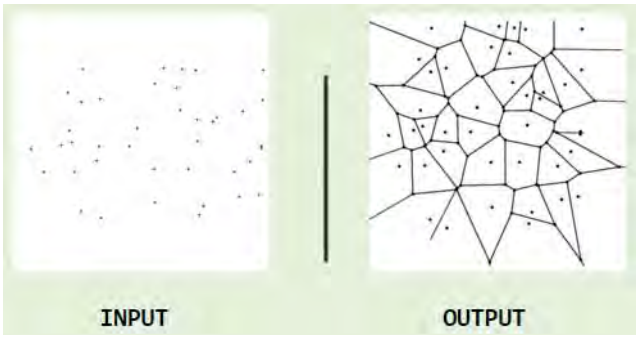

Figure 3: *Voronoi diagram (Skiena, 2008)*

Each point and its nearest sample points have the same value. In another words, whole points have same value inside the same polygon. If surface is not regular and there is no homogenous sampling, this method can be used (Li and Heap, 2008; URL-1).

The lines that are used to establish Thiessen polygons are the sides of Delaunay triangles. In Delaunay triangle, a circle is formed along its three corners that never involve another sample points. There are several methods to form polygons like pycnophylactic interpolation which was developed by Waldo Tobler. In this technique, the volume of the data is preserved, but moved inside the area in order to generate a continuous surface (URL-1).

The algorithm of this exact interpolation method runs fast and hence suitable for interpolation over large areas. This method is useful especially for completing datasets (e.g. repairing grids with missing values). Nevertheless, it does not allow data extrapolation process.

2.3 Triangulation with Linear Interpolation Method

Triangulation with linear interpolation bases on Delaunay triangulation procedure and thus requires a medium-large number of data point to generate acceptable results (de Smith et al., 2015). If the data is distributed homogenously over the study area, this exact and rapid interpolation method gives better results.
In this exact interpolation method, triangles are generated by drawing lines between data points and they never intersect each other (URL-3).

The equations of the method are provided below (Soycan and Soycan, 2003);

$$N_1 = a_0 + a_1\varphi_1 + a_2\lambda_1$$

$$N_2 = a_0 + a_1\varphi_2 + a_2\lambda_2 \,, \varphi_1, \lambda_1 = 0, \qquad \underline{N} = \begin{vmatrix} N_1 \\ N_2 \\ N_3 \end{vmatrix} = \begin{vmatrix} 1 & 0 & 0 \\ 1 & \varphi_2 & \lambda_2 \\ 1 & \varphi_3 & \lambda_3 \end{vmatrix} \begin{vmatrix} a_0 \\ a_1 \\ a_2 \end{vmatrix} \qquad (2)$$

$$N_3 = a_0 + a_1\varphi_3 + a_2\lambda_3$$

where a_0, a_1, a_2 coefficients are estimated from following equations;

$a_0 = N_1$

$$a_1 = \frac{[(\lambda_2 - \lambda_3)N_1 + \lambda_3 N_2 - \lambda_2 N_3]}{(\varphi_2\lambda_3 + \varphi_3\lambda_2)} \quad (3a)$$

$$a_2 = \frac{[(\varphi_3 - \varphi_2)N_1 + \varphi_3 N_2 - \varphi_2 N_3]}{(\varphi_2\lambda_3 + \varphi_3\lambda_2)} \quad (3b)$$

2.4 Local Polynomial Method

In this fast and non-exact interpolation method, which is most applicable to locally smooth dataset, samples are located equally on a grid by using weighted least squares (de Smith et al., 2015). Similarly, the data values, within the searching neighborhood, are distributed normally. Various degrees of polynomials (first, second, third, etc.) are used within a defined neighborhood, moreover; depending on the degree of polynomial it smooths the model surfaces. This method gives more realistic results and shows better characteristics in case the data is locally smooth.

The single order local polynomial performs a plane through the data, the second order local polynomial performs a surface with a bend while third order local polynomial performs two bends. The local polynomial equations based on polynomial degree are given below;

$$\begin{aligned} &1: N(\varphi,\lambda) = a + b\varphi + c\lambda \\ &2: N(\varphi,\lambda) = a + b\varphi + c\lambda + d\varphi\lambda + e\varphi^2 + f\lambda^2 \\ &3: N(\varphi,\lambda) = a + b\varphi + c\lambda + d\varphi\lambda + e\varphi^2 + f\lambda^2 + g\varphi^2\lambda + \\ &\qquad h\varphi\lambda^2 + i\varphi^3 + j\lambda^3 \end{aligned} \quad (4)$$

The accuracy of surface is higher when the multiple planes are described. The computation speed is independent from data size; therefore, this method can be used for large data. If the data is getting closer to the grid nodes, the higher weight is obtained.

Depending on the degree of polynomial, model surfaces are smoothed. This method gives more realistic results and shows better characteristics in case the data is locally smooth.

2.5 Radial Basis Function (RBF) Method

RBF method that is a special case of spline and identified as a distance from the location of each points; uses a range of kernel functions likewise variogram models in Kriging. Nevertheless, in comparison with Kriging method, there are no additional assumptions regarding the statistical properties of the input data in RBF method. The flexibility of the model can be increased with additional parameters (de Smith et al., 2015).

In this method, reverse cone over each location is generated and smooth surfaces from a large dataset are obtained. When the surface has intense changes in short distance, this interpolation algorithm does not provide suitable results (URL-2 and URL-3). The equations of the method and relevant figure (see Figure 4) are shown below.

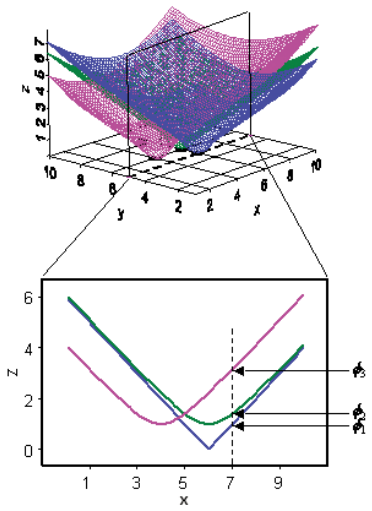

Figure 4: *Radial basis functions for different locations (URL-2)*

$$Zp = \sum_{i=1}^{n} Pi\phi(ri) + m \qquad (5)$$

where z_p is z value at point, P_i is weight for i^{th} point, $\phi(r_i)$ is radial basis function for radius r_i and m is the bias or offset value.

Radial basis function method looks like Kriging since they both perform an accurate data.

The types of radial basis function (RBF) are listed below;

- Inverse Multiquadratic
- Multilog
- Multiquadratic
- Natural Cubic Spline
- Thin Plate Spline

2.6 Biharmonic Spline Method

This flexible but relatively unaffected and unsteady interpolation method is a linear combination of Green function that is located at the center of the data. This interpolation method, whose running speed is fast, is an exact interpolator and allows smoothing. Biharmonic spline interpolation is available as a district procedure and can be used in tandem with other methods. (de Smith et al., 2015).

Slope measurements can be used when the accuracy of slopes are higher than heights. Another benefit of this method is that the degree of Green functions can be less than the number of data. Therefore, interpolating surface can be independent from inaccurate sample points. The degree of this differentiation can be high, but not useful if it is more than 4. In this thesis, this method is used as two dimensional. The equation of the method is described as follow (Sandwell, 1987);

$$\nabla^4 f(x) = \sum_{j=i}^{n} a_j \delta(x - x_j)\,, \quad w(x_i) = w_i \tag{6}$$

where n is the number of data points in m dimensions, ∇^4 is the biharmonic operator and x is the position in m dimensions.

2.7 Kriging Method

Kriging, which is one of the most common interpolation methods, is an exact, local and stochastic method and estimates the values at unsampled points by using sampled points at surrounding locations. Kriging is one of the main techniques of geostatistical interpolation

(Isaaks and Srivastava, 1989). Geostatistics is a branch of statistic which is used to perform continuous surface by estimating and evaluating the spatial attributes of sampled points.

This method is based on the statistical illustration of the best linear unbiased estimate. In another word, the variance of the observations is minimized (best) and the true expected value of data is matched (unbiased) in Kriging method that is a linear estimator (URL-4). The processes of this method include exploratory statistical analysis of the data, variogram modelling that is a mathematically illustration of spatial variability of data, performing the surface, and exploring a variance surface arbitrarily. When there is a directional bias in the data or spatially correspond distance, Kriging is one of the most useful interpolation technique (URL-5).

In this technique, firstly, the variation on spatial data that is usually too complicate to be modelled mathematically with a simple function are defined and modeled as a stochastic surface or random field. The equation belongs to Kriging method is given below (URL-1);

$$Z(x) = m(x) + \varepsilon'(\mathrm{x}) + \varepsilon'' \qquad (7)$$

where $Z(x)$ is a random variable at x, $m(x)$ is a constructional component, $\varepsilon'(\mathrm{x})$ is auto-correlated residual from $m(x)$ and ε'' is random noise.

Point and block Kriging are two types of Kriging methods, and the value of the points are calculated via neighbor values in point Kriging while the mean value of the rectangular blocks that are located on the center of the grid nodes are estimated in block Kriging. The drift may not be applied, which is called as ordinary Kriging; or can be determined as linear or quadratic, which is referred as universal Kriging, in this method. Ordinary Kriging is a linear prediction considering stationary mean structure. In another words, the mean is constant within region of interest. However, universal Kriging is a linear prediction considering non-stationary mean structure which means linear or higher order trend in values of the data are fitted. The data can be predicted easier in ordinary Kriging. In contrast to ordinary Kriging, the universal Kriging method relies on more complicate predicting algorithm (URL-3).

When there is no nugget effect introduced into computations, this geostatistical method is stated as an exact interpolator. These are quite flexible range of methods due to the fact that they are based on variogram modeling and not easy to programing the computations. Extrapolation and

error prediction can be carried out in spite of slow computation speed. Size of the data does not influence the running speed significantly. (de Smith et al., 2015).

3. NUMERICAL TEST

After subtracting the blunders (3 points), which are detected visually and statistically, from the data set, the validations of the interpolation techniques are realized using 1201 GPS/leveling points which are between 40°30' N - 42°00' N latitudes, 27°30' E - 30°00' E longitudes. The 3D coordinates of the points are obtained through GPS observations in ITRF96 datum in addition to the orthometric heights from the adjustment of leveling observations. The accuracies of the ellipsoidal heights are 1.5 cm and the orthometric heights are 2.0 cm.

The data used in this study (IGNA) is provided by Istanbul Technical University Geodesy Division. The coordinates of IGNA 2005 data is obtained in ITRF96 datum and orthometric heights of the C order densification points are obtained in TUDKA99 (Turkey National Vertical Control Network Datum 1999) through adjustment of leveling observations in the network (Ayan et al., 2006).

In order to test the performance of the geoid model objectively; homogenously distributed 50 test points, which are equal to 50% of the entire GPS/Leveling data and represent topography well, are identified. While selecting the test points, it is also considered not to harm the distribution of reference benchmarks that contributes to calculation of grid models. The rest of the points after choosing test points are referred as geoid reference points (1151 points).

The distribution of the points on SRTM3 data, 1151 geoid control benchmarks (reference points) and 50 test points are illustrated in Figures 5, 6a, 6b respectively.

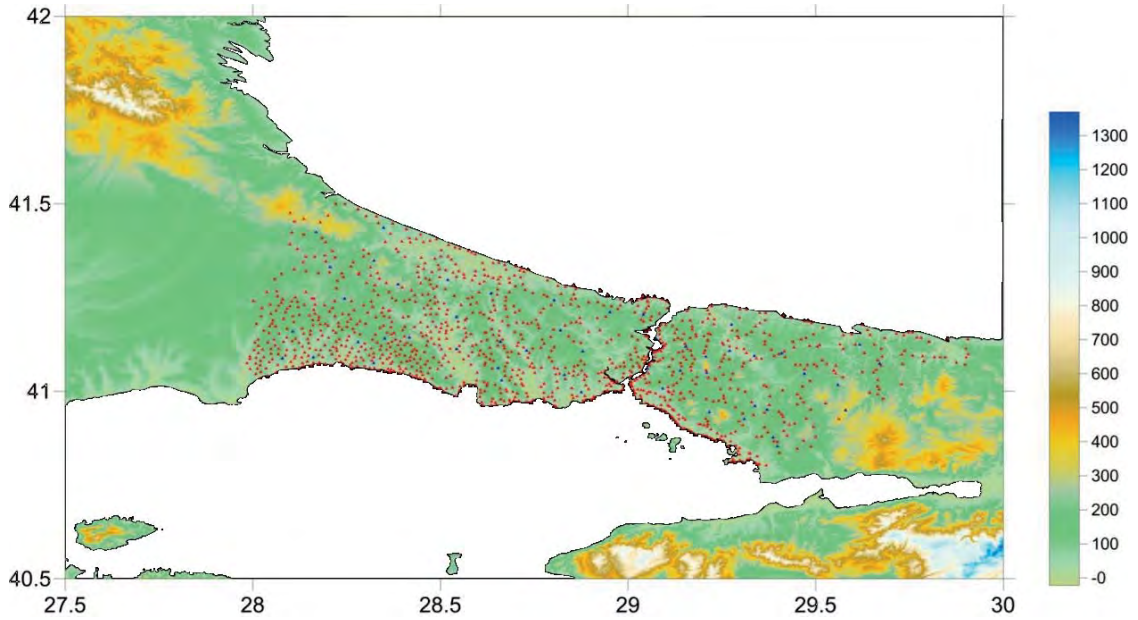

Figure 5: *Geoid reference points and test points on SRTM3 data* **(URL-6)**

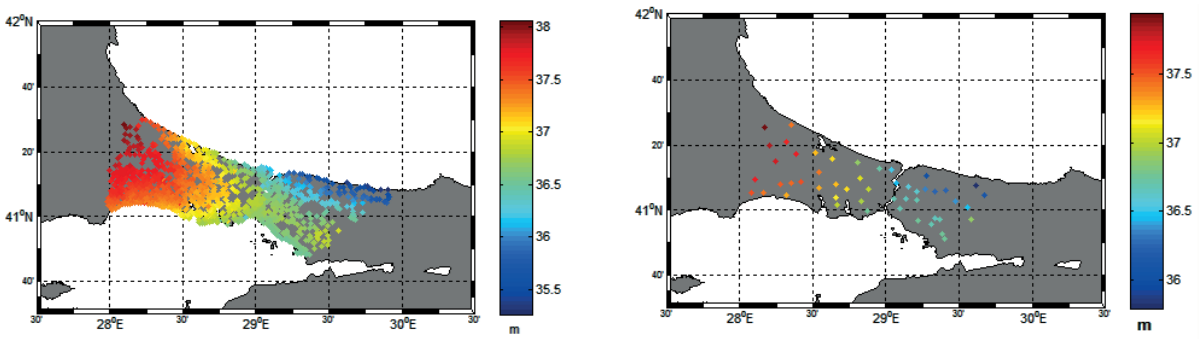

Figure 6: *the distribution of* – **a)** 1151 *Geoid control points* **b)** 50 *test points. The color bar shows the observed geoid heights at these points in meter*

In order to assess he performances of the interpolation techniques objectively that are used for geoid modeling, gridded data with 1151 points are interpolated with linear, nearest, cubic and spline interpolation methods by using 50 test points. The results of the interpolations are given statistically in Tables 1, 2, 3, 4 following:

Table 1: The statistics of linear interpolation results of geoid height residuals at geoid control points and test points

	(cm)	Min	Max	Mean	Std	Rmse
INVERSE DISTANCE to a POWER	Ref. Points	-42.0	28.7	0.0	3.9	3.9
	Test Points	-8.5	24.7	1.7	5.2	5.4
KRIGING	Ref. Points	-37.8	28.7	0.0	2.9	2.9
	Test Points	-6.8	9.5	0.2	3.1	3.1
NEAREST NEIGHBOR	Ref. Points	-50.8	32.6	-0.1	3.3	3.3
	Test Points	-7.8	7.3	0.2	3.3	3.3
RADIAL BASIS FUNCTION Thin Plate Spline	Ref. Points	-34.2	17.9	0.0	2.5	2.5
	Test Points	-6.6	8.8	0.1	3.1	3.1
TRIANGULATION WITH LINEAR INTERPOLATION	Ref. Points	-26.0	23.5	0.1	3.0	3.0
	Test Points	-6.6	10.0	0.4	3.1	3.1
LOCAL POLYNOMIAL 1. Order	Ref. Points	-45.2	37.6	2.0	5.5	5.9
	Test Points	-10.9	25.4	3.9	5.8	6.9
LOCAL POLYNOMIAL 2. Order	Ref. Points	-47.4	35.0	0.0	4.5	4.5
	Test Points	-8.4	13.2	0.4	4.1	4.1
LOCAL POLYNOMIAL 3. Order	Ref. Points	47.7	34.8	0.0	4.3	4.3
	Test Points	-7.7	12.6	0.3	3.9	3.9
BIHARMONIC SPLINE INTERPOLATION	Ref. Points	-10.8	10.3	0.0	1.2	1.2
	Test Points	-6.4	9.1	-0.1	3.2	3.2
TRIANGUALTION WITH LINEAR INTERPOLATION (Matlab)	Ref. Points	-18.2	13.3	0.1	1.8	1.8
	Test Points	-5.6	9.7	0.1	2.9	2.9

Table 2: Nearest interpolation results belong to different gridding methods

	(cm)	Min	Max	Mean	Std	Rmse
INVERSE DISTANCE to a POWER	Test Points	-12.3	28.6	1.7	6.1	6.3
POINT KRIGING	Test Points	-9.2	12.0	0.2	4.2	4.2
BLOCK KRIGING	Test Points	-8.8	13.7	0.8	4.2	4.3
NEAREST NEIGHBOR	Test Points	-15.8	10.1	0.1	5.1	5.1
RADIAL BASIS FUNCTION Thin Plate Spline	Test Points	-7.2	10.6	-0.1	4.3	4.3
TRIANGULATION WITH LINEAR INTERPOLATION	Test Points	-8.2	12.6	0.4	4.2	4.2
LOCAL POLYNOMIAL 1. Order	Test Points	-13.5	27.2	4.0	6.3	7.4
LOCAL POLYNOMIAL 2. Order	Test Points	-10.0	15.0	0.5	4.7	4.7
LOCAL POLYNOMIAL 3. Order	Test Points	-10.3	14.3	0.3	4.6	4.6
BIHARMONIC SPLINE INTERPOLATION	Test Points	-6.8	9.5	-0.3	3.5	3.5
TRIANGULATION WITH LINEAR INTERPOLATION (Matlab)	Test Points	-6.8	9.5	0.0	3.2	3.2

Table 3: Cubic interpolation results belong to different gridding methods

	(cm)	Min	Max	Mean	Std	Rmse
INVERSE DISTANCE to a POWER	Test Points	-8.3	24.5	1.6	5.2	5.4
POINT KRIGING	Test Points	-6.1	8.8	0.1	3.1	3.1
BLOCK KRIGING	Test Points	-6.3	10.9	0.7	3.2	3.2

Table 3 (continued): Cubic interpolation results belong to different gridding methods

	(cm)	Min	Max	Mean	Std	Rmse
NEAREST NEIGHBOR	Test Points	-9.8	8.0	-0.1	3.5	3.5
RADIAL BASIS FUNCTION Thin Plate Spline	Test Points	-8.3	11.0	-0.1	3.6	3.6
TRIANGULATION WITH LINEAR INTERPOLATION	Test Points	-13.9	114.2	4.7	21.0	21.5
LOCAL POLYNOMIAL 1. Order	Test Points	-11.0	25.7	3.8	5.8	6.9
LOCAL POLYNOMIAL 2. Order	Test Points	-8.1	13.2	0.3	4.2	4.2
LOCAL POLYNOMIAL 3. Order	Test Points	-8.0	12.3	0.2	3.9	3.9
BIHARMONIC SPLINE INTERPOLATION	Test Points	-6.4	9.5	-0.1	3.3	3.3
TRIANGULATION WITH LINEAR INTERPOLATION (Matlab)	Test Points	-5.6	9.7	0.1	3.0	3.0

Table 4: Spline interpolation results belong to different gridding methods

	(cm)	Min	Max	Mean	Std	Rmse
INVERSE DISTANCE to a POWER	Test Points	-8.3	24.5	1.6	5.2	5.4
POINT KRIGING	Test Points	-6.1	8.8	0.1	3.1	3.1
BLOCK KRIGING	Test Points	-6.3	10.9	0.7	3.2	3.2
NEAREST NEIGHBOR	Test Points	-9.8	8.0	-0.1	3.9	3.9

Table 4 (continued): Spline interpolation results belong to different gridding methods

RADIAL BASIS FUNCTION Thin Plate Spline	(cm)	**Min**	**Max**	**Mean**	**Std**	**Rmse**
	Test Points	-8.3	11.0	-0.1	3.6	3.6
TRIANGULATION WITH LINEAR INTERPOLATION	Test Points	-13.9	114.2	4.7	21.0	21.5
LOCAL POLYNOMIAL 1. Order	Test Points	-11.0	25.7	3.8	5.8	6.9
LOCAL POLYNOMIAL 2. Order	Test Points	-8.1	13.2	0.3	4.2	4.2
LOCAL POLYNOMIAL 3. Order	Test Points	-8.0	12.3	0.2	3.9	3.9
BIHARMONIC SPLINE INTERPOLATION	Test Points	-6.4	9.8	0.0	3.3	3.3

As we compare the applied interpolation methods, the following conclusions are drawn:

- This can be seen on Table 1 that, the gridded data performed by biharmonic spline interpolation has the best results for linear interpolation. Geoid undulation residuals at reference benchmarks vary between -10.8 cm and 10.3 cm, and standard deviation is 1.2 cm. The values at test benchmarks vary between -6.4 cm and 9.1 cm, and standard deviation at these benchmarks is 3.2 cm. Triangulation with linear interpolation, Radial Basis Function and Kriging methods also give targeted results.
- According to nearest interpolation results in Table 2, the gridded data computed by triangulation with linear interpolation gridding method (in Matlab) gives the most accurate results. Geoid undulation residuals at test benchmarks vary between -6.8 cm and 9.5 cm, and standard deviation is 3.2 cm.
- Considering the cubic interpolation results in Table 3, the gridded data performed by triangulation with linear interpolation in Matlab gives the most accurate result. Geoid undulation residuals at test benchmarks vary between -5.6 cm and 9.7 cm, and standard deviation is 3.0 cm.

- In the light of the results of Table 4, this can be seen that point Kriging gridding method has the highest accurate value for spline interpolation. Geoid undulation residuals at test benchmarks vary between -6.1 cm and 8.8 cm, and standard deviation is 3.1 cm for both methods.
- Triangulation with linear interpolation technique is computed during gridding process by using both Surfer and Matlab codes. The different triangulation geometry and using different reference points for estimation may cause standard deviation differences between the result of the evaluations that are done by Surfer and Matlab codes.

4. CONCLUSION

Within the scope of this study, several interpolation algorithms are used when performing GPS/Leveling surfaces in local area and the drawn conclusions reveal 2.9 cm absolute accuracy as the best for the models using Triangulation with Linear Interpolation method.

When considering from the viewpoint of geodesy discipline, the highly accurate geoid model is an essential part of geodetic infrastructure. Although the accuracy of Turkish National Geoid is not within desirable range, local GPS/Leveling geoids are computed by using more dense data in transformation of ellipsoidal heights into orthometric heights in regional vertical datum. Descriptions about density, distribution and quality of the reference data when performing local geoids are given in Large Scale Map and Spatial Data Production Regulation (LSMSDPR, 2005).

The local GPS/leveling geoids provide short-term and limited solution for the problem in height transformation. Therefore; regional geoid, whose accuracy is within cm, have to be performed across the country. In addition to usage of other types of the data, calculations with finite elements and soft computing methods can contribute to the improvements of the researches in future.

ACKNOWLEDGEMENT

The Istanbul GPS/Leveling data (IGNA) used in this research is provided by Istanbul Technical University Geodesy Division.

REFERENCES

Ayan, T., Deniz, R., Arslan, E., Çelik, R. N., Denli, H. H., Akylmaz, O., Özşamlı, C., Özlüdemir, M. T., Erol, S., Erol, B., Acar, M., Mercan, H., Tekdal, E. (2006). Istanbul GPS Nirengi Ağı (İGNA) 2005-2006 Yenileme Ölçü ve Değerlendirmesi. Istanbul Technical University Report, Volume 1, Istanbul. (In Turkish)

de Smith, M. J., Goodchild, M. F. and Longley, P.A. (2015). A comprehensive Guide to Principles, Technqiues and Softwere Tools. Geospatial Analysis (5th ed.), The Winchelsea Press, Winchelsea, UK.

LSMSDPR, 2005. Large Scale Map and Spatial Data Production Regulation (LSMSDPR) of Turkey, legalized in July 2005, Turkey.

Isaaks, E. H. and Srivastava, R. M., (1989). An Introduction to Applied Geostatistics. Oxford University Press, Oxford.

Li, J. And Heap, A. D. (2008). A Review of Spatial Interpolation Methods for Environmental Scientists. Geoscience Australia, Record 2008/23, 137 pp.

Robeson, S. M. (1997). Spherical Methods for Spatial Interpolation: Rewiev and Evaluation. Cartography and Geographic Information Systems, 24, 3-20.

Sandwell, D. T. (1987). Biharmonic Spline Interpolation of Geos-3 and Seasat Altimeter Data. Geophysical Research Letters, 14: 2, 139-142.

Skiena, S. S. (2008). The Algorithm Design Manual (2nd ed.), Springer-Verlag, London.

Soycan, M. and Soycan, A. (2003). Surface Modeling for GPS/Leveling Geoid Determination. International Geoid Service, 1:1, 41-51.

Sutton, T., Dassau, O. And Sutton, M. (2009). A Gentle Introduction to GIS. Chief Directorate: Spatial Planning & Information, Department of Land Affairs, Eastern Cape, South Africa.

URL1- Spatial Interpolation Techniques. National University of Ireland, Maynooth. Retrieved from http://www.nuim.ie/staff/dpringle/gis/gis09.pdf, (February, 2016).

URL2- An Introduction to Interpolation Methods. Retrieved from http://pro.arcgis.com/en/pro-app/help/analysis/geostatistical-analyst/an-introduction-to-interpolation-methods.htm, (February, 2015)

URL3- A Basic Understanding of Surfer Gridding Methods. Golden Software Newsletter. Retrieved from http://www.goldensoftware.com/newsletter/issue71-surfer-gridding-methods-part1, (March, 2016).

URL4- Geostatistics in Hydrology: Kriging Interpolation. Retrieved from http://www.dmsa.unipd.it/~berga/Teaching/STAM/stat.pdf, (March, 2016).

URL5- How Kriging Works. Retrieved from http://desktop.arcgis.com/en/arcmap/10.3/tools/3d-analyst-toolbox/how-kriging-works.htm#ESRI_SECTION1_E112B7FAED26453D8DA4B9AEC3E4E9BF, (April, 2016).

URL6- Sandwel, D. T. Scripps Institution of Oceanography University, University of California. ftp://topex.ucsd.edu/pub/, (February, 2016).

Use of Transferable Development Rights (TDR) Method on the Preservation of Historic Buildings in Turkey

Yunus Konbul[1], Mustafa Yanalak[2]

[1]Alanya Alaaddin Keykubat University, Akseki MYO, Land Registry and Cadaster Program, Akseki/Antalya, Turkey,
E-mail: yunus.konbul@alanya.edu.tr
[2]Istanbul Technical University, Geomatics Engineering Department 34469 Istanbul, Turkey
E-mail: yanalak@itu.edu.tr

ABSTRACT

Historic buildings are one of the few objects that can connect a country to its past, build national pride, and also provide urban aesthetics and bring touristic income. Therefore it is important to preserve them. Today, the practice of preservation of historic landmarks in Turkey is considered to be a successful one with its strong legislation and well-functioning preservation boards. However in this study, we will look at the situation from the perspective of building owners. When a building is decided to be preserved, put aside its demolition, even minor changes require the approval of preservation boards. This might be a great method for the sake of preservation, however from the owners' perspective, it is problematic to impose restrictions on "development rights" of people without the compensation of any kind (e.g. expropriation). For example, when a two-storey historic building is preserved in a neighborhood where development plan (zoning) allows five-storey buildings, because of the preservation decision, the owner of the historic building is prevented from his/her "right to build", which is causing an enormous amount of loss of "development gain" for the owner. On the other hand, this is a fact that public finances of countries cannot afford to expropriate every preserved real estate in whole country. At this point, Transferable Development Rights (TDR) (in Turkish, İmar Hakkı Transferi-İHT) can be a good method in Turkey as well, which has been used in many other countries for quite a long time. TDR simply means that the owner of a preserved real estate is allowed to transfer his/her development right to somewhere else. They can use their development right either by physically building it on another land parcel, or sell their right to someone else. By this way, the cost of preservation is financed by the real estate market or the community, not by the State. In other words, the economic loss (because of the restriction) of the owner is compensated without the State spending any money. In fact, TDR method already has clauses in the Turkish legislation, however it has never been used. This study tries to shed light on the TDR method to be used on historic buildings in Turkey by analyzing how it can be implemented, what the barriers are, and finally its advantages and disadvantages.

KEYWORDS: Transferable development rights; historic buildings; preservation; development right; development gain

1. INTRODUCTION

Lands, sites, buildings and other ground details which have historical, cultural or environmental significance are important elements of civilizations. The preservation of them is a not only a historical duty, but also a responsibility of the society. However, this study is focused on the owners of historic buildings and their rights, rather than the buildings itself.

Historic buildings are very important elements for the countries. They connect a country to its past, provide and sustain national pride. They have materialistic benefits as well, such as providing urban aesthetics and bringing touristic income to the country.

Today, the case of preservation of historic buildings in Turkey can be considered a successful one with its strong and strict preservation legislation, well-established preservation boards and not-to-be-ignored public grants and subsidies for their restoration. When a building is decided to be preserved by public authorities, not only their demolition is forbidden, even minor changes on them requires the approval of preservation boards, which are established by serious and picky academics and professionals. Widely known that it is quite a hassle to get their approval for the restoration projects. This is great for the sake of preservation. However, in this study we focus on the least-spoken and maybe least-cared part of the story: the owners of restricted historic buildings.

In this study, complicated technical issues are simplified as much as possible in order to facilitate the understanding of the subject and to focus on key points. For instance, the case of preservation can include many different types such as preservation of natural areas, agricultural lands and archeological sites. However, the subject is limited to only preserved historic buildings in this study, because of its simplicity. Also, development rights will be discussed as "storeys" (or floors) instead of FAR (floor area ratio), and lot coverage ratio will be accepted as 1.0, etc.

When a building is decided to be preserved by a preservation board, the development potential of that land parcel is frozen. This causes an enormous amount of loss of "development gain" or "development right" for the owner. Development right simply means the maximum building permissions according to the development plan (zoning) decisions. For instance, when a two-storey historic building is decided to be preserved (without any means of compensation by the

authorities) in a neighborhood where the development plan actually allows four-storey buildings, the historic building owner cannot use his/her "development right" fully, while the neighboring parcel owners can fully enjoy the enrichment of development gains without any obstacles. It looks like the authorities punish some people in the society for owning a historic preserved building, and ironically the building is decided to be preserved by the authorities as well. This causes unfairness. Because, development decisions must be equal for every landowner in the same zone. However with the decision of preservation, these landowners are prevented from their development rights without compensation (Figure 1).

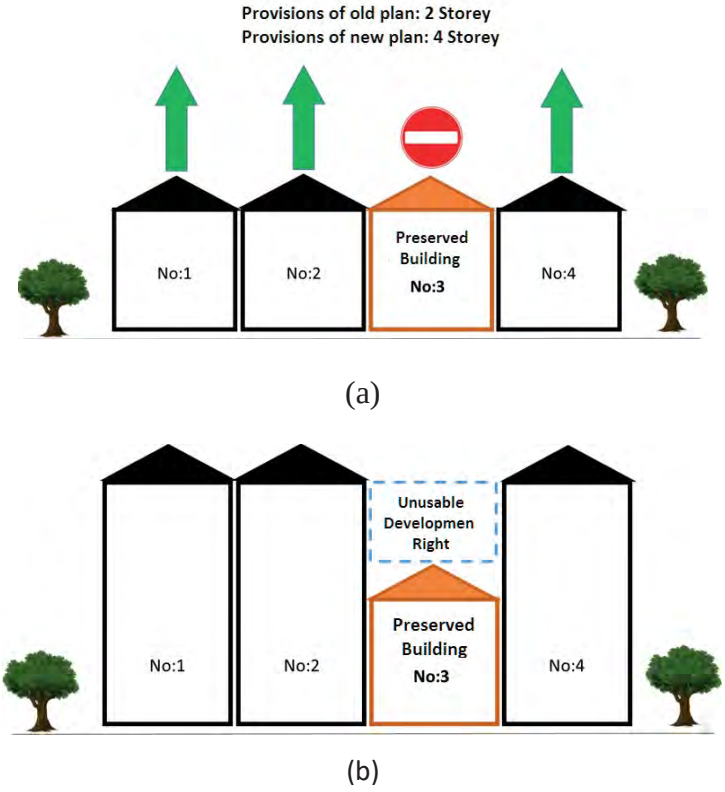

Figure 1: Restricted development right.

In order to solve this problem, the first solution comes to mind is the *expropriation* method. The State can purchase the preserved real estate from the owner. However it is a fact that public finances of countries cannot afford to expropriate all preserved real estate in whole country. There can also be other social disadvantages of doing so. Such as, a family can ask to keep their real estate which was inherited from their grand-grandparents. Those real estate should stay with the family, and should be protected that way.

At this point, the method of Transferable Development Rights (TDR) (in Turkish, İmar Hakkı Transferi-İHT) can be used in Turkey as well, which has been used for a long time in many other countries. TDR simply means that the owner of a preserved real estate is allowed to transfer his/her frozen/blocked/unused development right to somewhere else. They can use their development right either by physically building it on another land parcel, or sell their right to someone else. By this way, the cost of preservation is financed by the real estate market and the community, not by the State. In another words, the preservation is realized without violating development rights of people, and also without forcing public finances of the State. Actually, there are already clauses in the Turkish legislation about using TDR method, however it has never been used. It is understandable that it could not be used until today, because it is not an easy task.

Almost 10 years after the first TDR legislation was enacted in 2004, a very important workshop was held in 2014 hosted by the Ministry of Environment and Urbanization of Turkey. Academics and professionals from the sector held meetings and discussed the possibilities of the implementation. The conclusions were made, however unfortunately no further action could be made in the sector. This study aims to support above mentioned movement and increase scientific awareness on this matter.

2. SOME TDR EXAMPLES IN THE WORLD

According to the literature, the first TDR project was implemented in the USA, however there are different suggestions on when the first TDR was made. According to one view, the first TDR was used in 1916 in New York, by the zoning legislation, the landowners who could not use their "air right" could transfer it to a neighboring land parcel. By this, the "receiving parcel" was allowed to exceed existing development limits [1]. Another view says that it was first introduced by Gerald Lloyd in 1961, the TDR was first mentioned in the New York City's Landmark Preservation Law of 1968, which was enacted in order to protect historic landmarks [2-3]. Either way, it shows that there is much experience in TDR in the USA. Since its adoption, the TDR method was used not only on historic landmarks, but also on protecting agricultural lands and natural areas which has special natural significance [4-5]. After the pioneer projects

of TDR in the USA, the concept was spread out to many other countries such as France, Germany, Holland, Italy, Canada, China and South Korea [4].

According to some statistics, in 1970s more than twenty TDR projects were implemented in eleven states in the USA. These projects include road construction and protection of agricultural lands as well. TDR projects which were made in Maryland, USA, are considered to be the most organized and successful one. According to the studies, 32374 hectares of agricultural lands were preserved [6]. In 1980s and 90s, more than 100 TDR projects were implemented in 32 states and projects continued in 2000s [7].

In Italy, the first TDR program was started in 2014, and until May 2017, 75000 m^2 of development rights were transferred in several TDR programs. Interestingly, it is reported that only %10 of the TDRs were turned into a building construction, the remaining 90% has been used as a negotiable instrument, being traded among investors [8].

3. PRESERVATION AND TDR LEGISLATION IN TURKEY

In the Turkish legislation, there are two Acts which open the way to implement the TDR method. One of them is targeting the TDR method directly on preserved areas, which is the subject of this paper. The Act is called "Preservation of Cultural and Natural Assets Act, No.2863" (Kültür ve Tabiat Varlıklarını Koruma Kanunu, 2863).

According to the Act, the restricted development rights of properties can be transferred to somewhere else. Article 17 (c) is completely dedicated to using TDR on preserved lands. The article can be translated as (not word-to-word):

"*Article 17 – (Amendment 14/7/2004 - 5226/8)*

c) Municipalities and governorships are authorized to transfer property ownership or restricted parts of development rights from the preserved cultural assets … which are determined by conservation development plans, to the receiving areas in public ownership (State ownership) or in the ownership of third persons which are determined by development plans and which are available to receive transferable rights, within the scope of a program together with determining the prior rights..."

(In Turkish: "*Yapılanma hakları kısıtlanmış tescilli taşınmaz kültür varlıklarına veya bunların koruma alanlarında bulunan ya da koruma amaçlı imar plânlarıyla yapılanma hakları kısıtlanan taşınmazlara ait mülkiyet veya yapılanma haklarının kısıtlanmış bölümünü, imar plânlarıyla yapılanmaya açık aktarım alanı olarak ayrılmış, mülkiyetlerindeki veya üçüncü şahıslara ait alanlara, aktarımdan yararlanacak öncelikli hakları belirleyerek bir program dahilinde aktarmaya, belediye sınırları ve mücavir alanlar içinde belediyeler, bunların dışında valilikler yetkilidir.")*

The remaining paragraphs of the Article 17 (c) explains more details of the transfer method, and ends with the clause that this article can only be valid after the Regulation is prepared by the relevant Ministry. However, that Regulation has never been prepared. Therefore, this article has never been able to be functional.

4. IMPLEMENTATION SUGGESTIONS FOR TDR METHOD IN TURKEY

Since the TDR method could not be used in Turkey until today, it is possible to start from the beginning. If we think about a restricted historic building, there are few options to compensate the loss of the landowner:

a) Expropriation (government buying private property)

b) Giving other unused public lands (lands that belong to the State) to the owner, as a compensation

c) The TDR owner can use his/her development right on another land parcel which belongs to him/her

d) The owner can sell the TDR to a third person to be used on another land parcel

It is obvious that (a) expropriation method cannot be affordable for the public finances to be used everywhere. (b) Giving state lands to the owners cannot be affordable either, because in such case the State can lose large amount of public lands. Therefore (a) and (b) is eliminated.

4.1 (c) The TDR Owner Transfers the Right on Another Land Parcel

In this option, theoretically the owner is pre-accepted to own two different land parcels (let's say parcel-1 and parcel-2). If the owner is restricted by a preservation decision on one parcel,

he can transfer that "unusable development right" on his second land parcel as an addition to the existing development right. For instance, the owner has two land parcels in a 4-storey permitted neighborhood. On parcel-1, there is a 2-storey preserved historic building, which means the owner cannot use the remaining 2 storeys on it. He can transfer that unusable 2 storeys on top of parcel-2, making it a total of 4 + 2 = 6 storeys permitted land parcel (Figure 2).

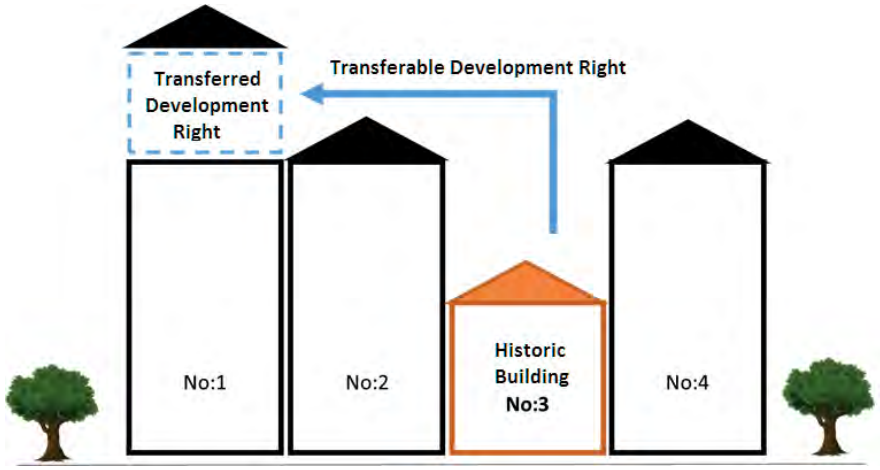

Figure 2: Transferring the restricted development right on another land parcel.

Benefits:

1) Historic building is preserved.
2) Owner can still use his/her development right.
3) The State did not pay anything.

Concerns:

1) Permitting a taller building in a neighborhood where all other buildings are shorter, it pulls attention. There are concerns about urban aesthetic.
2) The taller building may block the view, sunlight or air circulation of the shorter buildings around.
3) Additional apartment units will increase the neighborhood population, it may put extra weight on the infrastructure (water, electricity or traffic).

Things can be easier to understand when we consider floor-area-wise. There is a landowner whose, let's say, 300 m^2 size of development is restricted. The owner can build his 300 m^2 on

another parcel exactly the same size, as 300 m^2. It looks legitimate. However, what if we consider it value-wise? What if the owner has another land parcel in a much more expensive neighborhood? For instance, the average value of the neighborhood where the historic building is located is 2.000TL/m^2. The owner has another parcel in another area where it is 10.000TL/m^2. The unused 300 m^2 is worth 600.000TL in the original neighborhood. If he uses the same size of development in the second neighborhood, his 300 m^2 makes 3.000.000TL. The owner gets 2.400.000TL extra money out of nowhere. How will the public conscience react to it?

If we take the value path, then we should equalize the values between the transfers. According to the example above, 300 m^2 is worth 600.000TL in the first area, and 600.000TL is worth only 60 m^2 of development in the second area. This time it can hardly make a small apartment unit in the second neighborhood, however the values are equal. In the Preservation of Cultural and Natural Assets Act, the value method is foreseen, however it has never been used.

4.2 (d) The Owner Sells the TDR to Someone Else

In case the restricted owner does not have another land parcel, the right can be sold to someone else. By this way, the owner gets the money, and the buyer gets the additional building right (Figure 3).

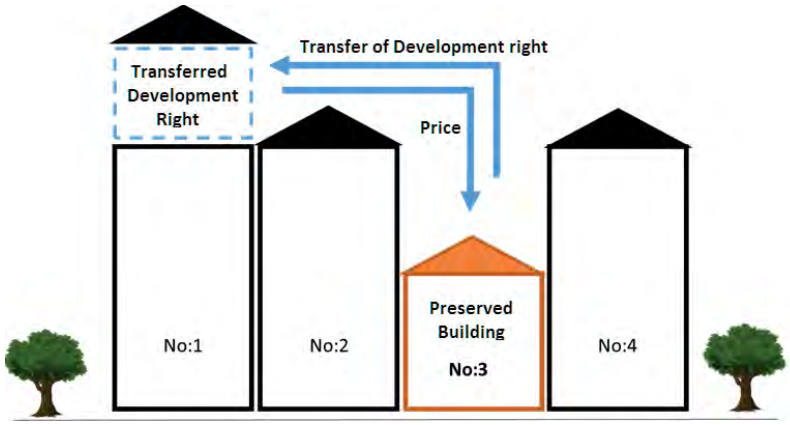

Figure 3: Selling of TDR to a third person.

Benefits:

1) Historic building is preserved.
2) Owner can turn his restricted development right into money.
3) The new buyer of TDR gets a larger or taller building permission.
4) The State did not pay anything.

Concerns:

1) Permitting a taller building in a neighborhood where all other buildings are shorter pulls attention. There are concerns about urban aesthetic.
2) The taller building may block the view, sunlight or air circulation of the shorter buildings around.
3) Additional apartment units will increase the neighborhood population, it may put extra weight on the infrastructure (water, electricity or traffic).
4) How will the TDR be valued? Will the value be a fixed price decided by the public authority? Or will it be decided among buyer and seller? Will it be according to the building size, or market price?

5. EVALUATION OF THE METHODS

5.1 The Concerns on Title 4.1

The concerns expressed on heading 4.1 (the owner uses his TDR on his/her other land parcel) is evaluated here.

1) **Permitting a taller building in a neighborhood where all other buildings are shorter can pull negative reactions. There are concerns about urban aesthetics.**

It is true that a taller building will pull attention among shorter buildings. Taller buildings are generally find aesthetically ugly and environmentally harmful. However they cannot be forbidden in most cases. We must put our aesthetical feelings aside and ask: what if that taller building brings more benefit than its harm? For instance, a hospital is going to be built in a 2-storey permitted neighborhood. What should be done? Should they build a fully equipped modern hospital in large building complex accordingly, or will they try to squeeze everything

into a small 2-storey building? Obviously, hospitals must be built according to the health and medical professional needs, and aesthetical concerns should come the second at this point.

Therefore, development plan decisions can be loosened for a higher public interest situations. TDR can be included here as well. Development plans can be made in a way that it tolerates exceeding maximum building height decisions in TDR situations. However, human nature will eventually try to abuse any tolerance if there is no regulation on it. In order to avoid the risk of abuse of building height tolerance, a maximum number of the tolerance can be set as well. Because, it can be tolerable to see a 6-storey building in a 4-storey neighborhood, however a 12-storey residence building would be looking too provocative. A maximum number for the extra-building can be determined, such as:

"The extra-building through TDR cannot exceed the 25% of the normal FAR of the building (according to the existing development plans)."

Which will mean that, accepting FAR as building height in a roughly calculation, the 25% of a 4-storey building will be made an extra 1 storey. So the building can be built a maximum of 5 storeys, in a 4-storey neighborhood. A maximum number for tolerance can be fixed this way.

The amount of extra building can be determined differently according to the unique situation of the areas in a way that the buildings (through TDR) will not be too tall to damage urban aesthetics.

2) **The 6-storey building may block the view, sunlight or air circulation of the buildings around.**

When it comes to sunlight or air blockage, it is the preserved building owners who suffer from it the most. Keeping a 2-storey building and permitting all other surrounding buildings to be 4 floors or even more, the sunlight and air usage of the preserved building is totally chocked. If there are concerns on sunlight and air usage when a taller building is permitted among other shorter buildings, then more empathy should be given to the very short preserved buildings among much taller buildings surrounding it. Because the conditions of the latter is much worse than the former (Figure 4).

(a)

(b)

Figure 4: Preserved historic building examples (Photographed by Y. Konbul).

The number of preserved historic buildings in urban areas is generally very few comparing with normal buildings. Therefore the TDR rights will be available in few parcels in the cities. If

considered this way, the disturbance made by taller TDR buildings among shorter buildings can be tolerable as well. Also, how much can a 5 or 6 storeys building among 4-storey buildings can create disturbance? Such information can be investigated in another study.

3) Additional apartment units will increase the population in the neighborhood, it can put extra weight on the infrastructure (water, electricity or traffic).

If the TDR is used in the same neighborhood of the preserved historic building, extra population will not be the case. Because, when the development plans are made, the population of the neighborhoods are calculated according to a fixed FAR (floor area ratio) or building heights without knowing/considering restricted buildings. When a building is decided to be preserved, the planned population of that particular parcel will be restricted. Therefore the population of the neighborhood actually will not reach to the pre-determined number. When the restricted part is used on another parcel through TDR in the same neighborhood, the missing population will be brought back to the area, which will meet up with the normal expected population. This means that if the TDR is used in the same neighborhood (or development zone), it will not bring extra population to the area, it will actually let the neighborhood meet the normally expected/calculated population density.

If the TDR is used in another development zone, then this concern can be valid. The prior calculated population of the area can be exceeded with the TDR transfers inside the area. However, vague thoughts can be misleading. How much increase in the population can be seen as a problem? Is bringing ten families (~40 people) in a 4000-people-neighborhood too many (1% increase)? Can it really make a big difference on the infrastructure? Probably not. However bringing 50% more people to an area can be a problem for the capacity of the existing infrastructure. Then what is the border? It can be a subject of another study. Summarizing all, population increase through TDR can be a valid concern if the incoming people is too many. For small number of transfers, it should not make a big problem. Therefore, numbers are important. It is unnecessary to categorically refuse such options.

5.2 The Concerns on Heading 4.2

The method explained in heading 4.2 (owner sells the TDR to someone else) is evaluated in this part. According to the experiences in other countries, selling of TDR is more complicated than its use by the original owner of the TDR. There are many questions to answer.

1) Will the TDR owner sell it to anyone, anywhere, with any price he/she wants?

2) How will the price be determined?

3) Will an authority regulate the sales of TDRs, or will it be completely market driven?

4) Will the new buyer of TDR use the exact number of restricted floor size (square meter), or will he/she need to convert the money paid into the development size for a particular neighborhood?

From the bureaucratic point of view, letting the TDR owner sell it anyone he/she wants is the simplest one. It is letting the owner of restricted building sell his/her TDR to anyone with a negotiated price between them, with minimum intrusion of public authorities. It is letting the free market take care of the business. The first problem that can occur here is the location that the purchased TDR will be used. Will the authority let TDR being used anywhere in the city? What if the restricted building is in an unpopular neighborhood in the city, and the purchaser wants to use the TDR on his very expensive land parcel in a high-class neighborhood? These are among many other big questions that academics, professionals and public administrators needs to find an answer before doing anything in the TDR practice. These questions should be answered on the paper first, before practicing anything in the real life. Perhaps this is the reason why the TDR legislation in Turkey could not be used since its enactment in 2004. The questions could not be answered on the paper yet.

As explained above, if the TDR is made completely according to the construction size (m^2-to-m^2), then 1 m^2 in the popular neighborhood can be priced many-many-times more than unpopular neighborhood. The owner can collect an enormous amount of "unearned income" through "development gain". Public conscience will protest it.

What if a person from an unpopular neighborhood wants to purchase a TDR from an popular neighborhood? If the trade is completely between a willing seller and a willing buyer without any intervention of public authorities, how much money will he pay? Maybe a real estate

appraisal can be made on the restricted building's unused development right, and the value of that part can be paid by the buyer. After that, how many square-meter can the buyer build on his land? This means that a regulatory authority is inevitable, such as local authority or the Ministry, which will issue TDR certificates and will calculate how many square-meter can be built in a specific neighborhood with a specific TDR.

5.3 Using TDR in Undeveloped Areas

Up till this point, TDR was evaluated only in developed urbanized areas in this paper. Using TDR in developed areas inevitably means that the pre-determined development limits (by development plans) must be exceeded in order to let a TDR to be used. What if the TDR is used in undeveloped empty areas, such as in urban peripheries?

Urban areas in Turkey are determined by development (zoning) plans, and these plans show urban boundaries. You can localize where an urban area starts and ends with the coordinates of those boundaries. If an urban area has potential to expand towards its peripheries, new areas can be opened to urbanization by additional development plans. Turkish urbanization today is keen on expanding cities by opening new development areas in the peripheries.

If we consider how to use TDRs in undeveloped areas in the peripheries, there must be very strong, very tight legislations. Because cities are already expanding with new additional development plans. If an undeveloped area is going to be available for TDR owners, it must be clear that the area can only be developed by incoming TDRs. There must be no other possibility to develop that area through regular development permissions.

For instance, there is an owner of preserved building who is given a TDR by the local authority for the restriction. The authority tells him/her to use that development right in the peripheries of the city. The person goes out and buys a land parcel in the undeveloped periphery of the city, and the public authority gives a 4-storey building permission to him for that land parcel. The TDR owner builds a 4-storey building on his land. However after 2 years, the authority makes a new development plan and open the whole periphery area for development and gives 4-storey building permissions for the whole area. In this case, the TDR owner is cheated. Because the TDR owner could normally buy a land in the periphery of the city, wait for 2 years and get a 4-storey building permit just like any other landowners. However, in this case, he is deceived by

the public authority into thinking that he was transferring his restricted development right into that area. The situation is, he used (or lost) his TDR certificate for a development right he would normally get without using a TDR. It is the same as paying money for something you would normally get for free.

In order to use a TDR right in an undeveloped area in a meaningful way, the area must be strictly forbidden for any development rights, except TDR owners. This way, the TDR owners will know that their neighborhood will not be opened for development to others for free. However, the whole peripheries of a city cannot be dedicated for only incoming TDRs, yet some part of it can be dedicated (Figure 5). A small part of the periphery can be reserved for TDRs, and can be named as "TDR-Privileged Zone" or "TDR-Reserved Zone" or somthing similar (in Turkish, İHT İmtiyazlı Alan, İHT Rezerv Alanı vb.). Any attempt of development permission other than incoming TDRs in TDR-Reserved Zone can put the authority in a bad position, such as asking money (in this case forcing a landowner use his TDR right) for something that they normally give for free.

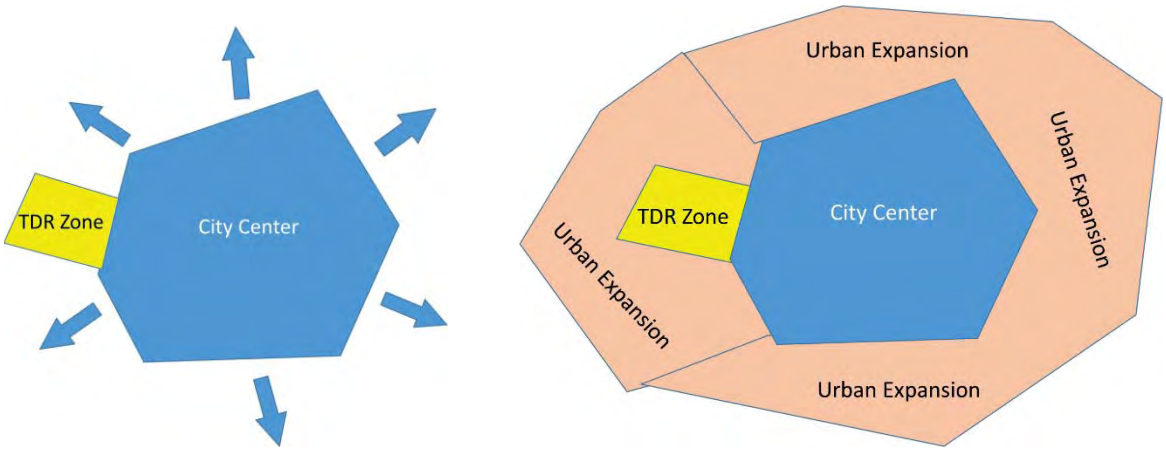

(a) (b)

Figure 5: Urban expansion and TDR Reserved Zone relationship.

CONCLUSIONS

Preservation of historic buildings is a must. However the restrictions on these real estate without a compensation is unfair for their owners. If authorities cannot purchase/expropriate those estates (public finance cannot handle purchasing every preserved estate), the best method seems

to be the Transferrable Development Right (TDR) method. By this way, the owner of a preserved estate can use his/her restricted development right somewhere else, or sell it to someone else. However, how it can be done is the difficult part to solve. This study tries to shed light on the subject and tries to answers some of those questions.

Even though the TDR legislation was enacted as early as 2004 in Turkey, it could not be used so far. Considering the few scientific studies on this title in the Turkish academia until today, it seems that this leading-edge legislation was too ahead of its time. If the legislation could have been supported by strong academic studies, the regulation may have already been prepared and we could have been able to see some TDR implementation examples in the country. Scientific studies should be increased on this subject in order to support and facilitate the realization of TDR method.

According to the literature, different methods are used in different projects. Therefore there is no one method fit-for-all. It seems that the system needs to be flexible with the idea of letting authorities find a way which fits to their specific conditions.

If the restricted development right is used in urbanized areas, than it will mean that the receiving land parcels (land parcel which host the incoming TDRs) will need to exceed the existing maximum development/construction limits determined by development (zoning) plans. Although development plan decisions must be equal for every landowners in the zone, some of the land parcels will be tolerated to pass the limits of regular development permissions in case of TDR.

If the restricted development right is used in un-urbanized, undeveloped areas of the cities (such as peripheries), the usage of TDR can be tricky. Because, if an undeveloped area will be opened for construction for a transferred TDR, it must be special for TDR only. In another words, if a person transfers his TDR to an undeveloped land parcel outside the city, gets a special building permission for that parcel, however after 6 months the local authority decides to open the whole periphery area to development will mean that the TDR owner is tricked. Because the TDR owner did not have to use his restricted right on that area, he could wait for 6 months and get a normal building permit for free (without using his TDR). This way, he pays money (the TDR in this case) to the authority for something that he could get for free. In order to avoid such

situation, an area in the periphery of a city can be dedicated to only TDR transfers, and they can be named as "TDR Privileged Zone", "TDR Reserved Zone" or something similar.

REFERENCES

1. Johnston, R. A., & Madison, M. E. (1997). From land marks to landscapes: a review of current practices in the transfer of development rights. Journal of the American Planning Association, 63(3), 365-378

2. Linkous, E. R. (2016). Transfer of development rights in theory and practice: The restructuring of TDR to incentivize development. Land Use Policy, 51, 162-171. doi:10.1016/j.landusepol.2015.10.031

3. Kaplowitz, M. D., Machemer, P., & Pruetz, R. (2008). Planners' experiences in managing growth using transferable development rights (TDR) in the United States. Land Use Policy, 25(3), 378-387. doi:10.1016/j.landusepol.2007.07.004

4. Falco, E., & Chiodelli, F. (2018). The transfer of development rights in the midst of the economic crisis: Potential, innovation and limits in Italy. Land Use Policy, 72, 381-388. doi:10.1016/j.landusepol.2017.12.069

5. Linkous, E. R. (2016). Transfer of development rights in theory and practice: The restructuring of TDR to incentivize development. Land Use Policy, 51, 162-171. doi:10.1016/j.landusepol.2015.10.031

6. Shahab, S., Clinch, J. P., & O'Neill, E. (2019). An Analysis of the factors influencing transaction costs in transferable development rights programmes. Ecological economics, 156, 409-419.

7. Dündar, S. (2010). İmar Hakkı Aktarımı-İstanbul Üzerine Bir İnceleme. (Yüksek Lisans Tezi), İstanbul Teknik Üniversitesi, İstanbul.

8. Falco, E., & Chiodelli, F. (2018). The transfer of development rights in the midst of the economic crisis: Potential, innovation and limits in Italy. Land Use Policy, 72, 381-388. doi:10.1016/j.landusepol.2017.12.069

Georeferencing in 3D point clouds with L1 norm (least absolute value) method

Ülkü Kırıcı Yıldırım[1] , Yasemin Şişman[2]

[1]Ondokuz Mayis University, Geomatics Engineering Department 55138 Samsun, Turkey
Phone: +90 362 312 1919, E-mail: ulku.kirici@omu.edu.tr

[2]Ondokuz Mayis University, Geomatics Engineering Department 55138 Samsun, Turkey
Phone: +90 362 312 1919, E-mail: ysisman@omu.edu.tr

ABSTRACT

A point cloud is a three-dimensional structure that consists of a large number of points at a certain distance to each other in a digital environment. The point cloud should best symbolize the surface being received. Georeferencing (transformation) should be performed to make the obtained point cloud useable. While performing georeferencing, the control points to be selected should cover the entire project. In a coordinate transformation, some different coordinate transformation methods might be choose according to shape of computation surface, aim of transformation and amount of the points with known coordinates in both coordinate systems. In applications corrected (adjusted) measurements can be determined with more than necessary measurements. Due to more measurements than necessary, the inconsistency between measurements results in no single meaningful solution. Therefore, only meaningful solution can be obtained by abide to different aim functions. One of these methods is L1 norm (Least Absolute Value Method- LAV) which solution aims to In L1 norm (LAV) method, the solution is made by trial and error or the problem is converted to linear programming While, the advantage of this method is that it has little or no effect on the big error. The disadvantages of this method are difficulties of solving and accepts the same number of unknown measurement as correct.

In this application L1 norm method was used on the georeferencing with Bursa-wolf model. 3D point cloud was used as a data. Common points were selected from the data set to cover the working area homogeneously. Georeferencing was done using these common points. The calculated transformation parameters were tested on other points and the correction values were calculated. Results were reviewed.

KEYWORDS: point cloud; L1 norm; georeferencing

1. INTRODUCTION

Georeferencing (coordinate transformation) is the process of transforming the points between two coordinate systems. For the process of coordinate transformation, both systems should have some common characteristics (same axes, same the angle in-between, etc) [1]. In the coordinate transformation process, transformation parameters are calculated by using common points in both systems. The coordinate transformation parameters numbers are vary according to transformation method will be used. Some geometric properties of both systems are protected from transformation [2]. The coordinates of any other points/objects are calculated using by these transformation parameters. There are many different coordinate transformation methods in use. These are 2D (Two Dimensional) and 3D (Three Dimensional) similarity, affine and projective transformation. Bursa-Wolf, Molodensky-Badekas, Veis, Hotine, Krakiwsky-Thompson and Vanicek-Wells models are examples of 3D similarity transformation models. Bursa-Wolf, Molodensky-Badekas and Veis models are the most used and most significant results of these models [3].

In applied sciences, measurements are made more than the number of unknowns in order to increase the accuracy and precision obtained from measurements and the results of measurements. In a problem, the number of unknown parameters is equal to the number of sufficient calculation and it is shown with u. If the number of measurements (n) is higher than the number of unknowns u, there is the more solution of the problem. In such as system, adjustment is made to obtain the only significant result. The objective of adjustment is to find out the most suitable and highest probability value of the unknown and unknown functions without leaving out any measurement from measurement groups which do not contain gross or systematic error [4].

In adjustment the solutions are made according to an objective function in order to determine unknown parameters. Objective function is chosen considering measurement residuals as minimum. The most frequently applied methods in adjustment are Least Squares Method (LS-L2 Norm), The Least Absolute Value Method (LAV-L1 Norm) and Total Least Squares Method (TLS) [1].

The aim of this study is to calculate the transformation parameters of 3D point clouds having two coordinate systems according to the 3D similarity transformation. 3D similarity transformation was performed according to the L1 norm method and L2 norm method.

2. MATERIAL AND METHOD

2.1 3D similarity transformation

3D similarity datum transformation is the most commonly used model for geodetic transformation and has attracted extensive attention. The purpose of 3D transformation is to predict the coordinates of new points in the target system by using their original coordinates and the coordinates of common points in both original and target coordinate systems. In order to achieve this goal, two necessary procedures, including the parameter estimation and new point transformation, should be implemented in practice.

Parameter estimation is an important part for the 3D similarity transformation problem, in which there are totally seven transformation parameters to be estimated, including three translation parameters (X_0, Y_0, Z_0), three rotation angles $(\varepsilon, \psi, \omega)$ and a scale ratio $(1+\Delta)$. In geodetic field, many algorithms have been developed to solve these parameters.

By using the transformation parameters, the original coordinates of the new points can be converted into the target coordinate system [5].

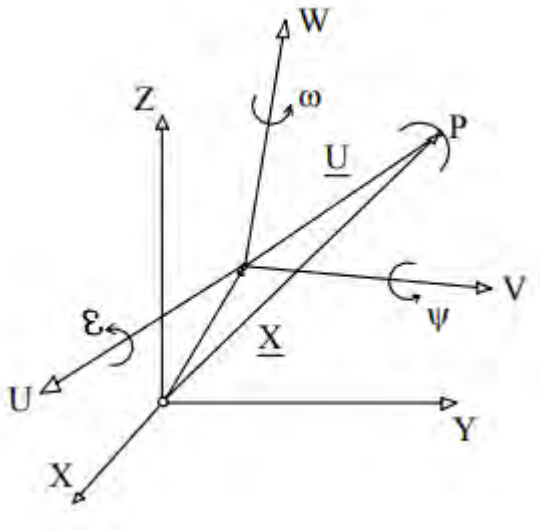

Figure 1. *3D similarity transformation [2]*

$$X = X_0 + (1+\Delta).R.U \qquad (1)$$

X : Coordinates of points in the 1st system (X, Y, Z)

U : Coordinates of points in the 2nd system (U,V,W)

The R return matrix is the result of three successive returns.

$$R=\begin{bmatrix} \text{Cos}\psi.\text{Cos}\omega & \text{Cos}\varepsilon.\text{Sin}\omega+\text{Sin}\varepsilon.\text{Sin}\psi.\text{Cos}\omega & \text{Sin}\varepsilon.\text{Sin}\omega-\text{Cos}\varepsilon.\text{Sin}\psi.\text{Cos}\omega \\ -\text{Cos}\psi.\text{Sin}\omega & \text{Cos}\varepsilon.\text{Cos}\omega-\text{Sin}\varepsilon.\text{Sin}\psi.\text{Sin}\omega & \text{Sin}\varepsilon.\text{Cos}\omega+\text{Cos}\varepsilon.\text{Sin}\psi.\text{Sin}\omega \\ \text{Sin}\psi & -\text{Sin}\varepsilon.\text{Cos}\psi & \text{Cos}\varepsilon.\text{Cos}\psi \end{bmatrix} \quad (2)$$

$$R=I+Q=\begin{bmatrix}1&0&0\\0&1&0\\0&0&1\end{bmatrix}+\begin{bmatrix}0&\omega&-\psi\\-\omega&0&\varepsilon\\\psi&-\varepsilon&0\end{bmatrix} \quad (3)$$

Since each point consists of three coordinate components, the following equations can be written for each point.

$$\begin{bmatrix}X_0\\Y_0\\Z_0\end{bmatrix}+(1+\Delta).R.\begin{bmatrix}U\\V\\W\end{bmatrix}-\begin{bmatrix}X\\Y\\Z\end{bmatrix}=\begin{bmatrix}0\\0\\0\end{bmatrix} \quad (4)$$

If we put 3 in 4;

$$X_0+(1+\Delta).(I+Q).U-X=0 \quad (5)$$

obtained. If the equation is opened and the second terms related to scale and rotation are neglected;

$$X_0+Q.U+(1+\Delta).U-X=0 \quad (6)$$

obtained. General adjustment model is written as follows [2].

$$A.v+B.x+w=0 \quad (7)$$

$$\begin{bmatrix}1&0&0&-1&0&0\\0&1&0&0&-1&0\\0&0&1&0&0&-1\end{bmatrix}.\begin{bmatrix}V_U\\V_V\\V_W\\V_X\\Y_Y\\V_Z\end{bmatrix}+\begin{bmatrix}1&0&0&U&0&-W&V\\0&1&0&V&W&0&-U\\0&0&1&W&-V&U&0\end{bmatrix}.\begin{bmatrix}d_{x_0}\\d_{y_0}\\d_{z_0}\\d_\Delta\\d_\varepsilon\\d_\psi\\d_\omega\end{bmatrix}+\begin{bmatrix}U-X\\V-Y\\W-Z\end{bmatrix}=0$$

2.2 Least absolute value method (L1 norm)

In the classical Gauss-Markov model, the unknown parameters x for a linear (linearized) parametric adjustment are determined based on the following functional and stochastic models [6]:

$$\begin{aligned} &l + v = A.x \\ &D^T.x = 0 \\ &P = Q_l^{-1} = \sigma_0^2 C_l^{-1} \end{aligned} \tag{8}$$

$v_{n\times 1}$:vector of residual

$l_{n\times 1}$: vector of observation

$A_{n\times u}$: rank deficient design matrix

$P_{n\times n}$: weight matrix of observations

$D_{u\times d}$: datum matrix of the network added to complete the rank deficiency of the design matrix

$O_{d\times 1}$: zero vector

$C_{j(n\times n)}$: covariance matrix of observations

$Q_{l(n\times n)}$: cofactor matrix

$\sigma_0^2 = a$: priori variance factor

The L1 norm is a method that minimizes the weighted sum of the absolute values of the corrections [7].

$$P^T|V| = \sum_{i=1}^{n} P_i|V_i| \rightarrow \min \tag{9}$$

To transform Eqs. (8) and (9) into something we can work with, the usual strategy is to borrow a trick from linear programming and introduce slack variables that guarantee nonnegative, and this allow us to write the objective function without absolute value signs.

As mentioned, setting up the L1 norm problem by a linear programming solution requires us to formulate a mathematical model where all variables, both parameters and residuals, are nonnegative. The development begins with the familiar parametric Eq. (8) and is then transformed into an L1 norm problem by adding slack variables. To convert these equations

into a form where there are nonnegative parameters and nonnegative residuals, we introduce two slack vectors, a and β, for the parameters, and two slack vectors, u and w, for residuals.

$$\begin{aligned} v &= u - w \qquad u, w \geq 0 \\ x &= \alpha - \beta \quad , \quad \alpha, \beta \geq 0 \end{aligned} \tag{10}$$

Rewriting the original parametric equations and datum constraints and the objective function in terms of slack variables yields

$$z = P^T |V| = P^T |u - w| = P^T (u + w) \rightarrow \min \tag{11}$$

where

$u_i = 0$ or $w_i = 0$

subject to

$$\begin{aligned} l + u - w &= A(\alpha - \beta) \\ D^T(\alpha - \beta) &= 0 \end{aligned} \tag{12}$$

and

$u, w, \alpha, \beta \geq 0$

or equivalently

$$z = \begin{bmatrix} 0^T & 0^T & P^T & P^T \end{bmatrix} \cdot \begin{bmatrix} \alpha \\ \beta \\ w \\ u \end{bmatrix} \rightarrow \min \tag{13}$$

subject to

$$\begin{bmatrix} A & -A & I & -I \\ D^T & -D^T & Z & Z \end{bmatrix} \cdot \begin{bmatrix} \alpha \\ \beta \\ w \\ u \end{bmatrix} = \begin{bmatrix} 1 \\ 0 \end{bmatrix} \tag{14}$$

Where Z is zero matrix. Denoting

$$\begin{bmatrix} \alpha \\ \beta \\ w \\ u \end{bmatrix} = x \; ; \quad \begin{bmatrix} 0 \\ 0 \\ P \\ P \end{bmatrix} = c \tag{15}$$

and

$$\begin{bmatrix} A & -A & I & -I \\ D^T & -D^T & Z & Z \end{bmatrix} = A \quad ; \quad \begin{bmatrix} 1 \\ 0 \end{bmatrix} = b \tag{16}$$

one gets

$$z = c^T . x \rightarrow \min$$

subject to

$$A.x = b \quad ; \quad x \geq 0$$

This is a special operations research problem that can be solved by linear programming [6].

2.3. The least square method (L2 norm)

The least squares method explained by Carl Friedrich Gauss in 1795 and Legendre in 1805. This method is used in many different applications [8]. Unknown parameters calculated with the following equation in this method.

$$\underline{X} = \left(\underline{A}^T P \underline{A}\right)^{-1} \underline{A}^T P \underline{\ell} \tag{17}$$

Root mean square error (RMSE);

$$m_0 = \pm\sqrt{\frac{\underline{V}^T \underline{P} \underline{V}}{f}} \quad ; \text{f = n – u} \tag{18}$$

The measurement errors of the LS method (L2 Norm) influence the residual of other calculations. Thus, this correction value may not always be due to an error in the measurement. This situation is called the spread and storage effect of LS method (L2 Norm). Different solution methods can be conducted for the analysis of spread and storage method.

3. RESULTS AND DISCUSSION

In this study, 35 points coordinates in both ED50 and ITRF coordinate systems of Samsun province were used. 3D similarity transformation was made with 5 homogeneously selected points from these points. (Figure 2, Table 1) Weighted L1 norm method and weighted L2 norm method were used in this 3D similarity transformation. Firstly, transformation parameters were calculated using selected common points. (Table 2) All of these studies were done in the Matlab program.

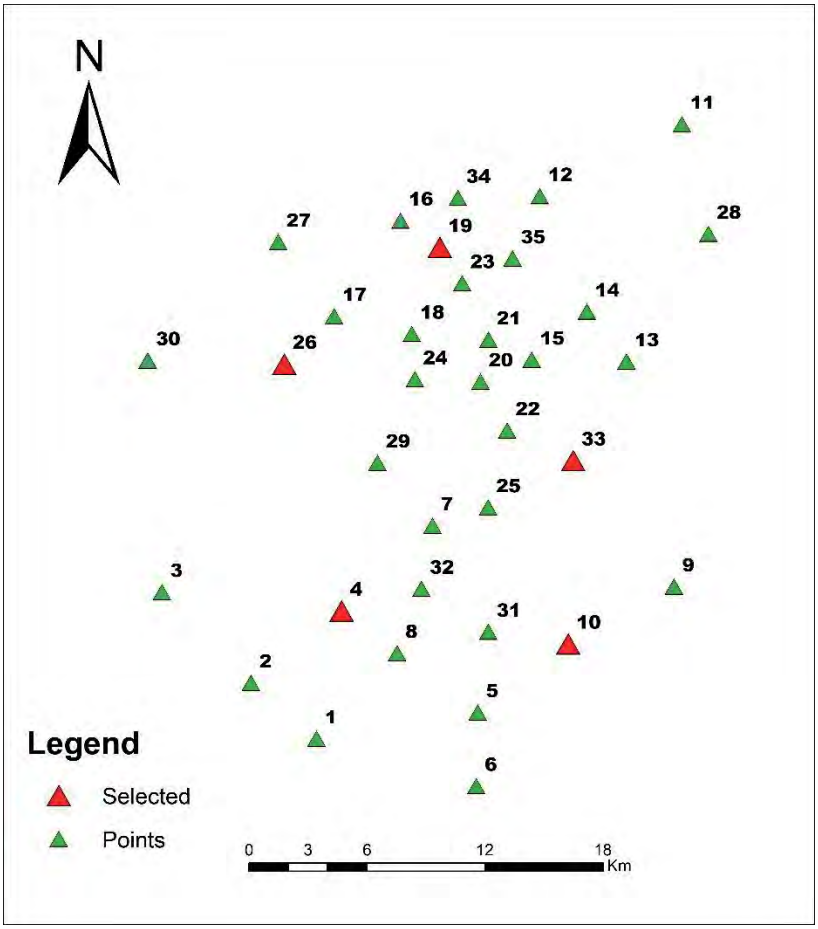

Figure 2. *Working area*

Table 1: Selected point coordinates.

	ED50			ITRF			
NN	**Y**	**X**	**Z**	**Y**	**X**	**Z**	**P**
4	469289,50	4535770,31	836,53	469267,86	4535586,50	871,62	1,000
10	480812,50	4534094,29	941,78	480791,11	4533910,60	976,71	0,563
19	474280,17	4554243,54	794,94	474259,25	4554059,61	829,06	1.041
26	466374,60	4548309,33	732,99	466353,58	4548125,62	767,53	1,500
33	481065,31	4543404,58	828,69	481044,25	4543220,86	863,13	0,250

Table 2: Calculated transformation parameters.

	Transformation parameters	
	L2 Norm	**L1 Norm**
X_0	-134,377	-155,684
Y_0	-143,455	-118,766
Z_0	258,520	252,894
ε	0,00001963	0,00001835
ψ	-0,00004723	-0,00004613
ω	-0,00002772	-0,00002189
$(1+\Delta)$	0,99999199	0,99999607

Using the calculated transformation parameters, the coordinates of the remaining 30 points in the new system were recalculated. The correction value (V) was found with the differences between the calculated coordinate and current coordinate. (Table 3, Table 4)

Table 3: Calculated correction value in L1 norm method.

NN	Vy(m)	Vx(m)	Vz(m)
1	0,229	0,102	0,438
2	0,299	0,011	0,169
3	0,551	0,206	99,875
5	99,933	0,006	-0,002
6	-0,142	-0,148	0,633
7	-0,212	0,202	-0,853
8	0,003	0,292	0,453
9	-0,482	-0,082	0,399
11	-0,136	0,119	-0,625
12	-0,022	-0,029	-0,228
13	-0,054	-0,047	-0,092
14	-0,044	-0,054	0,394
15	-0,166	999,863	0,001
16	0,020	-0,124	-0,216
17	0,065	-0,014	0,018
18	0,004	0,006	-0,008
20	-0,147	-0,176	0,185
21	-0,113	-0,100	-0,059
22	-0,284	-0,111	-0,037
23	0,004	0,075	0,020
24	-0,067	-0,002	0,068
25	21,590	1,139	1,112
27	0,435	-0,036	0,077
28	-0,207	0,131	0,223
29	-0,121	0,146	0,240
30	0,242	-0,173	-0,123
31	-0,171	-0,028	0,178
32	-0,034	0,209	0,240
34	0,009	-0,028	0,113
35	1000,019	-0,046	-0,075

Table 4: Calculated correction value in L2 norm method.

NN	Vy(m)	Vx(m)	Vz(m)
1	0.309	-0.083	0.464
2	0.388	-0.144	0.195
3	0.647	0.096	99.901
5	99.960	-0.205	0.012
6	-0.099	-0.380	0.650
7	-0.210	0.056	-0.846
8	0.041	0.115	0.468
9	-0.539	-0.297	0.393
11	-0.292	0.039	-0.657
12	-0.121	-0.099	-0.248
13	-0.144	-0.185	-0.108
14	-0.132	-0.169	0.378
15	-0.234	999.740	-0.009
16	-0.032	-0.174	-0.225
17	0.052	-0.079	0.020
18	-0.028	-0.080	-0.011
20	-0.190	-0.290	0.182
21	-0.167	-0.204	-0.066
22	-0.325	-0.246	-0.040
23	-0.054	-0.006	0.011
24	-0.091	-0.102	0.069
25	21.571	0.986	1.114
27	0.423	-0.067	0.079
28	-0.348	0.014	0.193
29	-0.117	0.029	0.246
30	0.293	-0.212	-0.107
31	-0.164	-0.218	0.186
32	-0.016	0.046	0.250
34	-0.065	-0.083	0.099
35	999.937	-0.124	-0.090

4. CONCLUSION

Although outlier measurement test has not been performed, points which ones have big error are seen from correction value (V). Calculations shows that correction values, we can say that points 3, 5, 15, 25 and 35 are big error.

Since the correction values of point 3 in the Z direction 99.875, point 5 in the X direction 99.933, point 15 in the Y direction 999.863, point 25 in the X direction 21.590 and point 35 in the X direction 1000.019 are higher than the other values, we can say that these coordinates are big error in L1 Norm.

Since the correction values of point 3 in the Z direction 99.901, point 5 in the X direction 99.960, point 15 in the Y direction 999.740, point 25 in the X direction 21.571 and point 35 in the X direction 999.937 are higher than the other values, we can say that these coordinates are big error in L2 Norm.

In both methods (L1 Norm, L2 Norm), the same points appear to contain big error, indicating that there are problems in these points.

Incorrect measurements must be removed from the data set and the calculation process must repeated. At the same time, by increasing the number of points in the data set, a more sensitive work can be done for a wider area.

REFERENCES

1. Sisman Y., 2015, The Different Adjustment Methods in 3D Coordinate Transformation, Internatıonal Symposıum On Innovatıve Technologıes In Engıneerıng And Scıence, Valencia, Spain.

2. Başçiftçi F., İnal C., 2008, Jeodezide Kullanılan Bazı Koordinat Dönüşümlerinin Programlanması, S.Ü. Müh.-Mim. Fak. Derg., c.23,s.1.

3. Uzun Y., Üç Boyutlu Astrojeodezik Dik Koordinat Sistemlerinde Dönüşüm Modelleri ve Uyuşumsuz Ölçü Gruplarının Belirlenmesi Yöntemlerinin Karşılaştırılması, Doktora Tezi, Karadeniz Teknik Üniversitesi Fen Bilimleri Enstitüsü, Trabzon, 2003.

4. Wang, Y., 1992, "A rigorous photogrammetric adjustment algorithm based on co-angularity condition" International Archives of Photogrammetry and Remote Sensing, 29(B5), 195-202.

5. Wang B., Li J., Liu C., Yu J., 2017, Generalized Total Least Square Prediction Algorithm For Universal 3D Similarity Transformation, Advances in Space Research 59, 812-823.

6. Simkooei A.A., 2003, Formulation of L1 Norm Minimization in Gauss-Markov Models, J.Surv.Eng., 129(1):37-43.

7. Yetkin M. , Inal C., 2011, L 1 Norm Minimization in GPS Networks, Survey Review, 43:323, 523-532

8. Sisman Y.,2014, Coordinate transformation of cadastral maps using different adjustment methods, Journal of the Chinese Institute of Engineers, Registered Number: 101080, Chinese inst. Engineers Tape 10019 Taıwan , Çin.

A Performance Analysis of Low-Cost GNSS receivers Using N-RTK

Nedret BOZKURT[1] , M. Halis SAKA[2]

[1,2] Gebze Technical University, Geomatic Engineering 41400 Kocaeli, TURKEY
Phone: +90 533 820 0317, E-mail: nbozkurt@gtu.edu.tr
Phone: +90 532 494 0227, E-mail: saka@gtu.edu.tr

ABSTRACT

Today, low-cost and high-performance GNSS devices can be successfully used in many fields including, autonomous vehicles, Unmanned Aerial Vehicles (UAVs), railways, maritime, agriculture, GIS, communication, energy, natural events, sports and meteorological studies. In real time positioning, the Radio Technical Commission for Maritime Services (RTCM) data structure including base station correction information can be transmitted to the receiver by The Networked Transport of RTCM via Internet Protocol (NTRIP) data transmission protocols. Thus, it can provide more flexible solutions for precise measurements compared with the standard Real-Time Kinematic (RTK) positioning technique can be achieved.

GNSS receiver manufacturers offer low cost products with acceptable accuracy for real-time analysis. In this study, a base station (NTRIP-Caster) was established using open-source software of U-Center and RTKLib to test the Ublox C94-m8p single-frequency GNSS receiver. RTCM correction data transmitted from this single frequency base station was transmitted over the internet to single-frequency C94m8p receiver (NTRIP-Client) and real-time network solutions, at the same time RINEX data were recorded at 1-second intervals. In order to compare the accuracy of low-cost devices with Post-Processing (PPK) data, RINEX data were collected and then the estimated solutions were analyzed using the dual-frequency receiver with RTKLIB software.

The results showed that the N-RTK results obtained with the U-Center software and the PPK solutions obtained with the RTKLib software were in the fix solution for single frequency receivers.

KEYWORDS: Low cost; Single Frequency; GNSS; N-RTK; PPK

1. INTRODUCTION

In the 1980s, the first commercially available GPS receiver could only perform C / A and P code measurements, and the initial sales prices were around $ 50,000- $ 250,000. Today, GNSS receivers capable of both code and phase measurements are available for up to $ 100[1].

GPS modules generally have a variety of positioning features, including standard positioning service (SPS), static positioning, precision point positioning (PPP), post-processing kinematics (PPK), and real-time kinematics (RTK) GPS [2]. Single-receiver, single-position solution accuracy may not be sufficient in many applications where low-cost high-accuracy location solutions are needed, such as automatic transport service, unmanned aerial vehicle, geodesy, agriculture and the GNSS mass market [3].

In this study, the positioning performance of single frequency receivers will be discussed by transmitting the correction data in a base station created with a single frequency GNSS receiver using the internet protocol (NTRIP) using open source U-Center and RTKLib software[4, 5].

2. METHODS AND DEVICES USED

In order to obtain real-time location data using the low-cost GNSS receiver, the base station correction data must be sent to the receiving part. In this study, single frequency Ublox C94m8p receiver was used as base station (Figure 1).

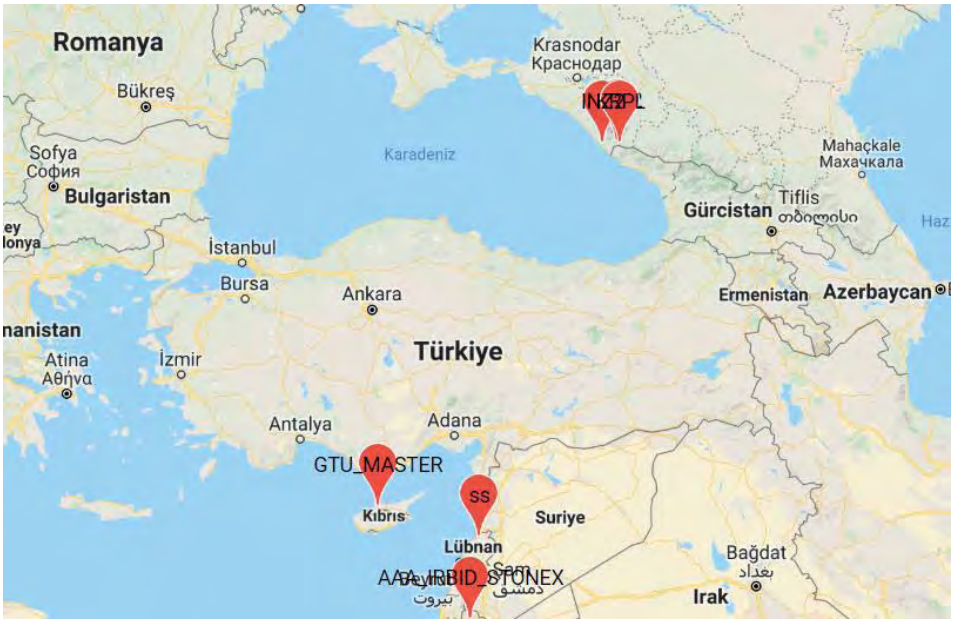

Figure 2. *GTU Base Station (RTK2go NTRIP-Caster user monitoring screen)*

U-Center software, which uses Ublox products and allows the configuration of the receiver, provides an NTRIP-Caster service to which correction data can be sent. However, RTK2go[6] base station operator, which is an NTRIP-Caster that does not require static IP, was preferred. Open source RTKLib server software was used to send RTCM correction messages to this base station operator.

Table 1: Devices used simultaneously

Location	Method	GNSS Receiver	Antenna-Frequency
Base1	(NTRIP Caster)	**Ublox C94m8p** (Low cost)	Ublox- Single f. (L1)
Base2	(RINEX data for PPK)	**Leica GS14** (High-Grade)	Leica –Double f. (L1-L2)
Rover	(NTRIP-Client)	**Ublox C94m8p** (Low cost)	Ublox -Double f. (L1-L2)
	(RINEX data for PPK)	**Ublox ZED-F9P** (Low cost)	

The Ublox C94-m8n receiver card is connected to the computer via a USB port. However, the transfer of the data on the radio on the UART-1 port is done. It is necessary to determine in advance which message data is transmitted via the RTCM. RTCM messages are defined as GPS+GLONASS configuration on the device. These messages are 1005 (Reference station coordinates), 1077 (GPS observations), 1087 (GLONASS observations) and 1230 (GLONASS code measurements). In order to eliminate the GLONASS integer ambiguity, the message 1230 must be forwarded. However, this is sent every 10 seconds to take advantage of the radio capacity. If BeiDou satellite data will be used, the message 1127 (BeiDou observations) will also have to be selected in the message settings. (Figure 2).

In the rover part, a single frequency Ublox C94m8p receiver was used and RINEX data was recorded with U-Center open source software to a computer in UBX format at 1 second intervals. The U-Center software also acts as the NTRIP client, and the position data after the received correction messages have been recorded. In order to compare the post-processing data, RINEX data were collected with Leica GS14, a dual frequency geodesic GNSS receiver located near the base station.

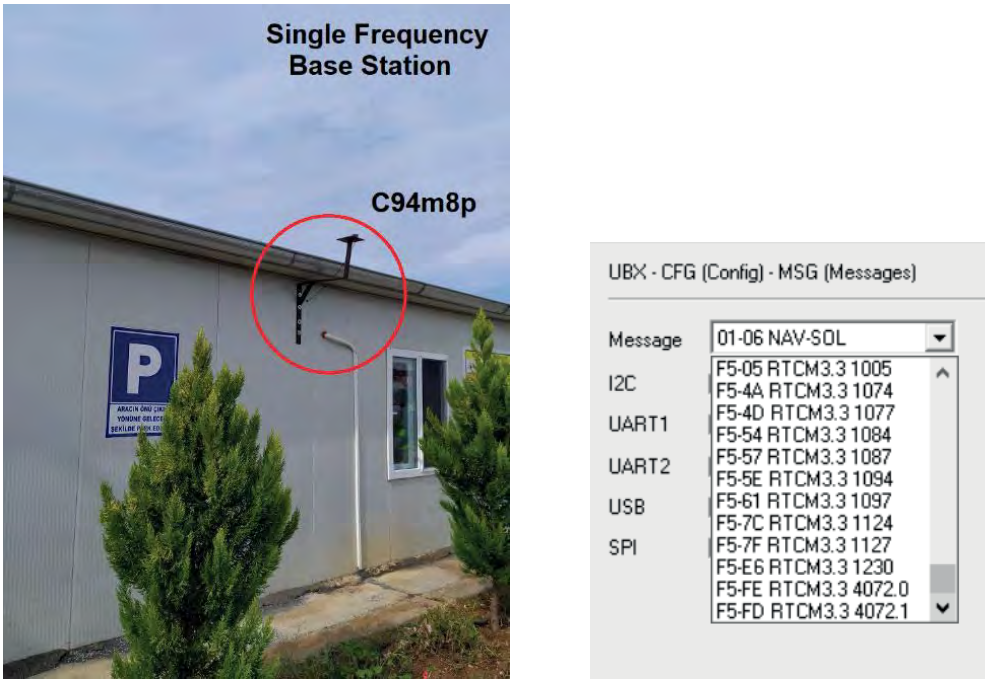

Figure 2. *Ublox C94-M8P base station on the left, messages sent to the rover on the right*

2.1 Single frequency C94m8p receiver

The Ublox C94M8P single frequency GNSS receiver card is sold as a single receiver if used via NTRIP-Caster (Figure 3). However, thanks to an internal radio transmitter on the card, it can be used as stationary and rover. In this application, the radio transmitter was disabled because correction data will be sent over the network. The 72-channel u-blox M8 engine supports GPS (L1C / A), GLONASS (L1OF), BeiDou (B1I) frequencies. RTK has a update rate of 5Hz in positioning. In static measurements, this is 10 Hz. However, in this application, 1 Hz data range was configured on the rover [7].

Figure 3. *Ublox C94-M8P single frequency RTK application card on the left ($ 180), GPS patch antenna on the right ($ 15-25)*

2.2 Dual frequency ZED-F9P receiver

The ZED-F9P receiver is a dual-frequency, low-cost GNSS receiver recently launched by Ublox. The 184 channel u-blox F9 engine supports GPS (L1C / A, L2C), GLONASS (L1OF, L2OF), GALILEO (E1-B / C, E5b), BeiDou (B1I, B2I) satellites. RTK has a update rate of 5Hz, while static measurement is 20Hz. The convergence time is less than 10s and it is 6 times faster than the C94M8P receiver (Figure 4) [8].

Figure 4. *Ardusimple SimpleRTK2B dual frequency RTK application card based on ZED-F9P ($ 200) on the left, multi-band GPS patch antenna on the right ($ 53)*

2.3 Dual-frequency Leica GS14 receiver

The Leica Viva GS14 is a professional dual-frequency GNSS receiver that supports 120 channels of GPS (L1, L2, L2C), GLONASS (L1, L2), BeiDou (B1, B2) and GALILEO (E1, E5b). It has 5 Hz position update and 20 Hz data record for RTK. The convergence time is 4 s (Figure 5) [9].

Figure 5. *Leica Viva GS14 dual frequency professional GNSS receiver*

3. RESULTS AND DISCUSSION

To test single and dual frequency Ublox GNSS receivers in a dynamic environment, the location data of a test site at a distance of 8.5 km and 3.6 km from the base station were collected with U-Center open source software. Both rovers were recorded in the same sky (Figure 5).

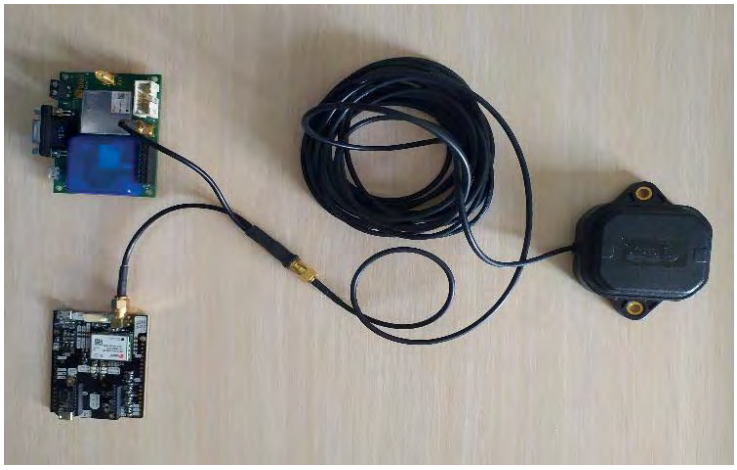

Figure 6. *Rover test platform (Ublox C94m8p and ZED-F9P)*

At the same time, RINEX data was recorded at 1 second intervals to obtain PPK data from the base station. PPK and N-RTK data of single frequency receiver were compared with PPK data of dual frequency ZED-F9P receiver.

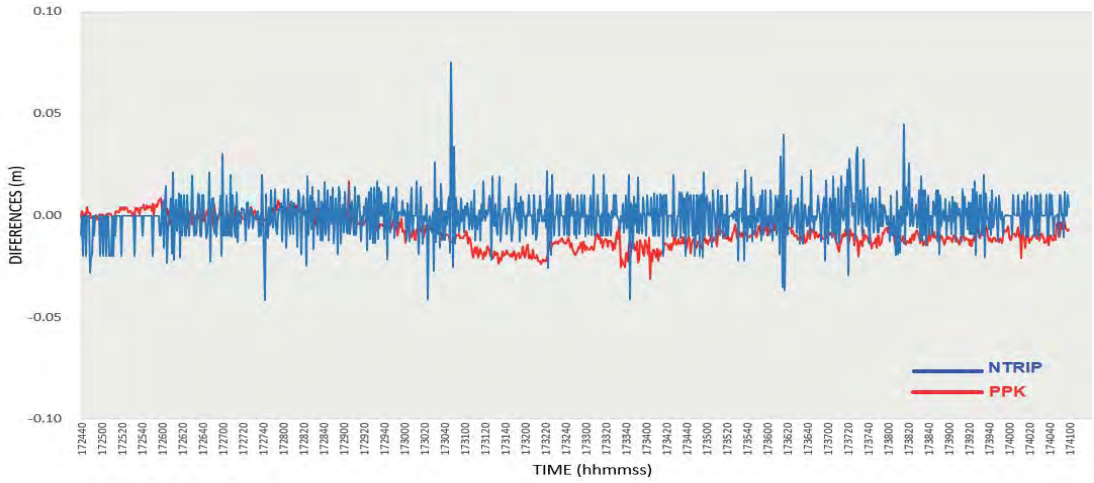

Figure 7. *Distance differences over time interval t_1-t_2*

The distance vector between time t_1 and t_2 was calculated as PPK with the dual frequency GNSS receiver. The distance vector of the single frequency receiver obtained by the N-RTK method was compared and a maximum error of 8 cm was observed. It was also compared with the PPK distance solution between the time t_1 and t_2 of the single frequency receiver. Here it is seen that the max 3 cm (Figure 7).

When the results obtained from the two-frequency PPK coordinates were considered fix and the coordinate data calculated for each t moment were examined, the differences in the north and east coordinates of PPK and N-RTK were found to be around a few cm, but the N-RTK up value reached dm level (Figure 8, Figure 9).

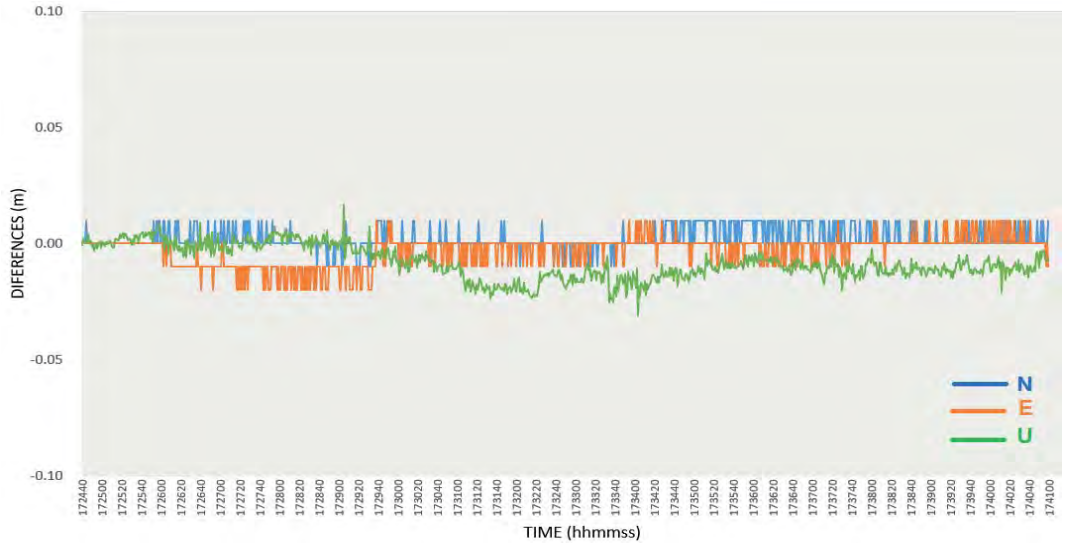

Figure 8. *PPK coordinate differences of single frequency GNSS receiver at time t*

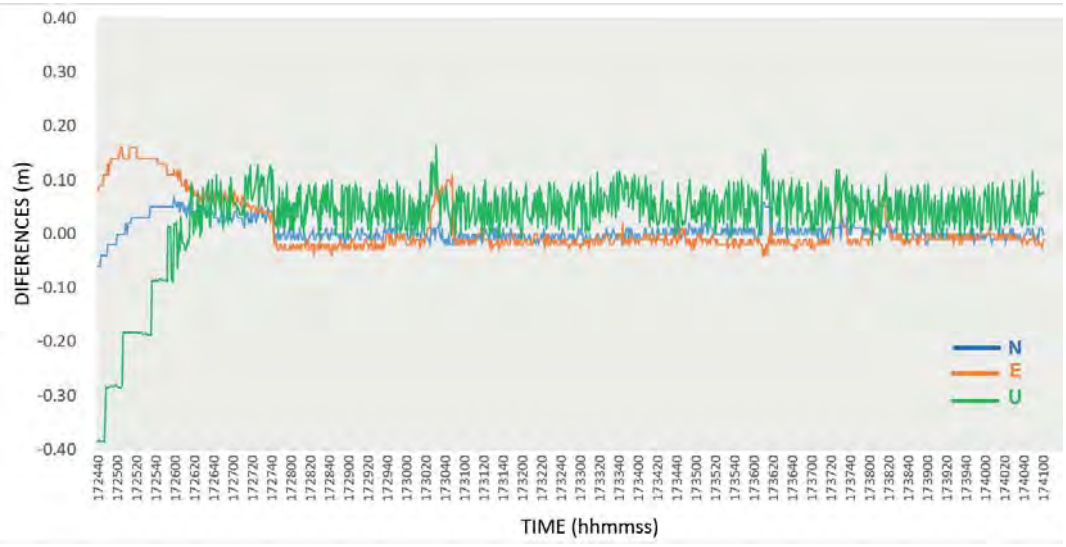

Figure 9. *N-RTK coordinate differences of single frequency GNSS receiver at time t*

4. CONCLUSION

The N-RTK and PPK performance of the low-cost single-frequency GNSS receiver is compared with the PPK performance of dual-frequency geodesic and high-performance GNSS receivers. The small size of the modules of single frequency devices and the good performance of open source software such as U-Center and RTKLib provide advantages in real-time positioning that require low-cost and centimeter accuracy. However, a good internet connection and clear sky conditions should be provided.

In this study, the PPK vertical positioning performance of the single frequency GNSS receiver appears to be more effective than the N-RTK positioning performance. However, both methods give precision of a few cm in the horizontal position. This location solution is slightly lower than that provided by geodesic receivers. However, the solution quality can be applied in systems that are cost-effective and reasonably require medium / high precision. On the other hand, low-cost GNSS modules have very small form factors and consume very low power compared to survey-grade GNSS receivers; All these features make these modules cost-effective for GNSS-based mass market applications and solution development.

ACKNOWLEDGEMENT

This study, published by the authors, is part of a dissertation on "Positioning Performance of Low Cost GNSS Receivers in Unmanned Aerial Vehicles (UAV)".

REFERENCES

1. Odolinski R.; Teunissen P. J. G. "GPS+BDS RTK: A low-cost single-frequency positioning approach" (2017), GPS World.

2. Atunggal D.; Ma'ruf B.; Sunantyo T.A.; Rokhmana C.A. "Evaluation on the Performance of Single and Dual Frequency Low Cost GPS Module Observation using Geodetic Antenna" (2018), Communications in Science and Technology.

3. Mahato S.; Santra A.; Dan S., Rakshit P., Banerjee P. ;Bose A. "Preliminary Results on the Performance of Cost-effective GNSS Receivers for RTK" (2019), URSI AP-RASC.

4. Ublox U-Center Open Source Software. https://www.u-blox.com/en/product/u-center (02.11.2019)

5. RTKLib Open Source Software. http://www.rtklib.com/ (02.11.2019)

6. RTK2go NTRIP Server. http://www.rtk2go.com/ (02.11.2019)

7. Ublox C94m8p RTK Application Board. https://www.u-blox.com/sites/default/files/C94-M8P-AppBoard_UserGuide_%28UBX-15031066%29.pdf (02.11.2019)

8. Ublox F9 high precision GNSS module. https://www.u-blox.com/sites/default/files/ZED-F9P_ProductSummary_%28UBX-17005151%29.pdf (02.11.2019)

9. Leica GS14. https://leica-geosystems.com/products/gnss-systems/smart-antennas/leica-viva-gs14 (02.11.2019)

Detection of ground motions in coastal area

Mila Atanasova [1], Hristo Nikolov [2]

[1]National Institute of Geophysics, Geodesy and Geography-BAS, Bulgaria
Phone: +359 2 979 33 54, E-mail: mila_at_zl@abv.bg

[2]Space Research and Technology Institute – Bulgarian Academy of Sciences, Bulgaria
Phone: +359 2 979 2458, E-mail: hristo@stil.bas.bg

ABSTRACT

Landslide processes are considered to be the major part of the natural hazards occurring on the northern part of the Bulgarian sea side. Their monitoring can be done by direct measurements in dedicated GNSS networks, which is the most accurate method. The objective of this study is to provide solid grounds for monitoring of the landslide processes using innovative methods by combining GNSS and SAR data. This goal will be to achieved by implementation the following two sub-objectives: first, establishment a verified methodology for extracting high-quality information from SAR images aimed at continuous monitoring of landslide areas integrating interferometric images (IFI) and in-situ GNSS data and second, based of freely accessible data provided by ESA and national sources to create a working prototype of an information system for monitoring and preventing the effects of earth crust movements (landslides, falls, etc.). One of the scientific tasks to be solved includes the development of methodological approaches to compare the results of the combined processing of interferometric images from SAR, in-situ measurements by permanent GNSS stations from the national NIGGG network in the area of study and geodetic measurements of a newly built test network a specific area on the Northern Black Sea coast of Bulgaria subject to landslide processes. After the primary processing of the data from three sources, their reconciliation which will form a geodatabase for subsequent spatial analysis envisaged in GIS environment.

KEYWORDS: ground motion, GNSS, InSAR, landslide monitoring

1. INTRODUCTION

The main objective of this research is monitoring the ongoing landslide processes by complementary use of SAR and GNNS data. It will be achieved by means of proved methodology for continuous monitoring of landslide areas by integrating information from interferometric images and GNSS data from permanent and local geodetic networks. The outcome of this study will deliver reliable information for the ongoing risky geo-processes for the region of the Northeastern Bulgaria, known with several large active landslides. These results could provide better understanding of the origin and dynamics of current landslide processes as well as assessing the resulting hazards by creating thematic maps. The selection of the mentioned area is based on information provided by the national authority responsible for the monitoring and keeping track of the landslides according to which over the past two years their number has almost doubled.

In this study are selected landslides located at the coastal zone of NE Bulgarian Black Sea. The selection of this region is based on the fact that until now more than 120 landslide events have been registered in the districts of Varna and Dobrich, and 80% of landslides affect the coast line. As contributing factor provoking the interest of this specific area is the fragile stability of its slopes which can be undermined even by single event such as abrasion, erosion, prolonged rainfalls, seismic, etc.

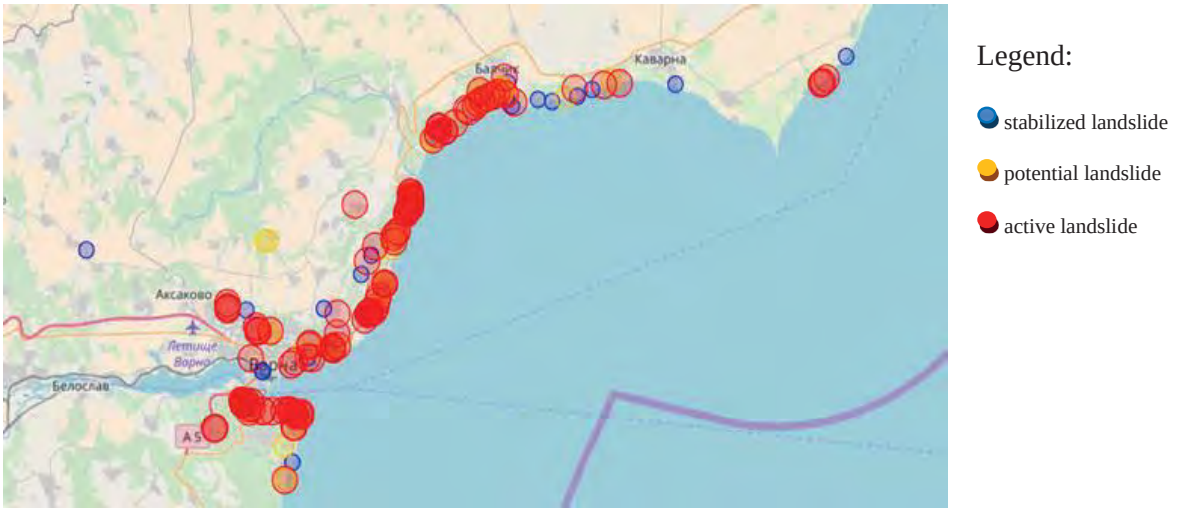

Figure 1 *Map of active, stabilized and potential landslides in NE Bulgaria (according to GIS of the Ministry of Regional Development and Public Works (MRDPW) [1].*

In the present research the authors investigated a short strip along the Black Sea starting from city of Varna and ending at Kaliakra cape. The area is about 80 km long, where large numbers (more than 120) of irregularly distributed landslides have been registered and are monitored by the competent authorities MRDPW (Fig.1). From geological point of view most of the landslides located in this region are of complex nature [2-3].

Obtaining reliable data on the ongoing risky geo-processes and obtaining adequate and reliable information about them on the current state of the Earth's surface is a key factor in tracking the origin and dynamics of landslide processes as well as assessing the resulting threats to the population and infrastructure. This is the main reason why it is necessary to develop and implement a rapid and accurate method for their operational observation. One possible solution proposed in this paper is to use the information derived from differential interferometric data processing from the synthesized aperture radar (SAR) data, based on which Earth's crust deformations are registered with magnitude of centimeters. Results from SAR data processing unambiguously indicate the presence of these movements in certain zones of these areas, but verified in-situ GNSS measurements are also required to obtain validated information. From what it was said above formulated is the main objective - studies of the landslide processes through the use of innovative methods. This objective is achieved through implementation of the following: extraction of high quality and reliable information on SAR images focused on regular monitoring of landslide areas integrating interferometric imaging and GNSS data. Based on the freely available SAR data and the software provided by ESA, as well as data from national sources is make a prototype of an archive for monitoring the movements of Earth's crust (landslides, subsidence, etc.).

In the past decades the northeastern Black Sea coast of Bulgaria has been the subject of scientific research and geodetic surveying by the former "Laboratory of Geotechnics" BAS and "Central Laboratory of Higher Geodesy" today, the Department of Geodesy. By the mid-1990s a geodynamic network was built for monitoring the landslide processes around the town of Balchik [4]. Due to intensive construction activities of the coastal area in the last 20 years and the lack of funding for research and its maintenance it is assumed that some of the points of the said network (pillars for precision instrument positioning) were destroyed. Nevertheless an extensive and comprehensive methodology for geodetic investigations of

landslides was developed [5]. In it underlined is the significance of the following issues – type, size and form of the landslide; velocity of the displacements; availability of stable areas in vicinity of the studied object; the capability of the equipment to be used as required by the desirable precision.

2. METHOD

2.1 Synthetic aperture radar (SAR) data and DInSAR processing

In the next paragraphs provided will be short description of the SAR data and the processing steps used to produce the interferometric images (IFIs) that were the combined with the geodetic data in studying the landslides. The SAR data that have been processed are from a constellation comprised of two satellites (A and B) Sentinel-1 mission freely distributed by ESA and can be obtained from Scientific Data Hub [6]. Every satellite has revisiting time of 12 days which means that one and the same area is imaged every 6 days by one of the satellites. The SAR instrument is a C-band radar (corresponding to a wavelength of 5.56cm) with right-looking line of sight (LOS) regardless of the orbit direction, and operates in four acquisition modes stripmap, interferometric wide swath (IW), extra-wide swath and wave mode. For interferometric processing single look complex (SLC) data obtained in IW mode are to be used since in it not only the amplitude of the backscattered signal is available, but its phase too. The phase signal is of crucial importance since after appropriate processing it delivers information about the changes in the distance to the objects on the Earth's surface between two satellite overpasses [7].

DInSAR (SAR Interferometry) is a method that uses SAR data to produce topographic and surface motion maps based on information about the deformations based on interferometric phase. It is based on the acquisition of complex-valued data over the same area at different time and uses the difference found in the phase signal to detect the horizontal/vertical changes caused by ground deformations. Since in the measured phase there are two components – one corresponding to the distance of single object from the surface and next reflecting the phase change by the environment – a measure of quality is introduced, known as coherence, an estimate for the noise level in the phase signal. It is widely accepted that for the single pixel

from the phase band of the IFI to be considered reliable the same pixel in the coherence band should have value above 0.3. Low values of this parameter are due to many external factors such as troposphere state at the time of acquisition, the position of the satellite in its "orbital tube" which defines perpendicular baseline, presence of vegetation in the area of study, etc.

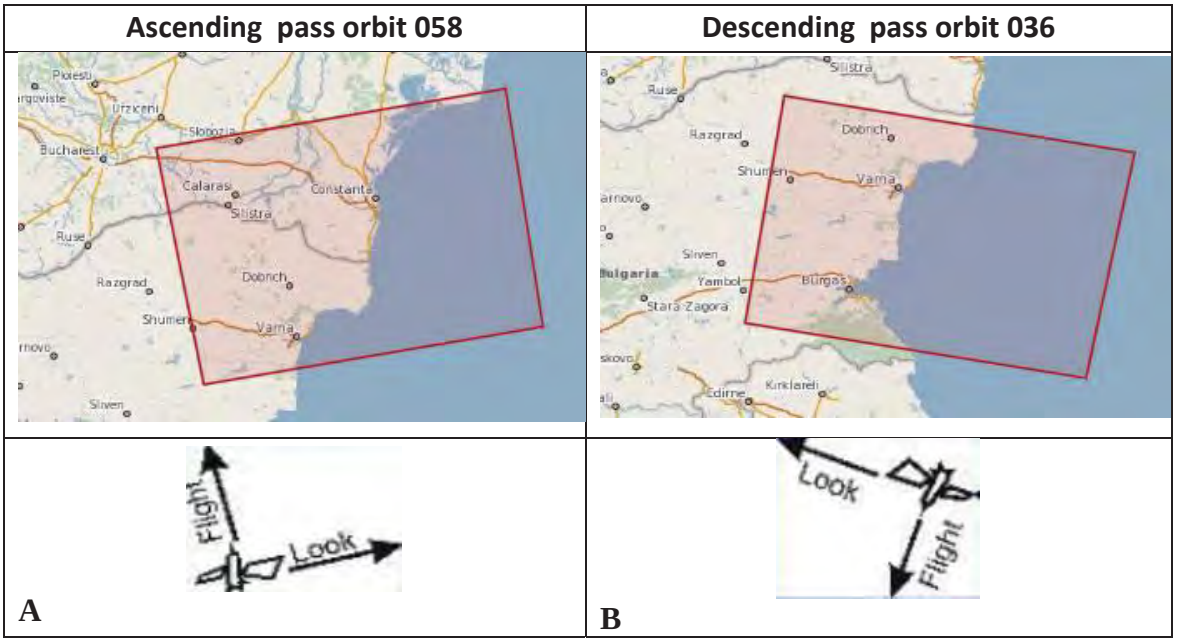

Figure 2. *Shape of the SAR images from ascending (A) and descending orbits (B)*

It needs to be underlined that the information provided by the phase signal is a relative with regard to the one of the SAR images, often called "master", and with regard to a point on the ground which is assumed to be stable. One more thing that needs to be addressed here is that all detected deformations are measured along the LOS of the SAR instrument and for this reason additional calculations are needed for properly combining GNNS and SAR data.

A drawback of the SAR data that needs mentioning is that they cannot detect ground changes along the track of the satellite which results in better registering movements in east-west direction then in north-south. This can be overcome by combining information derived from IFIs from both ascending and descending orbits (see fig. 2). An advantage offered by the DInSAR method is the possibility to register ground changes over large or difficult-to-access areas thus delivering more information than by single in-situ acquisition. This does not mean

that it can completely substitute terrain measurements, but rather to provide details on the surface movements for larger areas in the investigated region.

The processing of the SAR data to produce deformation map includes the following steps – precise coregistration of both images used in the IFI based on the orbital data, formation of the interferogram, filtering and speckle reduction, phase unwrapping, and geocoding. The most important step is the phase unwrapping since only after it the information contained in the phase signal is converted into ground displacements. At this step by integrating the phase difference between neighboring pixels at every 2π the difference in altitude in LOS is generated after any integer number of altitudes of ambiguity has been deleted.

2.2 GNSS for landslide monitoring

When geodynamic networks are used to study landslide processes several types of surveying points are used – ones fixed on geologically stable terrain, others located inside the landslide.
In order to accomplish the objectives of the present study targeted at regular monitoring of the Earth's crust movements geodetic data from two sources are needed – a time series from stable points in vicinity of the investigated area and such from built geodynamic network in and around the landslide body. The former the stable points situated in non-deformable zone are provided by the permanent GNSS network, while the latter shall originate from already established network.
Newly created one located inside the specific landslide, which will is being measured few cycles. The main advantage of GNSS measurements is the fact that no direct visibility is required between the points at which high precision receivers are placed and thus making this technology competitive to the classical geodetic measurements. Sometimes it is difficult to make measurements of the landslide processes at the GNSS points of the geodetic network due to technical reasons e.g. the presence high trees result in deterioration and lack of GNSS signal from the satellites; difficult terrain; the danger posed by semi-destroyed buildings and facilities; administrative obstacles - private ownership of the properties in the active part of the landslide. Here it needs to be stated that the deformation analysis of the geodynamic networks will be made after the third measurement cycle which will result in real assessment of the local movements of Earth's crust [8].

3. RESULTS AND DISCUSSION

The outcomes of this research can be summarized as follows – extensive research was performed on the recent activations of landslides, collected were historical and contemporary geodetic data about the deformations caused by them, created was a local image archive of Sentinel-1 satellites for the region of Northeastern Bulgaria; justified was the need to use local DEM in order to improve the quality of the produced interferometric images; created was a set of interferometric images at fixed intervals - monthly, every 4 months, 8 months, a year; generated are thematic interferometric images used in mapping deformations for the region of Northern Black Sea coast, confirmed is the strong relationship between geodetic and satellite derived information concerning ongoing landslide activities.

First step to achieve the main objective was to create a local archive with Sentinel-1A/B images for the region of Northeastern Bulgaria consisting of about 300 SLC images. For mapping the deformations in the studied region produced were interferometric images at intervals 4 and 8 months.

The stated time intervals were used since one of the main factors influencing the quality of the IFIs is the vegetation and for this reason only autumn and spring scenes were processed. Also most of the landslides activations are taking place at those seasons a fact which is supporting justification for this selection. Another factor that should be accounted before producing IFI is the presence of snow – used data are from days with no snow coverage [9]. In the figure 3 presented are the displacements found in an IFI produced from images dated Nov 26th 2014 an Dec 27th 2015.

In figure 4 are shown the displacements obtained from the IFI 01Jan2015-21Dec2016. The color of the pixel represents the surface movement in metric unit for the investigated period ranging from dark blue to purpura. Particularly vulnerable areas are shown in purpura, less vulnerable in yellow and green. The landslide activity assessment resulting from this research shows (Fig. 4) that subsidence range from -48 mm to -69 mm.

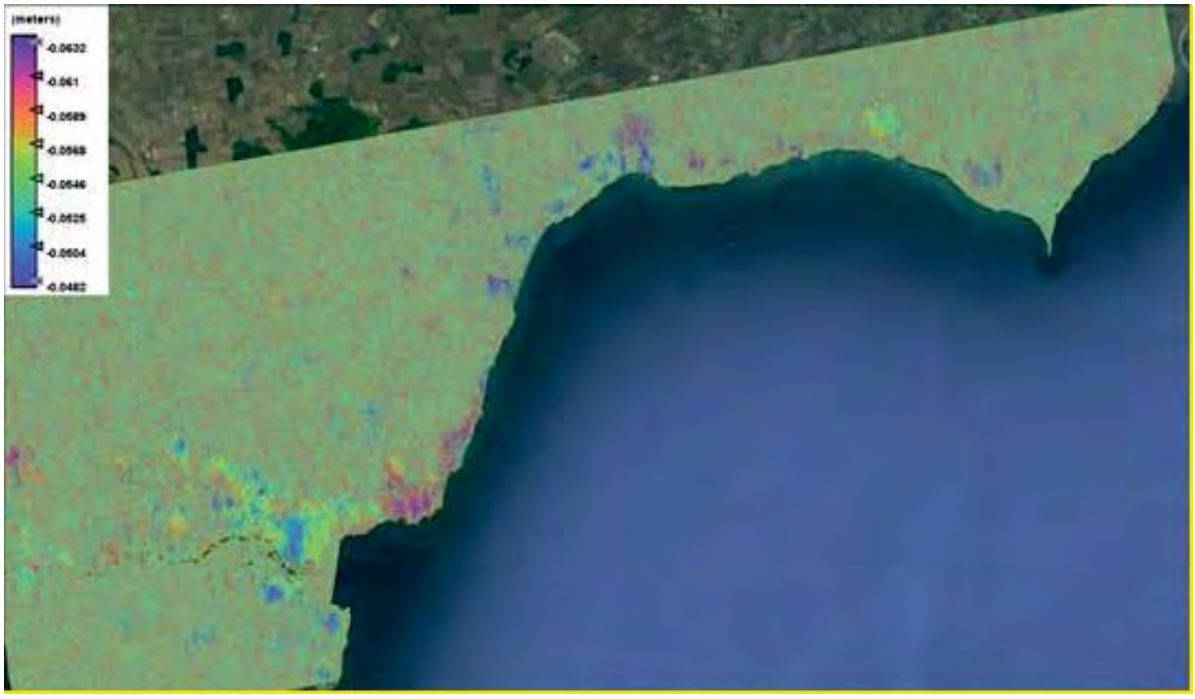

Figure 3. *Displacements obtained from IFI 26Nov2014-27Dec2015*

Figure 4. *Displacements obtained from IFI 01Jan2015-21Dec2016*

.

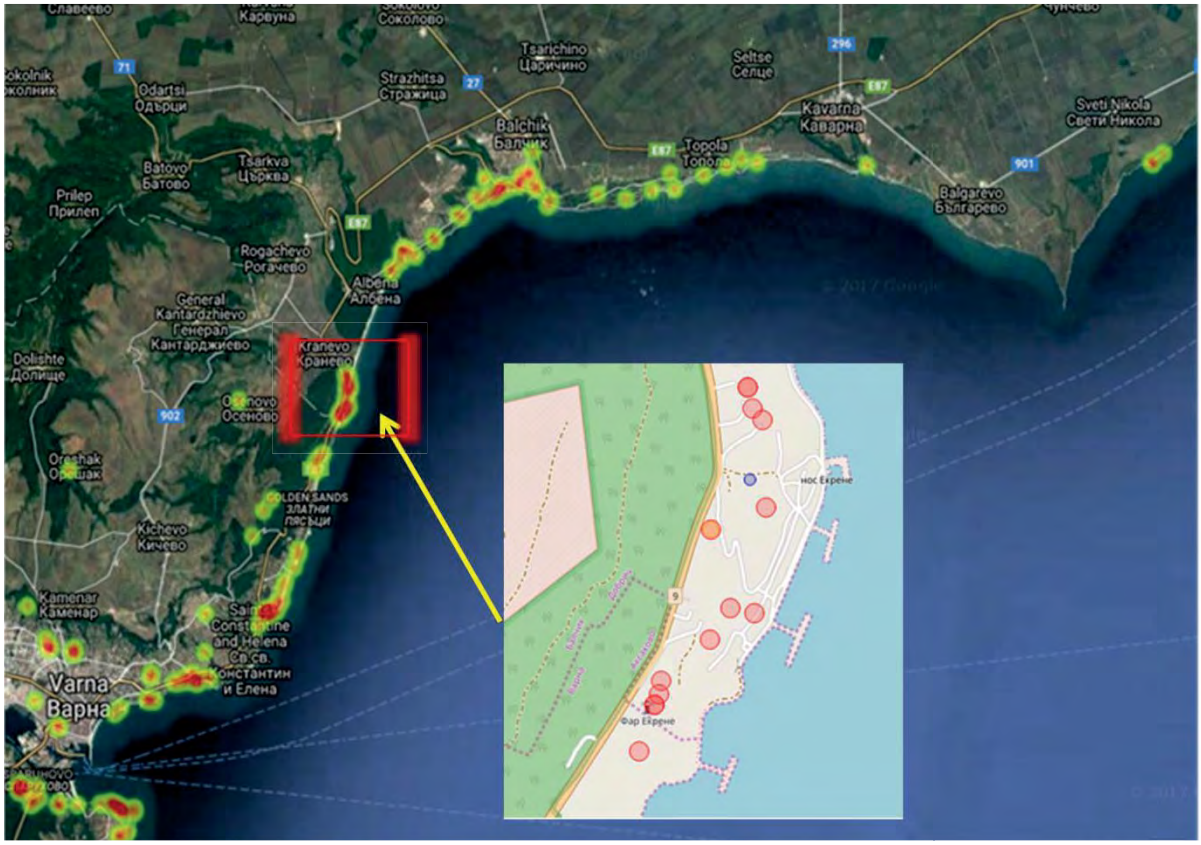

Figure 5. *Raster heat map based on displacement values at the points of landslides registered*

The area of interest or this study is the one marked by the shaded red quadrate in which concentration of ground deformations has been observed (see Fig. 5). This area is called "Dalgiya yar" - a landslide circus that covers several active landslides, whose boundaries overlap and for this reason difficult to differentiate. Even for some of the investigated landslides located in this area, a smaller landslide could be delineated inside them. This phenomenon can be seen on figure 6. On this figure shown are the registration landslide codes as they appear in the landslide register maintained by MRDPW and the boundaries of the separate landslides are shown in different colours.

The landslide "Fara" located between the village of Kranevo and the touristic resort "Panorama" covers only the low stage of the circus. This landslide with assigned

identification number VAR 02.54145-01-17 in the register of landslides in the Republic of Bulgaria activated on October 13th 2012 destroying the lighthouse and villas.

Figure 6. *ID codes from MRDPW register and the boundaries of the investigated landslides.*

The landslides and collapses in the activated area in 2013 are due to human activities that took place in the last 20 years mainly the illegal construction, as well as to the fact that the requirements for civil engineering were not respected. For example instead of building small bungalow houses two- and three-storey buildings were erected. In some of them swimming pools have been built whose waters flow down the slope of the landslide. Those flows had

very serious impact, as the water from the said pools flows down the slope where there is no drainage. Water supply network accidents often occur there, because landslides that tear the water mains slip and, in turn, water – regardless of its origin (from the water supply system, rains, or pools) leads to activation and development of landslide and collapse processes.

In this research the authors set their attention on a landslide located in the investigated area – "Dalgiya yar" – "Fara". This specific object was selected since only for it old data from previous geodetic measurements and geological observations was made available. This fact made possible the comparison between in-situ data and data obtained from satellites. For landslide "Fara" two measurement cycles were carried out (one in 2013 and one in 2018) on a network consisting of 8 points located on the road I-9 above the landslide [10]. The geodetic data were gathered by Geozastita Varna Ltd. according to the assignment by the Ministry of Regional Development which concludes Contract № RD-02-29-372/11.11.2013. under the Law on Public Procurement for Execution with the subject "Geodetic survey of landslides between bus stop Fara and bus stop Obzor, and Kranevo village". The contractor is Survey Group" Ltd., (see fig 7).

Figure 7. *The geodetic network used by Survey Group" Ltd. to measure the displacements along the road (colored in blue).*

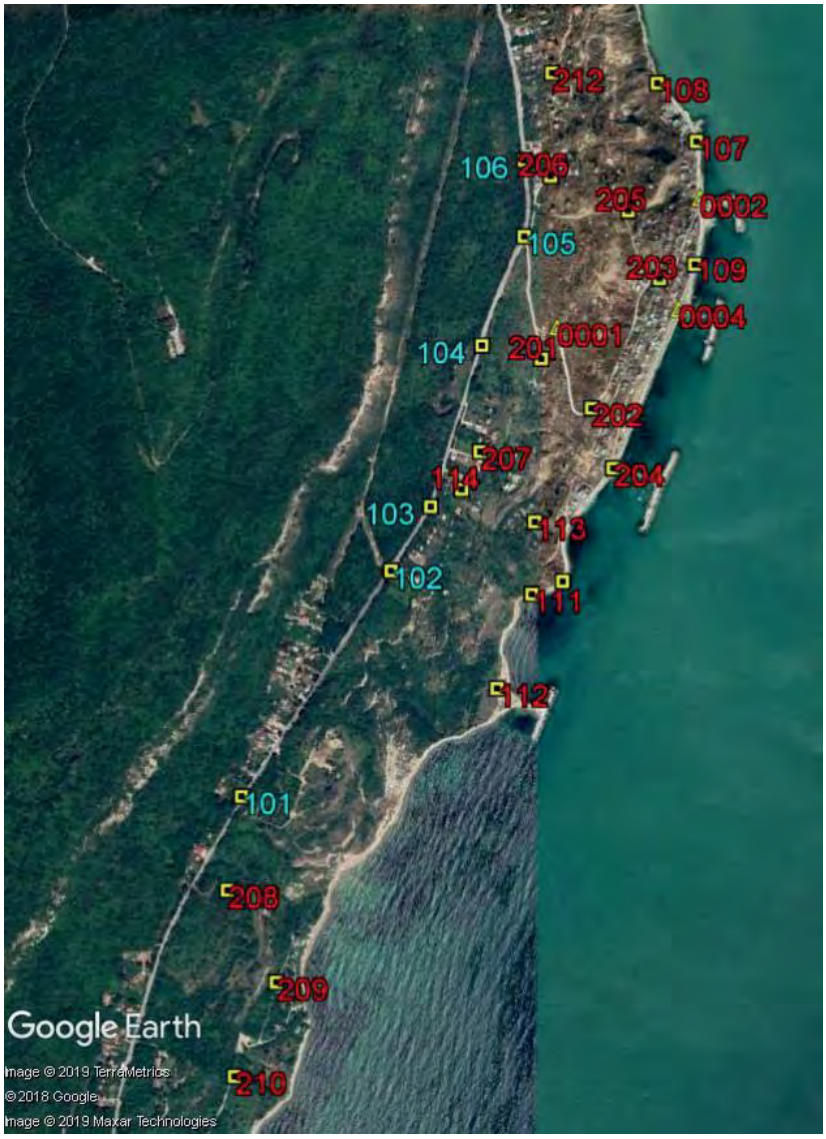

Figure 8. *Points of the new geodynamic network in and around the landslide "Dalgiya yar"*

For this specific study a geodetic geodynamic network in and around the landslide area "Dalgiya yar" – "Fara" (see fig 8) was created. It consists of of a total of 30 stabilized points with some being metal pipes 35 cm long while other are metal bolts nailed in the rock. The GNSS measurements were made with 2 receivers of type CHC i80 GNSS System, with horizontal precision 2.5 mm + 0.1 ppm RMS and vertical 3.5 mm + 0.4 ppm RMS and 1 receiver - P3E GNSS sensor used for reference station. All measurements were made in the static method. For stable points located in the non-deformable zone of the landslide used were

stations of permanent GNSS network maintained by the private company GeoVara Ltd. In this research used were 2 stations Varna and Krushartsy. The newly created geodynamic network (see Fig.8) located inside the landslide investigated will is being measured once a year. In the said geodynamic network "Dalgiya yar" are included all old six points that were discovered on the ground from the network used to track deformations along the road (the blue colored in Fig. 7 and Fig 8). The first measurement cycle in the geodynamic network was performed during a campaign in June 19-23 2019. Thus we have a third cycle of measuring road deformations The results of the GNSS measurements were processed using „CHC Geomatics Office 2" software in the WGS Coordinate System. "BGSTrans" software was used for transformation of coordinates from the World Geodetic System WGS-84 to national coordinate system the 1970, K-7. Also created was general reference register for points in the 1970 coordinate system and Baltic height system order to compare years 2013 and 2018 (see Table 1).

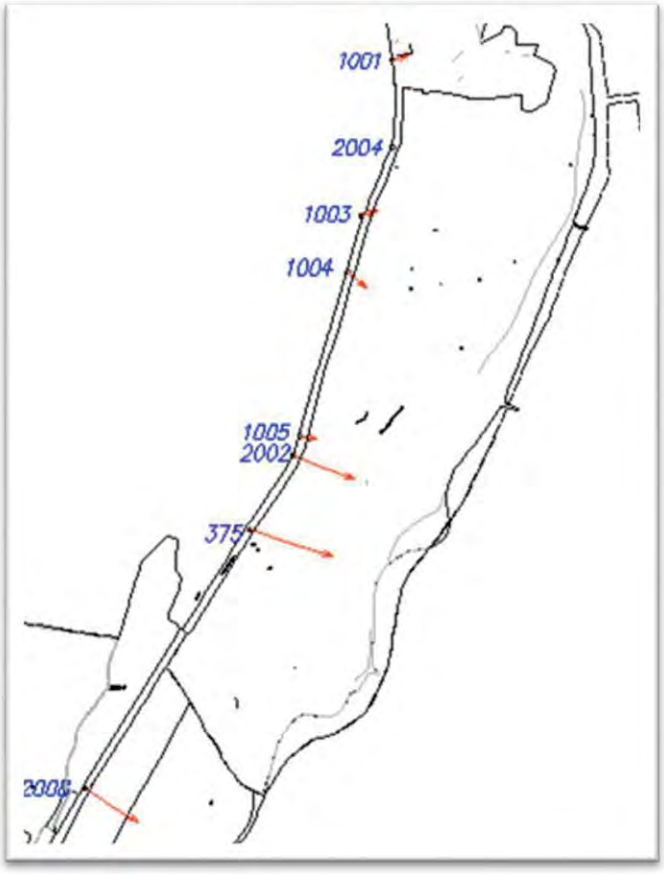

Figure 9. *Horizontal displacements for the period 2013–2018*

The results of 2013 were compared to those from 2018 (see Table 1). A drawing was created with the horizontal displacements of 8 points along the road to illustrate the analysis of the displacements of the section under consideration from 2013 until 2018 (see Fig 9). The largest displacements for the area under consideration were found in the southwest part of the site. A register of points for landslide deformation analysis has been developed.

Table 1: *Tables should horizontal and vertical deformations for the I period 2013 – 2018; II period June 2019 - August 2018 yr.*

old	***new***	***2018 - 2013***				***June 2019 - August 2018***			
point	**name**	**ΔX /m/**	**ΔY /m/**	**S /m/**	**ΔH/m/**	**ΔX /m/**	**ΔY /m/**	**S /m/**	**ΔH/m/**
2008	101	-0.325	0.513	0.607	-0.088	-0.033	0.079	0.085	-0.056
375	102	-0.265	1.00	1.034	-0.465	-0.068	0.066	0.094	-0.072
2002	103	-0.278	0.586	0.648	-0.375	-0.002	0.148	0.148	-0.054
1004	104	-0.161	0.181	0.242	-0.068	0.048	0.094	0.105	-0.074
2004	105					0.001	0.092	0.092	0.019
1005		-0.034	0.161	0.164	-0.038				
1003		0.035	0.155	0.159	0.017				
1001	106	0.039	0.134	0.139	0.054	0.053	0.069	0.087	-0.037

After analysis of horizontal and vertical deformations recorded for the period 2013 - 2018 along the road I-9 it was found that the values of horizontal displacements are in the range 0.61 - 1.04 m and vertical are in the range -0.09- -0.47m.. It was established that the overall movement of the terrain lies in ~~its~~ southwestern part of the area after one of the turns of the road I-9 (for all 4 points considered). The maximum displacements are at point numbered 375 – horizontal -1.04m and vertical – 0.47m. In the northern part of the road I-9 in the considered range slight movements of the terrain were found in the range 0.14-0.24 m in the horizontal plane and from 0.05 to –0.07 m in height (for all 4 points considered). The maximum displacement was found to be at point 1004 –0.24 m the horizontal plane [10].

For II period (June 2019-August 2018, only 10 months), horizontal and vertical deformations are at lower values 0.08-0.10 m in the horizontal plane and vertical max.0.075 m.

4. CONCLUSION

The obtained results provide grounds to draw the conclusion that both data sources used lead to similar results (the displacements are in the range of centimeters) confirming the overall behavior of the studied landslides. The differences between them could be contributed to large number of external factors affecting the SAR data such as vegetation and temporal decorrelation. When comparing the two methods it should be taken into account that the values of the IFIs elements correspond much larger area (15m by 15m) while the GNNS are point measurements. Nevertheless the outcomes of this study are encouraging and the authors will continue their research of investigating landslide zones by means of SAR data. It should be noted that for more of them no data from GNSS surveys are available and this is one possibility to register their development. Other factor that supports the usage of IFIs in landslides investigation is that the price of the final product and the man effort both being much lower compared to those necessary for GNSS measurements.

ACKNOWLEDGEMENT

This paper has been made available with the financial support provided by National Science Fund, call identifier "Financial support for basic research projects on societal challenges – 2018" Project number КП-06-ОПР 06/1. The authors would like to express their gratitude to GeoVARA Ltd, Geozastita Varna Ltd., Ministry of Regional Development and Public Works и Survey Group Ltd. for the provided data.

REFERENCES

1. Ministry of Regional Development and Public Works, Map of landslide http://gis.mrrb.government.bg/

2. Berov B., Ivanov Pl., Dobrev N., Nankin R., Krastanov M.,(2013) State of the Art for Landslides Along the North Bulgarian Black Sea Coast, Landslide Science and Practice Volume 5: Complex Environment, Springer, Editors: Claudio Margottini, Paolo Canuti, Kyoji Sassa, 2013 pp 97-102.

3. Bruchev, I., Dobrev, N., Frangov, G., Ivanov, Pl., Varbanov, R., Berov, B., Nankin, R. Krastanov, M. The landslides in Bulgaria — factors and distribution, Geologica Balc. 36, 3-4; pp 3-12, 2007.

4. Tsenko T. (1993) Assessment of the use of geodetic methods in the study of landslides, abrasion and erosion. Journal of the Bulgarian Geological Society, Laboratory of Geotechnics - BAS, year LIV, vol. 1, 1993 (in Bulgarian)

5. Milev G., Tsenko T., Avdzhiev M., Vassileva K., Simeonova R., Tosheva R., Filipov V., (1987) Instruction for the study of landslides by geodetic methods, Sofia, GUKK, 143c. 1987 (in Bulgarian)

6. https://scihub.copernicus.eu/dhus/#/home

7. Luis Veci, TOPS Interferometry Tutorial http://sentinel1.s3.amazonaws.com/docs/S1TBX%20TOPSAR%20Interferometry%20with%20Sentinel-1%20 Tutorial.pdf, 2016

8. Vassileva, K., G. Valev, Atanasova-Zlatareva M. (2017) Deformation analysis of the Balkan Peninsula from GPS data 2011-2016. Coordinates, XIII, 12, Thomson Press (India), 2017, ISSN:0973-2136, 31-34 http://mycoordinates.org/deformation-analysis-of-the-balkan-peninsula-from-gps-data-2011-2016/

9. https://www.stringmeteo.com/ (accessed January 2019)

10.Ministry of Regional Development Contract /№ RD-02-29-372/11.11.2013 subject "Geodetic survey of landslides between bus stop Fara and bus stop Obzor, and Kranevo village"- contractor - Survey Group" Ltd.

11.Geozastita – Varna Ltd. (2018), Annual Report under Contract No РД-02-29-198 / 02.05.2018 and Additional Agreement № РД-02-29-198 (1) / 06.11.2018 Preventive activities related to registration and monitoring of the landslide areas on the territory of the Republic of Bulgaria and the areas with abrasive processes along the Black Sea coast in the regions of Dobrich, Shumen, Varna, Burgas (in Bulgarian).

On the use of genetic algorithm in component substitution-based pansharpening

Volkan Yilmaz

Artvin Coruh University, Geomatics Engineering Department 08100 Artvin, Turkey
Phone: +90 462 377 2761, E-mail: volkanyilmaz.jdz@gmail.com

ABSTRACT

Pansharpening aims to transfer the spatial details of a high resolution panchromatic (PAN) image into a lower resolution multispectral (MS) image, producing an image of superior spatial and spectral quality. Various pansharpening methods have been reported so far. Of these, the component substitution (CS)-based pansharpening methods are among the most widely used ones, owing to their advantages of being fast and easy to implement. The biggest advantage of the CS-based pansharpening methods is that they are very good in enhancing the spatial resolution. However, they tend to distort the colors of the input MS image. This is due to the fact that there is not a standard color preservation procedure when producing the intensity component used by the CS-based methods. This, of course, motivates the analysts to develop more advanced approaches to produce more efficient intensity components. This study utilized the genetic algorithm (GA) within a CS-based pansharpening framework (GA-CS) to produce the optimum intensity component to eliminate the CS-based methods' disadvantage of distorting the color characteristics. The GA-CS framework estimated the optimum band weights using the GA. The GA-CS framework was conducted in two test sites, which were acquired by the WorldView-2 and IKONOS satellites. The performance of the GA-CS method was qualitatively and quantitatively compared against those of widely-used CS-based methods Gram-Schmidt (GS), Brovey, Modified Intensity-Hue-Saturation (MIHS), Principal Component Analysis (PCA) and Ehlers. Qualitative and quantitative evaluation results showed that the GA-CS framework produced images of superior color quality, compared to the other methods used. It was also concluded that the metaheuristic algorithms may be used as an efficient means of optimizing pansharpening results.

KEYWORDS: pansharpening; genetic algorithm; image fusion; metaheuristic algorithms; component substitution

1. INTRODUCTION

Pansharpening enables the production of images of superior spectral and spatial resolution by integrating the spatial details of a higher-resolution panchromatic (PAN) image and a lower-resolution multispectral (MS) image. Pansharpening process aims to identify the contributions of the input MS and PAN images to the pansharpening result. To this aim, a wide variety of approaches have been developed to produce spatially superior images without deteriorating the color characteristics. However, none of the pansharpening methods developed so far is able to properly keep the color content while increasing the spatial detail quality. In fact, some pansharpening methods focus much on producing sharper images, whereas some of them on keeping the color content [1]. For example, the multiresolution analysis-based methods, which aim to combine the spectral and spatial features in sub-levels of the input images, are more successful in keeping the color content than in transferring the spatial details of the input PAN image [2]. The component substitution (CS)-based pansharpening methods transform the input MS image from Red-Green-Blue (RGB) space into another one, where the color and spatial detail features can be separated in different components. In this new space, the input PAN band is swapped with the intensity component containing the spatial detail features. An inverse transform results in the pansharpened image in RGB space [3]. The CS-based methods offer spatially superior images, however, they tend to distort the color characteristics of the input MS image [4]. The CS-based methods are also fast and easy-to-implement, which makes them open for any improvements.

The success of the CS-based pansharpening methods is highly dependent on the procedure followed to produce the intensity component. To find an optimum compromise between the color and spatial detail quality, it is necessary to produce an intensity component that is statistically very similar to the input PAN image [1]. An inefficient procedure is likely to lead to color distortions. Hence, this study used the genetic algorithm (GA) to optimize the intensity component used by the CS-based methods.

The reminder of the paper is as follows. Section 2 will provide theoretical information about some of the most widely-used CS-based pansharpening methods. Section 3 will introduce the test sites and the used GA-based pansharpening procedure. Section 4 will provide the qualitative and quantitative evaluation results for all pansharpening methods used. Section 5 will present the conclusions drawn from this study.

2. CS-BASED PANSHARPENING METHODS

This study compared the performance of the used GA-based pansharpening method against those of the Brovey (BRV), Principal Component Analysis (PCA), Gram-Schmidt (GS), Modified Intensity-Hue-Saturation (MIHS) and Ehlers (EHL). This section provides some brief theoretical information about the principles of these methods.

The BRV method produces an intensity component by summing all the input MS bands. Each MS band is then multiplied by the input PAN band and the result is divided by the intensity component to obtain the pansharpened bands [5].

The PCA method transforms the input MS image into another space where there is almost no correlation between the transformed components. The input PAN band is substituted by the first principal component, which contains the spatial detail information. A reverse PCA transform results in the pansharpened image [6].

The GS, which is very similar to the PCA, simulates a low-resolution PAN image by using all input MS bands. The obtained low-resolution PAN image is combined with the input MS bands. A GS transform is then applied to the combined data. The input PAN band is replaced by the first GS component and an inverse GS transform is conducted to produce the pansharpened bands [7].

The IHS pansharpening method applies an IHS transform on the input MS bands. The intensity component produced from the transform is replaced by the input PAN band and an inverse IHS transform gives the pansharpening result. The limitation of the IHS method is that it is able to cope with three MS bands. Siddique [8] developed the MIHS method to process MS images with more than three spectral bands. The MIHS method benefits from trilateral band combinations of the input MS image.

The EHL method applies an IHS transform on the input MS image. A fast Fourier transform (FFT) is then applied on the intensity component and the input PAN band. The intensity spectrum is filtered with a low-pass filter and the PAN spectrum is filtered with a high-pass filter. An inverse FFT is applied on both filtered spectrums and the results are summed to obtain the new intensity component. Finally, an inverse IHS transform is applied using the new intensity component to produce the pansharpened image [9,10].

2. MATERIAL AND METHOD

2.1 Test sites and data

This study was conducted in two test sites, which are in the city of Trabzon, Turkey. The first test site is a mixture of an urban and rural area monitored by the WorldView-2 satellite in 2012. The WorldView-2 image offers eight MS bands with a spatial resolution of 2 m and a PAN band with a spatial resolution of 50 cm. The radiometric resolution of the WorldView-2 image is 11 bits. The second test site is an urban area monitored by the IKONOS satellite in 2003. The IKONOS satellite provides four MS bands with a spatial resolution of 4 m and a PAN band with a spatial resolution of 1 m. The IKONOS image has a radiometric resolution of 11 bits. The test sites are shown in Figure 1.

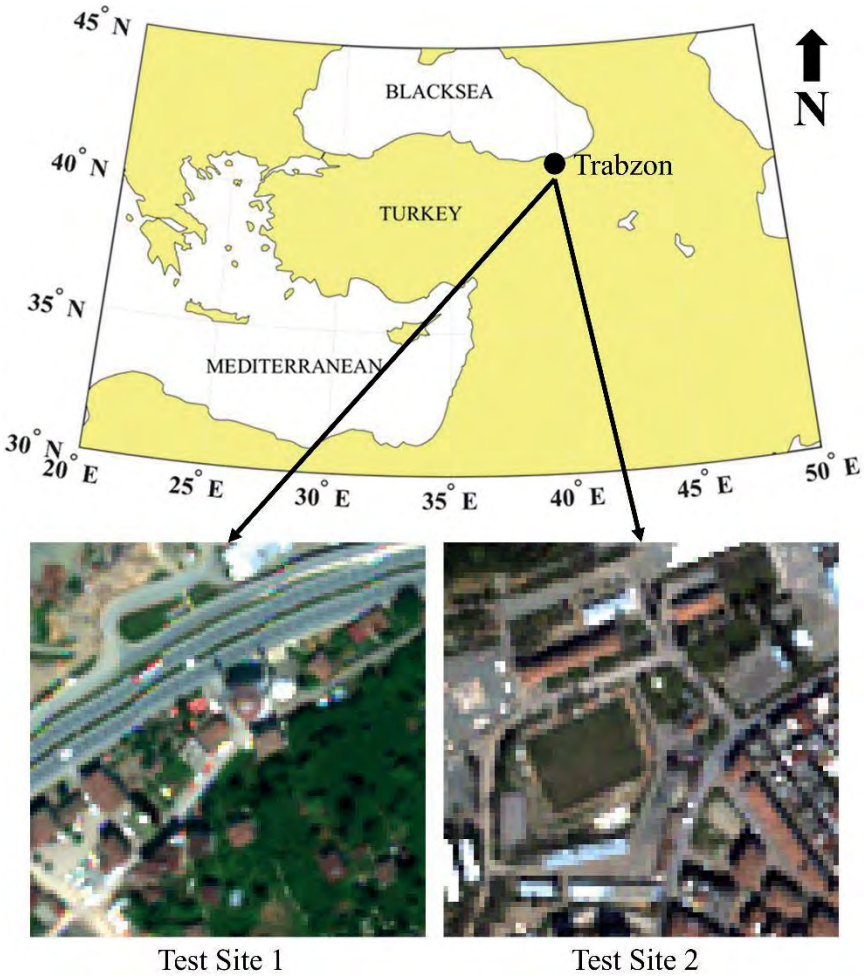

Figure 1. Test sites

2.2 GA-based pansharpening approach

A general CS-based pansharpening framework can be defined as follows [11-13]:

$$\mathrm{P}_n^h = \mathrm{MS}_n^r + g_n \cdot (\mathrm{PAN} - \mathrm{I}) \quad (1)$$

where, $n = 1, \dots, N$ (N is the total number of the input MS bands), MS_n^r is the nth band of the upsampled MS image, P_n^h is the nth band of the pansharpened image, PAN is the input PAN image, I is the intensity component and g_n is the nth gain. The intensity component (I) can be defined as a linear combination of the input MS bands:

$$\mathrm{I} = \sum_{n=1}^{N} w_n \cdot \mathrm{MS}_n^r + b \quad (2)$$

where, w_n denotes the band weights and b is a constant. The $(\mathrm{PAN} - \mathrm{I})$ image is used to inject the spatial details into the MS bands. This study proposed to use the GA to estimate the optimum band weights (w_n). The GA, which is a randomized search and optimization technique, is based on the principles of evolution [14]. The GA searches for the optimum solution in a population that is composed of randomly-generated chromosomes [15]. The genes, which are the possible solutions, form the chromosomes. The first step of the used framework was to generate a population randomly. All the elements of each chromosome was used to calculate an intensity component (see Eq. 2), which was used to compute the objective function given in Eq. 1. The fitness of each chromosome was investigated by calculating the Erreur Relative Globale Adimensionalle de Synthese (ERGAS) [16] metric between each MS band and corresponding pansharpened band. Considering the principle of the survival of the fittest, a group of chromosomes were selected to produce new offsprings through the crossover and mutation [15]. The crossover operator exchanges a certain amount of information between two parent chromosomes to generate two child chromosomes. On the other hand, the mutation operator makes random changes on the chromosomes to increase the variety in the population. Once the crossover and mutation operators were applied, the old offsprings were replaced by the new ones. The selection, crossover and mutation operations were implemented on new populations until a termination criterion was met or the maximum iteration number was reached. In this study, the population size was set to 50, the maximum number of iterations were set to 100, the crossover rate was chosen as 0.95 and the mutation rate was chosen as 0.001 for both test sites.

3. RESULTS

This section provides the qualitative and quantitative evaluation results for all the pansharpening methods used. It should be noted that any successful pansharpening method should keep the color features of the input MS images while improving the spatial detail quality. Figure 2 shows the pansharpening results for the sites 1 and 2. As seen in the figure, in both sites, the GA-based CS pansharpening framework (GA-CS) produced the most consistent colors with the input MS images while increasing the spatial detail quality. In the site 1, the EHL method was found to be the second most successful one after the GA-CS. Figure 2 also shows that the BRV, PCA, GS and IHS methods distorted the colors of the input MS image in the site 1. As seen in the figure, these methods produced colors that are visually different from those in the input MS image. It can also be inferred from Figure 2 that all pansharpening methods except the PCA managed to transfer the spatial details of the input PAN image of the site 1. In the site 2, the EHL and PCA methods produced the most consistent colors after the GA-CS method. It can also be concluded from Figure 2 that the GS and IHS methods caused paleness in the site 2. When it comes to spatial detail quality, all pansharpening methods were successful in producing images of high spatial detail quality in the site 2.

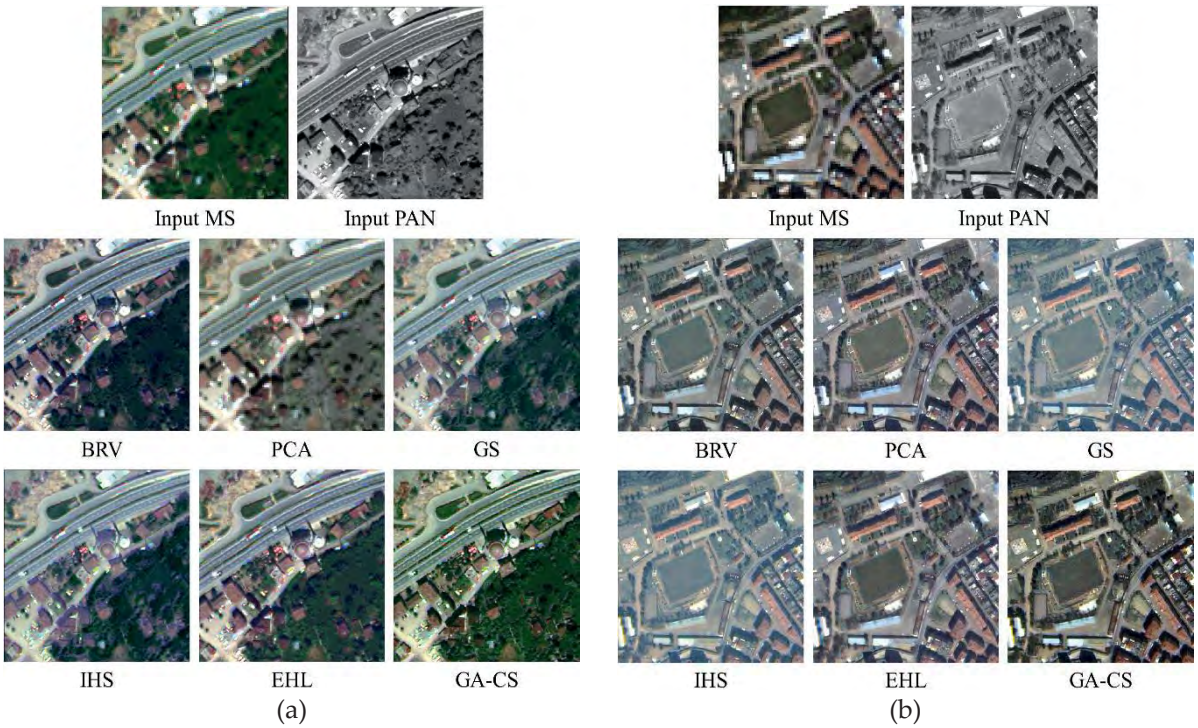

Figure 2. Pansharpening results for the sites 1 (a) and 2 (b)

For a robust performance evaluation, the spectral quality of each pansharpened image should be investigated with quality metrics. To this aim, the Structural Similarity Index (SSIM) [17], ERGAS, Spectral Residual Based Similarity (SR-SIM) [18], Spectral Information Divergence (SID) [19] and correlation coefficient (CC) [20] metrics were computed between the pansharpened bands and corresponding input MS bands. These metrics were applied considering the widely-used spectral quality evaluation protocol proposed by Wald et al. [21]. This protocol implies that any pansharpened image degraded to the size of the input MS bands should be identical to the input MS image. Hence, the spectral quality evaluation metrics used in this study were computed between the input MS bands and degraded pansharpened bands. Table 1 shows the spectral quality metric values calculated for the test sites. It should be noted that the best value for each metric is shown bold. As seen in the table the GA-CS results achieved the bets values from almost all metrics, which is in good agreement with visual findings (see Figure 2). In the site 1, the GA-CS result got the best SSIM, ERGAS and SR-SIM values of 0.879, 2.459 and 0.953, respectively. Table 1 also shows that, in the site 1, the GS, MIHS and EHL methods achieved the best metric values after the GA-CS. On the other hand, the BRV and PCA caused the greatest amount of color distortion in this site. In the site 2, the pansharpened image obtained by the GA-CS method received the best SSIM, ERGAS, SR-SIM and CC values of 0.866, 3.650, 0.938 and 0.923, respectively. The GS and MIHS methods achieved the best spectral metric values after the GA-CS. It should be noted that the EHL method showed a lower performance in the site 2, compared to the site 1.

Table 1: Spectral quality evaluation metric values.

Site	Method	SSIM	ERGAS	SR-SIM	SID	CC
1	**BRV**	0.073	23.554	0.587	**0.004**	0.941
	PCA	0.291	27.894	0.832	0.293	0.640
	GS	0.798	3.016	0.945	0.011	0.958
	MIHS	0.776	3.231	0.936	0.012	0.950
	EHL	0.869	3.435	0.945	0.016	**0.968**
	GA-CS	**0.879**	**2.459**	**0.953**	0.005	0.966
2	**BRV**	0.174	3.916	0.676	0.008	0.908
	PCA	0.824	4.285	0.921	0.014	0.913
	GS	0.855	3.982	0.933	0.006	0.917
	MIHS	0.841	3.927	0.930	**0.005**	0.907
	EHL	0.804	7.714	0.919	0.048	0.920
	GA-CS	**0.866**	**3.650**	**0.938**	0.007	**0.923**

The biggest advantage of the used GA-CS method is that it is easy-to-implement and does not rely one complex computations. The GA's ability to search the optimum results in very large populations brought a huge advantage when estimating the optimum band weights. It is possible to further improve the performance of the GA-CS method by changing the crossover and mutation rate parameters at the expense of a higher computation time. These parameters should be selected carefully to ensure the diversity of the population. However, finding the optimum population size parameter is very challenging and the users generally find it by trial-and-error, which is a disadvantage for the GA-CS method.

4. CONCLUSION

This study utilized the GA to optimize the band weights used to produce the intensity component within the CS-based pansharpening. The qualitative and quantitative evaluation results showed that the used GA-CS methodology achieved the best color quality, compared to the other CS-based methods used. It can be concluded from the results that the optimizing the band weights with the GA enabled the preservation of the color content while increasing the spatial detail quality, which eliminated the biggest disadvantage of the CS-based methods. Future studies will focus on developing more efficient metaheuristic algorithms-based pansharpening approaches to achieve spectrally and spatially superior results.

REFERENCES

1. Yilmaz, V.; Serifoglu Yilmaz, C.; Güngör, O.; Shan, J. A genetic algorithm solution to the gram-schmidt image fusion. Int. J. Remote Sens. 2019, just-accepted, 1-28.

2. Gogineni, R.; Chaturvedi, A. Sparsity inspired pan-sharpening technique using multiscale learned dictionary. ISPRS J. Photogramm. Remote Sens. 2018, 146, 360-372.

3. Ghassemian, H. A review of remote sensing image fusion methods." Inform. Fusion. 2016, 32, 75-89.

4. Ghahremani, M.; Liu, Y.; Yuen, P.; Behera. A. Remote sensing image fusion via compressive sensing. ISPRS J. Photogramm. Remote Sens. 2019, 152, 34-48

5. Hallada, W.A.; Cox. S. Image sharpening for mixed spatial and spectral resolution satellite systems. Proceedings of the 17th International Symposium on Remote Sensing of Environment, Ann Arbor, MI, 1983, 1023-1032

6. Chavez, P.S.; Kwarteng, A.Y. Extracting spectral contrast in Landsat Thematic Mapper image data using selective principal component analysis. Photogramm. Eng. Remote Sens. 1989, 55 (3), 339-348.

7. Laben, C.A.; Brower, B.V. Process for enhancing the spatial resolution of multispectral imagery using pansharpening. US Patent No. 6,011,875, filed 29 April 1998 and issued 4 January 2000 to the Eastman Kodak Company, 2000.

8. Siddiqui, Y. The modified IHS method for fusing satellite imagery. Proceedings of the ASPRS Annual Conference, Anchorage, Alaska, 2003, 5-9.

9. Ehlers M. Spectral characteristics preserving image fusion based on Fourier domain filtering. Remote Sensing for Environmental Monitoring, GIS Applications, and Geology IV, Proceedings of SPIE, 2004, 5574, 1, 1-13.

10. Klonus, S.; Ehlers, M. Image fusion using the Ehlers spectral characteristics preserving algorithm. GIsci Remote Sens. 2007, 44, 93–116.

11. Choi, J.; Yu, K.; Kim, Y. A new adaptive component-substitution-based satellite image fusion by using partial replacement. IEEE Trans. Geosci. Remote Sens. 2011, 49 (1), 295-309.

12. Dou, W.; Chen, Y.; Li, X.; Sui, D.Z. A general framework for component substitution image fusion: An implementation using the fast image fusion method. Comput. Geosci. 2007, 33 (2), 219-228.

13. Wang, W.; Jiao, L.; Yang, S. Novel adaptive component-substitution-based pan-sharpening using particle swarm optimization. IEEE Geosci. Remote Sens. Lett. 2014, 12 (4), 781-785.

14. Holland H. Adaptation in Natural and Artificial Systems. Ann Arbor: The University of Michigan Press, 1975.

15. Tang, K.S.; Man, K.F.; Kwong, S.; He, Q. Genetic algorithms and their applications. IEEE Signal Process. Mag. 1996, 13 (6), 22-37.

16. Wald, L. Data Fusion. Definitions and Architectures - Fusion of Images of Different Spatial Resolutions. Presses de l'Ecole, Ecole des Mines de Paris France, 2002.

17. Wang, Z.; Bovik, A.C.; Sheikh, H.R.; Simoncelli, E.P. Image quality assessment: from error visibility to structural similarity. IEEE Trans. Image Process. 2004, 13 (4), 600-612.

18. Zhang, L.; Li, H. SR-SIM: A fast and high performance IQA index based on spectral residual. 19th IEEE International Conference on Image Processing, Orlando, FL, USA, 2012, pp. 1473-1476.

19. Strait, M.; Rahmani, S.; Markurjev, D. Evaluation of Pan-Sharpening Methods, UCLA Department of Mathematics, 2008.

20. Zeng, Y.; Huang, W.; Liu, M.; Zhang, H.; Zou, B. Fusion of satellite images in urban area: Assessing the quality of resulting images. 18th IEEE International Conference on Geoinformatics, Beijing, China, 2010, pp. 1-4.

21. Wald, L.; Ranchin, T.; Mangolini, M. Fusion of satellite images of different spatial resolutions: Assessing the quality of resulting images. Photogramm. Eng. Remote Sens. 1997, 63, 691-699.

Improving the classification accuracy of hyperspectral images: An analysis of feature selection approaches

Akhtar Jamil[1], Bulent Bayram[2], Erdal Alimovski[1]

[1]Istanbul Sabahaattin Zaim University, Department of Computer Engineering,34303 Istanbul, Turkey
Phone: +90 212 692 8780, E-mail: akhtar.jamil@izu.edu.tr; erdal.alimovski@izu.edu.tr

[2]Yildiz Technical University, Department of Geomatics Engineering, 34469 Istanbul, Turkey
Phone: +90 212 383 5329, E-mail: bayram@yildiz.edu.tr

ABSTRACT

The recent years have witnessed development of advanced airborne and spaceborne hyperspectral imaging systems which are capable of acquiring images with high spectral and spatial resolutions. These data are valuable source of information which can be used in various application to derive useful information such as land cover classification, precision agriculture, environmental monitoring etc. The presence of hundreds of bands in the acquired images provide fine details which can help identify even small objects. Although, the hyperspectral data provides detailed information about objects of interest, yet in the presence of the high dimensionality of data, we may run the risk of overfitting our model. Such models may show optimal performance on the training data however, they usually fail to generalize well for the unseen data and ultimately show very poor performance. This problem can be addressed by applying feature selection approach whose goal is to select the most relevant features out of the all available features. In this paper, we focus on dimensionality reduction techniques for classification of hyperspectral images. We particularly compare the performance of principal component analysis (PCA) and independent component analysis (ICA) methods for feature selection. The subset of selected features is then used to classify the input images into different land cover classes using random forest (RF) classifier. We tested our method on publicly available data set of Pavia University, Italy. The results indicated that both feature selection methods were effective for the classification of the hyperspectral data into nine different land cover classes.

KEYWORDS: land cover classification; hyperspectral data classification; principal component analysis; independent component analysis

1. INTRODUCTION

The classification of remote sensing images obtained with modern airborne and spaceborne sensors has recently become a popular research subject due to the increasing amount of data. With the advancement of sensor technology, hyperspectral images with high spatial resolution are constantly becoming more usable. Nowadays hyperspectral images are used in many fields such as agriculture, forestry, geology and military systems.

Hyperspectral images generally consist of more than a hundred spectral bands (usually 224) in the wavelength range of 400–2500nm [1]. Although, it provides detailed information about the earth surface, yet the presence of multiple spectral bands may cause the images to contain redundant information too, due to presence of high dimensionality of data also known as curse of dimensionality. Such redundant information in hyperspectral images not only increases the processing time but also can adversely affect the classification accuracy of the classifier. Therefore, it is more imperative to perform dimensionality reduction in the hyperspectral images as a pre-processing step to minimize the redundant information before the classification step is applied [2]. According to [3] and [4] it is possible to divide dimensionality reduction techniques in two main categories: supervised and unsupervised. Supervised techniques include linear discriminative analysis (LDA) [5], local Fisher discriminate analysis (LFDA) [6] etc. Whereas unsupervised techniques include principal component analysis (PCA) [7], Independent component analysis (ICA) [8], minimum noise fraction (MNF) [9] etc.

Dimensionality reduction in the domain of hyperspectral images is not a new research area as it is evident from the literature that a number of approaches have been proposed to overcome the curse of dimensionality. For instance, in [10] the authors evaluated the performance of PCA and ICA for classification of land use/land cover (LULC) over some parts of Nilgiris district. The experimental results show that ICA based classification performs better with an accuracy of %76.38 compared with PCA which accuracy ratio is %78.06. [11] presented comparison of PCA with non-linear techniques like Isomap, Multidimensional scaling (MDS), Local Tangent Space Alignment (LTSA) etc. for image classification. From obtained results, it is concluded that non-linear techniques for dimensionality reduction were more effective than PCA despite their high variance. To reduce the computational time in the classification task of hyperspectral images, authors in [12] applied dimensionality reduction

as a preprocessing step before applying the classification step. Instead of using PCA, they choose to use a noise-adjusted principal-components (NAPC) for dimensionality reduction. The results indicated that NAPC was effective for dimensionality reduction compared to the traditional PCA. Moreover, the results demonstrate that NAPC can better preserve the object information than PCA. [13] developed a parallel and distributed implementation of PCA based on cloud computing architectures. The proposed method was applied on several hyperspectral datasets, and obtained results demonstrates that presented method produced very high performance. In paper [14], a novel dimension reduction technique called minimum change rate deviation (MCRD) was introduced which is focused on spatial relation among neighboring pixels. In the paper it is highlighted that, proposed method surpassed PCA in retaining the required information for classification goal. In [15], a dimensionality reduction method based on neural networks is proposed. Researches presented a novel penalty function which successfully reduces the number of active neurons, that neurons correspond to the dimensionality of the data. It is concluded in the paper that the proposed penalty function is more efficient compared with the conventional penalties.

From literature we can deduce that the dimensionality reduction is a crucial preprocessing step that should be performed before the data is passed to the classifier. The output of this step will be the spectral information with less redundant information which means the selected channels will have high discrimination power. The selection of the dimensionality reduction methods is a matter of user preference, however, the method which is simple to implement, computationally inexpensive and provides optimal results will be highly preferred. Therefore, our focus in this research paper is to compare the performance of two simplest and easy to implement algorithms, i.e. PCA and ICA, as a preprocessing step for dimensionality reduction in hyperspectral image classification.

2. STUDY AREA AND DATA SET

We used the open source hyperspectral data set available online which is obtained for University of Pavia, Pavia, Italy. These images were acquired with the Reflective Optics System Imaging Spectrometer (ROSIS-03) optical sensor. The spatial size of this hyperspectral image is 610 × 340 pixels which was taken near the Engineering School at University of Pavia. The ROSIS-03 sensor provides 115 bands with spectral coverage ranging

from 0.43 to 0.86 μm. The spatial resolution is 1.3 m per pixel. The noisy channels were removed while remaining 103 spectral channels were used in the study. There are 43923 labeled samples in total and nine classes of interest. Figure 1 (a) presents false color images of this ROSIS-03 data while (b) shows the ground truth data for this image.

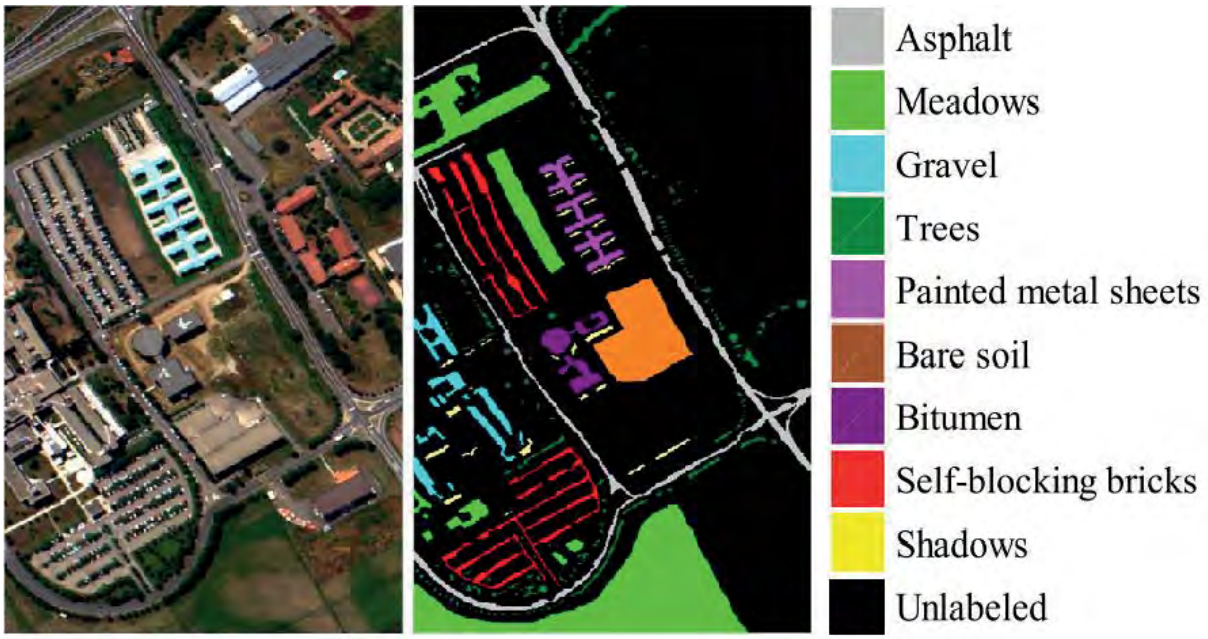

(a) (b)

Figure 1. *Pavia University a) Original data and b) Ground truth*

3. PROPOSED METHOD

The classification of hyperspectral data using RF classifier along with two feature reduction techniques (PCA and ICA) is evaluated. The spectral features are first passed though PCA and ICA individually and their output are classified by the RF classifier. The main objective was to evaluate the performance of PCA and ICA for dimensionality reduction to improve the overall classification accuracy for hyperspectral data classification. The following sections summarize the concepts of PCA, ICA and RF.

3.1 Principal Component Analysis

PCA is a technique of multivariate analysis that can be used to reduce a complex data set to a lower dimension which may help to reveal some hidden structures/patterns within the data. The main goal of PCA is to obtain the most important characteristics from data.

PCA calculates a feature subspace that maximizes the variance along the axes within the data. The covariance matrix is calculated from the input data and its Eigen vectors and their corresponding eigenvalues are obtained, which form the basis of PCA. The eigenvectors determine the direction to the new features space and eigenvalues determine their magnitude. The features with higher eigen values will be selected for further classification step.

3.2 Independent Component Analysis

ICA has been in use for long time and is one of the popular algorithm used for dimensionality reduction. It is a statistical technique which is particularly very useful for multivariable data analysis. Its main objective is to transform from a high dimensional space to relatively a lower n-dimensional space such that the new space with the transformed variables (components) describes the essential structure of the data containing the more relevant information from the sensors. The features present in the new feature space are supposed to be highly discriminative, therefore, they will be selected for classification in the next step.

3.3 Random Forest

The Random Forest algorithm is a supervised classification algorithm widely used in different classification tasks. This algorithm was proposed by Leo Breiman and Adèle Cutler in 2001 [16]. The random forest algorithm consists of a number of decision tree classifiers combined such that the final decision is based on the individual decisions made by each tree. This make the RF classifier more robust for decision making. The trees present in RF are characterized by the same number of nodes, but different data. The decisions of these different decision trees will be combined to give a final answer that represents an average response of all these decision trees.

3. RESULTS

In this paper, the most widely used hyperspectral data has been used to generate nine different classes using RF classifier. For training we used 80% of the available data for each class and tested with remaining 20%. Table 1 summarizes the land cover classes and the number of samples for each class. The RF classifier was trained with the default setting using Scikit-Learn library in python and anaconda environment. The obtained average classification

accuracies for each class have been reported in Table 2. The average overall accuracy for PCA and ICA remained 95.88 % and 95.22% respectively. These results indicate that both PCA and ICA are every effective for feature dimensionality reduction as they produced almost similar high classification accuracy on the test data.

Figure 2 shows the classification results obtained for PCA and ICA. It can be seen that the results are visually very similar which are also consistent with quantitative results. It is also worth mentioning that the processing time of ICA was little higher than the PCA. We run the experiments on a laptop with 2.7GHz processor and 16 GB RAM. We believe that both are equally efficient when it comes to the problem of feature reduction.

Table 1: ROSIS Pavia University lands cover classes and samples for each class.

Class	Land Over Class	Samples
1	Asphalt	6631
2	Meadows	18649
3	Gravel	2099
4	Trees	3064
5	Painted metal sheets	1345
6	Bare Soil	5029
7	Bitumen	1330
8	Self-Blocking Bricks	3682
9	Shadows	947

Table 2: Classification results for RF classifier using dimensionality reduction PCA and ICA

Land Over Class	RF Accuracy (%)	
	PCA	ICA
Asphalt	98.1	97.8
Meadows	95.3	96.5
Gravel	95.3	95.65
Trees	89.2	90.3
Painted metal sheets	93.1	90.25
Bare Soil	97.9	95.65
Bitumen	98.6	97.65
Self-Blocking Bricks	97.8	96.85
Shadows	97.65	96.36
Overall Accuracy	**95.88**	**95.22**

4. CONCLUSION

In this work a comparison between the results obtained for two methodologies in damage detection (PCA and ICA) using data driven from a Piezoelectric active system, were shown. Both methodologies allowed detecting the damages showing in most cases a clear distinction between the data from undamaged structure and the other three damage states. The results can change depending of the phase to being analyzed but in all cases it is possible to distinguish the presence of damage. In addition, it was shown some differences between the results using both methodologies, for instance the definition of the number of Components or the possibility of define different data set by identifying the kind of damage due to the separation that is possible to see in some of the phases. An important difference between PCA and ICA is related to the number of components used in each methodology, in the PCA case this number can be determined by the variance criteria, but in the ICA case don't exist a criteria for determining how many components represent the dynamic of the data, despite this, was showed that with just two components is possible to define the presence of damages, of course is necessary to evaluate all the combinations to determine which components show better results. One way to improve the results with ICA could be using another tool that includes all the Independent Components by each phase or performing data fusion including the components from all phases.

(a) (b)

Figure 2. *Classification results obtained from RF classifier, a) PCA b) ICA*

In this study we focused on dimensionality reduction for hyperspectral images to improve the classification accuracy of the classifiers. The presence of redundant data in the form of spectral information in hyperspectral images may adversely affect the classification accuracy of supervised classifiers. To alleviate the problem of curse of dimensionality we selected a subset of spectral information with higher discrimination power. To obtain this subset, we evaluated two well known and simple approaches: PCA and ICA. We found that both dimensionality techniques along with RF classifier were effective for classification of the hyperspectral images into nine different classes. Both approaches produced higher classification accuracies for University of Pavia data set.

In future, we would like to extend our method by applying deep learning based method for classification. The advantage of deep learning based approaches is that it can extract high level features from the input data automatically. Moreover, the classification accuracy of the deep learning methods are usually better than the traditional methods.

REFERENCES

[1] K. Thilagavathi and A. Vasuki, "Dimension reduction methods for hyperspectral image: A survey," *Int. J. Eng. Adv. Technol.*, vol. 8, no. 2, pp. 160–167, 2018.

[2] P. Ghamisi *et al.*, "Advances in Hyperspectral Image and Signal Processing: A Comprehensive Overview of the State of the Art," *IEEE Geosci. Remote Sens. Mag.*, vol. 5, no. 4, pp. 37–78, Dec. 2017.

[3] S. G. Bajwa, P. Bajcsy, P. Groves, and L. F. Tian, "Hyperspectral image data mining for band selection in agricultural applications," *Trans. Am. Soc. Agric. Eng.*, vol. 47, no. 3, pp. 895–907, 2004.

[4] P. S. Thenkabail, M. K. Gumma, P. Teluguntla, and A. Irshad, "PE & RS," vol. 80, no. 8, 2014.

[5] L. Zhang, Y. Zhong, B. Huang, J. Gong, and P. Li, "Dimensionality reduction based on clonal selection for hyperspectral imagery," *IEEE Trans. Geosci. Remote Sens.*, vol. 45, no. 12, pp. 4172–4186, 2007.

[6] W. Li, S. Prasad, J. E. Fowler, and L. M. Bruce, "Locality-preserving dimensionality reduction and classification for hyperspectral image analysis," *IEEE Trans. Geosci. Remote Sens.*, vol. 50, no. 4, pp. 1185–1198, 2012.

[7] C. Syms, "Principal Components Analysis," *Encycl. Ecol. Five-Volume Set*, vol. 1, pp.

2940–2949, 2008.

[8] P. Comon, P. Comon, I. Component, and P. Comon, "Independent Component Analysis , a new concept ? To cite this version : HAL Id : hal-00417283 Independent component analysis , A new concept ?*," . *Signal Process. Elsevier*, vol. 36, no. 94, pp. 287–314, 1994.

[9] A. A. Green, M. Berman, P. Switzer, and M. D. Craig, "A transformation for ordering multispectral data in terms of image," *IEEE Trans. Geosci. Remote Sens.*, vol. 26, no. 1, pp. 65–74, 1988.

[10] V. S. Pooja, M. Rafiq, and V. N. Mariappan, "Classification of Hyperspectral Image Using Principal Component and Independent Component Analysis," vol. 04, no. 03, pp. 145–154, 2017.

[11] J. Khodr and R. Younes, "Dimensionality reduction on hyperspectral images: A comparative review based on artificial datas," *Proc. - 4th Int. Congr. Image Signal Process. CISP 2011*, vol. 4, pp. 1875–1883, 2011.

[12] I. Kopriva, "Independent-component analysis for hyperspectral remote sensing imagery classification," *Opt. Eng.*, vol. 45, no. 1, p. 017008, 2006.

[13] Z. Wu, Y. Li, A. Plaza, J. Li, F. Xiao, and Z. Wei, "Parallel and Distributed Dimensionality Reduction of Hyperspectral Data on Cloud Computing Architectures," *IEEE J. Sel. Top. Appl. Earth Obs. Remote Sens.*, vol. 9, no. 6, pp. 2270–2278, Jun. 2016.

[14] R. Dianat and S. Kasaei, "Dimension reduction of optical remote sensing images via minimum change rate deviation method," *IEEE Trans. Geosci. Remote Sens.*, vol. 48, no. 1, pp. 198–206, 2010.

[15] N. Carolina, "Nc 27695-791 1," pp. 3–6, 2004.

[16] L. Breiman, "Random Forests," *Mach. Learn.*, vol. 45, no. 1, pp. 5–32, 2001.

A Low Cost Method UAV-PPK - Accuracy and Application

Davis Dinkov

National Institute of Geophysics, Geodesy and Geography at the Bulgarian Academy of Sciences, 1000 Sofia, Bulgaria
E-mail: davis.dinkov@gmail.com

ABSTRACT

In recent years, the unmanned aerial vehicle systems (UAVs) have demonstrated significant potentialities with potential for applications in many fields. Mapping of inaccessible and dangerous territories through field study methods is a challenging task. Remote sensing techniques may provide an alternative solution to such tasks. Usually single GNSS receivers of consumer UAVs cannot deliver submetric positioning accuracy. Therefore it is necessary to use Ground Control Points (GCPs), measured with precise GNSS systems for accurate geodetic positioning. The purpose of this study is to evaluate the accuracy and application of a PPK (Post Processed Kinematic method) solution used for accurate georeferencing of UAV images by post processing measurements from Global Navigation Satellite Systems (GNSS). For comparison of the PPK solution with methods using ground control points (GCP), a comparative analysis of the result of the study on the same test area by the two methods was carried out. Additional factors that can affect the accuracy of the final digital data (cloud points, digital surface models – DSM and orthophoto images) are also analyzed. Experiments with different number of GCPs used, and different image resolution (different UAV altitude) were made.

For the purposes of this study, a UAV Phantom 4 Pro was used. Its weight is approximately 1.4 kg and its diagonal size is 35 cm. The maximum flight duration is 28 min. Phantom 4 Pro comes with a 20 MP CMOS (Complementary Metal-Oxide Semiconductor) sensor with 1 inch (25.4 mm) size. The DJI camera uses a mechanical shutter that eliminates at maximum level the distortion that occurs at high flying speed. To experiment with the PPK method, a low-cost Emlid Reach M + single frequency GNSS receiver and a specially designed kit (SNAP-PPK) were used for installation of the receiver to the UAV.

KEYWORDS: UAV; Structure from Motion; low-cost system; Photogrammetry; PPK Method

1. INTRODUCTION

Depending on the specifics of the tasks being solved, a number of measurements can be made using GNSS (Global Navigation Satellite Systems), and the mathematical processing can be performed in several ways. High-precision relative phase GNSS measurements are paramount to achieve precise coordination (centimeter precision in position). They are carried out simultaneously on two points – base point (reference) and determinable (mobile). Depending on the way of running on the measurements and their processing, the following methods differ: 1) static and kinematic; 2) In real time and with subsequent data processing. Most commonly used UAVs (for example, the DJI Phantom series) use GNSS receiver for navigation purposes and can be used to add positional information and coordinates to EXIF metadata of images acquired during flight. However, the positioning accuracy of these receivers is in meters, which necessitates the use of differential GNSS solutions for UAVs to achieve centimeter accuracy in positioning of the taken images. In this study is used post-processed kinematic method (PPK) for accurate georeferencing images from UAVs. In the PPK method, GNSS measurements are carried out at a stationary reference station and mobile receivers. Very specific for this method is the relatively short duration of the observation in the mobile receivers – the subsequent processing of kinematic GNSS measurements with duration of seconds secures centimeter to millimeter accuracy at the location of the recorded point.

High resolution topography data (HRTD) (i.e. cloud points, digital surface models – DSM or digital elevation model – DEM) can be acquired by using various techniques for example: Light Detection and Ranging (LIDAR), Synthetic Aperture Radar (SAR), SfM – method (Structure-of-Motion), etc. The main advantage of LIDAR and SAR is that both techniques are not limited by the illumination of the study object or the shading of the clouds/tree crowns [1]. However, these techniques have high operating costs and produce very large datasets that are difficult for interpretation. Alternatively, the SfM method provides alternative and budget options for acquiring HRTD [2]. The combination of aerial photographs captured by UAVs and processed by the SfM algorithm allows the reconstruction of three-dimensional (3D) surface models based on a set of digital RGB images from different points of view [3,4,5].However, the resulting models have no spatial reference information (scale and geolocation). Different techniques are applied to georeferencing spatial data depending on the software used. If absolute orientation

is required (obtaining HRTD in a particular coordinate system), georeferencing using GCPs is the standard approach.

In the past few years, the development of high-quality IMU (Inertial Measurement Unit) and GNSS technologies, as well as specialized RTK (Real Time Kinematic) and PPK (Post-Processed Kinematic) UAVs solutions, can provide accurate parameters for the external orientation of the cameras which are used. Using such approach has the potential for the elimination of the need of GCPs [6]. Recently, both methods (RTK and PPK) for georeferencing are gradually evolving and can provide centimeter level accuracy in specialized studies.

The purpose of the study is to evaluate the geospatial accuracy of the photogrammetric products (HRTD), obtained by the UAV/PPK method using a low cost configuration one-band GNSS receiver (Emlid M+), DJI Phantom 4 pro serial drone and Snap-PPK kit for DJI Phantom. The results are compared to the traditional georeferencing approach – by using ground control points (GCP).

2. MATERIAL AND METHOD

2.1 Study Site

The study site is located in outskirts of Sofia and is a suburban park Figure 1 (Botanical Garden of BAS), with various land cover (mowed green areas, unpowered grass with shrubs, wooded areas, alleys and buildings). The study area is about 16 ha and is characterized by diverse terrain with transverse slope of about 12.7 % with highest point of 722 m a.s.l. and lowest point of 695 m a.s.l.

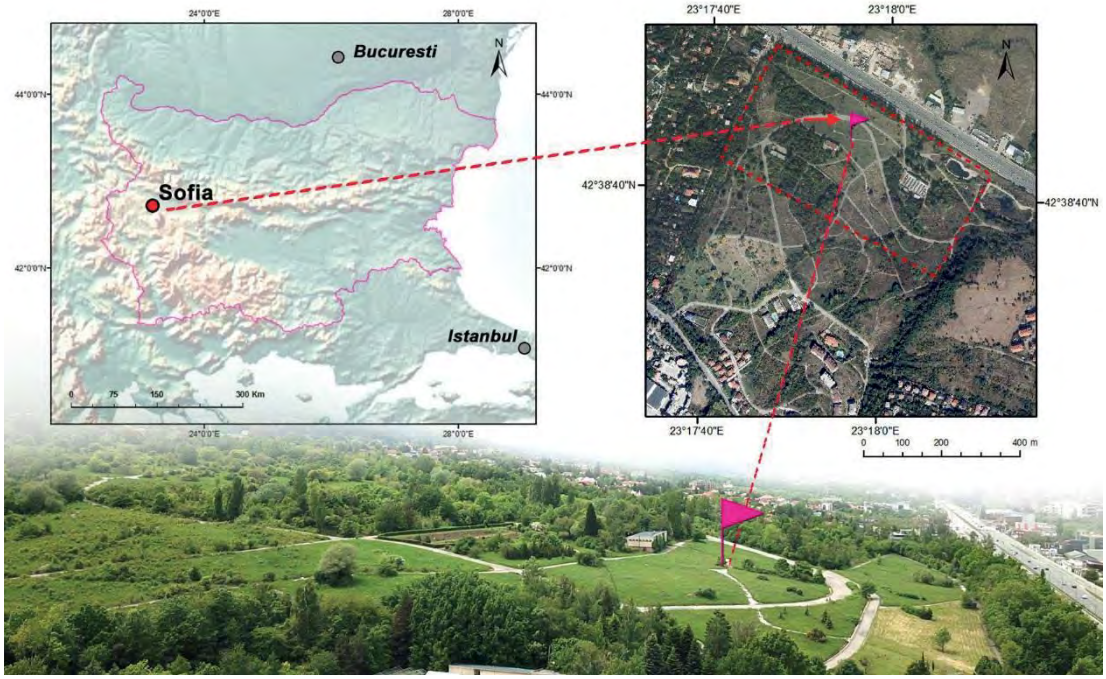

Figure 1. *Location of study site*

2.2. UAV Configuration

2.2.1. Platforms and Payloads

This study uses a consumer class of UAV - DJI Phantom 4 Pro (P4P) – Figure 2(a). The P4P is equipped with a DJI FC6310 camera with a nominal focal length of 8.8 mm and a 1 "CMOS" 20 megapixel sensor with 2.41 x 2.41 μm nominal pixel size. The DJI FC6310 creates an image of 5472 x 3648 pixels, which corresponds to 13.2 x 8.8 mm. For implementation of the PPK-GNSS experiment, the platform is equipped with compact multi-GNSS-RTK receiver (Reach RTK kit, Emlid Ltd) with RTK / PPK capability as described below.

(**a**) (**b**) (**c**)

Figure 2. *UAV and PPK-GNSS module : (a) Phantom 4 pro ; (b) Emlid Reach M+ and Tallysman antenna; (c) Snap PPK adapter kit for Phantom 4 pro [7]*

2.2.2. PPK-GNSS Module

During the UAV flights, a Reach RS (Emlid Ltd) was mounted on a tripod located upon GCP to provide positioning correction input. The maximal distance between the UAV and the base station was 405 m. The receiver of the base is configured to log the raw data in a RINEX file at 5 Hz using the satellite GPS, GLONASS and GALILEO. UAV was equipped with a Reach GNSS receiver (Figure 2b) to log the raw data as UBX format using GPS and GLONASS satellites. The antenna model was Tallysman's TW2710, which covers the GPS L1, GLONASS G1, BeiDou B1, Galileo E1, and SBAS (WAAS, EGNOS, and MSAS) frequency bands. The antenna was mounted on a special plate, with the center right above the camera lens center to minimize the offset the shift between the antenna phase center and camera projection center. The antenna height was 23 cm and this difference between the antenna and camera projection center was considered during the post-processing.

Snap PPK - Figure 2(c) is an adapter kit to connect an Emlid Reach GNSS receiver to a Phantom 4 Pro [7]. The kit snaps on in seconds to Phantom 4 Pro - without any modifications. The front LEDs on a Phantom 4 Pro blink each time a picture is taken. A phototransistor detects the blink and a time mark is recorded in the Reach's log file. The time marks are extracted and combined with the pictures as precision geotags. Accuracy is further improved by setting the Phantom on a GCP target and taking a picture while stationary. This position is free from shutter timing errors, lever-arm errors, and camera calibration errors.

2.3. Ground Control and Validation points

For assessment of the accuracy were used 7 (11) ground control points (GCP) and 37 (42 during the second flight) validation points (VP) - Figure 3.

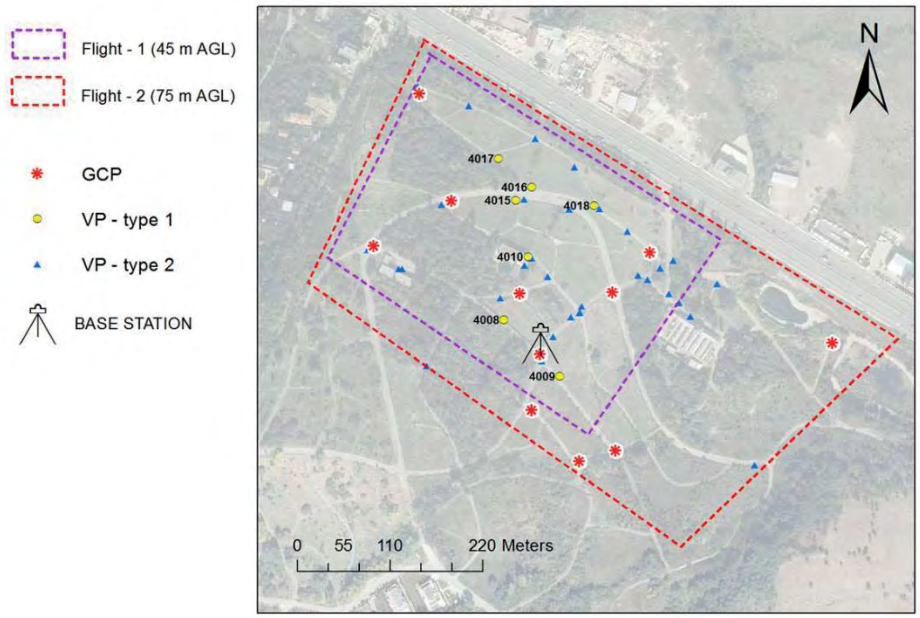

Figure 3. *Test area with control and validation points*

All control points are marked on the ground with permanent signs using 2 perpendicular shoulders 100/20 cm – Figure 4(a). The control points are always located in the inner corner of the marked sign. The validation points are in two categories: First category – marked points with clear and permanents terrain signs (forced centering pillars – Figure 4(b) and Second category – distinct topographic elements – Figure 4(c).

(**a**) (**b**) (**c**)

Figure 4. *Ground Control Points and Validation Points*

GCPs are used only for georeferencing and do not participate in the final accuracy analyzes where VPs are used. The coordinates of the marked points were obtained by the GNSS RTK

method with geodetic two-frequency receiver (Kolida – K5 PLUS), RTK solution with the 1YOCTO network [8]. For a fixed solution, the declared accuracy of 1YOCTO is up to 5 cm.

2.4. Acquisition of Photogrammetric Data and Processing

2.4.1 Flight Planning

Flight missions were planned using the UgCS Desktop application and were performed with UgCS for DJI. The UgCS Photogrammetry Tool [9] allows flight planning at constant altitudes over mapped terrain (AGL). This feature ensures preset image overlap and consistent GSD (Ground Sample Distance). UgCS uses SRTM data (or Shuttle Radar Topography Mission), but there is an option to enter a more accurate DEM.

The flight missions are designed with 80% forward overlap and 70% side overlap of the images. The first mission (Figure 5a) was carried out at the altitude of 45 m from the terrain and maximum speed of UAV of 2.2 m/s, and the second mission (Figure 5b) was carried out at the altitude of 75 m from the terrain and with maximum speed of 3.5 m/s, leading to a ground sample distance (GSD) of 1.27 cm and 2.08 cm.

(a) **(b)**

Figure 5: *Flight Planning*

2.4.2 Georeferencing of images

To evaluate the accuracy of the different georeferencing options, the datasets were processed with six configurations at two altitude flights:

- First flight (Dataset-1): Flight altitude 45 m, built-in GPS solution + 7 GCP, only PPK and PPK + 1 GCP (Figure 6);
- Second flight (Dataset-2): Flight altitude 75 m, built-in GPS solution + 11 GCP, only PPK and PPK + 1 GCP (Figure 7).

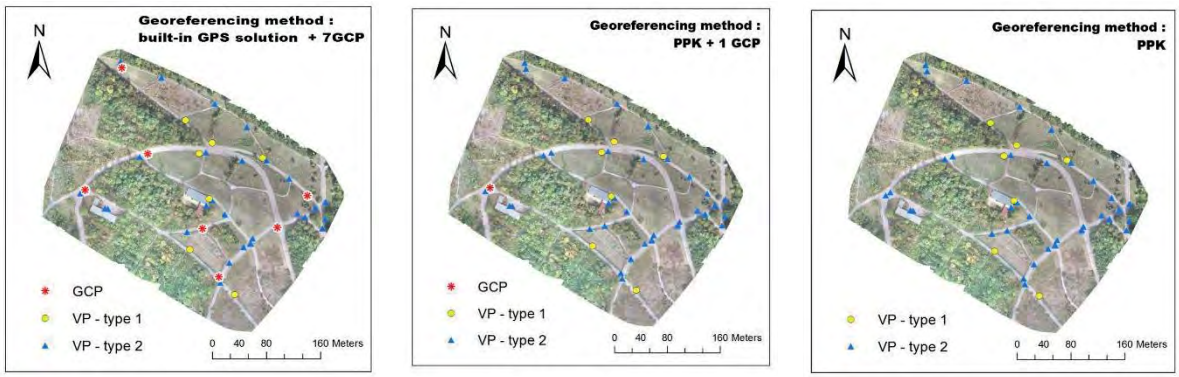

(**a**) (**b**) (**c**)

Figure 6: *Distribution of GCPs and VPs and illustration of the different georeferencing configurations:*

a) built-in GPS solution + 7 GCP ; b) PPK + 1 GCP ; c) PPK.

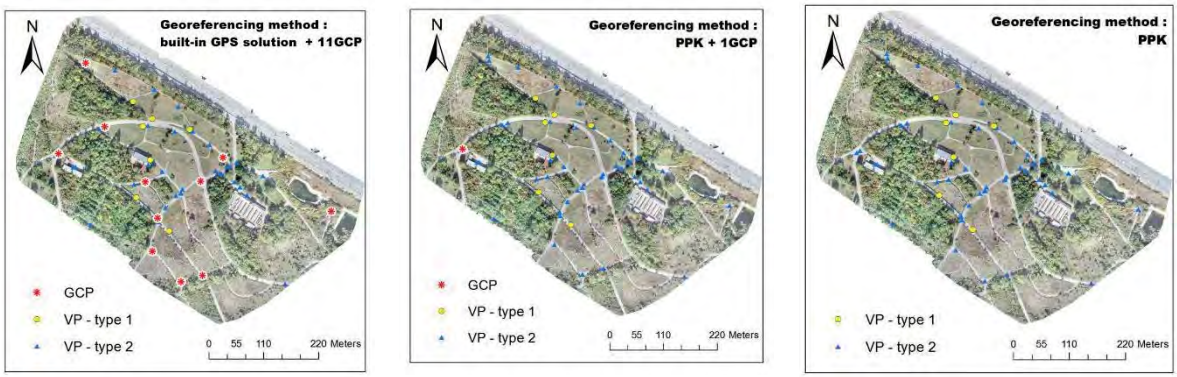

(**a**) (**b**) (**c**)

Figure 7: *Distribution of GCPs and VPs and illustration of the different georeferencing configurations:*

a) built-in GPS solution + 11 GCP; b) PPK + 1 GCP; c) PPK.

For conventional methods using GCP and built-in GPS solution, we used built-in single GPS solution to acquire the coordinates of the images. In the PPK solution test, the image coordinates

were calculated using the RTKLib open source software package [10]. Raw GPS data from the UAV-mounted Snap-PPK kit with additional GNSS receiver Emlid Reach M+ and the base station (Emlid Reach RS+) were extracted and corrected by post-processing using RTKLib.

2.4.3 Data Processing

Georeferenced images were processed with Pix4D Mapper software [11]. The software uses the SfM algorithm to generate 3D cloud points, DSM and orthophoto mosaics in the study area. The procedure consists of three main steps: (i) Initial processing, (ii) Generating cloud of points and (iii) Generating of DSM and orthophoto mosaic. All next steps are made separately, with some differences between the configurations – . First, six subprojects were created to allow independent evaluation of all variables and their possible combinations (three georeferencing approaches, two flight altitudes). In the PPK solution method, the calculated camera positions are attached to the EXIF metadata of each taken image. For the 7GCP (11 GCP) configuration this information has been removed and geotags from the original Phantom 4 Pro images were used. After the initial processing, all validation points (Check points) were entered for calculation of the accuracy. Next steps include generation of solid cloud of points, orthophoto mosaics and DSM. Orthophoto mosaics are generated with resolution of 5 cm/pixel and DSM is with resolution of 10 cm/pixel.

2.4.4 Evaluation of Accuracy

The evaluation of point cloud accuracy was performed using 37 (42 for the second flight) validation points (VPs) (which were not used in the cloud generation) by computing the differences between the coordinates of the checkpoints in the 3D cloud and those measured in the field by GNSS. Mean values and the root mean square error (RMSE) of the differences were computed for each flight to detect systematic shifts and block deformations.

The positions of the validation points were determined directly on the point clouds. The GCPs and VPs were marked in the Pix4D using built-in RayCloud 3D Editor.

Export the vectorized validation points in .shp format and it is used for subsequent analyses. The coordinates of the validation points (In the PPK configuration, the ground control points are used as validating) were compared to the coordinates in the outputs as follows:

Calculation of the root mean square coordinate errors:

$$RMSE_x = \sqrt{\frac{\sum_{i=1}^{n} \Delta x_i^2}{n}} \quad (1)$$

$$RMSE_y = \sqrt{\frac{\sum_{i=1}^{n} \Delta y_i^2}{n}} \quad (2)$$

$$RMSE_z = \sqrt{\frac{\sum_{i=1}^{n} \Delta z_i^2}{n}} \quad (3)$$

where Δxi, Δyi and Δzi are the differences between reference coordinates and the coordinates determined from the remote sensing data and n is the number of points in the set.

The RMSEx and RMSEy errors were used for the calculation of the root mean square horizontal error RMSExy as follows:

$$RMSE_{xy} = \sqrt{RMSE_x{}^2 + RMSE_y{}^2} \quad (4)$$

The RMSExy is one of the most common horizontal accuracy criteria for sets of points and was used as the main measure to compare data between the test sites and between various configurations of GCPs/VPs.

3. RESULTS AND DISCUSSION

For the purpose of the study, two flights were made for obtaining images for the tested site with the following parameters:

Table 1: First flight (F1) – Figure 5a:

Altitude of the Flight (AGL) (m)	Area Covered (ha)	Dataset (Images)	Number of Calibrated Images	GSD
45	11.36	598	582	1.28 cm

Table 2: Second flight (F2) – Figure 5b:

Altitude of the Flight (AGL) (m)	Area Covered (ha)	Dataset (Images)	Number of Calibrated Images	GSD
75	24.2	422	422	2.08 cm

3.1 Accuracy of different georeferencing methods

Table 1 summarizes the RMSE ranges in the X, Y and Z directions for the all validation points for the different configurations. For the datasets acquired from the built-in GPS in UAV configuration and the use of ground control points for georeferencing, an average planimetric accuracy of RMSExy = 0.06 m and corresponding altimetric accuracy were obtained at 45 m flight altitude of RMSEz = 0.14m and at 75 m flight altitude RMSEz = 0.07 m. The configurations of PPK and PPK + 1 GCP at flight altitude of 45 m also showed a planned accuracy of about 0.06 m, in altitude the error dropped to 0.051 m (PPK + 1 GCP). In the PPK configuration during a flight in a height of 75 m, the addition of 1 GCP significantly improved the accuracy, especially in altitude.

Table 3: *Mean errors (ME), Standard deviation (SD) and Root mean square errors (RMSExy) on validation points respectively for horizontal and vertical coordinates, for the different configurations for each of the two flights (flight 1 (F1) - height at 45 m, flight 2 (F2) - height at 75 m*)

Flights	Georeferencing method	Mean (m)				SD(m)				RMSE(m)			
		X	Y	XY	Z	X	Y	XY	Z	X	Y	XY	Z
F1(45m)	7 GCP	-0,019	0,010	**0,021**	-0,045	0,042	0,038	**0,057**	0,164	0,046	0,039	**0,060**	0,145
F1(45m)	PPK	-0,018	-0,007	**0,019**	0,055	0,044	0,038	**0,058**	0,038	0,047	0,039	**0,061**	0,067
F1(45m)	PPK+1GCP	-0,014	0,001	**0,014**	0,033	0,040	0,039	**0,056**	0,038	0,043	0,039	**0,058**	0,051
F2(75m)	11 GCP	-0,019	0,014	**0,024**	0,002	0,030	0,040	**0,051**	0,070	0,036	0,043	**0,056**	0,070
F2(75m)	PPK	-0,092	-0,123	**0,153**	0,550	0,044	0,053	**0,069**	0,074	0,102	0,133	**0,168**	0,555
F2(75m)	PPK+1GCP	-0,059	-0,071	**0,092**	-0,058	0,034	0,045	**0,057**	0,069	0,068	0,084	**0,108**	0,090

3.2 Accuracy and Precision of PPK Solution in Direct Georeferencing

This study is focused on the application of a budget PPK solution for direct georeferencing. The PPK approach provided results comparable to those that can be acquired by using GCPs, i.e. with RMSExy 0.06 – 0.11 m. This shows that direct georeference with accurate positioning and orientation is able to replace the conventional ground control and to provide centimeter accuracy. The quality if georeferencing through ground control points depends on the number and distribution of GCPs [12,13]. The accuracy is improved by adding more and more tightly distributed GCPs, which would increase the time of the study. In this study, the use of PPK method (without any GCP) for precise georeferencing of the camera positions indicates that the same level of accuracy is provided as the GCP solution. Deviations are possible (at an altitude of 75 m, the error in altitude is above normal for the method) due to incorrect solutions that may remain undetected (e.g., false fix in resolving ambiguities) or from an uncalibrated camera. Using only one GCP significantly improved the results (F2 (75m) PPK+1GCP) of this study, so it is recommended to use at least one GCP as a good operational compromise to eliminate GNSS interference. Discussion of the SNAP-PPK kit is also the exact fixation of the moment of capture (use of a photodetector to the lights of P4P), with a offset between 12-15ms [14]. This time shift and its effect on accuracy is subject of our further researches.

3.3 Application of UAV-PPK method

In the present study, we tested the applicability of the UAV-PPK method for the precise positioning of geodetic pillars for forced centering (Validation points type-1), which are part of the monitoring network established in 1989. Such control pillars (Fig. 4b) are placed for monitoring of landslides and other disturbed terrains and serve for precise measurements and analysis of the movements of the upper layers of the earth's surface. High precision measurements are made (angular-length, leveling, gravimetric and GNSS) and the data is processed by specialized technology with the aim for accurate determination of the coordinates of the points, respectively the displacement of the researched points [15]. The test site includes pillars № 8,9,10,15,16,17,18 from the geodetic monitoring network (respectively numbered as follows VP 4008,4009,4010,4015,4016,4017 – Figure 3). We cannot look for planimetric and height accuracy commensurate (equal) with precise geodetic measurements, but the idea is the possibility to detect deviations in the location of the studied points, which will draw attention to further high-precision studies. This hypothesis can be applied for complex and hard to reach territories where a monitoring observation can include high financial costs and a lot of time.

From the presented histograms of the planimetric and height errors for the validation points from the geodetic pillars for forced centering (Figure 8 and Figure 9) can be seen that at a flight altitude of 45 m and a PPK georeferencing method, a planimetric error was reported RMSExy = 0.050 m and height RMSEz = 0.035 m (Figure 8b). At a flight altitude of 75 m the PPK solution gave results with significant deviation in the Z direction, but as with studies for all validation points of the project, the adding of a single ground reference point can eliminate deviations. If we assume that 0.05-0.10 m is the border for changing the location of the studied point, then the UAV-PPK georeferencing method is an alternative and cost-effective solution when it comes to monitoring control points for large areas that are poorly accessible or require repeated study.

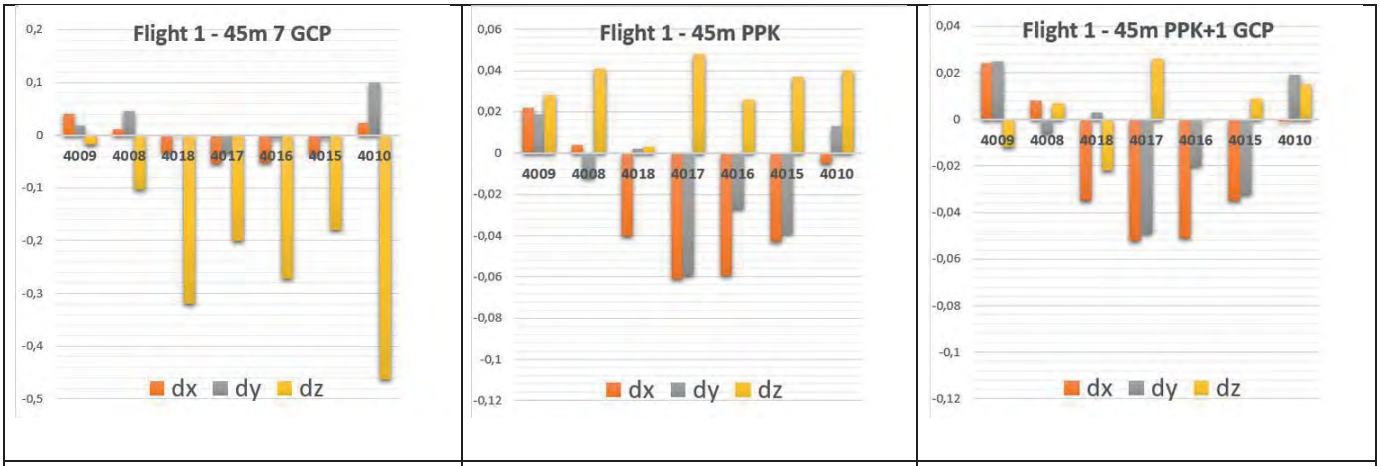

(a)	(b)	(c)
RMSExy = 0,058 m , RMSEz = 0,260 m	RMSExy = 0,050 m, RMSEz = 0,035 m	RMSExy = 0,044 m , RMSEz = 0,015 m

Figure 8: *Histograms of planimetric and vertical errors (dx,dy,dz) for the validation points of geodesic pillars for the different methods for georeferencing of the images for* **Flight-1**

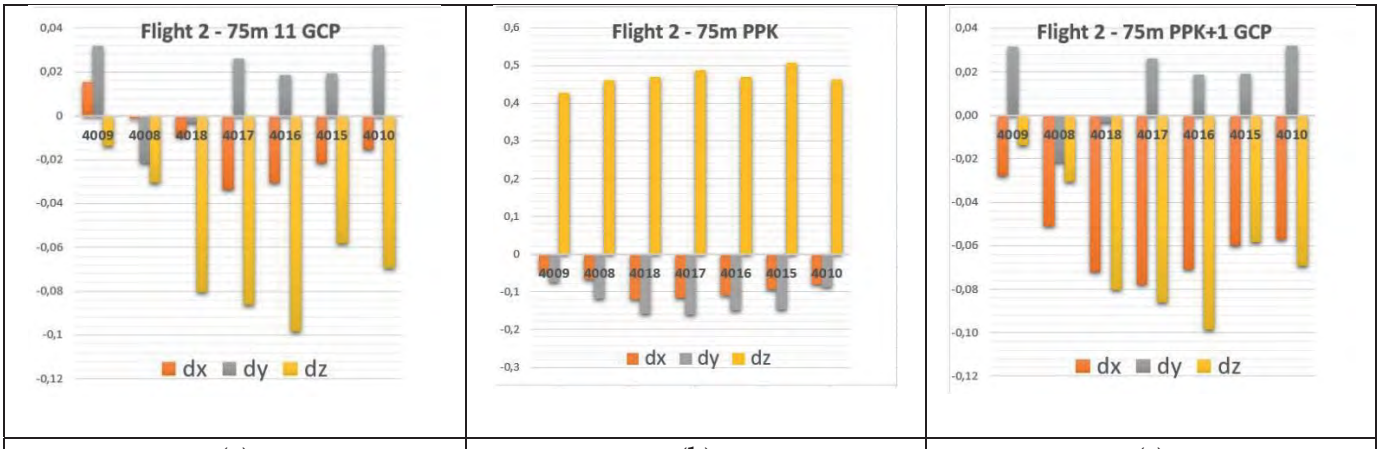

(a)	(b)	(c)
RMSExy = 0,032 m , RMSEz = 0,069 m	RMSExy = 0,162 m , RMSEz = 0,470 m	RMSExy = 0,098 m , RMSEz = 0,102 m

Figure 9: *Histograms of planimetric and vertical errors (dx,dy,dz) for the validation points of geodesic pillars for the different methods for georeferencing of the images for* **Flight-2**

4. CONCLUSION

We tested the ability of the PPK budget system for UAVs and demonstrated accurate spatial data comparable to those obtained using standard approaches (GCP).

The UAV-SfM framework is used in geomorphology, open pit mines, monitoring of disturbed territories to accurately capture the surveyed surface. Our study showed that the application of PPK (Post-Processed Kinematic) in direct georeferencing can provide cm-level accuracy and precision with greatly improved field survey efficiency, and this without the need to survey a single GCP. Overall, the PPK-SfM workflow overcomes the limitations of GCP, providing a

high-precision and high-efficiency solution in surveying. The results suggest that the PPK method can provide data with comparable or even higher accuracy compared to the GCP approaches, independently on the terrestrial measurements. This is the main requirement for remote sensing of inaccessible and hazardous areas.

REFERENCES

1. Passalacqua, P., Belmont, P., Staley, D. M., Simley, J. D., Arrowsmith, J. R., Bode, C. A., Crosby, C., DeLong, S. B., Glenn, N. F., Kelly, S. A., Lague, D., Sangireddy, H., Schaffrath, K., Tarboton, D. G., Wasklewicz, T. and Wheaton, J. M.(2015):Analyzing high resolution topography for advancing the understanding of mass and energy transfer through landscapes: A review, Earth-Science Rev., 148, 174–193
2. James, M. R. and Robson, S.: Straightforward reconstruction of 3D surfaces and topography with a camera: Accuracy and geoscience application,(2012) J. Geophys. Res. Earth Surf., 117(3), 1–17
3. Eltner, A., Kaiser, A., Castillo, C., Rock, G., Neugirg, F. and Abellán, A.: Image -based surface reconstruction in geomorphometry-merits, limits and developments, (2016), Earth Surf. Dyn., 4(2), 359–389
4. Dinkov, D. 3D Modeling Of Natural Landscapes Using Unmanned Aerial Systems. Problems of Geography, Vol.1-2, Press BAS "Prof. Marin Drinov", (2018), ISSN:0204-7209; 2367-6671 (online), 139-163
5. Dinkov, D. 3D Modeling Of Cultural Historical Heritage Sites Using Unmanned Aerial Systems. Problems of Geography, Vol. 3-4, Press BAS "Prof. Marin Drinov", (2018), ISSN:0204-7209; 2367-6671 (online), 139-160
6. James, M. R., Robson, S. and Smith, M. W.: 3-D uncertainty-based topographic change detection with structure-from-motion photogrammetry: precision maps for ground control and directly georeferenced surveys, (2017), Earth Surf. Process. Landforms, 42(12), 1769-1788
7. www.tuffwing.com, Available online: http://www.tuffwing.com/products/Phantom_Reach_PPK_Integration_kit.html (accessed on 01.11.2019)
8. 1YOCTO, Available online: http://www.1yocto.bg (accessed on 01.11.2019).
9. www.ugcs.com, Available online: https://www.ugcs.com/photogrammetry-tool-for-land-surveying, (accessed on 01.11.2019).
10. Takasu, T. and Yasuda, A.: Development of the low-cost RTKGPS receiver with an open source program package RTKLIB, in:International Symposium on GPS/GNSS, 4–6 November 2009, Jeju, Korea.
11. www.pix4d.com, Avaliable online: https://www.pix4d.com/product/pix4dmapper-photogrammetry-software, (accessed on 01.11.2019).
12. Sanz-Ablanedo, E., Chandler, J. H., Rodríguez-Pérez, J. R., and Ordóñez, C.: Accuracy of Unmanned Aerial Vehicle (UAV) and SfM Photogrammetry Survey as a Function of the Number and Location of Ground Control Points Used, (2018), Remote Sens., 10,1606, https://doi.org/10.3390/RS10101606

13. Rangel, J.M.G.; Gonçalves, G.R.; Pérez, J.A. The impact of number and spatial distribution of GCPs on the positional accuracy of geospatial products derived from low-cost UASs. Int. J. Remote Sens. 2018, 39,7154–7171.
14. www. community.emlid.com, Avaliable online: https://community.emlid.com/t/affordable-way-to-integrate-reach-m-with-dji-phantom/13414/5, (accessed on 01.11.2019).
15. Tsenkov, T., Georgiev,I., Pashova, L., Radev I., Georgiev, D.: Monitoring of landslide processes in the region of the Botanical garden of BAC, Sofia, "GEOSCIENCES 2006" – Proceedings, 2006, 362-365.

ASSESSMENT OF SATELLITE DERIVED BATHYMETRY DATA USAGE IN THE HYDROGRAPHIC SURVEY PLANNING PHASE

Koray Açar, Dursun Zafer Şeker

[1]Istanbul Technical University, Geomatics Engineering Department 34469 Istanbul, Turkey
Phone: +90 216 322 2580, E-mail: acar17@itu.edu.tr

[2]Istanbul Technical University, Geomatics Engineering Department 34469 Istanbul, Turkey
Phone: +90 212 285 3755, E-mail: seker@itu.edu.tr

ABSTRACT

Bathymetric data, needed to determine sea floor topography is obtained by the ship based SONAR as sound source method and aircraft based LIDAR as light source method. These active hydrographic survey methods present high resolution and accuracy but they are expensive and need relatively long survey time because they require survey hardware and field work. Satellite Derived Bathymetry, obtained in shallower waters than 30 meter by processing high resolution multi-band satellite images, increases its potential as a fast and economical remote sensing hydrographic data collection method, although it does not replace traditional survey methods at present. In this study, the determination of the Satellite Derived Bathymetry methods to be applied and evaluation with the relevant stakeholders is discussed. It will be useful to concentrate the survey line planning on shallows, shipwrecks or dangerous areas by using the Satellite Derived Bathymetry data for exploration purposes before the depth measurement studies to be carried out by the survey ships. The study is performed on the east coast of Saros Gulf with the 167 square kilometers sea area and the depths vary between 0-102 meters. Multi-band satellite image data obtained from the Landsat 8 satellite is processed with Geographical Weighted Regression method by i.image.bathymetry module in an open source GIS software. Calculated water depths compared with the updated navigation chart depths and the shallower areas marked and noted as areas to survey primarily. The results did not achieve the accuracy standards of the International Hydrographic Organization Standards for Hydrographic Surveys (S-44). It is considered to be helpful that the Satellite Derived Bathymetry data can be used for reconnaissance but not for chart production.

KEYWORDS: Hydrography; Bathymetry; Satellite Derived Bathymetry; Remote Sensing

1. INTRODUCTION

Bathymetry is the measuring of underwater topography and the bathymetric data obtained as a result of hydrographic research is the basic need for human use of the sea. The earliest and most basic method was to measure depth by a weight (lead line) attached to the end of a rope marked with length signs and to determine the position by angle/bearing measuring device (sextant). Over the years, lead line has been replaced by acoustic sounding devices using sound waves and sextant by the satellite based positioning systems.

The single-beam Echosounder (SBES) gathers the depth data by measuring the time elapsed between the sound wave transmitted from the platform on the sea surface and the reflection of the sound wave back to the sea floor. With each sound wave transmission, a single depth value is recorded which is reflected from the shallowest point falling into the fingerprint of the sound beam at the sea floor.

The multi-beam Echosounder (MBES) works like a SBE, but with each soundwave transmission, the beam rays are opened as a fan, creating a covering area perpendicular to the direction of heading of the platform. As the platform moves forward, an area is formed at the seabed where full coverage is provided along the exploration line.

The purpose of Side Scanning Sonar (SSS) is to determine the underwater heights by detecting the shipwrecks, heel and rock elevations on the sea floor with a towing fish. Since the location of the fish, which is towed under water by the ship and where the sonars are located, cannot be determined in IHO S-44 standards, the depth data obtained with SSS is not used in chart production, but information such as height from the sea floor and the orientation of the detected objects is taken into consideration.

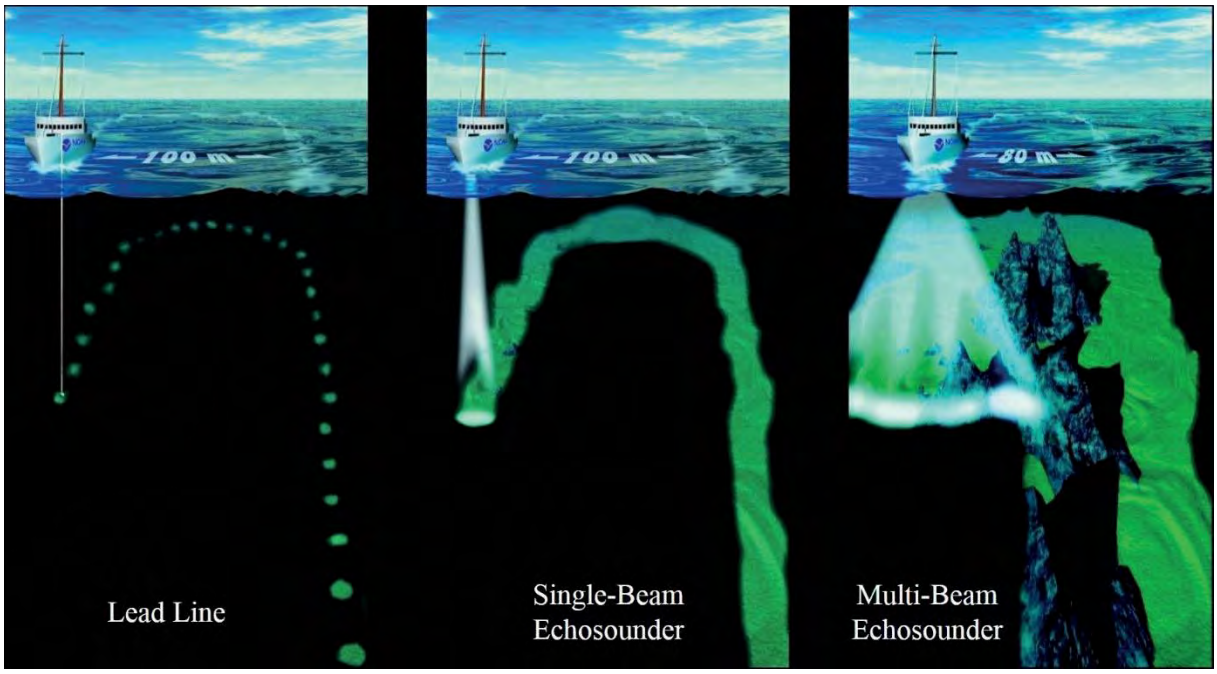

Figure 1. *Coverage areas of the ship-borne hydrographic survey methods* [1]

LIDAR (Light Detection and Ranging) transmits light instead of sound and obtains the distance and bearing of the features according to the return time as a dense cloud of data. There are two types of LIDAR, the topographic LIDAR maps the terrain with infrared light and the bathymetric LIDAR maps the sea floor with green light. It uses air-based flying vehicles as a platform and uses motion sensors and satellite-based positioning systems to detect the orientation of light.

Together with satellites with multi-band sensors such as LANDSAT, the energy reflected from certain wavelengths of the electromagnetic spectrum was collected and processed. The basis of the Satellite-Derived Bathymetry (SDB) method is that the difference/ratio between the reflected energy from the sea surface and the sea floor is due to the depth of the sea/water column and that the water depth can be calculated using certain algorithms [2,3].

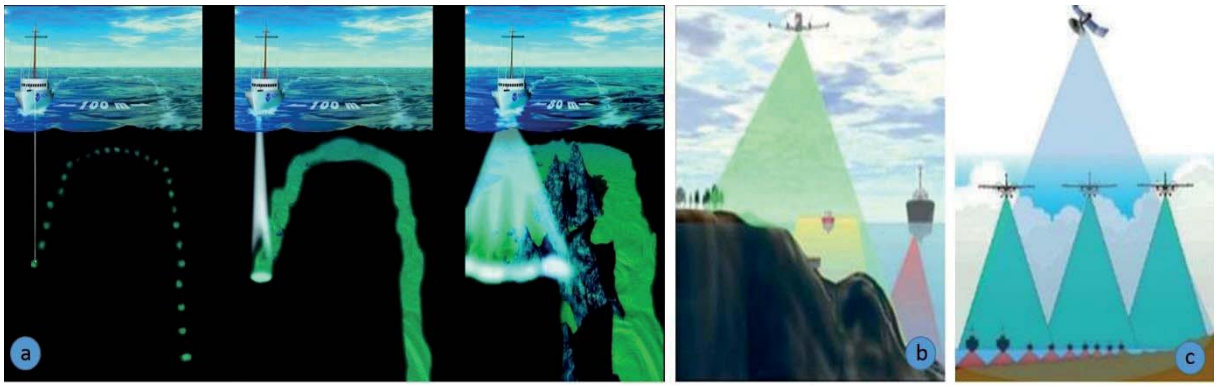

Figure 2. Comparison of Ship, Air and Space Borne systems coverage areas [1]. a) Ship-Borne Systems (Lead Line and Sonar), b) Air-Borne Systems (LIDAR), c) Space-Borne Systems (SDB)

The SDB method calibrates the results using reference depths. There are factors affecting the calculations such as light absorbing sediments, turbid waters, undulating sea surface.

Bathymetric surveys of marine areas deeper than 20 meters on our coasts are currently being carried out by research ships using the acoustic active MBES system. With the increase in depth, the survey coverage area increases and the depth collection activity of more areas per unit time can be completed.

The most effective method, MBES system, requires relatively larger platforms in terms of size. Since the activities on shallow waters jeopardize the survey ships, surveys between 0-20 meters are now perform with relatively small boats equipped with SBES. However, SBES only measures the depth under the hull and does not have full coverage capability. There is a possibility that wrecks and deed-like shallows in the areas between the survey lines cannot be detected. In order to avoid this situation, SSS is used to cover the survey gaps formed between the survey lines, but at least as many as the number of SBES lines should be carried out and the detailed survey of the detected underwater heights should be done again with the SBES/MBES to use the depth data in navigation charts within the IHO S-44 standards. This process, which includes planning, transfer to the study area, survey, data control, re-investigation of hazardous areas and data processing activities, is quite costly and long time consuming compared with the SDB methods.

Currently, survey line planning is carried out by considering the map scale to be produced based on the most recent depth data of the study area. For example, survey lines are planned perpendicular to the shore at 10 meter intervals in order to obtain 1/1 000 scale data with SBES. Data is not collected in the 10-meter area between the two planned lines, and it is important to identify any underwater obstacles in the area. In this study, the process of concentrating line planning on shallows, shipwrecks or hazardous areas by using the proposed SDB data for exploratory purposes prior to the depth measurement studies to be carried out is evaluated with the relevant stakeholders.

2. MATERIAL AND METHOD

2.1 MATERIAL

The study area in Figure 3, which is located to the east of Saros Gulf, was selected for SDB data processing. The sea area is 167 square kilometers and the depths vary between 0-102 meters. The 1/50 000 scale navigation chart of the study area is shown in Figure 4.

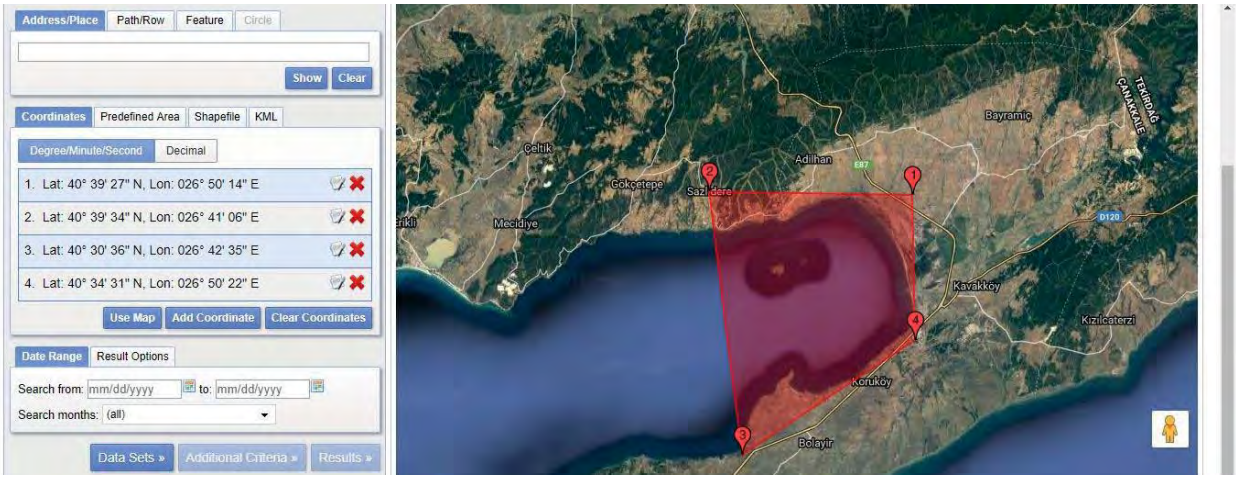

Figure 1. *Study area*

In this study, it is preferred to use free data and open source software in order to reduce cost. In this context, multi-band satellite image data were obtained from the United States Geological Research website at https://earthexplorer.usgs.gov/ with UTM coordinate system WGS84 datum. The specifications of the supplied Landsat 8 multi-band satellite imagery in the Landsat 8 (L8) Data User Manual are summarized below.

Landsat 8 is NASA's eighth satellite, ensuring that the Landsat program continues to play a key role in organizing, monitoring and understanding the resources needed for human livelihoods such as food, water and forests. Landsat 8 participates in Landsat 7's orbit and provides scientific data as well as images it collects. Landsat 8 satellite collects images in visible, near-infrared, short-wave infrared and thermal infrared ranges and has a 15-meter panchromatic, 30-meter multispectral and 100-meter thermal resolution depending on the spectral range.

OLI collects data in nine spectral bands. Seven of these nine bands have the ranges found in the Landsat 5 TM and Landsat 7 ETM sensors, making it compatible with older Landsat data. With the new two spectral bands deep blue / aerosol and short wave infrared cirrus bands, it is aimed to detect high and thin clouds and to measure water quality.

Figure 2. *Navigation Chart of the study area*

Table 1: Landsat 8 Band Specifications

Spectral Band	Wavelength	Resolution
Band 1 - Coastal Aerosol	0.433 - 0.453 µm	30 m
Band 2 - Blue	0.450 - 0.515 µm	30 m
Band 3 - Green	0.525 - 0.600 µm	30 m
Band 4 - Red	0.630 - 0.680 µm	30 m
Band 5 - Near Infrared	0.845 - 0.885 µm	30 m
Band 6 - Short Wavelength Infrared 1	1.560 - 1.660 µm	30 m
Band 7 - Short Wavelength Infrared 2	2.100 - 2.300 µm	30 m
Band 8 - Panchromatic	0.500 - 0.680 µm	15 m
Band 9 - Cirrus	1.360 - 1.390 µm	30 m
Band 10 - Thermal Infrared Sensor 1	10.30 - 11.30 µm	100 m
Band 11 - Thermal Infrared Sensor 2	11.50 - 12.50 µm	100 m

The images named LC08_L1TP_181032_20180703_20180717_01_T1 were collected between 08:50:47.13 and 08:51:18.90 on 03 July 2018 with a cloudiness ratio of less than 10%.

2.2 METHOD

Lyzega [4] laid the foundation for the current SDB methods. Theoretically, the physical properties of the light moving through the water column begin to disappear, and as a result, the data reflected by the satellite from the shallow water are brighter and more realistic than the deep water. Scattering in deep waters is high and there is no bottom reflection, so the recorded light intensity is less [5].

SDB methods are divided into spectral rationing and radiative transfer model. In the calculations made with single band satellite images, the fact that the study area is in a single type of sediment structure gives good results. However, there are different sediment and water column properties under real conditions and the use of radiative transfer model using Geographical Weighted Regression method of satellite images with multispectral bands gives good results [2].

In this study i.image.bathymetry module, created by Poliyapram et al. [2], which runs on the open source GRASS GIS software, is used. The main functions of the module, as shown in the flow diagram indicated in Figure 5, are Sea Areas Detection, Water Level (Tide) Correction, Atmospheric and Water Corrections. As input data, 3rd Band (Green Band), 4th Band (Red Band), 5th Band (Near Infrared Band) and 6th Band (Correction Band) of Landsat 8 satellite images were used. The Navionics-based navigation chart of the Saros Gulf was provided with the open-source SAS-Planet software and the depth values were digitized. A total of 355 reference depth points ranging from 0 to 102 meters were created.

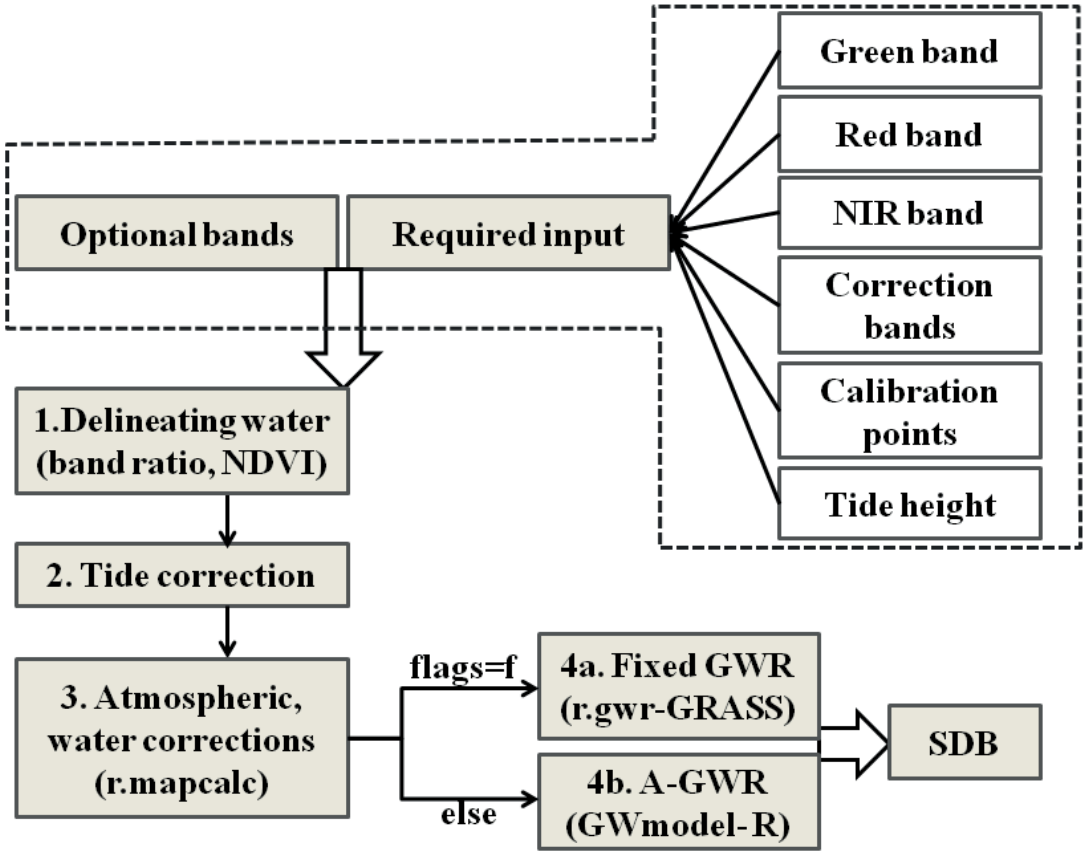

Figure 5. *Flowchart of the workflow of i.image.bathymetry*. [2]

A. Delineation of Water Region: Band ratio between the green and infrared bands were used for delineation of water region. A band ratio of greater than or equal to 1 was classified as water and for further processing this water region is used. Normalized Difference Vegetation Index (NDVI) has been used to remove the cloud. GRASS GIS r.mapcalc module is used for these calculations [2].

B. Tide Correction: In the process of obtaining the satellite image, this correction was omitted by selecting the time period at which the water level was at the Lowest Astronomical Water level where the map depths were reduced. Considering that satellite images are acquired in about 30 seconds, a single water level value to be added to or removed from all calculations will increase the accuracy of the calculations at the calibration stage.

C. Atmospheric and Water Corrections: The radiance observed by a satellite sensor on shallow water basically consists of four components, namely, atmospheric scattering, surface reflection, in-water volume scattering, and bottom reflection components [2].

Since there is no sea floor reflection in deep water areas, areas where less reflection is recorded than the limit value can be identified as deep water. In deep areas there is no sea floor reflection and the water and atmospheric corrections in the deep areas are the same in shallow areas. Water and atmospheric correction coefficients in deep areas formed from reference depth points are used in water and atmospheric correction calculations of shallow water areas. Therefore, the SDB calculations should include both deep and shallow water areas within the study area.

D. Geographical Weighted Regression (GWR):GWR determines the weight coefficient for each pixel. In the i.image.bathymetry module used in the study, Gauss and Bi-square methods can be calculated. In the bi-square method, the weight decreases with the bi-square function as the wavelength when moves away from the relevant pixel. The weight became zero further away as the wavelength from the pixel. The Gauss method also works on pixels farther away as the wavelength, and the weight decreases gradually with the continuous Gaussian function relative to the distance to the relevant pixel.

In the GWR model, the concept of bandwidth refers to the diameter of the kernel window. Bandwidth assignment has two methods, fixed and adaptive. Fixed Geographic Weighted Regression uses the same size kernel in the entire model regardless of the distribution of depth calibration points. Fixed Geographic Weighted Regression gives faster results because less data processing is required. Adaptive Geographical Weighted Regression, kernel size varies according to the density of depth calibration points. Small/decreasing kernel is used in areas with dense depth calibration points, larger/increasing kernel is used in areas with dense depth calibration points, and works better when randomly distributed calibration points are available.

3. RESULTS AND DISCUSSION

In this study, first SDB data on Turkish seas is evaluated after the SDB study conducted at Seyhan Dam Lake by Akgül at al. [6].

In the hydrographic survey performed in the "special order", which is the most accurate survey in IHO S-44 standards [7], the horizontal position accuracy should be ≤ 2 meters. The horizontal position accuracy should be ≤ 6 meters in 1a and 1b orders up to 20 meters of water depth as shown in Table 2. In this context, the spatial resolution of the depth data to be obtained by

Landsat 8 satellite data and SDB methods does not meet the survey standards of IHO S-44 special order but can meet the survey standards of IHO S-44 1a and 1b orders.

Table 2: IHO S-44 Standards for Hydrographic Surveys

Order	**Special**	**1a**	**1b**	**2**
Description of areas.	Areas where under-keel clearance is critical	Areas shallower than 100 meters where under-keel clearance is less critical but *features* of concern to surface shipping may exist.	Areas shallower than 100 meters where under keel clearance is not considered to be an issue for the type of surface shipping expected to transit the area.	Areas generally deeper than 100 meters where a general description of the sea floor is considered adequate.
Maximum allowable THU 95% ***Confidence level***	2 m.	5 m. + %5 of depth	5 m. + %5 of depth	20 m. + %10 of depth
Maximum allowable TVU 95% ***Confidence level***	a = 0.25 m. b = 0.0075	a = 0.5 m. b = 0.013	a = 0.5 m. b = 0.013	a = 1.0 m. b = 0.023
Full Sea floor Search	Required	Required	Not required	Not required
Feature Detection	Cubic *features* > 1 meter	Cubic *features* > 2 meters, in depths up to 40 meters; 10% of depth beyond 40 meters	Not Applicable	Not Applicable
Recommended maximum Line Spacing	Not defined as *full sea floor search* is required	Not defined as *full sea floor search* is required	3 x average depth or 25 meters, whichever is greater	4 x average depth

Recognizing that there are both constant and depth dependent *uncertainties* that affect the *uncertainty* of the depths, the formula below is to be used to compute, at the 95% *confidence level*, the maximum allowable TVU. The parameters "a" and "b" for each Order, as given in the Table, together with the depth "d" have to be introduced into the formula in order to calculate the maximum allowable TVU for a specific depth is in Eq.1.

$$+/- \sqrt{(a)^2 + (bxd)^2} \quad (1)$$

a represents that portion of the *uncertainty* that does not vary with depth

b is a coefficient which represents that portion of the *uncertainty* that varies with depth

d is the depth

Total Vertical Uncertainty (TVU) limits calculated for 5, 10, 15 and 20 meter water depths as explained in the IHO S-44 standards and shown at Table 3. TVU limits of 2. Order are not included the table because 2.Oder is applicable for deeper than 100 meter water depth but SDB is not applicable for deeper than 30 meter water depth.

Table 3: Total Vertical Uncertainty

IHO Survey Orders	Total Vertical Uncertainty			
Depth	5 meter	10 meter	15 meter	20 meter
Special Order	25 cm	26 cm	27 cm	29 cm
1a Order	50,42 cm	51,66 cm	53,67 cm	56,36 cm
1b Order	50,42 cm	51,66 cm	53,67 cm	56,36 cm

Bathymetry chart of Saros Gulf which is created with GRASS GIS software and *i.image.bathymetry* module by Sattellite Derived Bathymetry method is shown in Figure 6.

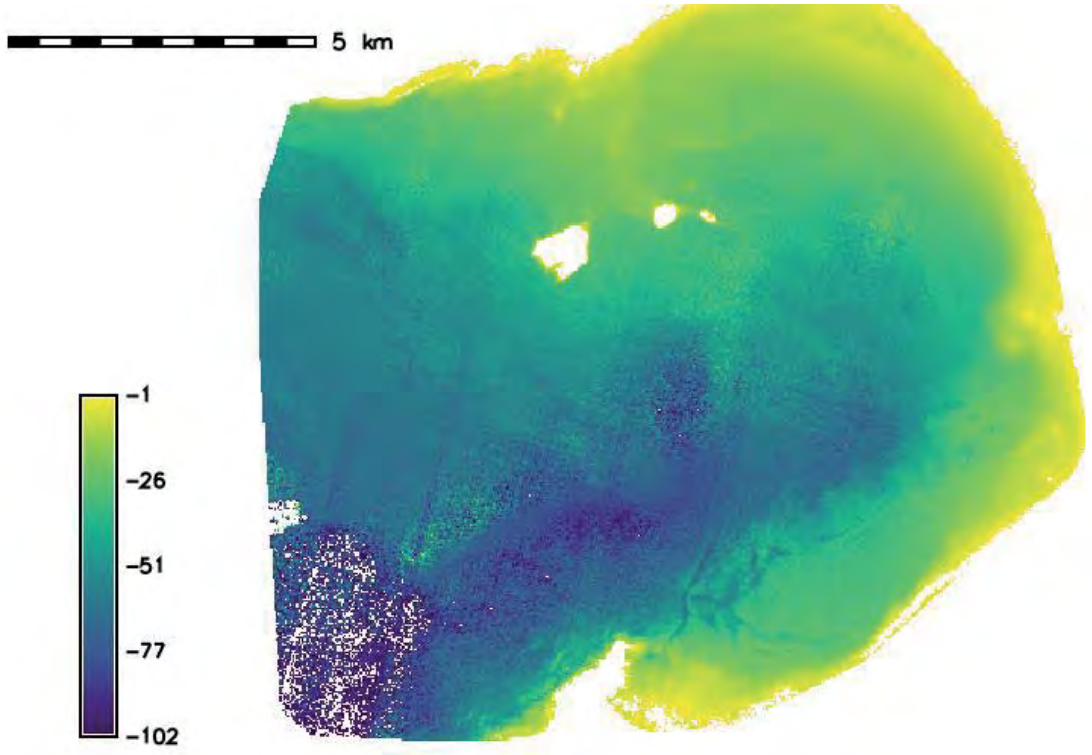

Figure 6. *Satellite Derived Bathymetry Chart*

Contour Line Bathymetry chart of Saros Gulf which is created from SDB depths is shown in Figure 7.

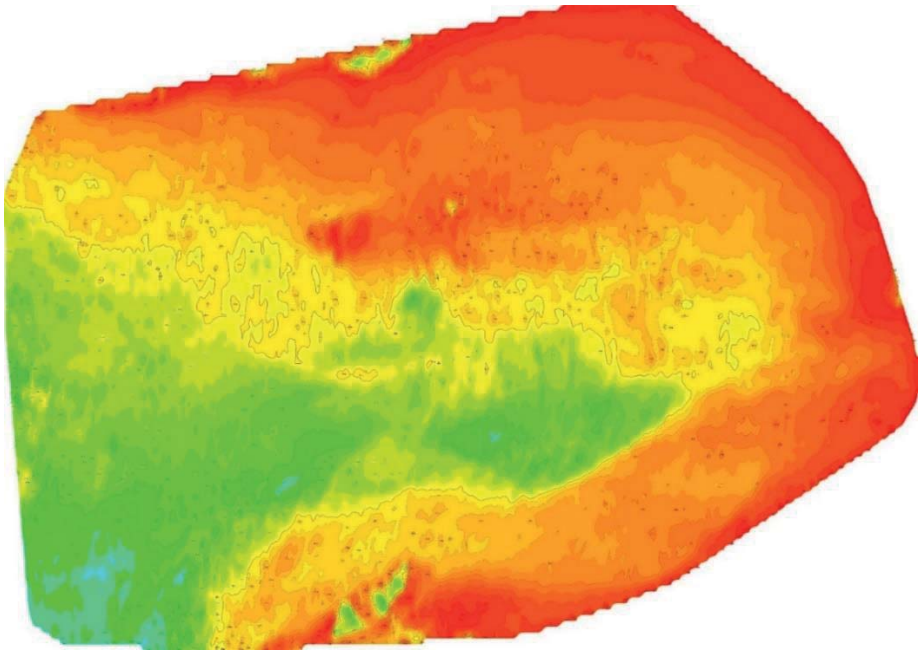

Figure 7. *Contour Line Bathymetry Chart*

SDB data compared with the updated navigation chart and shallower areas than the updated navigation chart is shown in Figure 8.

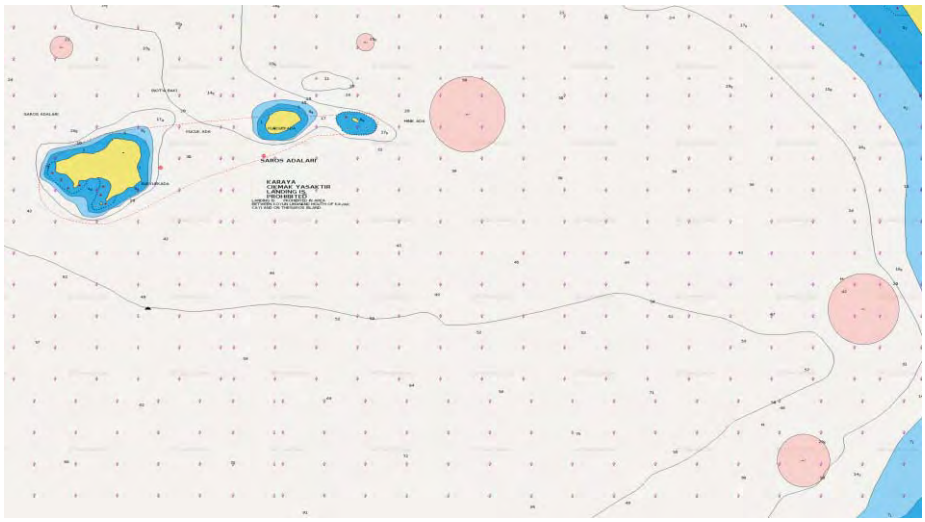

Figure 8. *Shallower areas on the navigation chart*

4. CONCLUSION

The implementation of the SDB method for the purpose of exploration and deceting navigation hazards prior to the research activity, reporting the underwater obstacles to the navigation charts as reported depth by the Office of Navigation, Hydrography and Oceanography and frequent line planning on points reported in subsequent survey activities is considered useful.

After the survey to be conducted with SBES between 0-20 meters, it will be much more efficient both time and economically to make the depth determination of the survey gaps between lines with the SDB method instead of SSS. Bathymetric accuracy obtained by using depth data collected by SBES in the field as control/reference points for the SDB can be greatly increased.

With the availability of satellite images with a spatial resolution of accurate than 2 meters, SDB data can be obtained to meet horizontal accuracy of IHO S-44 special order standards. To include the bottom and water column reflectance coefficients which may be calculated from the Office of Navigation, Hydrography and Oceanography database in the calibration stage, it was evaluated that the accuracy of the obtained SDB data could be improved.

REFERENCES

1. National Oceanic and Atmospheric Administration (NOAA). (2019, April 17). History of Hydrographic Survey. Retrieved from the NOAA Office of Coast Survey website: https://www.nauticalcharts.noaa.gov.

2. Vinayaraj, P & Raghavan, Venkatesh & Metz, Markus & Delucchi, Luca & Masumoto, Shinji. (2017). Implementation of Algorithm for Satellite-Derived Bathymetry using Open Source GIS and Evaluation for Tsunami Simulation. ISPRS International Journal of Geo-Information. 6. 89. 10.3390/ijgi6030089.

3. Vinayaraj, P.; Raghavan, V.; Masumoto, S. Satellite derived bathymetry using adaptive-geographically weighted regression model. Mar. Geod. 2016, 39, 458–478.

4. Lyzenga, D. R. (1978). Passive Remote Sensing Techniques for Mapping Water Depth and Bottom Features. Applied Optics, 17:3, 379-383.

5. Su, H., Liu, H. and Heyman, W. D. (2008). Automated Derivation of Bathymetric Information from Multi-Spectral Satellite Imagery Using a Non-Linear Inversion Model. Marine Geodesy, 31, 281-298.

6. Akgül, M., Dağdeviren, M., Biroğlu, İ. (2018). Satellite-Derived Bathymetry Using Multi-Temporal Satellite Images. DSİ Teknik Bülteni, 127, 14-27.

7. International Hydrographic Organization (2008). IHO Standards for Hydrographic Surveys (5th Edition). Monaco: IHO Publication S-44.

Direct Geo-referencing of UAV Images for Orthophoto Generation based on RTK GNSS Positioning

Burak Akpinar[1], M. Oğuz Selbesoglu[1], N. Onur Aykut[1],
O. Can Bayrak[1], Bülent Bayram[1]

[1] Geomatic Engineering Department, Yildiz Technical University, Istanbul,Turkey, (bakpinar, oguzs, oaykut, onurcb, bayram@yildiz.edu.tr)

ABSTRACT

Aerial or satellite imagery technologies have conventionally been used as a data source for geographic data collection, surveillance, mapping, and 3D modelling issues. However over the past decade, unmanned aerial vehicle (UAV) low-altitude remote sensing technologies are widely used as an effective, fast and inexpensive tool for creating accurate orthophoto maps. The accuracy and precision of orthophoto generated by Structure from Motion (SfM) photogrammetry tool based on UAV photographs depends on many parameters including camera/image quality, flight plan, SfM algorithms and geo-referencing strategy. Taking into consideration the advantages and disadvantages of using ground control points in orthophoto production, a process based on resolution, point density, accuracy, time, expertise and costs is required. On the other hand, conventional geo-referencing based on ground control points provides high accurate positioning but the geometrical accuracy critically depends on the number and spatial distribution of the ground control points. However, direct geo-referencing of the UAV images by using the high accurate positioning ability of Network RTK and Single Base RTK methods may overcome these limitations. Therefore, the automated extraction of control points by the double frequency GNSS receivers can be eliminate the need for ground control points especially for emergency mapping applications. The main purpose of the study is the investigation of the accuracy of orthophoto production without ground control points for mapping applications. In the study, Single Base RTK and Network RTK methods based on GNSS techniques were used during AUAV's flight for direct geo-referencing. 16 ground control points were placed homogeneously at the test area for the validation of the orthophoto accuracy generated by direct geo-referencing. The ground control points were measured with Network RTK method. The images were collected using a UAV and professional camera, at a flight height of 40 m above the ground. Analysis has been carried out in order to reveal the effect of the direct geo-referencing by Single Base RTK and Network RTK positioning methods on orthophoto generation in terms of accuracy and precision.

KEYWORDS: UAV; Orthophoto; GNSS; RTK

1. INTRODUCTION

Photogrammetry is an effective remote sensing method for determination of the objects and details on the topographic earth with the production of topographic vector and orthophoto maps at different scales. Over the last decade, close-range photogrammetry based on UAV technology has become an important tool for producing orthophoto with sufficient accuracy in fast and cost-effective way. The geo-referencing step for processing of imagery based on UAV systems is of great importance for acquiring high accurate orthophoto maps[1]. There are number of methods for geo-referencing of the images for orthophoto generation applications. One of the method is based on IMU devices with integration of the projection center coordinates. However, the low-cost IMU devices cannot provide sufficient accuracy for accurate orthophoto production [2]. In many applications, high-performance aerial mapping systems use GSP/IMU-based direct geo-referencing and the imaging sensor for orientation is computed in post-processing mode[3]. Light UAV models including only a camera and sensor orientation is achieved by the indirect approach by using ground control points (GCP) and performing aerial triangulation (AT). In fact, indirect geo-referencing are more accurate than direct geo-referencing in order to reach sufficient accuracy [2,4]. However, there are requirements in order to achieve sufficient accuracy with direct geo-referencing. The GNSS positioning technique and receiver type is very important to determine orientation of images is directly during the flight in terms of accuracy. For instance, the receiver must has the ability to collect data with two frequencies and should receive the corrections generated by the reference station/s. Single Base RTK method use only reference station for computing the real time corrections based on double difference positioning approach. Moreover, Network RTK method use the multiple reference stations for computing the corrections based on comprehensive methods such as Virtual Reference Station (VRS), Master-Auxiliary Concept (MAC) and Flächen Korrektur Parameter (FKP). In the study, the VRS method which is widely used method for correction modelling in Continuous Operating Reference Stations (CORS) Networks was used. The VRS methods positioning accuracy has been evaluated by many scientists [5-7]. The main purpose of the study is to investigate the accuracy of orthophoto generation based on direct geo-referencing with Single Base RTK and Network RTK methods. The images were collected using Phantom 4 RTK at a flight height of 40 m above the ground.

2. MATERIAL AND METHOD

Images were collected by using a Phantom 4 RTK and is given in the Figure 1. Flights were performed with fully autonomous mode based on the planned coordinates of waypoints. The Phantom 4 RTK contain accurate sensors allowing positioning and orientation of the platform and, subsequently, images.

Figure 1. *The photo of UAV*

The UAV flight was performed in the Football field at Davutpasa Campus of Yildiz Technical University (Figure 2). The generated orthophoto are given in the Figure 3.

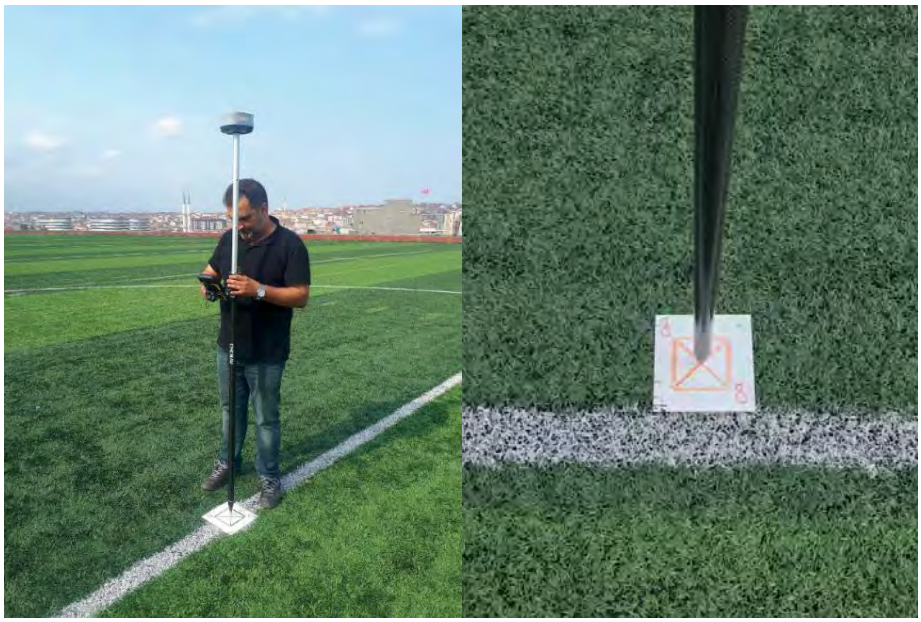

(a) (b)

Figure 2. *Study area and GPCs.*

Figure 3. *The orthophoto of the football field*

The GPCs coordinates were measured with Network RTK method by using the optimum configuration that allows 1 cm accuracy for positioning applications. The configuration of the Network RTK positioning is given in Table 1.

Table 1: Configuration of measurement.

GPCs Name	Method	Number of Observations	Elevation Angle
P1-P13	**VRS**	**10**	**10^0**

The Phantom 4 RTK has the ability for collecting data from GPS, GLONASS and Galileo Satellite systems. The L1 and L2 GNSS signals can be received for GPS and GLONASS system. Furthermore, the B1 and B2 signals can be received for the BEIDOU system and E1 and E5a for GALILEO System. Positioning accuracy of the system is 1 cm + 1ppm horizontally and 1.5 cm + 1 ppm vertically. The UAV is equipped with a 20 mega pixel 1" CMOS sensor camera and a gimbal with a pitching interval between -90° to +30°. In the analysis, 13 GPCs were used and coordinates were given in Table 2.

Table 2: Coordinates of GPCs

P.Name	y	x	h
1	**406275.450**	**4544092.599**	**101.248**
2	**406365.760**	**4544070.295**	**101.153**
3	**406249.156**	**4543952.502**	**101.010**
4	**406301.018**	**4544017.208**	**101.500**
5	**406333.794**	**4544008.882**	**101.182**
6	**406342.615**	**4544043.708**	**101.186**
7	**406309.971**	**4544052.315**	**101.394**
8	**406277.171**	**4544060.709**	**101.232**
9	**406328.830**	**4543937.413**	**101.318**
10	**406325.057**	**4543973.955**	**101.182**
11	**406292.125**	**4543982.436**	**101.338**
12	**406259.469**	**4543990.895**	**101.167**
13	**406268.350**	**4544025.837**	**101.240**

Direct geo-referencing by GPS and GLONASS dual-frequency data in differential mode by Single Base RTK and Network RTK methods were used. In the flight with Single Base RTK method, YLDZ reference station located 400 m away from the test site was used. In Network RTK method, TUSAGA-ACTIVE CORS Network which has an inter-station distances approximately 30-40 km was used for direct geo-referencing.

3. RESULTS AND DISCUSSION

In the study, automatic geo-referencing by the onboard dual-frequency GNSS receiver based on Single and Network RTK positioning techniques was investigated. In our tests, two different orthophoto-mosaic were generated based on the RTK positioning methods. Table 3 shows the impact of the RTK method on orthophoto generation accuracy. Orthophoto based on Single Base RTK method provided 1 cm mean error for horizontal plane while 2 cm in vertically. The Network RTK method's mean errors were found 0.6 cm in horizontally and 3.5 cm in vertically.

Table 3: Coordinate differences of Single Base RTK and Network RTK method.

	Single Base RTK			Network RTK		
	DY (cm)	DX (cm)	Dh (cm)	DY (cm)	DX (cm)	Dh (cm)
MAX	0.3	0.7	3.5	1.4	0.7	5.4
MIN	-2.1	-2.6	0.9	-0.4	-1.9	1.1
MEAN	-1.1	-0.8	2.0	0.9	-0.3	3.5
SD	0.59	1.11	0.83	0.51	0.84	1.37

Important point that the GNSS data recording rate was equal to 0.1 s equivalent to 0.4 m in distance for the flight speed of 4 m/s. However, the images were not collected at the GNSS epochs. Therefore, image positions might be less precise due to the synchronization error coming from the interpolation.

On the other hand, the distance between the reference station and the UAVs GNSS receiver is the important parameter in order to reach high accurate orthophoto by direct geo-referencing. In contrast with our expectation, the results demonstrate that the Single Base RTK method provided more accurate results in terms of standard deviations. Especially for vertical component, Network RTK coordinate differences approximately 50% higher than the Single Base RTK method. In practical case, Network RTK provide higher accuracy than the Single Base RTK method in positioning for various purposes. These results can be explained by the distances of TUSAGA-ACTIVE CORS Network stations to the flight area. On the other hand, the results obtained both two methods demonstrate that the accuracy of orthophoto production by direct geo-referencing based on RTK positioning techniques allows 1 cm accuracy.

4. CONCLUSION

This study compares two different approaches of UAV image geo-referencing and its impact on orthophoto generation accuracy. The Network RTK positioning method was used to measure the coordinates of the GPCs for validation. Two flights were performed with Phantom 4-RTK device by geo-referencing based on Single Base RTK and Network RTK method. The results demonstrate that the sufficient accuracy can be achieved by both two methods. According to the results, dual frequency GNSS receivers might be used for orthophoto generation that in areas where acquisition of GCPs is impossible.

REFERENCES

1. Forlani, G.; Dall'Asta, E.; Diotri, F.; Cella, U.M.d.; Roncella, R.; Santise, M. Quality assessment of DSMs produced from UAV flights georeferenced with on-board RTK positioning. *Remote Sens-Basel* **2018**, *10*, 311.

2. Jozkow, G.; Toth, C. Georeferencing experiments with UAS imagery. *ISPRS Annals of the Photogrammetry, Remote Sensing and Spatial Information Sciences* **2014**, *2*, 25.

3. Rehak, M.; Mabillard, R.; Skaloud, J. *A micro-UAV with the capability of direct georeferencing*; ISPRS Archives: 2013.

4. Stöcker, C.; Nex, F.; Koeva, M.; Gerke, M. Quality assessment of combined IMU/GNSS data for direct georeferencing in the context of UAV-based mapping. *The International Archives of Photogrammetry, Remote Sensing and Spatial Information Sciences* **2017**, *42*, 355.

5. Rizos, C.; Han, S. Reference station network based RTK systems-concepts and progress. *Wuhan University Journal of Natural Sciences* **2003**, *8*, 566-574.

6. Kahveci, M.; Karagöz, H.; Selbesoğlu, M.O. Statik ve RTK GNSS ölçüm ve hesaplamalarının karşılaştırılması. *HKM Jeodezi, Jeoinformasyon ve Arazi Yönetimi Dergisi* **2011**, *104*, 3-13.

7. Gumus, K.; Selbesoglu, M.O.; Celik, C.T. Accuracy investigation of height obtained from Classical and Network RTK with ANOVA test. *Measurement* **2016**, *90*, 135-143.

Comparison of different deep learning based face recognition systems

M. Taha Aydin[1], Metehan Dogan[2], O.Can Bayrak[3], Bulent Bayram[4]

[1]Yildiz Technical University, Technopark Davutpasa Campus, Cifte Havuzlar. Eski Londra Asfalti Street., No: 151/1B B1 Blok No:201A Esenler – Istanbul, Turkey,
E-mail: mtaha.aydin@ayvos.com

[2]Yildiz Technical University, Department of Geomatics Engineering, Davutpasa Campus, 34220 Esenler-Istanbul, Turkey
E-mail: metehandogn@gmail.com

[3] Yildiz Technical University, Department of Geomatics Engineering, Davutpasa Campus, 34220 Esenler-Istanbul, Turkey
E-mail: onurcb@yildiz.edu.tr

[4] Yildiz Technical University, Department of Geomatics Engineering, Davutpasa Campus, 34220 Esenler-Istanbul, Turkey
E-mail: bayram@yildiz.edu.tr

ABSTRACT

Face recognition systems are widely used in the fields of security, criminal identification, advertising and marketing. Nowadays, with the development of deep convolutional neural networks (CNN), significant success has been achieved in face recognition systems. One of the most important steps in the deep learning (DL) based face recognition architectures is the determination of loss functions. Loss functions directly affect facial features embedded in the Euclidean space during training. Euclidean distance is expected to be minimum for same person but maximum for different person. Therefore, it is critical to determine the optimal loss function. Another factor is face detection which directly affects the success of face recognition process. Accuracy and reliability of face detection has vital importance for extracting of facial features.

In this study, Facenet and Arcface facial recognition systems were integrated with Multi-Task Convolutional Neural Networks (MTCNN) and RetinaFace facial detection systems, respectively using VGGFace2 and Casia WebFace datasets. The obtained results from both Facenet+MTCNN and Arcface+Retinaface systems were evaluated. As a result, 86.1% accuracy was achieved in the VGGFace2 dataset by integrating FaceNet and MTCNN architectures. 99.2% accuracy was obtained by integrating ArcFace and Retinaface for the same dataset.

KEYWORDS: Deep learning, Loss function, face recognition, face detection

1. INTRODUCTION

Nowadays, many civil and governmental organizations use face recognition and detection systems for security, crime and missing persons' detection and smart advertising. Two CNN based approaches have been proposed for facial recognition and detection. The first of these approaches is to train a classifier to classify different identities with the softmax classifier. The other approach is based on embedded learning. The facial features learned in Softmax [4, 7] are not sufficiently distinctive. The error rate is highly dependent on increase of dataset. Therefore, Softmax loss is combined with loss functions such as center loss [1], contrastive loss [2, 5] and marginal loss [10] to enhance its distinctive features.

Facenet [3] is an embedded approach and its output directly uses triple loss function. In this approach, selection of semi-hard triplets is very important and directly affects the success of the model. Cosface [6] proposed large margin cosine loss. It maximizes inter-class cosine margin. Sphereface [8] modifies softmax loss and distributes it angularly. Thus, the loss function has a geometric interpretation. Arcface [11] proposed Additive Angular Margin Loss to enhance the distinctive features in the face recognition model. It creates a constant linear angular margin between all classes using Additive Angular Margin Loss to make system undependent to data increase.

Face detection is another important issue for face recognition. Face detection systems are used to create bounding boxes for each detected face. Face recognition systems have two purposes; Face detection and alignment. MTCNN (Multi-Task Convolutional Neural Network) [13] proposed a three-stage CNN structure. In the first stage, a shallow CNN (P-Net) quickly identifies the frames where the face may be included. In the second stage, another CNN (R-Net) search the bounding boxes that are created and incorrect detections are eliminated. Finally, with a stronger CNN (O-Net), the results are improved and their locations are determined. Retinaface [12] proposed a one-stage training by creating a feature pyramid. The common feature of these two approaches is that they create 5 face landmarks and bounding boxes for each face. The alignment is utilized using these landmarks.

In this study, the embedded Facenet+MTCNN approach has been compared with Arcface (creates a constant linear angular margin between classes) +Retinaface. The main factors which play key role for accuracy were investigated and both integrated systems have been tested under different conditions.

2. MATERIAL AND METHOD

In this study, pre-trained Arcface system consists of Resnet100 [16] architecture and Arcloss function [17] and pre-trained Facenet system [3] which consists of Inception Resnet v1 [18] and Triplet Loss function have been used. This is a face recognition system which embeds cropped face images (detected by MTCNN) into embedding array in Euclidean space. Facenet proposes an approach to direct embedding learning, unlike softmax classification [3]. Although this approach is successful in small datasets, but, the selection of semi-hard triplets is very important for large data sets. However, the selection of semi-hard triplets is a very difficult and time-consuming process and it effects directly the accuracy of the system [11].

Arcface and Facenet systems have been trained using Ms-Celeb-1m [15] and VGGFace2 [9] data set, respectively. Facenet training process is given in Figure 1.

Figure 1. *Facenet training process* [3]

One of the main components of Facenet system is triple loss function. According to this function, the Euclidean distance [3] between anchor image and its positive images is expected as minimum. Opposite to this, Euclidean distance between anchor image and negative image is expected as maximum (Figure 2). Thus, the system learns to embed the output and aims to increase the distance between positive and negative pairs during training.

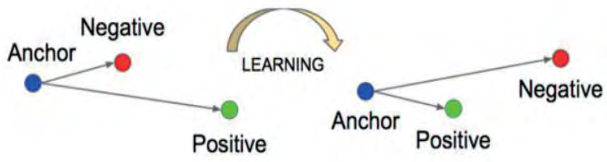

Figure 2. *Triplet Loss Function* [3]

Another used face recognition system is Arcface which embeds cropped face images (detected by Retinaface or MTCNN) into embedding array. It has been trained using Resnet100 architecture. This system learns to classify output similar to Softmax. For this purpose, Arcloss function is used. Since, Softmax classifiers do not create a margin value between classes, Arcface proposes the Arcloss function to maximise face class separability [11].

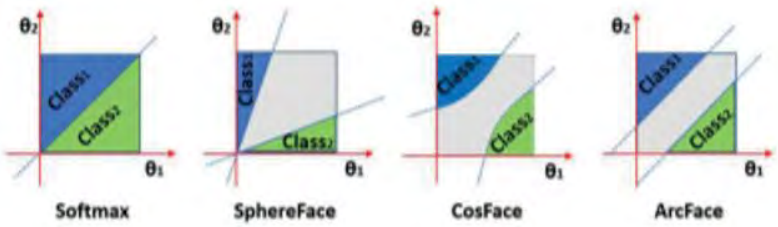

Figure 3. *Classes of different face recognition systems* [11]

Arcloss function creates a constant linear angular margin between classes (Figure 4). This function is based on the Large Margin Cosine Loss [6] function. Unlike Large Margin Cosine Loss, Arcloss has a constant distance between classes. Thus, a more stable model is trained [11].

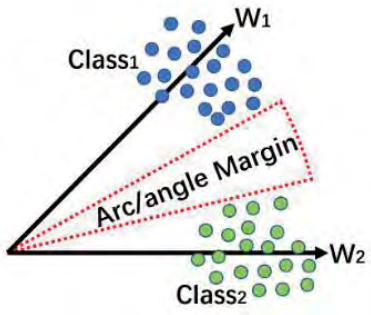

Figure 4. *Additive Angular Margin Loss* [11]

In this study, MTCNN and Retinaface face detection systems have been integrated with Facenet and Arcface systems, respectively.

MTCNN has 3-stage trainings for face detection which are P-Net, O-Net and R-Net, respectively. All steps result with creation of bounding box and 5 landmarks for considered image. MTCNN is successful to detect foreground faces in the image but not efficient to detect background faces as it can be seen in the Figure 5 [13].

Figure 5. *World's Largest Selfie detected by MTCNN* [21]

Retinaface is trained by Resnet50 [16] architecture using Widerface dataset. It generates bounding box coordinates and 5 landmarks as output similar to MTCNN. Unlike to MTCNN, Retinaface can detect very small faces in image since it trained using the feature pyramid. Its false detection rate is very low. Therefore it is very useful for face recognition systems. Although Retinaface trained with the Resnet50 is very successful but it is very slow and not efficient for face detection from real-time video sequences (Figure 6). However, Retinaface trained with Resnet25 architecture is faster than Resnet50 architecture but its face detection accuracy is lower than Resnet50 version of Retinaface (Figure 7).

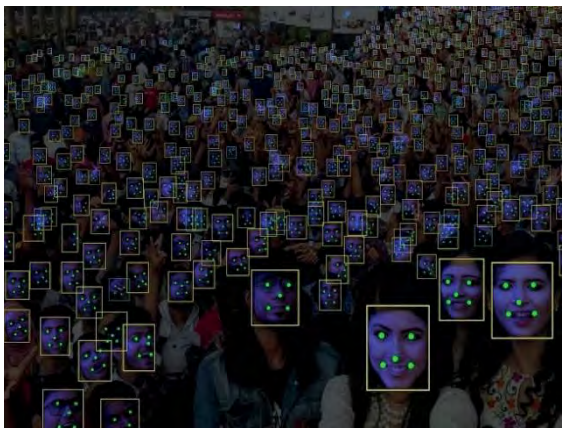

Figure 6. *World's Largest Selfie detected by Retinaface – Resnet50* [20]

Figure 7. *World's Largest Selfie detected by Retinaface – Resnet25* [20]

Two data sets have been used for accuracy assessment. The first dataset consists of 2.000 frontal images which have been selected from the VGGFace2 dataset. Deepgaze Head Pose Estimator [14] has been used to select frontal images from VGGFace2 dataset (Figure 8). The second

dataset is a randomly selected 4.000 images from the Casia WebFace dataset which consists of profile, rotated and frontal images.

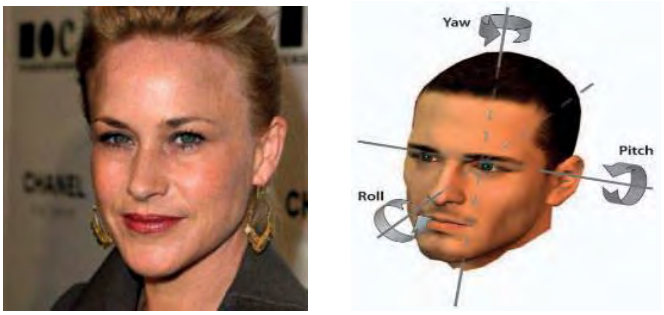

Figure 8. *Separated frontal face image with DeepGaze (roll=7.7°, pitch=-15.1°, yaw=23.5°)* [9, 14]

3. RESULTS AND DISCUSSION

Two images from for each person from each dataset (Casia Webface and VGGFace2) have been used. Total 8.000 and 4.000 images have been processed for accuracy assesment from Casia Webface and VGGFace2 datasets. In the first step, accuracy assessment has been realised using 4.000 frontal images. 2.000 of them have been used to determine ID of person and the rest of 2.000 images have been used for testing. The first images were used to determine the person's id and the second ones were used for testing. The embedding arrays of the test images are created. The Euclidean distances between identified persons and embedding arrays are calculated. The IDs which have minimum Euclidean distance have been compared. For this comparison, empirically defined threshold values have been selected which are 0.85 and 1.25 for Facenet and Arcface, respectively. Calculated Euclidean distances higher than defined threshold values for two dataset were considered as incorrect.

The calculated accuracies for Facenet and Arcface using VGGFace2 dataset are %47 and %90.6, respectively. The erroneous results were classified into 4 different groups as given in Table 1. For each removed images from dataset proper images have been replaced and accuracy assessment updated.

This section can also be divided by subtitles if necessary. It should provide a concise and precise description of the study results, their interpretation as well as the experimental conclusions that can be drawn.

Table 1: Erroneous results in 4 different groups

Error Sources	Facenet	Arcface
Obtained accuracy after removing low resolution images	%67.4	%93.7
Obtained accuracy after removing images include contrast problems	%70.7	%95.2
Obtained accuracy after removing semantically changed images (hair, beard, etc. changes)	%77.9	%97.8
Obtained accuracy after removing cap and glass contained images	%86.1	%99.2

In a randomly selected test data set of 4000 people separated from the Casia WebFace dataset: The calculated accuracies for Facenet and Arcface using Casia Webface %25.1 and %77.5, respectively. Unlike VGGFace2 dataset, the randomly selected images from Casia Webface dataset consist of:

- Profile, frontal and rotated images
- Images have contrast problems
- Low resolution images
- Semantically changed images (hair, beard, etc. changes)
- Cap and glass contained images

4. CONCLUSION

The test results of Facenet+MTCNN and Arcface+Retinaface systems showed that Arcface+Retinaface system is more capable for face detection and recognition compared to Facenet system. However, the results obtained from Casia Webface dataset indicate that face detection and recognition process is highly dependent on quality and semantic content of the images. Although Facenet+MTCNN and Arcface+Retinaface systems have been compared using image datasets, face recognition and detection from real-time video frames are required. Although the accuracy of Arcface +Retinaface system has been calculated as %77.5, but %94 of the incorrect results were higher than defined thresholds. This result depicts that Arcface+Retinaface system can be used efficiently for this purposes.

As a future project, it has been planned to use Arcface+Retinaface system which trained by Resnet25 architecture for video and real-time face detection.

REFERENCES

1. Y. Wen, K. Zhang, Z. Li, and Y. Qiao. A discriminative feature learning approach for deep face recognition. In ECCV, 2016.

2. Y. Sun, Y. Chen, X. Wang, and X. Tang. Deep learning face representation by joint identification-verification. In NIPS, 2014.

3. F. Schroff, D. Kalenichenko, and J. Philbin. Facenet: A unified embedding for face recognition and clustering. In CVPR, 2015.

4. Y. Taigman, M. Yang, M. Ranzato, and L. Wolf. Deepface: Closing the gap to human-level performance in face verification. In CVPR, 2014.

5. Y. Sun, X. Wang, and X. Tang. Sparsifying neural network connections for face recognition. In CVPR, 2016.

6. H. Wang, Y. Wang, Z. Zhou, X. Ji, Z. Li, D. Gong, J. Zhou, and W. Liu. Cosface: Large margin cosine loss for deep face recognition. In CVPR, 2018.

7. O. M. Parkhi, A. Vedaldi, and A. Zisserman. Deep face recognition. In BMVC, 2015.

8. W. Liu, Y. Wen, Z. Yu, M. Li, B. Raj, and L. Song. Sphereface: Deep hypersphere embedding for face recognition. In CVPR, 2017.

9. Q. Cao, L. Shen, W. Xie, O. M. Parkhi, and A. Zisserman. Vggface2: A dataset for recognising faces across pose and age. In FG, 2018.

10. J. Deng, Y. Zhou, and S. Zafeiriou. Marginal loss for deep face recognition. In CVPR Workshop, 2017.

11. J. Deng, J. Guo, N. Xue and S. Zafeiriou. ArcFace: Additive Angular Margin Loss for Deep Face Recognition In CVPR, 2019.

12. J. Deng, J Guo, Y. Zhou, J. Yu, I. Kotsia, S. Zafeiriou. RetinaFace: Single-stage Dense Face Localisation in the Wild In CVPR, 2019.

13. K. Zhang, Z. Zhang, Z. Li, Y. Qiao. Joint Face Detection and Alignment using Multi-task Cascaded Convolutional Networks In CVPR, 2016.

14. M. Kummerer, T. S. A. Wallis, M. Bethge DeepGaze II: Reading fixations from deep features trained on object recognition In CVPR 2016.

15. Y. Guo, L. Zhang, Y. Hu, X. He, and J. Gao. Ms-celeb-1m: A dataset and benchmark for large-scale face recognition. In ECCV, 2016.

16. He, K., Zhang, X., Ren, S., & Sun, J. (2016). Deep residual learning for image recognition. In *Proceedings of the IEEE conference on computer vision and pattern recognition* (pp. 770-778).

17. Deng, J., Guo, J., Xue, N., & Zafeiriou, S. (2019). Arcface: Additive angular margin loss for deep face recognition. In *Proceedings of the IEEE Conference on Computer Vision and Pattern Recognition* (pp. 4690-4699).

18. Szegedy, C., Ioffe, S., Vanhoucke, V., & Alemi, A. A. (2017, February). Inception-v4, inception-resnet and the impact of residual connections on learning. In *Thirty-First AAAI Conference on Artificial Intelligence*.

19. Carneige Mellon University, https://www.cs.cmu.edu/~peiyunh/tiny/, 05.11.2019

20. Deng, J., Guo, J., Zhou, Y., Yu, J., Kotsia, I., & Zafeiriou, S. (2019). RetinaFace: Single-stage Dense Face Localisation in the Wild. *arXiv preprint arXiv:1905.00641*.

21. Yin, X., & Liu, X. (2017). Multi-task convolutional neural network for pose-invariant face recognition. *IEEE Transactions on Image Processing*, *27*(2), 964-975.

Project CABARET – WP7 Educational Development and Deliverables

Boyko Ranguelov[1], Fathimath Shadiya[2], Fathimath Nistharan[2], Mariyam Humra[2], Mariyam Eeman[2], Mohamed Haikal Ibrahim[2]

[1]Mining and Geology University, Geophysics Department 1700 Sofia, Bulgaria
Phone: +359 2 8060 436, E-mail: branguelov@gmail.com

[2]Faculty of Engineering, Science & Technology, Maldives National University, Male, Maldives (fathimath.shadiy@mnu.edu.mv)

ABSTRACT

The **CABARET** (**C**apacity **B**uilding in **A**sia for **R**esilience **E**duca**T**ion) Project is funded by the European Union under the Erasmus+ program, to foster regional cooperation for more effective multi-hazard early warnings and increased disaster resilience among coastal communities. The goal of the Project is to strengthen the evidence-base in support of the implementation of the new framework. The participants constructed of a consortium of 14 European and Asian higher education institutions from nine countries - four from Europe and five from Asia. The Project covers three years period and intend many meetings among participants for data and knowledge exchange. The MGU and MNU participation are active as co-chairs of the WP7 – "Learning and teaching tools methodologies and approaches to the MHEW (Multi Hazards Early Warnings) and sustainable development of the resilience". The progress and achievements of the WP7 co-chaired by MGU and MNU are presented and the developments of MOOC's (Major Online Open Courses) are under discussion. The intended deliverables include MOOC's, Educational Platform development, Manual for use, Technical and Functional Specifications, Implementation actions, Students and wider public presentations about MHEWS, International Cooperation among partners, Sandpit Events, Promotions, etc.

KEYWORDS: Project CABARET; WP7; MOOCs; deliverables

1. INTRODUCTION

One of the most important packages due to the deliverables listed in the Project targeted to all participants is the WP7 entitled "Learning and teaching tools methodologies and approaches" for the mulihazards early warning systems and their applications [1]. The intended Educational Platform (EP), MOOCs (Massive Online Open Courses), technical manuals and brochures, together with the use of the Internet abilities for distant education are the modern tools for Higher Educational Institutions (HEI's) and their high effective performance of the knowledge for real practical purposes could be the most useful outputs [2]. During the last months many activities like bilateral cooperation, new concept about EP, curriculum of the MOOC's, etc. have been performed and executed following the research program and the practical applications [3], [4], [5]. The part of MOOC's is good to follow the Curriculum of Maldives education course (undergraduate level). There some links to other materials (such like larger and deeper content about Multihazards, MHEWS, case studies etc.) could be incorporated for students who like to extend their knowledge about different topics of this issue, because the Platform is targeted to the students of MNU. Another part could be effective for the wide public, containing materials for education and familiarization to the topics of CABARET Project [6].

2. MATERIAL AND METHOD

Massive open online courses (MOOCs) is a mode of e-learning which allows students to study courses from different universities geographically located anywhere in the world. MOOCs are classified in to various groups based on pedagogical approaches and training functions. The MOOC to be developed would follow content-based MOOC (xMOOC). It's goal is to effectively deliver the content to a wider audience making use of behavioral principles of acquiring knowledge through repetitive testing of knowledge [5]. This consists of lectures and quizzes to test the mastery of the theory taught, assessments complying to deadlines, discussion forum to connect student with lecturers/instructors and other students enrolled in the course. The course and content of the course is open to anyone interested MHEW systems [6]. Registration is free and requires only a click in the relevant link in the platform and filling up information to sign up [7]. The WP7 is targeted to the creation of MOOC's, Educational Platform (EP), Informative materials to the wide public, and all these tools in electronic based Platform. Some elements are presented next:

Course duration and content break down include:

100% online learning (start instantly and learn at own schedule).

Flexible deadlines (reset deadlines in accordance to the schedule).

Beginner Level (approximately 12 hours to complete).

Suggested 10-15 hours of lectures, quizzes, and assignments

Language – English, Subtitles: English

3. RESULTS AND DISCUSSION

The results (different modules, thematic, time duration etc. are summarized in a comparative Tables and adapted to the conditions in South-East Asia.

Table 1: Tables of the modules, thematic topics and time duration.

3.1. Module 1 - Multihazards

Upon the completion of this module, the learner will be to understand the different types of hazards, how hazards become disaster. Conditions, complexity and negatives effects of hazards. Measuring risk assessments and economic losses.

4 hours to complete

18 videos (Total 158min), 6 readings, 5 quizzes

Introduction to risk frame work	1	m
Define hazard, exposure, vulnerability and risk	10	m
Introduction to hazards	2	m
Earthquake	8	m
Cyclone	8	m
Tsunami	8	m
Flooding	8	m
The nature of multi-hazards	5	m
Conditions, complexity and negative effects	10	m
Economical losses	10	m
Single to multiple consequences	10	m
Nonlinearities of the damages	10	m
Hazard assessment	5	m
Exposure assessment	5	m
Vulnerability assessment	5	m
Integrating the risk framework with impact	10	m
Why hazard become a disaster?	10	m

SDGs, SENDAI framework, local frameworks	10	m

6 Readings

Learning Objectives	5	m
Syllabus	5	m
Risk framework	10	m
Hazards in Asian Region	10	m
Multi-hazards	10	m
Disaster Risk Analysis	10	m
DRR policies	10	m

5 Quizzes

Introduction to risk framework	5	m
Hazards in Asian Region	10	m
Introduction to multi-hazards	10	m
Disaster Risk Analysis	10	m
Introduction to DRR policies	10	m

3.2. Module 2 – Multihazards Early Warning Systems

Upon the completion of this module, the learner will be introduced to early warning systems and available technologies. Will have a understanding of Indian Ocean and Pacific Tsunami warning systems, the effectiveness of these systems along with regional and local mechanism used.

4 hours to complete

8 videos (Total 70 min), 5 readings, 4 quizzes

Introduce the framework of early warning systems	5	m
Available technologies	5	m
Indian Ocean and Pacific Tsunami warning systems	10	m
Effectiveness of the existing systems	10	m
National, regional and local mechanisms	10	m
Existing initiatives and upcoming initiatives	10	m
The concepts of upstream, interface and downstream	10	m
Effectiveness of the upstream, interface and downstream mechanisms	10	m

5 Readings

Learning Objectives	5	m
Syllabus	5	m
Introduction to multi-hazard early warning systems	20	m
Existing early warning systems	20	m

Governance mechanisms in place	20	m

4 Quizzes

Framework of early warning systems	10	m
Available technologies	10	m
Indian Ocean and Pacific Tsunami warning systems	20	m
Effectiveness of the existing systems	10	m
National, regional and local mechanisms	20	m
Existing initiatives and upcoming initiatives	10	m
The concepts of upstream, interface and downstream	10	m
Effectiveness of the upstream, interface and downstream mechanisms	10	m

3.3. Module 3 – Community Based Disaster Management (CBDRM)

Upon the completion of this module, the learner will understand the basic concepts of CBDRMs their best practices along with the challenges faced, and how to link multi-hazards systems to CBDRM systems

4 hours to complete

5 videos (Total 50 min), 5 readings, 5 quizzes

Basic concepts of CBDRM	10	m
CBDRM in process	10	m
Best practices of CBDRM	10	m
CBDRM challenges	10	m
Link multi-hazards with CBDRM systems	10	m

5 Readings

Learning Objectives	5	m
Syllabus	5	m
Basic concepts of CBDRM	20	m
CBDRM in process	20	m
Best practices of CBDRM case studies country specific	20	m
CBDRM challenges Case studies	20	m
Link multi-hazards with CBDRM systems	20	m

5 Quizzes

Basic concepts of CBDRM	10	m
CBDRM in process	10	m
Best practices of CBDRM	20	m
CBDRM challenges	20	m
Link multi-hazards with CBDRM systems	20	m

4. EDUCATIONAL PLATFORM

The Educational Platform (EP) has to respond the following technical specifications.

Context	• Course description • Course schedule • Syllabus • FAQ
Resources and assessments	• Individual modules to support self-placed learning • Resources shown in context of learning activity • Support of different content format (text, presentations, image, video) • Self-test quizzes at the end each lesson. • Case study along with readings to assess mastery of knowledge at the end of each module • Language - English
Interactivity	• Discussion forum - Link provided takes students and instructor to space where they can interact in real-time and contribute ideas offline.
Technical support	• Free and open access to course content • Course and material always available and downloadable • Course content under open-license to be used without restrictions

5. CONCLUSIONS

- The international cooperation in the frame of the WP7 – CABARET Project is established to the creation and development of the educational tools for HEI's and wider public.
- A progress of the work performed in the frame of the WP7 of CABARET Project is displayed including technical specifications of the educational platform development and MOOC's structure and content.
- The co-chaired WP7 by MGU and MNU is under development according to the time schedule of the Project. First results of MOOC's are available – educational modules are established by content and temporal structure.
- New concept for the further development of the structure of the Educational Platform (EP) of the CABARET Projects is proposed.
- Intended international cooperation among participants of the Project is an essential topic for the coastal resilience educational platform development.

ACKNOWLEDGEMENT

This work is supported by the CABARET Project No 573816-EPP-1-2016-1-UK-EPPKA2-CBHE-JP of EU Erasmus+ Program.

The European Commission support for the production of this publication does not constitute an endorsement of the contents which reflects the views only of the authors, and the Commission cannot be held responsible for any use which may be made of the information contained therein.

REFERENCES

1. Capacity Building in Asia for Resilience Education – CABARET Project. Detailed Description of the Project. Annex IV. Version 1., 2016, 201 pp.

2. Ranguelov, B. K. The EU ERASMUS+ Project CABARET and MGU Participation., Ann of Mining and Geology University, 2017, Volume 60 (1), pp.90-93.

3. Ranguelov B. K., Shadiya F. A. The CABARET ERASMUS+ Project - WP7 (Progress and Achievements), Proc. S E S 2 0 1 8 , 7 – 9th November 2018, Sofia, Bulgaria.

4. Ranguelov, B. K. Project C A B A R E T - E U Tool for Sustainable MHEW Education for Coastal Communities., Proc. „ОБРАЗОВАНИЕ И НАУКА – ЗА ЛИЧНОСТНО И ОБЩЕСТВЕНО РАЗВИТИЕ"., 27–28th October, 2017. pp. 396-404. https://uni-plovdiv.bg/pages/index/1318/ (accessed on 12 08 2019)

5. Seidametova, Z. Design and Development of MOOCs. 2018. Available online: http://ceur-ws.org/Vol-2104/paper_244.pdf (accessed on 10 09 2019)

6. Guidelines for Development and Implementation of MOOCs, 2015. Available online: https://www.aicte-india.org/downloads/MHRD%20moocs%20guidelines%20updated (accessed on 07 08 2019).

7. Oniţa, M., Mihăescu, V., & Vasiu, R. Technical Analysis of MOOCs. 2015. *TEM Journal 4*(1). Available online: http://www.temjournal.com/content/41/07/temjournal4107.pdf (accessed on 12 08 2019)

VR Technologies in Geospatial Education

Tanya Slavova[1], Deyan Sosserov[2], Asparuh Kamburov[3], Krasimima Gachevska[4], Nikola Kostalov[5], Vanya Stoyanova[6]

[1] University of Mining and Geology 'St. Ivan Rilski', 'Prof. Boyan Kamenov' Str., Sofia 1700, Bulgaria (tanya.slavova@mgu.bg)

[2] University of Mining and Geology 'St. Ivan Rilski', 'Prof. Boyan Kamenov' Str., Sofia 1700, Bulgaria, (sosserov@abv.bg)

[3] University of Mining and Geology 'St. Ivan Rilski', 'Prof. Boyan Kamenov' Str., Sofia 1700, Bulgaria, (asparuh.kamburov@mgu.bg)

[4] University of Mining and Geology 'St. Ivan Rilski', 'Prof. Boyan Kamenov' Str., Sofia 1700, Bulgaria, (krasi_roko@abv.bg)

[5] University of Mining and Geology 'St. Ivan Rilski', 'Prof. Boyan Kamenov' Str., Sofia 1700, Bulgaria, (nikola.lek13@gmail.com)

[6] University of Mining and Geology 'St. Ivan Rilski', 'Prof. Boyan Kamenov' Str., Sofia 1700, Bulgaria, (iwankastoqnowa@gmail.com)

ABSTRACT

Virtual reality (VR) is an interactive computer-generated simulation of a real or fictional environment. This term, that is widely used nowadays, has history dating back to the 1960s. Since then different types of virtual reality have been defined. This requires to outline what exactly is meant by this term in the current paper and where its place is in comparison to the other "realities". During the last decade VR, traditionally associated with video games, is gaining a contemporary increasing popularity in other divisions including education and engineering. On one hand, in the current paper it is investigated the role of computer simulations and gamification in modern education, how these improve teaching results, what are the strengths and the problems. On the other hand, it is studied how this technology is currently implemented in engineering and geospatial science and workflow in particular and how this could be developed in future. The study on the available practical examples is supplemented by analysis of the measurement tools and the data appropriate for rendering a real-world simulation.

The available technical solutions on the market are reviewed in terms of building up a VR laboratory. The hardware classification, including VR visualization tools like head-mounted displays and CAVE automatic virtual environments, is defined by properties like a degree of immersion and affordability. Regarding to software, a subject of interest are game engines which main characteristics are presented in the paper. Bearing in mind the possible options for future development and extension of a system it is proposed a solution for the needs of geospatial education.

KEYWORDS: Virtual Reality, Geospatial, Education

1. INTRODUCTION

Training has a key role in education as learning in authentic situations evokes and comprises real-life experience. For some people modern technologies provide the opportunity to approach similar experience in a virtual environment, others are sceptic. Nevertheless technologies are taking greater and greater part of our personal and professional life, so it is natural to consider how to take an advantage of them to build a bridge between these two spheres as education does.

Regarding to studies dedicated to virtual education most of them have been published since 2010 which shows clear interest on applying such tools for this purpose. A large part of them is focused on the pedagogical aspect, whereas technological development is reviewed by a few. In terms of teaching disciplines, VR has no borders gaining popularity in science, technology and engineering (STE) 16, astronomy, physics, chemistry, archaeology, medicine, etc. In terms of VR application in geospatial education, the study was extended with a research on VR application in the working process of a variety of applications – urban planning4, 17, 21, geosciences 13, 18, engineering 2, mining7, etc.

This study was set as a base for the establishment of a new VR laboratory so it was made a system overview, followed by a case study. The process of field data logging and visualization in a virtual environment are described, as well as the chosen equipment for a newly established VR laboratory for the needs of geospatial education. Finally, the attitude on VR technology is validated through a questionnaire on a public event attended by both specialists and non-specialists.

2. BASIC DEFINITIONS

Regarding to Boton's study 2, some of the definitions of the term "Virtual Reality" given by different authors include "computers, head-mounted displays, headphones, and motion-sensing gloves" and "electronic simulations of environments experienced via head-mounted eye goggles and wired clothing enabling the end user to interact in realistic three-dimensional situations" but these device-oriented definitions does not seem acceptable to convey the whole complexity of the concept, while other definitions try to avoid any "reference to a particular hardware system". For some authors the three most important properties of virtual reality are the so-called "3 Is": immersion, interaction and imagination 8, while for others there are four key elements to consider and combine: the virtual world, immersion, sensory feedback, and interactivity 2. While they slightly differ, both of them include "immersion" and "interactivity" which refer respectively to the sensation of being in an environment and the respond of the VR system to the actions of the user. These two are essential features of a VR system.

Four main types of "realities" are distinguished today (Fig.1). On the one end of the reality-virtuality (RV) continuum stands the real environment (RE), which spills into augmented reality (AR), transforming into augmented virtuality (AV) which immerse into the virtual environment. This final stage on the second line of the RV continuum is the subject of the

current paper. By definition a virtual world is a computer-generated, boundless, immersive "game-like" environment 3. Such environments are called virtual environments (VE).

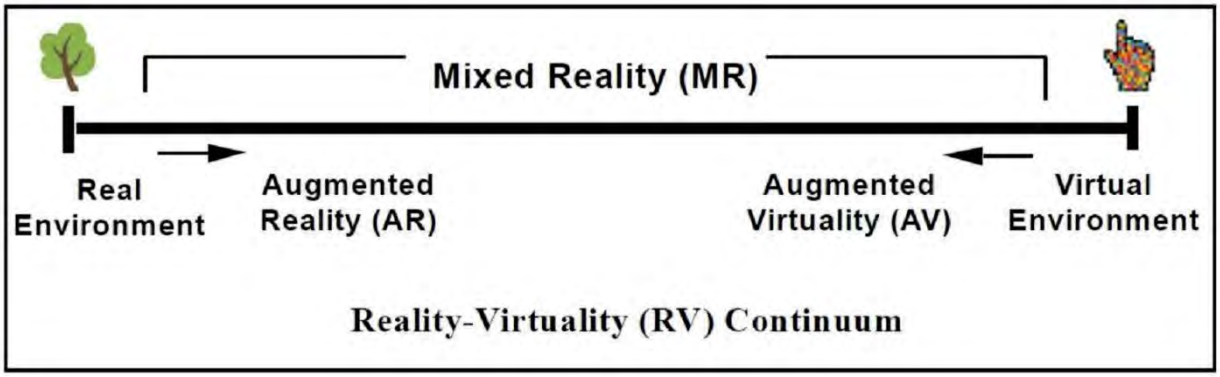

Figure 1. *RV continuum*

3. VR IN EDUCATION

3.1 Main Aspects

According to Beguin, 2002, cited in Paravizo 15, three main goals can be pursued with simulations: observation, learning and designing. Traditionally associated with video games, currently VR is also widely used in medicine, chemistry, physics, engineering, archaeology, entertainment and so on, and therefore it is suitable for education in all these disciplines.

The review on papers dedicated to VR application in education shows that most of them are not older than a decade - a confirmation of a currently hot topic. Considering the wide usage of computers and internet for teaching, two main divisions are outlined – virtual and remote computer-based laboratories. The first group refers to computer simulations with typically high visualization and interaction capabilities, aimed to help students perform a given (simulated) scientific or engineering experiment, whereas the second one represents computer programs that provide a graphical user interface (GUI) to interact with real hardware performing the experiment 5. In terms of this paper the focus falls solely on virtual laboratories (VL).

The term "virtual laboratory" first appeared in 1992. The idea of its application in education/learning is to visualize geospatial structure in three-dimensional space, and use the virtual reality to render the 3D model and further bring the stereoscopic perception to the users so they can understand the geospatial structure and enhance their memory 13. The design strategy of 3D interaction is mainly guided by the experience of the users in the real world. It is expecting the user adopts the real world knowledge but also to go beyond their perception of it. One to one correspondence interaction may reduce the efficiency, comfort and usability of the VR system so a rational interaction design not only enhance these but also avoid possible chaos and unexpected interaction.

Gained growing popularity among universities and educational institutions in the past two decades and especially in the 2010s, it seems that using virtual worlds for teaching and learning possesses great potential for students and teachers. Keeping a realistic view requires to bear in mind both advantages and disadvantages of virtual tools. Regarding to different studies (11, 14, 16, 13), they are summarized in Table 1:

Table 1: Advantages and disadvantages of VR education for teachers and students.

	Teachers	Students
Advantages	- Adding experience in the classroom - Control of the experience - Making the "unseen" seen - Custom design regarding to individual learners - Easily reproduced experiments - Damage resistance - Setting a greater variety of simulations than practical experiments - Providing experimental situations not observable in reality - Not so complex and/or expensive as actual experiments - Cost effective	- Better understanding of the covered topics - Learning is not dependent on specific time and place - Learning materials adapted in the learning environment to the learner's needs
	- Safe environment	
Disadvantages	- Extensive planning and time for preparation - Dependence on computer tools	- Lack of interaction with the experience - Possible lack of seriousness - Possible need of final stage of training through actual hands-on experience

A growing trend in contemporary education is game-based learning, and game design principles and gamification theories can be found underlying in development of VE 15. The advanced technology of video games attracted great attention from the scholars to promote the motivation, excitement and participation of users, which represents to be a major concern in the design of human-computer interaction 13. It is proven that this kind of interactive engagement improves students' understanding, motivation and learning outcomes 5. According to different studies conducted in the last decade and summarized by Estriegana 6, game-based learning environments have significant potential to challenge and involve students in an active learning process, improving their attitudes, interest in learning and acceptance of technology.

The use of computer games and game engines in environmental applications and planning is increasing due to their advanced performance and interactivity capabilities 17. If well designed,

games enable the inclusion of target groups without expert proficiencies into a multidisciplinary environment since they provide familiar settings for unfamiliar subjects. This makes games an effective educational tool that facilitates knowledge and information exchange.

The application of VR in education enables training in a safe environment as well. During the teaching process in some disciplines, such as mining specialty for example, it is usually difficult, costly to organize, time-consuming and has high risk to take students into a real mine and let them deeply comprehend the structure and procedure of various mining methods7. According to Fei a virtual mine teaching platform can greatly enhance the vitality, efficiency and safety in mining education both for students and for mining workers training and mining experiments.

3.2 VR in Engineering

According to Berg and Vance's study on industry use of VR 1, the technology is defined as mature, stable, and, most importantly, usable in industries such as architecture, engineering and construction. In the areas of knowledge, related to practical and technological fields, students must spend much of their working time to solving practical problems and simulating experiences 6. Regarding to Estriegana's literature review on VL, simulators and hands-on exercises, properly designed virtual experiences may replace real-life experimentation, facilitate learning process and enhance learning outcomes. Additional advantages of VL are their potential of distance learning to increase flexibility and accessibility.

The use of VR for scientific and information visualization can provide useful insights on many datasets, for example allowing users to explore information from the inside-out in contrast to 2D techniques which give an outside-in view 9. Compared with traditional CAD tools and approaches, the inherent simplicity of the 3D environment exploration can make user involvement in design process more effective 15. As it is said in Paravizo's study: "[then, using traditional CAD software] we went as passengers. In this one [the GE-based VE], we go as drivers. […] This tool enables us to share more the analysis of the environment. The analysis and design of the environment".

Contemporary science and industry are also characterized with a growing complexity. This requires well-prepared specialists who are able to solve problems efficiently and to work in interdisciplinary teams 8. Technology enhanced learning will lead to pan disciplinary, interdisciplinary and multidisciplinary education content in various forms which focus on various cultures 13.

3.3 VR in Geospatial

While VR has its roots in the 1950s and 1960s, concerted research only began in the 1980s when computers became adequate to allow the creation of realistic virtual worlds 18. First studies of the combination of VR and geographic information systems (GIS) dates back to the

beginning of the 1990s 4 which led to the concept of VRGIS. At the end of the 2010s it has turned into a hot topic 21.

A Geographic Information System (GIS) is often defined as a combination of a database management system, a set of operations for examining data, and a graphic display system which are tied to the process of spatial analysis 19. GIS environments are also cartographic tools that allow for building maps in real time and examining the impacts of changes to the map interactively. VRGIS represents VR technology as a front-end interface with users and support of spatial GIS data in areas related to modern cities and urban management, such as transport and traffic, e-business and e-government, ocean and island management, scenic area management, virtual community and geography education. It is considered by many as a substantial potential for developing efficiency and increasing interaction in spatial decision-making and a good tool for audiences as the public contemplates design ideas relying on their experience of viewing space. Roaming in virtual cities and touristic sites has become a substitute for traditional maps to represent, describe, examine and design concepts. Places are displayed clearly to people, creating an immersive environment for utilization of spatial GIS data allowing users to navigate and interact. After using VR technology, decision-makers, designers, engineers and the public can see the real-time effects of different "what-if scenarios" that otherwise would take a lot of resources and time.

Simultaneously with developing VR technology and broad applications, the basic requirements are also growing rapidly – users require not only to obtain geospatial data dynamically but want also to apply controls, evaluations, calculations and transfers in the light of existing data 4. Regarding to Herwig's case study 10 some features for a professional use of game engines in landscape planning include GIS interface, geo-reference, interactive orientation, selection, analysis and editing functions.

The landscape visualization offered by the graphics-assisted games triggers significantly public interest in the planning process 10. The case study explored by El halabi 4 gives some important results on personal experience of a VRGIS. All participants preferred the use of modern means to facilitate the decision-making process.

The entertainment industry is interested in the landscape theme (terrain, vegetation etc.) 10. Both landscape planning and the entertainment industry could benefit from this concern to produce realistic games and tools for professional landscape visualization. For that purpose landscape planners (among others) should offer their professional knowledge of real landscapes and the specific needs for interactive landscape visualizations.

4. SYSTEM OVERVIEW OF A VR LABORATORY

VLs are a convenient and cost effective way of improving education. After the initial investment on building up such a laboratory there are no additional payments on special equipment, consumables and transportation that are usually related to field activities. Aside from the benefits it does not mean it is easy to create and deploy. The difficulties are mainly

related to the hardware and especially software expertise required to create and maintain the VR environment, as well as training students to use and take advantage of it.

A VR laboratory consist of hardware and software. It is recommended to follow industry standards in order to not waste effort, time and money working on a platform that doesn't seem to be valid for a longer period. It is also advisable to carefully choose the most appropriate and affordable, if not completely free, tools so a future lack of funds won't affect the project life, and this also increments the opportunities on collaboration 5.

4.1 VR Devices

VR systems are traditionally classified into two main categories: "immersive" (or egocentric) VR which uses a helmet-mounted video/audio system to give the user the experience of interactive immersion within the virtual world; and, desktop, "through-the window" (or exocentric) VR which displays the virtual world on a traditional 2D monitor screen 18. Other authors extend this classification with a mid-group called semi-immersive 2 which includes more complex solutions than the basic non-immersive VR and yet not as comprehensive as the fully-immersive VR. The focus of the current study falls on the last, fully-immersive group. According to Mengoni et al. cited in 2, it is divided into seven subclasses according to the different display technologies: HMD, auto-stereoscopic display, curved screen, stereoscopic projection, holographic display, CAVE-like display, and dome-shape display, and their comparison is extended by several performance metric including: the image resolution, the haptic feedback, the sound and the motion feedbacks, the ease of learning, the mental load, the user centrality, and the ease of use.

VR is realized through multiple devices which enable bidirectional information flow between the user and the virtual world. From technological point of view, it is immersive if it provides stereoscopic presentations of objects in real size as well as head-tracking of the user 8. Since its introduction in 1960s **Hata! Başvuru kaynağı bulunamadı.** the VR technology has experienced several waves of interest – in the 1980s and 2000s, and evolved significantly 9. Its development led to the high-quality consumer-grade HMD devices currently available on the market, like HTC Vive, Oculus Rift and Valve Index. Widely used HMDs are complemented by user tracking, immersive audio and haptics to improve the user experience. Liagkou's study 12 evaluates the costs of several high-end and yet affordable VR solutions and the complementary PC equipment for training and education purposes. Showing proportionality between these two factors, HTC Vive and Vive Pro have the highest prices, followed by Oculus Rift and other solutions. HMD solutions are described as moderately immersive but affordable for the end-user in comparison to the highly immersive but much more expensive cave automatic virtual environments (CAVEs).

4.2 Game Engines

Game engines represent a powerful software package that enables developers to build games and applications using pre-existing modules of 2D/3D rendering, game physics, input manipulation and so on, speeding up virtual environment development process 15. They are versatile and low-cost tools, with a worldwide user community that provides help and resources via Internet 10.

A 3D game engine includes numerous key runtime components that enable efficient game development and performance, such as rendering engine, physics engine, animation modules, collision detection, scripting, visual effects, math libraries, etc. 17 The possible interactions that could be implemented on a virtual environment include interacting with the environment and equipment (e.g. information spots), interacting with non-playable characters – NPCs (e.g. dialogues for working conditions) and interactions with the resources available to the user 15.

Using 3D game engines for landscape visualization requires a fundamental knowledge in 3D designing 10. Trial-and-error methods are often necessary to import terrain, 3D objects, and other data from CAD/GIS software. Game engines have great potency as a design platform due to their optimized performance, graphic abilities and user-friendly interface, but their detachment from the GIS environment limits their ability to be used stand-alone in a planning process since most existing geospatial information and the analytical impact calculation functionalities are usually only available in GIS environment but the integration of GIS in a game engine, wherein geographic coordinate systems and GIS functionalities are managed, is a crucial step.

In order to ease development of VR software, most hardware vendors provide plugins which integrate into the most common game engines, specifically Unity 3D and Unreal 9. Software companies can then use these plugins to develop VR experiences for multiple devices.

5. CASE STUDY

5.1 Data logging and processing

The implementation of digital environments in the field of mining and engineering education and their visualization through virtual reality systems is dependent to availability of different geospatial information. Related to this, with the help of existing geospatial technologies and software in the cathedra of "Mine surveying and geodesy" of the university, geospatial data from various objects in the country was acquired. The new subway tunnel in the Sofia city, fully functioned quarry, underground and open mine, as well as transport and micro water tunnels were captured via technologies like terrestrial laser scanning (TLS) and aerial digital photogrammetry through UAV, suplemented with the conventional total station and GNSS measurements. All this has ensured approaching to the state-of-the-art geospatial solutions, where this technologies works integrated to each other and secured realization of accurate measurements with interesting content and variety.

The acquired geospatial information, in the form of point clouds, were than merged through the CloudCompare software. This led to generation of digital environments of the sites and their visualization through virtual reality system, integrated in the Unreal game engine, through a specific plug-in. These virtual places are going to be a base for an ongoing educational purposes like different training activities, practices and science developments in a future VR Lab.

5.2 VR Visualization

The Unreal Engine 4.23 was the game engine selected for designing the VE, mainly due to its visual graphics capabilities and support for interactions without the need of employing a traditional programming language known as Blueprints. Other of its main features include C++ source code and Python scripting, not only VR, but also AR and MR solution, landscape system, content browser, etc. More information, as well as download through registration is available on 22.

A key factor in Unreal Engine is its extensibility through plugins many of which are available for free. A Point Cloud Plugin 22 was used to upload the available through field measurements point clouds. Its features include simple drag-and-drop import, support of most column-based source files, large data support, color support, level of detail, etc. With the use of this plugin were created several VEs to represent different working sites (Fig.2).

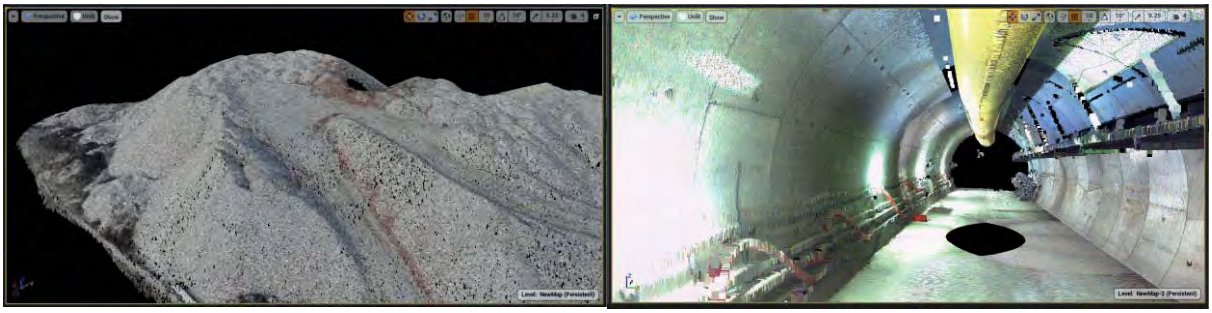

a) *b)*

Figure 2. *Visualization of geospatial data in a VE: a) aerial surface view; b) underground view*

5.3 VR Equipment

Following a detailed market analysis in terms of pricing, functionality, robustness and processing power requirements, two systems are purchased and integrated into the newly developed university VR laboratory – HTC Vive (PC-based device) and Oculus Go (autonomous device). The necessary funding – 1750 € - is provided from a dedicated university project, funded by the Ministry of Education and Science of Bulgaria though the "Ordinance #3 on the terms and procedure for evaluation, planning, distribution and spending of the state budget to finance scientific or artistic activity in state higher schools." The HTC Vive kit includes 2 base stations, 2 controllers, wireless adapter, audio strap and other related

accessories, which are installed inside a dedicated classroom within the department premises, which may be easily transformed into a fully-functional mobile VR laboratory (Fig. 3).

Figure 3. *Demonstration of HTC Vive kit inside the mobile VR laboratory during the European Researchers' Night 2019*

Unlike VR devices like Google Daydream and Zeiss, which either support only several smart-phone models or require special adapters, Oculus Go is a rather open autonomous VR system. It may utilize the upbeat of VR/GIS integration, (e.g. through the supported ArcGIS 360 VR App) and thus provide another level of functionality inside the laboratory.

6. PUBLIC APPROVAL

In 2019 the University of Mining and Geology hosted two public events where the VR laboratory was demonstrated. The first one was an Open Doors Day dedicated to mid- and high-school students and the second one was the European Researchers' Night (ERN) dedicated to non-scientists.

On both of them the interest on this technology was visible. In order to "measure" the public approval on it a questionnaire was prepared for the second of these two events. 43 people participated, almost half of whom were between 18 and 24 years old (Fig. 4), and, respectively, the answer on the question about occupation was 50% for "student". 79% from the respondents answered they know what VR is, 14% have some idea, and 7% - no idea (Fig. 5). On the question "What's your opinion on integration of VR in working/learning process?" the positive attitude was declared by 86%, 75% of which answers were "strongly positive", and negative - by 9% (Fig. 6).

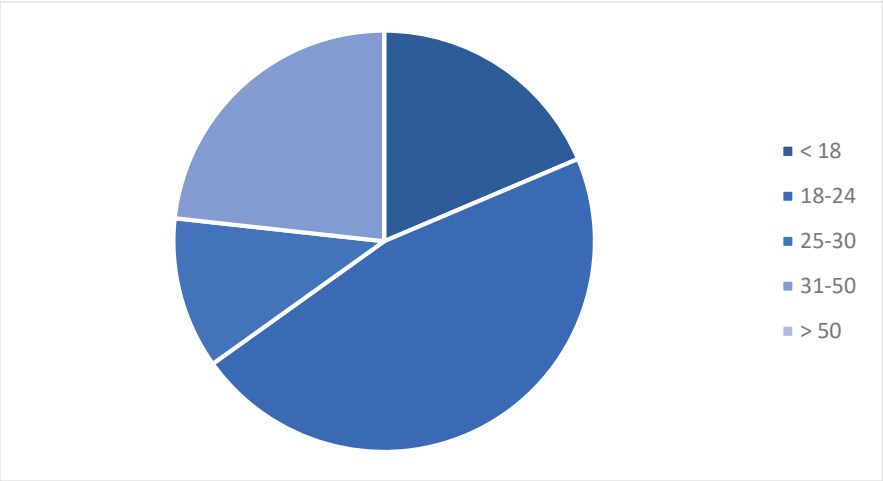

Figure 4. *Age of the participants (in years)*

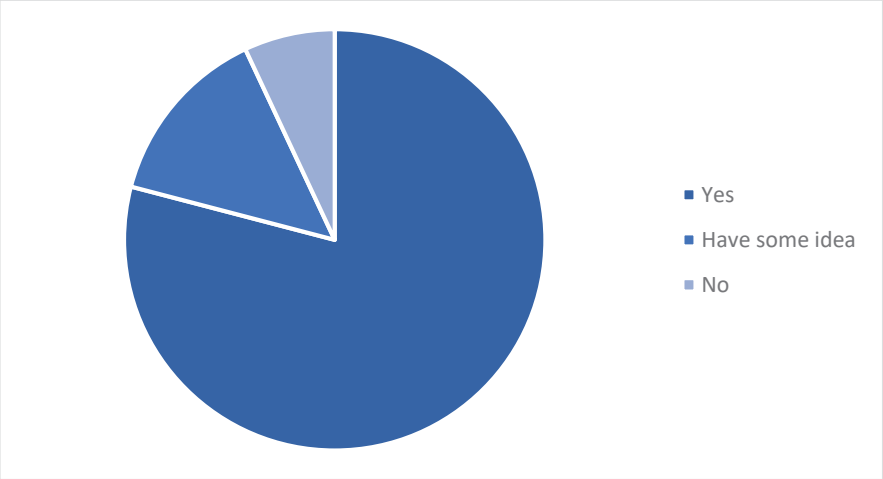

Figure 5. *The answers on the question "Do you know what VR is?"*

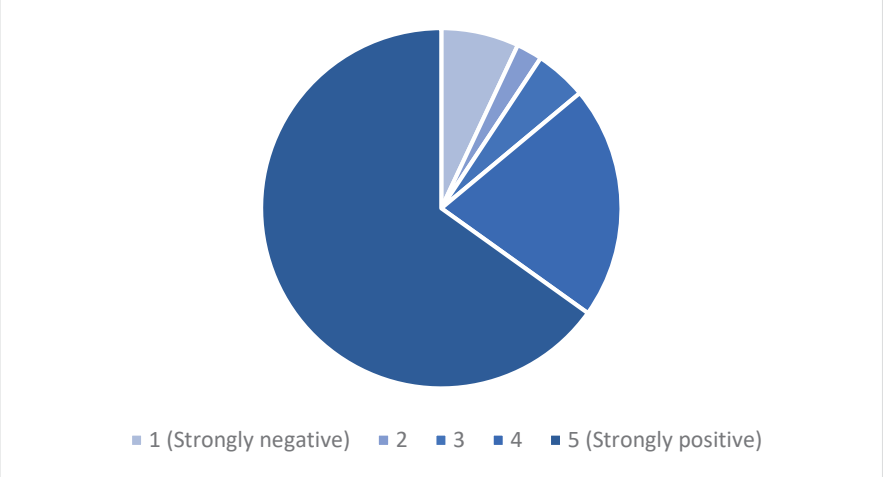

Figure 6. *The answers on the question "What's your opinion on integration of VR in working/learning process?"*

7. CONCLUSIONS

For the last decade VR technology has been gaining popularity in more and more areas. With only a bit of skepticism it is valued as a highly promising tool for education. Its strengths exceeding its weaknesses are the reason to explore available hardware and software for establishment a VR laboratory.

The presented solution is a qualitative and yet affordable one. It is well-accepted by both specialists and non-specialists. Therefore the current case study is considered only the first step of a platform that it is about to extend.

ACKNOWLEDGMENT

The authors express their gratitude to the University of Mining and Geology "Saint Ivan Rilski" and the Ministry of Education and Science of Bulgaria for their funding though the "Ordinance #3 on the terms and procedure for evaluation, planning, distribution and spending of the state budget to finance scientific or artistic activity in state higher schools."

REFERENCES

1. Berg L., Vance J. Industry use of virtual reality in product design and manufacturing: a survey. Virtual Reality 21 (2017), 1-32
2. Boton C. Supporting constructability analysis meetings with Immersive Virtual Reality-based collaborative BIM 4D simulation. Automation in Construction 96 (2018), 1-15
3. Chau M., Wong A., Wang M., Lai S., Chan K., Li T., Chu D., Chan I., Sung W. Using 3D virtual environments to facilitate students in constructive learning. Decision Support Systems 56 (2013), 115-121
4. El halabi A., El Sayad Z., Ayad H. VRGIS as assistance tool for urban decision making. Alexandria Engineering Journal (2019) 58, 367-375
5. Esquembre F. Facilitating the Creation of Virtual and Remote Laboratories for Science and Engineering Education. IFAC-PapersOnLine 48-29 (2015), 049-058
6. Estriegana R., Medina-Merodio J., Barchino R. Student acceptance of virtual laboratory and practical work: An extension of the technology acceptance model. Computers and Education 135 (2019), 1-14
7. Fei D., Anbi Y. Safety education based on virtual mine. Procedia Engineering 26 (2011) 1922-1926
8. Häfner P., Häfner V., Ovtcharova J. Teaching Methodology for Virtual Reality Practical Course in Engineering Education. Procedia Computer Science 25 (2013) 251-260
9. Hernandez J., Kranzlmüller D. NOMAD VR: Multiplatform virtual reality viewer for chemistry simulations. Computer Physics Communications 237 (2019) 230-237
10. Herwig A., Paar Ph. Game Engines: Tools for Landscape Visualization and Planning? Trends GIS Visualization Environ. Plan. Des. (2014) 161-172
11. Jorda J. Virtual tools: virtual laboratories for experimental science – an experience with VCL tool. Procedia – Social and Behavioral Sciences 106 (2013) 3355-3365

12. Liagkou V., Salmas D., Stylios Chr. Realizing Virtual Reality Learning Environment for Industry 4.0. Procedia CIRP 79 (2019) 712-717
13. Lv Zh., Li X., Li W. Virtual reality geographical interactive scene semantics research for immersive geography learning. Neurocomputing 254 (2017) 71-78
14. Mikhaylov N, Chernov D. From Virtual Lab to Virtual Development Lab. 9th IFAC Symposium Advances in Control Education Nizhny Novgorod, Russia, June 19-21, 2012
15. Paravizo E., Braatz D. Using a game engine for simulation in ergonomics analysis, design and education: An exploratory study. Applied Ergonomics 77 (2019) 22-28
16. Potkonjak V., Gardner M., Callaghan V., Mattila P., Guetls C., Petrovic V., Jovanovic K. Virtual laboratories for education in science, technology, and engineering: A review. Computers & Education 95 (2016) 309-327
17. Rafiee A., Male P., Dias E., Scholten H. Developing a wind turbine planning platform: Integration of "sound propagation model-GIS-game engine" triplet. Environmental Modelling & Software 95 (2017) 326-343
18. Raper J., McCarthy T., Williams N. Georeferenced four-dimensional virtual environments: principles and applications. Comput., Environ. and Urban Systems 6 (1998), 529-539
19. Rhyne Th. Going Virtual with Geographic Information and Scientific Visualization. Computers & Geosciences 23 (1997) 489-491
20. Sutherland I. A head-mounted three dimensional display. Proceedings of the AFIPS Fall Joint Computer Conference (1968) 757-764
21. Wang W., Lv Zh., Li X., Xu W., Zhang B., Zhu Y., Yan Y. Spatial query based virtual reality GIS analysis platform. Neurocomputing 274 (2018), 88-98
22. Point Cloud Plugin. www.pointcloudplugin.com (2019)
23. Unreal Engine. www.unrealengine.com (2019)

Analysis of GNSS satellite visibility according to the max(GDOP) criteria for the region of Turkey

Sinan BİRİNCİ[1], Furkan SOĞUKKUYU[2], M. Halis SAKA[3]

[1] Gebze Technical University, Department of Geodetic and Photogrammetric Engineering (s.birinci@gtu.edu.tr)

[2] Gebze Technical University, Department of Geodetic and Photogrammetric Engineering (fsogukkuyu@gtu.edu.tr)

[3] Gebze Technical University, Department of Geodetic and Photogrammetric Engineering (saka@gtu.edu.tr)

ABSTRACT

Global Navigation Satellite Systems (GNSS) provide globally the geospatial positioning needs. The GNSS systems mainly consist of four independent satellite systems, namely, GPS, GLONASS, GALILEO and BeiDou. The reliable positioning capability with GNSS satellite systems is related to the number of visible satellites and their distribution in the space. Therefore, the contribution of the use of GNSS satellite systems together has been discussed in many studies as multi-GNSS.

In this study, the use of the GNSS systems for Turkey and its immediate surroundings has been examined. The utility of GNSS satellite systems in the worst visibility situation was identified according to the GDOP value with 10 degrees elevation for GPS, GLONASS, GALILEO and BeiDou in their ground truck period to test which system is individually enough for positioning.

The GDOP estimation performed use of each satellite systems precise orbit data. The process achieved by in house Matlab program developed in this project. The region selected for covering Turkey district. The selected region border limit is (11^o-47^o) north latitude and (12^o-60^o) east longitude. The grid size of the region selected as 1.5^ox1.5^o. The GDOP value estimated for each satellites system ground track period in five minutes interval for each grid point.

It was observed that the GPS system fully met the expectations. Others were found to be insufficient in their ground truck period. The second simulation performed for pairs of satellite system combination except GPS. The combination uses of GLONASS/GALILEO, BeiDou/GLONASS and GALILEO/BeiDou was analyzed to find out which combination is performing. The results are intensely discussed in this study.

Keywords: *GNSS*; GDOP; Satellite Visibility; Ground Truck Period

1. INTRODUCTION

GNSS satellite systems provide accurate and reliable positioning on the earth-surface since the GPS constellation was completed in 1990s. The GNSS systems mainly consists of two categories of satellite systems. These are Global systems such as GPS, GLONASS, GALILEO and BeiDou and regional systems as QZSS and IRNSS[1-4]. Today's many receiver manufacturer productions measure the all GNSS satellites system signals simultaneously. This situation gives us a prospect to analysis the combination of using the all GNSS satellite systems. In the GNSS positioning, there are many shortage situations such as urban canyon, tree canopies and indoor[5]. Therefore, using the combination of satellite systems for reliable positioning are become a necessity. Combined GNSS systems were discussed in many studies[6-8].

The performance of GNSS system depends on the GDOP criteria which shows the geometry of satellite distribution [7].

In this study, the use of the GNSS systems for Turkey region has been examined. The utility of GNSS satellite systems in the worst visibility situation was identified according to the GDOP value with 10 degrees elevation for GPS, GLONASS, GALILEO and BeiDou in their ground truck period to test which system is individually enough for positioning.

2. MATERIAL AND METHOD

Data acquisition of precise ephemerides of satellites and derivation of quantities to be used were explained at following sections. Sampling and simulating of ground points were conducted by gridding 1.5^o interval between 11^o – 47^o N and 12^o – 60^o E with homemade MATLAB program. Topocentric coordinates were computed for each simulated point. The azimuth and elevation quantities of satellites with respect to each point were evaluated. Elevation mask were selected 10^o avoiding due to the natural and unnatural obstacles [9]. GDOP values at every point were estimated for each GNSS system at their ground tracking period. The second GDOP computation were performed for analyzing of which GNSS combination is better.

2.1 Data Processing

Precise ephemerides were obtained for all GNSS systems (Table 1) from Center for Orbit Determination of Europe (CODE) for the time 1-10 June 2019. The reason of using ten days data for analyzing of the positioning capability of the satellite systems is that the maximum ground track period length is ten days. The ground track period of GNSS systems GPS, GLONASS and GALILEO repeats one day, eight days and ten days, respectively. The elevation information of the satellites was used to identify the satellites appearing at each point. The cut of angle is taken as 10 degrees. The elevation quantity of a satellite less than 10 degrees for every point implies that the satellite is not visible at the point.

Table 1: GNSS System and used satellites

GNSS Systems	Number of SV	Satellites
GPS	32	G01, G02, G03, G04, G05, G06, G07, G08, G09, G10, G11, G12, G13, G14, G15, G16, G17, G18, G19, G20, G21, G22, G23, G24, G25, G26, G27, G28, G29, G30, G31, G32
GLONASS	23	R01, R02, R03, R04, R05, R07, R08, R09, R10, R11, R13, R14, R15, R16, R17 ,R18, R19, R20, R21, R22, R23, R24, R26
GALILEO	24	E01, E02, E03, E04, E05, E07, E08, E09, E11, E12, E13, E14, E15, E18, E19, E21, E24, E25, E26, E27, E30, E31, E33, E36
BeiDou	9	C06, C07, C08, C10, C11, C12, C13, C14, C16

2.2. Design Matrix and GDOP

The use of GDOP (Geometric Dilution of Precision) to describe the effect of receiver-satellite geometry on accuracy of point positioning has become quite common[9,10]. Following model were constructed for derivation of design matrix and calculation of GDOP values based on all combinations of GNSS :

$$H_i = \begin{bmatrix} \cos(Az_1)\cos(El_1) & \sin(Az_1)\cos(El_1) & \sin(El_1) \\ \cos(Az_2)\cos(El_2) & \sin(Az_2)\cos(El_2) & \sin(El_2) \\ \vdots & \vdots & \vdots \\ \cos(Az_j)\cos(El_j) & \sin(Az_j)\cos(El_j) & \sin(El_j) \end{bmatrix} \quad (1)$$

where Hi is design matrix, i and j denote individual navigation system and the number of satellites, respectively. Consideration of solution matrix for all navigation systems yields:

$$H = \begin{bmatrix} H_G & I_G & 0_G & 0_G & 0_G \\ H_R & 0_R & I_R & 0_R & 0_R \\ H_E & 0_E & 0_E & I_E & 0_E \\ H_C & 0_C & 0_C & 0_C & I_C \end{bmatrix} \quad (2)$$

where H is design matrix for combined navigation systems and indices G, R, C, E denote GPS, GLONASS, BeiDou, GALILEO respectively[11]. The cofactor matrix follows:

$$Q = (H^T H)^{-1} \quad (3)$$

$$GDOP = \sqrt{tr(Q)} \quad (4)$$

It can be clearly seen that the minimum number of satellites is equal four for individual solutions. When the whole satellite systems is used in the solution, the minimum number of satellites should be equal seven.

3. RESULTS AND DISCUSSION

The first processing result is computation of GDOP values for GPS alone processing using one-day data shown in Figure 1. The left figure shows that almost %97 of GDOP values below four. In the right figure, maximum GDOP values below nine. This results shows the use of GPS alone is sufficient for all navigation purposes.

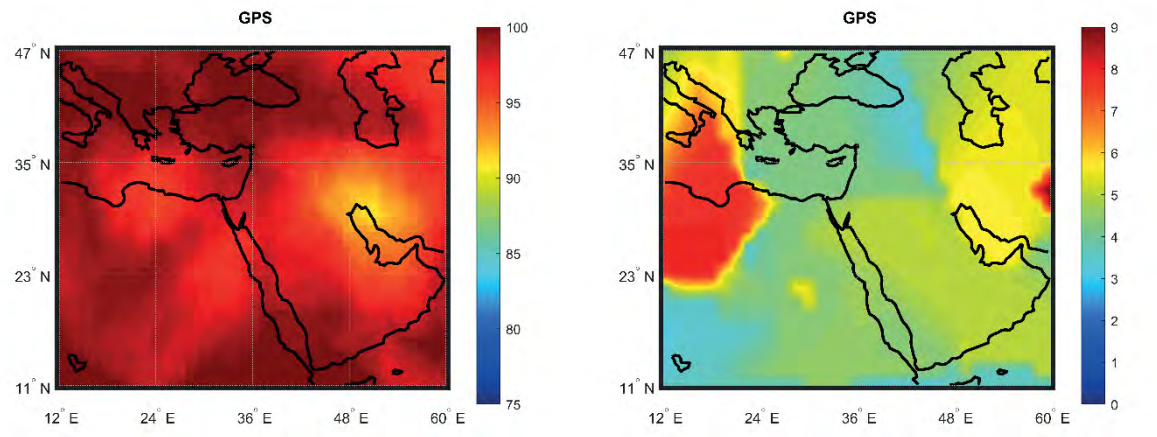

Figure 1. *Percentage of epochs with GDOP below four (left) and Maximum GDOP values (right) for GPS constellation in their ground track period.*

The second processing result is computation of GDOP values for GLONASS alone processing using eight days data shown in Figure 2. The left figure shows that the GDOP value below four at the between 11º - 30º N latitude reach to the %80. Between 30º - 47º N latitude reach to the %90. The right figure shows that no acceptable solution obtained for maximum GDOP criteria.

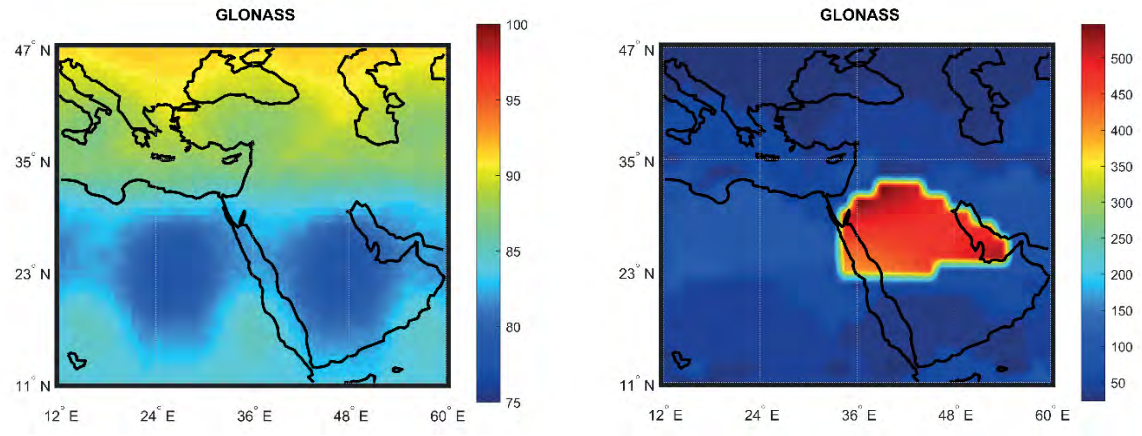

Figure 2. *Percentage of epochs with GDOP below four (left) and Maximum GDOP values (right) for GLONASS constellation in their ground track period.*

The third processing result is computation of GDOP values for GALILEO alone processing using ten days data shown in Figure 3. The left figure shows that almost %95 of GDOP values below four. The right figure shows that %40 of the solution below ten for maximum GDOP criteria.

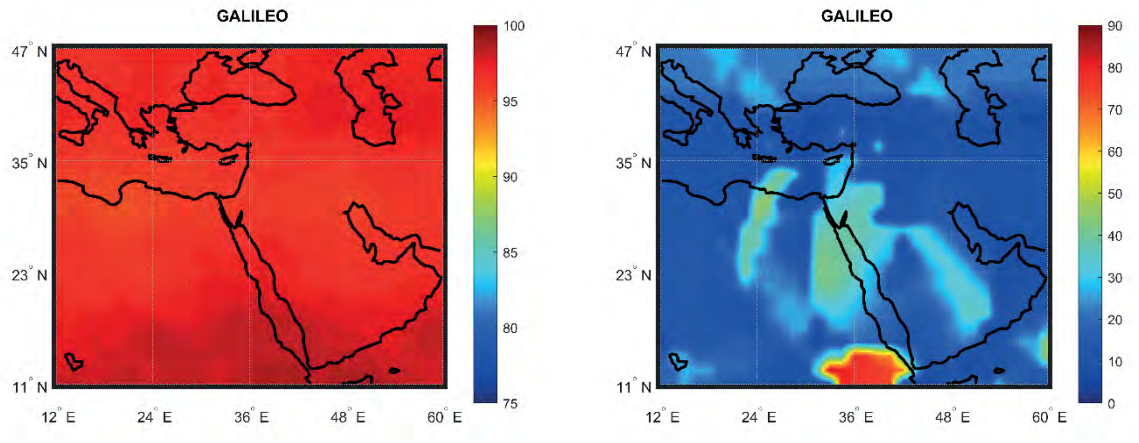

Figure 3. *Percentage of epochs with GDOP below four (left) and Maximum GDOP values (right) for GALILEO constellation in their ground track period.*

It can conclude that GPS system provides superior result then the others GNSS systems. The GALILEO has better results than the GLONASS satellite systems in the study area. BeiDou satellite system has no solution in the study area.

The combination solution of GNSS systems was performed as GLONASS/GALILEO, GLONASS/BeiDou and GALILEO/BeiDou. In the left subplot of Figure 4, GLONASS/ GALILEO results show that %99 of GDOP values below four. The right figure shows that %95 of the solution below ten for maximum GDOP criteria.

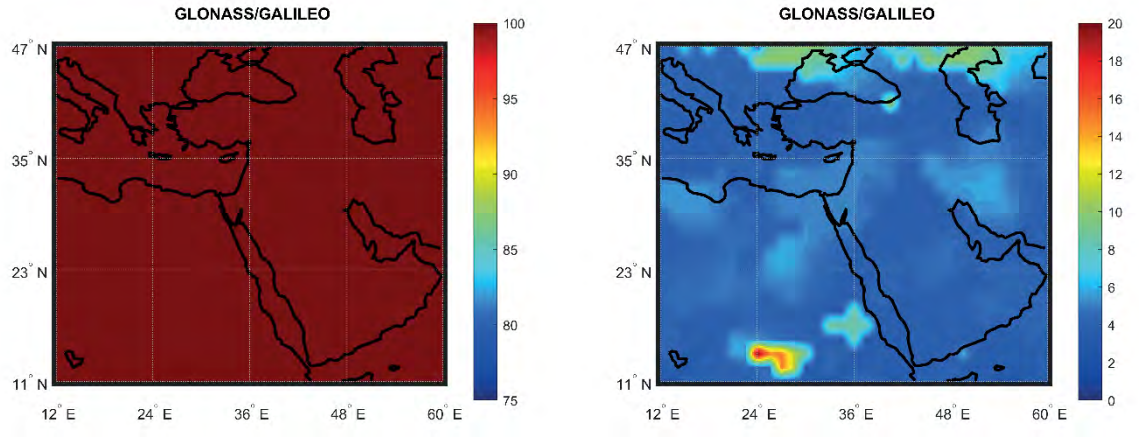

Figure 4. *Percentage of epochs with GDOP below four (left) and Maximum GDOP values (right) for GLONASS/GALILEO constellation in their ground track period.*

In the left subplot of Figure 5, GLONASS/BeiDou results show that %90 of GDOP values below four except the west-south quarter. The right figure shows that almost no solution obtained for maximum GDOP criteria.

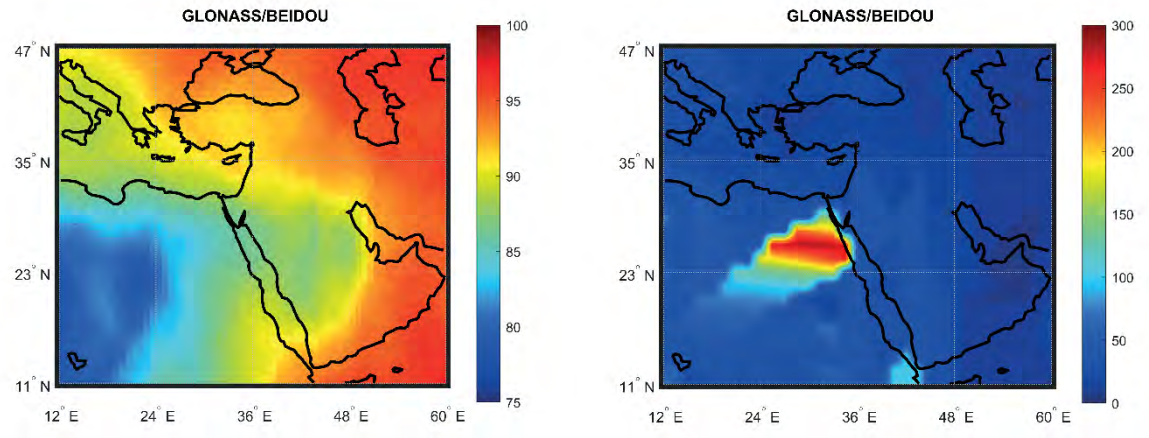

Figure 5. *Percentage of epochs with GDOP below four (left) and Maximum GDOP values (right) for GLONASS/BeiDou constellation in their ground track period.*

In the left subplot of Figure 6, GALILEO/BeiDou results show that %95 of GDOP values below four. The right figure shows that %40 of the solution below ten for maximum GDOP criteria.

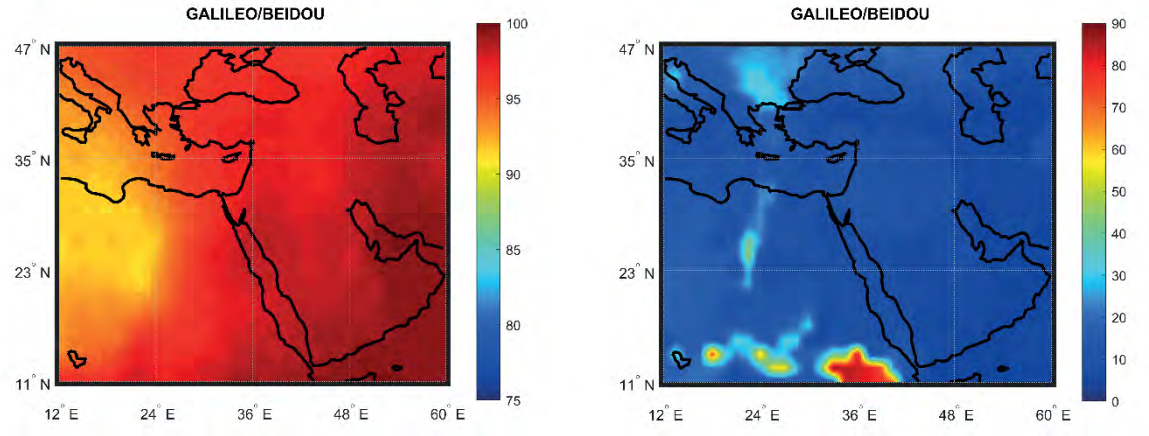

Figure 6. *Percentage of epochs with GDOP below four (left) and Maximum GDOP values (right) for GALILEO/BeiDou constellation in their ground track period.*

In the study area, it can conclude that GNSS dual satellite system combinations results for GLONASS/GALILEO, GLONASS/BeiDou and GALILEO/BeiDou were compared with each other. The results show that GLONASS/GALILEO combination give better results. This results is identical as GPS only solution. GALILEO/BeiDou combination result is better than GLONASS/BeiDou combination results. It can clearly be seen in the Figures that BeiDou combination supports GALILEO and GLONASS at the east part of the study region.

4. CONCLUSION

The motivations of this study is which GNSS systems support the navigation requirements for selected study area. The data analyzed for reliable results using the maxGDOP computation for (1.5x1.5) gridded study area and five minutes interval with their ground track period. It can be shown that the GPS system gives the best performance and superior results in its ground tracking period with 32 satellites. GALILEO gives better results than GLONASS with their ground tracking period with 24 and 23 satellites respectively. The BeiDou satellite system does not provide any solution for the region with their 9 satellites. The combinational analysis of GNSS system as GLONASS/GALILEO gives acceptable results due to maxGDOP. The failed situations occurred only few epoch in few grid points. It can be concluded GPS only and GLONASS/GALILEO combination gives identical results in the study area.

REFERENCES

1. The Global Positioning System. Available online: https://www.gps.gov/systems/gps/ (accessed on 1 November 2019)

2. Official information of the GLONASS SCC. Available online: https://www.glonass-iac.ru/en/ (accessed on 1 November 2019)

3. Galileo-Satellite Navigation. Available online: http://ec.europa.eu/growth/sectors/space/galileo/ (accessed on 1 November 2019)

4. BeiDou Navigation Satellite System. Available online: http://en.beidou.gov.cn/ (accessed on 1 November 2019)

5. Li, T., Zhang, H., Gao, Z., Chen, Q., & Niu, X. (2018). High-Accuracy Positioning in Urban Environments Using Single-Frequency Multi-GNSS RTK/MEMS-IMU Integration. Remote Sensing, 10(2), 205.

6. Meneghini, C., & Parente, C. (2017). Advantages of multi GNSS constellation: GDOP analysis for GPS, GLONASS and Galileo combinations. International Journal of Engineering and Technology Innovation, 7(1), 1–10.

7. Hadas, T., Kazmierski, K., & Sośnica, K. (2019). Performance of Galileo-only dual-frequency absolute positioning using the fully serviceable Galileo constellation. GPS Solutions, 23(4).

8. Li, X., Ge, M., Dai, X., Ren, X., Fritsche, M., Wickert, J., & Schuh, H. (2015). Accuracy and reliability of multi-GNSS real-time precise positioning: GPS, GLONASS, BeiDou, and Galileo. Journal of Geodesy, 89(6), 607–635.

9. Leick, A., Rapoport, L., & Tatarnikov, D. (2015). Gps satellite surveying. Hoboken, NJ: Wiley.

10. Zarei, N. (2014). Artificial Intelligence Approaches for GPS GDOP Classification. International Journal of Computer Applications, 96(16), 16–21.

11. Misra, P., & Enge, P. (2012). Global positioning system: signals, measurements, and performance. Lincoln, MA: Ganga-Jamuna Press.

Analyses on High Resolution Global Digital Terrain Model Qualities and Their Use in Gravity Reductions

Aslınur Bahçekapılı[1], Bihter Erol[2]

[1]Istanbul Technical University, Geomatics Engineering Department 34469 Istanbul, Turkey
Phone: +90 212 285 3826, E-mail: bahcekapiliaslinur@gmail.com

[2]Istanbul Technical University, Geomatics Engineering Department 34469 Istanbul, Turkey
Phone: +90 212 285 3821, E-mail: bihter@itu.edu.tr

ABSTRACT

Gravity of a point on Earth is affected by the topographic masses around it. In order to remove the attraction of these topographic masses, terrain corrections (TCs) are computed and applied to gravity reductions. Digital terrain models (DTMs) are widely used in TC calculations. This study mainly aims to determine an optimal DTM resolution for TC calculations and see the effects of TCs on geoid. DTMs that were used in this study are SRTM, ASTER GDEM2, AW3D30, TSYM3, EU-DEM, GTOPO30, GMTED2010 and HGM DTED-2 for the selected area of Turkey. An extensive comparison of these global and regional high resolution DTMs were provided and DTMs were validated with GPS/leveling benchmarks and global and regional geopotential models. TCs were calculated by using different resolution DTMs and different integration radius combinations. TC effect on geoid, indirect effects on geoid and geoid undulations were computed by using different resolution DTMs. Geoid undulation accuracies were tested. According to the main outcomes, 3″× 3″ resolution DTMs can be used in replacement of 1″× 1″ resolution DTMs. The desired radius as outer radius with a small inner radius saves a lot of time in TC calculations. The main factor which causes the changes in geoid undulations is the effect of TCs on geoid. The differences between the geoid undulations, that were computed with 30″× 30″, 2.5′× 2.5′ and 5′× 5′ resolution DTMs, are not significant.

KEYWORDS: digital terrain model; terrain correction; gravity reduction; geoid modelling

1. INTRODUCTION

Gravity reductions are commonly used for investigations of Earth's crust, interpolation and extrapolation of gravity anomalies and geoid determination. Gravity reductions are implemented by two steps. First, topographic masses above the geoid is removed. Second, gravity g at a point P on Earth's surface is reduced to the geoid. As a result, the disconformity of gravity values which are caused by height differences of gravity stations can be eliminated [1]. Bouguer gravity reduction admits the region around the gravity station P as horizontal and plane. This surface is named as Bouguer plate (Figure 1). The attraction of topographic masses on gravity is removed by subtracting the attraction of Bouguer plate from the measured gravity. Nevertheless, in this process, the topographic masses above the Bouguer plate is not considered although they have an upward attraction effect to the gravity on the calculation point. Moreover, the areas which does not have topographic masses below the Bouguer plate are considered as effective in the computations although they do not have any attraction to the calculation point. These diversions between the Bouguer plate and the real topography are named as terrain corrections ([2], [3]). In order to correct these errors, the refined Bouguer gravity g_B is determined by applying the terrain correction to the equation [1]:

$$g_B = g - A_B + A_t - F \tag{1}$$

where g is the measured gravity on point P, A_t is the terrain correction, A_B is the attraction of an infinite Bouguer plate, F is free-air anomalies.

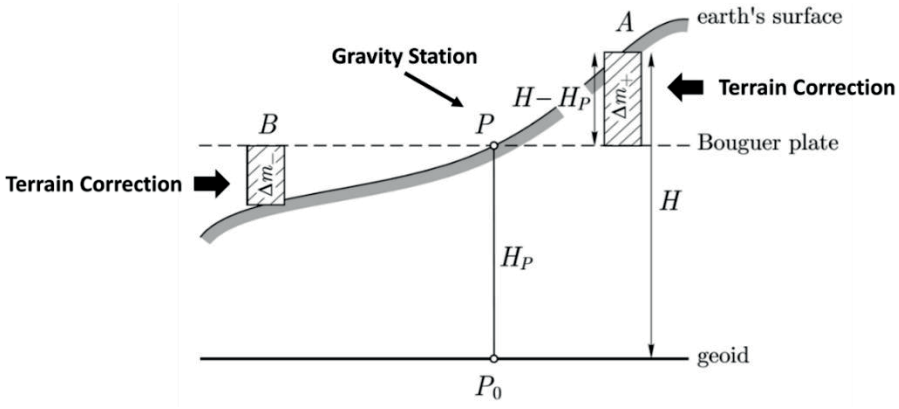

Figure 1: Bouguer gravity reduction where (Δm_+) and ($\Delta m\_$) are the topographic masses, P is the gravity station, P_0 is the reduced gravity station, H_P is the orthometric height of point P and H is the orthometric height of the area A [2].

A DTM consists of elevations of the points on Earth's bare surface which does not contain human-made structures and vegetation cover. DTMs are widely used for computing terrain corrections and modeling geoid. There are a lot of high resolution global and regional DTMs that are freely available. The accuracies and resolutions of DTMs affect the quality of TCs. It is important to choose the most accurate DTM for the study area. In the literature, Il (2018) estimated the performances of SRTM1 and ASTER DTMs in regional gravimetric geoid modeling and no significant difference was seen. Yahaya and El Azzab (2018) established that the precision of terrain effects was affected by height inconsistencies between the gravity stations and SRTM heights. Kiamehr and Sjöberg (2005) emphasized that when DTMs were used in the interpolation of Bouguer gravity anomalies, blunders in elevations would cause errors in gravity anomalies and geoid models. Merry (2003) also stated that when DTMs were used in the interpolation of free-air gravity anomalies and the computation of the Molodensky G1 term, errors in DTM heights would generate errors in geoid and quasi-geoid models. It is observed that these errors were significant and determining an optimum DTM were important.

High resolution DTMs provide high accuracy results. However, the use of high resolution DTMs in computation of TCs can be excessively long and time consuming due to the large amount of data. Lower resolution DTMs may show similar results to the higher resolution DTMs. In these situations, using the lower resolution DTM instead of the higher one is more advantageous by means of short computation time and less data storage. Moreover, the inner and outer zones, which TCs are computed within, can also affect the calculation time. Therefore, defining an optimal DTM resolution with an optimum integration radius combination is important.

In this study, a comprehensive comparison of global and regional high resolution DTM heights were presented. DTM heights were validated. The results and calculation times of TCs that were generated by using different resolution DTMs and different integration radius combinations were evaluated. In order to see the effects of DTM resolutions on geoid, TC effect on geoid, indirect effects on geoid and geoid undulations that were generated with different resolution DTMs were examined. Geoid undulations were validated on GPS/leveling benchmarks.

2. MATERIAL AND METHOD

2.1 Study Area and Data

The study area is between 39°N to 42°N latitudes and 28°E to 32°E longitudes of Turkey (Figure 2). 109 GPS/leveling benchmarks were used for DTM validations. DTMs that were used in this study are SRTM (The Shuttle Radar Topography Mission Global DEM, 1″× 1″, 3″× 3″ and 30″× 30″), ASTER GDEM2 (The Advanced Spaceborne Thermal Emission and Reflection Radiometer Global DEM Version 2, 1″× 1″), AW3D30 (The ALOS World 3D, 1″× 1″), TSYM3 (Turkish Digital Elevation Model, 3″× 3″), EUDEM (Digital Elevation Model Over Europe, 1″× 1″), GTOPO30 (Global 30 Arc-Second Elevation, 30″× 30″) and GMTED2010 (The Global Multi-Resolution Terrain Elevation Data 2010, 7.5″× 7.5″ and 30″× 30″) and HGM DTED-2 (General Directorate of Mapping 1″× 1″ Interval Digital Terrain Data) (Table 1).

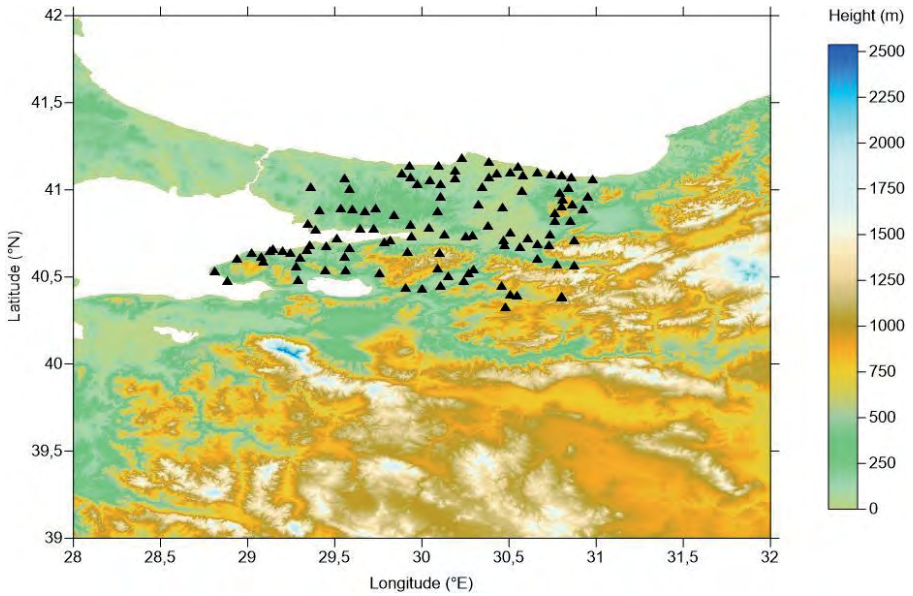

Figure 2: Distribution of GPS/leveling benchmarks on the study area.

Table 1: Properties of the DTMs used in this study.

DTM	DTM Data Sources	Spatial Resolution	Version	Coverage	Datum		Source
					Horizontal	Vertical	
SRTM1	Radar Interferometer, ASTER GDEM2, GMTED2010	1″× 1″ (~30 m)	Version 3	60°N to 56°S	WGS84	EGM96	[8], [9]
ASTER GDEM2	Infrared cameras	1″× 1″ (~30 m)	Version 2 (2011)	83°N to 83°S	WGS84	EGM96	[8], [9]
ALOS World 3D (AW3D30)	PRISM	1″× 1″ (~30 m)	Version 2.1	83°N to 82°S	WGS84	EGM96	[10]
EU-DEM	SRTM1, ASTER GDEM2 and Russian topographic maps	1″× 1″ (~30 m)	Version 1.1	Full coverage of the EEA countries.	ETRS89	EVRS2000	[11]
HGM DTED-2	25K national topographic maps	1″× 1″ (~30 m)	Version 2	36°N to 45°N and 26°E to 45°E	WGS84	TUDKA99A	[12]
SRTM3	SRTM1	3″× 3″ (~90 m)	Version 3	60°N to 56°S	WGS84	EGM96	[8], [9]
TSYM3	SRTM1, 25K national topographic maps.	3″× 3″ (~90 m)	Version 2	36°N to 45°N and 26°E to 45°E	WGS84	EGM96	[13]
GMTED2010	SRTM, ICESat, Canadian elevation data, Spot 5 Reference3D data	7.5″× 7.5″	2010	84°N to 56°S	WGS84	EGM96	[9]
GMTED2010	SRTM, ICESat, Canadian elevation data, Spot 5 Reference3D data	30″× 30″ (~1000 m)	2010	84°N to 56°S	WGS84	EGM96	[9]
GTOPO30	DTED, Digital Chart of the World, USGS 1-degree DEM's, Army Map Service 1:1,000,000-scale maps, International Map of the World 1:1,000,000-scale maps, Peru 1:1,000,000-scale map, New Zealand DEM, Antarctic Digital Database	30″× 30″ (~1000 m)	1996	90°S to 90°N and 180°W to 180°E	WGS84	Mean Sea Level	[9]
SRTM30	SRTM1, GTOPO30	30″× 30″ (~1000 m)	Version 2.1	60°N to 56°S	WGS84	EGM96	[8], [9]

2.2 Methodology for DTM Validations

The height differences between the two DTMs were calculated at the grid nodes by using Surfer software. The height differences were visualized by generating image maps and 3D maps. Minimum, maximum, mean, standard deviation, median and median absolute deviation values of the differences were computed. For the 109 GPS/leveling benchmarks, geoid undulations which were derived from EGM96, EGM2008 global geoid models and TG99A geoid model were subtracted from the ITRF96 ellipsoidal heights and the orthometric heights are obtained. These calculated orthometric heights were subtracted from the interpolated DTM orthometric heights. TUDKA99A orthometric heights are also subtracted from interpolated DTM orthometric heights. Minimum, maximum, mean and standard deviation values of the differences were calculated.

2.3 Methodology for Terrain Correction Calculations

Terrain corrections were computed by using the TC module of Gravsoft software. At a point $P(x_i, y_i)$, the terrain correction $c(i,j)$ is [14]:

$$c(i,j) = G\rho \sum_{n=0}^{N-1} \sum_{m=0}^{M-1} \{x\, ln[y + r(x,y,z)] + y\, ln[x + r(x,y,z)] - z arctan \frac{z}{zr(x,y,z)}\} \begin{vmatrix} x_i - (x_n + \Delta x/2) & y_i - (y_m + \Delta y/2) & 0 \\ x_i - (x_n - \Delta x/2) & y_i - (y_m - \Delta y/2) & h_{ij} - h_{nm} \end{vmatrix} \quad (2)$$

where G is Newton's gravitational constant, $\rho(x,y,z)$ is the topographic density at the running point, h_{ij} is the topographic height at point $P(x_i, y_i)$, E indicates the integration area, and $r(x,y,z)$ is the distance kernel defined as:

$$r(x,y,z) = (x^2 + y^2 + z^2)^{1/2} \quad (3)$$

$$r\left(x_i - x, y_j - y, h_{ij} - z\right) = \sqrt{(x_i - x)^2 + \left(y_j - y\right)^2 + \left(h_{ij} - z\right)^2} \quad (4)$$

The Gravsoft program uses DTM data sets to calculate TCs by using the formulas of the rectangular prism. Each grid compartment and its elevation identify a rectangular prism which is evaluated to generate the complete terrain effect [15]. As it can be seen in Figure 3, two DTMs are used in TC computations. One of them is a detailed inner grid which is used with the computation radius R, the other one is a coarse grid which is used with the computation radius R2.

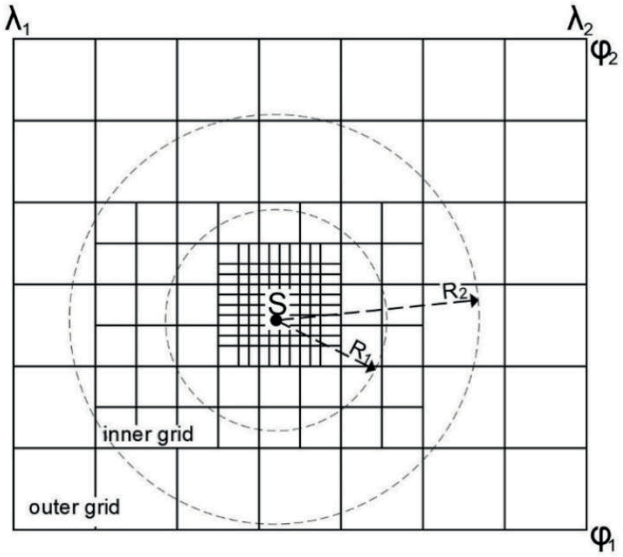

Figure 3: Representation of inner grid and outer grid with inner and outer radiuses (R1 and R2) centered at the computation point S.

Terrain corrections were computed with 20 km inner radius and 100 km outer radius by using 1″× 1″, 3″× 3″, 30″× 30″, 1′× 1′, 2.5′× 2.5′ and 5′× 5′ resolution DTMs as detailed grids for the area between 40.3ºN to 41.2ºN latitudes and 28.8ºE to 31ºE longitudes of Turkey. Coarse grids were selected as 5″× 5″, 15″× 15″, 2.5′× 2.5′, 5′× 5′, 12.5′× 12.5′ and 25′× 25′ respectively for the area between 39ºN to 42ºN latitudes and 28ºE to 32ºE longitudes of Turkey. Then, the calculations were repeated with the 1″× 1″ resolution DTM as detailed grid by selecting different inner and outer radius combinations which are R1=6.5 and R2=0 km, R1=6.5 and R2=20 km, R1=6.5 and R2=50 km, R1=6.5 and R2=100 km, R1=6.5 and R2=200 km, R1=20 and R2=0 km, R1=20 and R2=50 km, R1=20 and R2=100 km, R1=20 and R2=200 km, R1=50 and R2=0 km, R1=100 and R2=0 km. The results were compared by means of minimum, maximum, mean, standard deviation and calculation time values.

2.4 Methodology for Geoid Modeling

In order to examine the terrain effect on geoid undulation due to the varying spatial resolution of the DTM, the regional geoid model in the study area was calculated by using Remove-Compute-Restore (RCR) technique. The RCR technique implies that the effect of the GGM and the effect of the topography with its compensation should be removed from the employed gravity anomalies

for computing the geoid; as it can be seen in the following mathematical expressions [16]. The GGM that is used in this study is GGM05C with 360 maximum degree of spherical harmonic expansion. The reduced gravity anomaly is:

$$\Delta g = \Delta g_{FA} - \Delta g_{GGM} - \Delta g_H \quad (5)$$

And the computed geoid height is:

$$N \quad = N_{GGM} + N_{\Delta g} + N_{topo} + N_{ind} \quad (6)$$

where Δg_{GGM} is the effect of the GGM on gravity anomalies, Δg_H is the terrain effect on gravity, Δg_{FA} is free-air anomalies, N_{GGM} is the contribution of the GGM, $N_{\Delta g}$ is the residual geoid height which is calculated using Stokes integral, N_{topo} is the effect of terrain corrections on geoid and N_{ind} is the indirect effect of the terrain on the geoid heights. The individual components (N_{GGM}, $N_{\Delta g}$, N_{topo} and N_{ind}) were summed and the gravimetric geoid heights (N) were computed by using 2D Fast Fourier Transform technique [17]. The overall geoid undulations (N) were interpolated on the GPS/leveling benchmarks by using Surfer software. The obtained heights were compared with GPS/leveling data.

3. RESULTS AND DISCUSSION

3.1 DTM Validation Results

As it can be seen in Table 2, the mean, standard deviation, median and MAD values are the lowest for SRTM3 – TSYM3 differences, it is because TSYM3 is mainly generated from SRTM data sets. The following low standard deviation value is for SRTM1-AW3D30 by 4.98 m. ASTER-GTOPO30 has the highest standard deviation value by 84.41 m. Overall, the statistical values are the lowest for 1″×1″ and 3″× 3″ DTM comparisons and the highest for 30″× 30″ DTM comparisons. From Figure 4, it can be said that the highest difference values are on the rugged regions.

Table 2: Statistics of the height differences between the DTMs.

$H_{DTM1} - H_{DTM2}$	Min. (m)	Max. (m)	Mean (m)	SD (m)	Mdn. (m)	MAD(m)
SRTM1 – ASTER	-337	187	1.14	6.41	1	4
SRTM1 – AW3D30	-376	188	-0.12	4.98	0	3
SRTM1 – EU-DEM	486	-304	1.06	8.80	1	-4
SRTM1 – GMTED2010	-405	223	0.15	16.47	0	9
SRTM1 – HGM	-293	178	1.74	5.17	2	3
SRTM3 – TSYM3	-204	207	0.00	0.31	0	0
SRTM30 – GTOPO30	-626	576	-3.55	80.41	-2	34
TSYM3 – ASTER	-223	172	1.13	6.33	1	-4
TSYM3 – AW3D30	-361	185	-0.12	5.12	0	-3
TSYM3 – EU-DEM	486	-195	1.05	8.38	1	-3
TSYM3 – GMTED2010	-421	255	0.15	16.77	0	9
TSYM3 – GTOPO30	-564	591	-0.32	83.66	-1	38
TSYM3 – HGM	-335	238	1.74	5.20	2	-3
TSYM3 – SRTM3	-207	204	-0.00	0.31	0	0
TSYM3 – SRTM30	-482	391	2.19	47.85	1	25
ASTER – AW3D30	-326	162	-1.26	7.65	-2	5
ASTER – EU-DEM	475	-197	-0.59	10.08	-1	-5
ASTER – GMTED2010	-365	214	-1.00	16.60	-2	10
ASTER – GTOPO30	-578	599	-1.99	84.41	-3	38
ASTER – HGM	-251	164	0.60	7.72	0	5
ASTER – SRTM1	-187	337	-1.14	6.41	-1	-4
ASTER – SRTM30	-453	388	1.04	48.34	-1	26
ASTER – TSYM3	-172	223	-1.13	6.33	-1	4
HGM – ASTER	-164	251	-0.60	7.72	0	-5
HGM – AW3D30	-290	196	-1.86	6.25	-2	-4
HGM – EU-DEM	480	-250	-1.47	10.18	-1	-5
HGM – GMTED2010	-398	260	-1.58	16.83	-1	9
HGM – GTOPO30	-566	578	-2.81	83.84	-3	38
HGM – SRTM1	-178	293	-1.74	5.17	-2	-3
HGM – SRTM30	-447	406	0.46	48.12	0	25
HGM – TSYM3	-238	335	-1.74	5.20	-2	3
AW3D30 – ASTER	-162	326	1.26	7.65	2	5
AW3D30 – EU-DEM	485	-174	1.14	9.76	1	-4
AW3D30 – GMTED2010	-341	241	0.31	15.22	0	8
AW3D30 – GTOPO30	-563	601	-0.24	82.94	-1	37
AW3D30 – HGM	-196	290	1.86	6.25	2	4
AW3D30 – SRTM1	-188	376	0.12	4.98	0	-3
AW3D30 – SRTM30	-448	389	2.31	48.09	1	25
AW3D30 – TSYM3	-185	361	0.12	5.12	0	3
EU-DEM – ASTER	-475	197	0.59	10.08	1	5
EU-DEM – AW3D30	-485	174	-1.14	9.76	-1	4
EU-DEM – GMTED2010	-367	179	-0.83	16.37	-1	7
EU-DEM – GTOPO30	-556	606	-1.47	83.44	-2	38
EU-DEM – HGM	-480	250	1.47	10.18	1	5
EU-DEM – SRTM1	-486	304	-1.06	8.80	-1	4
EU-DEM – TSYM3	-486	195	-1.05	8.38	-1	3
GMTED2010 – ASTER	-214	365	1.00	16.60	2	-10
GMTED2010 – AW3D30	-241	341	-0.31	15.22	0	-8
GMTED2010 – EU-DEM	367	-179	0.83	16.37	1	-7
GMTED2010 – GTOPO30	-547	442	-1.65	62.27	-2	28
GMTED2010 – HGM	-260	398	1.58	16.83	1	-9
GMTED2010 – SRTM1	-223	405	-0.15	16.47	0	-9
GMTED2010 – SRTM30	-396	534	1.33	44.28	0	20

GMTED2010 – TSYM3	-255	421	-0.15	16.77	0	-9
GTOPO30 – ASTER	-599	578	1.99	84.41	3	38
GTOPO30 – AW3D30	-601	563	0.24	82.94	1	-37
GTOPO30 – EU-DEM	556	-606	1.47	83.44	2	-38
GTOPO30 – GMTED2010	-442	547	1.65	62.27	2	-28
GTOPO30 – HGM	-578	566	2.81	83.84	3	-38
GTOPO30 – TSYM3	-591	564	0.32	83.66	1	-38

Table 3: Statistics of the height differences at GPS/leveling benchmarks.

$H_{DTM} - (h - N_{Geoid})$	Minimum (m)	Maximum (m)	Mean (m)	Std. Dev. (m)
HGM – TG99A	-107.44	38.37	-21.03	20.51
HGM – EGM96	-72.81	38.08	-17.99	17.39
HGM – EGM2008	-72.11	38.17	-17.84	17.32
HGM – TUDKA99A	-72.09	37.88	-17.95	17.25
SRTM1 – TG99A	-99.74	43.00	-20.18	19.54
SRTM1 – EGM96	-70.46	42.71	-17.14	16.58
SRTM1 – EGM2008	-69.76	42.80	-16.98	16.51
SRTM1 – TUDKA99A	-69.74	42.51	-17.09	16.45
ASTER - TG99A	-91.60	41.90	-19.05	19.80
ASTER – EGM96	-73.74	41.61	-16.01	17.60
ASTER – EGM2008	-73.04	41.70	-15.86	17.54
ASTER – TUDKA99A	-73.02	41.41	-15.96	17.48
AW3D30 – TG99A	-94.45	39.91	-19.60	19.47
AW3D30 – EGM96	-74.19	39.62	-16.56	16.44
AW3D30 – EGM2008	-73.49	39.71	-16.41	16.37
AW3D30 – TUDKA99A	-73.47	39.42	-16.52	16.31
EU-DEM – TG99A	-99.22	55.08	-21.01	23.07
EU-DEM – EGM96	-73.20	55.10	-17.97	20.92
EU-DEM – EGM2008	-72.50	54.94	-17.82	20.85
EU-DEM – TUDKA99A	-72.48	54.52	-17.92	20.78
TSYM3 – TG99A	-94.45	39.91	-19.60	19.47
TSYM3 – EGM96	-74.19	39.62	-16.56	16.44
TSYM3 – EGM2008	-73.49	39.71	-16.41	16.37
TSYM3 – TUDKA99A	-67.18	41.37	-17.91	16.71
GMTED2010 (7.5″) – TG99A	-93.09	44.71	-22.96	25.10
GMTED2010 (7.5″) – EGM96	-84.08	44.55	-19.92	21.91
GMTED2010 (7.5″) – EGM2008	-83.78	44.71	-19.77	21.88
GMTED2010 (7.5″) – TUDKA99A	-83.86	44.66	-19.88	21.83
GTOPO30 – TG99A	-278.47	292.35	-53.35	95.72
GTOPO30 – EGM96	-248.01	292.28	-50.31	94.04
GTOPO30 – EGM2008	-247.72	292.24	-50.16	93.99
GTOPO30 – TUDKA99A	-247.73	292.12	-50.27	93.96
SRTM30 – TG99A	-227.71	177.09	-52.06	67.34
SRTM30 – EGM96	-198.11	176.80	-49.02	65.89
SRTM30 – EGM2008	-197.84	176.89	-48.87	65.86
SRTM30 – TUDKA99A	-198.11	176.60	-48.98	65.81

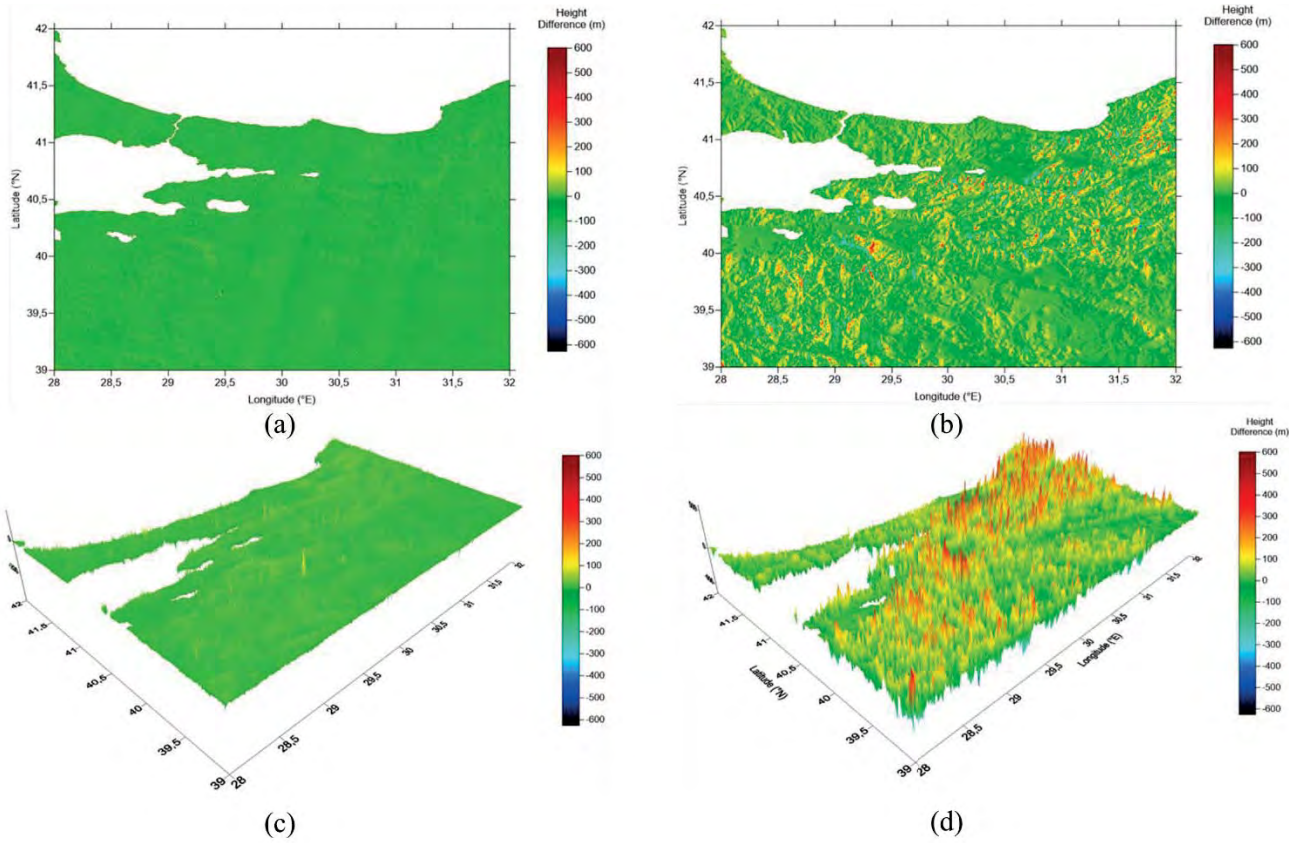

Figure 4: (a) and (c) shows the height differences between SRTM1 and AW3D30, (b) and (d) shows the height differences between SRTM30 and GTOPO30.

According to Table 3, the statistical values, that show the compatibility between DTMs and the geopotential models, are the lowest for 1″× 1″ and 3″× 3″ DTMs and the highest for 30″× 30″ DTMs. Comparison of AW3D30 and TUDKA99A orthometric heights has the lowest standard deviation value.

3.2 Terrain Correction Calculation Results

The terrain correction values vary between 0 mGal and 16.956 mGal. As it can be seen in Table 4, for 20 km inner radius and 100 km outer radius, minimum, maximum, mean and standard deviation values of 1″× 1″ resolution DTM and 3″× 3″ resolution DTM are approximately the same. However, the calculation time of 3″× 3″ DTM is approximately 9 times shorter than the calculation time of 1″× 1″ DTM. Besides, 30″× 30″ DTM gives similar results to 3″× 3″ DTM and the calculations of 30″× 30″ DTM are completed approximately 35 times faster than the

calculations of 3″× 3″ DTM. Moreover, 30″× 30″ and 1′× 1′ DTM has similar statistics and similar calculation times with 1′× 1′ DTM being 10 seconds faster. With 1′× 1′, 2.5′× 2.5′ and 5′× 5′ resolution DTMs, minimum, maximum, mean and standard deviation values start to differ more, although the processing time remains nearly the same. It can be deduced that TC values and DTM resolutions are directly proportional.

Table 4: Statistics of the terrain corrections for R1=20 km R2=100 km.

DTM Resolution	Minimum (mGal)	Maximum (mGal)	Mean (mGal)	Standard Deviation (mGal)	Time (s)
1″× 1″	0	16.887	2.944	2.587	7840
3″× 3″	0	16.956	2.928	2.584	864
30″× 30″	0	15.094	2.509	2.337	25
1′× 1′	0	14.717	2.192	2.063	16
2.5′× 2.5′	0	10.427	1.691	1.589	15
5′× 5′	0	6.319	1.363	1.202	14

As it can be observed from Table 5, minimum, maximum, mean and standard deviation values of TCs which are computed with R1=6.5 R2=20 and R1=20 R2=0 are the same. However, the calculation time with R1=6.5 R2=20 is approximately 6 times shorter. The statistics of R1=6.5 R2=50 and R1=20 R2=50 and R1=50 R2=0 results are also the same while the processing times are different. The outcomes can be obtained in approximately 745 s with 6.5 km inner radius (50 km outer radius), 6478 s with 20 km inner radius (50 km outer radius) and 34953.000 seconds with 50 km inner radius (0 km outer radius). Moreover, minimum, maximum, mean and standard deviation values of TCs which are computed with R1=6.5 R2=100 and R1=20 R2=100 are the same while the processing times are 3630 s and 16940 s respectively. The overall statistics of R1=6.5 R2=200 and R1=20 R2=200 are also the same in contrast with the processing times which are 21579 s and 33571 s respectively. Also, it can be seen that TC values increase as the outer radius increases (Figure 5).

Table 5: Statistics of the terrain corrections for 1″× 1″ resolution HGM DTED-2.

R1 (km)	R2 (km)	Minimum (mGal)	Maximum (mGal)	Mean (mGal)	Standard Deviation (mGal)	Time (s)
6.5	0	0.001	15.771	2.003	2.166	491
6.5	20	0.023	16.708	2.547	2.605	745
6.5	50	0.031	17.296	2.785	2.676	1639
6.5	100	0	16.887	2.944	2.587	3630
6.5	200	0	17.204	3.286	2.335	21579
20	0	0.023	16.708	2.547	2.605	4980
20	50	0.031	17.296	2.785	2.785	6478
20	100	0	16.887	2.944	2.587	16940
20	200	0	17.204	3.286	2.335	33571
50	0	0.031	17.296	2.785	2.676	34953
100	0	0	16.887	2.944	2.587	114795

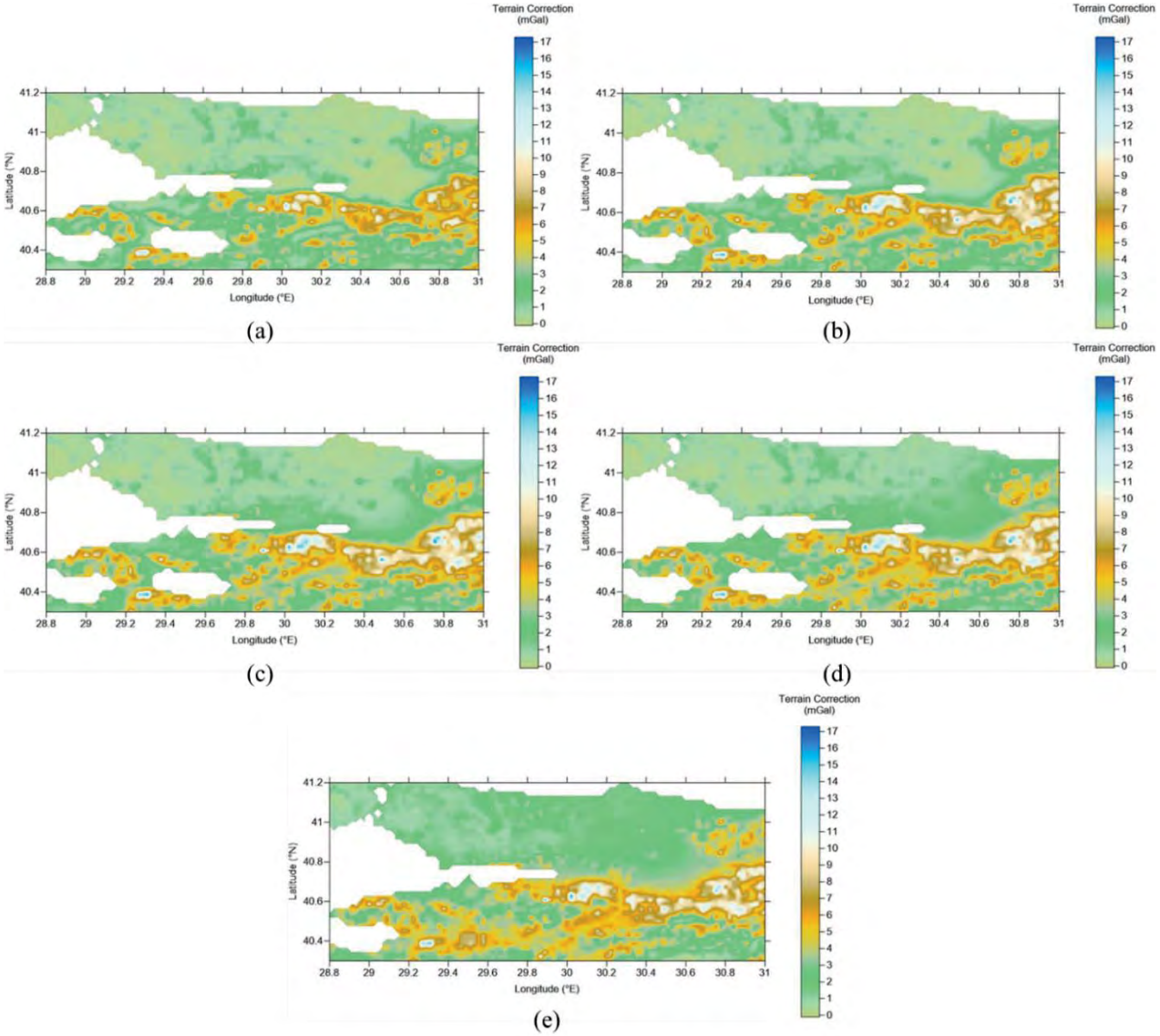

Figure 5: Terrain corrections for R1=6.5 km R2=0 km (a), for R1=6.5 km R2=20 km (b), for R1=6.5 km R2=50 km (c), for R1=6.5 km R2=100 km (d), for R1=6.5 km R2=200 km (e).

3.3 Geoid Modeling Results

As it can be seen in Tables 6 and 7, the minimum, maximum, mean and standard deviation values of the terrain correction effect on geoid undulations (N_{topo}), which were calculated by using 2.5′× 2.5′ and 5′× 5′ resolution DTMs, are approximately the same with the exception of centimeter or millimeter level differences. The results of 30″× 30″ resolution DTM shows an apparent difference with the other two DTM results. As Figure 6 illustrates, terrain correction effects on geoid are higher where the elevations are higher and the topography is rough. According to the comparison of the three image maps, it can be deduced that the effects derived from 30″× 30″ resolution DTM are the highest.

Table 6: Statistics of the effects of terrain corrections on geoid.

DTM Resolutions	Minimum (m)	Maximum (m)	Mean (m)	Standard Deviation (m)
30″× 30″	0.055	0.255	0.134	0.046
2.5′× 2.5′	0.039	0.176	0.093	0.032
5′× 5′	0.032	0.147	0.077	0.027

Table 7: Differences of the different resolution terrain correction effects on geoid.

DTM Resolutions	Minimum (m)	Maximum (m)	Mean (m)	Standard Deviation (m)
30″× 30″ - 2.5′× 2.5′	0.016	0.079	0.041	0.014
2.5′× 2.5′ - 5′× 5′	0.023	0.108	0.057	0.019
30″× 30″ - 5′× 5′	0.007	0.029	0.016	0.005

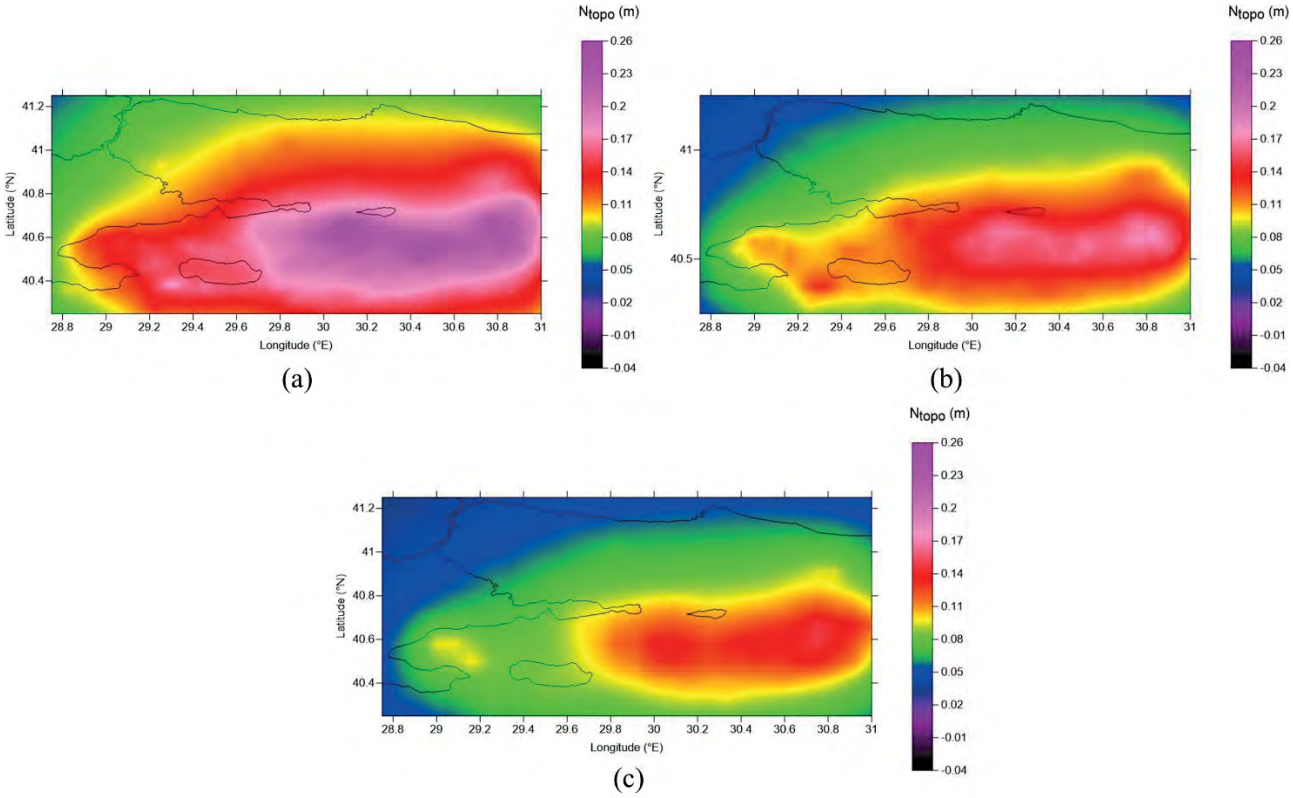

Figure 6: Effect of terrain corrections which were calculated with 30″× 30″ resolution DTM (a), with 2.5′× 2.5′ resolution DTM (b) and with 5′× 5′ resolution DTM (c).

According to Tables 8 and 9, the minimum, maximum, mean and standard deviation values of the indirect effects on geoid, that were computed from 30″× 30″, 2.5′× 2.5′ and 5′× 5′ resolution DTMs, are almost the same and have only millimeter level changes. This indicates that using either one of the 30″× 30″, 2.5′× 2.5′ and 5′× 5′ resolution DTMs does not make a considerable difference on the indirect effects. As Figure 7 demonstrates, indirect effects on geoid get smoother from 30″× 30″ resolution DTM to 5′× 5′ resolution DTM.

Table 8: Statistics of the indirect effects on geoid.

DTM Resolutions	Minimum (m)	Maximum (m)	Mean (m)	Standard Deviation (m)
30″× 30″	-0.133	0.000	-0.011	0.020
2.5′× 2.5′	-0.130	0.000	-0.011	0.020
5′× 5′	-0.137	0.000	-0.011	0.021

Table 9: Differences of the different resolution indirect effects on geoid.

DTM Resolutions	Minimum (m)	Maximum (m)	Mean (m)	Standard Deviation (m)
30″× 30″ - 2.5′× 2.5′	-0.003	0	0	0
2.5′× 2.5′ - 5′× 5′	0.004	0	0	-0.001
30″× 30″ - 5′× 5′	0.007	0	0	-0.001

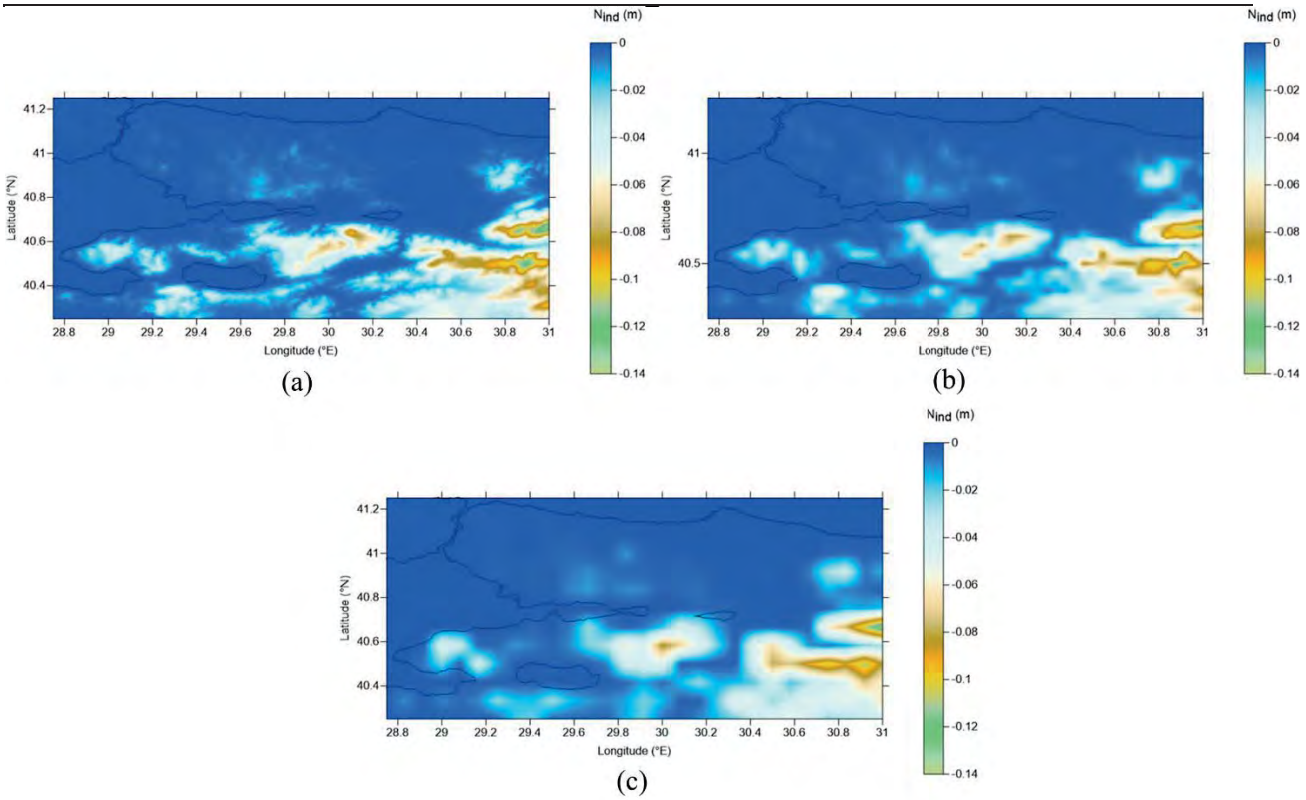

Figure 7: Indirect effects on geoid which were calculated with 30″× 30″ resolution DTM (a), with 2.5′× 2.5′ resolution DTM (b) and with 5′× 5′ resolution DTM (c).

As it can be seen in Table 10, the statistical values of geoid undulations, that were computed by using 30″× 30″, 2.5′× 2.5′ and 5′× 5′ resolution DTMs, are approximately the same and the values differ from each other in centimeter or millimeter levels. These small discrepancies indicate that using either one of the 30″× 30″, 2.5′× 2.5′ and 5′× 5′ resolution DTMs in terrain correction and indirect effect calculations does not make a remarkable amount of difference in overall geoid undulation values. Figure 8 indicates that the geoid undulations derived from 30″× 30″, 2.5′× 2.5′ and 5′× 5′ resolution DTMs do not show an apparent difference.

Table 10: Statistics of the geoid undulations.

DTM Resolutions	Minimum (m)	Maximum (m)	Mean (m)	Standard Deviation (m)
30″× 30″	35.689	41.093	39.939	1.150
2.5′× 2.5′	35.668	41.039	40.358	1.141
5′× 5′	35.662	41.013	39.886	1.136

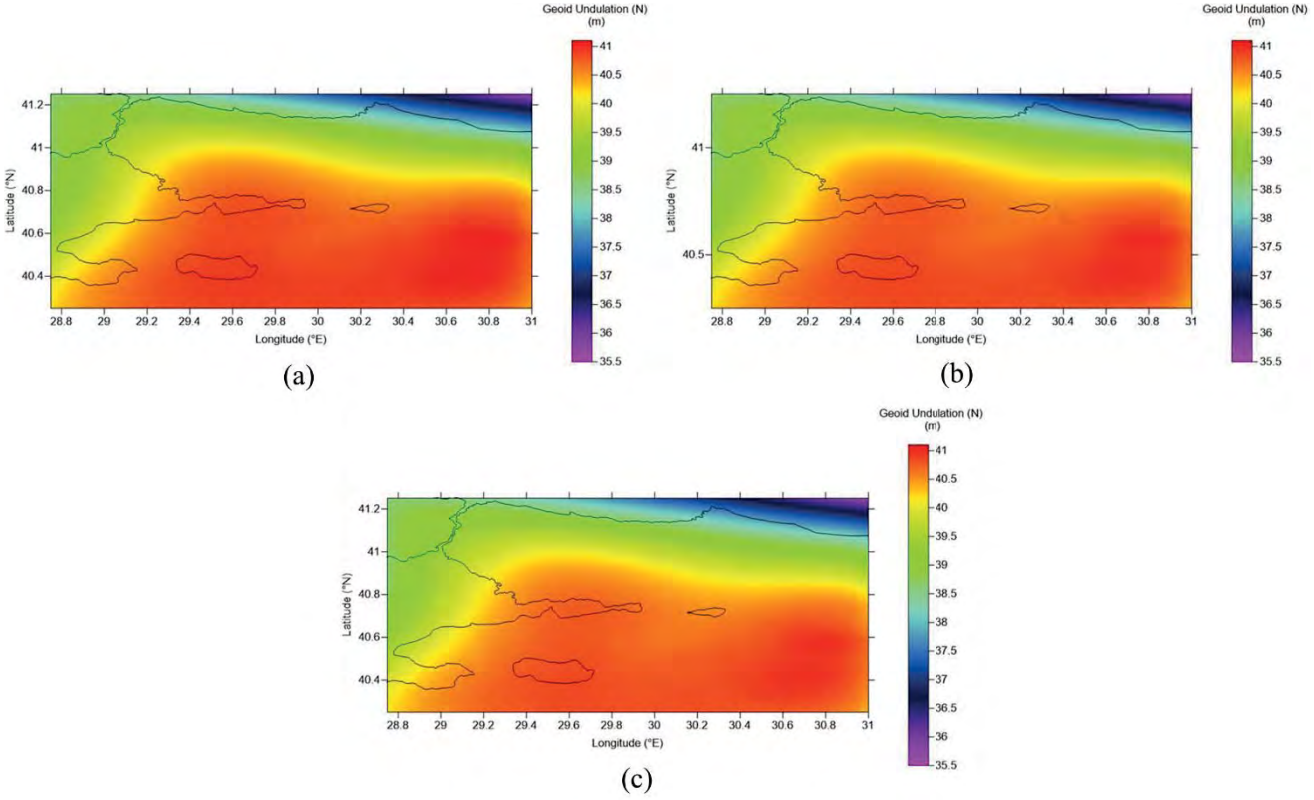

Figure 8: Geoid undulations that were derived from 30″× 30″ resolution DTM (a), from 2.5′× 2.5′ resolution DTM (b) and from 5′× 5′ resolution DTM (c).

According to Table 11, the centimeter and millimeter level changes in geoid undulations are not considerable for the accuracy in geoid modelling. The reason of obtaining low accuracy results is mostly the fault anomalies which have low resolution (5′× 5′).

Table 11: Statistics of the comparison between calculated geoid undulations and 109 GPS/leveling benchmark geoid undulations.

DTM Resolutions	Minimum (m)	Maximum (m)	Mean (m)	Standard Deviation (m)
30″× 30″	2.445	4.707	3.641	0.505
2.5′× 2.5′	2.422	4.662	3.598	0.501
5′× 5′	2.410	4.646	3.583	0.501

4. CONCLUSION

TSYM3 - SRTM3 and SRTM1 – AW3D30 DTMs have the highest similarity. According to their compatibility with TUDKA99A, it can be deduced that AW3D30 has the highest accuracy, meanwhile GTOPO30 has the lowest. In TC calculations, since 1″× 1″ and 3″× 3″ resolution DTM outputs do not show significant differences in statistics and do show a significant difference in calculation time, using 3″× 3″ DTM instead of 1″× 1″ DTM can be beneficial for saving time without lowering the accuracy. Moreover, keeping the desired radius as outer radius with a small inner radius saves a lot of time in the TC calculation process. It can be established that using either one of the 30″× 30″, 2.5′× 2.5′ and 5′× 5′ resolution DTMs does not make a significant difference on TC effect on geoid, indirect effects on geoid and geoid undulations. Since the statistical values of the indirect effects are almost the same, it can be deduced that the main factor which causes the changes in geoid undulations is the effect of the terrain corrections. For 30″× 30″, 2.5′× 2.5′ and 5′× 5′ resolution DTMs, it can be seen that the differences between the accuracies of the calculated geoid undulations are not considerable. These centimeter level differences can be ignored in the overall 3 to 4 m accuracy that is obtained for geoid undulations by 5′× 5′ resolution fault anomalies. For future studies, high resolution gravity anomalies can be used with 1″× 1″ and 3″× 3″ resolution DTMs in geoid modelling and the results can be evaluated.

REFERENCES

1. Heiskanen, W. A., & Moritz, H. (1967). Physical geodesy. Bulletin Géodésique (1946-1975), 86(1), 491-492.

2. Hofmann-Wellenhof, B., & Moritz, H. (2006). Physical geodesy: Springer Science & Business Media.

3. Vermeer, M. (2016). Physical Geodesy. Aalto University and the University of Helsinki: Helsinki, August 1, 89.

4. Il, H. T. A. (2018). Contribution of SRTM1 and ASTER Digital Elevation Models to Gravimetric Geoid Determination. (Master dissertation).

5. Yahaya, S. I., & El Azzab, D. (2018). High-resolution residual terrain model and terrain corrections for gravity field modelling and geoid computation in Niger Republic. Geodesy and Cartography, 44(3), 89-99.

6. Kiamehr, R., & Sjöberg, L. (2005). Effect of the SRTM global DEM on the determination of a high-resolution geoid model: a case study in Iran. Journal of Geodesy, 79(9), 540-551.

7. Merry, C. (2003). DEM-induced errors in developing a quasi-geoid model for Africa. Journal of Geodesy, 77(9), 537-542.

8. <https://search.earthdata.nasa.gov/>, date retrieved 05.03.2019.

9. <https://earthexplorer.usgs.gov/>, date retrieved 05.03.2019.

10. <https://www.eorc.jaxa.jp/ALOS/en/aw3d30/>, date retrieved 07.03.2019.

11. <https://land.copernicus.eu/imagery-in-situ/eu-dem/eu-dem-v1.1?tab=download>, date retrieved 12.03.2019.

12. <https://www.harita.gov.tr/urunler>, date retrieved 07.03.2019.

13. <http://galileo.selcuk.edu.tr/~tsym3/trdem2/>, date retrieved 07.03.2019.

14. Li, Y., & Sideris, M. (1994). Improved gravimetric terrain corrections. Geophysical Journal International, 119(3), 740-752.

15. Forsberg, R. (1984). A Study of Terrain Reductions, Density Anomalies and Geophysical Inversion Methods in Gravity Field Modelling. Ohio State University Reports, no.355, Ohio, US.

16. Erol, B. (2007). Investigations on Local Geoids for Geodetic Applications. (Doctoral dissertation).

17. Sideris, M. G. (2005). Geoid Determination by FFT Techniques. International School for The Determination and Use of The Geoid, Budapest, Hungary.

Assessments On Temporal Variations of Earth Gravity Field With Grace Observations Using Different Computation Services

Bilal MUTLU[1], Muhammed Raşit ÇEVİKALP[2], Bihter EROL[3]

[1]Istanbul Technical University, Geomatics Engineering Department 34467 Istanbul, Turkey
Phone: +90 536 848 5685, E-mail: mutlubil@itu.edu.tr

[2]Istanbul Technical University, Geomatics Engineering Department 34467 Istanbul, Turkey
Phone: +90 506 957 4369, E-mail: cevikalpm@itu.edu.tr

[3]Istanbul Technical University, Geomatics Engineering Department 34467 Istanbul, Turkey
Phone: +90 212 285 3826, E-mail: bihter@itu.edu.tr

ABSTRACT

Water is one of the most important needs of human life and plays a very important role in maintaining a healthy life. Nowadays, because of reasons such as global warming, water resources are under threat. Hence, humanity may face such a problem as water scarcity. Therefore, continuous monitoring and control of the water resources is necessary and essential, but since water basins are very large areas, it is difficult and expensive to carry out these observations using ground-based measurements accurately. In addition, these analyses are possible using satellite gravimetry. The gravitational field of the Earth continuously changes depending on time, and the redistribution of the water reservoir, which makes up three quarters of the globe, play vital role for gravitational field of the Earth. The vertical variation of these water bodies distributions can be investigated using the GRACE satellite pair, launched in 2002 by NASA. There are 4 different types of GRACE data and several analysis centers that provide and evaluate these data. Based on these, the problems come into minds such as how to model GRACE data and which GRACE data product must be used for more precise analyses and predictions. In addition, the interfaces or applications in which this data will be compiled is a separate problem and will be considered in this study. In the study, the Euphrates / Tigris basin, which is located between 30^o-40^o north latitudes and 37^o-52^o east longitude, is selected as the study area, and the Equivalent Water Thickness(EWT) based on these mass changes is calculated with GRACE (Gravity Recovery and Climate Experiment) satellite gravimetry data. The study was conducted in 3 different interfaces (applications): IGiK-TVGMF, EGSIEM Plotter and ICGEM. Common data set must be selected to investigate the differences between the results obtained in these different interfaces. In this context, Level-2 GRACE product with the DDK5 filtered was chosen, which was published by Astronomical Institute of the University of Bern (AIUB).

KEYWORDS: Earth gravity Field; Temporal Variation; IGiK-TVGMF; EGSIEM; ICGEM

1. INTRODUCTION

The world is a dynamic system consisting of continuously changing groundwater, soil moisture, snow and glaciers, and the water cycle formed by the fluid, mobile atmosphere and oceans. The change in any dynamics of these systems corresponds to changes in the field gravity field. Changes in the temporal and spatial scale in the gravitational field are used to define changes in the mass distribution. Because the short-term (monthly) changes of the gravity (gravitational field) signals can be said to consist of signals from the fluid-coated sources of the earth, rather than the signals of the solid world. In fact, the fluid world components are more moving than the solid world components [1]. For this reason, high accuracy satellite gravity measurements are one of the most important information stores about the changes in oceanography, cryosphere and atmospheric sources over time, especially hydrological.

New generation gravity field detection satellites CHAMP (Challenging Minisatellite Payload), GRACE (Gravity Recovery and Climate Experiment) and GOCE (Gravity Field and Steady-State Ocean Circulation Explorer) have been developed which aim to measure the world gravitational field and time changes with high accuracy. While CHAMP was the first satellite to determine the long wavelength components of the Earth's gravitational field, GRACE, the continuation of CHAMP, describes the world gravity field and its temporal changes. GOCE is focused on defining the world static field with the highest positional resolution possible. Although common missions determine the gravity field; GRACE stands out in terms of its ability to precisely identify the gravity field and the sources that cause it to change [2]. GRACE, aiming to measure the world gravitational field and its temporal changes with high accuracy, was launched on March 17, 2002 in order to investigate the water reservoirs on land, sea and glaciers by making high accuracy gravity measurements of the world.

By calculating Equivalent Water Thickness (EWT) changes, water redistribution in terrestrial areas can be detected and this quantity is obtained from GRACE products. If these obtained EWT values are analyzed according to Time-Series Method, trend and behavior of water bodies are detected. Computation also is important to analyze and model time varying gravity/mass functionals from GRACE data. Recently, there are different applications which are compiled in different computer programing languages to compute gravity/mass functionals from GGMs some of these applications are web-based and some work in environments like Matlab. Although the

data used are the same, the result may be different. There are main differences of currently available software and interactive online tools for the computations: some software were mainly developed to determine static gravity functionals so that time varying gravity functionals cannot be detected, some programs do not include some of functionals like water height or deflection of verticals, and there are differences at quality, speed and stability of software.

In this study, the Euphrates / Tigris basin, which is located between 30 °-40° north latitudes and 37 ° -52 ° east longitude and it is a transboundary basin with a total area of 879.790 km2 distributed between Iraq (46 percent), Turkey (22 percent), the Islamic Republic of Iran (19 percent), the Syrian Arab Republic (11 percent), Saudi Arabia (1.9 percent) and Jordan (0.03 percent)[3], is selected as the study area, and the Equivalent Water Thickness (EWT) based on these mass changes is calculated with GRACE (Gravity Recovery and Climate Experiment) satellite gravimetry data. The study was conducted in 3 different interfaces (applications): IGiK-TVGMF, EGSIEM Plotter and ICGEM. Common data set must be selected to investigate the differences between the results obtained in these different interfaces. In this context, Level-2 GRACE product (RL-02) with the DDK5 filtered was chosen, which was published by Astronomical Institute of the University of Bern (AIUB).

2. MATERIAL AND METHOD

The determination and the analysis of temporal variations of gravity/mass functionals (TVGMFs) such as Equivalent Water Thickness (EWT) and Geoid Height play vital roles within the Earth-science disciplines, especially since it is related to the depletion of water resources that have become important today [4].

$$N(\theta,\lambda) = a\sum_{l=0}^{\infty}\sum_{m=0}^{l}\hat{P}_{lm}\cos(\theta)\left(C_{lm}\cos(m\lambda) + S_{lm}\sin(m\lambda)\right) \quad (1)$$

$$\Delta EWT(\theta,\lambda) = \frac{a\rho_{ave}}{3\rho_w}\sum_{l=0}^{\infty}\sum_{m=0}^{l}\hat{P}_{lm}\cos(\theta)\frac{(2l+1)}{(k_l+1)}\begin{pmatrix}\Delta C_{lm}\cos(m\lambda)\\ +\\ \Delta S_{lm}\sin(m\lambda)\end{pmatrix} \quad (2)$$

On account of determination and analyzing TVGMFs using GGMs from GRACE data products, a befitting computational tool is essentially needed. Within the scope of this study, these 2 software are examined:

1. IGiK-TVGMF (Instytut Geodezji i Kartografii–TVGMF)
2. EGSIEM Plotter (European Gravity Service for Improved Emergency Management)

2.1 IGiK-TVGMF

IGiK–TVGMF (Instytut Geodezji i Kartografii–TVGMF) is an application, which is compiled as a MATLAB package, allows computing and analyzing TVGMF from Global Geopotential Models(GGMs) which is derived by using monthly interval GRACE satellite gravimetry mission data.

IGiK–TVGMF can compute analyze and model 13 parameters at a single point or a grid of points using GRACE-based GGMs. In addition to Plotter, there are two different techniques for analyzing and modelling TVGMFs in this application package; The Seasonal Adjustment(SA) and The Principal Component Analysis/Emprical Orthogonal Function(PCA/EOF) [5].

Level-2 products are used released by 7 different computation centres: GFZ (GeoForschungs Zentrum), the CSR (Centre for Space Research) and the JPL (Jet Propulsion Laboratory), the ITG (Institut für Geodäsie und Geoinformation of Bonn University), the AIUB (Astronomical Institute of Bern University), the HUST (Huazhong University of Science and Technology) and the Tongji (Tongji University).

Also, C_{20} spherical harmonic coefficient which represents dynamic oblateness changes of Earth, can be estimated from GRACE, Ocean Bottom Pressure (GRACE-OBP) and SLR data.

There are 3 different Reference Model in application; EGM2008, EIGEN-6C4 and GECO.

In addition, 9 different filter such as Gaussian and DDK1 – DDK8 can be used for computations.

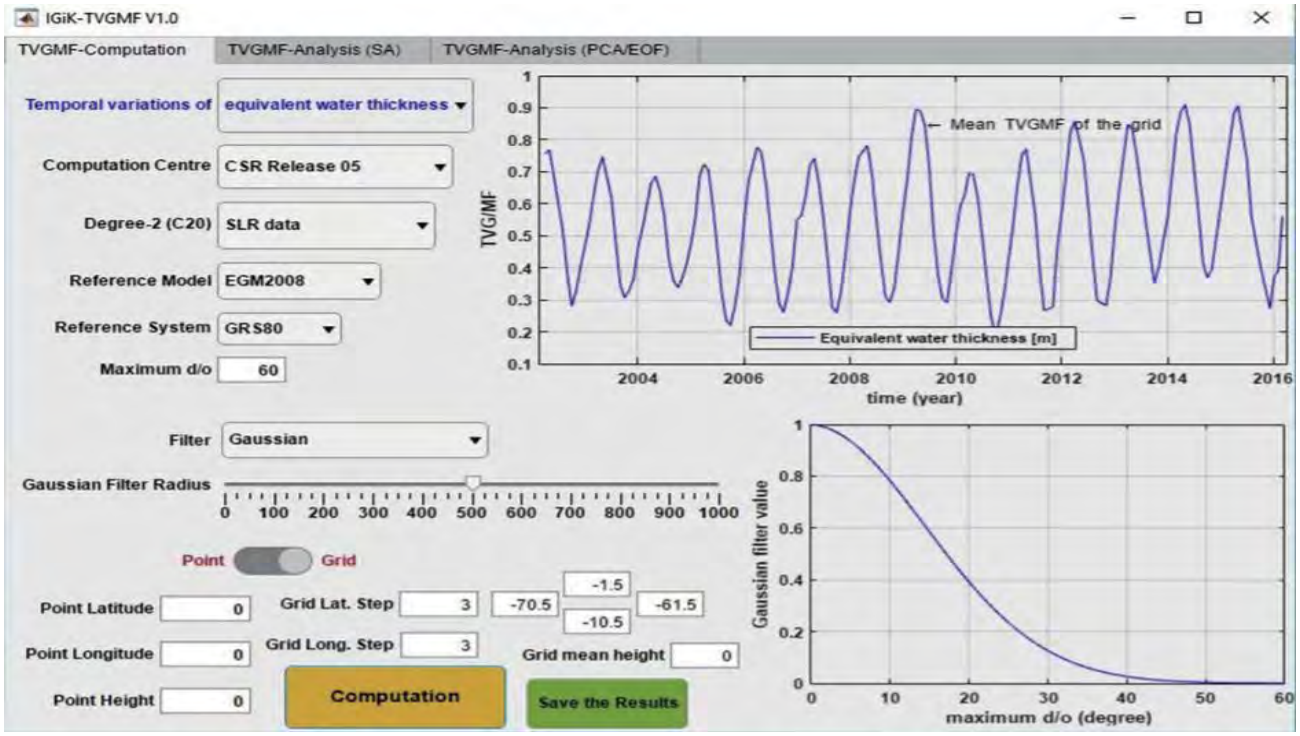

Figure 1. TVGMF computation in IGiK

The main aim of the SA method is to separate the time series signal into three components; Trend, Seasonal and Random components.

These two models of the SA method are defined as:

1. Additive model (common method) :Trend + Seasonal + Random
2. Multiplicative model (alternative) :Trend × Seasonal × Random

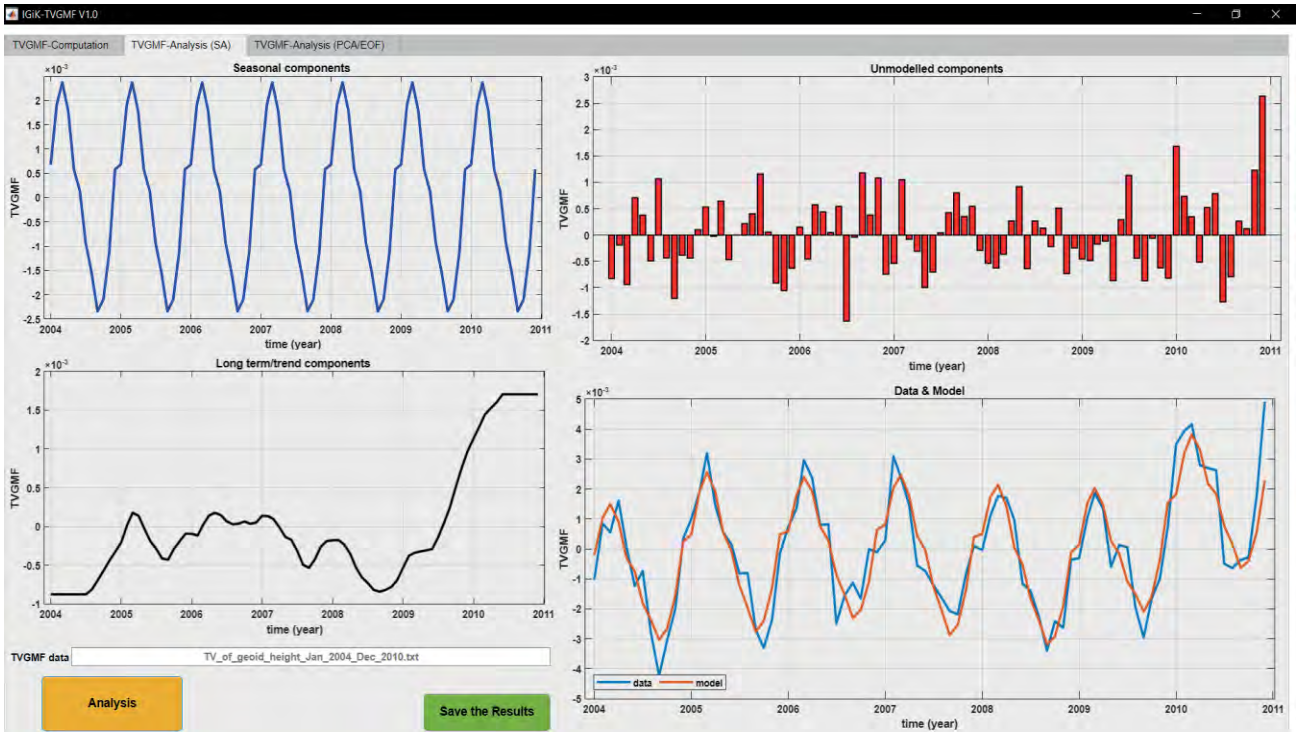

Figure 2. The SA TVGMF analysis in IGiK

The main aim of the PCA/EOF (Principal Component Analysis/Empirical Orthogonal Function) is to reduce the dimensionality of the data vector and to identify the most important patterns explaining the variability within the data. PCA/EOF method analyze the TVGMF in the spatio-temporal domain. The main advantage of the PCA/EOF method against the SA method is that behaviors in TVGMF can spatially be illustrated. The PCA/ EOF method also better than the SA method for areas characterized with negligible variation patterns of TVGMFs in the space domain [5].

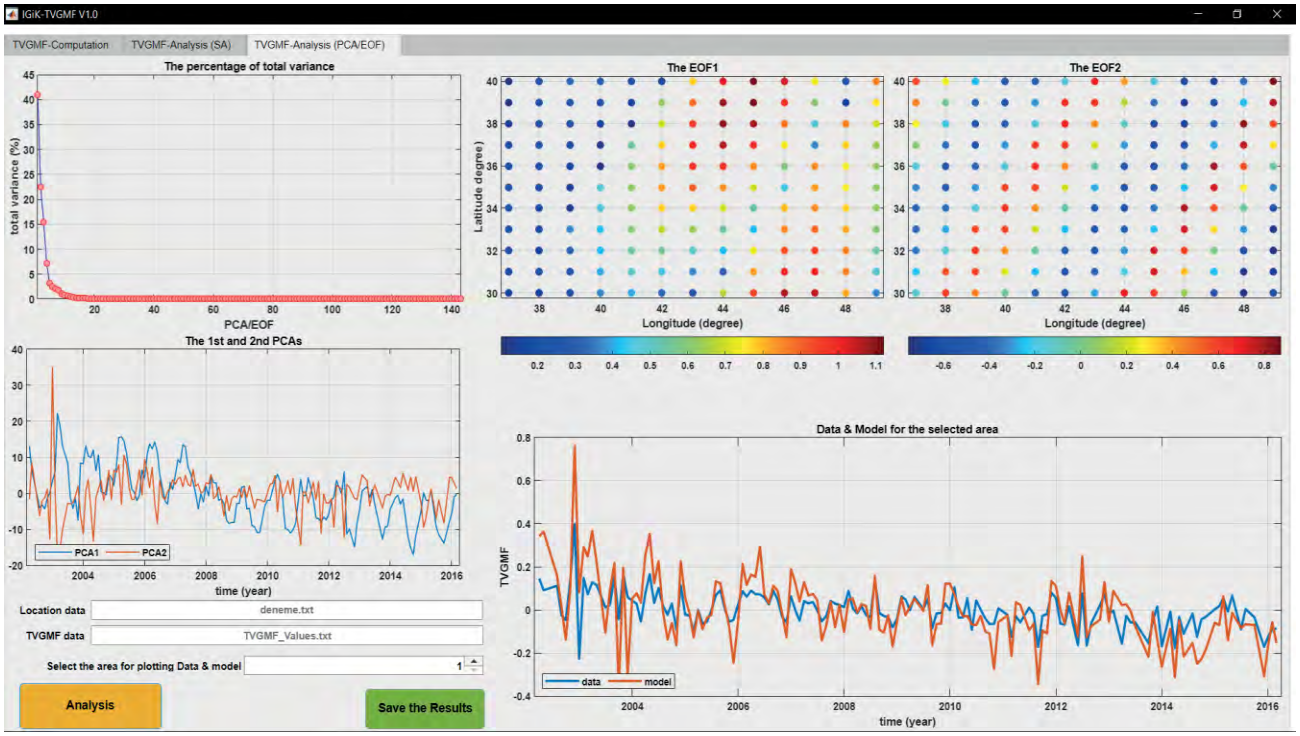

Figure 3. The PCA and EOF analysis in IGiK

2.2 EGSIEM

EGSIEM project has received funding from the European Union's Horizon 2020 research and innovation program. The extreme changes in the continental water storage can cause floods and droughts that require high damage to infrastructure, economy and human life. The aim of this project is to demonstrate that Gravity Recovery and Climate Experiment(GRACE) data allows for innovative approaches to monitoring and forecasting flood and drought. This project has been initiated to prevent these disasters by using an early warning system. Timely and reliable information is a top priority for any early warning system. The objectives will be achieved by setting up three dedicated services:

1. A scientific combination service;
2. A near real-time (NRT) / regional service; and
3. A hydrological/early warning service

Graphs of time variation of Gravity/mass functionals such as Water Heights, Geoid Heights and Spherical Harmonics can be plotted. As a data set, EGSIEM mascon data or Level-2 products

which is served by analysis centres can be used. Spherical harmonic models are converted into 1°x1° grids after replacement of the C20 by the SLR series provided in GRACE Technical Note 07, and subtraction of the mean over the time span. Coefficients taken into account for the conversion to grid go from degree 2 to degree 89 [6].

3. RESULTS AND DISCUSSION

As a data set, time series of monthly gravity models AIUB-RL02 with DDK5 filter are used in the study. Time interval of data set is between March 2003 to March 2014.

Table 1: Data gaps in the data set.

	Jan	Feb	Mar	Apr	May	Jun	Jul	Aug	Sep	Oct	Nov	Dec
2003			✓	✓	✓		✓	✓	✓	✓	✓	✓
2004		✓	✓	✓	✓	✓	✓	✓			✓	✓
2005	✓	✓	✓	✓	✓	✓	✓	✓	✓	✓	✓	
2006	✓	✓	✓	✓	✓	✓	✓	✓	✓	✓	✓	✓
2007	✓	✓	✓	✓		✓	✓	✓	✓	✓	✓	✓
2008	✓	✓	✓	✓	✓	✓	✓	✓	✓	✓	✓	✓
2009	✓	✓	✓	✓	✓	✓	✓	✓	✓	✓	✓	✓
2010	✓	✓	✓	✓	✓	✓	✓	✓	✓	✓	✓	✓
2011		✓	✓	✓	✓		✓	✓	✓	✓	✓	✓
2012	✓	✓	✓	✓		✓	✓	✓	✓		✓	✓
2013	✓	✓		✓	✓	✓	✓			✓	✓	✓
2014	✓	✓	✓									

The Euphrates/Tigris basin in which Turkey is located has been selected as study area. Water scarcity and disagreements in sharing the resources of the Middle East have been effective in this selection. In addition, the resolution of the GRACE satellite makes sense for this large basin.

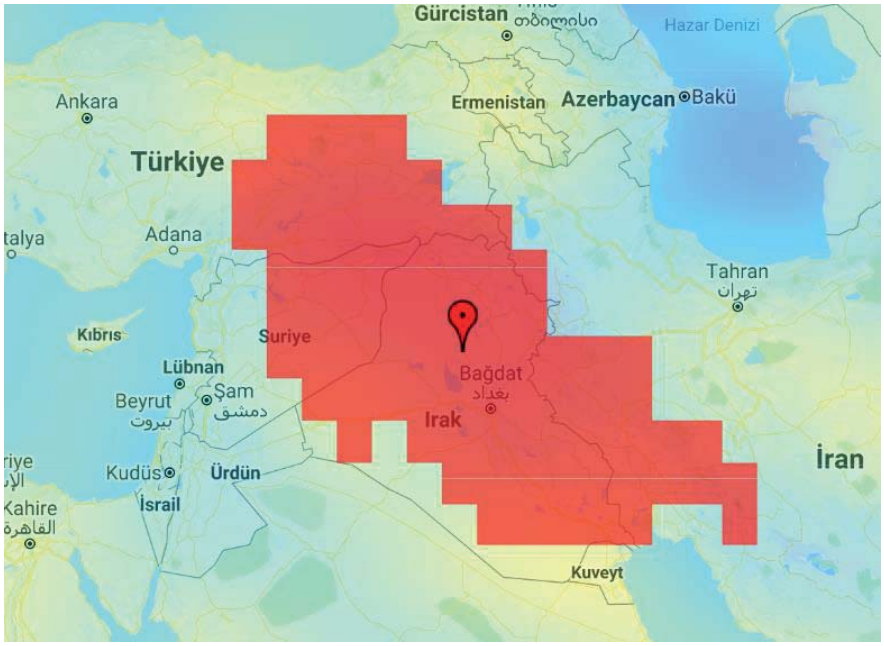

Figure 4. Area selection (Euphrates Basin).

Time series solution of IGIK Matlab package is shown below for equivalent water thickness. Seasonal adjustment and Principal Components analysis process cannot be done because there must be no time gap in the data set for these analysis.

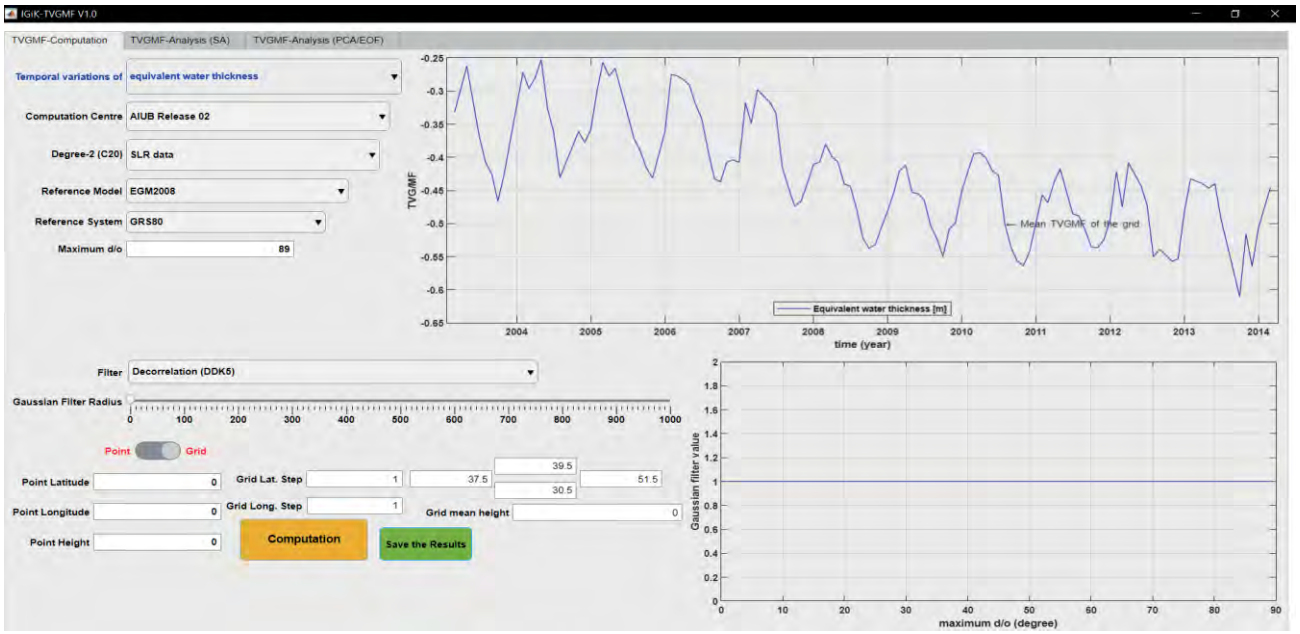

Figure 5. Time Variation solution of area (1°x1° grids) between 37,5°E-51,5°E longitudes.

Time series solution of EGSIEM plotter is also demonstrated in figure 7

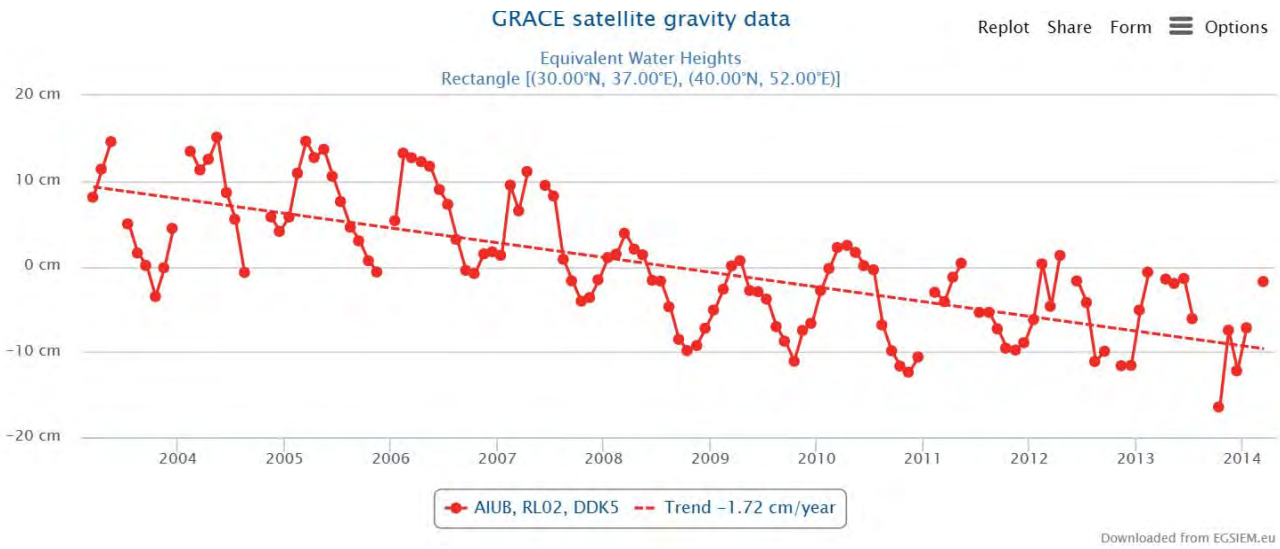

Figure 6. EGSIEM solution of area (1°x1° grids) between 37,5°E-51,5°E longitudes with Linear Regression.

Minimum and maximum values are different to each other but they were obtained at the same dates and trends are almost similar, there are 2 millimeter differences in each other. Finally, if the equivalent water height differences multiplied by the area, volume of displaced water can be determined in related interval.

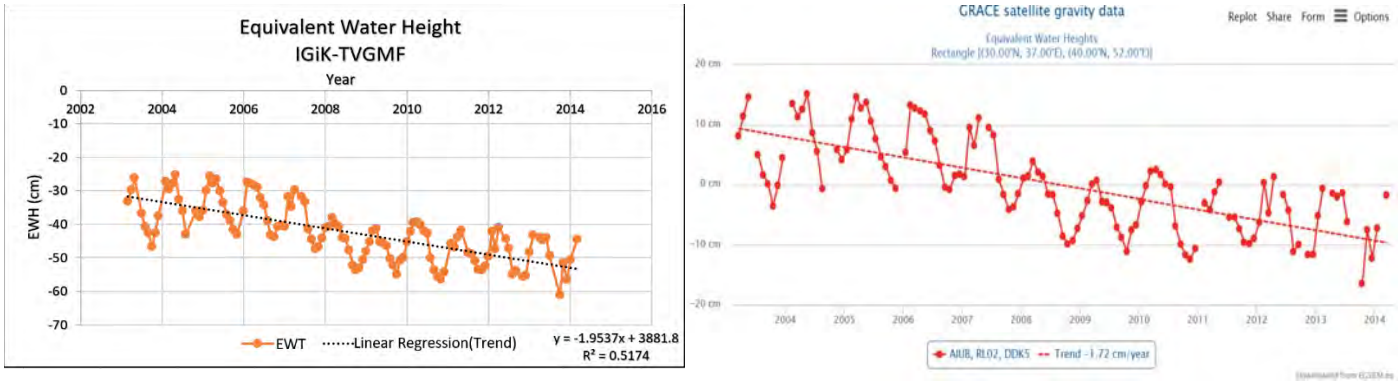

Figure 7. IGiK and EGSIEM solution of area (1°x1° grids) between 37,5°E-51,5°E longitudes with Linear Regression.

Table 2: Comparison of results.

	Maximum (cm)	Minimum (cm)	Trend (cm/year)	Volume(gigatons) $\Delta EWT\ x\ \frac{Area}{100000}$
EGSIEM	15.134	-16.433	-1.72	15.173
IGiK-TVGMF	15.4593	-20.352	-1.93	17.391

Also, Voss et. al found that there is -2.72 cm/year trend of interval between 2003 January and 2009 December for Euphrates/Tigris basin in their study (2013). Trend value is calculated as a -2.73 by using IGIK solution for related time interval in figure 9.

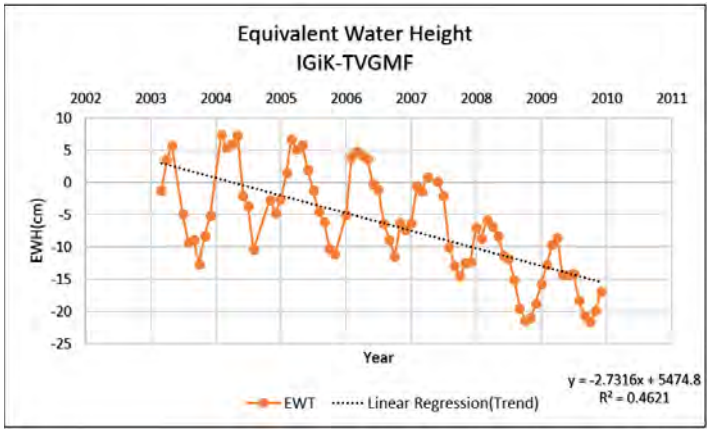

Figure 8. IGiK Time Variation solution of area (1°x1° grids) between 37,5°E-48,5°E longitudes with Linear Regression (between 2003-2010).

4. CONCLUSION

As a conclusion, web-based and desktop applications are used to analyzing and modeling time-variable gravity/mass functionals from GRACE data. In spite of using the same data, the different output can be obtained. Because of their features, quality, speed, and stability of application are the different each other. Moreover, some of the applications are not capable of computing a few functionals such as water height or deflection of verticals, and some cannot detect the time variable gravity functionals. The comparison of two applications is summarized in the table 3.

Table 3: Comparison of IGiK-TVGMF and EGSIEM Plotter.

IGiK-TVGMF	EGSIEM PLOTTER
• Matlab package.	• Web-based online tool.
• 13 different gravity functionals can be computed.	• Only 2 different functionals.
• Reference Models are used	• Reference time is used
• 9 different filter can be used	• There are no filter option but there are already filtered (ddk) Level-2 and Level-3 data can be used.
• Level-2 data sets released by GFZ, CSR, ITG, JPL, AIUB, HUST and Tongji are contained.	• Level-3 products which are released by EGSIEM and Level-2 products released by GFZ, AIUB, CNES, TUGRAZ, JPL and CSR are contained.
• There are only one series can be processed.	• Different series can be drawn in the same graph
• There are no graph export.	• Graphics can be downloaded and features can be modified.
• There are no trend calculation.	• Trend can be computed based on different regression models.
• Users are able to make changes in data set.	• Users can use only existed data sets.
• Time variation solution for all grid points in study area in output for related Monthly solution.	• Time variation solution for mean of all grid points in output for related Monthly solution.

ACKNOWLEDGEMENT

We would like to thank Assoc. Prof. Dr. Serdar EROL and Research Asst. M. Serkan IŞIK for all their supports.

REFERENCES

1. Swenson S., Wahr J., (2002), "Methods for Inferring Regional Surface-Mass Anomalies from Gravity Recovery and Climate Experiment Measurements of Time Variable Gravity", Journal of Geophysical Research: Solid Earth (1978– 2012), 107 (B9), ETG-3.

2. Yıldırım, Y. Ö. (2015). GRACE Uydu Verileri ile Türkiye'nin Uzun Dönemli Su Kütle Değişiminin İncelenmesi. Gebze Technical University.

3. Lehner, B., Verdin, K., Jarvis, A., (2008). New global hydrography derived from spaceborne elevation data. Eos, Transactions, AGU, 89(10): 93-94. HydroSHEDS.

4. Wahr, J., F. Molenaar, and F. Bryan (1998), Time variability of the Earth's gravity field: Hydrological and oceanic effects and their possible detection using GRACE, J. Geophys. Res., 103(B12), pp. 30,205-30,229

5. Godah, W. (2019). IGiK–TVGMF: A MATLAB package for computing and analysing temporal variations of gravity/mass functionals from GRACE satellite based global geopotential models.

6. Jäggi, A., Weigelt, M., Flechtner, F., Güntner, A., Mayer-Gürr, T., Martinis, S., ... & Meyer, U. (2019). European Gravity Service for Improved Emergency Management (EGSIEM)—from concept to implementation. Geophysical journal international, 218(3), 1572-1590.

Precise Orbit Determination (POD) of LEO Satellite Missions: Preliminary Results

Ilker Ustuner[1] , Serdar Erol[2]

[1]Osmaniye Korkut Ata University, Geomatics Engineering Department 80000 Osmaniye, Turkey
Phone: +90 328 827 10 00, E-mail: ilkerustuner@osmaniye.edu.tr

[2]Istanbul Technical University, Geomatics Engineering Department 34469 Istanbul, Turkey
Phone: +90 212 212 285 38 26, E-mail: erol@itu.edu.tr

ABSTRACT

Low Earth Orbiters (LEO) are orbiting satellites at an altitude of 200 and 2000 km above the earth, such as GRACE, SWARM, SENTINEL satellites. The orbits of these satellites rotating the earth need to be precisely determined for geodetic purposes. Precise orbits of a LEO that is equipped with a GPS (Global Positioning System) receiver can be determined by GPS observations. There are two main models of POD: kinematic orbit determination and reduced-dynamic orbit determination. Kinematic orbit determination of a satellite depends on getting three-dimensional coordinates on GPS observations without considering the external forces acting on the satellite. The result of the kinematic solution is discrete and has data gaps. Reduced-dynamic orbit determination takes external forces into account in position models of satellite. Although this study mainly focused on kinematic orbit determination, both two models that are introduced were produced. In this study, POD of one-day SENTINEL-3A and SWARM-A were performed. The processing strategy depends on precise point positioning (PPP) technique and zero-differenced LEO GPS data. The PPP technique is a zero-difference processing in which satellite final orbit, clock information, and biases are introduced in solution equations. The process was carried out for each satellite in Bernese GNSS Software version 5.2 that is GNSS (Global Navigation Satellite System) data processing software for geodetic purposes improved by University of Bern. In the term of POD, it is possible to process LEO data manually or automated Bernese PCF (Processing Control File) mode. In the process, CODE (Center for Orbit Determination in Europe) final products that are GPS final orbit and clocks were used. The main results of process are Kinematic and Reduced-dynamic orbits of each satellite in 10s sampling. When SENTINEL-3 results are compared to ESA (European Space Agency) solution, the difference in results is in cm level. On the other hand, SWARM-A satellite results have cm difference in X and Y axes compared to Astronomical Institute of University of Bern solution. Due to the lack of antenna phase center corrections of GPS receivers on Swarm satellites and specific satellite information, such as attitude information, they could not be used in this process. It can be stated that it should be evaluated in further researches whether these differences result from indicated situations for LEO satellites.

KEYWORDS: *Precise Orbit Determination*; POD; *LEO*; *GPS*; *Bernese; SWARM; SENTINEL*

1. INTRODUCTION

Since the first artificial satellite, SPUTNIK 1, was launched into orbit in 1957, the process of launching many artificial satellites developed for different purposes began. In terms of positioning and navigation applications, military purposes, telecommunication and information technologies, monitoring the atmosphere, obtaining images of continents and oceans, monitoring environmental impacts and changes, many artificial satellites have been launched into space. Along with the first artificial satellite sent to space, orbital tracking or trajectory calculations of the satellites gained importance. Following this situation, the orbit determination studies of satellites became one of the main study subjects of satellite geodesy.

For the purpose of geodetic and geodynamic purposes, CHAMP, GRACE and GOCE satellites are sent to space to provide gravity field information of the earth, and SWARM satellite mission is responsible for the observation of the earth's magnetic field, and SENTINEL satellites are responsible for earth observation. GNSS (Global Navigation Satellite System) satellite missions are examples of satellite systems developed for navigation and positioning and orbiting the earth.

Satellites can be classified depending on the height of the orbits they travel through the earth as low earth orbit, medium earth orbit, and geostationary earth orbit [1].

Low earth orbit satellites are orbiting between 200 and 2000 km altitude above the earth [2]. Medium earth orbits are the navigation orbits around the earth for satellite missions used for navigation purposes and are approximately 20000 km altitude, such as GNSS satellites [2]. Ground-stationary orbits are used for communication satellites. The satellites are orbiting the Earth's observation area at a constant 24-hour period of approximately 35800 km altitude, and global coverage is possible with at least 3 satellites [2].

Achieving the objectives of all satellite missions is provided by precise orbit information. The precise orbit determination of the satellites in navigation systems is important for precise positioning, which is the main purpose of navigation systems. On the other hand, in the gravity field determination studies, the distorting effects that have effect on the satellite dynamics can be modeled and the gravity field determination studies are carried out thanks to the precise position information of the satellites. These examples can be given for the importance of obtaining precise orbit determination of the satellites.

Orbit determination studies with GPS receivers placed on LEO satellites have contributed positively to the results of precise orbit determination studies with improvements in GPS technology and calculation methods. Two strategies can be defined in precise orbit determination studies: Kinematic and reduced-dynamic orbit determination based on GPS. Another strategy is dynamic orbit determination that can be called as the conventional model [2].

In this study, it is aimed to produce precise orbits of Sentinel-3 and Swarm-A LEO satellites. To achieve this, it was decided to use Bernese v5.2 software for precise orbit determination. Bernese software is a GNSS processing software developed by the University of Bern and has an automated orbit determination module for LEO satellites.

2. MATERIAL AND METHOD

To produce the precise orbits of LEO's by using spaceborne GPS receivers, there are two main models of POD: kinematic orbit determination and reduced-dynamic orbit determination.

The kinematic orbit determination strategy is directly dependent on the accuracy potential of the satellite positions that GPS can provide. This orbit determination model is to determine the satellite positions of the satellite completely dependent on GPS observations and fully independent of external forces. Thus, the quality of the data obtained directly affects the quality and continuity of the calculated satellite orbits. Although kinematic orbit determination strategy is the most practical method in terms of applicability, data is not continuous. Three different solution approaches can be shown in the kinematic model: zero differences (ZD), double differences (DD), and triple differences (TD) approaches [1; 3]. Kinematic orbit determination is performed by using high-rate GPS clock and ephemeris information by ZD method. In this process, it is possible to use zero differences approach and ionosphere-free linear combination [1]. Precise GPS time and orbit information are ephemeris information from the International GNSS Service (IGS) and one of its analysis centers. By using double differences and triple differences, kinematic solution is achieved by using bases between GPS receiver and IGS ground stations on LEO satellites. However, this greatly

increases the amount of data involved and requires strong computing capabilities for the solution. Since it is possible to achieve the desired result in a simpler way by using zero differences, it is preferred to use the ionosphere free linear combination with zero differences approach in kinematic solutions [1; 4]. Approaches in kinematic POD can be seen in the Figure 1.

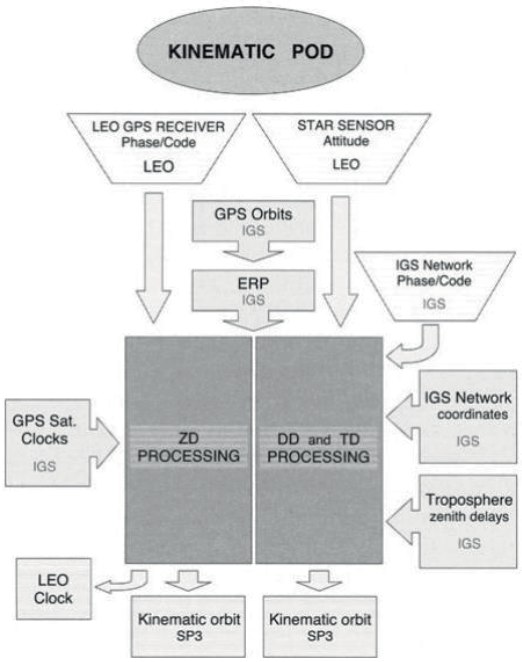

Figure 1. *Zero and double difference approach in kinematic POD* [5]

The dynamic orbit determination strategy estimates the time-dependent acceleration changes of the satellite using a mathematical model of external forces acting on the satellite, and the optimal orbit is developed for GPS measurements [2]. If the information about the dynamic behavior of the satellites is insufficient and the estimation time increases, deterioration of the orbital solutions will be seen. In the dynamic force model, all perturbed forces are added to the basic satellite motion equation as in the Equation 1 [2; 3; 6]. The components of the dynamic force model include gravitational or non-gravitational perturbations [1]. Gravitational perturbations can be listed as inhomogeneous gravity field of the earth, gravitational effect of other celestial bodies such as sun and moon, irregularities caused by tides, and relativistic effects. Non-gravitational perturbations can be sampled as atmospheric drift, solar direct radiation pressure.

$$\ddot{r} = -G\frac{Mm}{r^3}r + \ddot{f_1}(t, r, \dot{r}, Q_1, \dots, Q_d) \qquad (1)$$

The notations shown in Equation 1 are as follows:

- r position of satellite
- $\dot{r}$ velocity of satellite
- $\ddot{r}$ acceleration of satellite
- f_1 perturbed acceleration
- f gravitational or non-gravitational perturbations
- $Q_1, \dots, Q_d$ dynamic orbit parameters.
- G gravitational constans
- M mass of the earth
- m mass of the satellite

The reduced-dynamic orbit determination strategy can be defined as a combination of these two methods, using the advantages and disregards of the disadvantages in kinematic and dynamic methods. The kinematic technique ignores the incorrect physical modeling of the dynamic model by not processing dynamic information. However, it has measurement noise from the GPS signals in the model. The use of both techniques together in an appropriate weight in a Kalman filter process compensates for the disadvantages. The basis of the reduced-dynamic orbit determination strategy is the restoration of the dynamic solution with continuous GPS data. Reduced-dynamic orbit determination uses both the geometric power of GPS observations and the fact that satellite orbits are specific solutions of a motion equation. The dynamic orbit parameters $(Q_1, \dots, Q_d)$ in the equation (1) are called deterministic motion equation parameters [6]. In addition to the deterministic parameters in the reduced-dynamic orbit determination, the experimental stochastic parameters $(P_1, \dots, P_s)$ are added to the Equation 2.

$$\ddot{r} = -G\frac{Mm}{r^3}r + \ddot{f_1}(t, r, \dot{r}, Q_1, \dots, Q_d, P_1, \dots, P_s) = f \qquad (2)$$

Both kinematic and reduced-dynamic orbit solutions were produced by Bernese v5.2 software. Bernese is capable to process LEO data, but some Swarm and Sentinel specific satellite informations should be introduced to Bernese software, such as antenna phase center variations or some technical corrections.

In this study, the strategy of precise orbit determination was determined as follows [7]:

- only GPS data because of the Bernese LEO POD processing restriction
- 1-day solution of each satellite
- Earth-Centered Earth-Fixed (ECEF) positions
- CODE (Center for Orbit Determination) in Europe final products «Final GPS orbits and final 5s clock»
- Ionosphere-free linear combination and zero-difference approach
- No tropospheric correction due to LEO's altitudes
- 10s sampling results
- Elevation cut-off angle is 0 deg

3. RESULTS AND DISCUSSION

The orbit solution results obtained were compared with the results of different institutions and the statistical information about the orbits was evaluated within the scope of the study. Precise orbit determination studies were carried out for Swarm-A and Sentinel-3A satellites.

In the precise orbit determination study for Swarm-A satellite, 1 full day solution on 29.10.2018 was obtained by using Bernese LEOPOD.PCF. The phase center corrections and satellite attitude information for Swarm-A could not be applied. For sentinel-3A, only satellite attitude information could not be applied. Instead of the original satellite attitude files from startrackers, the nominal attitude mode was applied in the solutions.

The kinematic orbit results obtained from the Swarm-A precise orbit determination study were compared with the kinematic solutions performed by the Institute of Astronomy (AIUB) of Bern University (Table 1). In the results obtained, a difference in cm level was observed in X and Y axes, but in Z axis differences are in dm level.

When the kinematic and reduced-dynamic orbit solutions compared to each other from Bernese process in satellite coordinate system (RSW), results are as Table 2.

Table 1: Comparing orbit solutions (Bernese-AIUB) for Swarm-A

	DX (cm)	DY (cm)	DZ (cm)
Maks	13,44	-14,6	54,3
Min	0,0	0,2	50,7
Ort	5,8	-2,0	53,1
Std	4,4	7,5	1,1

Table 2: Comparing the kinematic and reduced-dynamic orbit solutions for Swarm-A

	Radial (cm)	Along-track (cm)	Out-of-plane (cm)
RMS	2.96	2.56	2.10
Mean	0.1	0.56	-1.28
Min	-10.11	-6.53	-8.19
Max	12.88	7.01	3.81

As the same way, 1 full day solution for Sentinel-3A on 29.10.2018 was obtained by using Bernese LEOPOD.PCF.

The kinematic orbit results obtained from the Sentinel-3A precise orbit determination study were compared with the kinematic solutions performed by European Space Agency (ESA) (Table 3). In the results obtained, a difference in cm level was observed in X, Y and Z axes.

When the kinematic and reduced-dynamic orbit solutions compared to each other from Bernese process in satellite coordinate system (RSW), results are as Table 4.

Table 3: Comparing orbit solutions (Bernese-ESA) for Sentinel-3A

	DX (cm)	DY (cm)	DZ (cm)
Maks	-18.6	-19.5	-13.9
Min	0.1	0.0	-2.4
Ort	-3.9	-4.0	-7.6
Std	4.2	8.5	1.4

Table 4: Comparing the kinematic and reduced-dynamic orbit solutions for Sentinel-3A

	Radial (cm)	Along-track (cm)	Out-of-plane (cm)
RMS	4.12	3.16	2.46
Mean	-0.06	0.26	-1.98
Min	-21.58	-8.71	-5.93
Max	41.93	24.57	2.64

The solutions show that the orbits for Swarm-A and Sentinel-3A is satisfying for many applications in the term of epoch based. However, it can be more precise after applying some corrections such as antenna phase center model and satellite attitude information, especially.

4. CONCLUSION

Precise orbits are crucial for many applications. The aim of the Swarm satellite mission is to provide the best exploration of the geomagnetic field and its time-dependent change [8]. For this purpose, magnetic and electric field observations, accelerometer observations should be accurately geographically referenced.

In order to improve altimeter performance, it is important to determine the precise orbits of Sentinel-3 satellites. On the other hand, the geographic referencing of the images obtained within the mission requires obtaining the precise orbit coordinates of the satellites.

For LEO POD, satellite attitude information plays an important role in producing precise orbits. In further studies, the orbits can be improved by using original satellite attitude information.

REFERENCES

1. Doğanalp, S. Gravite Alanı Belirleme Amaçlı Yakın Yer Uyduları için Duyarlı Yörünge Belirleme Teknikleri. PhD Thesis, Selçuk Üniversitesi, 2013.

2. Seeber, G. (2003). Satellite Geodesy. Walter de Gruyter, Berlin, 2nd edition.

3. Bock, H. (2003). Efficient Methods for Determining Precise Orbits of Low Earth Orbiters Using the Global Positioning System. PhD thesis, Institut f*ür* Geodäsie und Photogrammetrie, Geodätisch-geophysikalische Arbeiten in der Schweiz. ISBN:3-908440-08-4.

4. Svehla, D. ve Rothacher, M. (2003). Kinematic and reduced-dynamic precise orbit determination of low earth orbiters. Advances in Geosciences, 1:47–56.

5. Svehla, D. ve Rothacher, M. (2002). Kinematic orbit determination of LEOs based on zero or double-difference algorithms using simulated and real sst GPS data. In Adam, J.; Schwarz, K.-P., editor, Vistas for Geodesy in the New Millennium, IAG Symposia, volume 125, pages 322–328. Springer.

6. Jäggi, A. (2007). Pseudo-Stochastic Orbit Modeling of Low Earth Satellites Using the Global Positioning System. PhD thesis, Institut fürr Geodäsie und Photogrammetrie, Geodätisch-geophysikalische Arbeiten in der Schweiz. vol.73, ISBN:978-3-908440-17-8.

7. Jäggi A et al. (2015): Swarm kinematic orbits and gravity fields from 18 months of GPS data. Adv Space Res 57 (2016) 218-233, doi: 10.1016/j.asr.2015.10.035.

8. ESA ePORTAL (2019). SWARM Uydu Misyonu. Erişim: 27.10.2019, https://directory.eoportal.org/web/eoportal/satellite-missions/s/swarm

Ecological monitoring with multispectral images

Yoana Tsarovska

University of Architecture, Civil Engineering and Geodesy, ul. Hristo Smirnenski 1, Sofia, Bulgaria, Phone: +359 889 30 20 35, E-mail: yoanatsarovska@abv.bg

ABSTRACT

One of the biggest advantages of remote sensing is the ability which they provide for receiving information based on images, made in different spectral diapasons of the spectrum. Along with traditional frequencies of visible light to which correspond monochromatic and color images, continuously is growing and improving the usage of channels in ultraviolet, infrared and thermal zones from the spectrum. In this paper is made research about distribution of vegetation indices onto multispectral images. For this purpose is used color infrared image, from which based on mathematical operations with spectral brightness of pixels are calculated different vegetation indices as normalized difference vegetation index and normalised difference water index. In conclusion, can be said that multispectral images can be used to define vegetation indices and researching the condition of vegetation itself.

KEYWORDS: electromagnetic spectrum, multispectral images, ecological monitoring

1. INTRODUCTION

Different sensors can be used to gather and analyze various data in order to obtain full and more accurate information about the researched objects. Remote sensing techniques are based on using sensors, recording electromagnetic energy from different spectrum's diapasons, which are located onto aerial or cosmic vehicles, which purposes are solving many practical and scientific tasks (for example exploring and earth surface monitoring, as well as buildings and objects located onto the earth [5]). Electromagnetic spectrum diapasons, shown on figure 1, are the following:

- 0.1-0.4 mkm ultraviolet;
- 0.4-0.7 mkm visible;
- 0.7-3.0 mkm near infrared zone;
- 7.0-30.0 mkm distant infrared zone [8].

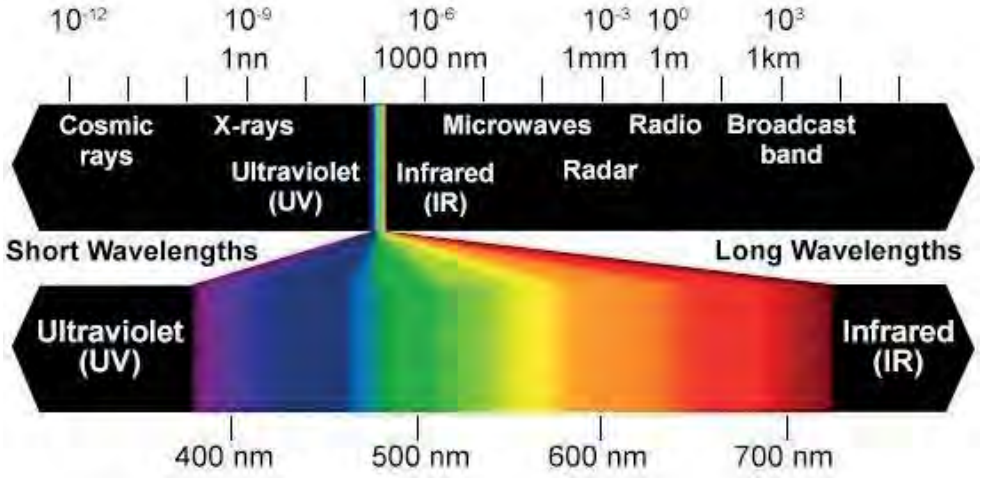

Figure 1. *Electromagnetic spectrum* [12]

2. COLOR INFRARED IMAGES (CIR)

A color infrared images (CIR) represents an image which is received from registration of reflected electromagnetic waves from the following types:

- infrared rays, which are visible for the human eyes as red (R);
- red rays, visible as green (G);
- green rays, visible as blue (B) [11].

These image types are especially valuable and applied as well as image classification and defining vegetation indices, because they have the unique ability to expose how an object reacts to infrared light (its absorbing and reflection). This is the reason why these images are very useful not only for identifying different vegetation types, but also for diagnostic of small changes in its condition. The American institute of agriculture gives the following definition of color infrared imagery: "multispectral data that contain a part of visible spectrum, as well as near infrared and it is useful when studying vegetation" [11].

The nature of aerial images (panchromatic, color or color infrared) is based on the fact that every type earth surface's covering absorbs exact portion of electromagnetic spectrum, transmits and reflects another one, which can be recorded thanks to passive systems.

Digital color infrared images filtrate the blue light that makes blue objects look like black. Therefore, onto that type of images water bodies, as well as roads are visible in black color. Onto digital color infrared images the vegetation that produces a big amount of chlorophyll, is presented in red color, whereas soil cover - in white color.

Without doubt color infrared images have a big impact in image analyzing and their classification. They are usually used to study vegetation cover with math functions for vegetation indices and find application in:

- defining vegetation types;
- evaluation of vegetation surface;
- mapping of vegetation surface;
- high-precision classifications;
- finding of ill and contaminated vegetation crops. [10]
- effective forest monitoring;
- realization of international and other meetings for forest protection;
- evaluation of wood supply and many others. [2]

3. VEGETATION INDICES

Vegetation indices show the vegetation condition and are obtained as a result of mathematical operations with pixels from images of different spectral diapasons. For example green

vegetation reflects very bright in near infrared diapason and reflects lower in visible red diapason. The indices can be two types - relative and perpendicular [6].

- Relative vegetation indices

With relative vegetation indices are formed izovegetation lines, which are drawing together at one point and their values form its inclination in RED-NIR graphic of distribution. Relative vegetation indices are the following: NDVI, SAVI, RVI.

- Perpendicular vegetation indices

Vegetation indices from this group (PVI, WDVI, DVI and etc.) are named "perpendicular" because their values express perpendicular distance from soil line to corresponding pixel in RED-NIR graphic of distribution. Izovegetation lines, produced from perpendicual vegetation indices are placed parallel to soil line.

The main purpose of vegetation indices is related with vegetation cover mapping, areas determination, that are covered with different crop types and evaluation and monitoring of the real state of vegetation cover. Vegetation indices determination usually is made based on series of multispectral images, made with time resolution [2].

In 3.1-3.4. are reviewed the most famous four vegetation indices, used in the following research.

3.1. Normalised difference vegetation index (NDVI)

NDVI is calculated by the following mathematical expression:

$$\mathbf{NDVI} = \frac{(\boldsymbol{\rho}\mathbf{NIR}-\boldsymbol{\rho}\mathbf{RED})}{(\boldsymbol{\rho}\mathbf{NIR}+\boldsymbol{\rho}\mathbf{RED})}, \qquad (1)$$

where ρNIR и ρRED are spectral brightness respectively in red and near infrared diapason. NDVI calculation is based on using two of most stable areas from the spectral curve of vegetations - in red area (0,6 - 0,7 mkm wavelength) is lying the maximum of chlorophyll absorption from sun radiation, and in near-infrared area (0,7 - 1,0 mkm wavelength) is located the area of maximum reflection of the cellular leaves structure. NDVI takes maximal values for the areas with thick vegetation and smaller values for different states of vegetation cover. Its values grow up with developing of green biomass and lower down with its drying (table 1) [2].

NDVI	Values interpretation
0 – 0-1	Bare soil
0.1 – 0.2	Almost absent canopy cover
0.2 – 0.3	Very low canopy cover
0.3 – 0.4	Low canopy cover, low vigour or very low canopy cover, high vigour
0.4 – 0.5	Mid-low canopy cover, low vigour or low canopy cover, high vigour
0.5 – 0.6	Average canopy cover, low vigour or mid-low canopy cover, high vigour
0.6 – 0.7	Mid-high canopy cover, low vigour or average canopy cover, high vigour
0.7 – 0.8	High canopy cover, high vigour
0.8 – 0.9	Very high canopy cover, very high vigour
0.9 – 1	Total canopy cover, very high vigour

Table 1: *NDVI interpretation[13]*

3.2. Normalised difference water index (NDWI)

It is suitable for water bodies and can be calculated from the following formula:

$$\mathbf{NDWI} = \frac{(\boldsymbol{\rho GREEN - \rho NIR})}{(\boldsymbol{\rho GREEN + \rho NIR})} \qquad (2)$$

They have high absorption power and low radiation in the limit from visible to infrared rays. This index use green and near infrared channel from the images. Values of water bodies are higher than 0,5. Vegetation has lower values, otherwise buildings have values from 0 to 0,2 [14].

3.3. Difference vegetation index (DVI)

It is slope oriented and is produced with extraction from red to near infrared channel. It is easier than NDVI and covers till infinity. Moreover, it is extremely suitable for distinguishing soil from vegetation. DVI is introduced at 1977 from scientists Richardson and Wiegand.

Values around zero identify bare soil, values higher than zero - water and values above zero - identify vegetation. DVI eliminates albedo effect (the relation between reflected and absorbed light) [9].

$$\mathbf{DVI = \rho NIR - \rho RED} \quad (3)$$

3.4. Ratio vegetation index (RVI)

It is common vegetation index, used more than 45 years in image analyses. The index is introduced from Roose at 1974 with aim to evaluate vegetation. It is defined as relation between near infrared and red channel. The areas with lots of vegetation have higher values, whereas areas with little vegetation - lower values [15].

$$\mathbf{RVI} = \frac{\boldsymbol{\rho NIR}}{\boldsymbol{\rho RED}} \quad (4)$$

4. DEFINITION OF VEGETATION INDICES

For the purpose of this paper is used Trimble software - eCognition Developer, which is specially made to work with multispectral images and allow producing different operations and calculations. It was made calculation of vegetation indices onto color infrared images that cover the area of La Puebla de Farnals, located in Valencia, Spain. The results are newly made indexed images, that show different values of vegetation indeces.

4.1. Normalized difference vegetation index (NDVI)

On figure 2 is shown distribution of this vegetation index in intervals (0,5-0,8), which show availability of good strength of vegetation cover. In light silver are presented values of the index lower than 0,5, but in dark silver - the lowest values, because there are water bodies, roads, parks and urbanized territory.

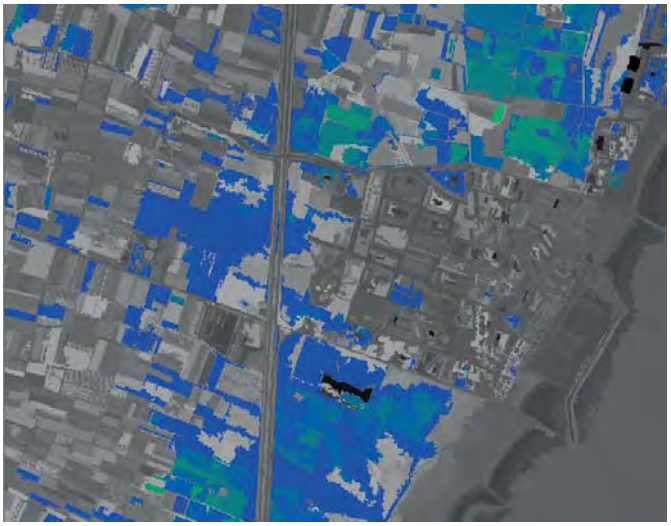

Figure 2. *Distribution of NDVI index in the area La Puebla de Farnals*

On figure 3 is shown distribution of some chosen objects from the imagery. From this graphic can be concluded that the analyzed vegetation is strength and the crop types can be classified as average canopy cover.

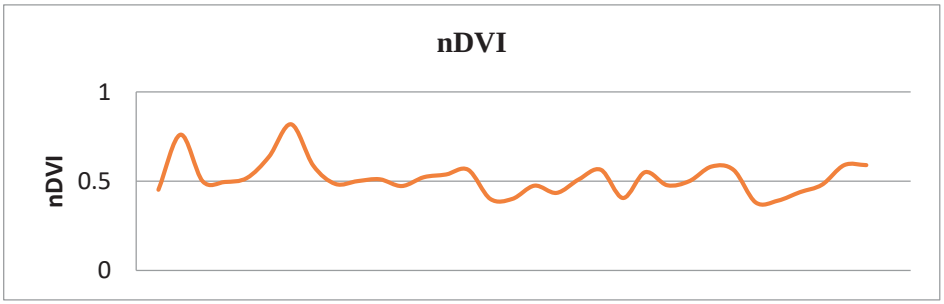

Figure 3. *Graphic of the vegetation state in the analyzed class*

4.2. Normalized difference water index (NDWI)

This index is used to define only water bodies. On figure 4 is shown the distribution of water bodies in defined values of the index (0,5-0,8).

Figure 4. *Distribution of NDWI vegetation index*

4.3. Ratio vegetation index (RVI)

On figure 5 is shown the distribtution of ratio index, that takes different values, which vary from low to high, respectively from white to saturated blue color, where vegetation is the most stable.

Figure 5. *Distribution of RVI vegetation index*

4.4. Difference vegetation index (DVI)

On figure 6 is shown the influence of the index in exact values, again varying depending on health of the crop types.

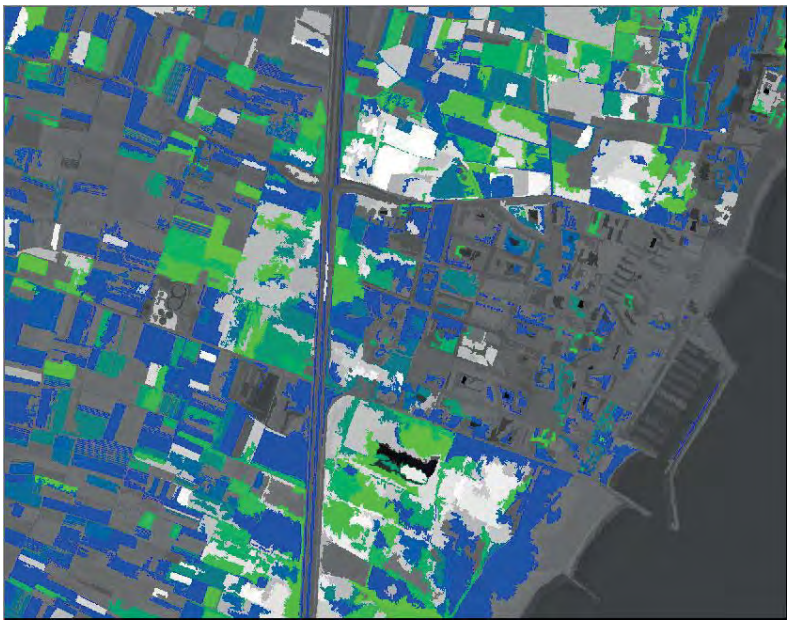

Figure 6. *Distribtuion of DVI vegetation index*

5. CONCLUSION

From the conducted survey of the distribution of vegetation indexes onto multispectral imageries, can be concluded that this is one fast method that allow studying of the vegetation crops. For the aim of this survey is used color infrared image, onto which are calculated vegetation indices, among which normalized difference vegetation index, normalized difference water index and ratio vegetation index. The results are new indexed images in the defined scale, ranging from white to blue color, which show respectively minimum to maximum values of vegetation index influence.

Generally, the researched territory has from very low to very high canopy cover, situated in forests. Thanks to vegetation indices can be made future researches of the vegetation state and moreover to observe for changes.

REFERENCES

1. Zdravcheva, Neli, Remote sensing lectures. Characteristics of GIS data.2018

2. Zdravcheva, Neli. Spectral transformations of multispectral satellites images. Annual of University of Architecture, Civil Engineering and Geodesy. 2017, Vol. 50, 1

3. Zdravcheva, Neli. Contemporary tools for ecological monitoring - University of Architecture, Civil Engineering and Geodesy, 2nd scientific applied conference with international participation "Management of civil engineering projects" 5-6 November, 2015

4. Zdravcheva, Neli. The role of photogrammetric and remote sensing for ecological and stable develeopment of contemporary society - 25 international sympozium "Contemporary technologies and professional practice in geodesy and other scientific fields"5-6 November 2015

5. Zdravcheva, Neli "Photogrammetric and GIS contribution for studying of global warming", "Geomedia", volume 1, january-february 2017

6. Zdravcheva, Neli. Application of vegetation indices, 25 International sympozium "Contemporary technologies, education and professional practice in geodesy and other scientific fields", 2017

7. Maldjanski, Plamen. Photogrammetric technologies, 2017, p.115

8. Maldjanski, Plamen. Photogrammetric technologies, 2017, p.284-288

9. Remotely sensed vegetation indices: Theory and applications for crop management. Basso, Bruno. 1, s.l. : Revista Idaliana de Agrometeorologia, 2004

10. Statewide Mapping Advisory Committee, Working Group for Orthophotography Planning. Guide for Understanding, Interpreting and Benefiting from CIR Imagery. July, 2011

11. United States Department of Agriculture, Four Band Digital Imagery INFORMATION SHEET, June, 2013

12. Web page: https://sites.google.com/site/mochebiologysite/online-textbook/light, 10.02.2019

13. Web page: https://www.agricolus.com/en/indici-vegetazione-ndvi-ndmi-istruzioni-luso/, 17.04.2019

14. Web page: https://www.sentinel-hub.com/eoproducts/ndwi-normalized-difference-water-index, 17.04.2019

15. Web page: https://prabugis.wordpress.com/2013/11/29/ratio-vegetation-index-rvi/, 20.04.2019

16. 3-band CIR, Digital orthoimages from Spanish photogrammetric society PNOA, 2018

Evaluation of Covariance Determination Procedure Using GOCE gradient data and Least Squares Collocation

Hadi Heydarizadeh[1], Sabah Ramouz[1], Aldolreza Safari[1], Riccardo Barzaghi[2]

[1]School of Surveying and Geospatial Engineering, College of Engineering, University of Tehran, Tehran, Iran, (hadi.heydarizadeh@ut.ac.ir, sabahramouz@gmail.com, asafari@ut.ac.ir)
[1]Politecnico di Milano, Department of Civil and Environmental Engineering, Milan, Italy, (riccardo.barzaghi@polimi.it)

ABSTRACT

Least Squares Collocation has been used in various fields of geodesy and geodynamics since 1963 when Kaula proposed a stochastic aspect of LSC in earth's gravity field determination for the first time with one of the first appearances in literature given by Krarup (1969). The most controversial part of the Least Squares Collocation is the covariance function which computes the correlation between different parameters involved within the procedure. The common way of determining the covariance function involves two steps: calculation of an empirical covariance function and then fitting an analytical covariance model to it under some assumptions, the expectation of the anomalous potential is equal to zero and the independency of the covariance function to spatial position and direction which are quiet violated in reality, especially in Iran with rough topography. In this study, the long-wavelength and topography/bathymetry effect have been removed from the radial in-orbit GOCE gradient data and then the empirical covariance has been created by these reduced data based on Remove-Compute-Restore technique. GOCE observations do not have a well-distribution data on the ground and this is an additional barrier to estimate and fit analytical covariance to empirical covariance function. So, to enhance the covariance determination, the effect of smoothing and averaging of the residual GOCE gradient has been analyzed. To make the assessment of the covariance determination possible, the residual vertical gravity gradient was divided into two datasets namely, observations and control points. The observations points served as an input data within the Least Squares Collocation procedure using Tscherning – Rapp covariance model and the control points used to evaluate the accuracy of the Least Squares Collocation gravity gradient predicting and then the covariance estimation. The results of this study show that the Tscherning-Rapp (1974) covariance determination by fitting of an analytical covariance to the empirical covariance derived from GOCE gradient data which resulted from the COVFIT module of the GRAVSOFT is accurate enough in gravity modeling.

KEYWORDS: Covariance determination; GOCE gradient; Least Squares Collocation; Remove-Compute-Restore

1. INTRODUCTION

Analysis and determination of the earth's gravity field and its corresponding issues have been controversial areas of the study which different scientists implemented various methods along with different data. Least squares methods for the prediction and interpolation of earth's gravity fields were introduced in geodesy by [1]. After that, Krarup in 1969 (2) modified and expanded it to Least Squares Collocation (LSC). LSC provides various advantages like combining heterogeneous observations, prediction of the values that are either different or the same with the observations, and also noise filtering which encourage the geodesians to use this method within their studies regarding earth's gravity field. To do this, LCS usually implemented among a Remove-Compute-Restore (RCR) procedure which the gravitational parts of the gravity signal related to global and topographical effects are first removed from the observations to reduce the irregularities and therefore guarantee the prerequisite of using LSC. The main step in using the LSC is the determination of the covariance function and its localization which describes the correlation between used parameters and is sensitive to the data distribution through the case study. Tscherning and Rapp in 1974 (3) introduced an analytical covariance model (A_COV) for the anomalous potential T as,

$$K(r_P, r_Q, \psi) = \alpha \sum_{n=2}^{N} \left(\frac{R_E^2}{r_P r_Q}\right)^{n+1} \sigma_n^2 \, P_n(\cos\psi) + \sum_{n=N+1}^{\infty} \left(\frac{R_B^2}{r_P r_Q}\right)^{n+1} k_n \, P_n(\cos\psi) \qquad (1)$$

where r_P and r_Q are the radii of the Earth in points P and Q, R_E is the mean radius of the Earth equal to 6371 km, R_B is the radius of the Bjerhammer sphere, N is the maximum degree of the global gravity model (GGM) used for removing long wave-length of the Earth gravity signal and σ_n^2 the error degree variance of this global model, k_n is the Tscherning-Rapp degree variance, P_n is the Legendre polynomial of degree n, ψ is the spherical distance between two points and α scale factor computed from the residual gravity observations which its value shows the agreement between the GGM with the gravity observations.

These days, satellite missions like GRACE, and GOCE provide valuable information regarding earth's gravity field. In particular, the GOCE is the first mission chosen to be launched by ESA (4) with the aim to recover the static gravity field of the Earth with outstanding high spatial resolution and accuracy. The GOCE was the first mission to implement the principle of gravity gradiometry in space with the help of Electrostatic Gravity Gradiometer (EGG) complemented with an onboard GPS to form the concept of Satellite Gravity Gradiometry (SGG). The aim of

SGG was providing the second order derivatives of the gravitational potential V (gravity gradient) in an arbitrary Cartesian coordinate system as follow,

$$M = \begin{bmatrix} V_{xx} & V_{xy} & V_{xz} \\ V_{yx} & V_{yy} & V_{yz} \\ V_{zx} & V_{zy} & V_{zz} \end{bmatrix} \quad (2)$$

which is known as Marussi tensor. Due to specific design of the used instrument within the GOCE mission, it is not plausible to retrieve every component of the Marussi tensor. According to Eq.2 V_{zz} can be obtained with highest precision. Furthermore, these gravity gradients are accurate in a certain frequency range, the so-called Measurement Bandwidth (MBW), which is defined from 5 to 100 mHz (5). This frequency rang can be approximately represented into spherical harmonic D/O 27 to 540 via the relation

$$\eta = \frac{D/O}{T_r} \quad (3)$$

according to (6) where η is the frequency and $T_r = 5383\text{s}$ is the approximated orbit revolution time of the GOCE satellite. On the other hand, GOCE mission has a dense distribution of data which using it in LSC procedure requires a high-performance system to implement the inversion of the covariance matrix between observations (C_{tt}) which is the key section of the Wiener-Kolmogorov formula as,

$$\hat{s} = C_{st}(C_{tt} + C_{nn})^{-1} l \quad (4)$$

where s is the unknown parameters, l is the observations, C_{st} is the covariance between unknown parameters and observations, and C_{nn} represents the covariance of the noise. Therefore, to overcome this defect, it is necessary to design a process strategy on GOCE gradient data to have a less dense input data while reaching to the proper results.

Ramouz et al. in (7) used the LSC method and terrestrial gravity data for gravity field modeling in Iran. Because of the poor spatial distribution of the gravimetric observations and rough topography over some regions of Iran, they have been challenged in forming the A_COV for this dataset. Ramouz et al. in (8) tried to enhance the procedure of LSC modeling through the covariance improvement attempts. They selected four areas with extreme situations based on data distribution and topography over Iran and evaluated the process of determining A_COV there. They found that the data distribution remarkably would affects the result of A_COV and

also the geometrical fitness of an A_COV to the empirical covariance model (E_COV) derived from the gravity observations in the region, could not be served as an appropriate or at least an adequate criterion in such a case study. Additionally, by analyzing the estimated parameters of A_COV, they achieved alternative LSC gravity models in the areas with averagely 10% improvement with regards to STD of the differences between models and the control points in the areas.

So, in this study, we investigate the same procedure for GOCE gradient data and assessed the quality of A_COV determination and attempt to improve LSC gravity modeling by A_COV parameters analyzing over Iran. The methodology of LSC modeling and GOCE gradient observations processing will be described in next section. After that, the used data and model will be introduced in section 3. In section 4, the results of the A_COV determination evaluation and LSC modeling improvement will be presented. Finally, the conclusion of the work will be discussed in section 5.

2. MATERIAL AND METHOD

As been discussed above, to implement LSC, usually RCR technique is used (9). To perform such a procedure, it is needed to have an information regarding the used data and models and also the overall schematic of the problem which will be described within the following sections.

2.1 Material

The second-order derivatives of the Earth's gravitational potential V_{zz} can be defined either in a gradiometer reference frame (GRF) whose X-axis is pointing approximately in the satellite's flight direction, the Z-axis radially downwards and the Y-axis complementing an orthogonal system or local north-oriented frame (LNOF) whose x-axis is pointing North, y-axis towards West and z-axis upwards in a geocentric radial direction. In this study, only the vertical gradient of the anomalous potential V_{zz} in LNOF provided by ESA through the EGG_TRF_2 series (10), after the implementation of the GRS80 normal potential i.e. $T_{zz} = V_{zz} - U_{zz}$, has been used as an observation. Five months of such a T_{zz} gradient data, from January to May 2012 were selected as a base observations. Figure 1 (a) depicts the used data in the area which is limited to 17 to 48 degree in North-South and 36 to 71 degree in East-West direction.

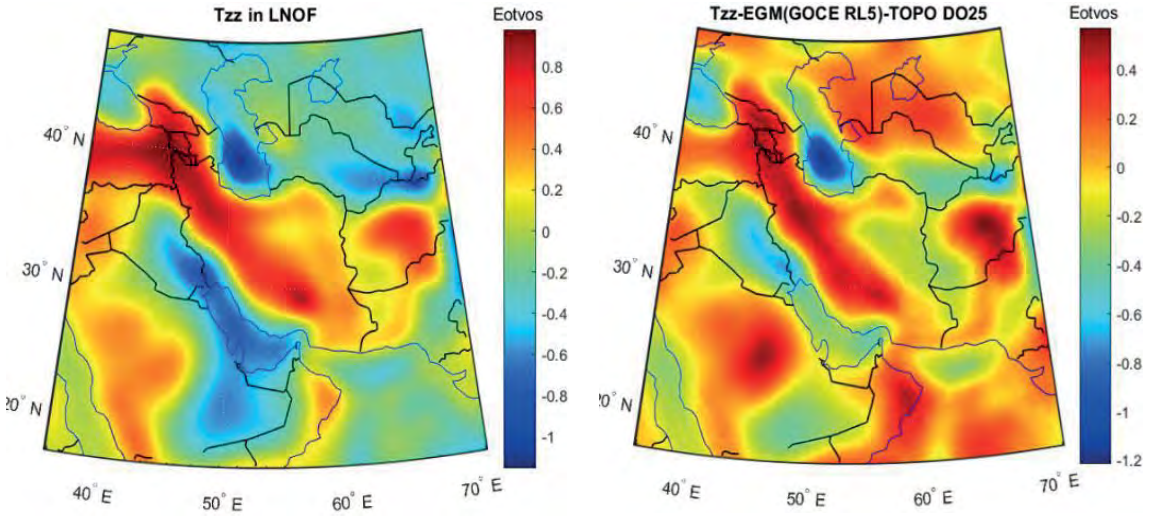

(a) (b)

Figure 1. *5 Months of T_{zz} gravity gradient data from January to May 2012 over Iran(left)and T_{zz} after full subtraction*

To reduce the irregularities of the observed data and smooth it, the long-wavelength and topography effects up to degree and order 25 have been removed from the gravity gradient signal (11). As for long-wavelength, the TIMe-wise geopotential model, namely GOCE_TIM_RL05 which can be considered as a 'GOCE-only' solution (12) is used and for topography, the GEBCO (13) model have been used in a 1*1-minute resolution. In Figure 1 (b) the gradient data after the full subtraction is shown. Also, Table 1 shows the statistical aspect of removing the global field and topographic effects. As can be seen in this table, the STD values of data after full subtraction reduced 33.6% with respect to the observations.

Table1: Statistics of removing global and topographic effects on the STD of the gravity gradient signal in the work area

Region	min	max	mean	STD
Observations	-1.1598	0.9866	0.0037	0.3729
Global	-1.2454	0.7515	-0.0076	0.2668
Global + Topographic	-1.2195	0.772	-0.0311	0.2475

2.1 Method

To implement the covariance analysis, the gradient data have been divided into two datasets namely observations and control points. The control points extracted in a grid of 15 minutes from gradient data. Figure 2 depicts the 3309 control points within the work area of 25 to 40 degree in latitude and 43 to 64 degree in longitude.

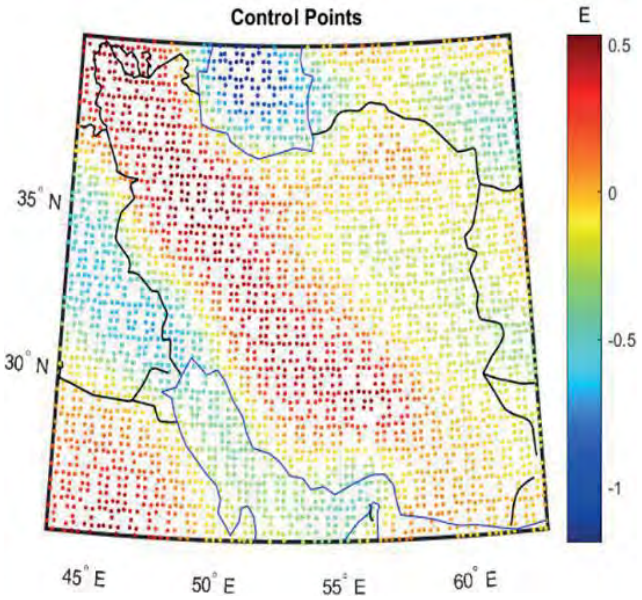

Figure 2. *Extracted control points within the work area with the resolution of 15 minutes*

The reminded gravity has been considered as observations in 4 cases namely grids of 10, 15, 20, and 30 minutes with 10179, 4524, 2494 and 1131 mean T_{zz} data. For instance, in case of the grid with 10*10 arc-minute grid-size, all the measurements which fall in the grid cell have been averaged and the value of this averaging is placed in the center of the cell. For each case, covariance estimation was executed according to the Tscherning-Rapp covariance model. Through this procedure, first, E_COV was calculated using residual gravity gradients according to Knudsen (14) for each the observation pairs l_i, l_j through the following formula,

$$E\_COV(k) = \frac{1}{N_k} \sum_{i,j}^{N_k} l_i l_j \tag{5}$$

where N_k denotes the number of observation pairs in the respective sample interval k. Then the following A_COV was fitted to it within a least square adjustment to find the best parameters of the used degree variance. This A_COV can be calculated by performing the covariance propagation on the base covariance function of Eq.1.

$$cov\left(T_{zz_P}, T_{zz_Q}\right) = \left(\frac{\partial^2}{\partial r_P^2}\right)\left(\frac{\partial^2 K}{\partial r_Q^2}\right) = \frac{\partial^4 K}{\partial r_P^2 \partial r_Q^2}$$
$$= \alpha \sum_{n=2}^{N} \frac{(n+1)^2(n+2)^2}{r_P^2 r_Q^2}\left(\frac{R_E^2}{r_P r_Q}\right)^{n+1} \sigma_n^2 \, P_n(\cos\psi) \qquad (6)$$
$$+ \sum_{n=N+1}^{\infty} \frac{(n+1)^2(n+2)^2}{r_P^2 r_Q^2}\left(\frac{R_B^2}{r_P r_Q}\right)^{n+1} k_n \, P_n(\cos\psi)$$

where k_n represents the Tscherning-Rapp degree variance as,

$$k_n = \frac{A}{(n-1)(n-2)(n+B)} \qquad (7)$$

As unknown variables, α, A (scale factor of the residual signal at higher degrees), and R_B are estimated by fitting the A_COV to E_COV computed from the residual observations. Moreover, B is a constant parameter which is considered equal to 4 in local usage.

According to the (8), the sample interval of Eq.5 for each case has been selected due to the overall distribution of the data in the region. By doing this, it is plausible to determine the two parameters of the E_COV, covariance at distance zero or variance (C0) and the correlation distance ($\boldsymbol{\xi}$). Moreover, to check the suitability of the selected sample interval, the covariance fitting and also observations prediction for different sample interval size in each case have been done and the estimated parameters have been compared with each other. After that, the best possible parameters for covariance model selected by trial and error according to the following flowchart which is depicted in Figure 3.

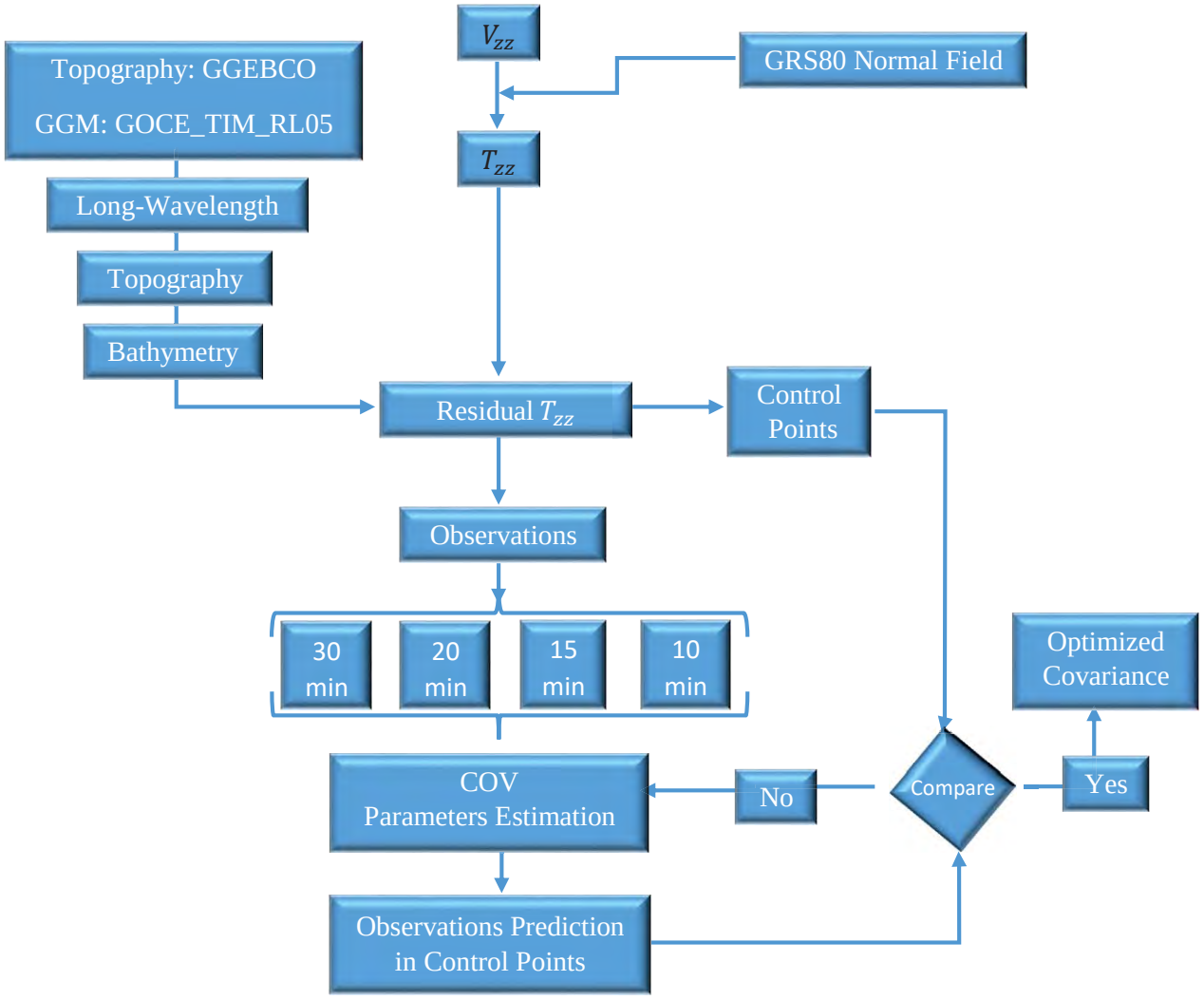

Figure 3. *Flowchart of the problem*

3. RESULTS AND DISCUSSION

After constructing residual data and dividing it into two subsets namely, observations and control points, it is plausible to perform the covariance estimation using Eq.5 and Eq.6. In the following figures, estimated E_COV (blue dots) along with fitted A_COV (red lines) for different interval size can be seen. As for the case of 10-minute resolution, we have considered the three-interval size as 6.5, 10, and 13.5 minutes. As for the case of 15-minute resolution, the interval size of 10, 15, and 20 minutes have been selected. In addition, for the case of 20- and 30-minute resolution, the interval size of 13, 20, 27 and 20, 30, 40 have been considered, respectively.

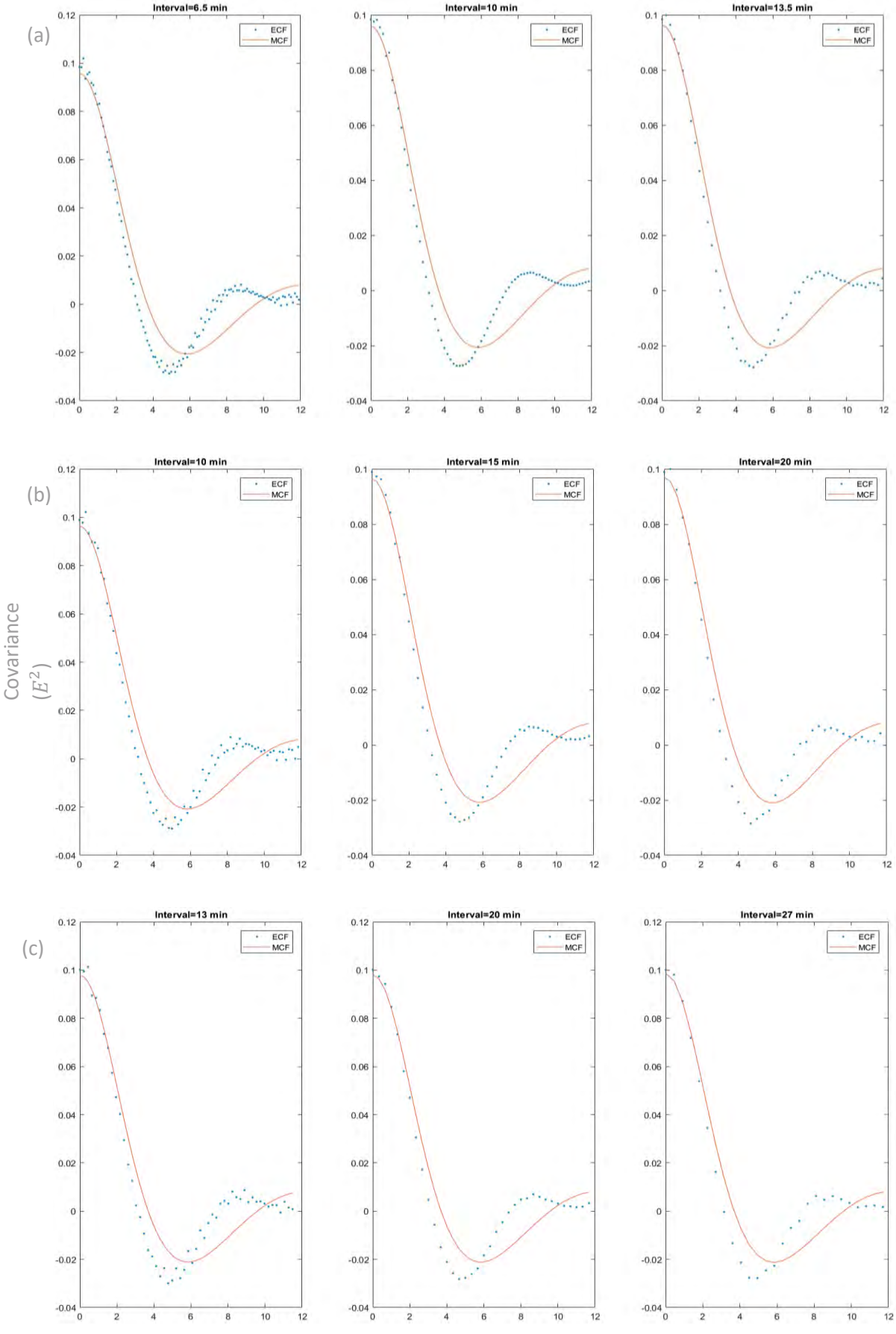
(a)
Interval=6.5 min
Interval=10 min
Interval=13.5 min
(b)
Interval=10 min
Interval=15 min
Interval=20 min
(c)
Interval=13 min
Interval=20 min
Interval=27 min
ECF
MCF
Covariance (E^2)
Spherical Distance (ψ)

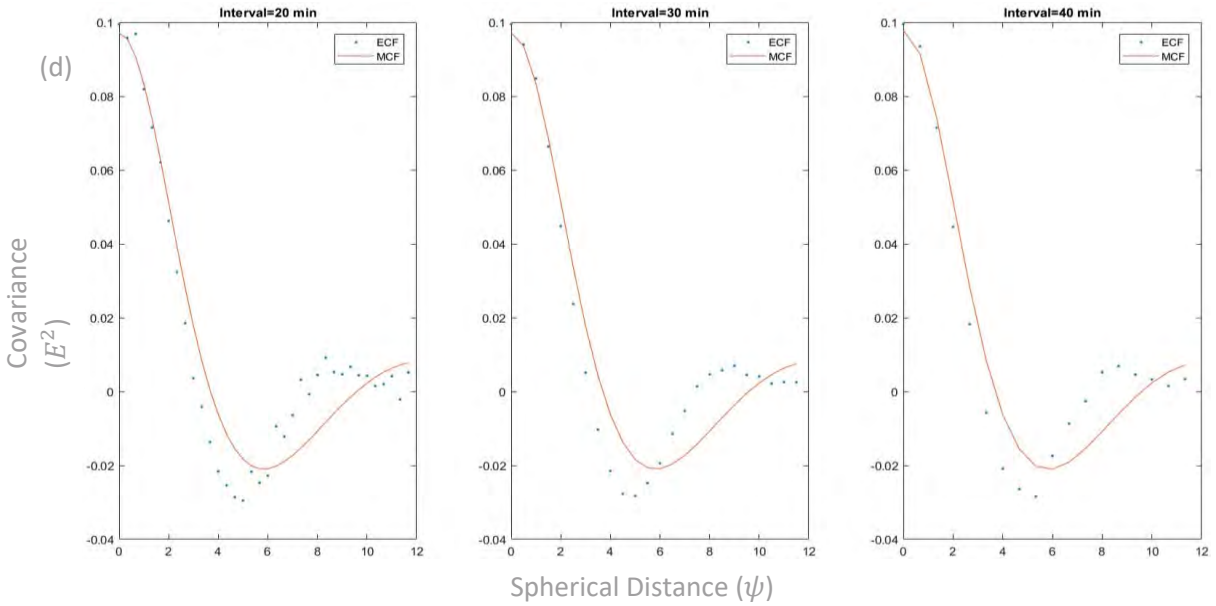

Figure 4. *Covariance Estimation: E_COVs (blue dots) and fitted A_COVs (red lines) in each sample interval. (a) is for, (b) is for 15, (c) is for 20, and (d) is for 30 minutes interval.*

Moreover, the statistics of the estimated parameters as well as the accuracy of observations prediction in terms of STD and mean of the difference between computed models and control points have been analyzed and reported within the Table 2 and the charts of the Figure 5. Because in this study, the used observations in the covariance estimation procedure to produce E_COV (i.e. residual GOCE gradients) are in almost complete agreement with the used GGM, predication and analysis of the parameter α in Eq.6 has been neglected. As can be seen in Table 2, for the case study with the resolution of 10 minutes, the results are more accurate in terms of STD, although in terms of mean, the case with 30 minutes resolution gave the better results. Also, from Figure 5, one can concludes that finer grid of mean residual GOCE data could result in more accurate modeling by respect with STD, however, in these cases the estimation involved with bias. As it is obvious from Fig. 5c and 5d, expect the mean of 30-minute grid resolution, changing the sample interval size has not a significant influence on the STD and mean of LSC modeling.

Table 2: Estimated values for each degree variance parameters within each sample interval

	Grid size	10			15		
	Sample interval	6.5	10	13.5	10	15	20
Before	$A\ (km/s)^4$	6833.1	6706.7	6639.6	6586.6	6457.9	6920.9
	$R_B - R_E\ (km)$	-4.47	-5.46	-6.25	-6.74	-8.11	-4.57
	Mean (Eotvos)	0.000344	0.000350	0.000354	0.000531	0.000562	0.000539
	STD (Eotvos)	0.014910	0.014914	0.014918	0.015049	0.015055	0.015040

Grid size	20			30		
Sample interval	13	20	27	20	30	40
$A\ (km/s)^4$	6598.1	6475.2	6409.9	5359.5	6214.9	6160.0
$R_B - R_E\ (km)$	-7.71	-9.31	-10.6	-45.4	-12.37	-14.1
Mean (Eotvos)	0.000007	0.000020	0.000030	-0.000014	-0.000129	-0.000119
STD (Eotvos)	0.016590	0.016606	0.016619	0.015721	0.015680	0.015681

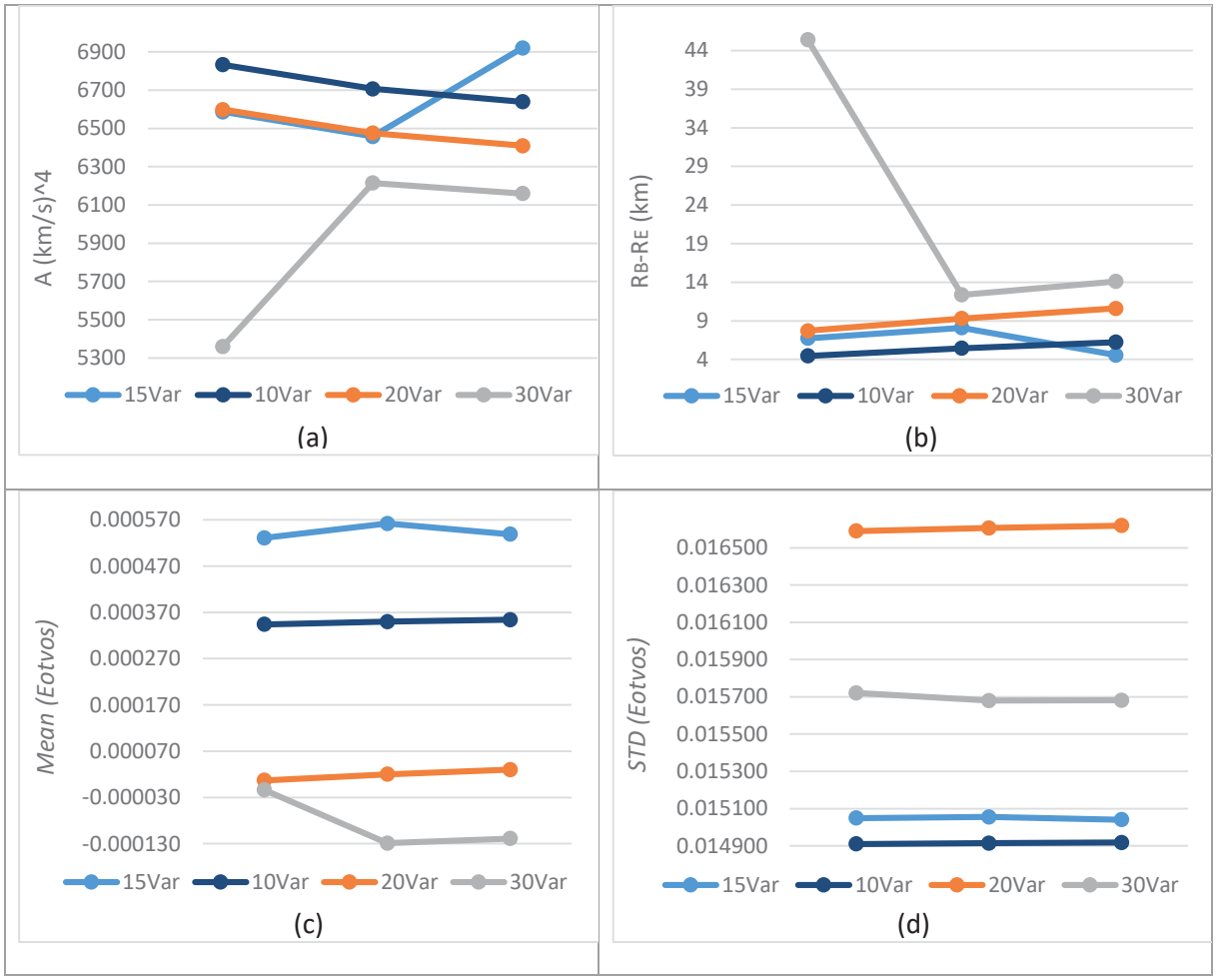

Figure 5. *Estimated covariance parameters and the accuracy of the observations' prediction in terms of STD and Mean. (a):* Scale factor of the residual signal at higher degrees, *(b): Bjerhammer Radius, (c): Mean, (d): Standard Deviation*

After the implementation of this stage and finding the best possible data distribution and also its covariance model parameters, the covariance enhancement has been done to check the idea that asserted in (8) regarding improvable covariance parameters within the trial and error technique. To do this, a procedure which is depicted in the flowchart of the Figure 3 have been performed on Tscherning-Rapp 1974 covariance determination algorithm. Within this procedure, after finding the best sample interval in each case study, the parameters $R_B - R_E$

and A of the corresponding covariance of that sample interval would change manually in order to the LSC model reach the best results in terms of STD and mean. In Table 3, the statics of covariance parameters refinement is reported and in the charts of the Figure 6, the process of changing the parameters after modification could be seen.

Table 3: *Estimated optimized values for each degree variance parameters within each selected sample interval after modification*

	Grid size	10	15	20	30
After Improvement	Sample interval	6.5	20	13	30
	$A\ (km/s)^4$	6590	6450	6465	5516
	$R_B - R_E\ (km)$	-1.9	-2.8	-4.1	-13
	Mean (Eotvos)	0.000306	0.000494	-0.000053	-0.000149
	STD (Eotvos)	0.014904	0.015038	0.016567	0.015669

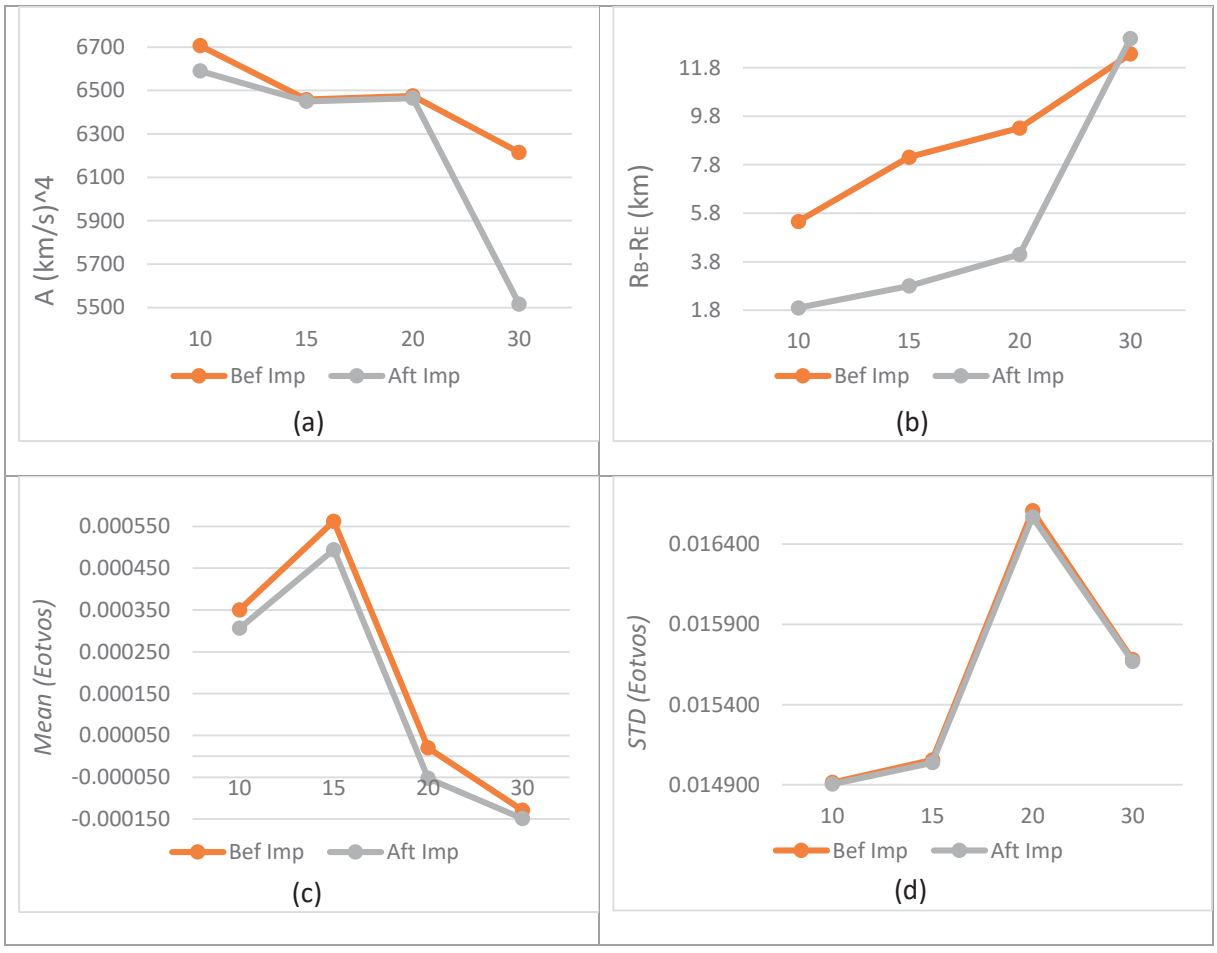

Figure 6. *Estimated covariance parameters and the accuracy of the observations prediction in terms of STD and Mean before (orange) and after (gray) modification. (a):* scale factor of the residual signal at higher degrees, *(b): Bjerhammer Radius, (c): Mean, (d): Standard Deviation*

As can be seen in Table 3 and Figure 6, manually changing the covariance parameters within the trial and error procedure could affects and refine the result, though the amount of refinement is not significant in comparison with that was detected for terrestrial gravity anomalies over Iran (8). According to Fig. 6, there is 0.04%, 0.01%, 0.13%, and 0.07% improvement in terms of STD for the 10-minute, 15-minute, 20-minute, and 30-minute case studies, respectively. This equals to averagely 0.07% improvement due to covariance refinement with regards to standard Tscherning-Rapp covariance estimation (1). Moreover, analyzing the covariance parameters during covariance refinement shows averagely 5.8% change in the estimation of parameter *A* which most of it related to 30-minute grid and not considerable in other grids, however, $R_B - R_E$ changes averagely 25.1%. In case of removing 30-minute grid from the comparison, changes related to parameters *A* and $R_B - R_E$ will be 4.2% and 47.5%, respectively. This remarkable change in parameter $R_B - R_E$ could be stemmed from this fact that the Earth is not a complete sphere as it is assumed in defining the mean radius for it, though this modification could not affect the LSC modeling significantly. Generally, this investigation shows that the standard Tscherning-Rapp covariance determination procedure which is executable using GRAVSOFT package, is accurate enough in gravity modeling using LSC method. Consequently, this study illustrates that merely geometrically fitting of E_COV to A_COV for gravity gradient recovery at the mean satellite altitude of 260 km could give the proper results and therefore the covariance refinement is not necessary in this case, though there is a slight improvement.

4. CONCLUSION

Based on the study which had been done by Ramouz et al., in (8), the distribution of the input terrestrial gravity data and also covariance fitting would affect the results significantly. This issue encouraged us to investigate such a problem for the GOCE gravity gradient recovery at the mean satellite altitude. To reach this aim, we have considered the 4 cases and 3 interval size within each case to analyze the data distribution on the results. In addition, as for covariance fitting, the best Tscherning-Rapp covariance parameters for each case are studied using the trial and error method. At the first stage, data reduction has been performed and got the refinement of 33.6% in the input data. After that the E_COV and A_COV have been created and analyzed in different cases to find the best data distribution and also optimized covariance parameters.

Covariance of T_{zz} is not sensitive to α. Because, α is a parameter which shows the agreement between the global model and terrestrial local observations. In this case, T_{zz} is satellite gravity measurements. In comparison with covariance assessment of terrestrial gravity anomalies (7),

Tscherning-Rapp 1974 covariance model has better performance with T_{zz}. The statistical information of the LSC modeling for T_{zz} using Tscherning-Rapp covariance shows acceptable results. And the implementation of refinement of covariance parameters - like the procedure which was done according to the flowchart in Fig 3 – could not enhance the result of T_{zz} modeling remarkably at the satellite altitude. Even this change lead to deterioration in the mean value of the difference between the estimated model and control points. Although according to Table 3, the result could be modified by changing the used covariance parameters within the trial and error procedure for T_{zz} at the satellite altitude, it's not a considerable amount of modification. On the other hand, the effect of data distribution has been studied in this study. According to Table 2 and 3, it can be seen that for the case with 10-minute grid and the sample interval of 6.5 minutes, the result of the prediction has more agreement with control points in terms of STD of the differences. So, data distribution could affect the result.

As for Future work, it is going to implement such a procedure for GOCE gradient data in geophysical proposes and found that at the earth's surface or lower altitude, Tscherning-Rapp covariance function will work or not.

REFERENCES

1. Heiskanen, W.A., Moritz, H. (1967). Physical Geodesy, W.H.Freeman, 364pp.

2. Moritz, H. (1980), Advanced Physical Geodesy, Herbert Wichmann Verlag Karlsruhe and Abacus Press Tunbrilge Wells Kent, Karlsruhe, Germany and England.

3. Ramouz, S., Afrasteh, Y., Reguzzoni, M., & Safari, A. (2019). Assessment of Covariance Estimation through Least Squares Collocation over Iran.

4. Rieser, Daniel and Mayer-Guerr, Torsten, (2014) A Least Squares Collocation Approach with GOCE gravity gradients for regional Moho-estimation, EGU General Assembly Conference Abstracts, 16.

5. Sansò, F., and M. G. Sideris (2013), Geoid Determination_ Theory and Methods, Springer-Verlag, Berlin Heidelberg, doi:10.1007/978-3-540-74700-0.

6. Tscherning, C. C., and R. Rapp (1974), Closed Covariance Expressions for Gravity Anomalies, Geoid Undulations, and Deflections of the Vertical Implied by Anomaly Degree Variance Models, Rep. 208,The Ohio State University, Department of Geodetic Science.

Sponsors

,

Engineering Measuring Map Construction
Floating Scaffolding Systems
Industry and Trade Limited Company

http://www.csymuhendislik.com.tr/

http://www.kentistmuhendislik.com/

http://www.atlihanharita.com/

https://www.elyatekno.com/

http://www.geotekniktd.com/

www.gravity.itu.edu.tr

İTÜ

İSTANBUL TEKNİK ÜNİVERSİTESİ

1773